Measurements of Quarkonia and Tetraquark Production in Jets at LHCb

Naomi Cooke

Thesis submitted for the degree of
Doctor of Philosophy

Particle Physics Group,
School of Physics and Astronomy,
University of Birmingham.

January 31, 2023

Abstract

The main subject of this thesis is to understand the production of quarkonia in more detail. Previous measurements from LHCb and CMS have shown discrepancies between data and current Pythia 8 MC predictions when measuring the normalised cross section *vs.* $z(J/\psi) \equiv p_{\mathrm{T}}(J/\psi)/p_{\mathrm{T}}(\mathrm{jet})$ for prompt J/ψ's, where J/ψ's are clustered into jets. Pythia 8 predicts an isolated peak at $z(J/\psi) \simeq 1$ in comparison to data which is less isolated. First, the implementation of incorporating quarkonia fragmentation functions into the Pythia 8 parton shower framework is discussed. The incorporated calculations are based on the effective field theory, non-relativistic QCD (NRQCD). Second, Run 2 data collected by LHCb is used to measure normalised cross sections *vs.* z for different quarkonia, namely the J/ψ, $\psi(2S)$, $\Upsilon(1S)$, $\Upsilon(2S)$ and $\Upsilon(3S)$, for jets with $p_{\mathrm{T}} > 15\,\mathrm{GeV}$. These are selected using the dimuon decay channel, where the Υ's are more isolated than the prompt J/ψ and $\psi(2S)$. Finally, the normalised cross section *vs.* z is measured for the X(3872), to better understand its production using the dimuon-dipion decay channel, alongside the $\psi(2S)$ for jets with $p_{\mathrm{T}} > 5\,\mathrm{GeV}$. Contributions to the LHCb Upgrades are also discussed, in particular work to characterise Low Avalanche Gain Detectors (LGADs) produced by *Micron*, before and after irradiation. These are a proposed timing-detector candidate for LHCb Upgrade 2.

DECLARATION OF AUTHOR'S CONTRIBUTION

The main work in this thesis is split into four different chapters. First, I contributed to all aspects of the work presented in chapter 3, to incorporate NRQCD fragmentation into the Pythia 8 framework, collaborating with Leif Lönnblad, Philip Ilten and Stephen Mrenna whilst I was at both Lund University and University of Birmingham. This would have not been possible without funding from MCnet with a Marie Sklodowska Curie Position within Horizon 2020, Innovative Training Network: European Training Network with grant number MCnetITN3 722104.

Second, the work on the LHCb detector upgrades presented in chapter 5 was split into three parts. The RICH detector work was my own, under the supervision of Antonino Sergi, Silvia Gambetta and Giovanni Cavallero. The trigger upgrade work was my own as part of the LHCb "QEE Run 3 Migration Task Force". The initial jet reconstruction was performed by Murilo Santana Rangel, and I received advice from William Barter and Ross Hunter. The work on testing the *Micron* LGADs was performed using experimental equipment already setup at the University of Birmingham; Jonathan Mulvey designed and commissioned the gain setup for use on *Teledyne* LGAD sensors. The setup was then adapted for testing the *Micron* sensors. I worked on testing the *Micron* LGADs with Niladri Sahoo and Nigel Watson, and used Dan Thompson's code for analysing the data.

Third, the work presented in chapter 6 is of my own, under the supervision of Philip Ilten. The unfolding procedure was performed in collaboration with Eliane Epple.

Finally, the work presented in chapter 7 was in collaboration with Eliane Epple, where I contributed to all aspects the analysis apart from the unfolding procedure. Preliminary investigations of the polarisation of J/ψ in jets in appendix E is of my own, under the supervision of Philip Ilten. This would not have been possible without funding from the University of Birmingham Physics department and STFC.

ACKNOWLEDGEMENTS

There are so many people to thank, that I could write a thesis of thank yous! First, I would like to thank my supervisor Philip Ilten, whose diverse physics knowledge is unparalleled. He saw my potential and pushed me for numerous opportunities such as leadership roles and to work on Pythia 8 at Lund University. He has been a constant source of advice, including to avoid spinny chairs when I go for interviews, and read my thesis at questionable hours. He has definitely made me a better physicist and I am deeply grateful for the knowledge he has taught me, and the chance I have had to work with him. I would also like to thank Nigel Watson, who has been an unwavering source of support and encouragement for me not only as a PhD student, but also as an undergraduate. I have thoroughly loved working with him.

I would also like to thank MCnet for giving me the opportunity to work on Pythia 8, and for Lund University for hosting me. All of the people were extremely welcoming, and the opportunity to work with world renowned researchers is a dream and experience I will never forget and treasure forever. I want to give my deepest thanks to Leif Lönnblad, my supervisor away from home, who was persistent in getting me a visa, and who always found time to discuss physics with me and I learned tremendously from. I really enjoyed working with him. Also to Torbjörn Sjöstrand who took time to teach me the intricacies of Pythia 8 and I loved having physics discussions with him. I would also like to thank all of the people I collaborated

with, in particular Eliane Epple and Stephen Mrenna who I loved working with and learned a lot from.

Also, to all of the staff at Birmingham, in particular the Particle Physics Department who are the friendliest people you could ever meet. During my undergraduate years, they always had an open door policy and I am deeply indebted to them for growing my passion of particle physics. In particular I would like to thank, Cristina Lazzeroni and Angela Romano, who were my masters supervisors and were amazing female role models to follow, and Maria who always sorted out any problems I had. I would also like to thank the LHCb particle physics group, Nathaniel, Georgios, Kristian, Ryan, Jon, Paul, Dan and Marcus who helped my with any coding problems and made work a great place to be. I want to particularly thank Niladri Sahoo, who I loved working on the LGADs with. Finally, Tom, Rob, António and Kal, who tormented me daily, but I loved going to work with and are friends for life.

Whilst I was on LTA at CERN, I met many amazing people. In particular, Katherine, Kathryn, Lakshan and Biljana who were my extended family during covid lockdowns and shared many amazing adventures with that I will remember forever, with many more to come! I also want to thank my friends from home, Michelle, Hannah, Rosalea and Helen, who I miss deeply when I am not with them and distract me with Taylor Swift, games and food.

Finally, last but not least, my family. My parents who always told me to dream big and to never limit myself. My sister, Abi, who is my daily inspiration and partner in crime. Finally, my nan who was my biggest cheerleader and I know who would be proud of me. I would not be where I am today without their love and support, and words cannot express how grateful I am to them.

To my family, I would not be where I am without you.

Contents

CHAPTER 1

Introduction

The main aim of this thesis is to better understand the production of a special set of particles called quarkonia. Quarkonia are a type of flavourless meson, where mesons are particles that contain an even number of quarks. Quarkonia are composed of a quark+antiquark pair of the same heavy flavour quark, *i.e.* a c or b quark. Examples for $c\bar{c}$ states are J/ψ, $\psi(2S)$ and for $b\bar{b}$ are $\Upsilon(1S)$, $\Upsilon(2S)$ and $\Upsilon(3S)$. What makes these particles interesting to measure is that they are a good probe for understanding quantum chromodynamics (QCD) in more detail. QCD is a quantum field theory (QFT) which describes the strong force which binds the quarks together that form the quarkonium state via the exchange of gluons [1]. QCD calculations can be performed using perturbation theory in a series expansion of a parameter called α_s at high energies. α_s denotes the strength of the QCD interaction. However, at low energy scales, α_s becomes larger than unity, and hence QCD can no longer be calculated perturbatively. When forming the quarkonia states, the heavy quarks are typically produced at high energy scales. However, for the quarks to form the quarkonia bound states, the relative velocity between the quarks must be small. This means the quarks evolve down to lower energy scales to form the bound state. Hence the formation of the quarkonia bound state needs to include perturbative and non-perturbative QCD calculations. As the quarkonia mass is at the energy scale

where these two regimes meet, quarkonia production can bridge the gap between these two regimes [2].

Various models have been used to describe quarkonia production, with varying rates of success, to try to describe the experimental data produced by the Tevatron, which measured the prompt and displaced production of J/ψ's. Displaced J/ψ's are those produced from the decays of b hadrons, in comparison to prompt production, where J/ψ's are produced directly at the primary electron-positron or proton-proton collision point. The probability of production, known as the cross section, was measured differentially *vs.* the transverse momentum of the J/ψ, $p_{\mathrm{T}}(J/\psi)$ for prompt and displaced J/ψ's. The first model to be tested was the colour singlet (CS) model, which predicts that J/ψ's are produced in a colour singlet state only. However, CS model predictions were compared to the experimental prompt J/ψ distributions, but found that the model underestimated production by an order of magnitude at large $p_{\mathrm{T}}(J/\psi)$ [3]. This can be seen in blue in fig. 1.1.

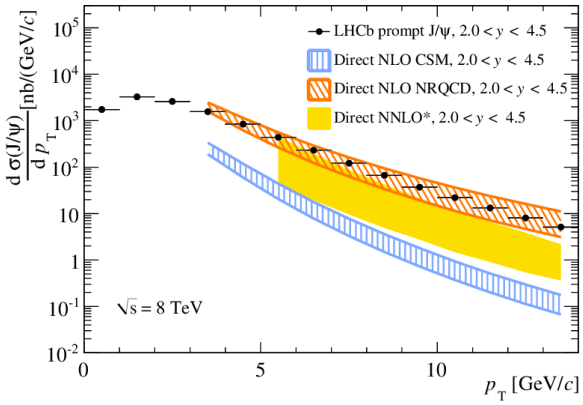

Figure 1.1: Differential production cross section *vs.* $p_{\mathrm{T}}(J/\psi)$ with LHCb including CS and NRQCD theory predictions [4].

This led to the introduction of the non-relativistic QCD (NRQCD) model, which is an effective field theory. This model takes into account the relative velocity between the quarks in the J/ψ bound state. The physical consequence of this is that not only are J/ψ's produced in colour singlet states as seen in the CS model, but also J/ψ's are produced in colour octet (CO) states [5, 6]. As these states carry colour charge, they need to radiate a gluon in order to be in a CS state. Feynman diagrams for these two mechanisms are shown in fig. 1.2. NRQCD predictions are compared with experimental data, as shown in dark orange in fig. 1.1, and match very well with data when CS and CO modes are included.

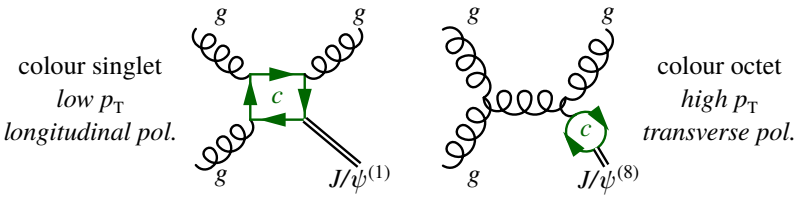

Figure 1.2: CS and CO Feynman diagrams [7].

However, there are still inconsistencies when comparing this NRQCD model with experimental data. The first instance is found when measuring the polarisation of the J/ψ *vs.* $p_T(J/\psi)$ as shown in fig. 1.3. NRQCD predicts that CS states are typically produced at low p_T values with a longitudinal polarisation, in comparison to CO states which are produced at high p_T values with a transverse polarisation. Hence, as $p_T(J/\psi)$ increases, one would expect the J/ψ to be increasingly more transversely polarised. Figure 1.3 shows measurements of λ_θ *vs.* $p_T(J/\psi)$, where λ_θ is a polarisation parameter. $\lambda_\theta = +1$ means the J/ψ is maximally transversely polarisation as opposed to λ_θ = -1 which is maximally longitudinally polarised and $\lambda_\theta = 0$ which is no polarisation. This is explained more in appendix E. As shown in fig. 1.3, the LHCb data shows minimal polarisation at all values of $p_T(J/\psi)$ [8]. This has been observed at other experiments such as ALICE, CDF and CMS [9–11]. No matter the corrections applied to the NRQCD model, as shown in blue, red and green in fig. 1.3, it still does not explain the minimal polarisation observed in data.

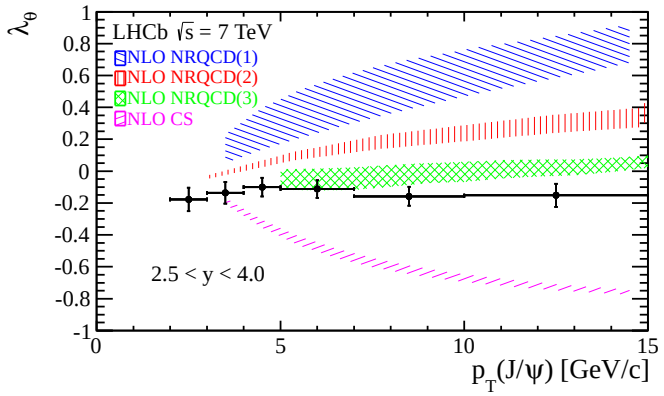

Figure 1.3: Polarisation of J/ψ, λ_θ, measured with LHCb data including CS and NRQCD theory predictions [8].

The second instance of inconsistencies of NRQCD predictions with experimental data, is recent measurements published by LHCb which look at J/ψ's clustered into jets [12]. In this case, the differential production cross section is measured *vs.* $z(J/\psi) \equiv p_T(J/\psi)/p_T(\text{jet})$, the fraction of the transverse momentum carried by the J/ψ in the jet. The cross sections were separated into the prompt and displaced components, as shown in fig. 1.4. For the displaced component shown in fig. 1.4a,

predictions match well with experimental data, where the predictions are calculated using a Monte Carlo (MC) generator called PYTHIA 8 [13, 14]. However, when comparing LHCb prompt distributions with LO NRQCD PYTHIA 8 predictions, the data are shifted to lower $z(J/\psi)$ values. These measurements were then repeated at CMS with similar conclusions, as shown in fig. 1.5.

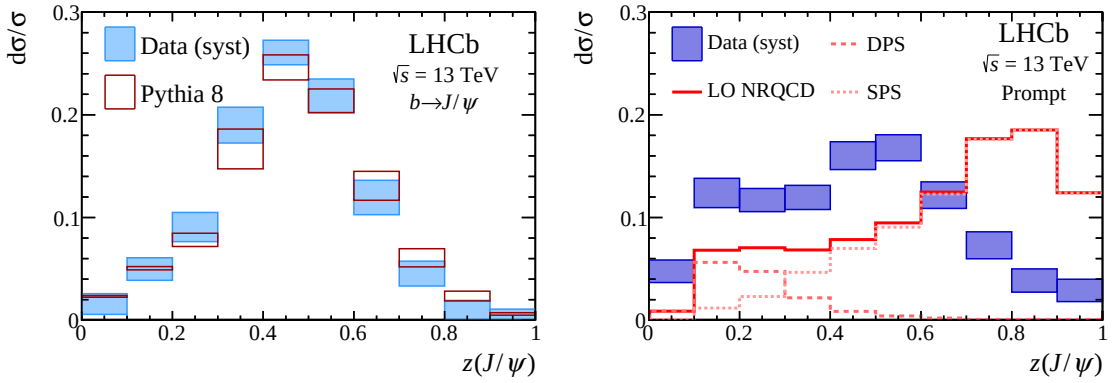

(a) Displaced. (b) Prompt.

Figure 1.4: Normalised LHCb cross section measurements *vs.* $z(J/\psi)$ [12].

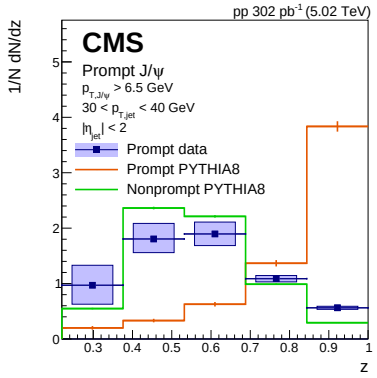

Figure 1.5: Normalised CMS prompt cross section measurements *vs.* $z(J/\psi)$ [15].

The physical interpretation of this is that the J/ψ's are produced less isolated than predicted, and have significantly more radiation surrounding them. In the current PYTHIA 8 release, only NRQCD calculations are performed in the hard production component of the Monte Carlo generation, with production diagrams that look like those shown in fig. 1.6a. This is at the highest energy scale of the generation, so has the effect of producing very isolated J/ψ's. However, calculations have been performed such as those explored in Refs. [16] and [17], to extend the NRQCD framework to not only include production through hard production, but through fragmentation processes. Fragmentation in this case is the emission of a J/ψ state from a high energy quark or gluon. $z(J/\psi)$ can hence be though of as a fragmentation variable, where the lower the $z(J/\psi)$ the larger the extent of the fragmentation. An

example process is shown in fig. 1.6b. Ref. [18] has shown the comparison of the LHCb data with different fragmentation calculations, such as using the fragmenting jet function (FJF) formalism. These are more consistent with the LHCb data than the current PYTHIA 8 release, which does not include fragmentation calculations.

(a) Hard production. (b) Fragmentation.

Figure 1.6: Different production methods of quarkonia [7].

The main aim of this thesis is to firstly include NRQCD fragmentation calculations into PYTHIA 8 by incorporating them into the parton shower for various quarkonia states in CS and CO states. Secondly, to extend the measurements performed by LHCb of the normalised cross section *vs.* $z(J/\psi)$ to other quarkonia states with LHCb data, namely, the $\psi(2S)$, $\Upsilon(1S)$, $\Upsilon(2S)$ and $\Upsilon(3S)$ states using the dimuon decay channel. Finally, this analysis is also extended to a potential exotic tetraquark state, called the X(3872), using the dimuon+dipion decay channel. This is to extend the work performed by many experiments to determine the true nature of the particle, *i.e.* is it a molecular or a true tetraquark state?

The thesis is structured as follows. Chapter 2 discusses general QCD theory, and jet clustering. Chapter 3 discusses the implementation of NRQCD fragmentation in the PYTHIA 8 framework, describing what a Monte Carlo generator is and the formalism behind parton shower and NRQCD theory. The implementation and results are shown, with the derived CS and CO fragmentation expressions shown in appendix A. The LHCb detector is explored in chapter 4, and in chapter 5 I will discuss contributions I made to the LHCb detector upgrades I and II, on the ring-imaging cherenkov detector (RICH), trigger framework and finally research and development (R&D) work on Low Gain-Avalanche detectors (LGADs). Chapter 6 will report the normalised cross section measurements for various quarkonia states, and chapter 7 will discuss the tetraquark measurement. Conclusions are then drawn in chapter 8. Appendix A shows all the fragmentation functions that were implemented into PYTHIA 8, and appendix B a more detailed discussion of the generation of a quarkonia splitting. Appendix C shows extra results for the tetraquark measurement and finally preliminary investigations into measuring the polarisation *vs.* $z(J/\psi)$ are shown in appendix E.

CHAPTER 2

Theory

In this chapter, firstly the Standard Model (SM) of particle physics will be discussed. Then the calculation of production and decay rates for different processes are discussed, and how this leads to the necessary modelling of the structure of the proton. Finally, as jets are used to measure the momentum fractions of different quarkonia and tetraquarks in jets as discussed in chapters 6 and 7, jets are defined and the different algorithms that cluster these are discussed.

2.1 The Standard Model

The Standard Model (SM) is the backbone for particle physics. It is used to explain what the fundamental particles are that make up matter, and how they interact with each other. Particles are split into two types, fermions and bosons, which are shown in fig. 2.1. The main characteristic that sets these apart is the spin. Fermions have half integer spin, in comparison to bosons which have integer spin of 0 or 1. Fermions obey a rule called the Pauli Exclusion principle, which says that fermions cannot share the same quantum state, in comparison to bosons which can. Fermions are split into two classes, quarks and leptons. These are fundamental particles, as they are not made up of any other particle, *i.e.* they are not divisible. There are

three generations of leptons. An electron is a first generation lepton and has a very light mass particle partner called an electron neutrino, which interacts very weakly with other particles. The second and third generation are the muon and the tau respectively, with partners muon neutrino and tau neutrino. The particle mass gets larger for each subsequent generation. All of these leptons (in fact all fermions) also have antiparticle partners, which means they are equal in mass to their particle partner, but other properties, such as charge, are equal and opposite. For example, the electron has an electric charge of -1. Its antiparticle partner is the positron (or antielectron) which has an electric charge of +1. All leptons can be detected individually, *i.e.* they do not have to combine with other leptons in a bound state to be detected.

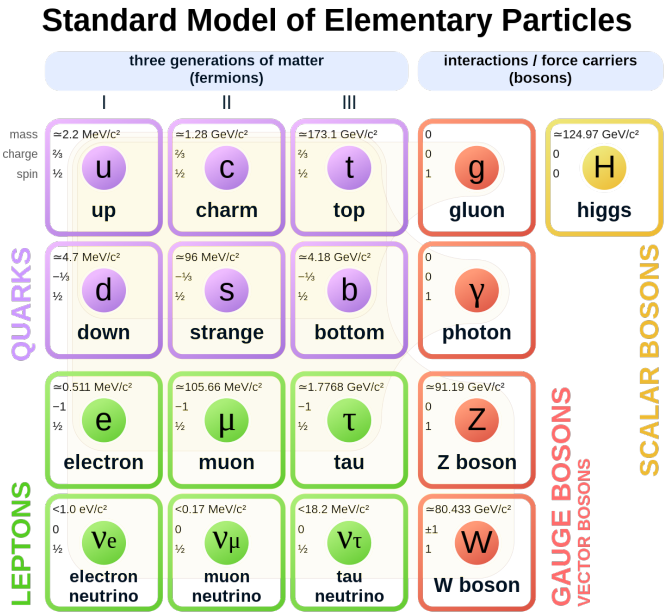

Figure 2.1: A schematic diagram showing all the fundamental particles and their properties [19].

Quarks also have three generations, where up and down are the two first generation quarks. Higher mass quarks are the charm, strange, top and bottom which are the second and third generation respectively. Up, charm and top have an electric charge of +2/3, in comparison to down, strange and bottom which have -1/3. For this thesis, the charm and bottom quarks are of particular interest. Quarks behave differently to leptons as they carry an extra property called colour charge. The consequence of quarks carrying colour charge is that they cannot be seen by themselves in nature. They need to be combined with other quarks to be in a colour neutral state. These make up particles that contain two or more quarks, which are

collectively called hadrons. These are split into two types, mesons and baryons. Mesons are bosons, as they contain an even number of quarks, with an example arrangement of $q\bar{q}$, where q is a quark, and $\bar{q}$ an antiquark. Tetraquarks are also mesons, as they contain four quarks. Baryons are fermions, as they contain an odd number of quarks. Two example quark arrangements are qqq or $\bar{q}\bar{q}\bar{q}$. An example baryon is the proton, which contains two up and one down valence quarks.

The gauge bosons are the second class of particles, which are mediators/force carriers for the interactions between particles. These mediate three of the four fundamental forces of nature. First, the electromagnetic force which interacts with particles that carry electric charge, is mediated by the boson called a photon. Second, the strong/nuclear force, which is mediated by the gluon. This interacts with particles that carry colour charge, hence quarks. This primarily binds quarks into bound states like hadrons mentioned previously. Third, is the weak interaction where heavier unstable particles decay to lighter particles via W and Z bosons. An example is seen in beta decays. For certain interactions to take place, different properties have to be conserved, such as charge, colour charge, baryon number and lepton number, for example. The fourth force, gravity, in not currently incorporated into the SM.

For the fermions, quarks interact via all three forces, in comparison to leptons which do not interact via the strong force, since they do not have a colour charge. Since neutrinos do not carry electric charge, they only interact weakly, which makes them very difficult to detect. For the bosons, there are eight kinds of gluons which carry different colour-anticolour combinations. Since the gluons carry colour, they can self interact. This leads to the confinement of quarks into bound hadron states, which will be discussed in section 2.2.1. Since photons do not carry electric charge, they do not self interact. At large energies, the electromagnetic force and the weak force unify into a single force, called Electroweak Unification.

In comparison to the gluon and photon which are massless, W and Z bosons have very large masses. This was originally a problem in particle physics, as the W and Z bosons could be calculated to have zero mass, even though they were measured experimentally to have large masses. The reason W and Z bosons have mass was found to be due to an effect called Electroweak Symmetry Breaking in Quantum Field Theory (QFT). The consequence of this is that the bosons obtain their masses from interacting with something called the Higgs field.

QFT is the framework which allows physicists to calculate how particles interact with each other using a fundamental set of rules. It states that each fundamental particle has a field associated with them. Particles are then the excited states, or quanta, of their field. So each of the three forces described above are carried by specific fields, which is what is meant when bosons are said to be force carriers. In the Higgs field, it does not cause a force, but instead particles obtain their mass from interacting with the Higgs field. The Higgs boson is then an excitation of the Higgs field. A particle consistent with the expected properties of the minimal SM Higgs boson was discovered in 2012, and is measured to have a mass of 125.25 $\pm$ 0.17 GeV [20]. More tests need to be performed to confirm this.

An important test of the SM is to check if the rate of production and decay of the Higgs boson matches SM predictions. The branching ratio (BR) is the probability that a Higgs boson will decay into a particular final state, e.g. $H^0 \to b\bar{b}$. This can be measured experimentally for all decay channels. Another important property is the strength of the interaction, called the coupling. An important property of the Higgs boson is that the Yukawa coupling strength is proportional to the mass of the particle it is decaying into. This can be seen in fig. 2.2, where the coupling strength is larger for higher mass decay products. Various couplings of the Higgs production and decays have been measured, and so far seem to be consistent with the SM.

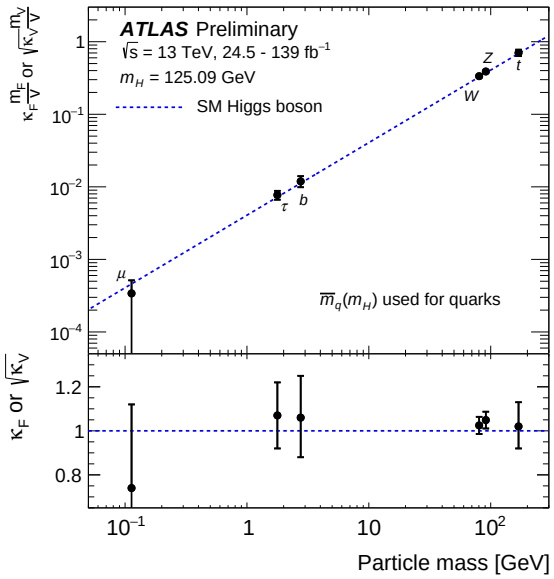

Figure 2.2: Reduced coupling strength modifiers of Higgs to various fermions and bosons *vs.* their respective masses [21, 22].

Inconsistencies with the SM have been observed in various physics areas. Some of

the most notable have been observed in astrophysics, for example where the stars at the edge of a galaxy have found to rotate faster than expected, assuming only luminal matter and Einsteinian gravity. There have also been inconsistencies in cosmic microwave background measurements. It has been theorised by the physics community that this gives hints for a new substance called dark matter. There are also many other beyond the SM (BSM) theories of interest such as supersymmetry (SUSY) for example. In particle physics, searches to find inconsistencies with the SM are split into two types, direct and indirect searches. Direct searches try and measure BSM particle signatures directly, where dark photons is one example [23]. Indirect searches aim to measure SM parameters, such as couplings, precisely and any deviation from the theory prediction could give hints for new physics. Three examples where deviations have been observed are in the mass of the W boson measured at CDF [24], the muon g-2 anomaly measured at Fermilab [25], and lepton universality measurements from LHCb [26].

2.2 Calculating the cross section of various processes

In particle physics, the probability that a specific process occurs per unit flux is called a cross section, and is measured in units of area called barns. The cross section for any process, such as $e^- e^+ \to q\bar{q}$ as shown in fig. 2.3, can be calculated from first principles using Fermi's Golden Rule. This states that for a general process of $a + b \to 1 + ... + n$, the cross section can be calculated with,

$$\sigma_{a+b\to 1+...+n} = \frac{1}{F} \int |\mathcal{M}_{a+b\to 1+...+n}|^2 \mathrm{d}\Phi_n, \tag{2.1}$$

where,

$$\mathrm{d}\Phi_n = (2\pi)^4 \delta^{(4)} \left(\sum_{l=1}^{n} p_l - p_a - p_b \right) \prod_{k=1}^{n} \frac{\mathrm{d}^3 \boldsymbol{p}_k}{2E_k (2\pi)^3}. \tag{2.2}$$

F is the Lorentz-invariant flux factor, $\mathcal{M}_{a+b\to 1+...+n}$ the matrix element and $\mathrm{d}\Phi_n$ the phase space in an elementary volume of the final state particles [27]. F and $\mathrm{d}\Phi_n$ are independent of the production process, in comparison to the matrix element which needs to be calculated for each separate process. The matrix element encodes all the possible interactions of the incoming and outgoing states. The rules that govern how the matrix element is calculated are derived using QFT. The electromagnetic interactions are calculated from Quantum Electrodynamics (QED), and the strong

interactions from Quantum Chromodynamics (QCD) which are QFTs. The important parameter is the coupling strength, and is denoted by α_{em} and α_s for QED and QCD respectively. Assuming α_{em} and α_s are small compared to unity, then the matrix element can be calculated perturbatively in a series expansion of α. An example for QCD is,

$$\mathcal{M}_{a+b\to 1+\ldots+n} \simeq \alpha_s^{p/2} \sum_{k=0}^{n'} C_k^{a+b\to 1+\ldots+n} \alpha_s^k, \tag{2.3}$$

where p depends on the process [27]. The full expression of $\mathcal{M}_{a+b\to 1+\ldots+n}$ would be calculated if $n' \to \infty$. However, this is not possible, so the sum is truncated. The first non-vanishing term calculated in the sum is referred to as leading order (LO) and the second term is next-to-leading-order (NLO). The coefficients, $C_k^{a+b\to 1+\ldots+n}$ are specific to the process and are calculated using Feynman rules from Feynman diagrams [27]. These will not be discussed in much detail in this thesis, as the calculations are not centrally involved in this research. Consequences for introducing corrections to LO and NLO contributions are described in the subsequent sections.

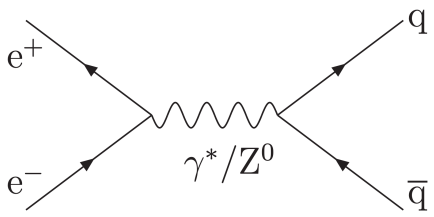

Figure 2.3: LO process for $e^-e^+ \to q\bar{q}$ [27].

2.2.1 Renormalisation of coupling

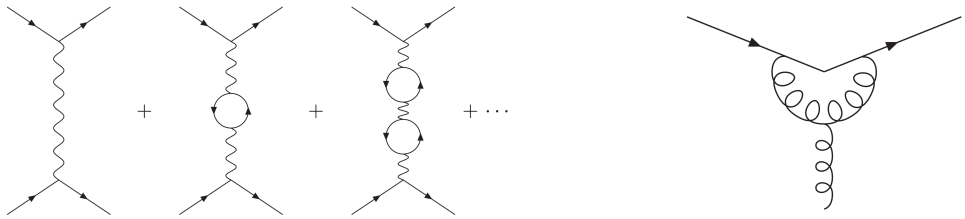

(a) QED.

(b) QCD.

Figure 2.4: Virtual loop corrections in the propagator for QED and QCD. The loops present in a) also take part in QCD, where the fermions in the loop would instead be quarks. Loop corrections like b) only take part in QCD, due to the self-interacting nature of the gluon [27].

Couplings are not constant and depend on energy scale. At leading order (LO) calculations of the cross section, this scale dependence is not seen. However, cor-

rections to the LO term introduce this scale dependence. This scale dependence of the coupling is what is seen experimentally, as all orders of α in the cross section are measured, not just the leading order. Primarily, this occurs when loop corrections are added to the mediator/propagator of the interaction. When performing calculations of the matrix element, the particles in the additional loop can take any value of momentum. Hence, when calculating the integral at large energy, it becomes divergent. This is called the ultraviolet divergence and is proportional to E^2. This divergence is handled with a procedure called renormalisation. This will not be derived here, but the physical consequences will be discussed. Inside the integral, a new energy scale parameter μ_R^2 is introduced, such that the integral is now a finite quantity. When introducing this scale, for example in QED, the electromagnetic coupling α_{em}, is now dependent on energy scale, Q^2, which is the virtuality of the propagating photon,

$$\alpha_{em}(Q^2) = \frac{\alpha_{em}(\mu_R^2)}{1 - \frac{\alpha_{em}(\mu_R^2)}{3\pi}\log(Q^2/\mu_R^2)}. \tag{2.4}$$

The divergences in the photon propagator from loop corrections are now absorbed into the coupling which is "running" with energy scale [27]. These loops are shown in fig. 2.4a. μ_R^2 is any chosen value, such that $\alpha_{em}(\mu_R^2)$ can be measured experimentally. When calculating the matrix element, for example $e^- q \to e^- q$,

$$\mathcal{M}_{e^- q \to e^- q}(Q^2) = \sum_{k=1}^{+\infty} C_k(Q^2, \mu_R^2)\alpha_{em}^k(\mu_R^2), \tag{2.5}$$

it is now dependent on scale Q^2 [27]. The matrix element is not dependent on μ_R^2, as the scale μ_R^2 is chosen such that the overall dependence cancels between the coefficients and α_s. However, in most calculations the full matrix element is truncated, so the coefficients can be dependent on factors of $\log(Q^2/\mu_R^2)$. Hence μ_R^2 is usually chosen such that $\mu_R^2 \sim Q^2$. μ_R^2 can then be varied by 1/2 or 2 to determine uncertainties for the calculation. An important consequence if introducing this scale, is that the electromagnetic coupling increases with μ_R^2 [27].

For the strong coupling, the same procedure is applied for loop corrections in the gluon propagator,

$$\alpha_s(Q^2) = \frac{\alpha_s(\mu_0^2)}{1 + \beta_0\alpha_s(\mu_0^2)\log(Q^2/\mu_0^2)}, \tag{2.6}$$

where $\alpha_s(\mu_0^2)$ is the known strong coupling value, and typically μ_0 is to be the Z^0

boson mass [27]. β_0 here is,

$$\beta_0 = -\frac{N_F}{6\pi} + \frac{11N_c}{12\pi}, \tag{2.7}$$

where N_F is the number of active quark flavours, and $N_c = 3$ which is number of colours [27]. This introduction of the second term in β_0 has important consequences. The first term behaves the same as for QED. However, because gluons can self-interact, unlike photons in QED, there are gluon loops as well as quark loops. This comes from the non-Abelian nature of QCD. This is shown in fig. 2.4b. These contribute a positive sign to β_0, hence $\beta_0 > 0$. This means α_s decreases with μ_R^2. This can be seen in fig. 2.5. This means that the strong coupling diverges at low energies, meaning that QCD calculations in this regime cannot be calculated with perturbation theory. Physically, this leads to colour confinement, as mentioned in section 2.1 that the quarks are confined into bound states by the surrounding gluons combining them together, as the coupling makes it hard for them to be pulled apart. At high energies, there is "asymptotic freedom", as the coupling between quarks and gluons is small, hence they interact feebly with each other. In this region, QCD calculations can be performed with perturbation theory. The transition between the perturbative and non-perturbative regions is given a value, called Λ_{QCD}. This will be discussed more in section 2.3 [27].

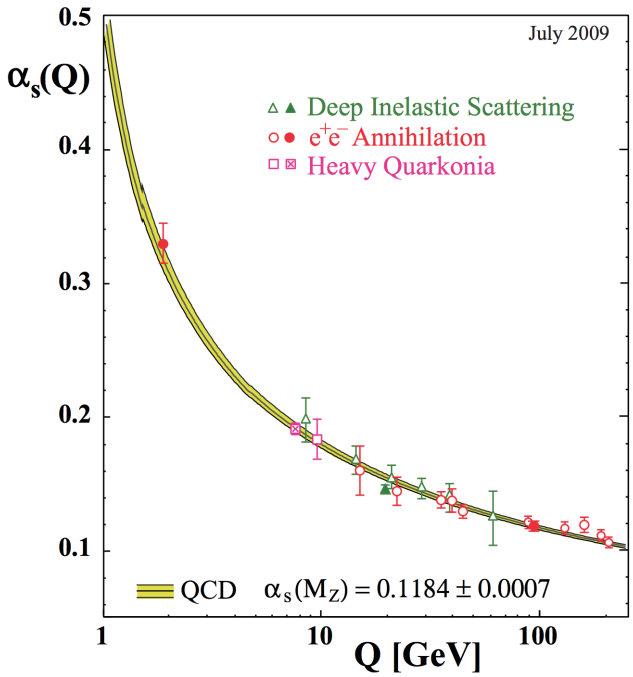

Figure 2.5: Strong coupling, α_s *vs.* energy scale, Q [28].

2.2.2 Infrared divergences and resummation

As well as ultraviolet divergences, there are infrared divergences in QED and QCD. These appear due to the massless nature of the gluon and photon. An example to explain this is the $e^+e^- \to q\bar{q}$ process shown in fig. 2.7a. At LO, the tree-level cross section is calculated as

$$\sigma_0(s) = N_c Q_q^2 \frac{4\pi\alpha_{em}^2}{3s} \tag{2.8}$$

where Q_q is the charge of the quark, s is the squared centre of mass energy and N_c is the number of colours which is equal to 3 [27]. This alone does not present any singularities. However, when the differential cross section is calculated for the process where an additional gluon is added to the final state, as shown in fig. 2.6, singularities are present. These are called real-emission diagrams, and the two diagrams in fig. 2.6 can also interfere with each other. This is calculated as,

$$\frac{\mathrm{d}\sigma_R}{\mathrm{d}x_1\mathrm{d}x_2} = \sigma_0 C_F \frac{\alpha_s}{2\pi} \frac{x_1^2 + x_2^2}{(1-x_1)(1-x_2)}, \tag{2.9}$$

where $C_F = 4/3$ is the colour factor and $x_i = 2(p_i \cdot p_0)/p_0^2$ which is a kinematic variable for the three parton final state, $q\bar{q}g$, which are each denoted with a label i = 1,2,3 [27]. p_i is the four momentum of each parton and p_0 is the sum of all these. In the e^+e^- centre of mass frame, $p_0 = (\sqrt{s}; 0, 0, 0)$, hence $x_i = 2E_i/\sqrt{s}$ where E_i is the energy of parton i. Hence, $0 \leq x_i \leq 1$ is always true, where the partons are massless. From eq. (2.9), there are two singularities at $x_1 = 1$ and $x_2 = 1$. These are infrared singularities, which can be explained by looking at the angles between the partons. θ_{13} is the angle between the quark and gluon, and θ_{23} is between the antiquark and gluon. Therefore,

$$1 - x_1 = \frac{x_2 x_3}{2}(1 - \cos\theta_{23}), \quad 1 - x_2 = \frac{x_1 x_3}{2}(1 - \cos\theta_{13}) \tag{2.10}$$

and $x_1 = 1$ when $\theta_{13} = 0$, and $x_2 = 1$ when $\theta_{23} = 0$ [27]. This means the gluon becomes collinear with the quark or antiquark. Here, these can be called collinear singularities. From energy conservation, the relation $x_1 + x_2 + x_3 = 2$, is also true. Hence if $x_1 = x_2 = 1$ simultaneously, then $x_3 = 0$, which means the gluon has infinitely small energy, otherwise called "soft". This is known as a soft singularity. The physical origin of these singularities is because the process $e^+e^- \to q\bar{q}g$ cannot be distinguished from $e^+e^- \to q\bar{q}$ in these limits, hence a divergence occurs. In

the case of massive quarks, collinear divergences are not much of an issue, but soft divergences can still occur. As infrared divergences occur, calculating the total cross section can lead to infinite values, which is not physical,

$$\sigma_R = \int_0^1 \int_0^1 \frac{\mathrm{d}\sigma_R}{\mathrm{d}x_1 \mathrm{d}x_2} \mathrm{d}x_1 \mathrm{d}x_2. \tag{2.11}$$

However, in this cross section, virtual contributions from loop diagrams as shown in fig. 2.7 have not been considered [27]. These virtual corrections also include infrared divergences, when the virtual gluon in the loop is soft, on the order of $\sim \log(E)$. This means graphs like b) in fig. 2.7 are not distinguishable from the tree level process of $e^+e^- \to q\bar{q}$, which is what is seen in the real emissions case. Collinear divergences also appear with the same principles. What is interesting is that when the real and virtual corrections are combined when calculating the integrated cross section, the collinear and soft divergences exactly cancel. This was proven in QED and QCD, by using the KLN theorem [29,30], where the total cross section $\sigma_T = \sigma_0 + \sigma_R + \sigma_V = \sigma_0(1 + \alpha_s/\pi)$. This is the total cross section of $e^+e^- \to q\bar{q}g$ at order α_s, as these processes are not distinguishable without divergences from $e^+e^- \to q\bar{q}$. To make the processes $e^+e^- \to q\bar{q}$ and $e^+e^- \to q\bar{q}g$ distinguishable, one can introduce a phase space cut off, such that the gluon kinematics never reach the infrared divergence limit. This is what would be seen experimentally as the resolving power of the detector is only finite, so it would not distinguish these two diagrams. For example, if the energy of the quarks is limited to $E_{1,2} < (\sqrt{s}/2)(1 - \lambda)$ where $\lambda > 0$, the real emission cross section for $e^+e^- \to q\bar{q}g$ is,

$$\hat{\sigma}_R(\lambda) = \int_0^{1-\lambda} \int_0^{1-\lambda} \sigma_0 C_F \frac{\alpha_s}{2\pi} \frac{x_1^2 + x_2^2}{(1 - x_1)(1 - x_2)} \mathrm{d}x_1 \mathrm{d}x_2. \tag{2.12}$$

This is convergent and simplifies to,

$$\hat{\sigma}_R(\lambda) \sim \sigma_0 C_F \frac{\alpha_s}{2\pi} \log^2(\lambda), \tag{2.13}$$

where gluons with $E_3 < \lambda\sqrt{s}$ cannot be measured [27]. An exclusive cross section for $e^+e^- \to q\bar{q}g$ can now be calculated with a finite answer without including the virtual and born level graphs. To deal with infrared divergences, one either calculates an inclusive cross section where the KLN theorem is applied for each order in α_s, or exclusively where an infrared cut off is applied. The later technique is typically

seen in MC event generators as virtual contributions cannot be directly simulated. However, this approach leads to logarithmically enhanced terms in the cross section as shown in eq. (2.13), which counteracts the fact that α_s is small. These are handled using a technique called resummation. The cross section of a process $ij \to A$ where A is any number of partons is,

$$\hat{\sigma}_{ij\to A}(\hat{s}, \mu^2; \lambda) = \alpha_s^p(\mu_R^2) \sum_{k=0}^{+\infty} C_k^{ij\to A}(\hat{s}, \mu^2, \mu_R^2; \lambda)\alpha_s^k(\mu_R^2), \tag{2.14}$$

where λ is the infrared cut off and $C_k^{ij\to A}$ here is slightly different to that defined in eq. (2.5) [27]. For massless partons,

$$C_k^{ij\to A}(\hat{s}, \mu^2, \mu_R^2; \lambda) = \sum_{l=0}^{2(p+k)} c_{kl}^{ij\to A}(\hat{s}, \mu^2, \mu_R^2)\log^l(\lambda), \tag{2.15}$$

where coefficients in $c_{kl}^{ij\to A}$ do not contain divergences, but the log terms, $\log^l(\lambda)$ are included at all orders in α_s [27]. The logarithms need to be resummed [31]. For leading logarithms (LL), the terms $c_{k,2(p+k)}^{ij\to A}\alpha_s^{p+k}\log^{2(p+k)}(\lambda)$ are evaluated for all values of k. For next-to-leading logarithms (NLL), these are $c_{k,2(p+k)-1}^{ij\to A}\alpha_s^{p+k}\log^{2(p+k)-1}(\lambda)$ for all values of k. This resummation technique is performed for example in parton showers in MC event generators, as discussed in section 3.2. There are various other ways to perform resummation, which will not be discussed here. For LO and NLO, these calculate $C_0^{ij\to A}$ and $C_1^{ij\to A}$ respectively. Hence, if one decides to calculate (LO or NLO) and (LL or NLL) simultaneously this can have overlap in some of the terms of the calculation. This is present in event generators in the parton shower for example. This leads to double counting and is solved using a technique called matching [27].

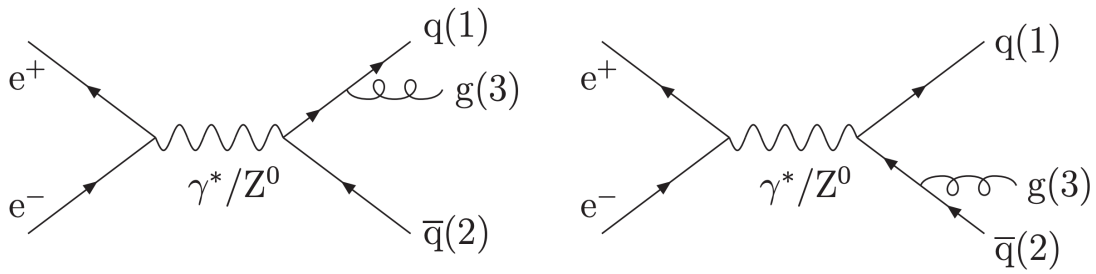

Figure 2.6: LO contributions to $e^+e^- \to q\bar{q}g$ [27].

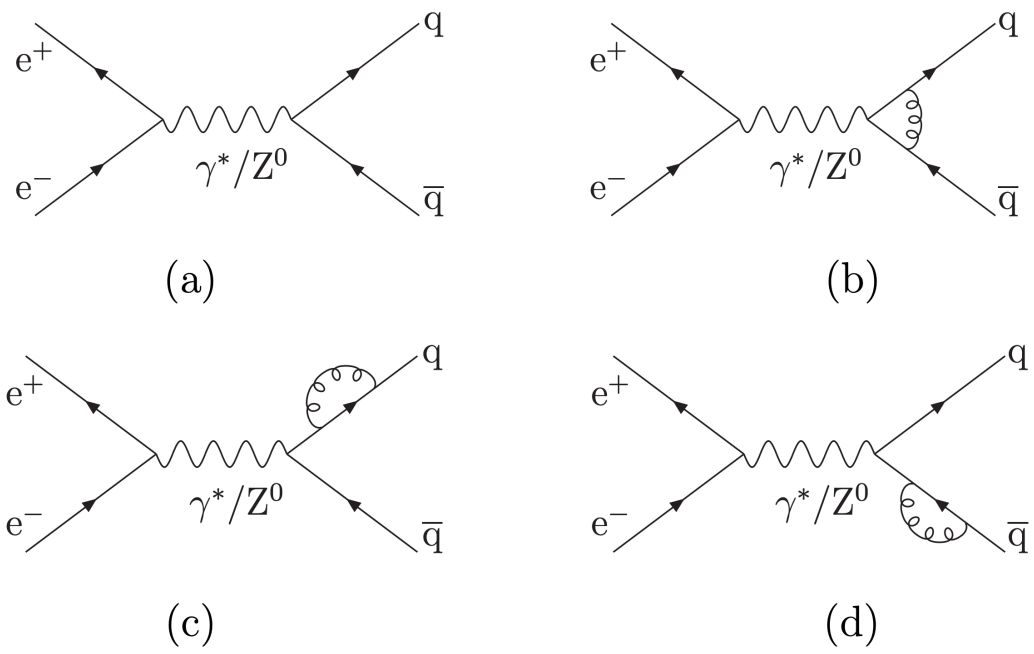

Figure 2.7: $e^+e^- \to q\bar{q}$ Feynman diagrams which contribute at a) LO, and b), c) and d) which are one loop virtual corrections [27].

2.3 The parton model of the proton

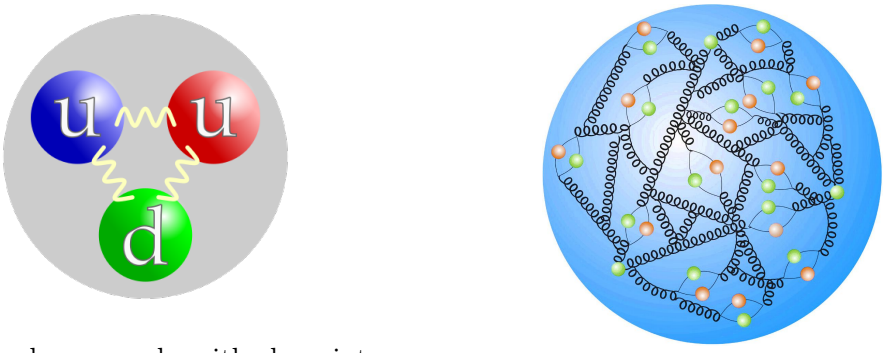

(a) Proton valence quarks with gluon interactions [32].

(b) More complex picture of proton [33].

Figure 2.8: The simple valence quark picture of the proton *vs.* the more complex structure that is seen as higher energy probes are used.

The parton model is used to describe how a proton behaves in proton-proton collisions. In the simple picture of the proton, it is made up of three valence quarks, two up quarks and one down quark. In reality, when one has a high energy probe, with energy Q, more internal structure of the proton is observed as shown in fig. 2.8b. The quarks in the proton are surrounded by a sea of virtual gluons and $q\bar{q}$ pairs, which appear for very short times. If the probe can interact with the proton at small enough timescales of $1/Q$, it can then interact with these virtual partons, *i.e.*

at scales where $Q \gg \Lambda_{\mathrm{QCD}}$. This is seen at the Large Hadron Collider, where the dominant production mode of the Higgs is from gluon fusion [27].

Parton density functions (PDFs), $f_i(x, \mu^2)$, are used to describe partons within protons, where x is the momentum fraction carried by the parton within the proton. $f_i(x, \mu^2)dx$ is the probability for a parton of flavour i, to have x between x and $x+dx$ at scale μ^2. These PDFs are not fully described by perturbative QCD [27]. However, in the perturbative regime, the PDFs evolution with scale μ^2 are calculated using DGLAP equations [34–36],

$$df_i(x, \mu^2) = \frac{d\mu^2}{\mu^2} \sum_k \int_x^1 \frac{dz}{z} \frac{\alpha_s(\mu^2)}{2\pi} P_{k\to i}(z) f_k(x/z, \mu^2), \tag{2.16}$$

where the renormalisation scale μ_R is also set to μ. $P_{k\to i}(z)$ are the Altarelli-Parisi splitting functions, also known as splitting kernels. These are related to branching contributions that happen at LO to the matrix elements in perturbative QCD. For a branching $k \to i + j$, z is the momentum fraction of a parton i branching off parton k. These are shown pictorially in fig. 2.9 [27].

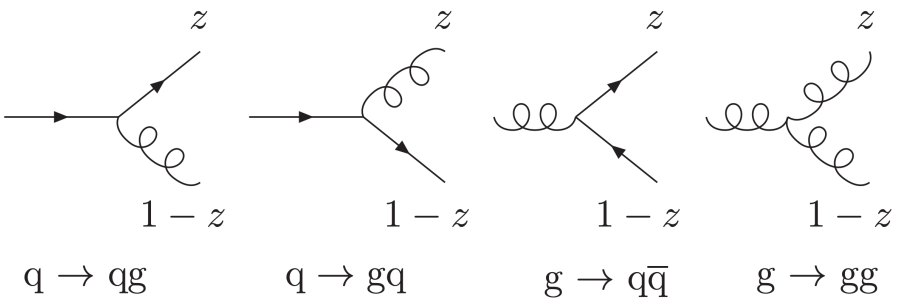

Figure 2.9: Various QCD branchings of the quark and gluon [27].

Mathematically, the splitting kernels for massless partons are:

$$P_{q\to q}(z) = P_{\bar{q}\to\bar{q}}(z) = C_F \left(\frac{1+z^2}{1-z} \right)_+, \tag{2.17}$$

$$P_{q\to g}(z) = P_{\bar{q}\to g}(z) = C_F \left(\frac{1+(1-z)^2}{z} \right), \tag{2.18}$$

$$P_{g\to q}(z) = P_{g\to\bar{q}}(z) = T_R(z^2 + (1-z)^2), \tag{2.19}$$

$$P_{g\to g}(z) = 2C_A \left(\frac{z}{(1-z)_+} + \frac{1-z}{z} + z(1-z) \right) + \frac{11C_A - 4N_F T_R}{6} \delta(1-z), \tag{2.20}$$

where $C_F = 4/3$, $T_R = 1/2$, $C_A = N_C = 3$, are the colour factors, and N_F is the number of active quark flavours. Equations (2.17) to (2.20) shown here are only

calculated to LO [27]. These can also be calculated at NLO and NNLO in α_s as with other cross section measurements,

$$P_{k\to i}(z,\mu^2) = P^{LO}_{k\to i}(z) + \frac{\alpha_s(\mu^2)}{2\pi}P^{NLO}_{k\to i}(z) + \left(\frac{\alpha_s(\mu^2)}{2\pi}\right)^2 P^{NNLO}_{k\to i}(z) + \dots \quad . \tag{2.21}$$

The + shown in eqs. (2.17) to (2.20) above means the functions are plus described. This means the divergence at $z \to 1$, which emerges from a soft singularity, is removed. For example, in $q \to qg$, as $z \to 1$, the gluon's energy $\to 1$. This is because this leads to an infrared divergence in the matrix element, as the mother and daughter quark cannot be distinguished. However, there are not only real branchings such as those shown in fig. 2.9, but also contributions from loop diagrams to NLO calculations of the cross section. These are called virtual corrections. When calculating the cross section using the KLN theorem, infrared divergences from real emissions can be cancelled by divergences that appear in QCD loop diagrams. The plus prescription in the splitting kernels handles these virtual contributions, where the splitting kernels are what remain after the cancellation of these divergences. In comparison, there is no singularity in $q \to gq$ as the daughter g and mother q are distinguishable. Collinear singularities are not fully handled by the KLN theorem. Hence, these divergences are absorbed into the PDFs. This leads to a scale dependence, μ, which is what was seen in the renormalisation case [27].

To understand the physical meaning of this, the quark PDF DGLAP equation $q(x,\mu^2)$ is,

$$dq(x,\mu^2) = \frac{d\mu^2}{\mu^2}\int_x^1 \frac{dz}{z}\frac{\alpha_s(\mu^2)}{2\pi}(P_{q\to q}(z)q(x/z,\mu^2) + P_{g\to q}(z)g(x/z,\mu^2)), \tag{2.22}$$

where $g(x/z,\mu^2)$ is the gluon PDF and $N_F = 1$ for simplicity. The plus prescription needs to be handled using a Heaviside function [27]. Incorporating this, the equation can be rewritten as,

$$\begin{aligned} dq(x,\mu^2) = \frac{d\mu^2}{\mu^2}\int_x^1 \frac{dz}{z}\frac{\alpha_s(\mu^2)}{2\pi}(\hat{P}_{q\to q}(z)q(x/z,\mu^2) + \hat{P}_{g\to q}(z)g(x/z,\mu^2)) \\ -q(x,\mu^2)\frac{d\mu^2}{\mu^2}\int_0^1 dz\frac{\alpha_s(\mu^2)}{2\pi}\hat{P}_{q\to q}(z) \end{aligned}, \tag{2.23}$$

where $\hat{P}_{q\to q}(z)$ and $\hat{P}_{g\to q}(z)$ are unregularised splitting functions where the plus prescription has been handled [27]. Equation (2.23) can be reinterpreted as a con-

tinuity equation, with the number of incoming and outgoing quarks that flows out of a system given by

$$dq(x,\mu^2) = \delta q_{in}(x,\mu^2) - \delta q_{out}(x,\mu^2), \tag{2.24}$$

where $\delta q_{in}(x,\mu^2)$ and $\delta q_{out}(x,\mu^2)$ are defined as,

$$\begin{aligned}\delta q_{in}(x,\mu^2) &= \int_x^1 \frac{dz}{z}\frac{d\mu^2}{\mu^2}\frac{\alpha_s(\mu^2)}{2\pi}(\hat{P}_{q\to q}(z)q(x/z,\mu^2) + \hat{P}_{g\to q}(z)g(x/z,\mu^2)),\\ \delta q_{out}(x,\mu^2) &= q(x,\mu^2)\int_0^1 dz\frac{d\mu^2}{\mu^2}\frac{\alpha_s(\mu^2)}{2\pi}\hat{P}_{q\to q}(z),\end{aligned} \tag{2.25}$$

and $dq(x,\mu^2)dx$, at scale μ^2, is the rate at which the number of quarks in a box of size dx changes [27]. Hence, when considering $\delta q_{out}(x,\mu^2)dx$, it resembles the number of outgoing quarks of flavour q, $q(x,\mu^2)dx$, multiplied by

$$d\mathcal{P}_{q\to q}(\mu^2,z) = \frac{d\mu^2}{\mu^2}dz\frac{\alpha_s(\mu^2)}{2\pi}\hat{P}_{q\to q}(z), \tag{2.26}$$

which is the probability that the $q \to qg$ branching occurs, at scale μ^2 and x. The integral is used to account of all values of z of the daughter quark [27].

Similar to the running strong coupling, the value of PDFs at scale μ can be found, given the PDF value at initial scale μ_0 by solving the DGLAP equations. The difference in this case is that the PDFs are not directly measurable at scale μ_0, hence they are estimated with phenomenological models with a parameterisation of x which are constrained by experimental measurements. The DGLAP equations then evolve the PDF inputs to the appropriate scale μ. All the perturbative branchings which occurred between μ_0 and μ are then contained in the PDF, as DGLAP is only valid in the perturbative regime. The inputs of various free parameters to the PDFs at scale μ_0 can be measured in experiments by looking at the cross sections of different processes, such as Drell-Yann. μ_0 is usually Λ_{QCD}, as α_s becomes unity and the non-perturbative regime is entered. Different calculations of the PDF evolution are provided by MSTW2008, NNPDF, CTEQ [37–39]. The PDF for each flavour of quark and gluon *vs.* x at scales $Q^2 = 10$ GeV^2 and $Q^2 = 10^4$ GeV^2 are shown in fig. 2.10 [27].

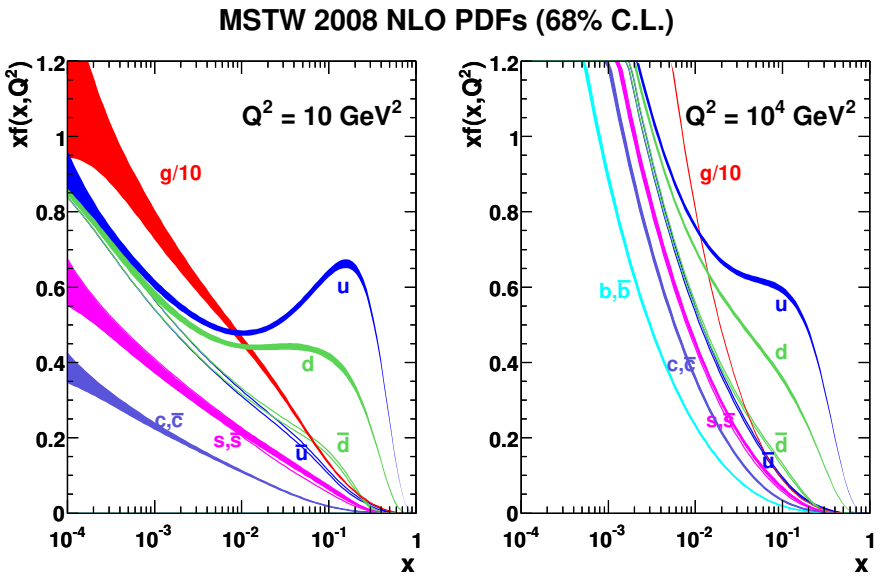

Figure 2.10: NLO PDFs derived from the MSTW 2008 set [37].

As Q^2 increases, the probe is more likely to interact with the virtual partons, hence contributions from virtual $q\bar{q}$ pairs increase. These are usually called sea quarks, which are different from the valence uud quarks of the proton. Hence these contributions can be separated in the u quark PDF,

$$u(x,\mu^2) = u_v(x,\mu^2) + u_s(x,\mu^2), \tag{2.27}$$

where s and v refer to the sea and valence quarks respectively. The PDFs also have different number and momentum sum rules, which will not be described in detail here [27].

The total cross section of a proton-proton collision to a final state A, $\sigma_A(s)$, at a centre of mass energy of $\sqrt{s}$ can hence be calculated using the proton PDFs with a factorisation approach,

$$\sigma_A(s) = \sum_{i,j} \int dx_1 \int dx_2 f_i(x_1,\mu^2) f_j(x_2,\mu^2) \hat{\sigma}_{ij\to A}(\hat{s} = x_1 x_2 s, \mu^2). \tag{2.28}$$

Parton i is selected from one proton, and parton j from the other, which are described by the proton PDFs, $f_i(x_1,\mu^2)$ and $f_j(x_2,\mu^2)$, respectively [27]. These partons then take part in the main part of the cross section $\hat{\sigma}_{ij\to A}$, each carrying the fractional momentum of the proton, x_1 and x_2, respectively. The perturbative and non-perturbative regimes are factorised into $\hat{\sigma}_{ij\to A}$ and the PDFs, respectively, and are separated by the factorisation scale μ. Below scale μ is non-perturbative and

above is perturbative. The PDFs are universal, and are independent of the process calculated, *i.e.* $ij \to A$. The perturbative and non-perturbative regimes are also known as short-distance and long-distance regimes respectively. This concept is also used when describing the production of quarkonia with NRQCD, which is discussed further in section 3.3. μ is chosen such that the cross section does not depend on not physical scales. $\hat{\sigma}_{ij\to A}$ is also dependent on μ_R, the renormalisation scale of α_s, as the cross section is usually calculated at fixed order, hence μ_R needs to also be chosen. These are usually chosen to be equal to the scale of the process, Q, so logarithmic terms do not become too large [27].

2.4 Jets

A jet can be defined as "the collimated sprays of hadrons that result from the fragmentation of a high-energy quark or gluon" [40] . It is not intrinsically a fundamental object and the definition depends on the algorithm chosen. Fragmentation is a combination of the branchings off a high energy parton as seen in the splitting kernels in section 2.3, and finally the hadronisation of the parton to a hadron. This will be discussed more in section 3.1. A jet algorithm is used to cluster the particles that are close together in an event. The final clustered jets depend on the jet algorithm used, so are not fundamental physics objects. However, the jet algorithm must be well-defined and reproducible for it to be used by physicists. Also, the jet object should resemble the initial parton object that is calculable as much as possible. Additionally, the jets must not change if a low energy or a parallel parton is emitted, *i.e.* they have to be infrared and collinear safe [41]. These requirements dictate the choice of how the jet is defined.

Sequential recombination and cone algorithms are the two main types of clustering algorithms. Cone algorithms are not discussed here, as sequential recombination algorithms are used in this thesis. The order of execution of the sequential recombination algorithm is:

1. For all the particles in an event, identify the pair of particles in some distance measure that are the closest together.

2. Find the total four momentum of the combined particles and assign it as a new pseudo-jet particle.

3. Repeat these steps until a stopping criterion is reached.

The distance measure and stopping criterion used depend on the jet algorithm, and are determined by the structure of perturbative QCD divergences, as seen in section 2.2.2 [40]. The k_t algorithm is an example of a sequential recombination algorithm, and uses two different distance measures. The first is d_{ij} which is defined as the distance between two particles i and j,

$$d_{ij} = d_{ji} = min(p_{Ti}^2, p_{Tj}^2)\frac{\Delta R_{ij}^2}{R^2}, \tag{2.29}$$

where the jet radius R is set, and $\Delta R_{ij}^2 = (y_i - y_j)^2 + (\phi_i - \phi_j)^2$ is the radial distance between the two particles. y is the rapidity and ϕ the azimuthal angle between particle of interest and the proton beam. These coordinates will be discussed more in section 4.1.1. The $\min(p_{Ti}^2,\ p_{Tj}^2)$ finds the particle with the smallest squared transverse momentum, p_{T}. The second, d_{iB}, is the distance between the beam and every particle,

$$d_{iB} = p_{Ti}^2. \tag{2.30}$$

Jet algorithms can be either inclusive or exclusive. For the exclusive case, a fixed jet radius is used. d_{ij} or d_{iB} is also calculated for each particle in an event. If d_{ij} is the smallest, particles i and j are replaced as a single pseudo-jet with momentum $p_i + p_j$. If d_{iB} is the smallest, particle i becomes part of the beam jet. This continues for each particle in an event, until d_{ij} or d_{iB} becomes larger than a cut off value, d_{cut}. The remaining particles are non-beam event jets. For inclusive algorithms, if d_{iB} is smallest, the particle is added to an "inclusive jet" instead of the beam jet. As there is no d_{cut} threshold, this continues until no particles remain. The jets that are above a p_{T} threshold are the only ones that are kept [40]. Other example algorithms are the Cambridge/Aachen (C/A) and anti-k_t algorithms. For the C/A algorithm, the distance measures are,

$$d_{ij} = d_{ji} = \frac{\Delta R_{ij}^2}{R^2}, \tag{2.31}$$

$$d_{iB} = 1. \tag{2.32}$$

For the anti-k_t algorithm, the distance measures are defined as,

$$d_{ij} = d_{ji} = min(p_{Ti}^{-2}, p_{Tj}^{-2}) \frac{\Delta R_{ij}^2}{R^2}, \tag{2.33}$$

$$d_{iB} = p_{Ti}^{-2}. \tag{2.34}$$

The anti-k_t algorithm is usually used because it performs like a perfect cone algorithm, producing jets that are circular in y -ϕ space [40]. This is shown in fig. 2.11, in comparison to the C/A and k_t algorithms [42]. However, different physics objectives may need more specialised jet algorithms, for example a Higgs decaying into $b\bar{b}$ can be identified with a mass-drop tagger method [43].

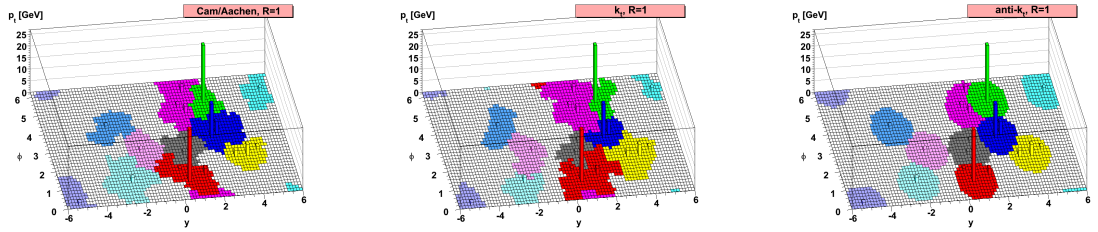

(a) Cambridge-Aachen. (b) k_t. (c) anti-k_t.

Figure 2.11: The phase space for different jet algorithms [42].

CHAPTER 3

Quarkonia showers in PYTHIA 8

As explained in the introduction in chapter 1, current Monte Carlo predictions produced by PYTHIA 8 do not effectively describe the J/ψ in jets fragmentation results produced by LHCb and CMS. One possible theory to describe quarkonia production is NRQCD, which is an effective field theory that theorises that quarkonia can be produced in colour singlet and colour octet states. The NRQCD formalism for quarkonia production is incorporated into PYTHIA 8, but only in the hard matrix element calculations. The work described in this chapter shows the incorporation of colour singlet and octet fragmentation processes into PYTHIA 8. This is achieved by including these calculations into the parton shower. Firstly, I will discuss in section 3.1 what a Monte Carlo event generator is, and describe different parts of the event generation. Then I will discuss parton showers in more detail in section 3.2 and how to sample important generation variables from a distribution. Then I will describe NRQCD theory and its formalism in more detail in section 3.3 and how this is incorporated into the PYTHIA 8 framework in section 3.4. Finally in section 3.5 I will discuss how this implementation has been tested with single dipole results and compare results to experimental data. Then I will give some conclusions and discuss possible future work in section 3.6.

3.1 What is Monte Carlo Generation?

Monte Carlo simulation (MC) is widely used in particle physics, and is a method that allows the user to predict possible outcomes of an event using pseudo-random number sequences. MC is essential for modelling particle physics collisions, as it used to connect calculations that can be performed from first principles, such as $e^+e^- \to q\bar{q}$, to those that can only be described by phenomenological models such as hadronisation or the evolution of a parton shower down to the hadronisation scale. Without MC, this is not possible. Probabilities are described by probability density functions (PDFs), which describe different aspects of the particle collision, and can be dependent on multiple variables. The PDFs can be randomly sampled according to their distribution, to find values for these variables for each event. This factorisation of different aspects of the collision is very important, as very complex probability combinations can be calculated.

Monte Carlo is also used in integration. For instance, if the integral needs to be found of an unknown PDF (where divergences are regulated with cut-offs), the maximum height of the unknown distribution can be measured, and a uniform distribution can be produced at this value. Data points are then randomly generated. The ratio of the number of data points that "land" inside the unknown distribution, *vs.* those that "land" within the total uniform distribution is then the integral value. This is called the accept-reject method which can be optimised. The value of the integral tends towards the true value, the larger the number of data points are generated, N. The error is then $\sqrt{N}$. Other integration techniques are available such as the trapezium rule *etc.* which are "quadrature" methods, but Monte Carlo is extremely good at determining multi-dimensional integrals. This is important in the particle physics context, for example to calculate a $2 \to n$ body process, requires a $3n-4$ integral, which comes from the n momentum vectors in the process. Considering spin, flavour *etc.* would require even more dimensions [44].

There are several general purpose Monte Carlo generators in particle physics. Three examples are HERWIG [45], SHERPA [46], and PYTHIA 8 [47]. PYTHIA 8 [47] will be the main focus of this thesis. The aim is to simulate a whole proton-proton collision, from the interaction of the partons from each proton, down to the final particles produced in an event. To make this achievable, the simulation is factorised into different sections. A schematic diagram of a simulated event is shown in fig. 3.1,

with the main components shown [44].

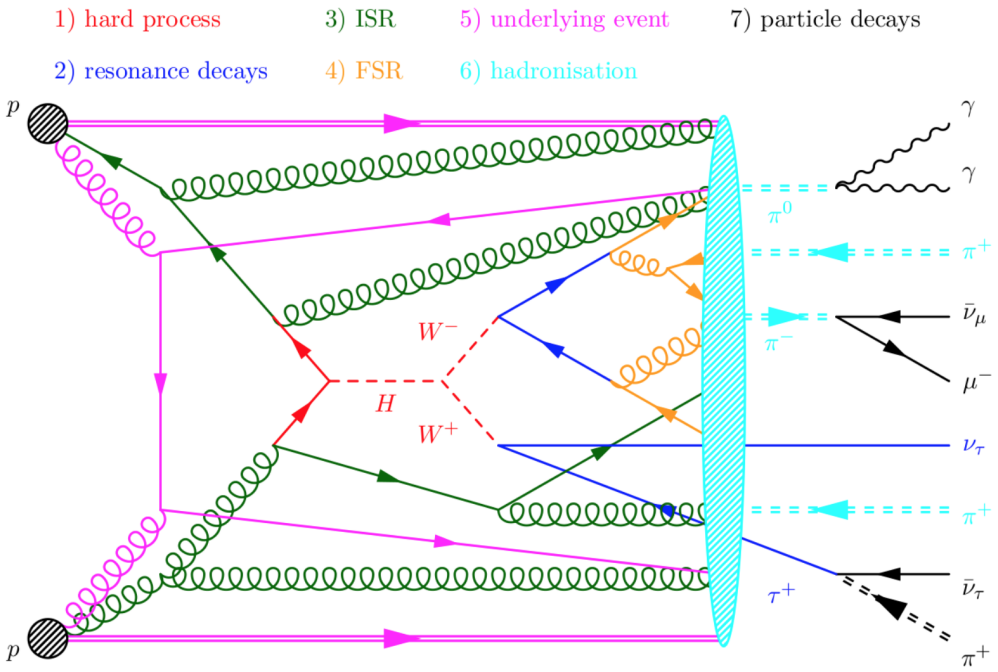

Figure 3.1: A schematic diagram of a simulated proton-proton collision with the different components shown [44].

The different aspects of the simulation need to be time-ordered. Firstly, two protons (also called beam particles) collide, each defined by a parton distribution function, as explained in section 2.3. The two partons from each proton then interact in the main process of the event, called the hard process. Hard and soft means high and low energy respectively. These are typically $2 \to 2$ processes, with an example of $q\bar{q} \to H \to W^+W^-$ shown in fig. 3.1. However, these partons can lose energy via QCD radiation before the hard process takes place, which are simulated as a series of branchings, for example $g \to gg$. These are called radiation emissions and are not particle interactions, as in MC it is assumed that the initial state particles are non-interacting in the past, and the final state particles are non-interacting in the future. This is shown in green and is called Initial State Radiation (ISR). Short-lived resonances can also be produced, such as the Z^0 or $W^\pm$ that need to be decayed. The outgoing partons also branch to more partons as the event evolves, which is called Final State Radiation (FSR). ISR and FSR are separated because they are simulated in slightly different ways. Once the energy of the final partons in the event evolve down to the Λ_{QCD} energy scale, α_s becomes divergent in the QCD processes, as discussed in sections 2.2.1 and 2.3. Hence, hadronisation takes place, which is the process where the partons (quarks and gluons) become observable colour-neutral

hadrons. This is due to QCD confinement which is shown in light blue. Many of these colour-neutral hadrons are not stable (exceptions being the p for example) and hence decay, shown in black. There is an additional component, shown in pink, called the underlying event or multiple parton interactions (MPI). Other partons from the proton may interact with each other, but with not as much energy as partons that took part in the hard process. "Beam remnant" also contributes to this, as the partons that interact still leave behind a net-coloured object from the rest of the proton. This can interact with the final state particles and can complicate the event structure. Colour reconnection [48] and Bose-Einstein effects [49] can also complicate events, as they provide phenomenological models for particle interactions beyond that of the hard process interaction [13]. These different components are described in more detail in this section. Proton PDFs are described in more detail in section 2.3. The ISR and FSR, collectively called the parton shower, are described separately in section 3.2, as the goal is to add additional branchings to the parton shower.

3.1.1 The Hard Process and Resonance Decays

Various hard processes (cross sections) are programmed into PYTHIA. $2 \to 1$ and $2 \to 2$ processes are the easiest to program, as more final state particles means implementing a more complicated phase space. Some example processes are hard QCD (*e.g.* $qg \to qg$), soft QCD (diffractive and elastic scattering), Onia production, deep inelastic scattering, W/Z, Higgs, prompt photon production ($qg \to q\gamma$) and photon induced processes [13].

Resonance decays are typically reserved for a class of particles which are above the b mass: *i.e.* t, Z^0, $W^{\pm}$, h^0 *etc.* Hence electroweak physics or beyond the standard model decays typically contribute here. Resonances can decay to other resonances, *e.g.* $h^0 \to W^+W^-$, and these decay until no other resonances are produced, hence the decay chains can be sizeable. Each decay may be perturbatively calculated, and occasionally spin information is used. Light resonances that are produced in abundance are typically not treated this way, for example the ρ meson. This is purely a technical distinction to allow for factorisation of the event [13] and avoid cross sections dependent upon variable final-state multiplicity.

3.1.2 Beam Remnants and Multiple Interactions

The beam remnant is the part of the proton that is left when one of the partons takes part in a hard interaction. For example, if one of the u quarks is used, this leaves behind a ud diquark which has an anti-triplet colour charge. A diquark is a theoretical concept of two quarks combined inside a baryon, to allow for colour and flavour conservation. This leaves then some colour connection between the beam remnant and the hard interaction. The colour connection is even more complex when a gluon is an initiator, as a uud is left behind in a colour antitriplet diquark and colour triplet quark states, each of which can interact with the hard process. The beam remnant is also left with some residual energy, as the initiator parton has some primordial transverse momentum (k_{T}), from the uncertainty principle due to the size of the proton. The beam remnant then takes up this recoil [13].

Usually, as there are multiple interacting partons in the proton, not only one hard interaction occurs per event, but several. These are called multiple parton interactions (MPI). The implementation of MPI in PYTHIA is handled by allowing several different partons to interact in separate $2 \to 2$ scatterings. Typically, $2 \to 2$ QCD calculated cross sections diverge as $p_{\mathrm{T}} \to 0$ and then decreases rapidly at high p_{T}. However, this divergence is not observed in MPI interactions in data. Hence a $p_{\mathrm{T,min}}$ scale is introduced at $\sim$ 1.5-2.5 GeV to damp the divergence. Hence, in an event where there are no hard interactions only soft scatterings, called minimum-bias, then scatterings are usually around the $p_{\mathrm{T,min}}$ scale. If there is a hard interaction, then if there are additional scatterings, these are typically also around the $p_{\mathrm{T,min}}$ scale. Events with several high p_{T} scatterings are not typically expected. However, this can happen and this is called double parton scattering (DPS). An example of where this has been observed was in the J/ψ in jets measurements as discussed in chapter 1, where a high p_{T} J/ψ and jet are measured in the same event [13].

There is also the pedestal effect to consider, which is the fact that the probability of additional soft scatterings increases if a hard scattering has taken place. This is because hard processes typically take place in more central collisions, *i.e.* a small impact parameter, as there are more partons present to interact with and at higher virtuality, in comparison to the peripheral region. This leads to a trigger bias on high p_{T} processes which are more central, and hence have a larger probability for a second interaction to take place anyway. In these events more event activity

is registered than in an average event [47]. These additional soft interactions are called underlying event, which is composed mainly of MPI, along with some ISR and beam remnant. This component is usually tuned to experimental data, *e.g.* Tevatron data [13]. There is also a connection between MPI and the parton shower in terms of p_{T} ordering, which will be discussed in more detail in section 3.2.2.

3.1.3 Hadronisation

As explained in section 3.1, hadronisation takes place when QCD reaches the non-perturbative regime at long distances due to α_s (perturbative at short distances), and the coloured partons become hadrons (colourless and bound). In event generators, hadronisation is the conversion of partons to hadrons plus the decays of the particles. This is used as the decay products are what is actually measured by the detector, and will also correctly model the multiplicity of events. For simplicity, the defined hadronisation in this thesis only includes the conversion of partons to hadrons, and decays are discussed separately. Due to the non-perturbative nature of hadronisation, its process is not known from first principles. Hence, this is described by phenomenological models, where the main models are cluster hadronisation and string hadronisation [13]. Independent hadronisation can also be used to handle individual hadronisation (exclusive) of a single parton to hadrons, using separate models in conjunction with string or cluster hadronisation (inclusive). In some texts, cluster/string hadronisation can be called cluster/string fragmentation. However, in this thesis, the term hadronisation will be used in this context, to separate this from parton shower fragmentation.

String hadronisation, also called the Lund model, is the model used in PYTHIA. Like the parton-shower it is iterative and probabilistic in nature. Firstly, consider a $q\overline{q}$ system. A charge and anti-charge together produce a colour dipole field, and as the distance between the two charges increases, the energy stored increases linearly. This is known as linear confinement. This is due to the self-interaction of the gluon mediator in QCD, which leads to the allowed three-gluon and four-gluon vertex Feynman diagrams. This linear confinement also seems to be confirmed by lattice QCD. This can be translated as a string model, where the colour dipole field can be re-interpreted as a physical colour flux tube (string) between the two charges, which has no transverse degrees of freedom. The constant in the linear increase in energy per unit length, called the string constant κ, was determined from hadron

spectroscopy and then later validated by lattice QCD calculations with a value of $\sim$ 1 GeV/fm. It can also be thought of as a mass density. Hadronisation now occurs from these strings. As the two quarks ($q + \overline{q}$) move apart, the string increases in length, leading to the potential energy increasing. The string can break, which leads to the creation of a $q'\overline{q}'$ pair. The remaining strings can be broken even more if the energy is large enough, until only on-mass-shell hadrons are left. The new $q'\overline{q}'$ pairs result from quantum tunnelling. This means heavy-quark production is suppressed, u:d:s:$c \sim 1{:}1{:}0.3{:}10^{-11}$. The probability of c and b quarks being produced is extremely slim, hence they are typically only produced in the parton shower. The allowed final combined mesons also need to be selected, where pseudoscalar or vector mesons can be produced. Due to the different spin states, there is expected to be a 1:3 ratio of production respectively. The hadronisation can start either at the q or $\overline{q}$ end of the string and works towards the other end of the string. This symmetry constrains the overall "Lund symmetric hadronisation function" shape, which gives the allowed momentum for a new particle to be produced. This function is tuned from data. Other influences can make event kinematics more challenging. For example, nearby gluons can create kinks in the string [13].

The model behind cluster hadronisation is very different to string hadronisation and is based on the idea of pre-confinement, where partons cluster together to form colour singlet states. This occurs at the end of the parton shower, where all of the remaining gluons split into quark-antiquark pairs. These then group together with surrounding partons to form clusters in colour singlet states. These clusters then decay via two-body decays until the generated final state hadrons are stable. Any kinematics/flavours that need to be rearranged after clustering can be corrected for, like in the string hadronisation model. PYTHIA implements the string hadronisation model, whereas HERWIG and SHERPA use the cluster hadronisation model. Both models describe data, however the cluster model has problems describing kinematics, while the string model describes kinematics well, but can have problems with flavour [50].

3.1.4 Decays

The hadrons produced from string hadronisation are often not stable and need to decay to stable states. Many of the branching ratios (BRs) to simulate the decays come from theory calculations. However, whenever quality experimental data is

available, it is used. About 50 % of decay products are distributed isotropically according to phase space, and 50 % are handled with matrix element calculations. This is where the models for decay are available and decaying non-isotropically has a sufficient effect. Some examples are if the decaying particle is polarised or proceeds through strong resonant structures. Secondly, if a charm or bottom hadron decays semi-leptonically as an example, then the weak matrix elements need to be taken into account [13]. A table of the non-isotropic decays are shown in Table 2 in Ref. [47]. All the branching ratios, particle properties *etc.* are stored in an external table for PYTHIA 8 to use, where the allowed decay products are hadrons, leptons or photons. There are special cases, *e.g.* $\Upsilon \to ggg$ and many B-decays, where the final decay products are partons, due to the heavy mass of the parent particle. Sometimes the final partons are showered, however others are just collapsed to hadronic systems using a simplified string model [13].

3.2 Parton showers

Parton showers are the collective term for ISR and FSR which was introduced in section 3.1. This is used to factorise between the various physics processes, from the high energy scale of the proton PDF, to the hard process discussed in section 3.1.1, and then to the lower energy scale of the hadronisation process discussed in section 3.1.3. In FSR, this is the process where the outgoing partons from the hard process take part in QCD radiation and continuously branch to lower energy quarks and gluons as they evolve from the hard process energy scale, to the lower cut off Λ_{QCD} energy scale. The radiation is softer than the core hard process. This branching process is called fragmentation. This has been discussed in the context of the parton model of the proton in section 2.3 and also in jets in section 2.4. Overall, this makes a simulated proton-proton collision have a more realistic representation of what is observed at a collider, as a hard process of $2 \to 2$ particles now becomes a $2 \to n$ particle process. These also better simulate jet events, as the branching of the additional particles are likely to take place collinearly to the original outgoing partons of the hard process. So this can broaden jets in the event [51].

3.2.1 Sudakov form factor

The probability for a branching can be described by the same evolution equations that are used for the proton PDFs, described in section 2.3, the DGLAP equations. The general differential probability for a parton a to branch to partons b and c is described in eq. (3.1),

$$d\mathcal{P}_a(z, Q^2) = \frac{dQ^2}{Q^2}\frac{\alpha_s}{2\pi}P_{a\to bc}(z)dz, \tag{3.1}$$

at a virtuality scale of Q^2, where b has the fraction z of a's energy and c has the fraction $(1-z)$ [51]. The choice of scale, Q^2, for the parton shower to evolve is dependent on the overall physics goals that need to be achieved, for example, applying angular ordering to correct for colour coherence effects. This is discussed more in section 3.2.2. Three different QCD splitting kernels for massless quarks, as discussed in section 2.3, are shown in eqs. (3.2) to (3.4),

$$P_{q\to qg}(z) = \frac{4}{3}\frac{1+z^2}{1-z}, \tag{3.2}$$

$$P_{g\to gg}(z) = 3\frac{(1-z(1-z))^2}{z(1-z)}, \tag{3.3}$$

$$P_{g\to q\bar{q}}(z) = \frac{N_f}{2}(z^2+(1-z)^2), \tag{3.4}$$

where N_f is the number of active flavours and the expressions are derived from the collinear limit of their respective matrix element expressions [51]. The emission probability described in eq. (3.1) can be above unity. This is because several emissions can occur for an inclusive rate. However, in a parton shower, the emissions are time-ordered, from the hardest scale to Λ_{QCD}. Hence, enforcing time-ordering makes this is an exclusive rate, so emission probabilities are less than unity [51].

Hence, this can be treated like the problem seen in radioactive decay. Solving the differential equation for radioactive decay,

$$\frac{dN}{dt} = -\lambda N, \tag{3.5}$$

gives the probability of the number of particles, N, that have not decayed after a given time t, where λ is the decay constant. In this case for FSR, $\mathcal{P}_a^{no}(Q^2_{max}, Q^2)$ is the probability that parton a will have no emissions between Q^2_{max} and Q^2 and the

differential equation to be solved is,

$$\frac{d\mathcal{P}_a^{no}(Q^2_{max}, Q^2)}{dQ^2} = \mathcal{P}_a^{no}(Q^2_{max}, Q^2)\frac{d\mathcal{P}_a(z, Q^2)}{dQ^2}, \tag{3.6}$$

where $d\mathcal{P}_a(z, Q^2)$ is the probability for parton a to branch, as expressed in eq. (3.1) [51,52]. Note, this is not a constant like λ in the radioactive decay case, as it depends on Q^2. Hence, solving the differential equation for the no emission probability gives [51],

$$\mathcal{P}_a^{no}(Q^2_{max}, Q^2) = \exp\left(-\int_{Q^2}^{Q^2_{max}}\int_{z_{min}}^{z_{max}} d\mathcal{P}_a(z', Q'^2)\right) = \Delta_a(Q^2, q^2). \tag{3.7}$$

In Monte Carlo generator terminology, $\mathcal{P}_a^{no}(Q^2_{max}, Q^2)$ is called the Sudakov form factor and is denoted by a Δ, $\Delta_a(Q^2, q^2)$, as shown in eq. (3.7). The limits of $z_{min} < z < z_{max}$ are from kinematic limits on the branching. Hence, the differential probability that the first branching occurs at $Q^2 = Q^2_a$ is $d\mathcal{P}_a(z, Q^2_a)\mathcal{P}_a^{no}(Q^2_{max}, Q^2)$. If this branching occurs, then the b and c partons can now branch at the scale where $Q^2_{max} = Q^2_a$. This is then an iterative process until Λ_{QCD} is reached, where later branchings are further suppressed by an extra Sudakov factor, to reduce the allowed phase space [51].

For ISR, the differential probability distribution is slightly different, the partons involved in the hard process evolve backwards to the proton PDF scale, hence the proton PDFs need to be taken into account. Hence, the starting point is DGLAP with the parton b density,

$$df_b(x, Q^2) = \frac{dQ^2}{Q^2}\frac{\alpha_s}{2\pi}\int\frac{dx'}{x'}f_a(x', Q^2)P_{a\to bc}\left(\frac{x}{x'}\right), \tag{3.8}$$

for a small increase in dQ^2, is the probability that parton a with momentum fraction x' becomes resolved into parton b at $x = zx'$ and parton c at $x' - x = (1-z)x'$ [51].

Hence, for backwards evolution, dQ^2 is decreased so parton b becomes unresolved into parton a. The differential probability of the branching, $d\mathcal{P}_b$, is then given by the ratio df_b/f_b as [51],

$$d\mathcal{P}_b(x, Q^2) = \left|\frac{dQ^2}{Q^2}\right|\frac{\alpha_s}{2\pi}\int dz\frac{x'f_a(x', Q^2)}{xf_b(x, Q^2)}P_{a\to bc}(z) \tag{3.9}$$

In the subsequent sections, less emphasis will be placed on ISR because for this work inclusion of quarkonia into the parton shower is only considered within the FSR framework. However, once the quarkonia branchings have been implemented in the FSR framework, these could also be easily implemented in the ISR framework.

3.2.2 Choice of evolution variable

There are many motivating factors which can make certain evolution variables for the energy scale of the parton shower better than others. Mainly, there have been three different approaches of evolution variable chosen to be implemented in parton showers. In PYTHIA 6 [13], m^2 was chosen. HERWIG [45] uses an energy-weighted emission angle variable, $E^2(1 - cos\theta) \sim m^2/(z(1-z))$, whereas, ARIADNE [53–55] chose to evolve in squared transverse momentum $\sim z(1-z)m^2$. Hence, these were ordered by large invariant mass, emission angle and p_{T} respectively. These will now be described about in more detail [51].

HERWIG orders emissions not only by energy, but also by angular ordering. This is to take into account coherence effects when soft gluons are emitted, which is explained in more detail in Ref. [56].This means that the first emission might not necessarily be the hardest (largest energy scale) emission, but the widest angle. Hence, this leads to regions of phase space which are not filled, for example in three jet events. These regions need to be filled separately after the parton shower has evolved, and the kinematics of each emission are treated at the end [51].

In PYTHIA 6, m^2 is used as the evolution variable. It was found this variable in fact overpopulates certain regions of phase space, as coherence effects are not inherently taken care of with this variable as there is no angular component. Hence an additional veto has to be included to remove the excess soft gluon emissions. The kinematics are constructed after the daughter virtualities are known [51].

ARIADNE is a slightly different shower concept. Instead of considering just single partons splitting to other individual partons, parton pairs are considered. These are called dipoles, where an example is a colour charge dipole between a quark and an antiquark. Another example is an EM dipole. The evolution of these dipoles is collectively called a dipole shower. Hence, if a dipole emits a gluon for example, the single dipole will split into two dipoles. Since a two-body system is now being considered, it is natural to consider emissions in terms of decreasing p_{T}^2. This in-

herently includes coherence effects and considers the hardness of the emission. The partons after each branching are on-mass shell in this picture, hence the kinematics can be performed immediately after each branching. This makes it easier to stop and restart the shower at any point. However, the main disadvantage is that all dipole types cannot be treated the same. For example, $g \to q\overline{q}$ cannot be easily implemented in the dipole picture [51].

All choices of evolution variable are valid and describe data fairly well, however ARIADNE's approach seems to describe data the best. Hence, the parton shower algorithm was altered in the newer version of PYTHIA, PYTHIA 8. Firstly, the evolution variable m^2 was replaced with p_{T}^2. This was to include some of the coherence effects inherently in the evolution. Also, p_{T}^2 can easily transform to m^2, to keep all of the hard matrix element corrections already implemented. As well as changing to p_{T}^2, some of the dipole approach implemented in ARIADNE was included. The branchings themselves are still considered as single partons. However, each "radiator" parton which takes part in the branching has a "recoiler" partner. This means the kinematics of the shower can be considered as a radiator+recoiler "dipole". These kinematics will be discussed in more detail in section 3.2.3. Splittings like $g \to q\overline{q}$ can now be considered on the same footing as other splittings, with the advantage that the kinematics can be considered after each individual splitting. Consequently, the shower can be stopped and restarted at any point, which is important when incorporating MPIs into an event. This is also very important for interleaved parton showers where ISR and FSR can be take place in any stage of the parton shower, as they are described by the same evolution variable, as for MPI. Underlying event is also characterised by the small p_{T} in comparison to the hard collision, so it is a useful variable in this case as well [51].

3.2.3 Branching kinematics

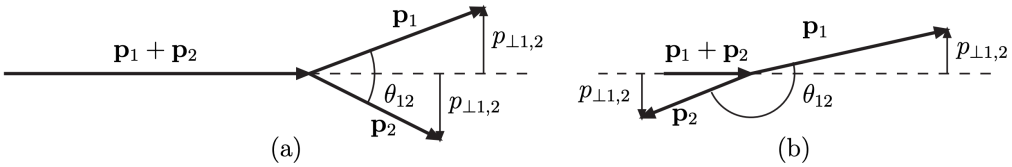

Figure 3.2: Branching kinematics for process $a \to bc$ expressed in a), and an example for large angle and small a momentum shown in b) [51].

In this section, the expression for p^2_{T} will be derived, for a general branching $a \to bc$. Light-cone definitions of the kinematics are used, where $p^{\pm} = E \pm p_z$ and $p^+p^- = m^2_{\mathrm{T}} = m^2 + p^2_{\mathrm{T}}$. If parton a is defined to be travelling the $+z$ direction, as shown in fig. 3.2, the kinematics for parton b and c can be defined as $p^+_b = zp^+_a$ and $p^+_c = (1-z)p^+_a$. z here is the light-cone z fractional momentum. Hence, using p^- conservation, the following expression can be derived [51]:

$$m^2_a = \frac{m^2_b + p^2_{\mathrm{T}}}{z} + \frac{m^2_c + p^2_{\mathrm{T}}}{1-z}. \tag{3.10}$$

This can be arranged to obtain p^2_{T}, as shown in eq. (3.11),

$$p^2_{\mathrm{T}} = z(1-z)m^2_a - (1-z)m^2_b - zm^2_c = p^2_{\mathrm{T,LC}}, \tag{3.11}$$

which can also be considered as the light-cone transverse momentum, $p^2_{\mathrm{T,LC}}$ [51].

For ISR and FSR, the evolution variable p^2_{T} and the final kinematics are handled differently. FSR is the succession of parton branchings to on-shell partons from the hard process to Λ_{QCD}, whereas ISR is the backwards evolution from hard interaction to shower initiators in proton PDFs. This leads to a difference in the virtuality of the process, where FSR branchings are time-like, whereas ISR branchings are space-like. This is demonstrated in fig. 3.3 [51].

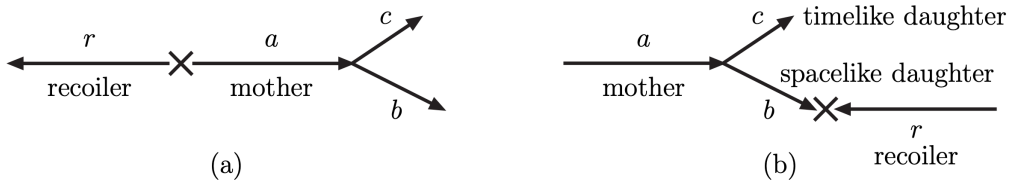

Figure 3.3: Diagram for a) an FSR type branching and b) an ISR branching. The cross denotes the central hard process, and r the recoiler which interacts on different sides [51].

For the time-like branching, $Q^2 = m^2_a$ and $m_b = m_c = 0$. Substituting these into eq. (3.11), leaves $p^2_{\mathrm{T,LC}}$ for FSR showers to be [51],

$$p^2_{\mathrm{T,LC}} = z(1-z)Q^2. \tag{3.12}$$

For the space-like branching, $Q^2 = -m^2_b$ and $m_a = m_c = 0$. Hence [51],

$$p^2_{\mathrm{T,LC}} = (1-z)Q^2. \tag{3.13}$$

Here, $p^2_{\mathrm{T,LC}}$ can be used as the evolution variable to order branching emissions. This is usually relabelled as $p^2_{\mathrm{T,evol}}$ [51].

In $p^2_{\mathrm{T,evol}}$, the z definition used is the light-cone z. This is not the same z that is used in the final kinematics of the radiator+recoiler dipole. The z in the kinematics is the same as for the DGLAP equations for the proton PDF. This is the energy shared between the daughters of parton a, *i.e.* $E_b = zE_a$ and $E_c = (1-z)E_a$. The kinematic z is Lorentz invariant. As the kinematic z expression is more complex than the evolution z, it is a harder expression to implement iteratively. Hence, the shower is evolved using $p^2_{\mathrm{T,evol}}$, and the final kinematics are corrected for afterwards using the kinematic z. This separation of evolution z and kinematic z is discussed in more detail in section 3.2.4, and further information on this is also discussed in Ref. [51].

3.2.4 PYTHIA 8 parton shower algorithm

The general algorithm used in PYTHIA 8 is described as follows and has been paraphrased from Ref. [51].

1. The evolution variable, $p^2_{\mathrm{T,evol}}$ is defined for FSR and ISR showers:

$$\mathrm{FSR} : p^2_{\mathrm{T,evol}} = z(1-z)Q^2, \tag{3.14a}$$

$$\mathrm{ISR} : p^2_{\mathrm{T,evol}} = (1-z)Q^2. \tag{3.14b}$$

2. All radiators in the shower evolve from $p^2_{\mathrm{T,max}}$ in $p^2_{\mathrm{T,evol}}$ from the hard process scale or from the previous branching. $p^2_{\mathrm{T,evol}}$ is then sampled from the evolution equation for FSR and ISR respectively:

$$\mathrm{FSR} : d\mathcal{P}_a = \frac{dp^2_{\mathrm{T,evol}}}{p^2_{\mathrm{T,evol}}} \frac{\alpha_s(p^2_{\mathrm{T,evol}})}{2\pi} P_{a\to bc}(z) dz \mathcal{P}^{no}_a(p^2_{\mathrm{T,max}}, p^2_{\mathrm{T,evol}}), \tag{3.15a}$$

$$\mathrm{ISR} : d\mathcal{P}_b(x,Q^2) = \frac{dp^2_{\mathrm{T,evol}}}{p^2_{\mathrm{T,evol}}} \frac{\alpha_s(p^2_{\mathrm{T,evol}})}{2\pi} \frac{x' f_a(x', p^2_{\mathrm{T,evol}})}{x f_b(x, p^2_{\mathrm{T,evol}})} \times P_{a\to bc}(z) dz \mathcal{P}^{no}_b(x, p^2_{\mathrm{T,max}}, p^2_{\mathrm{T,evol}}). \tag{3.15b}$$

3. From all the possible radiator+recoiler combinations, the radiator+recoiler with the hardest (largest) $p^2_{\mathrm{T,evol}}$ is then picked to perform the branching.

4. z is then also sampled to determine virtuality Q^2,

$$\text{FSR} : m_a^2 = Q^2 = \frac{p_{\text{T,evol}}^2}{z(1-z)}, \tag{3.16a}$$

$$\text{ISR} : -m_b^2 = Q^2 = \frac{p_{\text{T,evol}}^2}{(1-z)}. \tag{3.16b}$$

5. Kinematics are then determined from Q^2 and z in rest frame of recoiler+radiator:

   a Define z from energy fractions.

   b Un-branched partons are assumed to be on-shell and the four momentum of the recoiler is redefined.

6. Branchings are then iterated to lower $p_{\text{T,evol}}^2$ values through steps (1)-(5), until $p_{\text{T,evol}}^2$ decreases below $p_{\text{T,min}}^2$ in step (3).

Some additional details need to be added to this to give the complete picture of the parton shower algorithm:

1. The selection of the radiator+recoiler dipoles. This is explained with the example event, $e^+e^- \to \gamma^*/Z^0 \to q\overline{q}g$, where g was the first emission, and now there will be a second emission. In PYTHIA, each coloured parton (*i.e.*q,$\overline{q}$,g) is assigned a colour using the approximation that $N_C \to \infty$. The consequence of this is that $q\overline{q}$ each have the same colour-anticolour, *e.g.* red and anti-red. Then when the gluon is radiated off the quark, it takes the colour of the quark, *e.g.* red and then a new generated anti-colour *e.g.* anti-blue. This then leaves the quark to have the colour blue. QCD dipoles are defined between the three partons which have the same colour-anticolour. In this example, this colour connection is between the $q-g$ and $g-\bar{q}$. In each pair, *e.g.* $q-g$, the quark can act as the radiator and the gluon the recoiler, but also the gluon can be a radiator and the quark a recoiler. Hence there are four QCD dipoles available. However, even though q and $\overline{q}$ carry different colours and so do not have a QCD dipole between them, the q and $\overline{q}$ carry electric charge. Hence, two QED dipoles can be generated between $q-\bar{q}$, where each can radiate a photon, *e.g.* $q \to q\gamma$. Hence in total there are six dipoles. All six dipoles are evolved in $p_{\text{T,evol}}^2$ from the scale of the first gluon emission to the scale of the second emission. The dipole with the largest end $p_{\text{T,evol}}^2$ is chosen as the dipole. This

is then iterated until $p^2_{\mathrm{T,min}}$. The colour flow of an event is generally simple for most splittings in the $N_C \to \infty$ limit. The exception is for $g \to gg$ where colour can be assigned in two in-equivalent ways [51]. This is overcome by modifying the splitting kernel, and is described more in Ref. [54].

2. Correcting the kinematics of the radiator+recoiler system. Here, the radiator is defined as a, and the recoiler as r. The frame is rotated so a moves in $+z$ and r in $-z$ direction. Hence, $m^2_{ar} = (p_a + p_r)^2$. The virtuality of the process, Q^2 needs to be included. This increases E_a from $m_{ar}/2$ to $(m^2_{ar} + Q^2)/2m_{ar}$ and E_r decreases by this. E_b and E_c definitions can then be used to define the transverse momentum of b and c, with the momentum of a still in the $+z$ direction [51],

$$p^2_{\mathrm{T}b,c} = \frac{z(1-z)(m^2_{ar}+Q^2)^2 - m^2_{ar}Q^2}{(m^2_{ar}-Q^2)^2}Q^2 \leq z(1-z)Q^2 = p^2_{\mathrm{T,evol}}. \tag{3.17}$$

To complete the kinematics, the two daughters (b,c) and the recoiler are rotated and boosted back to the original frame. The allowed z range is then defined as [51],

$$z_{min,max} = \frac{1}{2}\left(1 \mp \frac{m^2_{ar} - Q^2}{m^2_{ar} + Q^2}\right). \tag{3.18}$$

Angular ordering from these kinematics is ensured by the choice of using dipoles and p^2_{T} as the evolution variable.

3. Partons up until now have been considered as massless. When considering massive partons, the virtuality, Q^2, is now modified to be $Q^2 = m^2_a - m^2_{a,0}$, where $m^2_{a,0}$ is the on-shell mass. Hence the evolution variable $p^2_{\mathrm{T,evol}}$ is generalised as [51],

$$p^2_{\mathrm{T,evol}} = z(1-z)(m^2_a - m^2_{a,0}). \tag{3.19}$$

This is important when incorporating quarkonia production in the parton shower, as described in section 3.4, because quarkonia have non-negligible mass. The kinematics of the radiator+recoiler dipole also therefore have to be changed to take into account masses, which is explained in more detail in Ref. [57].

4. p^2_{T} is sampled using a running α_s at first order, which is matched at the different quark flavour thresholds [51]. How this is implemented is explained in section 3.2.5.2.

5. The azimuthal angle, ϕ, in the kinematics of the dipole depends on the gluon polarisation. For splittings such as $q \to qg$, this can be selected isotropically. However, ϕ needs to be selected non-isotropically for splittings such as $g \to q\bar{q}$ and $g \to gg$ [51].

6. A matching and merging procedure is performed on the parton shower. As seen in PYTHIA 6, the parton shower can overpopulate the phase space with gluon splittings. This concept was introduced in section 2.2.2 with the idea of implementing real and virtual corrections to cross section calculations. In practice, a veto is put in place to merge the hard matrix element process to the parton shower [51]. A more detailed explanation of matching and merging is described in Ref. [58].

Overall, the p_{T}^2 algorithm implemented in PYTHIA 8 was tested by comparing ALEPH data at the Z^0 peak with the algorithm implementation. This was found to match data quite well, and better than the previous mass-ordered algorithm which was implemented in PYTHIA 6 [51].

3.2.5 Sampling $p_{\mathrm{T,evol}}^2$ and z variables from a distribution

As explained in section 3.2.4, $p_{\mathrm{T,evol}}^2$ and z describe the evolution of the parton shower to lower scales. $p_{\mathrm{T,evol}}^2$ and z are sampled randomly from their respective probability distributions using Monte Carlo techniques. An example of the sampling of z is demonstrated in section 3.2.5.1, and the sampling of $p_{\mathrm{T,evol}}^2$ using the veto algorithm with a fixed α_s and a running first order α_s is discussed in section 3.2.5.2.

3.2.5.1 Simple QCD parton shower overestimate example

This first example shows how z is sampled from the $q \to qg$ QCD splitting kernel. As explained in section 3.2.1, the splitting kernel that describes the $q \to qg$ branching is defined as

$$P_{q\to qg}(z) = \frac{1+z^2}{1-z}. \tag{3.20}$$

Equation (3.20) is actually an approximation of

$$P_{q\to qg}(z,y) = \frac{2}{1-z(1-y)} - (1+z), \tag{3.21}$$

where y is another kinematic variable that describes the splitting of $q \to qg$. However, to simplify the example, only the z dependent form of eq. (3.20) is considered. To sample a value of z from this distribution, one can use inverse transform sampling. The general expression for this is shown in eq. (3.22),

$$z = F^{-1}[F(z_-) + R[F(z_+) - F(z_-)]]. \tag{3.22}$$

$F(z)$ denotes the integral of $f(z)$ and $F^{-1}(z)$ is the inverse function of $F(z)$, where $f(z)$ is the expression to be sampled, which here would be $P_{q\to qg}(z)$. z_- and z_+ are the minimum and maximum allowed z values respectively which z can be sampled from. R is then a random number between 0 and 1 which is used to randomly select a z value in the z_- to z_+ range. However, in most cases the function $f(z)$ is not directly integrable, or the inverse of its integral cannot be found.

Hence, $f(z)$ can be overestimated using a function that is integrable and the inverse can be found. This is called an overestimate function. This fact that the z is sampled from an overestimate function can be corrected for afterwards. The main feature in $P_{q\to qg}(z)$ that needs to be taken care of is the pole of $(1-z)$. Hence the overestimate function $f_{q\to qg}(z)$ can be used,

$$f_{q\to qg}(z) = \frac{2}{1-z}. \tag{3.23}$$

As shown in fig. 3.4, the overestimate function shown in purple (estimate) covers all z values that the $P_{q\to qg}(z)$ does shown in brown (review). Even when $P_{q\to qg}(z, y)$ is dependent on y, it covers this function as well.

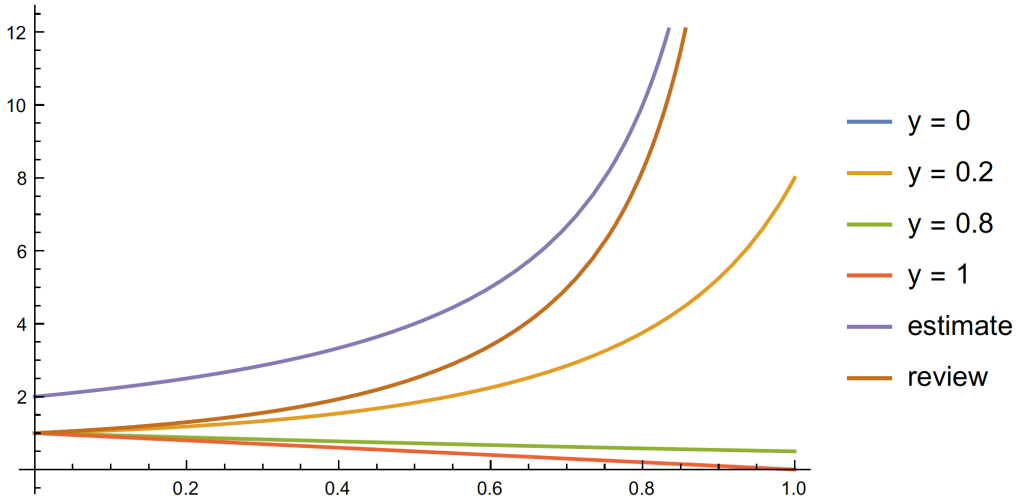

Figure 3.4: Comparison of the overestimate function (purple - estimate) with $P_{q\to qg}(z, y)$ at different fixed y values, and $P_{q\to qg}(z)$ (brown - review) [59].

The integral of $f_{q\to qg}(z)$ is then defined by $F_{q\to qg}(z)$ in eq. (3.24), where the definite integral is defined in eq. (3.25),

$$F_{q\to qg}(z) = \int f_{q\to qg}(z) = -2\ln(z-1) + c \tag{3.24}$$

$$F_{q\to qg} = \int_{z_-}^{z_+} f_{q\to qg}(z) = 2(\ln(z_- - 1) - Ln(z_+ - 1)) \tag{3.25}$$

The inverse of $F_{q\to qg}(z)$ is then defined as,

$$F^{-1}_{q\to qg}(z) = 1 + e^{\frac{-z}{2}}. \tag{3.26}$$

Substituting eq. (3.24) and eq. (3.26) into eq. (3.22), a z value can then be generated from eq. (3.27) named z_g,

$$z_g = 1 + (z_- - 1)^{1-R}(z_+ - 1)^R, \tag{3.27}$$

where R is a random number between 0 and 1. As mentioned previously, z_g is sampled from the overestimate function, $f_{q\to qg}(z)$, not the true function $P_{q\to qg}(z)$, which needs to be corrected for. z_g is substituted into both functions, $f_{q\to qg}(z)$ and $P_{q\to qg}(z)$. The ratio, R_a of $P_{q\to qg}(z)/f_{q\to qg}(z_g)$ is then calculated. If a new random number R' is generated where $R' < R_a$, then z_g is kept. Otherwise, it is thrown away and z_g is generated again until this condition is met. This allows z to be generated following the probability distribution of $P_{q\to qg}(z)$.

3.2.5.2 Veto algorithm

$p^2_{\mathrm{T,evol}}$ is sampled from the Sudakov factor expressed in eq. (3.7). The expanded form of eq. (3.7) which uses a general splitting kernel, $P_{ji}(z)$, is defined as,

$$\Delta_i(Q^2, q^2) = \exp\left\{ -\int_{q^2}^{Q^2} \frac{dp^2_{\mathrm{T,evol}}}{p^2_{\mathrm{T,evol}}} \frac{\alpha_s}{2\pi} \int_{Q_0^2/p^2_{\mathrm{T,evol}}}^{1-Q_0^2/p^2_{\mathrm{T,evol}}} dz P_{ji}(z) \right\}, \tag{3.28}$$

where the limits on z are dependent on the minimum value Q_0^2. Due to the extra exponential suppression of the probability distribution from the Sudakov, the simple inverse transform method shown in eq. (3.22) cannot be used directly. This expression must be altered slightly. This is called the veto algorithm as is defined

in eq. (3.29) which samples $p^2_{\mathrm{T,evol}}$ [13],

$$p^2_{\mathrm{T,evol}} = F^{-1}[F(p^2_{\mathrm{T,evol,0}}) + Ln(R)]. \tag{3.29}$$

$p^2_{\mathrm{T,evol,0}}$ is the starting scale of the parton shower branching, and F^{-1}, F and R follow the same meaning as in section 3.2.5.1. How $p^2_{\mathrm{T,evol}}$ is sampled for fixed α_s and first-order running α_s is explained in the following sections.

3.2.5.2.1 Sample fixed α_s

The function inside the exponential of the Sudakov expression in eq. (3.28) is what is sampled to determine, $p^2_{\mathrm{T,evol}}$. In this example, α_s is fixed. This is redefined as,

$$f(p^2_{\mathrm{T,evol}}) = \frac{\alpha_s}{2\pi}\frac{1}{p^2_{\mathrm{T,evol}}}\int dz P_{ji}(z). \tag{3.30}$$

The method for estimating the integral in eq. (3.30) has been seen before in section 3.2.5.1, where a z value is sampled. This sampled z value can hence be used to find the value of the z integral. Hence, the z integral over the splitting function can then be estimated as a constant, ϵ_{tot}, shown in eq. (3.31),

$$f(p^2_{\mathrm{T,evol}}) = \frac{\alpha_s}{2\pi}\frac{1}{p^2_{\mathrm{T,evol}}}\epsilon_{tot} \tag{3.31}$$

The same method as outlined in section 3.2.5.1 can then be used. The integral of eq. (3.31) is shown in eq. (3.32), with the inverse of the integral defined in eq. (3.33) with a fixed α_s,

$$F(p^2_{\mathrm{T,evol}}) = \int dp^2_{\mathrm{T,evol}} f(p^2_{\mathrm{T,evol}}) = \frac{\alpha_s \epsilon_{tot}}{2\pi}\ln\left(p^2_{\mathrm{T,evol}}\right) + c', \tag{3.32}$$

$$F^{-1}(p^2_{\mathrm{T,evol}}) = \frac{2\pi}{\alpha_s \epsilon_{tot}}\exp(p^2_{\mathrm{T,evol}}). \tag{3.33}$$

Substituting eq. (3.32) and eq. (3.33) into the veto algorithm in eq. (3.29), $p^2_{\mathrm{T,evol}}$ can be sampled from,

$$p^2_{\mathrm{T,evol}} = p^2_{\mathrm{T,evol,0}} R^{\frac{1}{\frac{\alpha_s \epsilon_{tot}}{2\pi}}}. \tag{3.34}$$

An important point to note is that ϵ_{tot} can not only be the overestimate of a single splitting, but a sum of all possible overestimates of different splittings. This means

that competition can be added between the different splittings, and the one that gives the hardest $p^2_{\mathrm{T,evol}}$ splitting is chosen. This becomes significant when including quarkonia production in the parton shower, in section 3.4.

3.2.5.2.2 First-order running α_s

In PYTHIA 8, $p^2_{\mathrm{T,evol}}$ is sampled from running α_s. This complicates the sampling as α_s is now dependent on $p^2_{\mathrm{T,evol}}$ as well as the general equation, shown in eq. (3.35),

$$g(p^2_{\mathrm{T,evol}}) = \frac{\alpha_s(p^2_{\mathrm{T,evol}})}{2\pi}\frac{1}{p^2_{\mathrm{T,evol}}}\epsilon_{tot}. \tag{3.35}$$

First order running α_s is defined in eq. (3.36), where β_0 is defined in eq. (3.37) and is dependent on the number of active quark flavours. Λ^2 is the minimum scale and is also dependent on the number of active quark flavours [60]. β_0 can be redefined as b_0 in eq. (3.38) which is the definition that is used in PYTHIA 8.

$$\alpha_s(p^2_{\mathrm{T,evol}}) = \frac{4\pi}{\beta_0 \ln\left(\frac{p^2_{\mathrm{T,evol}}}{\Lambda^2}\right)} \tag{3.36}$$

$$\beta_0 = 11 - \frac{2}{3}N_f \tag{3.37}$$

$$b_0 = \frac{\beta_0}{2} \tag{3.38}$$

Hence, substituting eq. (3.36) into eq. (3.35), the distribution for $p^2_{\mathrm{T,evol}}$ to be sampled from becomes,

$$g(p^2_{\mathrm{T,evol}}) = \frac{\epsilon_{tot}}{b_0 \ln\left(\frac{p^2_{\mathrm{T,evol}}}{\Lambda^2}\right)}\frac{1}{p^2_{\mathrm{T,evol}}}. \tag{3.39}$$

The integral and inverse integral of $g(p^2_{\mathrm{T,evol}})$ are shown in eqs. (3.40) and (3.41) respectively,

$$G(p^2_{\mathrm{T,evol}}) = \frac{\epsilon_{tot}}{b_0}\left[\ln\left[\ln\left(\frac{p^2_{\mathrm{T,evol}}}{\Lambda^2}\right)\right]\right], \tag{3.40}$$

$$G^{-1}(p^2_{\mathrm{T,evol}}) = \Lambda^2 \exp\left[\exp\left[\frac{p^2_{\mathrm{T,evol}} b_0}{\epsilon_{tot}}\right]\right]. \tag{3.41}$$

Equations (3.40) and (3.41) can then be substituted into the veto algorithm eq. (3.29)

to obtain $p^2_{\mathrm{T,evol}}$ from running α_s,

$$p^2_{\mathrm{T,evol}} = \Lambda^2 \left(\frac{p^2_{\mathrm{T,evol}}}{\Lambda^2} \right)^{R \frac{b_0}{\epsilon_{tot}}}. \tag{3.42}$$

The next section will discuss the theory behind quarkonia production, and how these calculations are implemented into the parton shower discussed above.

3.3 NRQCD Theory

As mentioned in chapter 1, measurements of prompt production of quarkonia were performed by Tevatron for J/ψ production, which showed discrepancies with theoretical models [61]. The main model at the time to try and describe these distributions was the colour singlet (CS) model. These calculations were performed at leading order (LO) in α_s. However, the CS model gave cross section predictions that were orders of magnitude less than what was actually observed at large transverse momentum, p_{T}. Two important developments in the theory have been included over the last two decades to try and explain this discrepancy. Firstly, fragmentation processes dominate at high p_{T}, *i.e.* the ISR and FSR processes shown in fig. 3.1, as most quarkonia are produced from high p_{T} partons. Secondly, the NRQCD factorisation formalism, which is an effective field theory, was introduced. Calculations are not only performed in a series expansion of α_s, but also the relative velocity between the two quarks in the bound state, v. The effect of this is that quarkonia are not only produced in CS states, but also colour octet (CO) states. In this section, the formalism of fragmentation in the quarkonia sector and NRQCD are introduced, and how this new type of production is included into PYTHIA 8 is discussed [62].

3.3.1 Colour singlet production

Quarkonia are mesons that contain the same heavy flavour quark and antiquark, *i.e.* $q\bar{q}$. These can be further subdivided into charmonium, $c\bar{c}$ mesons, and bottomonium, $b\bar{b}$ mesons. In this section, charmonium will be discussed as an example. When describing the different charmonium states, spectroscopic notation will be used, ${}^{2S+1}L_J$, where S is the total spin, L is the orbital angular momentum and J is the total angular momentum ($L+S$). For L, these are usually denoted by letters instead

of numbers, so ($S = 0$, $P = 1$, $D = 2$, $F = 3$). Some examples are J/ψ which is ${}^3S_1$, and different χ_{cJ} states which are ${}^3P_J$, where $J = 0, 1, 2$. Due to the higher orbital angular momentum, the χ_{cJ} states can decay to J/ψ's via the radiation of a photon. Hence, there are different classes of production of J/ψ states, which are summarised as,

1. Displaced: J/ψ's produced directly from b-decays. These are weak interactions, and hence take place at large enough time scales that a displaced vertex can be seen in the detector.

2. Displaced feed-down: there is an intermediate state between the b-decay and the J/ψ, for example the decay chain $B^+ \to \psi(2S)K^+ \to J/\psi\pi^+\pi^-K^+$. These are again weak interactions, but oftentimes displaced and displaced feed-down are not easily distinguishable experimentally. Hence, in experimental papers these two types typically come under one category called displaced.

3. Prompt: J/ψ's are produced directly in the proton-proton collision and decay.

4. Prompt feed-down: J/ψ's are produced from decays of higher angular momentum states such as χ_{cJ} states. These are still prompt decays as they take place through QCD and EM interactions, so they occur at very small timescales. Hence experiments usually classify prompt and prompt feed-down as prompt production.

In this section prompt production will be the main focus.

Charmonium can be thought as being produced in two steps. First, the production of a $c\bar{c}$ pair of quarks. Second, if in the $c\bar{c}$ rest frame, the relative momentum between the quarks is small enough compared to their masses, m_c, then they will bind to form the charmonium bound state. The production of the $c\bar{c}$ pair is from a process which has a virtuality, $Q^2 \geqq 4m_c^2$. To calculate the production cross section, as $Q^2 > m_c^2$, this part of the amplitude can be calculated perturbatively. This is called the short distance part of the calculation, and has a Short Distance Matrix Element (SDME). However, to form the charmonium bound state, this crosses to the region where $Q^2 \sim 4m_c^2$, hence α_s is large, so the amplitude is non-perturbative. This is called the long-distance part and is not directly calculable using perturbative methods. Hence, it is separated from the short distance part and is thought of as a constant to the amplitude of the process. This is called the Long Distance Matrix

Element. This constant is then determined from experimental measurements. An example is the general production cross section of colour singlet J/ψ's, $d\sigma(J/\psi + X)$,

$$d\sigma(J/\psi + X) = d\hat{\sigma}(c\bar{c}[^3S_1(1)) + X)|R_{J/\psi}(0)|^2, \tag{3.43}$$

where $d\hat{\sigma}(c\bar{c}[^3S_1(1)) + X)$ is the short distance calculation, (1) denotes the colour singlet state, and $|R_{J/\psi}(0)|^2$ is the long distance factor [62]. $|R_{J/\psi}(0)|$ physically is the value of the radial wavefunction at the origin of the J/ψ state. This can be determined experimentally by measuring the decay of the J/ψ state to electrons [62],

$$\Gamma(J/\psi \to e^+e^-) \approx \frac{4\alpha^2}{9m_c^2}|R_{J/\psi}(0)|^2. \tag{3.44}$$

This can be expressed for any other quarkonium state [62], for example the χ_{cJ} states,

$$d\sigma(\chi_{cJ} + X) = d\hat{\sigma}(c\bar{c}[^3P_J(1)) + X)|R'_{\chi_c}(0)|^2. \tag{3.45}$$

These types of production processes are usually called short distance CS model production [62].

3.3.2 Colour singlet fragmentation

However, the short distance CS model showed discrepancies with data from the Tevatron. First, the production of J/ψ states was underestimated at high p_T by orders of magnitude [62]. An example of a short distance process is $Z^0 \to J/\psi\, gg$, which is shown in fig. 3.5a [63]. Even though the $gg \to J/\psi\, g$ is one of the primary mechanisms from $p\bar{p}$ or pp collisions, $Z^0 \to J/\psi\, gg$ is a simpler example to discuss as it factorises out colour, and the virtuality of the process is large.

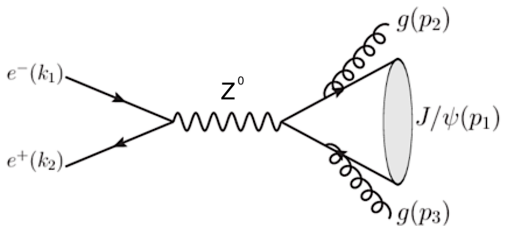

(a) $Z^0 \to J/\psi\, gg$ [63].

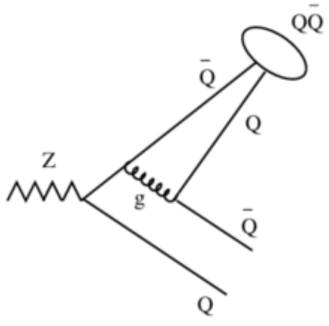

(b) $Z^0 \to J/\psi\, c\bar{c}$ [64].

Figure 3.5: Feynman diagrams comparing the short distance processes in $Z^0 \to J/\psi\, gg$ and fragmentation processes in $Z^0 \to J/\psi\, c\bar{c}$.

This process has a small BF $\sim 10^{-7}$, due to a contributing factor to the BF of $|R_{J/\psi}(0)|^2/(m_c M_Z^2)$. The $c\bar{c}$ pair is produced on a scale of M_Z from the Z^0, hence initially has a transverse separation of $\sim 1/M_Z$. However, the $c\bar{c}$ pair needs to become a bound state. The $|R_{J/\psi}(0)|^2/(m_c M_Z^2)$ factor is hence proportional to the probability that the $c\bar{c}$ pair is produced in a region with size $1/(m_c M_Z^2)$ to form the bound state. Hence, the BF for the short distance processes is suppressed by a factor of m_c^2/M_Z^2 [16].

In the early 1980's, it was theorised that short distance processes do not dominate the production at high p_{T}, but instead production is through fragmentation. An example of colour singlet fragmentation is shown in fig. 3.5b, with the decay $Z^0 \to J/\psi\, c\bar{c}$. Fragmentation is the mechanism where the Z^0 decays to a set of high energy partons, and one of these partons splits into a charmonium state along with other partons. This has already been seen in the context of proton PDFs in section 2.3 and parton showers in section 3.2. The fragmentation function $D(z, \mu)$ describes the probability that a parton with mass $< \mu$ will split to a charmonium state with longitudinal momentum fraction z, where μ is the scale of the process involved. These functions can be calculated using perturbative QCD.

The $Z^0 \to J/\psi\, gg$ and $Z^0 \to J/\psi\, c\bar{c}$ BF's can be compared, where the first is through short distance processes and the second is through fragmentation. The resulting calculations show that $Z^0 \to J/\psi\, c\bar{c}$ BF is $\sim 10^{-5}$ which is 100 times larger than the $Z^0 \to J/\psi\, gg$ BF. This is a surprising result, considering they are calculated at the same order in α_s, of ${\alpha_s}^3$. In the fragmentation case, $D_{c\to J/\psi}(z, \mu)$ is calculated at leading order α_s at the scale of $\mu = m_c$, and then evolved to larger scales $\mu = M_Z/2$ using the Altarelli-Parisi evolution equations discussed in section 2.3. This sums up the leading logs of μ/m_c. Hence, the probability for the $c\bar{c}$ pair to combine to a charmonium state is only suppressed by $m_c^3/m_c^3 = 1$, unlike for $Z^0 \to J/\psi\, gg$ which is suppressed by m_c^2/M_Z^2. This section will describe a walk through of the calculation of the fragmentation $D_{c\to J/\psi}(z, \mu)$. This and similar fragmentation functions are then used as inputs into the parton shower of the PYTHIA 8 framework. This is because these fragmentation functions act like the QCD splitting kernels which were introduced in sections 2.3 and 3.2. This will be described in more detail in section 3.4.2 [16].

To calculate this, the general process of $Z^0 \to J/\psi\,(E)+X$ is used. This is because for both production mechanisms, via the short distance mechanism and fragmentation,

production via Z^0 provides an easier calculation for both aspects, due to it's large virtuality and factorisation of colour. The differential equation calculated for the fragmentation production of J/ψ at energy E is,

$$d\Gamma(Z^0 \to J/\psi\,(E) + X) = \sum_i \int_0^1 dz d\hat{\Gamma}(Z^0 \to i(E/z) + X, \mu) D_{i\to J/\psi}(z, \mu), \quad (3.46)$$

where all parameters have been defined previously, and the sum is over all final state partons [16].

Physically, this means a parton i of energy E/Z splits into a J/ψ of energy E and longitudinal momentum fraction z, and another parton. The different energy scales are factored into different parts. The E scale is factored into $d\hat{\Gamma}$, whereas the m_c scale is factored into $D_{i\to J/\psi}$. This factored form is created by introducing a factorisation scale μ, which is chosen so that E is on the order of μ to remove the large E/μ logarithms that occur. The large logs of μ/m_c are then summed up in the standard way of using evolution equations,

$$\mu\frac{\partial}{\partial\mu} D_{i\to J/\psi}(z, \mu) = \sum_j \int_z^1 \frac{dy}{y} P_{i\to j}(z/y, \mu) D_{j\to J/\psi}(y, \mu), \quad (3.47)$$

where the Altarelli-Parisi function, $P_{i\to j}(z/y, \mu)$, describes splitting parton i to j with a longitudinal momentum fraction of z/y [16]. This was introduced in section 2.3. An example is $c \to c$ [16],

$$P_{c\to c}(x, \mu) = \frac{\alpha_s(\mu)}{2\pi}\left(\frac{4}{3}\frac{1+x^2}{(1-x)_+} + 2\delta(1-x)\right). \quad (3.48)$$

$D_{i\to J/\psi}(z, m_c)$ is then used as a boundary condition for eq. (3.47). Here only $D_{c\to J/\psi}(z, \mu)$ is being calculated, so only the c and $\bar{c}$ are kept in eq. (3.46), hence,

$$\frac{d\Gamma}{dz}(Z^0 \to J/\psi\,(E) + X) = 2\hat{\Gamma}(Z^0 \to c\bar{c}) D_{c\to J/\psi}(z, M_Z/2), \quad z = \frac{2E}{M_Z}, \quad (3.49)$$

where the factor of two accounts for contributions from c and $\bar{c}$ [16]. The only term that survives at leading order α_s in eq. (3.47) is [16],

$$\mu\frac{\partial}{\partial\mu} D_{c\to J/\psi}(z, \mu) = \int_z^1 \frac{dy}{y} P_{c\to c}(z/y, \mu) D_{c\to J/\psi}(y, \mu). \quad (3.50)$$

The inclusive J/ψ production rate is then found by integrating eq. (3.49) over energy [16],

$$\Gamma(Z^0 \to J/\psi + X) = 2\hat{\Gamma}(Z^0 \to c\bar{c}) \int_0^1 dz D_{c\to J/\psi}(z, m_c). \tag{3.51}$$

$\mu = m_c$ as at leading order α_s, $\int_0^1 dx P_{c\to c}(x,\mu) = 0$ is satisfied. This means the fragmentation probability $\int_0^1 dz D_{c\to J/\psi}(z,\mu)$ does not evolve with μ. Hence, the fragmentation probability $\int_0^1 dz D_{c\to J/\psi}(z)$ can be calculated by dividing the decay rate for $Z^0 \to J/\psi\, c\bar{c}$ by the decay rate for $Z^0 \to c\bar{c}$, where each are calculated at leading order in α_s. These are calculated using the usual Feynman rules and Fermi's golden rule.

The final fragmentation probability for $c \to J/\psi\, c$ is then derived to be,

$$\begin{aligned}\int_0^1 dz\; D_{c\to J/\psi}(z) \;=\; & \frac{8\alpha_s^2 |R(0)|^2}{27\pi m_c} \int_0^\infty ds\; \frac{1}{(s-m_c^2)^4} \int_0^1 dz\; \theta\left(s - \frac{4m_c^2}{z} - \frac{m_c^2}{1-z}\right) \\ & \left((s^2 - 2m_c^2 s - 47 m_c^4) \;-\; z(s-m_c^2)(s-9m_c^2) \;+\; 4\frac{z(1-z)}{2-z} s(s-m_c^2) \right. \\ & \left. - 4\frac{8-7z-5z^2}{2-z} m_c^2 (s-m_c^2) \;+\; 12\frac{z^2(1-z)}{(2-z)^2}(s-m_c^2)^2 \right).\end{aligned} \tag{3.52}$$

where $\sqrt{s}$ is the centre of mass energy of the fragmenting c (or $\bar{c}$) quark, and the other parameters have already been defined. The θ function gives the minimum allowed s value [16]. When substituting eq. (3.52) into the general equation, eq. (3.46), which composed of a short distance component and a fragmentation component, it is observed that both components contain a SDME and an LDME part. This is similar to what is seen in eq. (3.43).

What makes these fragmentation functions special is that they are universal, and are independent of the starting collision, such e^+e^- collisions or proton-proton collisions. For example, the fragmentation function derived in eq. (3.52) from the process $Z^0 \to J/\psi\,(E) + X$ would be the same even if it was calculated from a different starting process. An example for a general proton-proton collision is shown in eq. (3.53),

$$\begin{aligned}d\sigma(AB \to H(p_T) + X) = & \sum_{ijk} \int_0^1 dx_1 f_{j/A}(x_1) \int_0^1 dx_2 f_{k/B}(x_2) \\ & \times \int_0^1 dz\; d\hat{\sigma}(jk \to i(p_T/z) + X) D_{i\to H}(z),\end{aligned} \tag{3.53}$$

where the functions f are the usual proton PDF's and H is a generic quarkonium particle [62]. Also, since $D_{c\to J/\psi}(z)$ is a probability distribution, this does not necessarily need to take place in the first splitting. For example, five QCD type splittings could take place before a $c \to J/\psi\, c$ takes place. This type of input is ideal for an iterative type of process, for example a parton shower. More details on this will be discussed in the next section.

3.3.3 NRQCD formalism + colour octet production

The colour singlet model with short distance production processes and with fragmentation included better models the high p_{T} region in prompt J/ψ production than just short distance production alone. However, there are still some inconsistencies in the theory. Firstly, logarithmic infrared divergences still appear in leading order CS state calculations of the cross section for P-wave states, *i.e.* χ_{cJ} [62]. Secondly, the relative velocity of the c and $\overline{c}$ to form the bound state have not been considered, where v^2/c^2 can be as large as $1/3$ [65].

Infrared divergences emerge from the radiation of a soft (low energy) gluon. These type of divergences appear in the S-wave CS cross sections also. However, as these are linear infrared divergences, they are able to be factored into the non-perturbative part of the cross section, $|R(0)|^2$. However, in the P-wave states, these divergences happen to be logarithmic, so can not be absorbed into the non-perturbative part of the cross section. Hence, the CS model does not fully describe the production of quarkonium states [62].

To tackle this, the different energy scales of the quarkonium bound states, $Q\bar{Q}$ need to be considered. The first scale is the mass of the quark, M_Q, which gives the allowed distance range for $Q\bar{Q}$ annihilation and creation. $M_Q v$ gives the typical momentum of the quark in the bound state and is inversely proportional to its size. Finally $M_Q v^2$ represents the kinetic energy and gives the idea of the constituents interaction time. As $M_Q \to \infty$, these scales can be very different [65],

$$(M_Q v^2)^2 \ll (M_Q v)^2 \ll M_Q^2. \tag{3.54}$$

To keep track of this scale hierarchy, the NRQCD effective field theory was introduced. Not only in this theory are power series in α_s considered, but also a power

series in the relative velocity, v, between the constituents in the bound state. In NRQCD, the χ_{cJ} wavefunction, $|\chi_{QJ}\rangle$, is composed into its different Fock states, each of which represents a physical quarkonium state. The consequence for this expansion is that not only are colour singlet states are produced, but also in colour octet states, shown in eq. (3.55),

$$|\chi_{QJ}\rangle = O(1)\left|Q\bar{Q}[^3P_J^{(1)}]\right\rangle + O(v)\left|Q\bar{Q}[^3S_1^{(8)}]g\right\rangle + ... \tag{3.55}$$

where the superscripts (1) and (8) represent the colour singlet and colour octet states respectively [65]. The presence of the colour octet states removes these infrared divergences for soft gluon emission, as the $c\bar{c}$ pair can be in a colour octet state before the gluon is radiated. These colour octet states are not physical final states, as they carry colour. But these states only exist for a short period of time before they radiate a gluon and end up as a colour singlet final state. Hence, the colour octet state can radiate in a parton shower just like a gluon. Another way to think of this is that the gluon wavelength inside the quarkonium bound state becomes larger than the bound states size, hence the bound state can not only be in a colour singlet configuration [65]. When calculating this as a physical cross section, this returns back the same form as in eq. (3.45),

$$\begin{aligned} d\sigma(\chi_{cJ} + X) = {} & d\hat{\sigma}(c\bar{c}(^3P_J(1)) + X)\langle\mathcal{O}_1^{\chi_{cJ}}(^3P_J)\rangle \\ & + (2J+1)d\hat{\sigma}(c\bar{c}(^3S_1(8)) + X)\langle\mathcal{O}_8^{\chi_c}\rangle, \end{aligned} \tag{3.56}$$

where the short distance parts are factored into $d\sigma$ and the long distance parts are factored into $\langle\mathcal{O}_1^{\chi_{cJ}}(^3P_J)\rangle$ and $\langle\mathcal{O}_8^{\chi_c}\rangle$ which are the Long Distance Matrix Elements (LDMEs) for the colour singlet and colour octet respectively [62]. The only addition is now the CO part of the calculation. The CS parts of the NRQCD calculation are nearly the same as when just using the CS model, and $\langle\mathcal{O}_1^{\chi_{cJ}}(^3P_J)\rangle$ can be related to $|R'_{\chi_c}(0)|^2$ using [62],

$$\langle\mathcal{O}_1^{\chi_{cJ}}(^3P_J)\rangle = (2J+1)\frac{9}{2\pi}|R'_{\chi_c}(0)|^2. \tag{3.57}$$

This NRQCD formalism can also be extended to not only the P-wave states, but also the S-wave states. Equation (3.58) shows that the colour octet states also appear

for the S-wave states [65],

$$|J/\psi\rangle = O(1)\left|Q\bar{Q}[^3S_1^{(1)}]\right\rangle + O(v)\left|Q\bar{Q}[^3P_J^{(8)}]g\right\rangle + O(v^2)\left|Q\bar{Q}[^3S_1^{(1,8)}]gg\right\rangle + O(v^2)\left|Q\bar{Q}[^1S_0^{(8)}]g\right\rangle + O(v^2)\left|Q\bar{Q}[^3D_J^{(1,8)}]gg\right\rangle + ... \tag{3.58}$$

Hence, the general cross section for any quarkonium, H, can be factorised as,

$$d\sigma(H+X) = \sum_n d\hat{\sigma}(c\bar{c}(n)+X)\langle\mathcal{O}_n^H\rangle, \tag{3.59}$$

where the sum is for the different physical states of the quarkonium, colour singlet or octet [62].

3.3.4 NRQCD formalism + fragmentation

To fully describe the data, the NRQCD formalism which introduced the colour octet states for short distance processes, and the fragmentation formalism need to be included together. The fragmentation functions can now be reformulated to not only include the colour singlet fragmentation, but also colour octet contributions. The general form is hence,

$$D_{i\to H}(z,\mu) = \sum_n d_{i\to n}(z,\mu)\langle\mathcal{O}_n^H\rangle, \tag{3.60}$$

where the sum is over the contributing colour singlet and colour octet states, and $\langle\mathcal{O}_n^H\rangle$ are the corresponding LDMEs [62]. An example fragmentation function for the χ_{cJ} states is [62],

$$\begin{aligned} D_{g\to\chi_{cJ}}(z,2m_c) = {} & \frac{\alpha_s^2(2m_c)}{m_c^5} d_J(z)\langle\mathcal{O}_1^{\chi_{cJ}}(^3P_J)\rangle \\ & + \frac{\pi\alpha_s(2m_c)}{24m_c^3}\delta(1-z)\langle\mathcal{O}_8^{\chi_{cJ}}(^3S_1)\rangle. \end{aligned} \tag{3.61}$$

The fragmentation function, $d_J(z)$, is exactly the same as that calculated from the colour singlet model. The fragmentation function for the colour octet state is represented as a delta function. This is due to the short existence time. This can also be thought of as a top hat function with a narrow width, which represents the

size of the quarkonium state. Again, these fragmentation functions are universal, and can be included in any type of collision process [62],

$$d\sigma(p\bar{p} \to H(p_T) + X) = \sum_{jk} \int_0^1 dx_1 f_{j/p}(x_1) \int_0^1 dx_2 f_{k/\bar{p}}(x_2) \\ \text{x} \int_0^1 dz d\hat{\sigma}(jk \to g(p_T/z) + X, \mu_{frag}) D_{g\to H}(z, mu_{frag}). \tag{3.62}$$

Feynman diagrams summarising the different contributions from CS and CO states, including fragmentation are shown in fig. 3.6 [64].

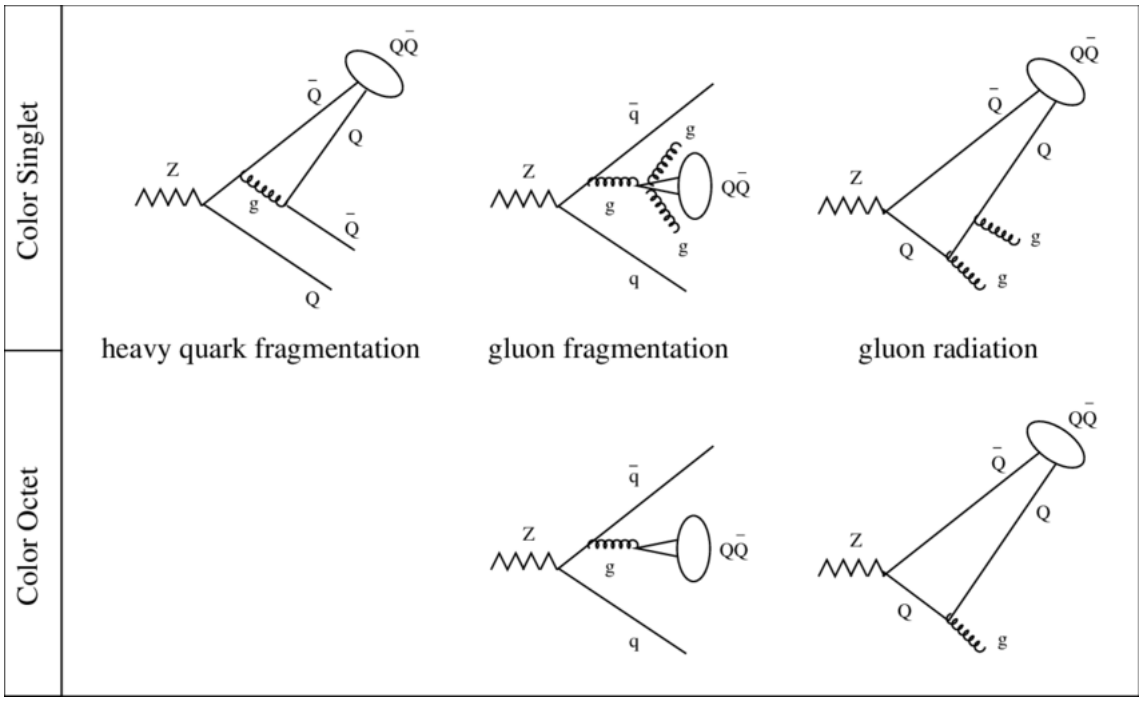

Figure 3.6: Feynman diagrams for various leading order processes for the production of colour singlet and colour octet states [64].

In the current version of PYTHIA 8, NRQCD formalism is used, where colour octet states are produced, as introduced in section 3.3.3. These only include the short distance processes, however. In Monte Carlo generators, short distance processes are called hard processes. These were introduced in sections 3.1 and 3.1.1. To truly describe data, the fragmentation contributions of colour singlet and colour octet states also need to be included. This is the topic of discussion in the next section, of how these fragmentation functions were included into PYTHIA 8.

3.4 Fragmentation implementation into PYTHIA 8

In the current implementation of PYTHIA 8, only the short distance processes (hard processes) of CS and CO production are included. Hence the fragmentation components of CS and CO production need to be included. This is achieved by incorporating the CS and CO fragmentation functions derived for different quarkonia (onium) into the parton shower framework in PYTHIA 8. The subsequent sections will detail its implementation and how it's run. The implementation is then tested by comparing the output with ARIADNE [53–55], another event generator, and then comparing the results with published data.

3.4.1 Program settings and code framework

PYTHIA 8 is an open source C++ based program, with each part of the generation split into different header and source files and classes. The parton shower is implemented into separate files. The FSR shower is handled in `SimpleTimeShower.cc` and ISR in `SimpleSpaceShower.cc`. Onium fragmentation is only included in the FSR shower for now. However it can be easily implemented in ISR using the same splittings as for FSR. Hence most changes are in the `SimpleTimeShower` methods. A separate file has been included in the PYTHIA 8 framework, called `OniaTools.cc`. This includes functions for the onium fragmentation functions which are then used in `SimpleTimeShower.cc`.

Various onium fragmentation processes have been implemented into PYTHIA. An example fragmentation process is $c \to J/\psi\,(1)c$, where (1) denotes a colour singlet state. The user has a choice whether these processes are turned on or off, where each process is set by a different flag. These flags are defined in an .xml file called `OniaShower.xml` and by default they are turned off. A summary of the different flags are shown in table 3.1. The onium production is separated into charmonium and bottomonium production. Charmonium can fragment from either a c, $\bar{c}$ or g, and bottomonium from a b, $\bar{b}$ or g. Charmonium and bottomonium can either be produced in ${}^1S_0$, ${}^3S_1$ or ${}^3P_J$ states, where J=0,1,2, with each in colour singlet or colour octet states. The flags for turning on individual processes are shown in purple in table 3.1. The nomenclature of the flag names follows a set pattern. An example flag for the $c \to J/\psi\,(1)c$ process is,

```
CharmoniumShower:c2ccbar(3S1)[3S1(1)]c = {on,off} ,
```

where `CharmoniumShower` is used as a J/ψ is a $c\bar{c}$ state. The pattern after the colon is `(initialStatePartons)2(finalStatePartons)`, where J/ψ is written as `ccbar(3S1)[3S1(1)]`. `3S1` denotes the ${}^3S_1$ state, and the `(1)` in brackets denotes it is produced in a colour singlet state. In this configuration there are two ${}^3S_1$ states, J/ψ and $\psi(2S)$, where $\psi(2S)$ is higher mass. Hence, `{on,off}` turns J/ψ production on, but leaves $\psi(2S)$ off. However, any arbitrary number of resonances can be included. The corresponding states for turning on each process are shown in light blue in table 3.1, with their corresponding MC PID numbers. Each process is associated with a Long Distance Matrix Element (LDME), as explained in section 3.3 with the notation of $\langle \mathcal{O}_1^{\chi_{cJ}}({}^3P_J) \rangle$ as an example, which is determined from fitting these functions to data distributions or lattice QCD calculations. The LDME value for each process is shown in the red flags in table 3.1. These are the same values used for the colour singlet and octet hard production processes, which are declared in `OniaProcesses.xml`. The flags in green turn on a range of processes at once, for example all of the onium processes, with `OniaShower:all = on`. The flags in yellow were used for testing the implementation of the parton shower. For example, to have α_s at a fixed value rather than running. Another example is not allowing QCD splittings to happen in the parton shower, but only allow splittings for onium processes.

Production	Flag	Purpose
All Production	`OniaShower:all = off`	All onia
	`OniaShower:all(1S0) = off`	All ${}^1S_0$ onia
	`OniaShower:all(3S1) = off`	All ${}^3S_1$ onia
	`OniaShower:all(3PJ) = off`	All ${}^3P_J$ onia
	`CharmoniumShower:all = off`	All charmonia
	`BottomoniumShower:all = off`	All bottomonia
Charmonium ${}^1S_0$ States	`CharmoniumShower:states(1S0) = {441}`	η_c
	`CharmoniumShower:O(1S0)[1S0(1)] = {1.16}`	η_c
	`CharmoniumShower:O(1S0)[3S1(8)] = {0.0119}`	η_c
	`CharmoniumShower:c2ccbar(1S0)[1S0(1)]c = {off}`	η_c
	`CharmoniumShower:g2ccbar(1S0)[1S0(1)]g = {off}`	η_c
	`CharmoniumShower:g2ccbar(1S0)[3S1(8)] = {off}`	η_c
Charmonium ${}^3S_1$ States	`CharmoniumShower:states(3S1) = {443,100443}`	J/ψ, $\psi(2S)$
	`CharmoniumShower:O(3S1)[3S1(1)] = {1.16,0.76}`	J/ψ, $\psi(2S)$
	`CharmoniumShower:O(3S1)[3S1(8)] = {0.0119,0.0050}`	J/ψ, $\psi(2S)$
	`CharmoniumShower:c2ccbar(3S1)[3S1(1)]c = {off,off}`	J/ψ, $\psi(2S)$
	`CharmoniumShower:g2ccbar(3S1)[3S1(1)]gg = {off,off}`	J/ψ, $\psi(2S)$
	`CharmoniumShower:g2ccbar(3S1)[3S1(8)] = {off,off}`	J/ψ, $\psi(2S)$
Charmonium ${}^3P_J$ States	`CharmoniumShower:states(3PJ) = {10441,20443,445}`	$\chi_{c0},\chi_{c1},\chi_{c2}$
	`CharmoniumShower:O(3PJ)[3PJ(1)] = {0.05,0.05,0.05}`	$\chi_{c0},\chi_{c1},\chi_{c2}$
	`CharmoniumShower:O(3PJ)[3S1(8)] = {0.0031,0.0031,0.0031}`	$\chi_{c0},\chi_{c1},\chi_{c2}$
	`CharmoniumShower:c2ccbar(3PJ)[3PJ(1)]c = {off,off,off}`	$\chi_{c0},\chi_{c1},\chi_{c2}$
	`CharmoniumShower:c2ccbar(3PJ)[3S1(8)]c = {off,off,off}`	$\chi_{c0},\chi_{c1},\chi_{c2}$
	`CharmoniumShower:g2ccbar(3PJ)[3PJ(1)]g = {off,off,off}`	$\chi_{c0},\chi_{c1},\chi_{c2}$
	`CharmoniumShower:g2ccbar(3PJ)[3S1(8)] = {off,off,off}`	$\chi_{c0},\chi_{c1},\chi_{c2}$
Bottomonium ${}^1S_0$ States	`BottomoniumShower:states(1S0) = {551}`	η_b
	`BottomoniumShower:O(1S0)[1S0(1)] = {1.0}`	η_b
	`BottomoniumShower:O(1S0)[3S1(8)] = {0.15}`	η_b
	`BottomoniumShower:b2bbbar(1S0)[1S0(1)]b = {off}`	η_b
	`BottomoniumShower:g2bbbar(1S0)[1S0(1)]g = {off}`	η_b
	`BottomoniumShower:g2bbbar(1S0)[3S1(8)] = {off}`	η_b
Bottomonium ${}^3S_1$ States	`BottomoniumShower:states(3S1) = {553,100553,200553}`	$\Upsilon(1S,2S,3S)$
	`BottomoniumShower:O(3S1)[3S1(1)] = {9.28,4.63,3.54}`	$\Upsilon(1S,2S,3S)$
	`BottomoniumShower:O(3S1)[3S1(8)] = {0.15,0.045,0.075}`	$\Upsilon(1S,2S,3S)$
	`BottomoniumShower:b2bbbar(3S1)[3S1(1)]b = {off,off,off}`	$\Upsilon(1S,2S,3S)$
	`BottomoniumShower:g2bbbar(3S1)[3S1(1)]gg = {off,off,off}`	$\Upsilon(1S,2S,3S)$
	`BottomoniumShower:g2bbbar(3S1)[3S1(8)] = {off,off,off}`	$\Upsilon(1S,2S,3S)$
Bottomonium ${}^3P_J$ States	`BottomoniumShower:states(3PJ) = {10551,20553,555}`	$\chi_{b0},\chi_{b1},\chi_{b2}$
	`BottomoniumShower:O(3PJ)[3P0(1)] = {0.085,0.085,0.085}`	$\chi_{b0},\chi_{b1},\chi_{b2}$
	`BottomoniumShower:O(3PJ)[3S1(8)] = {0.04,0.04,0.04}`	$\chi_{b0},\chi_{b1},\chi_{b2}$
	`BottomoniumShower:b2bbbar(3PJ)[3PJ(1)]b = {off,off,off}`	$\chi_{b0},\chi_{b1},\chi_{b2}$
	`BottomoniumShower:b2bbbar(3PJ)[3S1(8)]b = {off,off,off}`	$\chi_{b0},\chi_{b1},\chi_{b2}$
	`BottomoniumShower:g2bbbar(3PJ)[3PJ(1)]g = {off,off,off}`	$\chi_{b0},\chi_{b1},\chi_{b2}$
	`BottomoniumShower:g2bbbar(3PJ)[3S1(8)] = {off,off,off}`	$\chi_{b0},\chi_{b1},\chi_{b2}$
Tests	`CharmoniumShower:test = off`	No QCD
	`OniaShower:alphaSvalue = 0.4`	Fixed α_s value

Table 3.1: Summary of the different flags incorporated into PYTHIA 8. Green flags turn on multiple processes at once. Blue gives the MC PID number. Purple gives the processes available for each particle type and the red gives the LDME related to these processes. Yellow flags are used for testing the parton shower.

3.4.2 Sampling variables from the quarkonium fragmentation distributions

In this section, the sampling and defining of the overestimate functions of the fragmentation functions that describe the quarkonia production are discussed, which follow similar methods to those presented in section 3.2.5.

A summary of the different fragmentation functions that need to be sampled are highlighted in the purple flags in table 3.1. The fragmentation functions themselves, along with the papers that derive them, are shown in table A.1 in section A.1 in the appendix. Three main examples are discussed in this section, $c \to J/\psi(1)c$, $g \to J/\psi(1)gg$ and $g \to J/\psi(8)$. The rest of the splitting kernels, such as $g \to \eta_c(1)g$ follow a similar pattern to determining the overestimates.

3.4.2.1 Sampling $c \to J/\psi\, c$ distribution

The expression for the $c \to J/\psi(1)c$ branching was derived from first principles in section 3.3.2, and the final expression is shown in eq. (3.52). This expression is however a function of s and z, where s is the scale of the virtuality of the process and z is the energy fraction carried by the J/ψ after branching. The overall aim is to incorporate this splitting into the PYTHIA 8 parton shower. In PYTHIA 8, the evolution variables of the parton shower are not s and z, but instead $p^2_{\mathrm{T,evol}}$ and z. Hence the variables in the expression need to be transformed from s and z to $p^2_{\mathrm{T,evol}}$ and z. A simplified form of eq. (3.52) is,

$$dP(s,z) = \frac{8\alpha_s^2 M^2}{27\pi m_c} f(s,z) ds dz, \tag{3.63}$$

where M^2 is the LDME, and α_s is the strong coupling constant. As discussed in section 3.2.4, since c is a massive quark, the relation of the scale s with $p^2_{\mathrm{T,evol}}$ is,

$$s = \frac{p^2_{\mathrm{T,evol}}}{z(1-z)} + m_c^2. \tag{3.64}$$

The transformation of s and z, to $p^2_{\mathrm{T,evol}}$ and z can be performed using a Jacobian,

$$ds dz = \frac{1}{1-z} dp^2_{\mathrm{T,evol}} dz, \tag{3.65}$$

which can be substituted into eq. (3.63) to give,

$$dP(p^2_{\mathrm{T,evol}}, z) = \frac{8\alpha_s^2 M^2}{27\pi m_c} f(p^2_{\mathrm{T,evol}}, z) \frac{1}{z(1-z)} dp^2_{\mathrm{T,evol}} dz. \tag{3.66}$$

As there are no obvious divergences in z, this can be sampled uniformly using

$$z = z_c + (1 - 2z_c)R, \tag{3.67}$$

where z_c is the minimum kinematically allowed z and R is a random number. Equation (3.66) can then be rearranged to find an overestimate for the function,

$$dP(p^2_{\mathrm{T,evol}}, z) = \frac{dp^2_{\mathrm{T,evol}}}{p^2_{\mathrm{T,evol}}} dz \frac{8\alpha_s^2 M^2}{27\pi m_c} f(p^2_{\mathrm{T,evol}}, z) \frac{p^2_{\mathrm{T,evol}}}{z(1-z)}, \tag{3.68}$$

then,

$$dP(p^2_{\mathrm{T,evol}}, z) = \frac{dp^2_{\mathrm{T,evol}}}{p^2_{\mathrm{T,evol}}} dz \frac{8\alpha_s^2 M^2}{27\pi m_c} F(p^2_{\mathrm{T,evol}}, z) \tag{3.69}$$

where,

$$dF(p^2_{\mathrm{T,evol}}, z) = f(p^2_{\mathrm{T,evol}}, z) \frac{p^2_{\mathrm{T,evol}}}{z(1-z)}. \tag{3.70}$$

Hence, if $F(p^2_{\mathrm{T,evol}}, z) < 1.0$, then

$$dP(p^2_{\mathrm{T,evol}}, z) < \frac{dp^2_{\mathrm{T,evol}}}{p^2_{\mathrm{T,evol}}} dz \frac{8\alpha_s^2 M^2}{27\pi m_c}. \tag{3.71}$$

To find the overestimate, z is integrated out, and then one α_s is left as running, and then the other is fixed at the mass of the onium (J/ψ), m_O^2,

$$dP(p^2_{\mathrm{T,evol}}, z) = \frac{dp^2_{\mathrm{T,evol}}}{p^2_{\mathrm{T,evol}}} \frac{\alpha_s(p^2_{\mathrm{T,evol}})}{\alpha_0} \int dz \frac{8\alpha_s(m_O^2)\alpha_0 M^2}{27\pi m_c}. \tag{3.72}$$

The limits of integration for the z are then taken, which are $z_c < z < 1 - z_c$,

$$dP(p^2_{\mathrm{T,evol}}, z) = \frac{dp^2_{\mathrm{T,evol}}}{p^2_{\mathrm{T,evol}}} \frac{\alpha_s(p^2_{\mathrm{T,evol}})}{\alpha_0} (1 - 2z_c) \frac{8\alpha_s(m_O^2)\alpha_0 M^2}{27\pi m_c}, \tag{3.73}$$

hence,

$$dP(p^2_{\mathrm{T,evol}}, z) = \frac{dp^2_{\mathrm{T,evol}}}{p^2_{\mathrm{T,evol}}} \frac{\alpha_s(p^2_{\mathrm{T,evol}})}{\alpha_0} C, \tag{3.74}$$

where C can now be used as the overestimate of the function,

$$C = (1 - 2z_c)\frac{8\alpha_s(m_O^2)\alpha_0 M^2}{27\pi m_c}.$$

The general procedure for the generation of $c \to J/\psi\,(1)c$ can be summarised as:

1. PYTHIA generates a $p^2_{\mathrm{T,evol}}$ from using the overestimate of C.
2. Generate z from a uniform z distribution.
3. Restart from step 1 if $z(1-z)W^2 \leq p^2_{\mathrm{T,evol}}$, where W is the mass of the dipole.
4. Restart from step 1 if $p^2_{\mathrm{T}} = p^2_{\mathrm{T,evol}} - (1-z)m_O^2 - zm_c^2 < 0$, where p^2_{T} is the physical kinematic p_{T} and not the evolution of the parton shower p_{T}.
5. Calculate s.
6. Restart from step 1 if the result is outside allowed limits, $0 < s < \infty$ and $0 < z < 1$.
7. Calculate the weight $F(p^2_{\mathrm{T,evol}}, z)$ and restart from 1 if less than a random number. Emit warning if > 1 or < 0 to ensure the validity of the overestimate.

A more detailed procedure for the $c \to J/\psi\,(1)c$ generation is discussed in section B.1.

3.4.2.2 Sampling $g \to J/\psi\, gg$

The fragmentation function of the $g \to J/\psi\, gg$ is a more complex expression to find an overestimate for, due to the fact it is a one to three body branching. The expression for this is shown in section A.4 in the appendix, and is dependent on three variables, r, y and z. z is the normal splitting function definition, $r = 4m_c^2/s$ where s is the virtuality of the process, and $y = p_O \cdot q/s$ where p_O is the four momentum of the J/ψ and q is the four momentum of the mother gluon. These three variables, r, y, z, need to be translated to the evolution variables of the parton shower. Two of these evolution variables are z and $p^2_{\mathrm{T,evol}}$. The third evolution variable was decided to be the combined mass of the two final state gluons which are produced in the branching, m^2_{gg}. This is because the di-gluon can be handled as a single body in the initial generation, *i.e.* to compute an overestimate, then this can be corrected for afterwards where the di-gluon is "decayed" to two gluons in the final kinematics.

The notation (p_+, p_-, p_x, p_y) is used, where the individual components are the light-cone definitions of the kinematics. This uses the rules that p·q $= (p_+q_- + p_-q_+)/2 - p_xq_x - p_yq_y$, and $p^2 = p_+p_- - p_x^2 - p_y^2$. Hence the four momentum vectors for the process is then defined as,

$$p_{e0} + p_{r0} \to p_O + P_{gg} + p_r \tag{3.75}$$

where p_{e0} is the initial gluon emitter four momentum vector, and p_{r0} is the recoiler in the dipole pair. p_O is the final onium (J/ψ), P_{gg} is the final di-gluon, and p_r is the final recoiler four momentum. The four momentum vectors of each component are then defined as,

$$p_{e0} = (P_+, 0, 0, 0) = (W, 0, 0, 0), \tag{3.76}$$

$$p_{r0} = (0, P_-, 0, 0) = (0, W, 0, 0), \tag{3.77}$$

$$p_O = (zW, \frac{p_\mathrm{T}^2 + m_O^2}{zW}, p_\mathrm{T}, 0), \tag{3.78}$$

$$p_{gg} = ((1-z)W, \frac{p_\mathrm{T}^2 + m_{gg}^2}{(1-z)W}, -p_\mathrm{T}, 0), \tag{3.79}$$

$$p_r = (0, W - \frac{p_\mathrm{T}^2 + m_O^2}{zW} - \frac{p_\mathrm{T}^2 + m_{gg}^2}{(1-z)W}, 0, 0), \tag{3.80}$$

where all of the components have the same means as stated previously. From these four vector definitions, r, y and z can be redefined into the evolution variables $p_{\mathrm{T,evol}}^2$, m_{gg}^2 and z.

The four momentum of the mother gluon, q can be defined as,

$$q = p_O + p_{gg} = (W, \frac{p_\mathrm{T}^2 + (1-z)m_O^2 + zm_{gg}^2}{z(1-z)W}, 0, 0) \equiv (W, \frac{p_{\mathrm{T,evol}}^2}{z(1-z)W^2}, 0, 0). \tag{3.81}$$

Hence, the virtuality of the branching, s, can be defined and related to $p_{\mathrm{T,evol}}^2$ using

$$s = \frac{p_\mathrm{T}^2 + (1-z)m_O^2 + zm_{gg}^2}{z(1-z)} \equiv \frac{p_{\mathrm{T,evol}}^2}{z(1-z)}, \tag{3.82}$$

and r can be redefined as,

$$r = m_O^2/s = z(1-z)m_O^2/p_{\mathrm{T,evol}}^2. \tag{3.83}$$

This also leads to y being redefined as,

$$\begin{aligned} y &= p_O \cdot q/s, \\ &= \frac{1}{2s}\left(\frac{p^2_{\mathrm{T,evol}}}{(1-z)} + \frac{p^2_{\mathrm{T,evol}} + zm^2_O - zm^2_{gg}}{z}\right), \\ &= \frac{p^2_{\mathrm{T,evol}} + z(1-z)m^2_O - z(1-z)m^2_{gg}}{2p^2_{\mathrm{T,evol}}}, \\ &= \frac{1}{2} + z(1-z)\frac{m^2_O - m^2_{gg}}{2p^2_{\mathrm{T,evol}}}. \end{aligned} \tag{3.84}$$

The defintion of z can then remain unchanged. The function given in section A.4 can then be simplified into the following form,

$$dP(z,r,y) = \frac{5\alpha^3_S(m^2_O)M^2}{648\pi m^2_O} f(z,r,y)dzdrdy, \tag{3.85}$$

where M^2 is the LDME and m^2_O is the mass of the onium (J/ψ). The variables $p^2_{\mathrm{T,evol}}$ and m^2_{gg} can be expressed as dimensionless variables,

$$x^2_{\mathrm{T,evol}} = p^2_{\mathrm{T,evol}}/m^2_O, \tag{3.86}$$

$$y^2_{gg} = m^2_{gg}/m^2_O, \tag{3.87}$$

which simplifies the construction of the Jacobian,

$$dzdydr = \frac{z^2(1-z)^2}{2x^6_{\mathrm{T}}} dx^2_{\mathrm{T,evol}} dy_{gg} dz, \tag{3.88}$$

giving,

$$dP(x^2_{\mathrm{T,evol}}, z, y_{gg}) = \frac{5\alpha^3_S(m^2_O)M^2}{648\pi m^3_O} f(x^2_{\mathrm{T,evol}}, z, y_{gg}) \frac{z^2(1-z)^2}{2x^6_{\mathrm{T}}} dx^2_{\mathrm{T,evol}} dy_{gg} dz. \tag{3.89}$$

This can be rearranged to give,

$$dP(x^2_{\mathrm{T,evol}}, z, y_{gg}) = \frac{dx^2}{x^2_{\mathrm{T,evol}}} \frac{dz}{1-z} dy_{gg} \frac{5\alpha^3_S(m^2_O)M^2}{648\pi m^3_O} f(x^2_{\mathrm{T,evol}}, z, y_{gg}) \frac{z^2(1-z)^3}{2x^4_{\mathrm{T}}}. \tag{3.90}$$

The last two factors give an expression which is fairly well behaved. However, there seems to be a divergence as $y_{gg} \to 0$. However, it seems to be integrable when a

correction factor of y_{gg}^p is included,

$$F(x_{\mathrm{T,evol}}^2, z, y_{gg}) = f(x_{\mathrm{T,evol}}^2, y_{gg}, z)\frac{y_{gg}^p z^2(1-z)^3}{2x_{\mathrm{T}}^4}, \tag{3.91}$$

and with $p \lesssim 1$, it is always $\lesssim 1$. The splitting function therefore looks like,

$$\begin{aligned} dP(x_{\mathrm{T,evol}}^2, z, y_{gg}) &= \frac{dx^2}{x_{\mathrm{T,evol}}^2}\frac{dz}{1-z}\frac{dy_{gg}}{y_{gg}^p}\frac{5\alpha_S^3(m_O^2)M^2}{648\pi m_O^3}F(x_{\mathrm{T,evol}}^2, z, y_{gg}), \\ &\lesssim \frac{dx^2}{x_{\mathrm{T,evol}}^2}\frac{dz}{1-z}\frac{dy_{gg}}{y_{gg}^p}\frac{5\alpha_S^3(m_O^2)M^2}{648\pi m_O^3}. \end{aligned} \tag{3.92}$$

To incorporate this into PYTHIA, z and y_{gg} need to be integrated out. The veto algorithm generates $p_{\mathrm{T,evol}}^2$ according to the Sudakov using,

$$\frac{dp_{\mathrm{T,evol}}^2}{p_{\mathrm{T,evol}}^2}\frac{\alpha_S(p_{\mathrm{T,evol}}^2)}{\alpha_0}, \tag{3.93}$$

so the running α_s needs to be changed. The overall scale would be on the order of m_O^2, however there are two soft gluons which can be emitted at much smaller scales to take into consideration (at $\sim p_{\mathrm{T,evol}}^2$ or p_{T}^2). Hence, one α_s is fixed at m_O^2 and the other two are allowed to run, as there are two gluons and one onium. This can then be rewritten as,

$$\begin{aligned} dP(x_{\mathrm{T,evol}}^2, z, y_{gg}) &= \frac{dp_{\mathrm{T,evol}}^2}{p_{\mathrm{T,evol}}^2}\frac{\alpha_S(p_{\mathrm{T,evol}}^2)}{\alpha_0}\int\frac{dz}{1-z}\frac{dy_{gg}}{y_{gg}^p}\frac{5\alpha_S(m_O^2)\alpha_S(p_{\mathrm{T,evol}}^2)\alpha_0 M^2}{648\pi m_O^3}, \\ &\lesssim \frac{dp_{\mathrm{T,evol}}^2}{p_{\mathrm{T,evol}}^2}\frac{\alpha_S(p_{\mathrm{T,evol}}^2)}{\alpha_0}\int\frac{dz}{1-z}\frac{dy_{gg}}{y_{gg}^p}\frac{5\alpha_S(m_O^2)\alpha_S(p_{\mathrm{T,evol}}^2)\alpha_0 M^2}{648\pi m_O^3}. \end{aligned} \tag{3.94}$$

The integration limits are then $0 < y_{gg} < (W/m_O - 1)^2$ and $z_c < z < 1 - z_c$ with $z_c = (1 - \sqrt{1 - 4p_{\mathrm{T,cut}}^2/W^2})/2$. Therefore,

$$\begin{aligned} dP(x_{\mathrm{T,evol}}^2, z, y_{gg}) &= \frac{dp_{\mathrm{T,evol}}^2}{p_{\mathrm{T,evol}}^2}\frac{\alpha_S(p_{\mathrm{T,evol}}^2)}{\alpha_0}\times\log\frac{1-z_c}{z_c}\times\frac{(W/m_O-1)^{2(1-p)}}{1-p} \\ &\quad\times\frac{5\alpha_S(m_O^2)\alpha_S(p_{\mathrm{T,cut}}^2)\alpha_0 M^2}{648\pi m_O^3}, \\ &= \frac{dp_{\mathrm{T,evol}}^2}{p_{\mathrm{T,evol}}^2}\frac{\alpha_S(p_{\mathrm{T,evol}}^2)}{\alpha_0}\times C, \end{aligned} \tag{3.95}$$

where C is the overestimate that PYTHIA needs to use in the veto algorithm.

The procedure to sample the splitting is then as follows:

1. PYTHIA generates a $p^2_{\mathrm{T,evol}}$.
2. Generate a z according to $dz/(1-z)$ using to the integration limits above.
3. Restart from step 1 if $z(1-z)W^2 \leq p^2_{\mathrm{T,evol}}$.
4. Generate a dy_{gg}/y^p_{gg} using to the integration limits above.
5. Restart from step 1 if $p^2_{\mathrm{T}} = p^2_{\mathrm{T,evol}} - (1-z)m^2_O - zm^2_O y_{gg} < 0$.
6. Calculate r and y .
7. Restart from step 1 if outside allowed limits, $(r+z^2)/(2z) < y < (1+r)/2$ and $0 < r < z$.
8. Calculate the weight $F(x^2_{\mathrm{T,evol}}, z, y_{gg})\alpha_S(p^2_{\mathrm{T,evol}})/\alpha_S(p^2_{\mathrm{T,cut}})$ and restart from 1 if less than a random number. Also emit a warning if > 1 to ensure the validity of the overestimate.
9. Save $m^2_{gg} = y_{gg}m^2_O$ in a new variable for the dipole.
10. The massive di-gluon then needs to be "decayed" to obtain the right kinematics.

The sampling of z according to a $dz/(1-z)$ distribution was discussed in section 3.2.5.1. The sampling of y_{gg} according to dy_{gg}/y^p_{gg} is as follows. y_{gg} is simplifies to y for now, to make it easier to read. The integral needs to be calculated of $1/y^p_{gg}$ where $p = 0.8$, which gives,

$$\int_{y_-}^{y_+} \frac{1}{y^p}\,dy = \left[\frac{y^{1-p}}{1-p}\right]_{y_-}^{y_+} = \frac{1}{1-p}\left[y_+^{1-p} - y_-^{1-p}\right]. \tag{3.96}$$

The inverse integral of this is then,

$$f = \frac{y^{1-p}}{1-p}, \tag{3.97}$$

$$y = (f(1-p))^{\frac{1}{1-p}}, \tag{3.98}$$

$$\therefore\ f^{-1}(y) = (y(1-p))^{\frac{1}{1-p}}. \tag{3.99}$$

A value of y, called G can then be generated with a random number R,

$$y = \text{inv}[\text{int}[x0] + R[\text{int}[x1] - \text{int}[x0]]], \tag{3.100}$$

$$y = \text{inv}\left[\frac{1}{1-p}\left[Ry_+^{1-p} + (1-R)y_-^{1-p}\right]\right], \tag{3.101}$$

$$y(1-p)^{\frac{1}{1-p}} = \left(Ry_+^{1-p} + (1-R)y_-^{1-p}\right)^{\frac{1}{1-p}}, \tag{3.102}$$

$$\therefore\ f^{-1}(y) = \left(Ry_+^{1-p} + (1-R)y_-^{1-p}\right)^{\frac{1}{1-p}}, \tag{3.103}$$

where inv is short for inverse, and int is short for integral. Here $y_- = 0$ and $y_+ = (\frac{W}{m_O} - 1)^2$. Therefore,

$$G = \left[Ry_+^{1-p}\right]^{\frac{1}{1-p}}, \tag{3.104}$$

$$G = R^{\frac{1}{1-p}} y_+. \tag{3.105}$$

3.4.2.3 Sampling colour octet

The fragmentation function for colour octet production is of a different form in comparison to the other splitting functions. This is because it consists of a delta function in z and s,

$$d_c^{\psi}(z,s) = \frac{\pi\alpha_s \langle 0|\, \mathcal{O}_8^{\psi}(^3S_1)\, |0\rangle}{24m_c^3}\delta(1-z)\delta\left(1 - \frac{s}{M_{\psi}^2}\right), \tag{3.106}$$

where $\langle 0|\, \mathcal{O}_8^{\psi}(^3S_1)\, |0\rangle$ is the LDME of the colour octet process and M_{ψ} is the mass of the J/ψ. To handle these delta functions in the parton shower algorithm, only when the $p^2_{\text{T,evol}}$ of the previous splitting is just above $M_{\psi} = 2m_c$, does the colour octet splitting have the opportunity to be able to branch. If the final $p^2_{\text{T,evol}}$ of this splitting is harder (higher $p^2_{\text{T,evol}}$) than the other potential splittings, then the colour octet component is selected. If not, it is not selected and does not have the chance to be produced again as $p^2_{\text{T,evol}}$ evolves downwards. If the splitting is selected, the colour octet state persists through the rest of the parton shower, and is then decayed in the hadronisation phase. This is because all the different decay modes of the colour octet channels are implemented in PYTHIA 8. This means there will be consistency in the decays from the hard process to the fragmentation processes. As this effectively leads to a $1 \to 1$ splitting, the kinematics of the branching are handled by radiating an infinitely soft photon, so it keeps the $1 \to 2$ branching

and does not effect the colour flow. All of the different colour octet contributions from different quarkonia are handled in this way, where the only major differences between them are the LDME's and the mass of the onium being used.

3.4.2.4 Other splittings and kinematics

With the exception of the $g \to J/\psi\, gg$ splitting which follows the procedure described in section 3.4.2.2, most of the colour singlet splittings are $1 \to 2$ branching processes. These follow the same procedure as described in section 3.4.2.1, where an overestimate is calculated for each process. This enables the sampling of a $p^2_{\mathrm{T,evol}}$ and z for each process. The colour octet splittings then follow the same procedure as outlined in section 3.4.2.3.

To account for the competition between the different quarkonia splittings, the sum of the overestimates of the different splittings are used, which is then used in the veto algorithm to sample $p^2_{\mathrm{T,evol}}$. A random number is then generated. To select a particular branching, from an example of three different branchings, if the random number is less than the first branching overestimate divided by the sum of the total overestimates, the first branching is picked. If not, and the random number is less than the sum of the overestimates of the first and second branching divided by the sum, then the second branching is selected, *etc.* In the end, a particular quarkonia branching is then selected, with $p^2_{\mathrm{T,evol}}$ and z values. This then competes with other types of splittings such as QCD, EW *etc.* The splitting out of these with the hardest $p^2_{\mathrm{T,evol}}$ is the one selected to do the final splitting, and evolve the parton shower. This process is then repeated again for the next set of splittings.

The kinematics of the selected quarkonia splitting are handled using the already defined framework in PYTHIA 8 which handles heavy quark splittings, described in more detail in Ref. [57]. It was also important to make sure that this splitting could occur in any of the available dipole pairs, such as gg or qg for example.

3.5 Testing the quarkonia shower

Finally, after the implementation of the different splittings these need to be tested. This is carried out as a two-step process, with each serving a different purpose:

firstly, by comparing the J/ψ splitting kernels to those implemented in ARIADNE [53–55] and analytic functions in the literature, when they are available; secondly, by comparing the MC generation results with experimental data. The methods for each are described in the next sections.

3.5.1 Single dipole results

To test the parton shower implementation, firstly results for different splittings were compared with ARIADNE [53–55]. ARIADNE is an event generator, which was the first to evolve the parton shower not as individual partons, but as colour dipoles. Hence, the evolution variable chosen for ARIADNE was the transverse mass of the dipole, m_T, rather than p_{T}^2 which is used in PYTHIA 8. It was also the first to implement J/ψ quarkonia splittings in the parton shower. Namely, the $c \to J/\psi(1)c$, $g \to J/\psi(1)gg$ and $g \to J/\psi(8)$ where $J/\psi(8) \to J/\psi(1)g$. Hence, the PYTHIA 8 implementation of these three splittings can be compared to ARIADNE to check consistency. This then forms a good basis for implementing the other splittings which are not included in ARIADNE like $g \to \chi_{c0}g$, as only the LDME values and fragmentation functions vary between these, so can follow similar methods. ARIADNE was programmed using FORTRAN. As the PYTHIA 8 framework is coded using C++, ARIADNE and PYTHIA were compiled to give binaries for each of its internal methods. Then these could be used in the same C++ program to run ARIADNE and PYTHIA concurrently.

To carry out initial testing of the implementation of the different quarkonia splittings into the PYTHIA 8 shower, only the FSR part of the event needs to be generated. This is to simplify the testing as the other parts of the event generation, such as MPI, ISR *etc.*, can complicate the event structure. To do this, firstly a dipole is generated of either $c\bar{c}$ or gg at a centre of mass energy E_{cm}. A $c\bar{c}$ dipole is used to test the $c \to J/\psi(1)c$ splitting, and a gg dipole for the $g \to J/\psi(1)gg$ and $g \to J/\psi(8)$ splittings. The c quarks in this case have mass of $m_c \approx 1.5\,\mathrm{GeV}$. An FSR parton shower can then commence from either of these partons. The splittings that occur can be either a QCD splitting or from the single onium splitting that is being tested. The parton shower then stops once the final partons reach a $p_{\mathrm{T,evol}}^2$ scale less than Λ_{QCD}^2. For each J/ψ that is generated in the parton shower using the `TimeShower` method, its information is stored. This includes events where multiple J/ψ's are generated.

The variable of interest to compare ARIADNE and PYTHIA is z, which is used in the fragmentation functions, such as in eq. (3.52). z in these fragmentation functions is defined as (energy of the J/ψ, $E_{J/\psi}$)/(energy of the radiator, E_{rad}). However, this is modified slightly in these tests to, $z = E_{J/\psi}/(E_{cm}/2)$. This is because when only looking at the single splitting, this can be dependent on the choice of evolution variable used. This is important as ARIADNE uses m_T rather than p_T^2 as its evolution variable. This dependence is averaged out if the whole shower is used, hence $z = E_{J/\psi}/(E_{cm}/2)$ is chosen.

To build a sufficiently large sample size for the tests the default value of the LDME for each splitting was artificially increased. A Newton minimiser method was used to be able to find the LDME value that gives an average of 0.1 J/ψ's per event. This value is chosen to enhance the number of J/ψ's generated but not so much that the distribution becomes skewed away from the true distribution by the Sudakov resummation. If output LDME values for ARIADNE and PYTHIA are similar, this means the splitting kernel used is similar between the two, and the implementation of the splitting function is not dependent on the overestimate used.

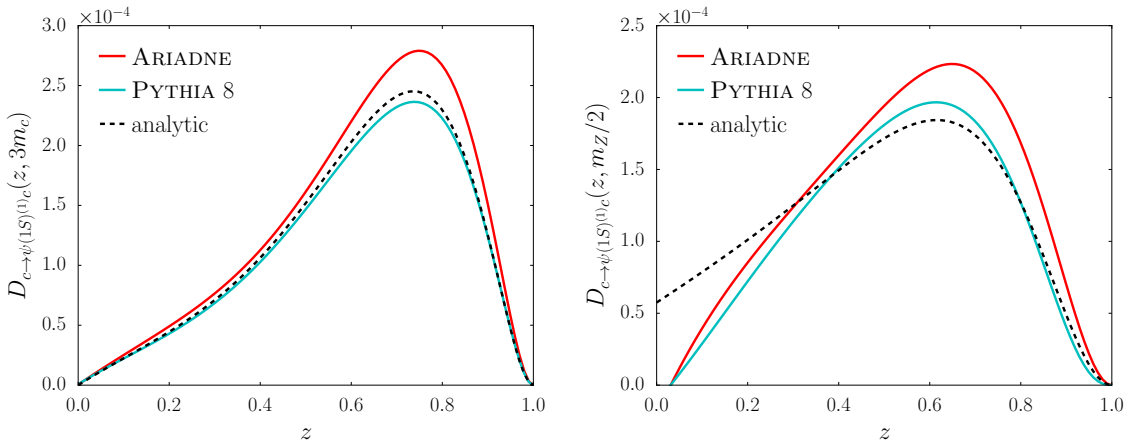

Figure 3.7: Comparison of the PYTHIA 8 and ARIADNE generation of $c \to J/\psi(1)c$ with the analytic expression at the energy scale of $3m_c$ *vs.* $M_Z/2$. The y-axis shows the value of the fragmentation function at each z value.

Firstly, the $c \to J/\psi(1)c$ splitting kernel was implemented, as this was the simplest kernel to put in. The overestimate and iterative generation process used is described in section 3.4.2.1. This was tested with various different settings, with z being the variable of interest. Figure 3.7 shows the results of PYTHIA implementation of $c \to J/\psi(1)c$ in comparison with ARIADNE and the analytic expression at different energy scales. The y-axis shows the value of the fragmentation function, $D_{c\to\psi(1S)^{(1)}c}$,

at each value of z, for a certain α_s value. The left hand plot has α_s fixed at $3m_c$ in the PYTHIA generation and does not include QCD splitting in the parton shower so it can be directly compared to the analytic expression. PYTHIA 8 is consistent with the analytic expression, in comparison to ARIADNE which is slightly more peaked. This could be due to differences in the evolution variable, the p_{T}^2 cut-off on which the parton shower ends, or the fact that ARIADNE at the moment can only have running and not fixed α_s values. However, the results are all relatively consistent with each other. The right hand plot in fig. 3.7 shows PYTHIA and ARIADNE evolved from $M_Z/2$, and hence includes the QCD splittings and running α_s for both distributions. Both distributions are consistent with each other, and differ by the same factor as seen in the left hand plot. They both differ from the analytic expression at low z, due to kinematic limits applied in the parton shower due to the mass of the c and J/ψ. Note that the analytic expression is an approximation, as it accounts for neither these kinematic effects nor the running of α_s. Since PYTHIA is consistent with both the analytic expression and ARIADNE, the $c \to J/\psi\,(1)c$ splitting kernel implementation has been validated. The same procedure was followed for the $c \to \eta_c(1)c$ splitting kernel, with results shown in fig. 3.8 in comparison to the $c \to J/\psi\,(1)c$ splitting kernel. PYTHIA in this case is also consistent with the analytic expression at both energy scales, and is hence validated.

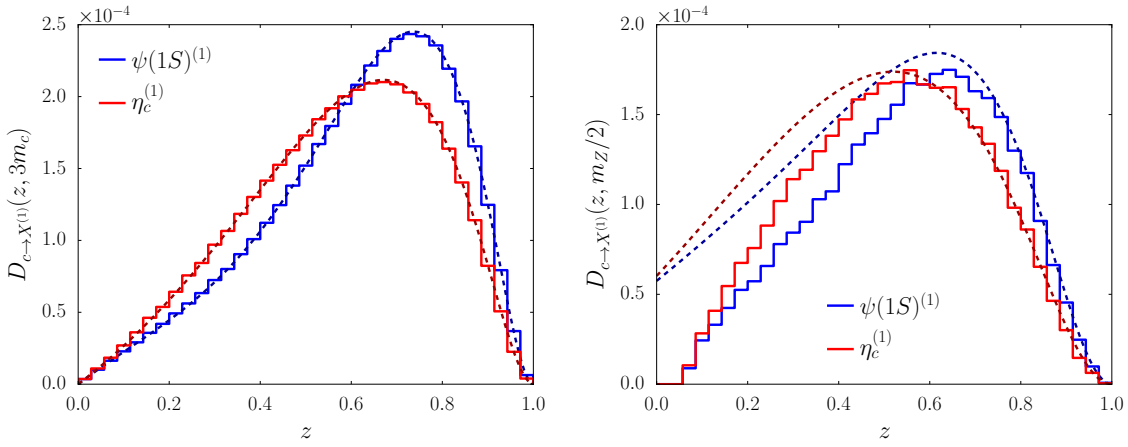

Figure 3.8: Production of colour-singlet S-wave states from charm splittings compared between (solid) PYTHIA 8 and (dashes) analytic expressions at the energy scales of (left) $3m_c$ and (right) $m_Z/2$. The y-axis shows the value of the fragmentation function at each z value.

The fragmentation of χ_{cJ} states from c's or g's have not been incorporated in any parton shower to date. This means the results cannot be compared with ARIADNE in these cases. However, they can be validated by comparing with the analytic

expression. The implementation of c splittings to the χ_{cJ} states is shown in the left hand plot in fig. 3.9 at the energy scale of $3m_c$. All the splittings have a central peak and are consistent with the analytic expressions. Hence, all of the c splittings have been validated. A comparison of the evolved splittings to S-wave and P-wave states from $m_Z/2$ are shown in the right-hand plot of fig. 3.9. The evolution behaves as expected, and shows that J/ψ and η_c are more likely to be produced from charm splittings than the χ_{cJ} states.

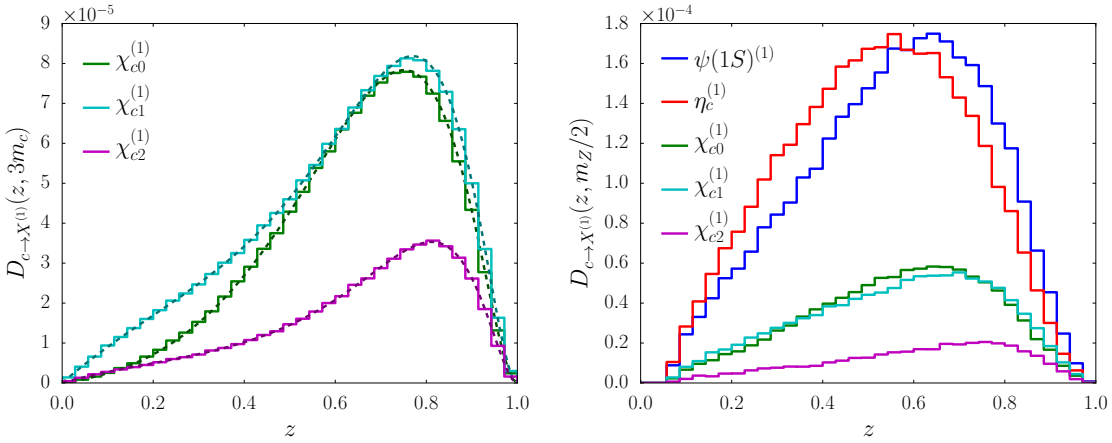

Figure 3.9: The left hand plot shows the production of colour-singlet P-wave states from charm splittings compared between (solid) PYTHIA 8 and (dashes) analytic expressions at the energy scale of $3m_c$. The right hand plot compares S-wave and P-wave states produced from charm splittings at the scale of $m_Z/2$. The y-axis shows the value of the fragmentation function at each z value.

Gluon fragmentation to the colour singlet η_c and χ_{cJ} states has been incorporated into the PYTHIA 8 framework, with results shown in fig. 3.10 for the η_c and χ_{cJ} states, at an energy scale of $2m_c$. For the χ_{c0} splitting to be visible on the plot, a scale factor of 20 was applied. Using the same procedure as for the charm splittings, as they all match the analytical expressions, they have been fully validated. The $g \to J/\psi\,(1)gg$ splitting is handled slightly differently to the η_c and χ_{cJ} colour singlet splittings, due to the fact it is a $1 \to 3$ splitting, instead of $1 \to 2$. The generation of $g \to J/\psi\,(1)gg$ follows the procedure outlined in section 3.4.2.2. ARIADNE's generation is different as it directly integrates out r and y to simplify the generation of the splitting. A validation of the $g \to J/\psi\,(1)gg$ splitting is shown in the left hand plot of fig. 3.10, and since the implementation matches the analytical expression, it is validated. To make the distribution visible on the plot, it is scaled by a factor of 100. Hence, $g \to J/\psi\,(1)gg$ is the least likely to occur out of all the gluon splittings to colour singlet quarkonia states. This effect is more visible in the left hand plot of

fig. 3.11, where all the gluon splittings to colour singlet quarkonia states are shown in one plot, and have been evolved from $m_Z/2$. The $g \to J/\psi(1)gg$ splitting is least likely to occur by two orders of magnitude, in comparison to $g \to \chi_{c1}(1)g$ and $g \to \chi_{c2}(1)g$ which are the most likely to occur.

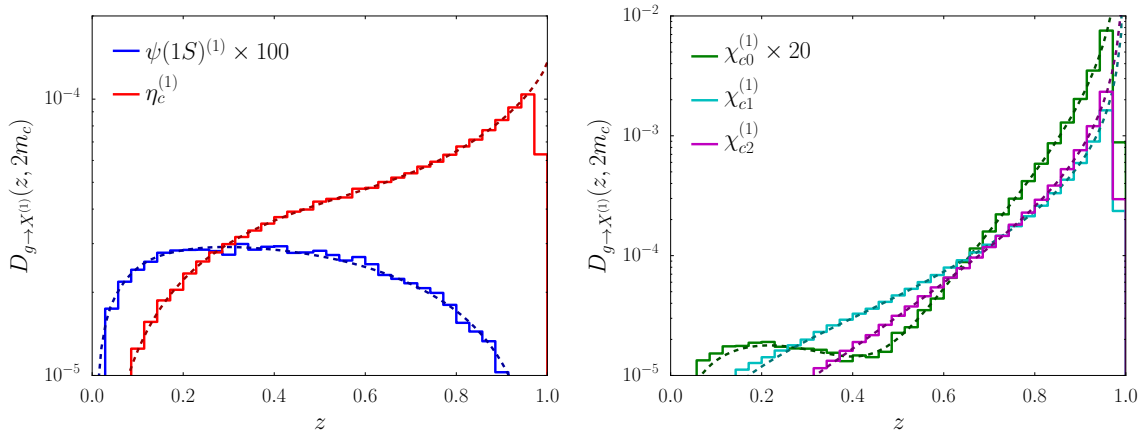

Figure 3.10: Production of colour-singlet (left) S-wave and (right) P-wave states from gluon splittings compared between (solid) PYTHIA 8 and (dashes) analytic expressions at the energy scale of $2m_c$. The y-axis shows the value of the fragmentation function at each z value.

The final splittings to validate are the colour octet splittings, such as $g \to J/\psi(8)$ to fully complete the quarkonia parton shower. The implementations of the colour octet state are slightly different in ARIADNE and PYTHIA 8. In PYTHIA 8, as mentioned in section 3.4.2.3 which discusses its implementation, the colour octet state is produced when $p^2_{\mathrm{T,evol}}$ is just above $4m_c^2$. The colour octet state then persists throughout the parton shower until it is decayed in the hadronisation phase through decay channels already implemented in PYTHIA. This colour octet state may further radiate through QCD emissions. In ARIADNE, the colour octet intermediate state does not exist through the decay chain of $g \to J/\psi(8)$ where $J/\psi(8) \to J/\psi(1)g$. It is forced to decay straight away through $g \to J/\psi(1)g$. This intermediate step is implemented by instead of having a delta function of z, $\delta(1-z)$, a top hat function with a finite width is used which is defined as, $\frac{1}{\epsilon}\theta(z-(1-\epsilon))\theta(1-z)$. ϵ is then dependent on the relative velocity of the two quarks in the quarkonium state. As the final colour octet state is not physical, in the testing of the parton shower, the $J/\psi(8)$ is forced to decay to $J/\psi(1)$. For this, the `forceHadronisation` method is used. The colour octet splittings for the η_c, J/ψ and χ_{cJ} states have been implemented into the PYTHIA 8 framework and validated, with results shown in the right hand plot in fig. 3.11, where they have been evolved from the energy scale $m_z/2$. For the

colour octet states, the most likely splittings to occur are the $g \to \chi_{c2}(8)[^3S_1]$ and $g \to J/\psi\,(8)[^3S_1]$ in comparison to $g \to \chi_{c2}(8)[^3S_1]$ which is the least likely.

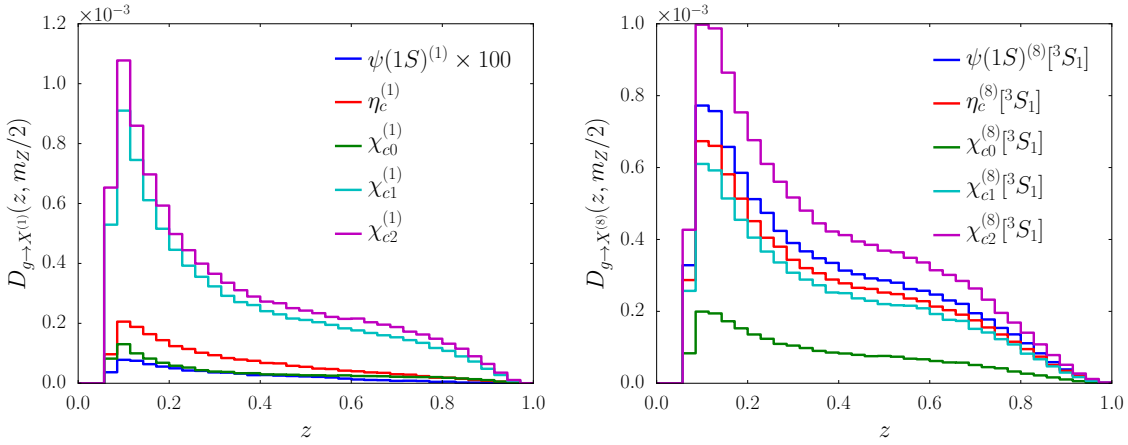

Figure 3.11: Production of (left) colour-singlet and (right) colour-octet states from gluon splittings with PYTHIA 8 at the energy scale of $m_Z/2$. The y-axis shows the value of the fragmentation function at each z value.

3.5.2 Data comparisons

The individual splittings have been implemented and tested in comparison to ARIADNE when only running the FSR part of the generation. Hence, to fully test the quarkonia shower splittings the full event needs to be generated, including the hard processes, ISR, MPI *etc.* As well as testing the individual splittings, the competition between the different splittings needs to be validated and the effects of feed-down in the $z(J/\psi)$ distributions need to be assessed.

This is tested by comparing the full event generation, including these additional quarkonium splittings, with experimental data. As explained in chapter 1, jet fragmentation measurements have been performed by LHCb and CMS which look at the J/ψ clustered in jets, and measure the fragmentation variable $z(J/\psi) = p_{\mathrm{T}}(J/\psi)/p_{\mathrm{T}}(\mathrm{jet})$. This variable is a good test for the implementation of the splittings, as it gives an idea of the isolation of the J/ψ. Lower values of z lean towards the J/ψ being produced from a fragmentation process. Also, both measurements are in different pseudo-rapidity and $p_{\mathrm{T}}(J/\psi)$ ranges, so they access different phase space regions of this variable. Results of z distributions for other quarkonium states have not been published yet, such as $\psi(2S)$, $\Upsilon(1S)$, $\Upsilon(2S)$ and $\Upsilon(3S)$. However these measurements at LHCb are the second subject of this thesis, and are presented in chapter 6 and chapter 7.

The Monte Carlo generation in PYTHIA 8 is cross checked with experimental data, by using a software package called RIVET [66]. RIVET is a generator-agnostic validation checker for generators, which compares MC predictions with experimental data, and is used for analysis preservation. As well as model checking, it is used for MC tuning. The idea is for a published analysis, such as a cross section measurement for J/ψ production, an experimentalist writes a RIVET routine for that analysis. A RIVET routine is a C++ program that runs the Monte Carlo generation and includes all the experimental cuts applied on the particles of interest. The MC predictions from the script are then compared to the experimental results, which are taken from HEPDATA [67]. HEPDATA stores all experimental data results so these can easily be used by everyone in the particle physics community in `.json` formats. RIVET hence is very useful for Monte Carlo developers as they do not have to look at individual papers to find the selection requirements applied on an analysis.

Each generator outputs an event record, which details for each event the order of particles produced, their properties, which type they are, for example if they are produced from a MPI or ISR, and what particles they are generated from and decay to. How the event record is recorded is usually dependent on the event generator used. HEPMC [68] is used to reorganise the output event record in a universal way, such that the output event record is the same no matter the generator used. This is then used as input into RIVET. Hence, RIVET is a generator-agnostic validation checker.

The quarkonium shower implementation in PYTHIA 8 needs to be compared with experimental data for standard variables. LHCb published cross section results for J/ψ, $\Upsilon(1S)$, $\Upsilon(2S)$ and $\Upsilon(3S)$ at $\sqrt{s} = 8\,\text{TeV}$ in bins of $p_\text{T}(J/\psi)$ and $y(J/\psi)$, where y is the rapidity. The experimental data has been published in HEPDATA. Unfortunately, a RIVET routine was not written for this analysis, hence this analysis was implemented into RIVET with number `LHCB_2013_I1230344`. The formalism used to identify the RIVET routine is `Experiment_YearPublished_InspireHEPID Number`. Finally, the quarkonium shower implementation needs to be tested with the $z(J/\psi)$ experimental results from LHCb and CMS. RIVET routines and HEPDATA were not available for these analyses, so these had to be implemented also. The names for the two implemented routines are `LHCB_2017_I1509507` and `CMS_2018_I1673584`.

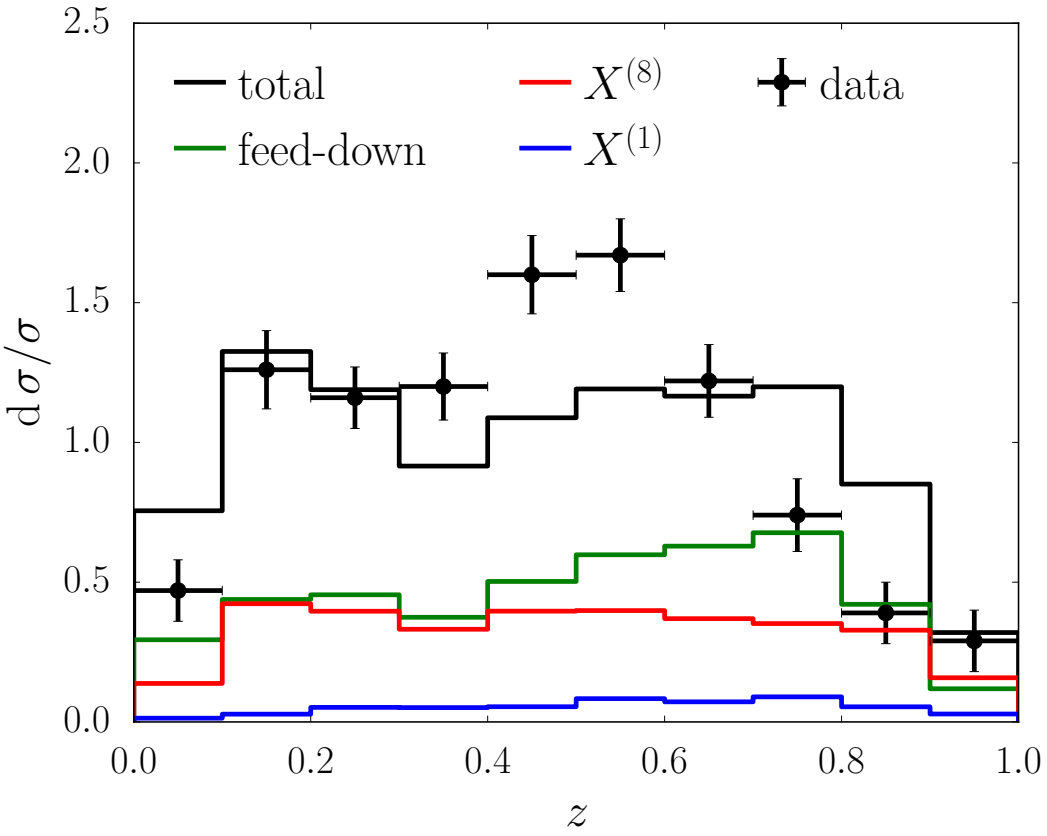

Figure 3.12: Comparison of the current PYTHIA 8 implementation, including all available splittings and feed-down, with LHCb data. This is generated with all hard QCD processes turned on and all the charmonium shower components, with the full event simulated. The production of quarkonia from the hard process is not included. Blue is the contribution from gluon and charm splittings to colour singlet J/ψ's ($X^{(1)}$), red is the contribution from gluon splittings to colour octet J/ψ's ($X^{(1)}$) and green is feed-down which includes charm and gluon fragmentation to colour singlet and colour octet χ_{cJ} states.

Preliminary results showing the current implementation of the quarkonia splittings in the parton shower in comparison to LHCb data are shown in fig. 3.12. The full event is generated, (*i.e.* with ISR *etc.*), with all the hard QCD processes turned on and all the charmonium shower components. The competition between the different quarkonia splittings is also taken into account. Here, the production of quarkonia from the hard process is not included. The final particles are clustered into jets and z is calculated for each jet that contains a J/ψ. In fig. 3.12, blue corresponds to the contribution from gluon and charm splittings to colour singlet J/ψ's ($X^{(1)}$), red is the contribution from gluon splittings to colour octet J/ψ's ($X^{(1)}$), green is feed-down which includes charm and gluon fragmentation to colour singlet and colour octet χ_{cJ} states and black is the total of all the contributions. All three components shift

the total distribution to lower z values, which lead to a significantly less isolated distribution than the current release of PYTHIA, which only implements the hard process component of onia production and has an isolated peak at $z(J/\psi) \simeq 1$. The component that contributes the least is the colour singlet J/ψ component (in blue), whereas the feed-down (green) component seems to contribute the most. The LDMEs that were used for each process were the default LDMEs that are used for the quarkonia production through the hard process. As these LDMEs were tuned to data assuming only the production of quarkonia through the hard process is possible, these will need to be re-evaluated. This can have a big effect on the shape of total distribution, as shown in Ref. [69]. This will be the subject of future work, in addition to validating the parton shower with the other RIVET routines.

3.6 Conclusions and future work

Overall, the current implementation does result in less isolated predictions of $z(J/\psi)$ which was observed in data. The next steps are to tune the LDME values for each splitting to data, by validating with the J/ψ in jets data by LHCb and CMS. Then also compare to data that are differential in p_{T} and rapidity. Once this baseline is set, the validation of the heavier mass states such as $\psi(2S)$ and the bottomonium states should be straightforward, using the jet measurements performed in chapters 6 and 7. Double counting of the parton shower with the hard process needs to also be taken into account. This may be solved by removing the processes from hard production, but this needs further investigation. Also the double counting from colour reconnection and refining the calculations by taking into account possible interference terms between emissions from the c or $\overline{c}$ states needs to be investigated.

Extensions of this could be to look at how the inclusive branching fractions for various processes are affected from including the additional contribution from parton shower production, for example Higgs decays into quarkonia. Also, how this effects production of quarkonia in heavy ion collisions. Finally, investigations of incorporating polarisation to the colour singlet and colour octet states in the parton shower could be explored.

CHAPTER 4

The LHCb detector in the LHC complex

In this chapter, I will describe the Large Hadron Collider (LHC) complex, and general kinematic variables used in particle physics across experiments. Then I will describe the LHCb physics goals, and the LHCb detector design used for Run 1 and 2 of the LHC.

4.1 The LHC complex

The Large Hadron Collider (LHC), currently the highest energy accelerator in the world, accelerates protons up to centre of mass energies of $\sqrt{s} = 13\,\text{TeV}$ [70]. It is run by the European Organisation for Nuclear Research (CERN). A schematic diagram of the LHC is shown in fig. 4.1. The circumference of the LHC is 26.7 km and it straddles the Switzerland-France border. The LHC tunnel is located 50–150 m underground and previously hosted the Large Electron-Positron collider (LEP) until 2000 [71]. The LHC has four interaction points (IP) where protons collide. Where these protons collide inelastically a large number of particles are produced, which may contain specific particles of interest. Detectors are then placed at these IPs to measure the properties of the particles in these collisions. The four detectors are ATLAS [72], CMS [73], LHCb [74] and ALICE [75]. Each collision in particle

physics is called an event.

To achieve centre of mass energies of this magnitude, the protons are accelerated through different stages: first with the Linear Accelerator 2 (LINAC 2), then to the Proton Synchroton Booster (PSB) and Proton Synchroton (PS) and then to the Super Proton Synchroton (SPS). The protons at this point have been accelerated to beam energies of 450 GeV. These beams are then injected into the LHC in bunches of $\sim 10^{11}$ protons. Bunches are accelerated in opposite directions with energies of up to 7 TeV each, until they are deflected towards the IP. The bunches are kept in a circular orbit using superconducting dipole magnets, generating a magnetic field of 8 T which operate at ~ 1.9 K temperatures. Quadrupole magnets are used to focus the beam at the IP [70].

As well as knowing the energy of the colliding protons, the instantaneous luminosity of the accelerator is necessary for many measurements. This is how many proton-proton interactions there are per second, per unit area. The smaller the width of the proton beams, the more likely the protons are to collide, and the larger the instantaneous luminosity. The targeted LHC instantaneous luminosity for Run 1 and Run 2 was $10^{34}\,\mathrm{cm}^{-2}\,\mathrm{s}^{-1}$, with the proton bunches crossing every 25 ns. The integrated luminosity is the instantaneous luminosity integrated over a given time period [70].

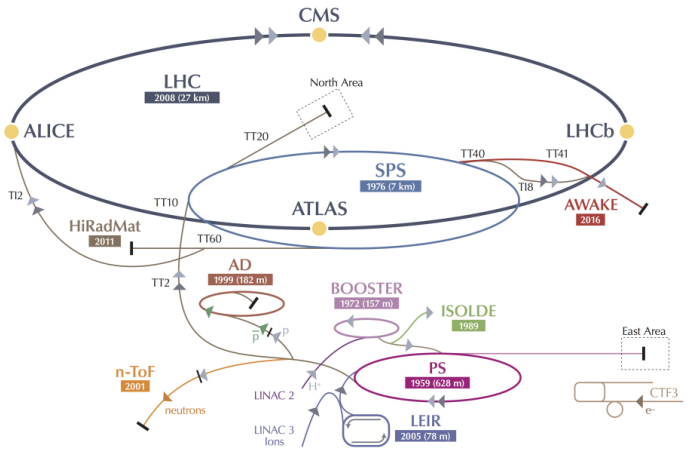

Figure 4.1: Schematic diagram of the LHC [76].

4.1.1 Coordinate system and kinematic variables

Figure 4.2 shows definitions of kinematic variables shared by all LHC experiments. The IP is where the protons are expected to collide. For a particle produced with a

momentum vector $\vec{p}$, the transverse momentum, $\vec{p}_T$, is the component perpendicular to the beam axis. A right-handed coordinate system is used with: $\vec{z}$ along the proton beam direction with positive sense into the LHCb detector from the IP; $\vec{y}$ points vertically upwards, and $\vec{x}$ is horizontal (right-handed definition means this points towards the centre of the LHC ring). θ is the polar angle relative to $\vec{z}$, while ϕ is the azimuthal angle in the x-y plane, with $\phi = 0$ along the positive $\vec{x}$ axis. Pseudorapidity, which is closely related to rapidity and experimentally more straightforward to determine, is defined as $\eta = -\ln\left(\tan\frac{\theta}{2}\right)$,

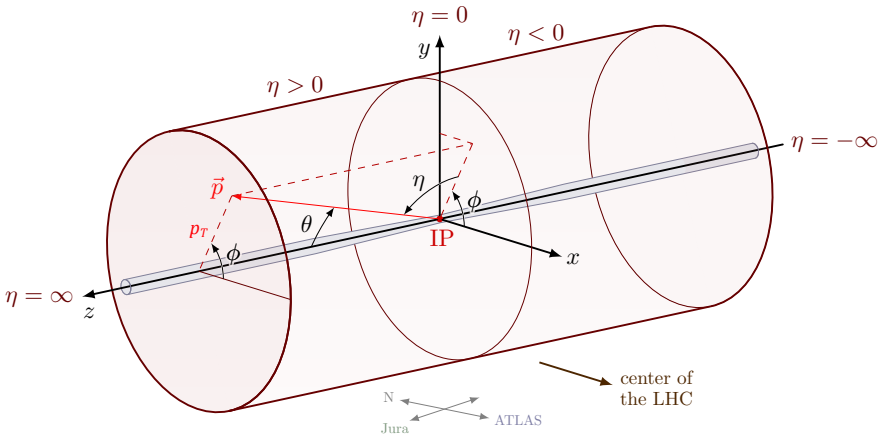

Figure 4.2: Definitions of kinematic variables [77].

4.2 LHCb Physics Programme

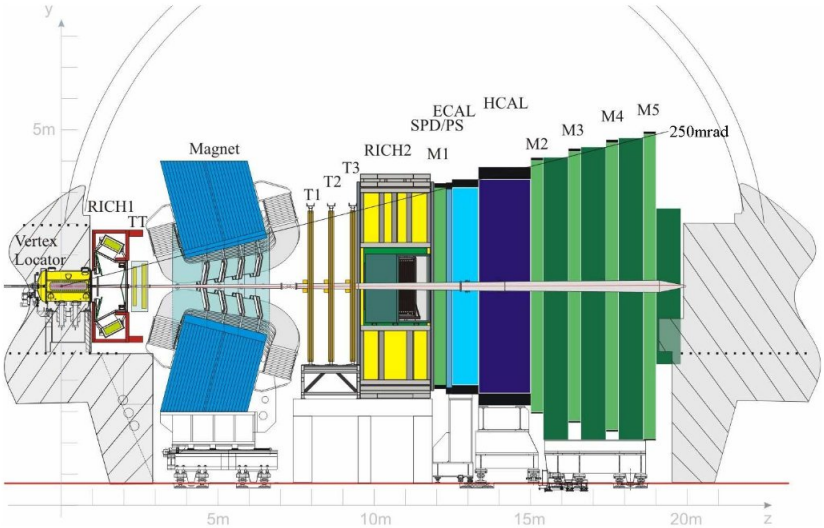

Figure 4.3: LHCb detector layout [78].

LHCb is a precision experiment at the LHC. Noteworthy measurements made by LHCb include observing potential pentaquark candidates in $\Lambda_b^0 \to J/\psi K^- p$ decays [79] and the first observation of CP violation in decays of charmed hadrons [80].

Its layout is illustrated in fig. 4.3 and designed with an angular coverage of all the particles produced from the collision point of the protons of $1.8 < \eta < 4.9$ [81]. This is in contrast to the three other experiments in the LHC, such as ATLAS, which typically provide more central coverage. Gluons from the colliding protons typically interact to produce either very forward or backward $b\bar{b}$ pairs as demonstrated in fig. 4.4a. The layout of LHCb enables it to be more effective at selecting b candidates by maintaining the angular coverage within the red region of fig. 4.4b. This ensures 24 % of $b\bar{b}$ quark pairs produced to be within the LHCb acceptance [81]. Therefore, to obtain precision measurements, such as CP violation in the charm sector, higher precision detectors can be installed covering only this relatively small acceptance.

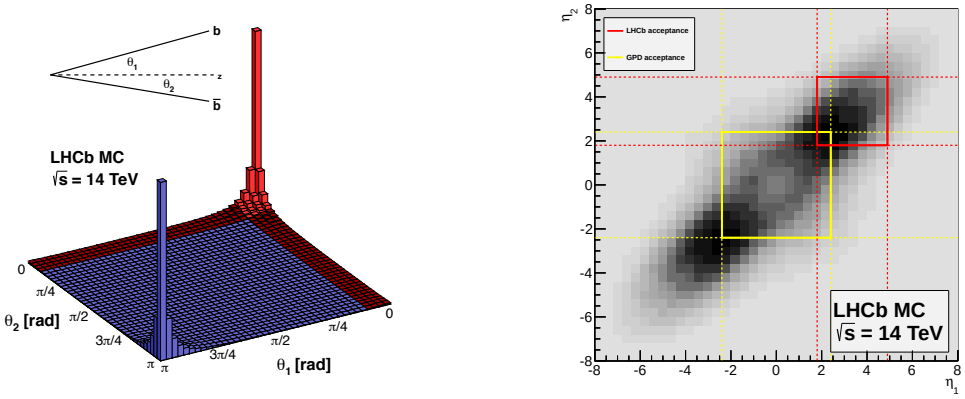

(a) Angular distribution.

(b) Pseudo-rapidity, η, distribution.

Figure 4.4: Angular and η distributions of $b\bar{b}$ pairs with PYTHIA 8 and the CTEQ 6 parton distribution functions [81].

The LHCb detector, shown in fig. 4.3, is composed of different sub-detectors, each with its own primary purpose to measure specific properties of an individual particle. Firstly, the protons (or heavy ions) travel through a beam pipe and collide at the IP. The resulting particles firstly pass through the VErtex LOcator (VELO), which is used to measure the secondary displaced vertices of b/c hadrons. The momentum of charged particles is measured by using a magnet to bend the particle's trajectory which is then measured using a silicon tracking system. This is composed of a Tracker Turicensis (TT) station and three Tracker (T) stations before and after the magnet respectively. Two Ring Imaging CHerenkov (RICH) detectors, RICH1 and RICH2, are used for particle identification (PID). These classify different hadron

types, primarily protons, pions and kaons. After these are the calorimeters, the Electromagnetic Calorimeter (ECAL) and Hadronic Calorimeter (HCAL) respectively. They are used to measure the energy of different types of particles and for Particle IDentification (PID). The ECAL measures electrons and photons, and the HCAL hadrons. A Preshower (PS) detector and a Scintillating Pad Detector (SPD) are placed before the ECAL to aid pion background rejection. The muon stations (M1–M5) then are used to identify muons. A trigger system is used to combine the outputs of each of these sub-detectors, and triggers on events which pass a specific set of criteria, before the information is saved to disk. If not, the information is not saved. Each detector component design and the trigger system will be described in more detail in the subsequent sections.

To increase the detector efficiency, interactions in the material are minimised. This can be achieved by reducing the material budget, hence reducing the multiple scattering of pions and kaons. This leads to improved pattern recognition and momentum resolution. It is anticipated that a single particle passes through only 60 % and 20 % of a radiation length and absorption length, respectively, before hitting RICH2. Access to the beam pipe is essential for maintenance, so the detector is divided into two sections [78].

For LHCb, the luminosity is decreased from the standard LHC luminosity of $10^{34}\,\mathrm{cm}^{-2}\,\mathrm{s}^{-1}$ to 4 x $10^{32}\,\mathrm{cm}^{-2}\,\mathrm{s}^{-1}$ [82]. This corresponds to $\sim$ 1.7 interactions per beam crossing, also called pile-up [82]. This is primarily to optimise the reconstruction efficiencies of secondary vertices from b-decays, but also of the primary vertices (PVs). It also reduces radiation damage to protect the detectors. The LHC has run for two periods, 2010–2012 (Run 1) and 2015–2018 (Run 2). The Long Shutdown between these two runs was used to upgrade the accelerator complex and detectors. During Run 1, $3\,\mathrm{fb}^{-1}$ of data was collected (integrated luminosity) and $5.7\,\mathrm{fb}^{-1}$ during Run 2 [83]. In this thesis, as all analyses used the data collected from Run 2, I will focus on the detector design of LHCb used for Run 2. There is not a huge difference in the detector design between Run 1 and 2.

4.3 The LHCb detector for Run 1 and 2

4.3.1 The Trigger system

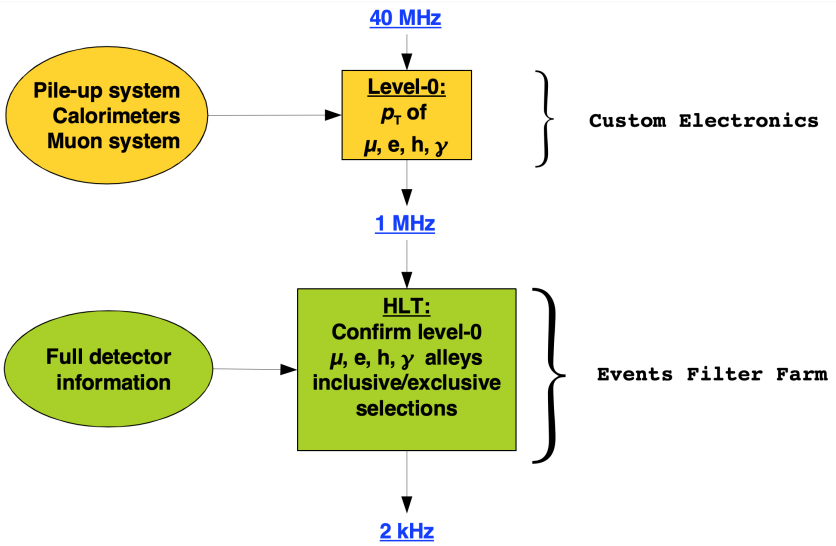

Figure 4.5: Schematic diagram of the LHCb trigger system [78].

The primary function of a trigger is to select events of interest, which may include a $J/\psi \to \mu^+\mu^-$ signal for example, and discard events that only include (abundant) background. During Run 2, it was problematic with an initial rate of 1 TB/s from the detector, to minimise the rate of gathered data to the required value of 0.7 GB/s in one step [84]. The trigger system is divided, therefore, into different levels. A schematic diagram of the LHCb trigger system is illustrated in fig. 4.5, with three trigger levels: L0 (hardware), and High Level Triggers HLT1 & HLT2 (software) [78].

L0 triggers are hardware triggers which are instrumented on Field Programmable Gate Arrays (FPGAs). Designed to meet the needs of event filtering, a limited selection of detectors are utilised at L0: calorimeters, muon system and the pile-up system [78]. These detectors define primitives for particles using coarse information to discard events. A combination of primitives can generate a distinctive trigger condition. To preserve an event, it must satisfy a specific trigger condition, namely, that the primitives must occur simultaneously, otherwise the event is discarded. HLT1 and HLT2 are software triggers and employ algorithms to reduce the rate. More comprehensive information is accumulated via the additional detectors used in HLT1 and HLT2, and filters events culminating in an eventual storage rate of 0.7 GB/s, which is shown in fig. 4.5 [78, 84].

4.3.2 The beam pipe

The beam pipe has protons which travel along it, interact, and then produce more particles which traverse through the pipe to the LHCb detector. Hence, it is important to minimise the amount of material in the beam pipe, whilst still maintaining a reliable vacuum. Hence, the beam pipe itself is made of beryllium, within 12 m from the interaction point. Then, for the next 7 m, stainless steel is used. The pipe itself consists of four main sections which are connected with flanged bellows made out of aluminium alloys [78].

4.3.3 The Magnet

A dipole magnet is utilised to establish the magnetic field at LHCb to measure the momentum of particles in combination with charged particle tracking detectors. Fifteen pancakes, made of annealed pure Aluminium-99.7 conductor, in each of the two saddle-shaped coils, form the magnet. It is set within a window-frame yoke with 100 mm laminated low carbon steel plates and provides an acceptance of ± 250 mrad (vertical) and ± 300 mrad (horizontal). A high momentum resolution requires a substantial field in between the VELO and RICH2. However, the field inside the RICH detectors demands a < 2 Tm field. This is because the RICH detectors contain photodetectors which generate photoelectrons. If the field is too large then the photoelectrons are deflected from the sensors active area [85]. These sensors are explained in more detail in section 4.3.6. To realise this compromise, an integrated field of 4 Tm for tracks of 10 m length was adopted [78].

4.3.4 The Vertex Locator

To identify b/c hadron decays, it is crucial to render precise track coordinates near to the interaction point as these decays are characterised by a displaced secondary vertex from the interaction point [78]. The VErtex LOcator system (VELO) is composed of 42 planes of silicon microstrip detectors, each incorporating an R sensor (*i.e.* microstrips along constant radii) and a ϕ sensor [86]. This enables the R and ϕ coordinates to be measured as the particle transits the VELO, providing a position resolution of 7 µm [86]. Ahead of the VELO sensors is the pile-up system formed up of two planes of R sensors. Sensors are arranged inside a vacuum vessel, called

an RF foil. This protects the VELO and provides an independent vacuum system. The material used is also minimised to reduce particle interactions [78].

4.3.5 The Tracking System

The magnet is sandwiched between two key components of the tracking system. Firstly, the Tracker Turicensis (TT), which is placed in front of the magnet, and covers the complete detector acceptance. Then the three Tracker (T) stations are placed after the magnet and are composed of inner and outer trackers (IT's and OT's). These are shown in a schematic diagram of the tracking system in fig. 4.6. The TT is a silicon microstrip detector with stations made up of four detector layers containing strips, each with a pitch of 200 µm and 30 cm in length [78]. The strips are arranged in different orientations in a pattern (x-u-v-x), with strips, x, organised vertically and strips, u and v, rotated by a stereo angle of -5° and +5° respectively.

Each of the three T stations comprises four modules. Situated near to the beam pipe is the IT, which is repeatedly made up of silicon microstrips with the same pitch of 200 µm and (x-u-v-x) arrangement as the TT. It is the size and arrangement of the shapes where the two tracker systems differ, however. Each strip is either 11 or 22 cm in length and arranged in a cross shape [78]. Surrounding the IT to cover the rest of the detector acceptance at lower pseudorapidity values are then the OT's which are made up of Kapton/Al straw-tubes, which emulate a drift-time chamber to track charged particles. Each drift tube comprises a gas mixture of 70 % Argon and 30 % CO_2. Two strips of thin foils of Kapton-aluminium are wound together to form the outer layer, and the inner foil (the cathode) consists of 40 µm Kapton-XC. A grounded cylinder with an anode wire running through makes up each straw-tube. Whenever a charged particle passes into the gas mixture ionisation takes place and produces charge deposition on the anode wire. An accurate measurement of the radius of curvature, and therefore momentum, of a particle is determined from the coordinates at the ionisation points. The momentum of a particle over a large area can therefore be established, providing sufficiently good momentum resolution to measure the invariant mass of a b hadron on the order of 0.4 %. This procedure is sufficient for events with high track multiplicity, where a high reconstruction efficiency is required. However, a coordinate resolution of 200 µm is required in conjunction with a drift time of < 50 ns. Each module has two layers of 64 drift tubes [78].

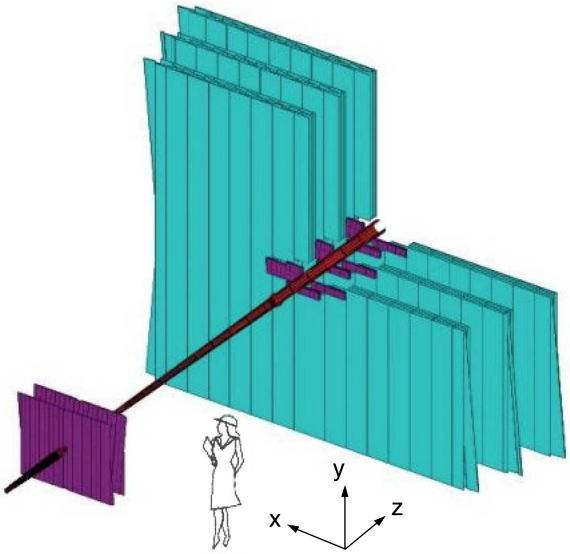

Figure 4.6: Schematic diagram of the tracking system. The silicon trackers, TT and IT, are shown in purple, and the OT is shown in blue [78].

4.3.6 The RICH detectors

The principal use for the Ring Imaging CHerenkov (RICH) detector is particle identification (PID), crucially differentiating pions from kaons. A conventional RICH detector design is employed for Run 2 (2015-2018). Particles traverse through its gas at speeds surpassing the speed of light in the medium and flashes of Cherenkov light are produced. This light is detected by arrays of photomultiplier tubes formed by a series of spherical and flat mirrors to reflect and focus the Cherenkov light onto the tubes. The photomultipliers used are Hybrid Photon Detectors. The radius of the path of the Cherenkov radiation is a function of both the speed of the particle in the medium and the pressure of the gas. Since the momentum of the particle is measured by the tracking system, and the speed of the particle is known from the radius of the Cherenkov radiation, the mass of the particle can be determined. Hence the particle can be identified. Two RICH detectors, RICH1 and RICH2, are deployed to cover the full momentum range of $\sim$ 1–100 GeV/c [78].

RICH1 is situated ahead of the magnet, as it is deployed to measure low momentum particles in the range of 1–60 GeV/c. It has a vertical optical layout and covers the full LHCb acceptance from $\pm$ 25–300 mrad (horizontal) and $\pm$250 mrad (vertical) utilising Aerogel and C_4F_{10} radiators [78].

RICH2 is placed after the magnet as it is utilised to measure high momentum particles in the range of 15–100 GeV/c and beyond. It has a horizontal optical layout and

the radiator used is CF_4. Additionally, its acceptance is limited from ± 15–120 mrad (horizontal) and ±100 mrad (vertical) [78].

In order to detect Cherenkov photons and determine their coordinates in the RICH detectors, Hybrid Photon Detectors (HPDs) are used. HPDs measure wavelengths within the range of ∼ 200–600 nm. When a photon hits the photocathode in the HPD it creates a photoelectron. A voltage of 10–20 kV accelerates the photoelectron onto a reverse-biased silicon detector, creating 1 electron-hole pair for every 3.6 eV of energy deposited, and the signal is read out with high efficiency. To ensure that each HPD can perform in magnetic fields up to 50 Tm, they are sheathed in iron shields in MuMetal cylinders, which is a nickel and iron ferromagnetic alloy. A schematic of a HPD is shown in fig. 4.7 [78].

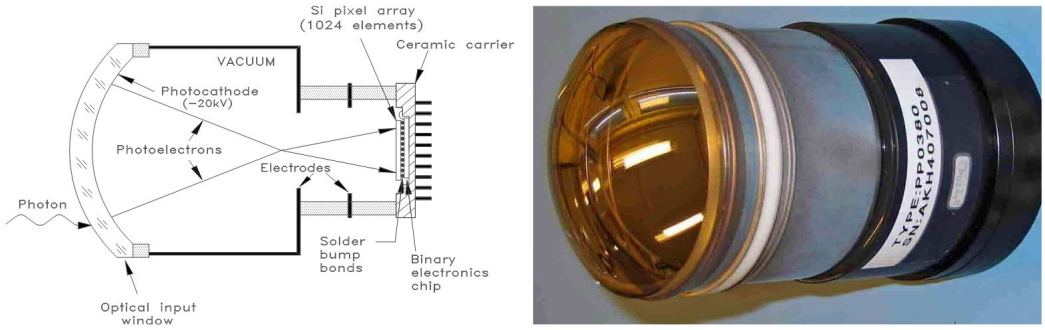

Figure 4.7: HPD layout [78].

4.3.7 The Calorimeters

LHCb has two calorimeters, the Hadronic CALorimeter (HCAL), which is a sampling device, preceded by a Shashlik type Electromagnetic CALorimeter (ECAL). The ECAL contains photomultipliers (PMT) which receive scintillation light read out by plastic wavelength-shifting (WLS) fibres. The HCAL comprises Fe and scintillator tiles and provides a number of functions, including the PID of hadrons, and determination of their transverse energy and position. The ECAL primarily performs PID of electrons and photons. The transverse energy measurement of the ECAL and HCAL is used in the L0 trigger decision to retain an event. This verdict is resolved in 4 µs as the L0 electron trigger needs to reject 99 % of pp interactions. To achieve this, electrons with high transverse energy in the trigger are selected and measured by the ECAL. Good shower separation and resolution are needed to ensure the calorimeter can perform the key function of background rejection. A preshower detector (PS) followed by an ECAL is employed when the longitudinal

segmentation of the EM shower is required to reject a charged pion background, for example. A scintillating pad detector (SPD) is inserted before the PS to identify charged particles, which supports π^0 background rejection in the electron trigger. Single fibres are read out by multianode photomultiplier tubes (MAPMT) in the SPD and PS, and a lead converter is inserted between them. The selected thickness of lead accommodates both the trigger performance and the energy resolution. The remaining background at L0 is provided by high energy photons which cannot be identified here. Complete confinement of the high energy photons is required to achieve a full energy resolution which requires an ECAL of 25 radiation lengths long. The HCAL does not have this requirement, so due to space restrictions, it is 5.6 interaction lengths long [78].

4.3.8 The Muon Stations

Muons are used to identify numerous CP-sensitive b decays, for example, in $B_d^0 \to J/\psi(\mu^+\mu^-)K_s^0$ and $B_s^0 \to J/\psi(\mu^+\mu^-)\phi$ decays and in the rare decay $B_s^0 \to \mu^+\mu^-$. It is essential, therefore, to have the means for their identification at LHCb and crucial for the analysis of this thesis as it is focused on the decay of quarkonia to oppositely charged muons. The muon detection arrangement at LHCb is comprised of five stations. In order to enable fast measurements of muon p_{T} in the trigger, the initial station is situated in advance of the calorimeters, and the others behind the calorimeters with 80 cm thick lead, sandwiched between each of the four stations. To ensure a 20 % acceptance for b semi-leptonic decays, the inner and outer acceptances are 20 (16) mrad and 306 (258) mrad in the bending (non-bending) plane. The five stations and calorimeters account for 20 interaction lengths collectively, and to navigate through this arrangement the transverse momentum of a muon p_{T} must be at least 6 GeV/c. The muon's track direction and p_{T} are determined partially by the first three stations. The last two distinguish the particle as a muon, as in all probability no other particle will arrive at these stations. Triple-GEM's are used in the vicinity of the beam pipe, and Multi-Wire Proportional Chambers (MWPC) are utilised to encompass the broad area of detector acceptance [78].

CHAPTER 5

Future LHCb detector upgrades

To achieve the physics goals of LHCb, the detector has been upgraded during Long Shutdown 2 (2019–2022), in preparation for Run 3 (2022–2025). This is Upgrade I. The detector will then be upgraded again during Long Shutdown 4 (2033–2034), in preparation for Run 5. This is Upgrade II. In this chapter, I will discuss contributions I made to both Upgrade I and Upgrade II.

5.1 LHCb Detector Upgrade I - Run 3

In this section, I will describe a general overview of the what parts of the detector were upgraded for LHCb Upgrade I (Run 3). Then I will discuss the contributions I made to the RICH commissioning, and to the trigger framework.

5.1.1 General overview of upgrade

A total of $9\,\text{fb}^{-1}$ has been collected by LHCb during Run 1 and Run 2. The goal for LHCb is to be able to collect $50\,\text{fb}^{-1}$ of data by the end of Run 4 of the LHC. In order to collect this much data, the trigger framework and different components of

the detector were upgraded during Long Shutdown 2. The trigger upgrade will be discussed in more detail in section 5.1.3, and the RICH upgrade in section 5.1.2 [87].

A number of upgrades were made to the LHCb subdetectors. The VELO was upgraded to be closer to the beam, reducing the inner radius from 8.4 mm to 5.1 mm. The amount of detector material has also been reduced from 4.6 % to 1.7 % of a radiation length. The VELO was also updated to a pixel detector, rather than the previous silicon strip design. All three of these updates improve the impact parameter resolution of tracks. The other tracking components, the T stations, have been replaced with the UT and SciFi Tracker as shown in fig. 5.1. In the UT, the inner sensors are closer to the beam pipe, and segmented to handle the expected radiation dose. The combination of the VELO + UT + SciFi detectors will allow the track algorithms to reconstruct fewer fake tracks, with a reduction by 50–70 %. This will help significantly with the trigger timing. The calorimeters and muon chambers have not been upgraded except for the readout electronics, and the removal of M1 [87].

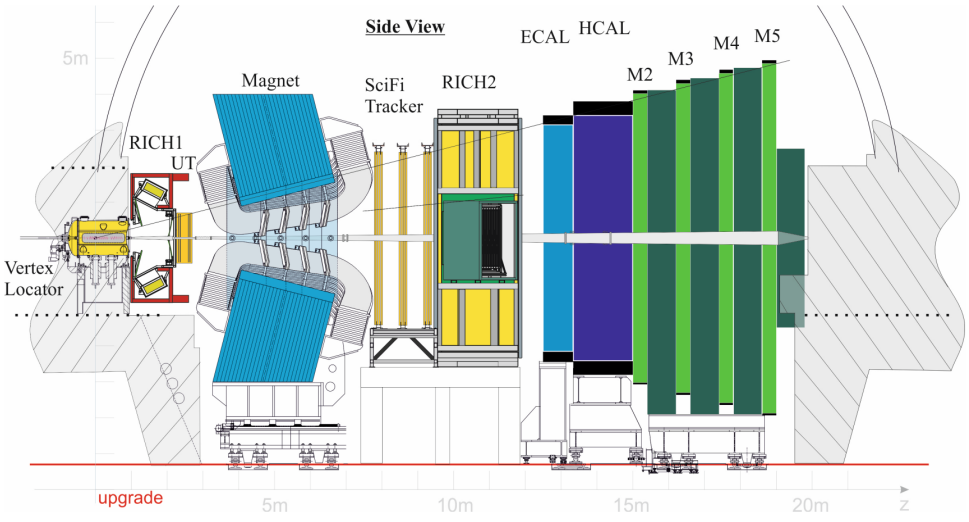

Figure 5.1: LHCb Upgrade I design [87].

5.1.2 Contributions to RICH detector commissioning

For Run 3 of the LHCb detector, both RICH detectors were upgraded. The aerogel was removed from RICH1 to increase the number of photons detected per track, which is important for high luminosity operation [88]. The mirror geometry was changed to take into account the higher occupancy the RICH has to withstand at

higher luminosity. Finally, the photon detector and readout system was upgraded. The requirement for the Run 1 and 2 readout was 1 MHz. As the hardware level in the trigger was removed, this requires that the different sub-detectors must be read out in real time during Run 3 at a 40 MHz rate. The photon detectors themselves also needed a higher spacial and angular resolution. The dark-count rate also needs to be reduced. This is the number of counts registered without any incident light shone on the photon detector, which arises mainly from thermal effects. Finally there must be a low cross-talk (interference) between readout channels. The previous photo-detectors were Hybrid Photon Detectors (HPD), shown in section 4.3.6, with a radius of 72 mm and contained a 1 MHz readout chip. These have been replaced with Multianode-Photomultiplier Tubes (MaPMTs) with external 0.35 µm CMOS chips for the 40 MHz readout called CLARO. There are two types of MaPMTs which were produced by Hamamatsu, R-type and H-type. R-type are Hamamatsu R13742 MaPMTs with 64 channels and $25.4 \times 25.4\,\mathrm{mm}^2$ in area. These are used to cover all of RICH1 and the inner parts of RICH2. H-type are Hamamatsu H21699 MaPMTs with 64 channels and are $50.8 \times 50.8\,\mathrm{mm}^2$ in area. These are used for the outer parts of RICH2. MaPMTs are vacuum photodetectors. When the photons enter the MaPMT, they are converted to photoelectrons by the photocathode. The signal is then amplified through a series of dynodes under a graded potential [89].

During Run 3, to make it easier to remove and repair or replace the photon detectors in case they are damaged, everything is contained within an elementary cell (EC). The major components are the MaPMTs, baseboard, CLARO and FPGA. A picture of an EC is shown in fig. 5.2. There are two types of EC: EC-R type which contains four R-type MaPMTs and EC-H type which contains one H-type MaPMT [89].

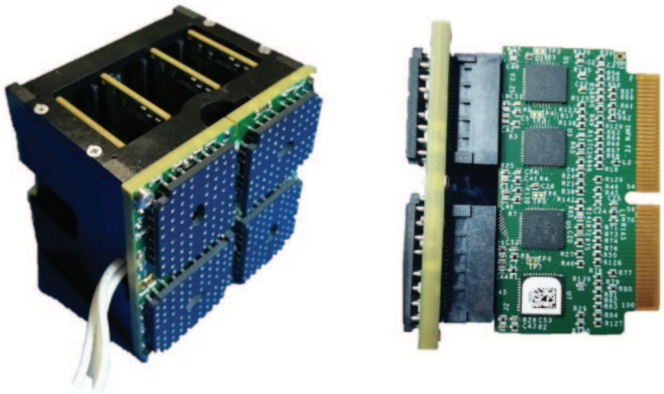

Figure 5.2: A picture of an EC-R. The CLARO chips are soldered onto the front-end boards [90].

As part of the RICH upgrade for Run 3, I was in charge of writing commissioning scripts that were used during the Long Shutdown to calibrate the readout of each CLARO. This involved calibrating the threshold for readout and maximising the signal-to-noise ratio for each readout channel of the MaPMTs. This was done by performing Data Acquisition (DAC) and threshold scans for each channel on each RICH detector column. These scans produced plots and log files which users used to check the CLARO calibration. These scans are described in more detail in the following sections.

5.1.2.1 DAC scan

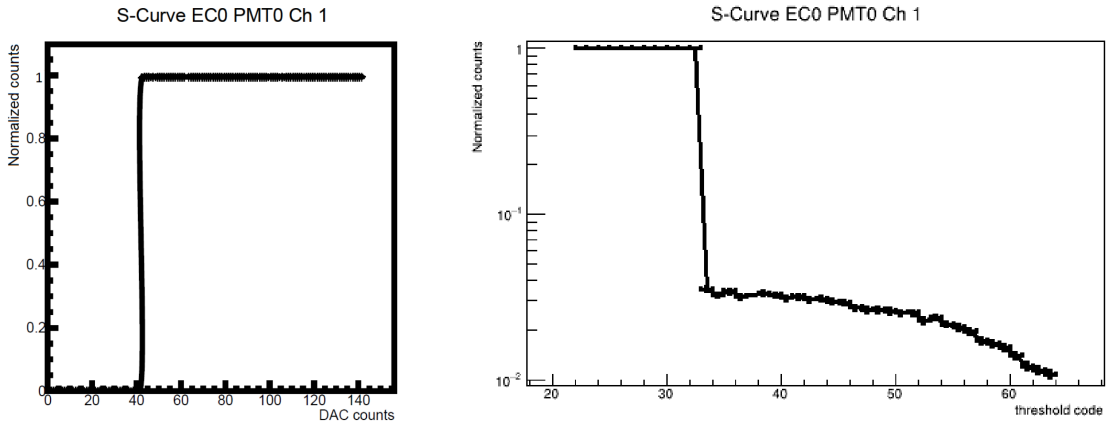

Figure 5.3: Left: DAC scan, right: Threshold scan [89].

This is performed to calibrate the CLARO. First, the readout threshold of the CLARO is programmed. Then a discrete charge is injected in steps into the CLARO chip capacitor into the MaPMT channel. The expected response of the CLARO is an s-curve going from 0 to 1, due to its binary response when it reaches the programmed threshold. This is called a DAC scan. An example plot is shown in fig. 5.3. The step size is referred to as a $\mathrm{DAC_{count}}$, which converts to injected charge as,

$$\mathrm{Charge[ke^-]} = 15.6\mathrm{[ke^-]} \times \mathrm{DAC_{count}}, \tag{5.1}$$

where Charge and 15.6 are in units of $\mathrm{ke^-}$, which is 1000 times a unit of elementary charge. The maximum number of $\mathrm{DAC_{count}}$ that can be injected is 256 [89]. From this s-curve a transition point, x_{trans}, and the width of the transition, σ_{trans}, can be found. In this case, the distribution $y_{\mathrm{DAC}}(x)$, which is defined as,

$$y_{\mathrm{DAC}}(x) = 0.5\left(1 + \mathrm{erf}\left(\frac{(x - x_{\mathrm{trans}})}{\sigma_{\mathrm{trans}}}\right)\right) \ , \tag{5.2}$$

is used to fit the data, where erf(x) is the error function [89]. To calibrate the CLARO, DAC scans are performed at different readout thresholds, z_{th}, of the CLARO. From this, x_{trans} and σ_{trans} can then be plotted *vs.* z_{th}. Here, x_{trans} *vs.* z_{th} is particularly important, as a linear fit results in,

$$x_{\mathrm{trans}}[\mathrm{ke}^-] = \Delta x[\mathrm{ke}^-] * z_{\mathrm{th}} + x(0)[\mathrm{ke}^-] \ , \tag{5.3}$$

where $\Delta x[\mathrm{ke}^-]$ gives the charge that corresponds to a CLARO threshold step, and $x(0)[\mathrm{ke}^-]$ is the intrinsic CLARO offset [89]. For each column of the RICH detector, there are a total of 6,144 channels that need to be calibrated. This is because each RICH detector column is made up of two halves. Within each half, there are three Photo-Detector Modules (PDMs). The PDMs are subdivided into four EC's and each of these is further subdivided into four MaPMTs. Finally, every MaPMT is made up of 64 channels. For each channel, Δx and $x(0)$ are determined from the procedure explained above. These values are then plotted in histograms shown in fig. 5.4 for different settings of the CLARO. The CLARO can program up to 64 different readout thresholds, 4 different attenuation schemes (0-3) and an offset (0 or 1). The attenuation is used to reduce the signal by $2^{\mathrm{attenuation}}$, which is useful to fit the pulse height of the single photon spectra. The offset of 1 shifts the programmed threshold by 32 threshold levels. This is useful to investigate noise (the pedestal effect) [89]. Figure 5.4 shows Δx and $x(0)$ for different settings of the CLARO. As well as the user being able to produce these plots, the channel numbers that fail to obtain a Δx and $x(0)$ value are saved into a log file, which the user can open and investigate further for each RICH column.

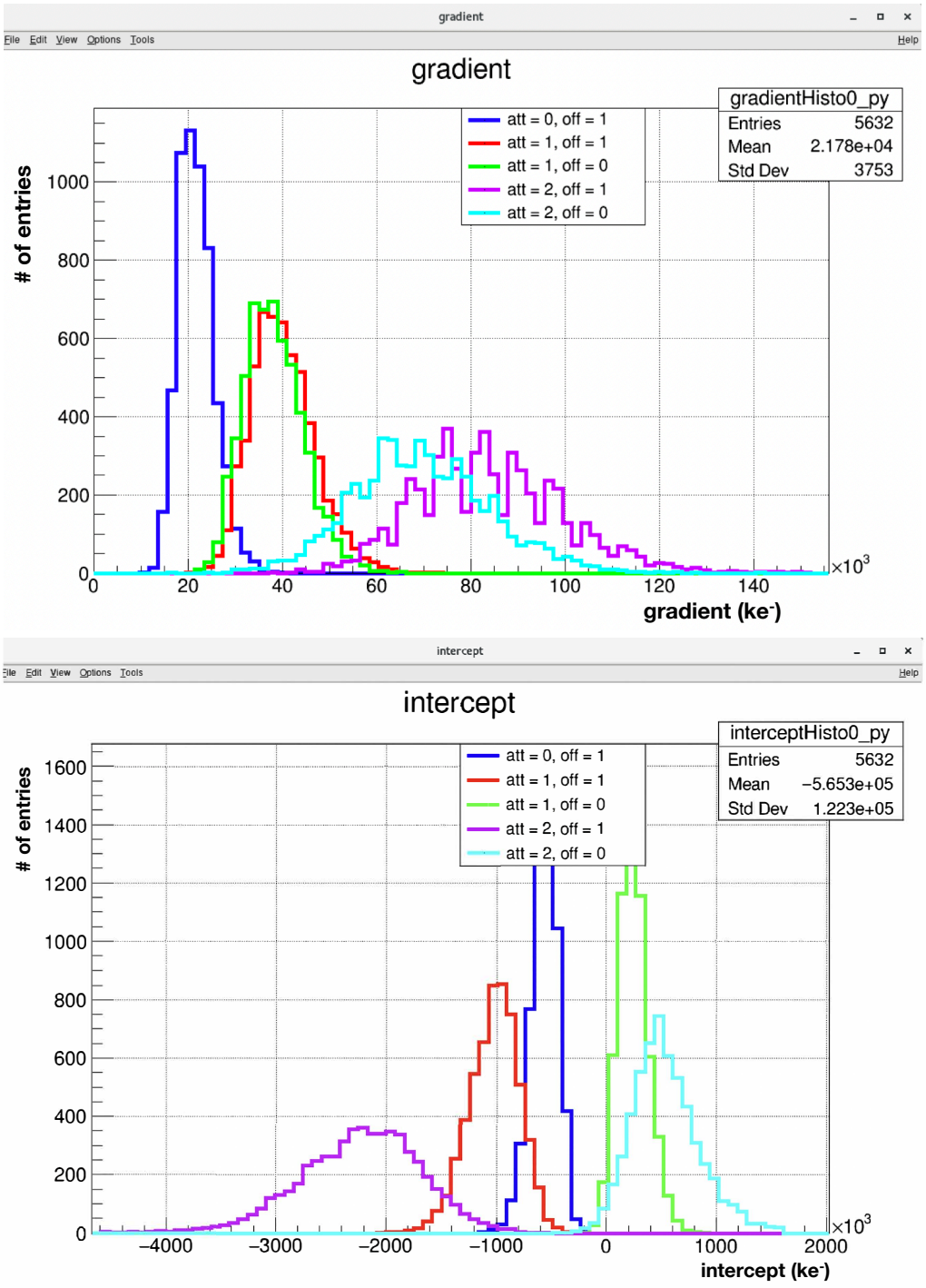

(b) Intercept

Figure 5.4: DAC scan output from the commissioning scripts with the CLARO showing a normal response. Different settings are used to calibrate the CLARO, where the attenuation (att) reduces the signal by a factor 2^{att} to fit the pulse height, and the offset (off) is used to investigate noise.

5.1.2.2 Threshold scan

The same method as the DAC scan is performed in a threshold scan, except now each channel of MaPMT is illuminated with a 405 nm laser, to measure its response. An example of a threshold scan is shown in the plot on the right-hand side of fig. 5.3. The left-hand part of the plot is noise from the oscilloscope, which has an exponential drop into the signal region. This signal is made mostly up of the single photon peak, where one photoelectron is amplified by the first dynode. Cross talk also contributes to this peak, as well as the rare case of a double photon peak, where two photoelectrons reach the first dynode. The optimal threshold voltage is chosen to maximise the signal-to-noise ratio, which is the cross point shown in fig. 5.3, where the exponential drop and signal bump meet [89].

5.1.3 Contributions to trigger upgrade / lines

As described in section 4.3.1, the first stage of the Run 1 and 2 trigger system was a hardware trigger (L0). However, this stage is more limited in the reconstruction and causes a bottleneck in the number of events that can be reconstructed, especially hadronic events. Figure 5.5 shows with the Run 1 and 2 trigger framework, that even if the luminosity is increased, the number of triggered hadronic events will eventually saturate [87].

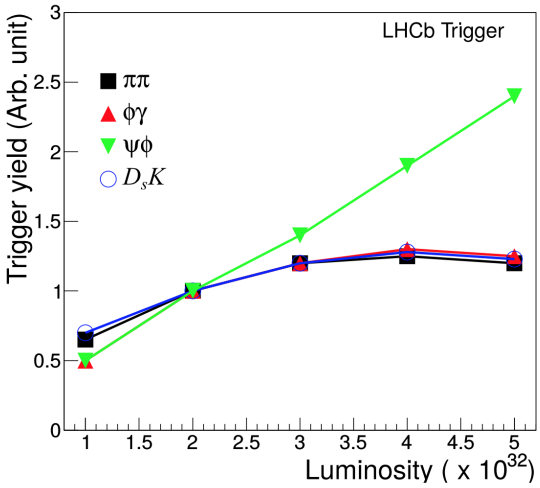

Figure 5.5: Trigger yield *vs.* luminosity with Run 1-2 trigger setup [87].

In Run 3, the L0 has been replaced with a fully software trigger, where full event reconstruction can take place and the detector is read out in real time at 40 MHz.

This is split into two levels, HLT1 and HLT2, where the HLT1 trigger selection is programmed onto GPUs whereas HLT2 is programmed onto CPUs. There are also options to reconstruct the whole event, or just the decay of interest [91]. Overall, this new framework increases the trigger efficiency by a factor of around 2 to 4 for hadronic channels [87].

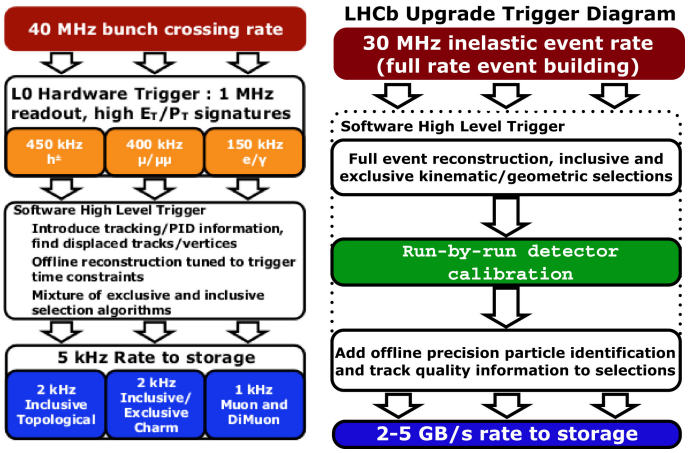

Figure 5.6: Comparison of the trigger framework for Run 1 and 2 *vs.* Run 3 [91].

As part of the trigger upgrade for Run 3, I was in charge of incorporating HLT2 jet lines into the Run 3 framework. In particular heavy flavour jets, which are important in QCD analyses, such as measuring the intrinsic charm content of the proton [92], and also for beyond the standard model physics signatures.

Heavy flavour particles, which contain a b or c quark, can be characterised by a displaced secondary vertex (SV) from the initial interaction at the PV. These usually have two to four tracks that originate from the SV. When clustered within a jet, they would also carry a significant amount of the energy of the jet. Hence, to identify heavy flavour jets, first a particle flow algorithm is applied, which combines information from the trackers and the calorimeters to form individual particles. These 'particles' are then clustered into jets using the anti-k_t algorithm [42] using FastJet [40]. Then a secondary vertex tagger is used to identify between b, c and light flavour (u, d, s and g) jets. This method was first implemented at LHCb in Ref. [93] during Run 2. The SV tagger gathers all of the tracks in an event into pairs. These pairs are then filtered with specific requirements, such as the distance of closest approach (DOCA) between any two tracks, the χ^2 of the SV vertex fit and χ^2_{IP} which is the difference in χ^2 of a PV reconstructed with and without a considered track. Once in pairs, a pair can still have the potential of sharing the same track with another pair. To remove duplicates, all the pairs that contain the

same track are linked within the same jet. Therefore the SV can contain any number of tracks.

The optimal cut values for the variables to create the SV object are obtained from two boosted decision trees (BDTs). The first separates b or c jets from light jets, the second separates b from c jets. These BDTs were trained from simulated b, c and light jet samples. The outputs of the BDTs are shown in fig. 5.7. The same optimised variable cut values obtained from the BDTs in Ref. [93] for the SV tag are used as the cut values in the trigger algorithm.

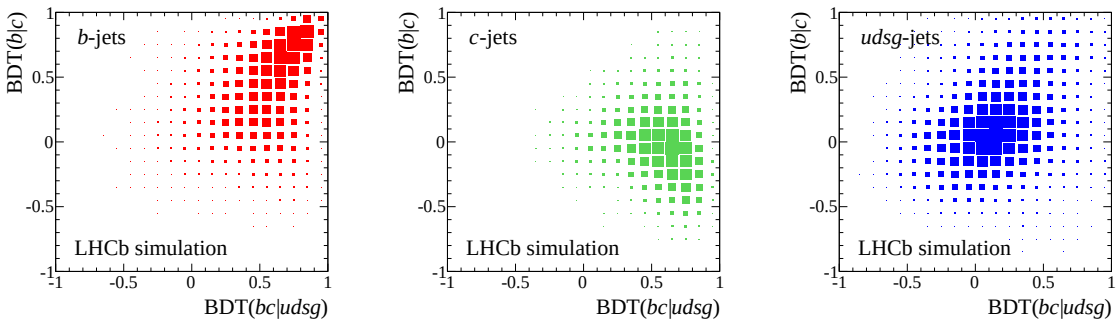

(a) b jets. (b) c jets. (c) light jets.

Figure 5.7: BDT($b|c$) *vs.* BDT($bc|udsg$) output distributions to distinguish between b, c and light flavour jets [93].

Hence, using the SV tagger method, various di-jet HLT2 lines have been written into the Run 3 trigger framework. Example lines are shown in table 5.1, as light flavour di-jets (`DiLightJet`), SV tagged di-jets (`DiSVTagJet`) and topological-trigger tagged di-jets (`DiTopoTagJet`) with different minimum p_{T}(jet) values. Topological-trigger tagged jets use the same method as SV-tagged jets, but with less stringent requirements imposed. The trigger rate and efficiency have been calculated for each trigger line using simulated $b\bar{b}$ jet events. Further cross-checks would be to use charm and light jet events also. The efficiency, ϵ_{trig}, is calculated as,

$$\epsilon_{\mathrm{trig}} = \frac{\text{number of triggered events that pass any HLT1 line + HLT2 line of interest}}{\text{number of triggered events that pass any HLT1 line}}, \tag{5.4}$$

using $b\bar{b}$ jet MC events. The trigger rate, R_{trig}, is then calculated as,

$$R_{\mathrm{trig}} = \sigma_{b\bar{b}}\, L_{\mathrm{inst}}\, \epsilon_{\mathrm{trig}} \tag{5.5}$$

where $\sigma_{b\bar{b}}$ is the cross section of $b\bar{b}$ jet events and L_{inst} is the instantaneous luminosity.

As the minimum p_{T}(jet) value decreases, the chance of the event being triggered

increases, and hence the rate increases, as shown in table 5.1. The acceptable rate for a single trigger line is $\lesssim 0.1\,\text{kHz}$. For the trigger lines shown in red, the rates are above the acceptable level. To reduce the trigger rates, lower momentum lines are prescaled.

Line	Prescale	Rates (kHz)	Efficiency ($b\bar{b}$ events)
Hlt2DiLightJet15GeV	1.0	15.10 ± 1.21	0.463 ± 0.016
Hlt2DiLightJet15GeV	0.01	0.2 ± 0.14	0.007 ± 0.003
Hlt2DiLightJet35GeV	1.0	0.1 ± 0.09	0.071 ± 0.008
Hlt2DiTopoTagJet15GeV	1.0	10.4 ± 1.01	0.408 ± 0.016
Hlt2DiTopoTagJet15GeV	0.01	0.2 ± 0.14	0.002 ± 0.001
Hlt2DiTopoTagJet35GeV	1.0	0.1 ± 0.09	0.067 ± 0.008
Hlt2DiSVTagJet15GeV	1.0	0.8 ± 0.28	0.268 ± 0.014
Hlt2DiSVTagJet15GeV	0.1	0.0 ± 0.0	0.020 ± 0.0044
Hlt2DiSVTagJet35GeV	1.0	0.0 ± 0.0	0.055 ± 0.007

Table 5.1: Jet trigger lines included in the Run 3 trigger framework, with various prescales and minimum $p_{\text{T}}(\text{jet})$ values.

5.2 Future detector upgrade R&D - LGADs

To exploit the full physics potential of LHCb, the detector will be upgraded again during Long Shutdown 4. The maximum luminosity will reach $1.5 \times 10^{34}\,\text{cm}^{-2}\,\text{s}^{-1}$ with the goal to acquire $300\,\text{fb}^{-1}$ of data. To achieve this, a maximum pile-up of $\sim$40 is expected so to reconstruct events with such a high level of activity, exploiting timing information will be crucial. Disentangling the information from distinct events that overlap within the detector to reduce the combinatorial component is possible by extending the tracking algorithms to use the arrival time of particles at individual sensors [94].

Studies by LHCb have defined the specification for all proposed sensors to meet for use in this high pile-up environment. The overall aim is to maintain the same impact parameter resolution expected after Upgrade I in the higher pile-up conditions of Upgrade II. In this environment, the sensors will also need to be extremely radiation hard. Depending on the final geometry of the detector, the timing resolution of the sensors must be $\leq 35\,\text{ps}$, handle integrated fluences between 1–6 $\times 10^{16}$ 1 MeV $\text{n}_{\text{eq}}/\text{cm}^2$ and have a pixel pitch of $\leq$ 42–55 µm [94].

Several timing detectors have been proposed, which can be classified into two dif-

ferent categories, both in early stages of development. One is to convert the current VELO 3D tracking detector into a 4D detector, by adding an ASIC that assigns a timestamp to a particle as it traverses the VELO; TimePix is an example of such an ASIC. The second is to add separate timing planes to the VELO detector that contain arrays of timing sensors. Examples of possible orientations of these planes are shown in fig. 5.8. This second option is explored in this thesis, where the potential candidates under test are called Low Gain Avalanche Detectors (LGADs) which have been produced by *Micron* [94].

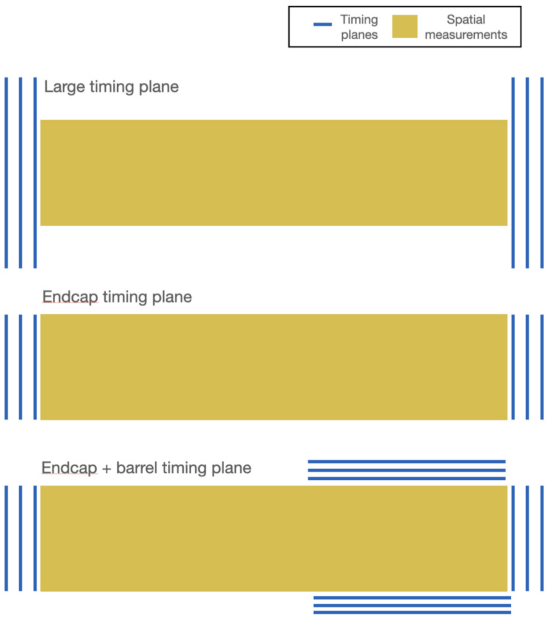

Figure 5.8: Possible timing plane orientations around the VELO [94].

In this section, I will firstly summarise the underlying principles and design of these LGADs. This will be followed by a discussion of the experimental set ups used to measure the gain and why this is important. Finally, I will show preliminary results of the gain measurements of the sensors, before and after they have been irradiated.

5.2.1 LGAD theory

5.2.1.1 LGAD design

An LGAD is a semiconductor device. The simplest type of semiconductor device to produce is a p-n diode. A diode usually consists of two types of silicon placed side-by-side, p-type and n-type. This p-type silicon is doped with boron, and n-type

silicon is doped with phosphorus. The n-type contains more electrons than the p-type, so when they are placed side-by-side, there is a charge density gradient and the electrons begin to diffuse from the n-type to the p-type. The absence of electrons or 'holes' , which behave as positively charged particles, then also start to diffuse from the p-type to the n-type. This diffusion leaves positive ions behind in the n-type as electrons diffuse near the junction, and negative ions in the p-type. This diffusion occurs until it is energetically favourable to stop. The region of excess charge around the p-n junction creates a potential barrier, which is called the depletion voltage, and an electric field is generated in this region. When a diode is put into forward bias, *i.e.* where an applied external voltage balances the depletion voltage of the diode, the electrons have sufficient energy to cross this potential barrier and current begins to flow. When a diode is put into reverse bias, free charges are pulled away from the p-n junction, hence the depletion width, and the electric field increases [95].

When a semiconductor device is in reverse bias and radiation is incident on the sensor and passes through the depletion region, electron-hole pairs are generated. Due to the electric field in the depletion region, these free charges move and an avalanche is produced. This produces a current that can be measured, with the signal peak height proportional to the energy of the incident radiation [95].

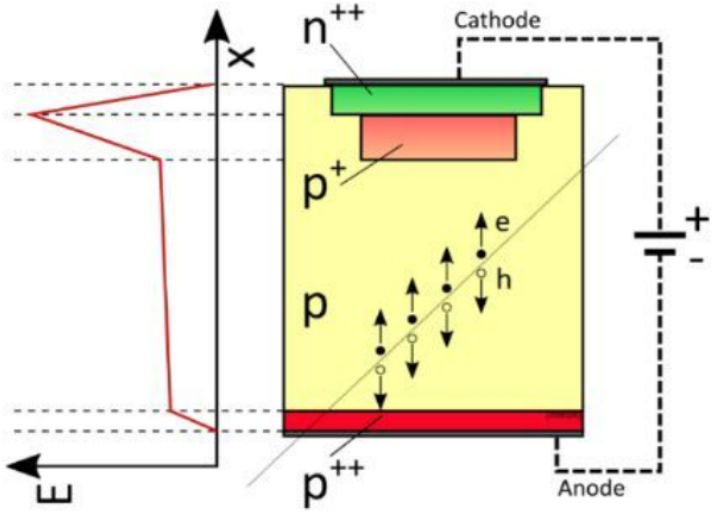

Figure 5.9: Simple LGAD design, showing the electric field profile. Electron-hole pairs are generated along the optical path of the incident laser [96].

An LGAD is a more complicated semiconductor device, which is shown in fig. 5.9 above. In an LGAD, a highly doped p+ layer between the p-bulk (the active zone) and the n++ layer is inserted. This layer gives an additional rise in the electric

field, as shown in fig. 5.9, and, if sufficiently high, can produce a large multiplication/avalanche of charges [96]. An example of a current *vs.* time plot is shown in fig. 5.10, where the back-side (the p-bulk side) is illuminated with a short pulse of laser light. For the LGAD shown in blue, first the laser light creates electron-hole pairs in the p-bulk. Second, the electrons drift and reach the top layer and are multiplied. Then the holes return, ending the drift and no current is produced. The amount of gain depends very much on the design of the gain layer, including its width, the p+ implant width and the level of impurities (such as carbon) added to the gain layer to reduce changes of the gain layer doping after irradiation. The orange distribution in fig. 5.10 is for a PIN. A PIN has the same design as an LGAD but lacks the inserted p+ layer, hence there is no amplification of the signal [97]. These devices are useful to characterise the gain of LGADs, as will be discussed further in section 5.2.2.3.

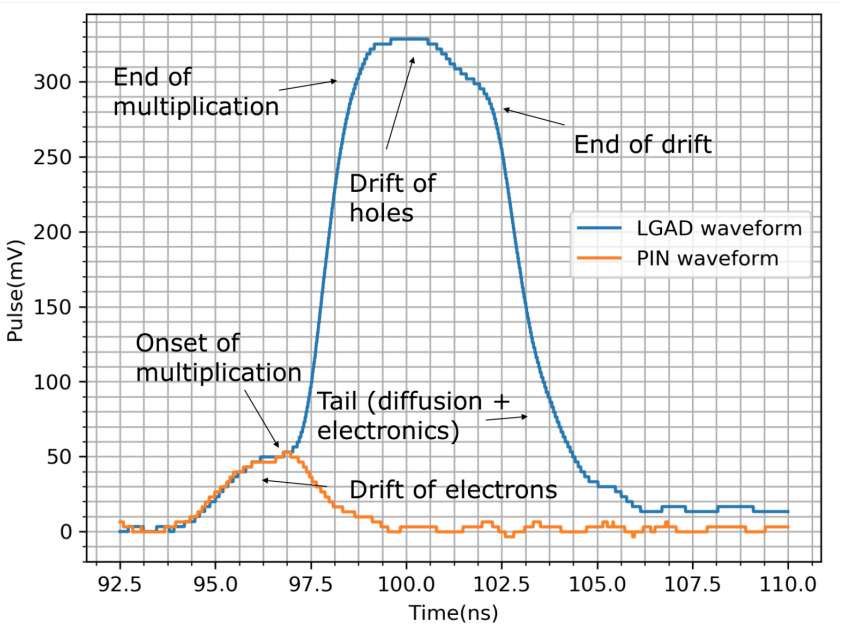

Figure 5.10: Voltage pulse *vs.* time for an LGAD (blue) and a PIN (orange) [97].

A more detailed design of an LGAD is shown in fig. 5.11. The Junction Termination Extension (JTE) is used to prevent premature breakdown at the edge of the gain layer which would give a sharp rise in the electric field. It also allows the sensors to be isolated from surrounding sensors on the same wafer. The guard-ring reshapes the electric field near the JTE and acts as a cathode for the peripheral region. The P-stop prevents a connection between the guard-ring and the JTE.

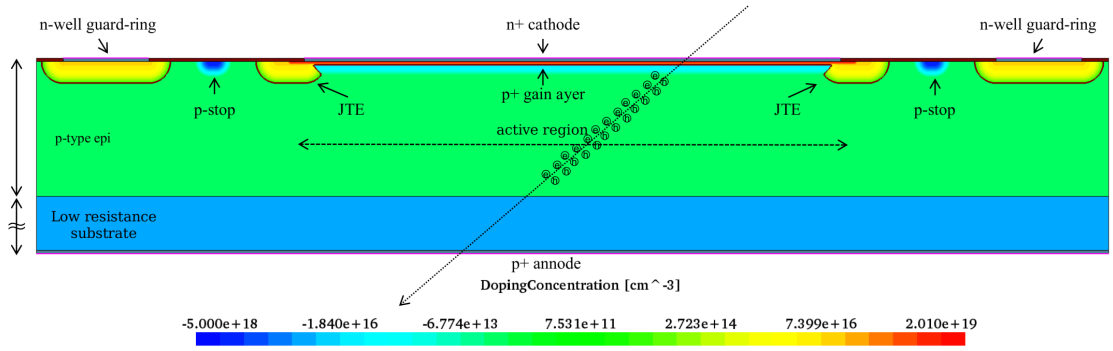

Figure 5.11: More detailed LGAD design, including JTE, P-stop & guard-ring [98].

5.2.1.2 Time resolution and gain

Excellent timing resolution, σ_t, is critical for the LGADs to be considered as a potential detector candidate. The timing resolution of a generic sensor itself depends on three parameters, σ_{jitter}, $\sigma_{\text{time-walk}}$ and σ_{TDC}, defined in eq. (5.6).

$$\sigma_t^2 = \sigma_{\text{jitter}}^2 + \sigma_{\text{time-walk}}^2 + \sigma_{\text{TDC}}^2 \ . \tag{5.6}$$

Here, σ_{jitter} is the error due to noise jitter in the signal being measured,

$$\sigma_{\text{jitter}} = \frac{\sigma_n}{\left|\frac{dV}{dt}\right|} \approx \frac{\sigma_n}{\left|\frac{S}{\tau_p}\right|} = \frac{\tau_p}{\frac{S}{N}}, \tag{5.7}$$

where σ_{jitter} depends on the rise time of the signal, $|dV/dt|$, and the signal to noise ratio, (S/N). The σ_n term represents the uncertainty in the noise and τ_p is the peak time [99]. This is illustrated schematically in fig. 5.12,

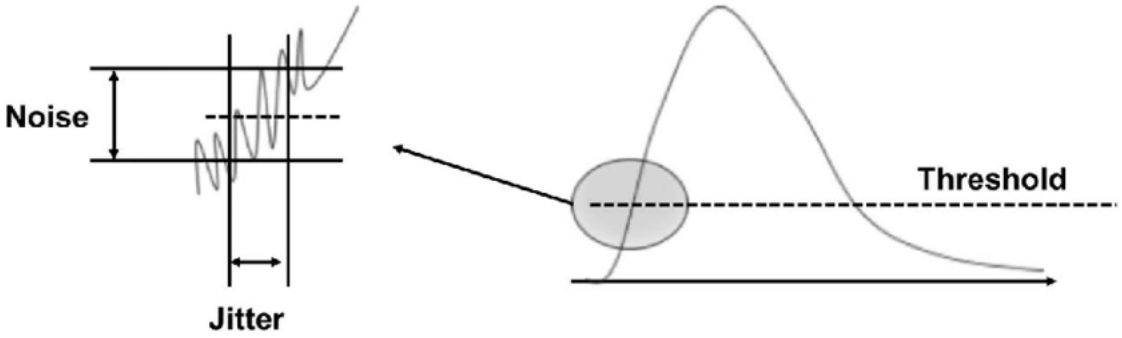

Figure 5.12: How noise translates into jitter in timing measurements [99].

Since σ_{jitter} depends on rise time of the signal, this term will be minimised with larger intrinsic gain, which is the ratio of output to input signal size. The σ_{TDC} is

the error due to the precision with which the oscilloscope can measure the pulse, in most cases usually negligible [99].

The most significant contributor that gives a natural limit to the time resolution of the sensor is the time-walk component, $\sigma_{\text{time-walk}}$ [99]. This is split into three components,

$$\sigma^2_{\text{time-walk}} = \sigma^2_{wf} + \sigma^2_{lf} + \sigma^2_{Q} \ . \tag{5.8}$$

First, when a sensor is injected with a laser, the response of the sensor is characterised by measuring the output signal voltage distribution as a function of time, $V(t)$, with an oscilloscope. The pulse is triggered when it reaches a certain threshold voltage. However, as demonstrated in fig. 5.13, if the amount of charge deposited in the sensor fluctuates, the pulse may be the same shape but may have a different amplitude. Consequently, the pulse crosses the threshold at different times and measuring the intrinsic time resolution of the sensor can therefore be affected. This is described by the σ_Q term. However, in the case where all signals have the same shape, this is not usually an issue as the measured amplitude can be corrected with a constant fraction discriminator (CFD) or a time-over-threshold (TOT)/time-of-arrival (TOA) algorithm. The problem arises when the signal shapes are not the same, which may arise due to Landau fluctuations, σ_{lf}. When a particle traverses a sensor, it can deposit variable amounts of charge along its path. When the charge reaches the top side of the electrode and is multiplied, it depends on where the charge was created. This cannot be avoided and determines the natural limit of the time resolution of the sensor. For example, the optimal time resolution of a 50 µm LGAD is ~ 25 ps. The σ_{wf} is the weighting field term. This depends on the hit position in a segmented device, *i.e.* depending if the hit is between two segmented electrodes or underneath one electrode, it will give different induced current pulses that are reflected in the timing measurement. Fortunately, if the design of the LGAD pad dimensions are much greater than its thickness, this term is negligible [99].

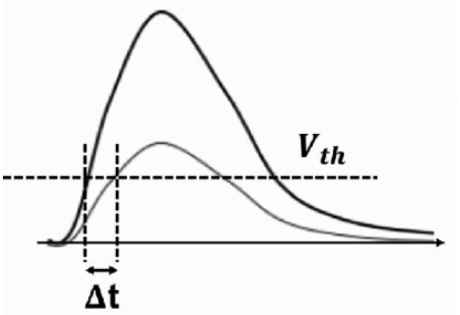

Figure 5.13: Schematic of charge injections leading to time-walk [99].

In summary, to optimise the time resolution, first, a large gain is needed to minimise the σ_{jitter} caused by large noise contributions from the large capacitance. Second, the sensor needs to be thin to reduce time-walk contributions. However, in reality a gain of < 100 is necessary. When considering the noise of a system, as shown in fig. 5.14, at high gain shot noise takes over. Shot noise occurs due to the charge carriers in the current of the system having discrete values of charge, which takes effect at low current values. Hence the signal to noise ratio does not improve with larger gain > 100 [99].

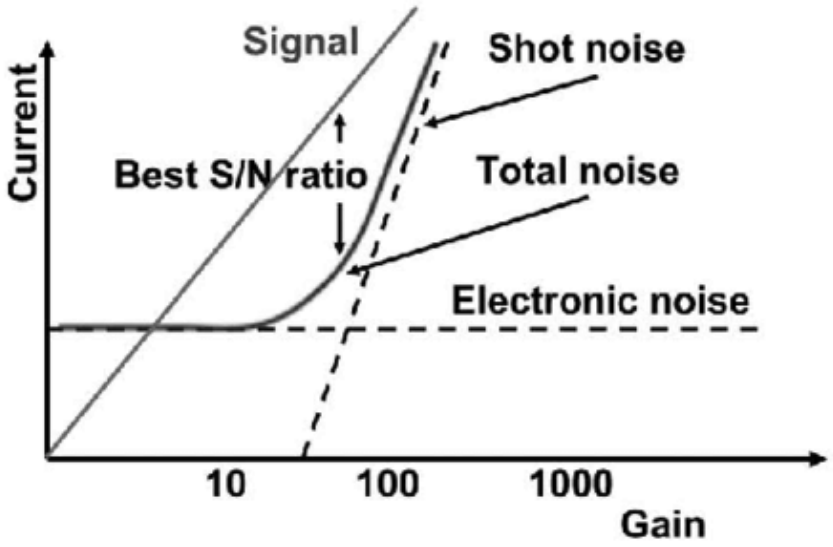

Figure 5.14: Optimising gain value for the best signal-to-noise ratio [99].

5.2.2 Experimental measurements

Gain, timing resolution and IV/CV measurements are the most important parameters used to characterise the behaviour of the LGADs. Experimental setups have been designed at Birmingham to measure these as a function of the applied voltage both before and after irradiation. These results will be compared with those from the LHCb group at the University of Glasgow for the same LGADs to check consistency of measurements between institutes. Initial work carried out and preliminary results are described below, with essential studies of timing resolution and further post-irradiation characterisation forming part of the ongoing programme of work that extends beyond this thesis.

5.2.2.1 Sensors tested

Sensor name		Type	Gain Doping	Pixel	JTE	Irradiated
Bham	Glasgow		($\times 10^{13}$cm^{-3})	(mm)	(µm)	
A	3331-16_East_38-2	LGAD	1.20	1.0	20	No
B	3331-16_East_7-1	LGAD	1.20	0.5	10	No
C	3331-16_East_7-2	LGAD	1.20	0.5	10	No
D	3331-19_East_38	LGAD	1.30	1.0	20	Yes
E	3331-19_East_4-1	LGAD	1.30	0.5	20	No
F	3331-19_West_7-2	LGAD	1.30	0.5	10	Yes
G	3331-19_West_2-1	LGAD	1.30	0.22	10	Yes
H	3331-19_East_29-2	LGAD	1.30	1.0	10	Yes
PIN 1	3331-19_East_30	PIN	N/A	1.0	10	N/A
PIN 2	3331-16_East_39-2	PIN	N/A	1.0	20	N/A

Table 5.2: Sensor naming conventions and properties, including physical dimensions.

A summary of the sensors tested at Birmingham and Glasgow is shown in table 5.2. The main characteristics of each sensor are the gain layer doping concentrations, pixel size and JTE size. Four sensors have been irradiated with a 8.9 $\times 10^{14}$ n_{eq}/cm^2 fluence, using the Birmingham cyclotron. The results presented in section 5.2.3 will use the Birmingham naming convention. An example sensor is shown in fig. 5.15.

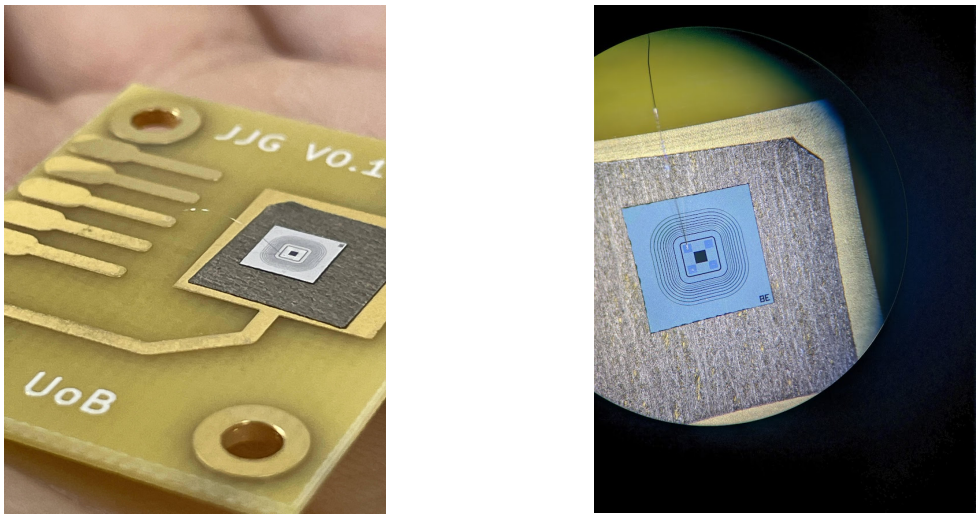

(a) Sensor on climate chamber board. (b) Sensor D under microscope.

Figure 5.15: Close up examples of LGAD sensors.

5.2.2.2 IV/CV setup

To measure the current *vs.* voltage (IV) and capacitance *vs.* voltage (CV) of the LGADs at room temperature and humidity, a probe station is used. This is shown

in fig. 5.16a. This applies a voltage on the back side of the sensor via the chuck, which is the gold metal plate. The probe (the thin metal object) is used as a ground, and placed on the aluminium band around the sensor. The purpose of this is that the sensor does not need to be wire-bonded to a Printed Circuit Board (PCB) to test IV/CV, which means there is less chance of breaking the sensor. An Inductance Capacitance Resistance (LCR) meter controlled by a computer is used to measure the IV and CV.

To perform IV and CV measurements at a controlled temperature and humidity, the sensor is placed into a climate chamber. This is shown in fig. 5.16b. These are also measured with an LCR meter, except the sensors need to be wire-bonded onto a PCB for electrical contact.

(a) Probe station. (b) Climate chamber.

Figure 5.16: Different setup for IV/CV measurements.

5.2.2.3 Gain method and setup

To measure the gain of an LGAD, the laser Transient Current Technique (TCT) is used [100]. Here, to mimic the passage of a charged particle, a pulsed laser is used to inject a constant charge into the LGAD by controlling the wavelength, intensity and frequency of the pulse. As explained in section 5.2.1, this will produce electron-hole pairs within the sensors that are then accelerated by the electric field in the LGAD. This current is measured using a charge sensitive pre-amplifier (CSP), which converts the current into a measurable voltage. This voltage pulse is then triggered and measured using an oscilloscope. An example pulse is shown in green in fig. 5.17.

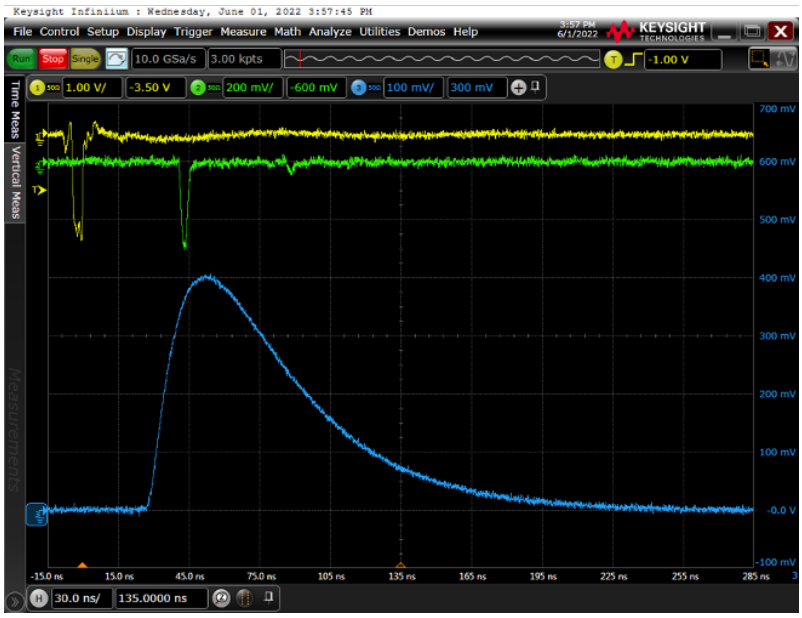

Figure 5.17: Output on oscilloscope of the laser (yellow), beam monitor (blue) and an LGAD (green).

To measure the intrinsic gain of an LGAD sensor, this voltage pulse needs to be integrated as it is proportional to the charge collected by the capacitor in the CSP. To demonstrate this, gain is defined as,

$$Q_L = qG_L, \tag{5.9}$$

where G_L is the gain of the LGAD, q is charge injected by the laser and Q_L is the total charge. Q_L can be determined by measuring the integral of the voltage pulse,

$$S_L = \int_{t0}^{t0+tw} V(t)dt = qAG_L, \tag{5.10}$$

where $V(t)$ is the voltage pulse waveform, S_L is the integral of voltage pulse of the LGAD, $t0$ is the start time of the integration, tw is the integral window and A is the amplification due to the CSP. The integral will include noise as well as signal; however, integration of noise should average to zero [101].

The quantities q and A are not easily measurable but, assuming that they remain stable between the time of performing measurements, they can be eliminated when taking the ratio of voltage integrals of eq. (5.10) for an LGAD and the corresponding PIN,

$$\frac{S_L}{S_P} = \frac{G_L}{G_P}, \tag{5.11}$$

where S_P and G_P are the integral and gain for a PIN respectively. As the two devices differ only by the absence of the gain layer in the PIN, *i.e.* $G_P = 1$, the gain of the LGAD is taken to be

$$G_L = \frac{S_L}{S_P} \, . \tag{5.12}$$

Hence, G_L can be measured by comparing the LGAD and PIN integrals at various bias voltages [101].

However, eq. (5.12) needs to be slightly modified. The charge q injected by the laser remains constant within the same session but not necessarily over longer time intervals. When LGADs from *Teledyne* were tested using the same apparatus, it was found that the charge injection from the laser may vary from day to day [102]. To take this into account, a beam monitor is used. The beam monitor consists of a beam splitter and a photodiode. A 90:10 beam splitter is used to split 90 % of the laser output to the LGAD and 10 % to the photodiode. The photodiode is used to measure the charge injection of the laser and has a voltage waveform that can be integrated and measured, as for the LGAD and PIN. The integral value of the beam monitor voltage waveform for different days, S_{bm} and S'_{bm}, is defined as,

$$S_{bm} = qB \tag{5.13}$$

$$S'_{bm} = q'B \tag{5.14}$$

where q and q' are different charge injections of the laser and B is a generic amplification value [101]. To remove the B dependence, again the ratio can be measured as,

$$\frac{S'_{bm}}{S_{bm}} = \frac{q'}{q} \tag{5.15}$$

Using eq. (5.10) but for a different day, this is re-written as,

$$S'_L = q'AG_L \tag{5.16}$$

Now replacing q' with eq. (5.15), S'_L can be measured as,

$$S'_L = qAG_L \frac{S'_{bm}}{S_{bm}}. \tag{5.17}$$

In the ratio of the LGAD and PIN, there is a constant q which now cancels out. This is the procedure used to measure the intrinsic gain of an LGAD, G_L [101].

Figure 5.18: Gain setup, including the laser, beam monitor and the LGAD on a mechanical stage.

The experimental configuration used is shown in fig. 5.18. The left-hand side connects to the external power supply. Inside the metal box is the infrared laser (1064 nm) which has a beam width of $\approx 50\,\mu m$. The LGAD is mounted on a PCB and placed underneath the laser, as seen in fig. 5.19. The PCB is then placed in a metal box on a stage, which is used to align the LGAD to the laser.

At the back of the box is the beam monitor that is used to record the output of the laser. A Neutral-Density (ND) filter can also be used to reduce the intensity of the laser if needed. The metal box is used to shield the setup from external light. The alignment and laser settings are controlled by a computer that is to the right of the laser. The computer also controls the oscilloscope, which measures the laser (yellow), beam monitor (blue) and LGAD (green) output as shown in fig. 5.17.

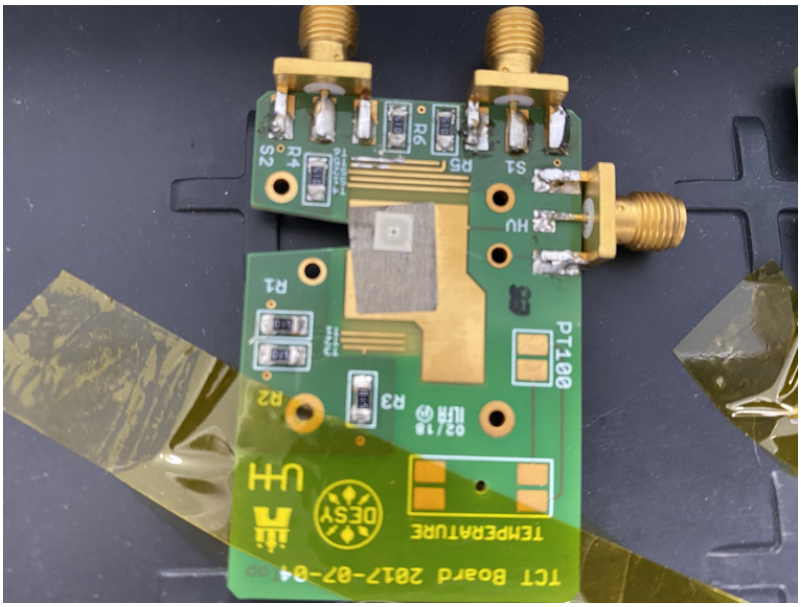

Figure 5.19: An example LGAD is attached onto a gain board with conductive tape, which is then wire-bonded.

The only difference between the setup before and after irradiation is that the LGAD needs to be kept at very cold temperatures (around $-20°C$) to reduce annealing of the LGADs that have been irradiated. Annealing can repair some of the damage arising from irradiation of the sensor and therefore should be avoided to evaluate the initial damage. A mixture of water and anti-freeze is used to cool the sensors, which are flushed with dry nitrogen to ensure low humidity and therefore prevent damage due to condensation forming on the sensor. The peltiers are used to further cool the sensors and maintain a stable temperature, with a surrounding foam enclosure which provides insulation. This is shown in fig. 5.20.

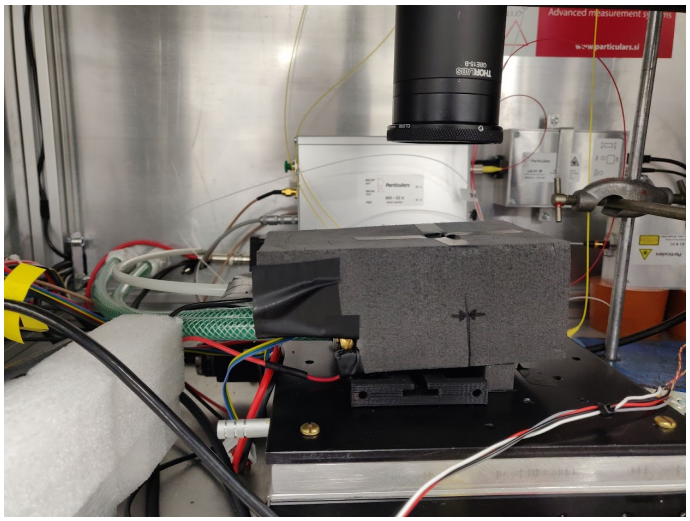

Figure 5.20: Gain set up including foam enclosure for cold measurements.

5.2.3 Results

This section describes first the IV/CV measurements of various LGADs and their gain measurements [103], before and after irradiation. All results are considered preliminary at the time of writing.

5.2.3.1 IV/CV measurements

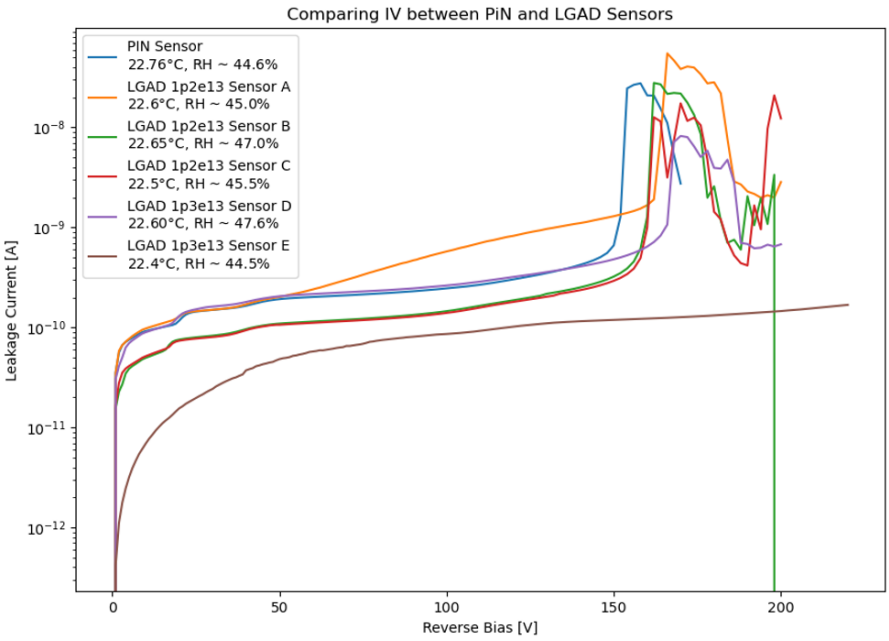

Figure 5.21: IV plots for sensors A-E and PIN.

First, IV measurements were performed for sensors A–E and the PIN (see table 5.2) to determine the breakdown voltage for each LGAD, which must not be exceeded in subsequent gain and time resolution measurements. These leakage currents shown in fig. 5.21 were measured using the probe station at room temperature, $\sim 22°C$, and at a humidity $\sim 45.0\,\%$. All sensors exhibit an exponential rise[1] and then fall back to the original current value at reverse bias voltages $> 140\,V$. This feature of the LGADs comes from a protective feature from the guard ring, which prevents leakage currents becoming too large in the LGAD. Hence, going up to $\sim 200\,V$ in the gain and time resolution measurements is sensible.

[1]Sensor E does not exhibit this behaviour as it broke in transit from Glasgow.

Other features can be explored in these plots. The breakdown voltage can be estimated by measuring the K factor from an IV distribution, defined as

$$K = \frac{V}{I}\frac{dI}{dV} \ . \tag{5.18}$$

A breakdown voltage for a given K factor value can then be measured. A K factor of 4 corresponds to a soft breakdown voltage value, whereas a K factor of 20 is a hard value. Plots of the K factor *vs.* breakdown voltage are shown in figs. 5.22a to 5.22c, which correspond to the PIN, sensor B and sensor D, respectively. Left to right in the plots increases the doping concentration in the gain layer from 0 to 1.2 $\times 10^{13}$ cm^{-3} to 1.3 $\times 10^{13}$ cm^{-3}, and as the doping concentration increases, the breakdown voltage increases.

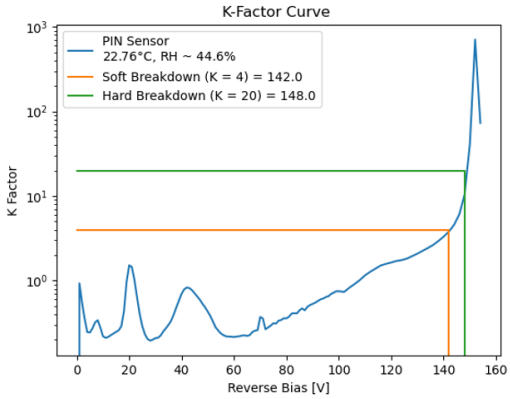

(a) PIN

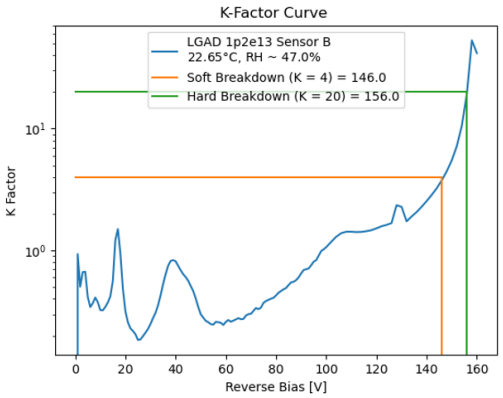

(b) Sensor B

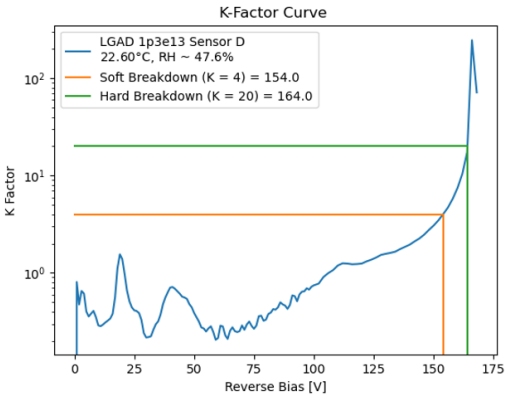

(c) Sensor D

Figure 5.22: K Factor *vs.* voltage for different sensors.

CV measurements provide further information on the sensors and were measured again using the probe station at room temperature, ~ 22°C, and at a humidity $\sim$ 45.0 %. A reverse bias is applied to the back of the sensor, and an AC supply with an

amplitude of 0.1 V is applied at different frequencies of [0.2,0.4,0.6,0.8,1,10,1000] kHz. These are performed in series and parallel, with an example CV distribution in series and parallel given in fig. 5.23.

As bias voltage increases up to ∼28 V, the gain layer is depleting. As soon as it has depleted, the capacitance starts to fall and reaches the full depletion voltage including the p-bulk at a value of ∼34 V. The CV measurements in series and parallel are independent of the frequency of the AC signal applied. This is expected, as differences would indicate the presence of a parasitic capacitance source. This could arise from the PCB on which the sensor is tested, but since the probe station does not need a PCB, this is not likely to occur.

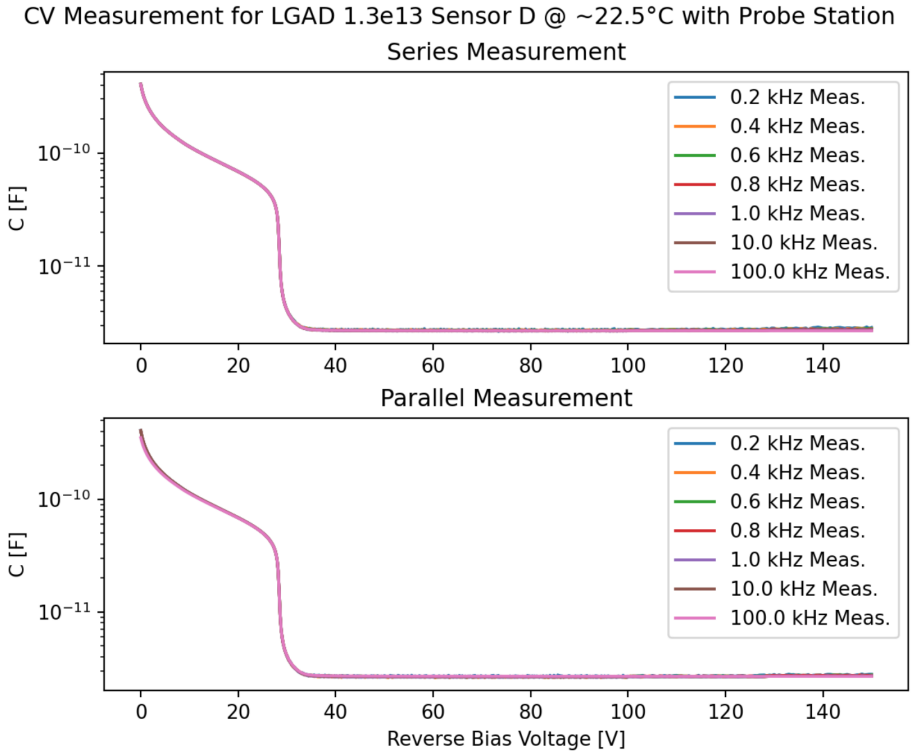

Figure 5.23: CV measurements for Sensor D in series and parallel at various frequencies.

From CV distributions, one can obtain the doping concentration at different reverse bias voltages and depth value of the LGAD using,

$$N_d = \frac{2}{\frac{dC^{-2}}{dV}} \frac{1}{q\epsilon_r A^2}, \tag{5.19}$$

where $\epsilon_r = 11.9$ for silicon and A $= 1\,\mathrm{mm}^2$ [98, 104]. The depth can be calculated

assuming that the LGAD acts as a parallel plate capacitor, with

$$C = \frac{\epsilon_r \epsilon_0 A}{d} \ . \tag{5.20}$$

Doping concentration *vs.* depth and reverse bias voltage are shown respectively in figs. 5.24a and 5.24b.

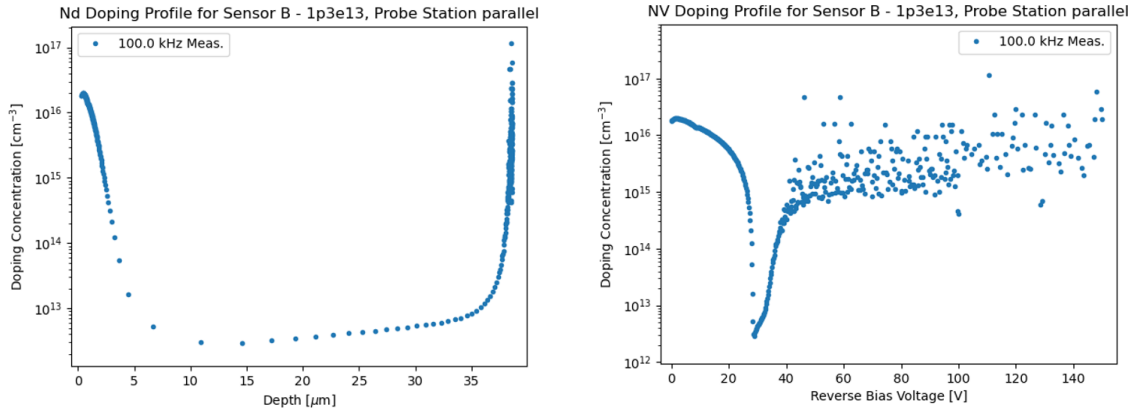

(a) Depth (b) Voltage

Figure 5.24: Doping concentration *vs.* (a) depth and (b) voltage.

5.2.3.2 Gain measurements

To measure the gain, first the output from the beam monitor is used to take into account the potential time variation of the charge injected by the laser, as shown in eq. (5.17). Figure 5.25 shows the beam integral *vs.* reverse bias for different days.

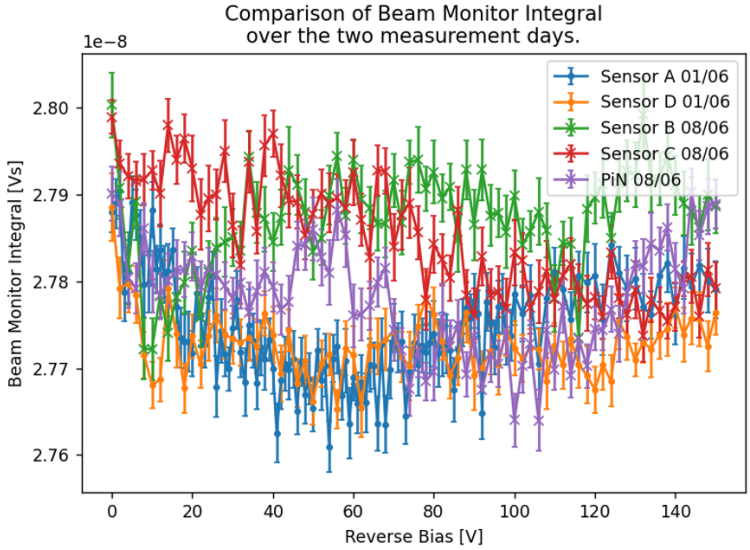

Figure 5.25: Beam monitor integral for different days of operation.

Estimating the integral of the LGAD pulse can be carried out using various methods. The integral of the pulse for different bias voltages with different methods is shown in fig. 5.26 for sensor B. All integration methods fit the pulses with a sixth order Savitzky-Golay smoothing filter [103]. The baseline voltage is also removed. In fig. 5.26, the blue distribution takes the peak voltage value and integrates within a symmetric window of $[-10\,\text{ns}, +10\,\text{ns}]$ around the peak. The orange distribution uses the same method, except with an asymmetric window of $[-10\,\text{ns}, +25\,\text{ns}]$. This provides a better estimate of the integral due to the tail in the signal peak. Both methods assume the noise in the integral should average to zero. However, both methods also assume the integral will always be calculated within this window. Hence, the best method tested was the first zero crossing method shown in green. This measures the timestamp of when the pulse first crosses the $V = 0$ threshold, on either side of the peak and then integrates between these points. Although this has the possibility of underestimating or overestimating the integral from noise fluctuations, all methods give very similar results [103].

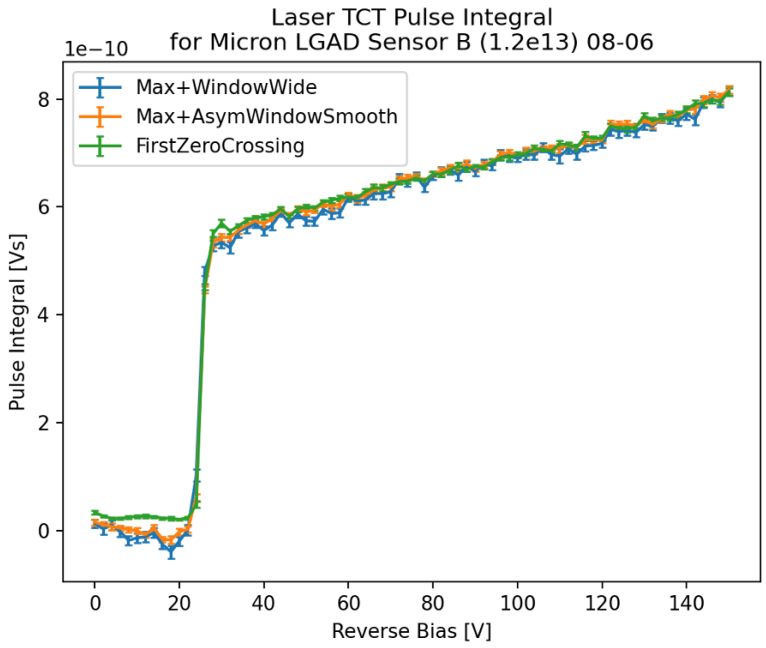

Figure 5.26: Pulse integral *vs.* voltage for sensor B with different integration methods.

With the integration methods in place, and also the beam monitor integral, the relative gain of the LGAD under test *vs.* a PIN can be measured. Figures 5.27a and 5.27b show the relative gain *vs.* reverse bias voltage for various doping concentrations and pixel sizes of the LGAD, respectively. The gain increases with reverse

bias voltage due to the increase in the electric field, and hence the increased acceleration of charges. Next, the relative gain increases with doping concentration and pixel size, due to the increase of free charges.

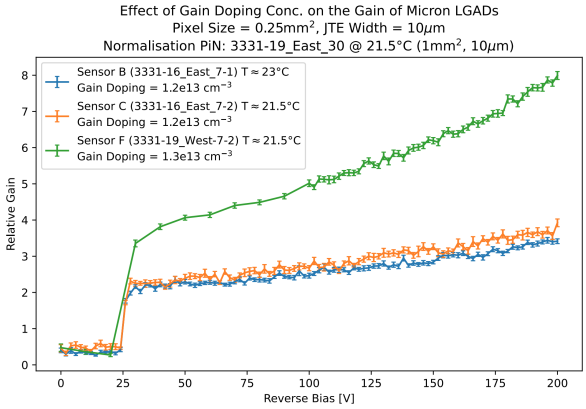

(a) Doping concentration.

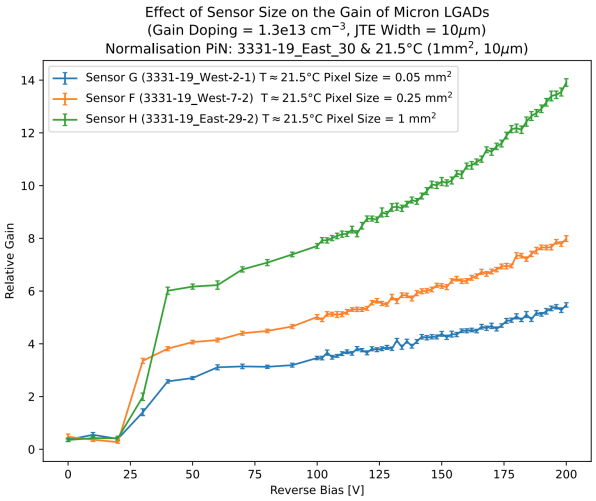

(b) Pixel size.

Figure 5.27: Gain *vs.* voltage at room temperature, varying (a) doping concentration and (b) pixel size.

Figure 5.28 shows relative gain *vs.* reverse bias voltage when varying the JTE size. The relative gain decreases with an increase in the JTE size. This is because some of the carriers created by the laser may drift to the JTE region, which is a region with no gain. Increasing the JTE area in the device will reduce the overall gain layer area, and hence reduce the overall gain.

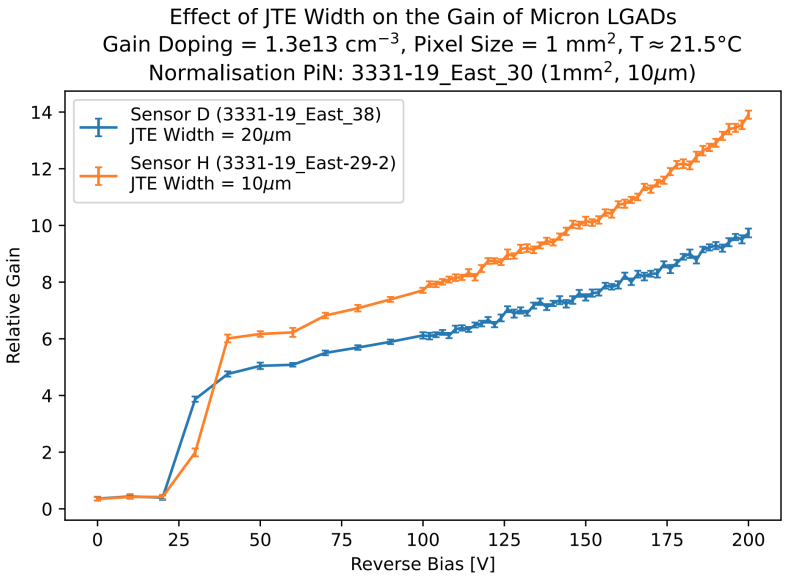

Figure 5.28: Gain *vs.* voltage, varying the JTE size at room temperature.

It is important to test the cold temperature behaviour of the sensors before they are irradiated as they will be tested cold after irradiation to reduce annealing. Figure 5.29 shows the relative gain *vs.* reverse bias voltage for two different sensors at room temperature and at cold temperatures between −15 and −18°C. For the relative gain of the LGAD to be properly normalised by the PIN, the PIN must be measured at the same temperature as the LGAD under test. Figure 5.29 shows that as the temperature is decreased the relative gain increases, as expected [100].

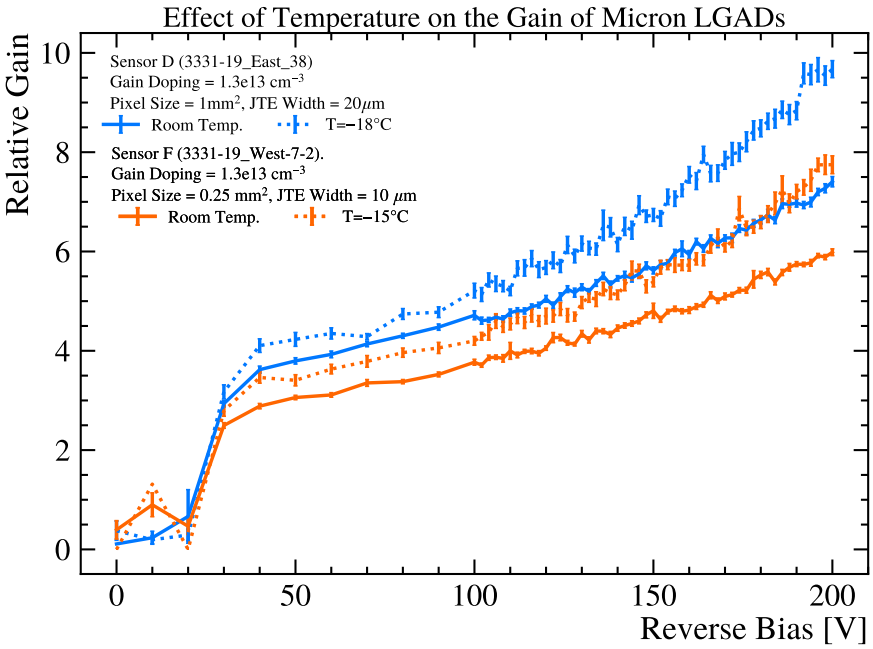

Figure 5.29: Gain *vs.* voltage for different sensors, comparing distributions at room temperature and between −15 and −18°C.

The measured gain at different temperatures have been compared using the University of Glasgow and the University of Birmingham setups. Figure 5.30 compares results for sensor F. Both institutes show that the gain increases with decreasing temperature. However, the absolute values of the relative gain at different temperatures are different between the two institutions. There may be two possible reasons for this. First, on the backside of the LGAD, there is an aluminium strip covering half of the sensor. This means that if the laser happens to hit the part of the sensor with the aluminium, it can cause reflections and hence artificially increase the measured gain. At Glasgow, a mechanism is in place to avoid regions of the LGAD where the aluminium has been placed, in comparison to Birmingham where this effect needs further investigation. The second reason could be due to a "Gain Supression" mechanism taking place with lasers that have a smaller spot size, which

is discussed in more detail in Ref. [105]. The laser beam used at Glasgow has a Full Width Half Maximum (FWHM) of 10 µm, in comparison to Birmingham which uses a laser beam of spot size ∼100 µm. Both reasons could explain the lower gains measured at Glasgow in comparison to Birmingham. However, the measured gains from Birmingham and Glasgow are roughly consistent.

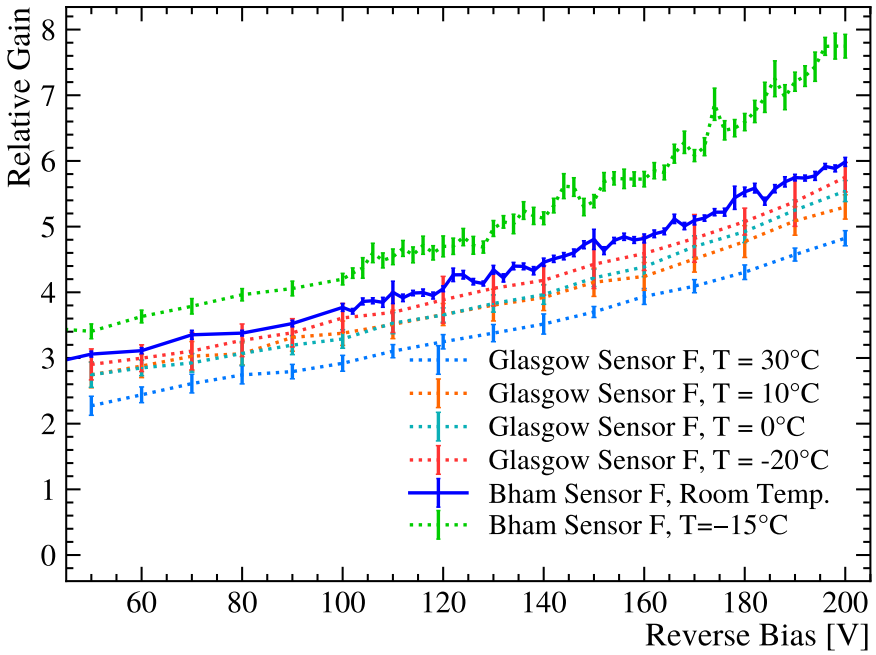

Figure 5.30: Comparison of Birmingham and Glasgow measurements of gain *vs.* voltage for sensor F at various temperatures.

5.2.3.3 Measurements after irradiation

Four of the LGAD sensors were irradiated with the in-house Birmingham cyclotron on 30th June 2022 with 8.9×10^{14} n_{eq}/cm^2 fluence, which are marked in table 5.2. These were then stored in a freezer to prevent annealing. Preliminary gain measurements have been performed on sensor D, with the results shown in fig. 5.31. Irradiating the sensors has decreased the gain. This is because irradiation decreases the doping concentration of the gain layer, so to achieve the same electric field in the gain layer, a higher bias voltage needs to be applied to mitigate this. To see this effect, a higher bias voltage possibly needs to be applied, which is the subject of future work.

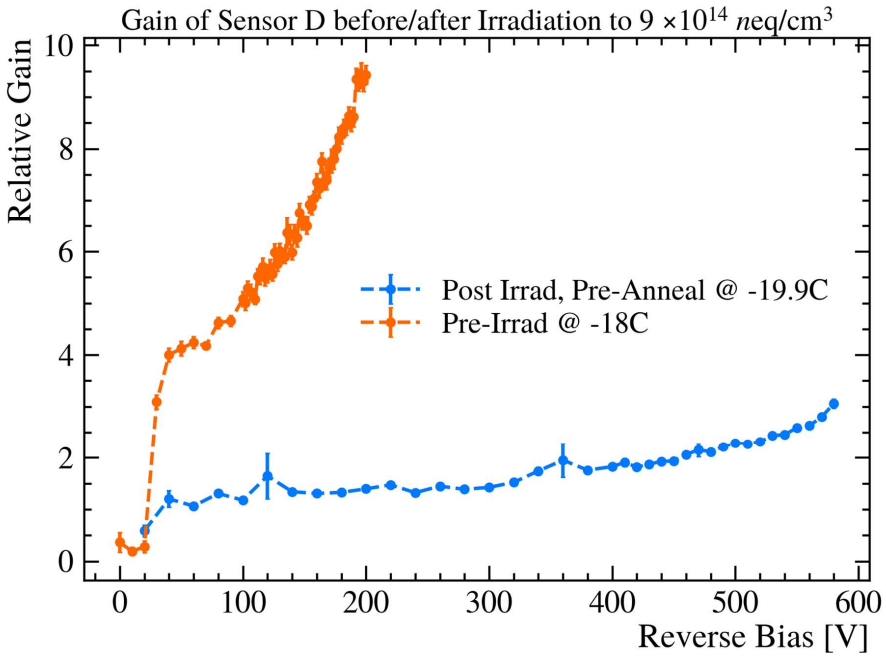

Figure 5.31: Preliminary gain *vs.* reverse bias voltage for pre-irradiated and post-irradiated sensor D.

5.2.3.4 Future prospects

Overall, preliminary results for different LGADs demonstrated expected behaviour, such as the gain increasing with decreasing temperature. This was consistent between Birmingham and Glasgow. Further work needs to be performed to explain the difference in absolute gain values between Glasgow and Birmingham, which may be due to gain suppression effects from the laser. Further testing needs to be done on the post-irradiated sensors, by testing gain at higher bias voltages and with more devices, and also their timing-resolution. Different designs of LGADs are also starting to be tested, which have the possibility of achieving larger and more uniform gain. These are iLGADs and trench LGADs. These will also be tested on TimePix sensors to test their readout capabilities.

CHAPTER 6

Quarkonia in jets measurements

As discussed in chapter 1, jet fragmentation measurements were performed by LHCb in 2017 [106] for J/ψ production. This showed that for prompt J/ψ production, there is a peak around $z(J/\psi) \equiv p_{\mathrm{T}}(J/\psi)/p_{\mathrm{T}}(\mathrm{jet}) \approx 0.5$, in comparison to current Pythia 8 predictions which show an isolated peak at $z(J/\psi) = 1$. CMS then repeated this measurement with CMS data [15], which observed the same trend in $z(J/\psi)$ as LHCb for prompt J/ψ's, *i.e.* a very depleted yield around $z(J/\psi) =1$ and an enhanced yield at $z(J/\psi) \approx 0.5$. This is shown in fig. 6.1. Unpublished results from ATLAS with $p_{\mathrm{T}}(\mathrm{jet}) > 50\,\mathrm{GeV}$ and $p_{\mathrm{T}}(J/\psi) > 45\,\mathrm{GeV}$, *i.e.* larger than the other results, show the peak at a higher $z(J/\psi)$ [107]. Preliminary results from STAR [108] show a rather flat distribution of $z(J/\psi)$ including yield around 1. This data has the lowest $p_{\mathrm{T}}(\mathrm{jet})$ values. This led to the work discussed in chapter 3 to incorporate new fragmentation calculations into the Pythia 8 framework, to try and explain data measurements better.

In this chapter, an expansion of the 2017 LHCb analysis of J/ψ production in jets was performed, by not only measuring the z parameter for J/ψ production, but also for other quarkonia. These are the $\psi(2S)$, $\Upsilon(1S)$, $\Upsilon(2S)$ and $\Upsilon(3S)$. The $\psi(2S)$ is of interest, due to the fact that it is a $c\bar{c}$ state like the J/ψ except with a higher mass. This leads to different size contributions from feed-down of higher excited

states, such as the χ_{cJ} states, which could effect the total z distribution. The decay of $\psi(2S)$ is also not very well modelled, with phenomena observed such as the "$\rho\pi$" puzzle [109]. Hence, knowing more about how the $\psi(2S)$ is produced could give further understanding to its decay. The Υ states are also interesting as they are $b\bar{b}$ states, so they have a significantly higher mass than the J/ψ and $\psi(2S)$. The $\Upsilon(1S)$ is $\sim$3 times the mass of the J/ψ, with a mass of 9,460.3 $\pm$ 0.26 MeV/c^2 [20]. Hence, this probes a different energy scale in comparison to the J/ψ, which could lead to a very different phenomenology of production. The $\psi(2S)$ like the J/ψ can be produced from b-decays as well as promptly, hence the final measurements are split into these two components. Υ's, however, cannot be produced from b-decays, since they are too massive, so only a prompt measurement is performed. These will be the first measurements produced by any experiment of $\psi(2S)$ and Υ jet fragmentation. These will be presented as normalised differential production cross sections, dσ/σ, *vs.* $z(Q)$, where Q denotes a quarkonium state.

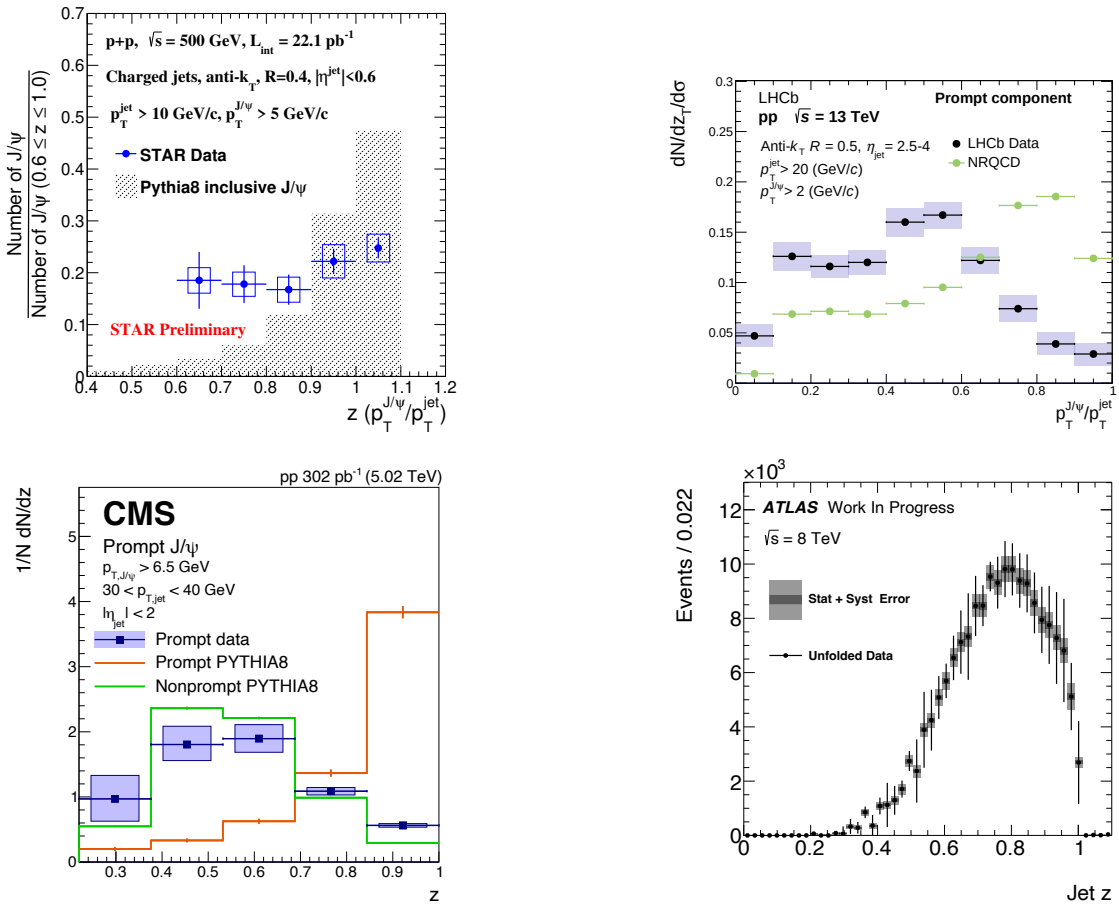

Figure 6.1: Fragmentation results of reconstructed prompt J/ψ production within jets. Top-left, STAR data [108]; Top-right, LHCb data; Bottom-left, CMS data [15]; Bottom-right, unofficial results using ATLAS data [107].

This chapter is structured as follows. Each section describes a particular aspect or method applied in the analysis. These methods are applied and discussed in detail for the J/ψ. As the methods applied for the other quarkonia are very similar, only the final result after applying each method will be shown for the $\psi(2S)$ and Υ's in each section. If there are any deviations from the standard method, these will then be explained in detail for each quarkonia. Section 6.1 will discuss the selection of the quarkonia candidates, then section 6.2 will explain the efficiency corrections that need to be applied to the signal after applying the selections. Section 6.3 will describe unfolding of the distributions to correct for the energy resolution of the jets, and section 6.4 will describe the calculation of the systematic uncertainties of the analysis. Section 6.5 will then show and discuss the final results and section 6.5.5 will discuss the future prospects of this analysis.

6.1 Selection of quarkonia

6.1.1 Data samples and tools used

For all the analyses presented here, the full 2016 LHCb "Turbo" data set was used. Run 1 data (2010-2012) was not used, as a transverse momentum cut, p_{T} was placed on the J/ψ. This means a lower limit would need to be placed on the measured $z(J/\psi)$, which was not wanted for this analysis. The 2017 and 2018 datasets were not used also, as a 0.001 prescale was placed on the trigger of the lines of interest. Consequently, the increase in statistics was not significant enough to outweigh the additional systematics introduced. Turbo data was used, as this only saves the triggered candidate, such as $J/\psi \rightarrow \mu^+\mu^-$, in comparison to a normal data set which saves the whole event to disk. However, "PersistReco" was also used, which saves other event information to be able to reconstruct the jets [110]. This led to a collected data set of $\sim$1.67 fb^{-1}. The DaVinci v45r6 [111] LHCb framework was used to select the data. Root [112] and RooFit [113] were used to analyse the data and fit data distributions.

6.1.2 Initial selection of candidates

To select J/ψ candidates, the $J/\psi \to \mu^+\mu^-$ decay channel was chosen. This is due to the relatively high branching ratio (BR) of $(5.961 \pm 0.033)\%$ [20], and also muons are the easiest particle to reconstruct in the detector, due to their charge and PID from the muon stations. Leptonic signatures are also easier to distinguish than hadronic signatures due to low background contributions. This decay channel is also used for the other quarkonia states.

Some selections were placed on the data in order to select $J/\psi \to \mu^+\mu^-$ decays. Firstly, a $J/\psi \to \mu^+\mu^-$ candidate must have a positive decision at each trigger level (L0, HLT1 and HLT2) in order for its information to be saved to disk. The three trigger lines chosen were: `L0DiMuon`, `Hlt1DiMuonHighMass` and `Hlt2DiMuonJPsiTurbo`. Each trigger line encompasses requirements on the $J/\psi \to \mu^+\mu^-$ candidate in order to select it, for example PID information on the muons, which become more selective the higher the level.

Secondly, there are selection requirements placed on the jets. Jets are reconstructed using the anti-k_t algorithm [42], with a radius of 0.5 and a minimum jet p_{T} of $15\,\mathrm{GeV}/c$. The pseudorapidity range of the jet axis value was chosen to be $2.5 < \eta < 4.0$, which is less than the LHCb detector acceptance of $2.0 < \eta < 4.5$. This is to ensure the jets are completely in the detector acceptance. The J/ψ's and μ's also have fiducial (kinematic) requirements placed on them and these are summarised in table 6.1. The J/ψ and μ's must also be clustered within the same jet. The jets themselves are built using the methods discussed in section 2.4, where the particle objects are built from tracker and calorimeter information in the particle flow, and then these are fed into the anti-k_t algorithm to be clustered into jets. The only difference with this analysis is that to avoid the muons being clustered into different jets, the J/ψ candidate itself is reconstructed, and the whole J/ψ candidate is fed into the particle flow and jet clustering algorithm, and the daughter muons are removed from the particle flow to avoid double counting. To improve the p_{T} resolution of the jets, only one reconstructed PV is allowed per event. Fake tracks can also be clustered into the jets, which would increase the p_{T} of the jet. Hence each clustered track has the probability that it is a fake track, GhostProb < 0.1. Each track must also pass through a unique VELO segment [114]. The overall selection criteria placed per event is shown in table 6.2.

particle	cut variable	value
μ	p_{T}	$> 0.5\,\mathrm{GeV}$
μ	p	$> 6\,\mathrm{GeV}$
μ	η	2-4.5
J/ψ	η	2-4.5
Jet	η	2.5-4
Jet	p_{T}	$> 15\,\mathrm{GeV}$

Table 6.1: Summary of fiducial requirements. These are not corrected for in the final results.

particle	cut variable	value
μ	IsMuon	True
μ	PIDmu	> 1
μ	ProbNNmu	< 0.8
μ	TRCHI2DOF	< 4
J/ψ	$\sqrt{p_T(\mu_1)p_T(\mu_2)}$	$\gtrsim 324\,\mathrm{MeV}$
J/ψ	decay vertex χ^2	< 25
J/ψ	$\mathrm{DOCA}_{\mu\mu}$	$< 0.2\,\mathrm{mm}$
J/ψ	$\mathrm{mass}_{\mu\mu}$	$\mathrm{M} < 2900\,\mathrm{MeV}$
J/ψ	$\lvert\mathrm{mass}_{\mu\mu}$ - $\mathrm{mass}_{J/\psi}\rvert$	$< 120\,\mathrm{MeV}$
Global	N_{SPD}	< 900
Global	N_{PV}	$== 1$

Table 6.2: Analysis selection to increase signal-to-background ratio in the mass spectrum. The loss of signal induced with these cuts is corrected for with efficiency corrections. IsMuon, PIDmu and ProbNNmu are PID variables for the muons. TRCHI2DOF is the track fit quality χ^2 per degree of freedom for the muons. $\mathrm{DOCA}_{\mu\mu}$ is the distance of closest approach between the muons. $\lvert\mathrm{mass}_{\mu\mu}$ - $\mathrm{mass}_{J/\psi}\rvert$ is the difference between the mass of the di-muon candidate and the world average mass of the J/ψ. N_{SPD} is the number of hits in the SPD detector and N_{PV} is the number of primary vertices per event.

Most of the selection requirements shown in table 6.2 are from the trigger lines. Collapsing these requirements into L0 +HLT1 +HLT2, the selection requirements placed on top of the trigger requirements are shown in table 6.3.

particle	cut variable	value
μ	ProbNNmu	<0.8
J/ψ	L0 && HLT1 && HLT2	True
Global	N_{PV}	$== 1$

Table 6.3: Selection criterion when everything is included in trigger selection.

The most notable selection cut is the ProbNNmu cut. This is a PID cut on the muons and is a harsher cut than those already used in the trigger lines. This is needed as large backgrounds appear at low $z(J/\psi)$ values, which is shown in fig. 6.2a. Pions may be mistaken as muons for example, as they decay $(99.98770 \pm 0.00004)\%$ of the time to muons via $\pi^+ \to \mu^+\nu_\mu$ [20]. This is calculated in the LHCb framework using an artifical neural network, where the inputs used are, the delta log likelihood of the particle being a muon *vs.* a pion, track p_{T}, tracks χ^2/ndf *etc.* The likelihoods are calculated from the product of likelihoods from each sub-detector, *e.g.* RICH, calorimeters and muon stations [115].

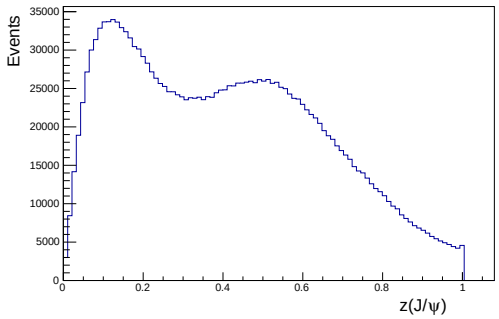

(a) No cut.

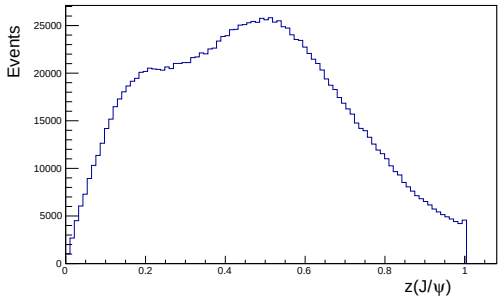

(b) Exponential cut depending on $p_{\mathrm{T}}(J/\psi)$: A = 0.69, tau = 2761 and c = 0.4.

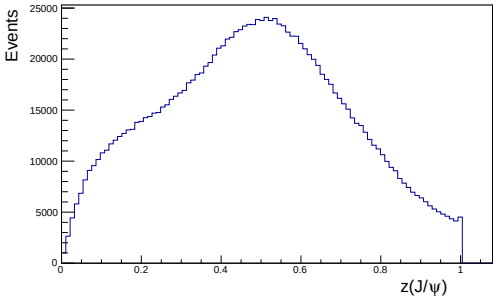

(c) ProbNNmu > 0.8.

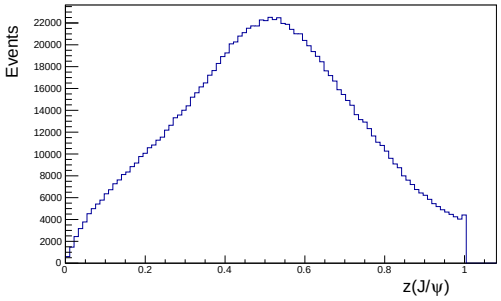

(d) ProbNNmu > 0.9.

Figure 6.2: Different ProbNNmu cuts on z isolation, $p_{\mathrm{T}}(J/\psi)/p_{\mathrm{T}}(\mathrm{jet})$.

Figure 6.2 shows the $z(J/\psi)$ distributions obtained by applying different ProbNNmu cuts on the muons to the data. The most effective cut to remove the background component at low $z(J/\psi)$ appears to be ProbNNmu > 0.9. However, when calculating the figure of merit (FOM) of removing the most background but keeping the most signal, which is defined as,

$$\mathrm{FOM} = (\text{efficiency on signal, } \epsilon) \text{ x } (\text{purity of sample, p}), \tag{6.1}$$

$$= \left(\frac{\text{signal yield after cut}}{\text{signal yield before cut}}\right) \text{ x } \left(\frac{\text{signal yield after cut}}{\text{total yield after cut}}\right), \tag{6.2}$$

it was found that the ProbNNmu cut value that optimised the FOM was ProbNNmu > 0.8 at low $z(J/\psi)$. Hence, this cut was used in this analysis.

6.1.3 Obtaining prompt and displaced fractions

J/ψ's can be produced in two different ways. Either directly in the proton-proton collision (prompt), or from b-decays (displaced). Prompt production of J/ψ's also include decays from particles that happen so fast they do not produce a displaced vertex in the detector, such as from χ_c states. Hence, after initial selections have taken place, the J/ψ's are separated into their production type, in 10 different $z(J/\psi)$ bins and 3 $p_{\mathrm{T}}(\mathrm{jet})$ bins. To obtain the best statistics in each bin, the bins are defined as follows:

$$z(J/\psi) : [0, 0.1, 0.2, 0.3, 0.4, 0.5, 0.6, 0.7, 0.8, 0.9, 1]$$

$$p_{\mathrm{T}}(\mathrm{jet}) : [15, 20, 30, \infty]\,\mathrm{GeV}/c$$

The fractions of prompt *vs.* displaced production are then used to obtain normalised $z(J/\psi)$ distributions in different $p_{\mathrm{T}}(\mathrm{jet})$ ranges. However, it is still possible even after the initial selections to select fake J/ψ candidates. For example, muons may happen to be close to each other in the detector, but do not originate from a J/ψ. This is called background. Hence, the total fraction of signal (J/ψ) *vs.* background needs to be obtained in each $z(J/\psi)$ and $p_{\mathrm{T}}(\mathrm{jet})$ bin. An invariant mass distribution of the selected J/ψ candidates is produced in each $z(J/\psi)$ and $p_{\mathrm{T}}(\mathrm{jet})$ bin, with an example shown in fig. 6.3. The true J/ψ's are in the signal peak. An unbinned extended likelihood fit is then performed to fit this peak using RooFit [113] in the mass range of $3.04 < \mathrm{m}(\mu\mu) < 3.16\,\mathrm{GeV}/c^2$. This is called the signal region. This range was chosen, as the true J/ψ mass is $3096.900 \pm 0.006\,\mathrm{MeV}/c^2$ [20]. However, LHCb has a finite detector resolution of $14.3 \pm 0.1\,\mathrm{MeV}/c^2$ [116] on the J/ψ mass. 4σ will contain most of the J/ψ signal peak, hence this signal range was chosen. The pull distribution shows the goodness of the fit. The J/ψ signal component is described by a probability density function (PDF) which is based on the sum of two anti-symmetric Crystal Ball functions (CB), called a Double Crystal Ball function (DCB) [117]. A single Crystal Ball (SCB) function is defined in eq. (6.3),

$$f_{CB}(m; M, \sigma, \alpha, n) = \begin{cases} \frac{(n/|\alpha|)^n \exp[-\alpha^2/2]}{(\frac{n}{|\alpha|} - |\alpha| - \frac{m-M}{\sigma})^n} & \frac{m-M}{\sigma} < -|\alpha| \\ \exp[-(\frac{m-M}{\sqrt{2}\sigma})^2] & \frac{m-M}{\sigma} > -|\alpha| \end{cases}, \tag{6.3}$$

where M is the mean, σ is the Gaussian core, α expresses the point when the function changes from a Gaussian to a power-law tail and n is the power of the tail. The two CB's shared the same mean and n value. The value of n is fixed to its theoretically preferred value of 1. However, α are equal values but opposite in sign. σ is also different, $\sigma_{CB2} = \sigma_{CB1} + \delta\sigma$ and $\delta\sigma > 0$ to remove degeneracy in the fit. The background component is from combinatorics of the muons only, hence an exponential function is used. From the invariant mass fits, the fraction of signal to background, and the total yields are then obtained in each $z(J/\psi)$ and p_{T}(jet) bin in the signal region.

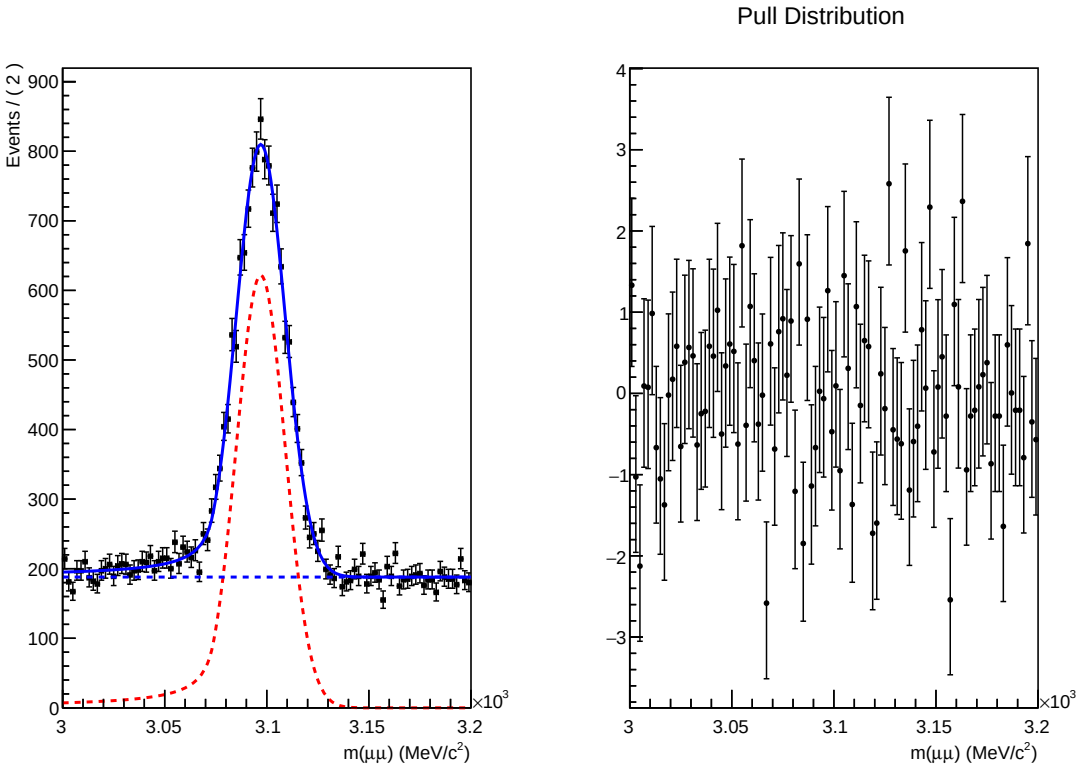

Figure 6.3: Invariant mass fit of J/ψ's for $20 < p_{\mathrm{T}}(\mathrm{jet}) < 30\,\mathrm{GeV}$ & $0 < z(J/\psi) < 0.1$. The signal is modelled with a DCB function, which is shown in red, and the background is modelled with an exponential function, which shown in blue.

Since the signal yield and fraction of J/ψ's have been obtained in each bin, this can now be separated into the prompt and displaced components in the signal region. These are characterised by the pseudo-lifetime of the J/ψ which is calculated in eq. (6.4),

$$t_z \equiv (x_{z,J/\psi} - x_{z,PV})\frac{m(J/\psi)}{p_z(J/\psi)}, \tag{6.4}$$

where $\mathrm{x}_{z,J/\psi}$ is the z position of the J/ψ decay vertex, $x_{z,PV}$ is the z position of

the primary vertex, m(J/ψ) is the J/ψ mass taken from the Particle Data Group (PDG) [20] and $p_z(J/\psi)$ is the z component of the J/ψ's momentum.

An example of a lifetime fit is shown in fig. 6.4. The prompt component (red) is described by a delta function, and the displaced component (green) by an exponential function. However, detector effects need to be taken into account which lead to a lifetime resolution ∼50 fs [116]. Hence the prompt and displaced components are smeared (convolved) with the same double Gaussian, $g_{resolution}(t_z)$. The requirement on σ_2 is the same as before to remove degeneracy.

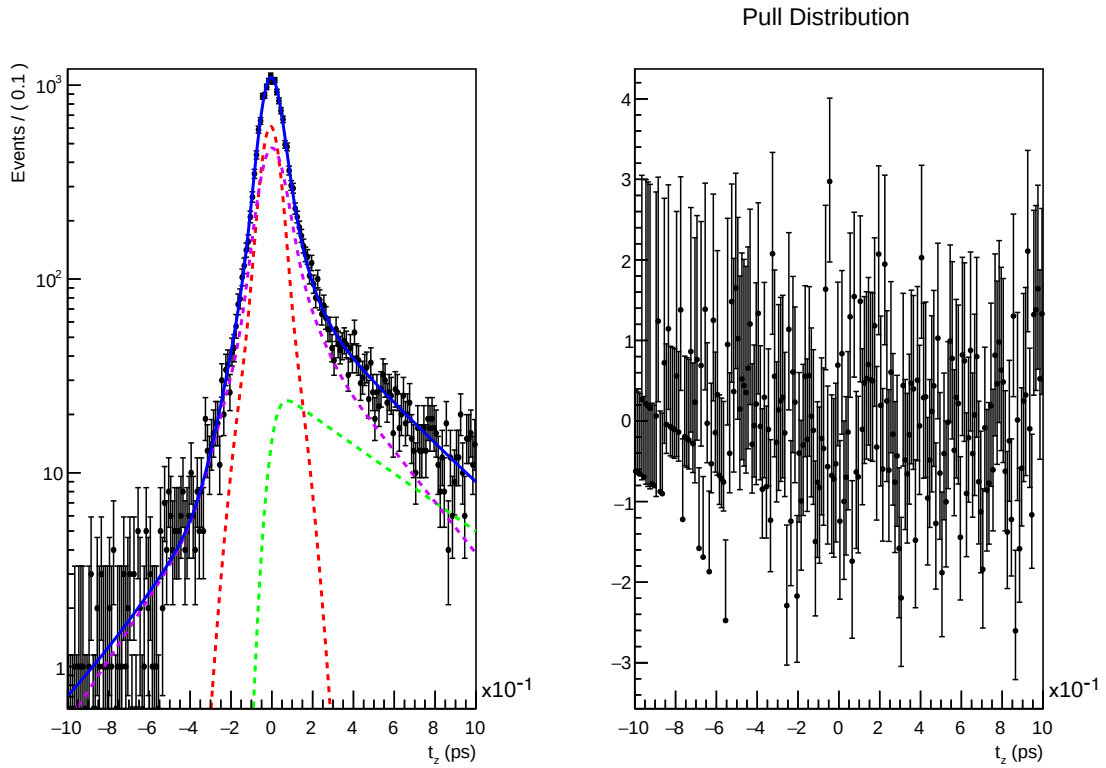

Figure 6.4: Signal lifetime fit, $20 < p_{\mathrm{T}}(\mathrm{jet}) < 30\,\mathrm{GeV}$ & $0 < z(J/\psi) < 0.1$, log scale. The background component, shown in purple, is modelled with an empirical fit to the sideband region of the mass fit in fig. 6.3 which is shown in fig. 6.5. The prompt component is modelled with a Double Gaussian, which is shown in red, and the displaced component is modelled with an exponential function convolved with a Double Gaussian, which is shown in green. The wrong PV component is too small to view.

However, there is still the background component (purple) to consider. To approximate the background component, firstly a mass region is chosen where only non-J/ψ candidates are selected. This is shown in fig. 6.3 where above and below the signal region only background exists. These are called the upper and lower sidebands re-

spectively. Hence particles within the lower sideband was selected with an invariant mass of $3.00 < \mathrm{m}(\mu\mu) < 3.04\,\mathrm{GeV}/c^{\,2}$ and the lifetime was measured for these particles. An example unbinned maximum likelihood fit to the background is shown in fig. 6.5 with RooFit [113]. The background PDF, $\mathrm{g}_{background}(t_z)$, was approximated using an empirical fit. It was best described by the sum of two negative exponentials and one positive exponential, each convolved with the same double Gaussian PDF which is then normalised.

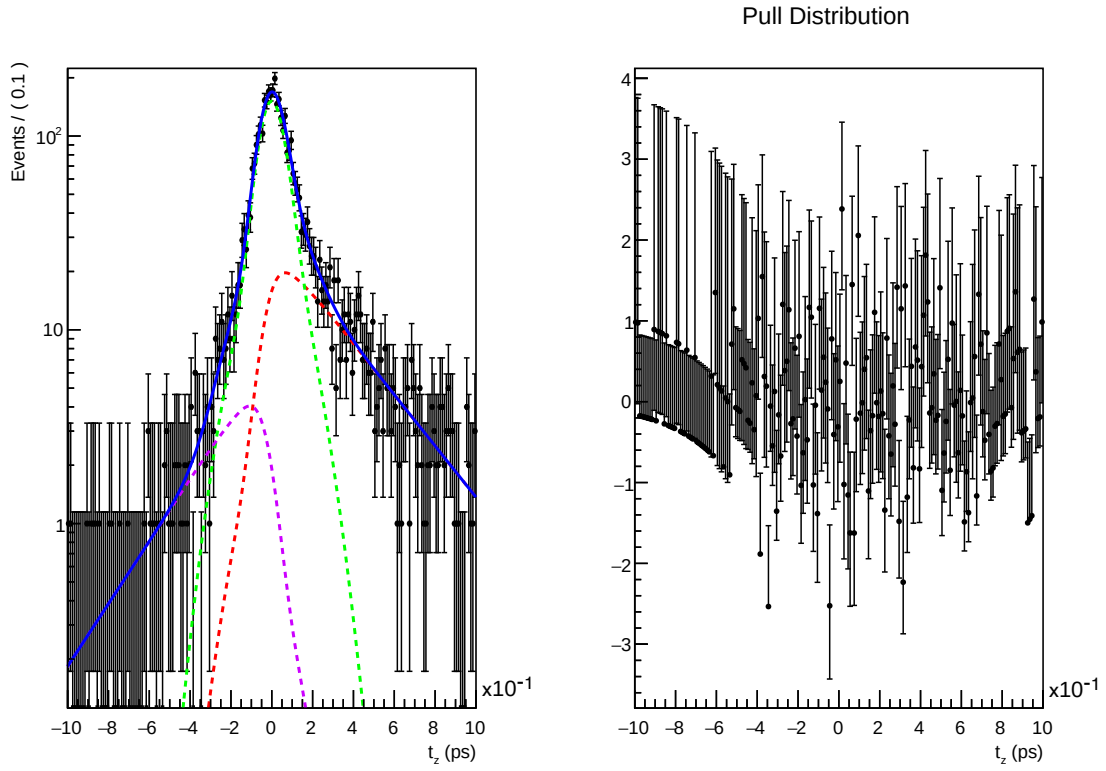

Figure 6.5: Background lifetime fit for $20 < p_{\mathrm{T}}(\mathrm{jet}) < 30\,\mathrm{GeV}$ and $0 < z(J/\psi) < 0.1$, log scale. It consists of two negative exponentials and one positive exponential, each convolved with the same Double Gaussian PDF.

There is also the wrong PV component (cyan) where the reconstructed J/ψ has been assigned to the wrong PV in an event. This can happen for two reasons [118]. Firstly, if two muons are close together, and combine to be a J/ψ candidate, but these muons actually originate from two different PV's, this could reconstruct a fake PV. Also, there is a chance the original PV might not be reconstructed at all, for various reasons. Hence the J/ψ can be associated with a completely different PV in the event. These effects are reduced by requiring one PV per event. This leads to long tails in positive and negative lifetime, which effects the displaced component. A PDF is simulated by using eq. (6.4) and replacing $\mathrm{x}_{z,PV}$ for the present event

with $x_{z,PV}^{NEXT}$ which is the z position of the PV in the next event. This is defined in eq. (6.5) [118],

$$t_z \equiv (z_{J/\psi} - z_{PV}^{NEXT}) \frac{m(J/\psi)}{p_z(J/\psi)}. \tag{6.5}$$

An example distribution is shown in fig. 6.6. A cross check was to store the PV's from all events and select a random one to use in eq. (6.5). This gave the same distribution. The PDF, $g_{wrongPV}$, is then estimated using kernel estimation [119]. RooFit [113] then normalises this distribution. It turns out the wrong PV component is a small correction on the order of 0.1%.

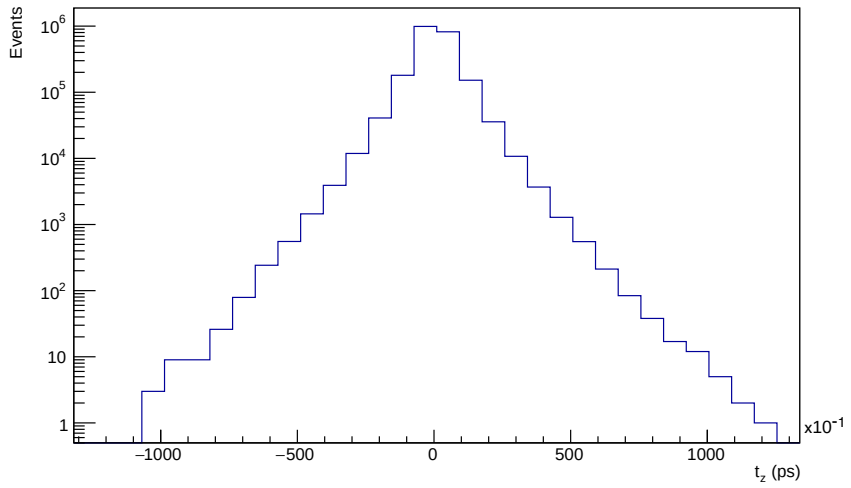

Figure 6.6: Lifetime distribution of the wrong PV component.

To produce fig. 6.4 with all four PDF components, an unbinned maximum likelihood fit of the lifetime, t_z, in the signal region was performed using the overall PDF, $g(t_z)$, defined in eq. (6.6) [118],

$$g(t_z) = \left[\left(f_{prompt}\delta(t_z) + f_{bdecay} \frac{e^{-\frac{t_z}{\tau_b}}}{\tau_b} \right) \otimes g_{resolution}(t_z) \right] + (f_{wrongPV}) g_{wrongPV}(t_z) + (f_{background}) g_{background}(t_z), \tag{6.6}$$

for each $z(J/\psi)$ and p_{T}(jet) bin. All PDF's are normalised. f_{prompt} is the prompt signal fraction, f_{bdecay} is the displaced signal fraction and $f_{wrongPV}$ is the wrong PV fraction. $f_{background}$ is the background fraction which is fixed from the invariant mass fit for each $z(J/\psi)$ and p_{T}(jet) bin. Hence, f_{prompt} and f_{bdecay} obtained for each bin can be used to measure the normalised $\mathrm{d}\sigma/\sigma$ *vs.* $z(J/\psi)$ distributions for both the prompt and displaced components.

6.1.4 Raw yields

Initial selection was applied on the 2016 Turbo data set as explained in section 6.1.2 to obtain J/ψ candidates with DaVinci [111]. RooFit [113] was then used to perform mass and lifetime fits, to obtain total signal yields and prompt and displaced J/ψ signal fractions in different $z(J/\psi)$ and $p_{\mathrm{T}}(\mathrm{jet})$ bins. The total signal yield is multiplied by these fractions to obtain the prompt and displaced yields. Figure 6.7 shows displaced and prompt yields *vs.* $z(J/\psi)$ for different $p_{\mathrm{T}}(\mathrm{jet})$ ranges. The error in each bin is the combination of the error in the signal yield obtained from the mass fit, and the error in the prompt or displaced fraction from the lifetime fit.

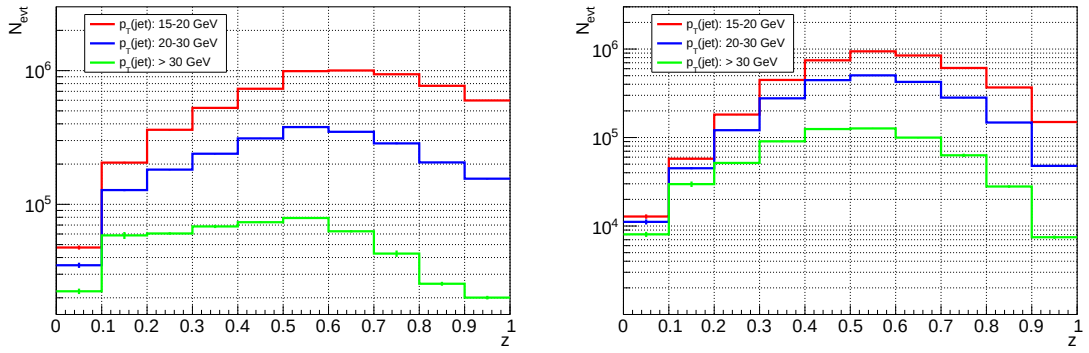

(a) Prompt. (b) Displaced.

Figure 6.7: Prompt and displaced yields *vs.* $z(J/\psi)$ in different $p_{\mathrm{T}}(\mathrm{jet})$ ranges.

The distributions in Figure 6.7 are then normalised using eq. (6.7), for example in the prompt case,

$$d\sigma/\sigma \text{ per z bin} = \frac{\text{prompt yield in that bin}}{\text{total prompt yield overall all z bins} \times \text{z bin width}}. \tag{6.7}$$

The resulting distributions are shown in fig. 6.8, which are split into the various $p_{\mathrm{T}}(\mathrm{jet})$ bins. All of the normalised z distribution plots presented in this thesis are normalised by the bin width. First observations show the prompt component peaks at around $z(J/\psi) \sim 0.5$, which is the same as the previous LHCb measurement [12]. As $p_{\mathrm{T}}(\mathrm{jet})$ increases, the mean value of $z(J/\psi)$ shifts towards lower values. This is in comparison to the displaced component, which also peaks ~ 0.5, but the distribution shape stays roughly constant with $p_{\mathrm{T}}(\mathrm{jet})$. This suggests that the fragmentation processes are different, and that the prompt component possibly has an additional double parton scattering (DPS) component. This is because a (J/ψ + jet) + (di-jet) DPS event can occur, where the J/ψ overlaps with a jet from the other process.

Hence a low energy J/ψ can be clustered into a high energy jet, which shifts the distribution towards lower $z(J/\psi)$ values.

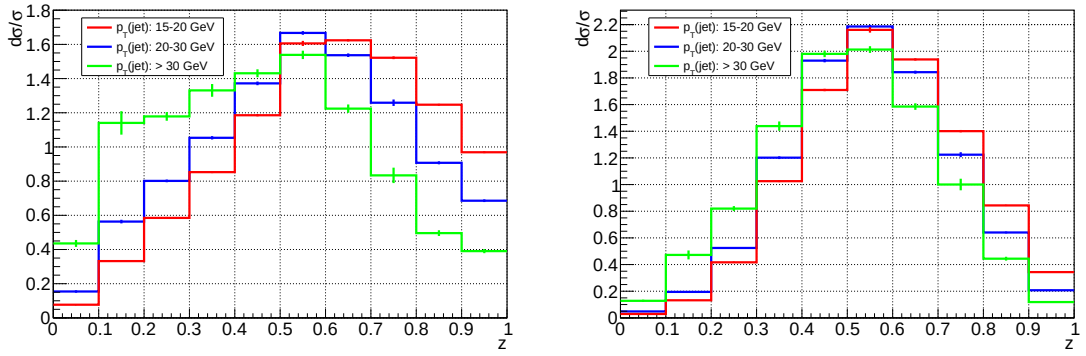

(a) Prompt. (b) Displaced.

Figure 6.8: Prompt and displaced normalised cross sections, $\mathrm{d}\sigma/\sigma$, *vs.* $z(J/\psi)$ in different $p_{\mathrm{T}}(\mathrm{jet})$ ranges. The plots are normalised as $1/N\ \mathrm{d}N/\mathrm{d}z$.

However, these distributions are not yet the true distributions of $z(J/\psi)$. Firstly, the detector is not 100% efficient at selecting J/ψ candidates. The data needs to be corrected to take into account reconstruction, trigger and muon PID efficiencies. This is discussed in section 6.2. Secondly, the finite jet energy resolution of each jet means that the true $p_{\mathrm{T}}(\mathrm{jet})$, $p_T^{true}(\mathrm{jet})$, may be different from the reconstructed $p_{\mathrm{T}}(\mathrm{jet})$, $p_T^{reco}(\mathrm{jet})$. This will lead to bin-migration effects in the $z(J/\psi)$ distributions. These are corrected for using a 2D Bayesian unfolding procedure using RooUnfold [120], which is explained in section 6.3. Typically, $\mathrm{p}_T^{reco}(\mathrm{jet}) < \mathrm{p}_T^{true}(\mathrm{jet})$, so this should shift the $z(J/\psi)$ distribution to lower values of $z(J/\psi)$.

6.1.5 Selection of $\psi(2S)$

The selection of the $\psi(2S)$ follows the same methods as for the J/ψ. The di-muon decay channel is used to select the initial $\psi(2S)$ candidate, with all the same software and tools. The only difference between the $\psi(2S)$ and J/ψ initial selection is that a different HLT2 trigger line is used, called `Hlt2DiMuonPsi2STurbo`. This has the same selection requirements as for the J/ψ HLT2 line, except the mass window cut of $\pm$ 120 MeV is around the $\psi(2S)$ nominal mass of 3686.10 $\pm$ 0.06 MeV [20], rather than the J/ψ mass. The signal yield is obtained in each $z(J/\psi)$ and $p_{\mathrm{T}}(\mathrm{jet})$ bin by performing a mass fit using a double crystal ball (DCB) function. An example mass fit is shown in fig. 6.9. The $\psi(2S)$ is then separated into the prompt and displaced components by performing a lifetime fit. The background lifetime fit is shown in fig. 6.10, and the signal lifetime fit in fig. 6.11.

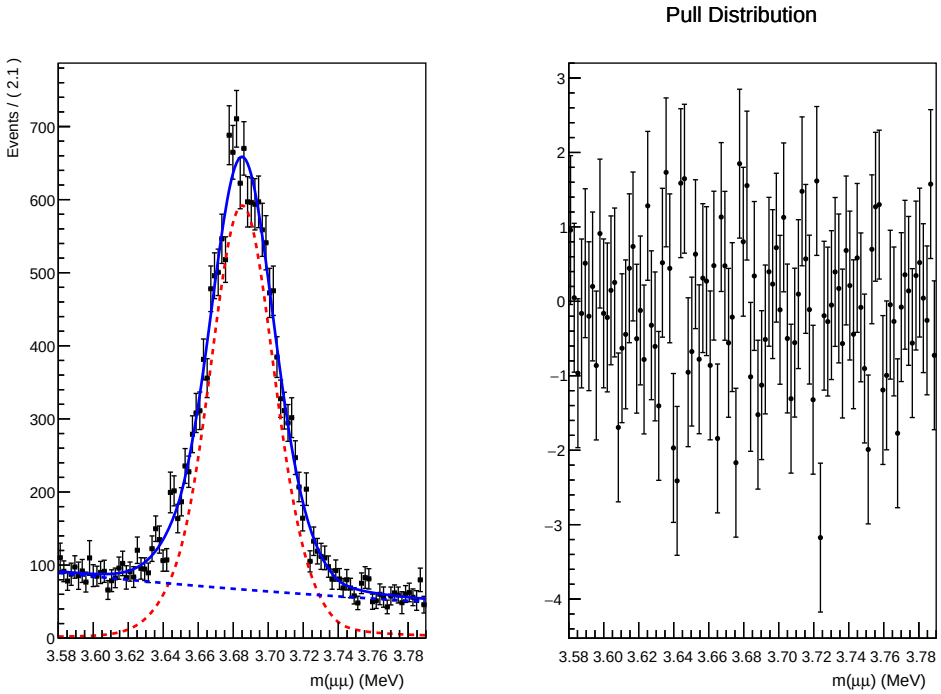

Figure 6.9: Invariant mass fit of $\psi(2S)$ for $0.8 < z(\psi(2S)) < 0.9$. The signal is modelled with a DCB function, which is shown in red, and the background is modelled with an exponential function, which shown in blue.

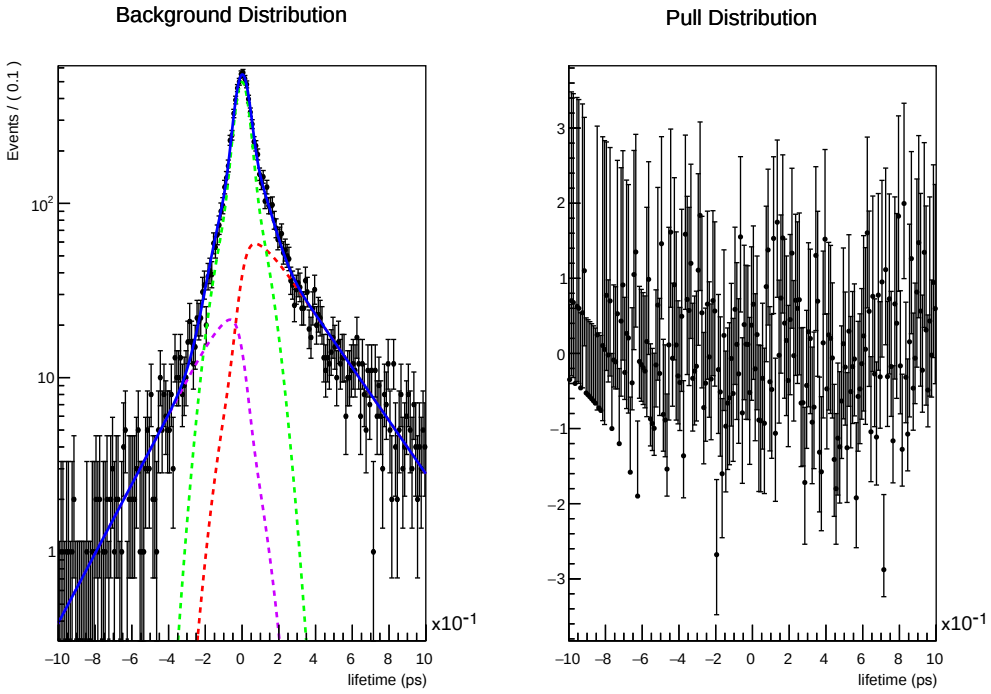

Figure 6.10: Background lifetime fit of $\psi(2S)$ for $0.3 < z(\psi(2S)) < 0.4$. It consists of two negative exponentials and one positive exponential, each convolved with the same Double Gaussian PDF.

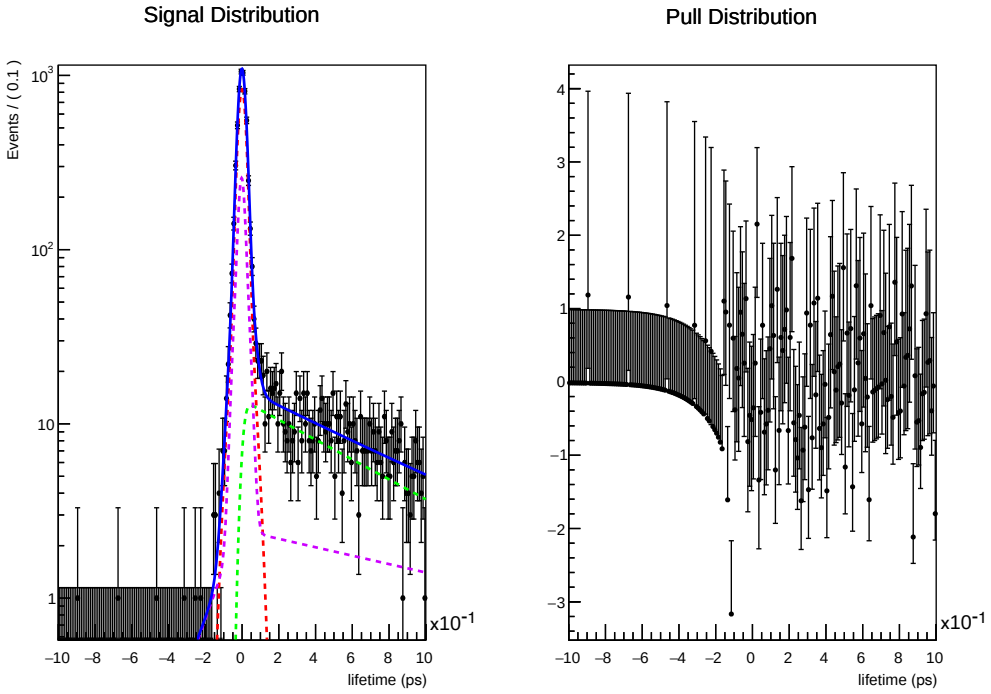

Figure 6.11: Signal lifetime fit of $\psi(2S)$ for $0.9 < z(\psi(2S)) < 1.0$. The background component, shown in purple, is modelled with an empirical fit to the sideband region of the mass fit in fig. 6.9 which is shown in fig. 6.10. The prompt component is modelled with a Double Gaussian, which is shown in red, and the displaced component is modelled with an exponential function convolved with a Double Gaussian, which is shown in green. The wrong PV component is too small to view.

The raw yields for the prompt and displaced component of the $\psi(2S)$ are shown in fig. 6.12. The yields are roughly 1-2 orders of magnitude smaller than for the J/ψ. This is expected as the branching fraction (BF) for $\psi(2S) \to \mu^+\mu^-$ is 0.80 ± 0.06 %, in comparison to the J/ψ's which is 5.961 ± 0.033 %. Also, the production cross section for $\psi(2S)$ is smaller than that of the J/ψ. Hence, due to statistics the average error in the yield is larger for the $\psi(2S)$ than for the J/ψ.

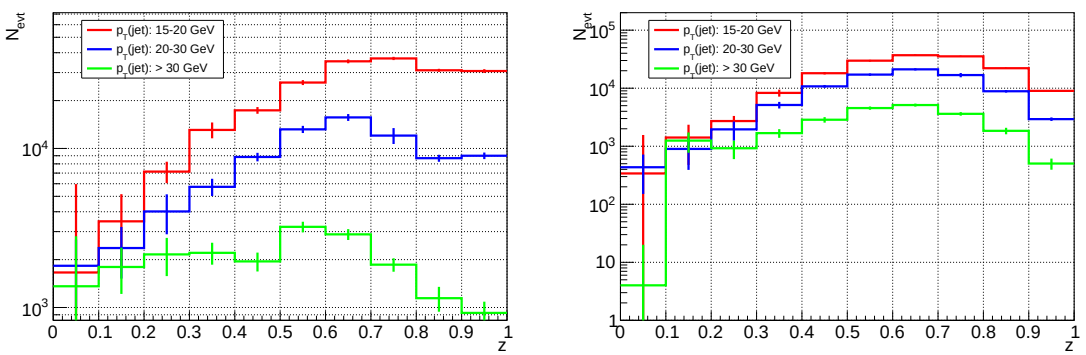

(a) Prompt. (b) Displaced.

Figure 6.12: Prompt and displaced yields *vs.* $z(\psi(2S))$ in different $p_{\mathrm{T}}(\mathrm{jet})$ ranges.

Normalised cross section distributions *vs.* $z(\psi(2S))$ are shown in fig. 6.13 with uniform binning. The distributions show similar behaviour to the J/ψ, where there is more of a central peak in the prompt distribution than the original expected isolated peak at $z(\psi(2S)) \simeq 1$. The mean $z(\psi(2S))$ value also shifts to lower values with increase in $p_{\mathrm{T}}(\mathrm{jet})$ for the prompt component, in comparison to the displaced component which stays pretty constant. However, the central $z(\psi(2S))$ peak is at a higher value of ~ 0.6, in comparison to both the prompt and displaced J/ψ distributions which had a central peak of ~ 0.5. This could be because the $\psi(2S)$ has a higher mass than the J/ψ, so shares more of the overall jet energy. However, different production mechanisms could come into play, such as fractions from feed down and b-decays *etc.* This will need to be explored in more detail.

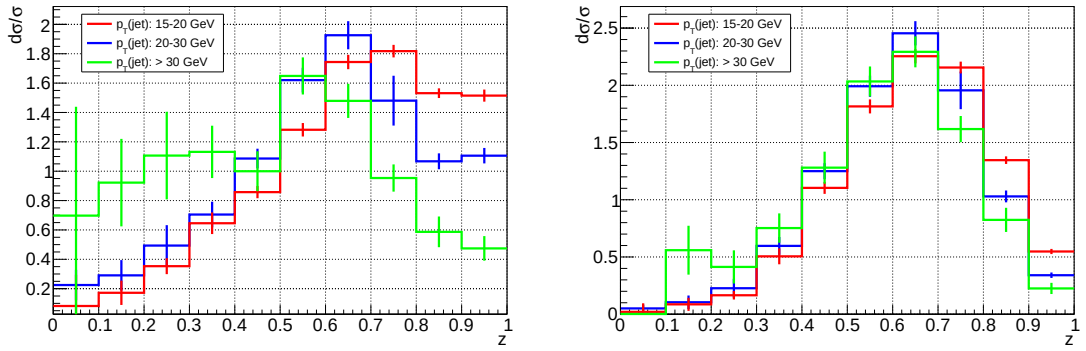

(a) Prompt. (b) Displaced.

Figure 6.13: Prompt and displaced normalised cross sections, $\mathrm{d}\sigma/\sigma$, *vs.* $z(\psi(2S))$ in different $p_{\mathrm{T}}(\mathrm{jet})$ ranges. The plots are normalised as $1/N\ \mathrm{d}N/\mathrm{d}z$.

6.1.6 Selection of $\Upsilon(1S)$, $\Upsilon(2S)$ and $\Upsilon(3S)$

The selection of $\Upsilon(1S)$, $\Upsilon(2S)$ and $\Upsilon(3S)$ uses the same software and tools as the J/ψ and $\psi(2S)$, and the di-muon decay channel is used. However, the method of their selection slightly differs from that of the J/ψ and $\psi(2S)$. Firstly, as for the $\psi(2S)$, a different HLT2 trigger is used called `Hlt2DiMuonBTurbo`. The selections are the same as for the J/ψ and $\psi(2S)$ again, except instead of using a mass window, any di-muon candidate that has a mass $> 4700\,\mathrm{MeV}$ is kept. This means all three Υ's are selected by the same trigger.

Secondly, the mass fits differ from that of the J/ψ and $\psi(2S)$. As the $\Upsilon(2S)$ and $\Upsilon(3S)$ are relatively close in mass, the upper tail of the $\Upsilon(2S)$ signal peak can bleed into the lower tail of the $\Upsilon(3S)$ signal peak, due to the fact that LHCb has

a finite mass resolution which is 0.4 % of the dimuon mass [116]. Hence, the Υ has a larger mass resolution than the J/ψ, because the Υ is more heavy, so decays to particles with higher p_{T} values which have a worse p_{T} resolution. This means that the three signal peaks need to be fit simultaneously along with the background component. An example mass fit is shown in fig. 6.14 with the selection $0.7 < z(\Upsilon) < 0.8$ applied. As the Υ is too heavy to be produced from b-decays, there is no displaced component. Hence, there is no need to perform a lifetime fit, and the final yield for each $z(\Upsilon)$ and $p_{\mathrm{T}}(\mathrm{jet})$ bin is just taken from the mass fit for each Υ. The signal region is chosen to be $9290 < \mathrm{m}(\mu\mu) < 9630\,\mathrm{MeV}/c^2$.

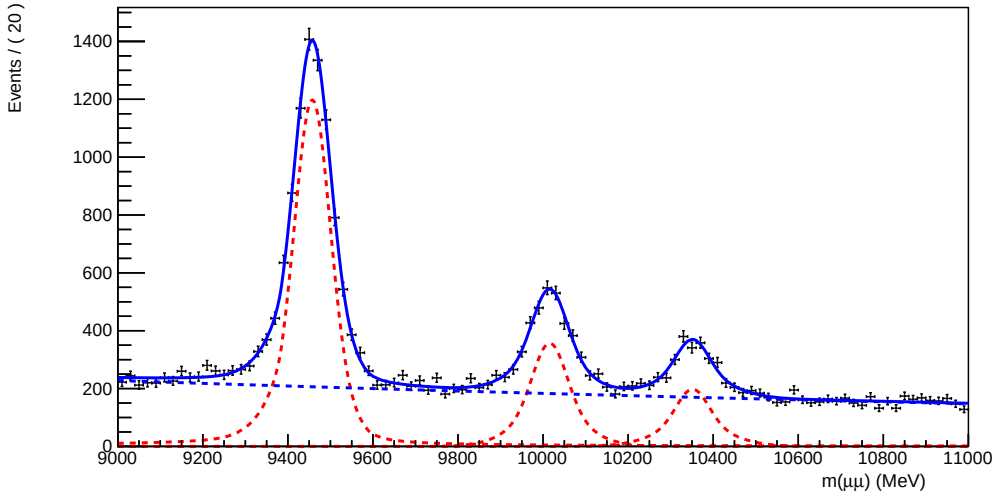

Figure 6.14: Invariant mass fit of Υ's for $0.7 < z(\Upsilon) < 0.8$. The signal is modelled with a DCB function for each Υ state (three in total), which is shown in red, and the background is modelled with an exponential function, which shown in blue.

The yield *vs.* $z(\Upsilon)$ for different $p_{\mathrm{T}}(\mathrm{jet})$ ranges for each Υ is shown in fig. 6.15. The yields at high $z(\Upsilon)$ are comparable to the J/ψ and $\psi(2S)$. However, the yields at low $z(\Upsilon)$ are roughly 3 orders of magnitude smaller. This leads to larger errors at low $z(\Upsilon)$, where the errors are taken directly from the mass fit signal uncertainty. The yield distributions in fig. 6.15 are normalised to give the result distributions shown in fig. 6.16. The resulting distributions are very different from those of the J/ψ and $\psi(2S)$, showing an isolated peak at $z(\Upsilon) \simeq 1$ for all Υ states. This again could be because the Υ is a higher mass than the J/ψ and $\psi(2S)$ so shares more of the jet energy. However, this needs to be investigated further. What is also interesting is that the peak gets less isolated with $p_{\mathrm{T}}(\mathrm{jet})$, where for the highest $p_{\mathrm{T}}(\mathrm{jet})$ bin the peak actually shifts to the next $z(\Upsilon)$ bin.

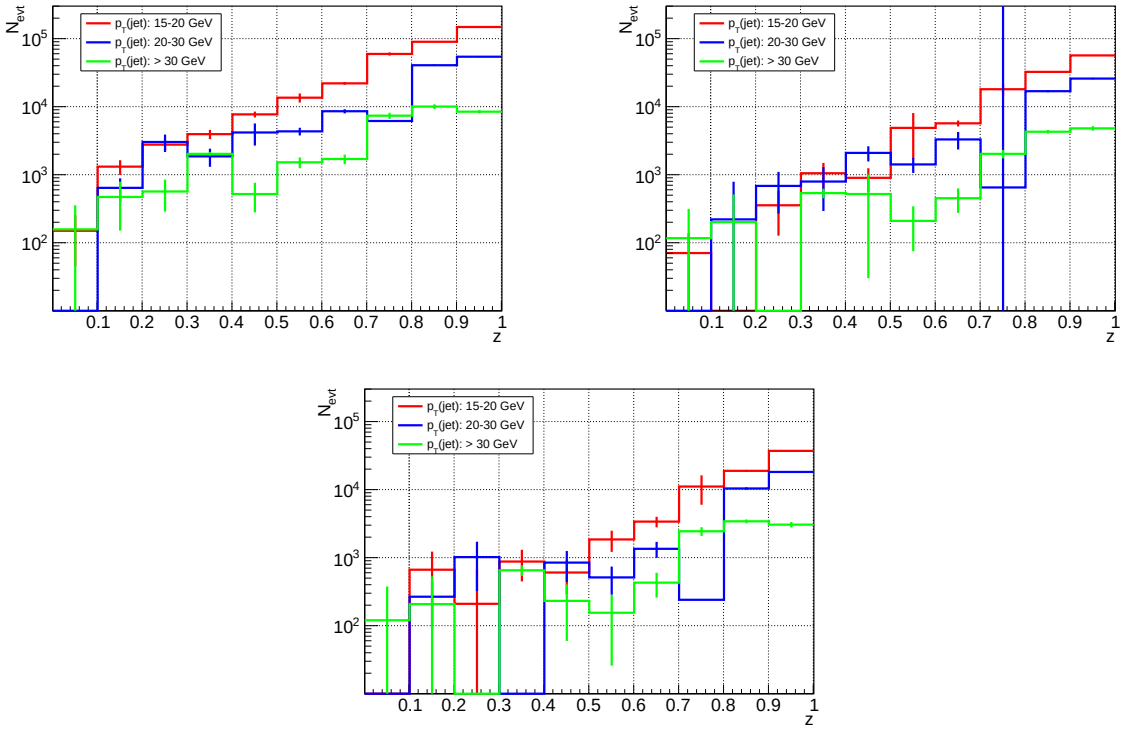

Figure 6.15: Yield distributions *vs.* $z(\Upsilon)$ in different p_{T}(jet) ranges for separated $\Upsilon(1S)$, $\Upsilon(2S)$ and $\Upsilon(3S)$. Left to right: $\Upsilon(1S)$, $\Upsilon(2S)$ and $\Upsilon(3S)$.

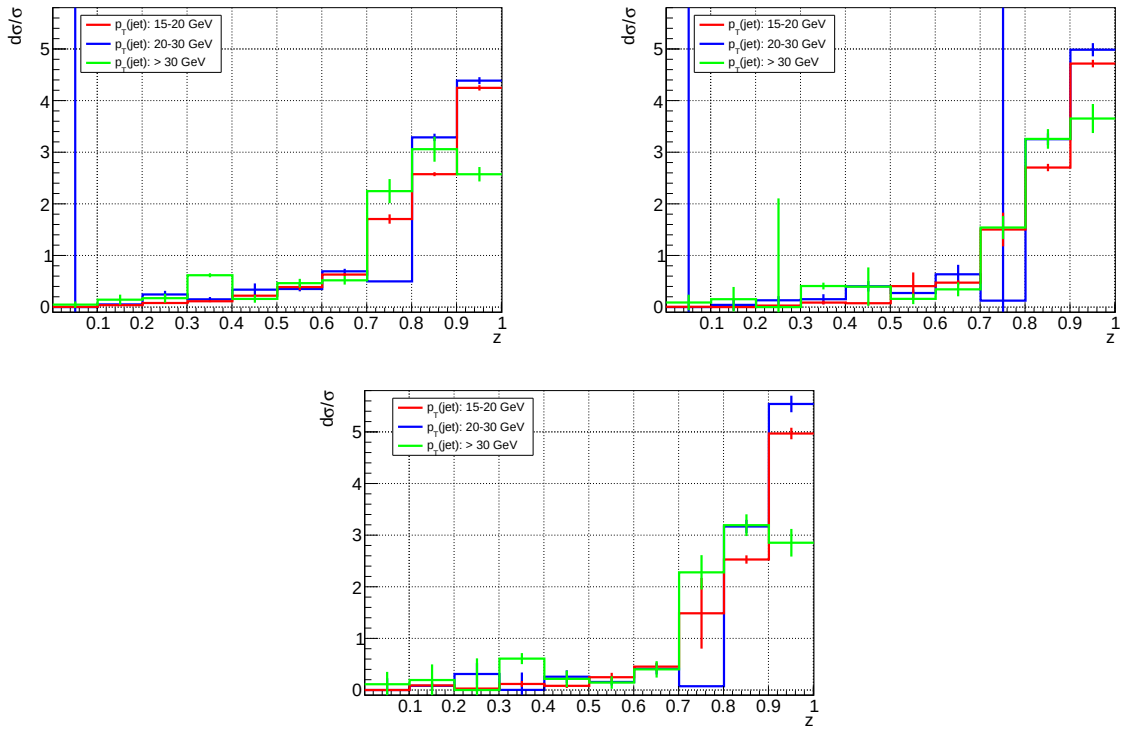

Figure 6.16: Normalised cross section distributions *vs.* $z(\Upsilon)$ in different p_{T}(jet) ranges for separated $\Upsilon(1S)$, $\Upsilon(2S)$ and $\Upsilon(3S)$. The plots are normalised as $1/N\ \mathrm{d}N/\mathrm{d}z$. Left to right: $\Upsilon(1S)$, $\Upsilon(2S)$ and $\Upsilon(3S)$.

To look at the distributions in a different way, instead of showing distributions for each individual Υ, the distributions for each $p_{\mathrm{T}}(\mathrm{jet})$ range are shown in fig. 6.17. This shows a general trend that the $z(\Upsilon)$ peak gets more isolated with each higher mass Υ state. Another interesting feature is that in the $p_{\mathrm{T}}(\mathrm{jet}) > 30\,\mathrm{GeV}$ distribution there is a slight peak at $z(\Upsilon) \simeq 0.35$. This may be another source of production, but will need to be investigated further.

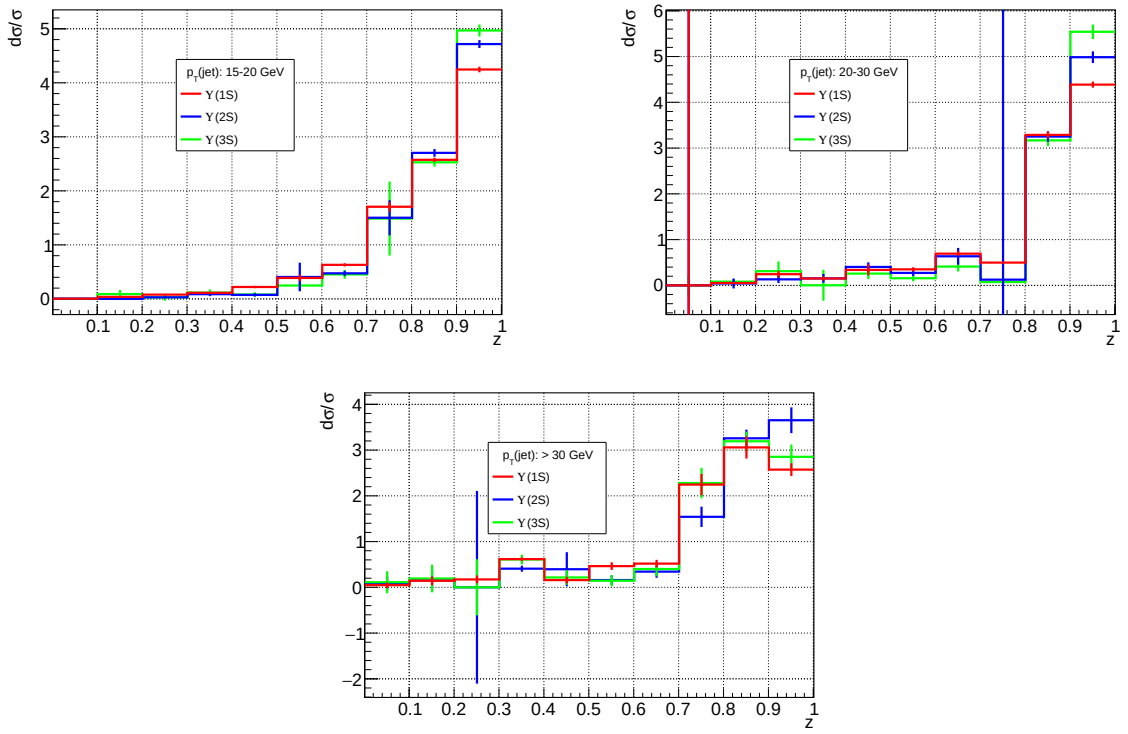

Figure 6.17: Normalised cross section distributions for $\Upsilon(1S)$, $\Upsilon(2S)$ and $\Upsilon(3S)$ *vs.* $z(\Upsilon)$ in different $p_{\mathrm{T}}(\mathrm{jet})$ ranges. The plots are normalised as $1/N\ \mathrm{d}N/\mathrm{d}z$. Left to right: $15 < p_{\mathrm{T}}(\mathrm{jet}) < 20\,\mathrm{GeV}$, $20 < p_{\mathrm{T}}(\mathrm{jet}) < 30\,\mathrm{GeV}$, and $p_{\mathrm{T}}(\mathrm{jet}) > 30\,\mathrm{GeV}$.

6.2 Efficiencies

This section will discuss how the efficiencies used for the signal correction of the J/ψ are obtained. The total efficiency, ϵ_{tot} can be factorised into several sub-components,

$$\epsilon_{tot} = \epsilon_{J/\psi} \cdot \epsilon_{global}, \tag{6.8}$$

where,

$$\epsilon_{J/\psi} = \epsilon_{trigger} \cdot \epsilon_{reco}(\mu_1) \cdot \epsilon_{reco}(\mu_2) \cdot \epsilon_{PID}(\mu_1) \cdot \epsilon_{PID}(\mu_2) \cdot (\epsilon_{lifetime}), \tag{6.9}$$

$$\epsilon_{global} = \epsilon_{nPV} \cdot \epsilon_{nSPD}. \tag{6.10}$$

To calculate each efficiency, fiducial cuts as defined in table 6.1 are always applied on the muons and J/ψ's. $\epsilon_{reco}(\mu)$ is the reconstruction efficiency for the muons. This only includes the probability that a track is reconstructed at all, not the quality of the reconstruction. $\epsilon_{trigger}$ is the trigger efficiency and $\epsilon_{PID}(\mu)$ is the PID efficiency of the muons, specifically a variable called ProbNNmu. ϵ_{global} is the global event efficiency. This includes the number of PV's, ϵ_{nPV}, and the nSPD cut, ϵ_{nSPD}, which is a measure of the multiplicity of an event. For displaced decays, a lifetime efficiency cut needs to be taken into account, which is taken from MC. Here, it can be assumed that the jet reconstruction can be factorised out, and does not effect the total efficiency of selecting J/ψ's. The jets are handled purely in the unfolding. The efficiencies themselves are measured as a function of different fiducial variables, to obtain an efficiency map. These maps are then used to reweight each event with an efficiency value to correct the distributions.

6.2.1 Reconstruction efficiencies

This section discusses the reconstruction efficiencies for the muons, $\epsilon_{reco}(\mu)$. The efficiency maps are obtained directly from LHCb simulations. When applying these reconstruction efficiency maps on data, however, an additional correction factor needs to be applied which takes into account the slight differences between MC and data. This is quantified by the data/MC ratio, $R_{data/MC}$. Hence, the reconstruction efficiency is factorised as follows,

$$\epsilon_{reco}(\mu) = \epsilon^{MC}_{reco}(\mu) \cdot R_{data/MC}. \tag{6.11}$$

How these quantities are obtained are presented in the next sections.

6.2.1.1 Muons

$\epsilon^{MC}_{reco}(\mu)$ is extracted from an inclusive $J/\psi \to \mu\mu$ MC sample, which contains both generator level and reconstruction information of the muons. Generator level MC is the particle generated directly from a MC generator such as Pythia 8. Reconstructed MC is this generated particle which is passed through a simulated LHCb detector to estimate its detector response.

All the reconstructed muons in an event are collected into a particle container (called

`StdAllNoPIDMuons`). The procedure is to loop over all the reconstructed muons available in the container. If this reconstructed muon links back to a generator level muon, then it is kept. If not, it is thrown away. (The reconstructed muon has to pass a certain number of MC generator level hits, *i.e.* matched energy deposits in the detector, to be classed as reconstructed). The ratio of these reconstructed muons to all muons generated at generator level gives the efficiency. Both samples, generator and reconstructed level, are only evaluated inside the fiducial volume of LHCb.

Figure 6.18 shows the muon reconstruction efficiency map, $\epsilon^{MC}_{reco}(\mu)$, in bins of $\eta(\mu)$ and $p_T(\mu)$. At higher $p_T(\mu)$ the efficiency values are extrapolated.

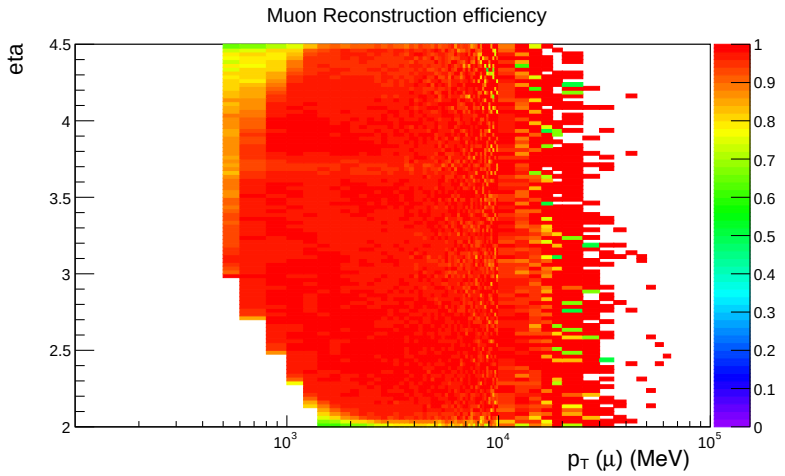

Figure 6.18: Muon reconstruction efficiency for 2016 MC (`StdAllNoPIDMuons`) *vs.* $\eta(\mu)$ and $p_T(\mu)$.

To check that the muon reconstruction efficiency, $\epsilon^{MC}_{reco}(\mu)$, is valid, a closure test is performed. In this closure test, it is assumed that the reconstruction efficiency of the J/ψ, $\epsilon^{MC}_{reco}(J/\psi)$, can be factorised as follows:

$$\epsilon^{MC}_{reco}(J/\psi) = \epsilon^{MC}_{reco}(\mu_1) \cdot \epsilon^{MC}_{reco}(\mu_2). \tag{6.12}$$

For the closure test both sides of eq. (6.12) are evaluated independently and then compared. $\epsilon^{MC}_{reco}(J/\psi)$ is calculated using the same method as the muons, except generator level matching the whole J/ψ candidate instead. This is shown in fig. 6.19(a). Figure 6.19(b) is evaluated using the right hand side of eq. (6.12). Each muon in the J/ψ candidate is assigned an efficiency using the muon reconstruction efficiency map, shown in fig. 6.18. The separate muon efficiencies are then multiplied together. Figure 6.19(a) and fig. 6.19(b) are very similar. Hence, dividing fig. 6.19(b) by fig. 6.19(a), should give a value of one. Figure 6.20 shows this division. Since all

bins are close to one the muon reconstruction efficiency map is validated.

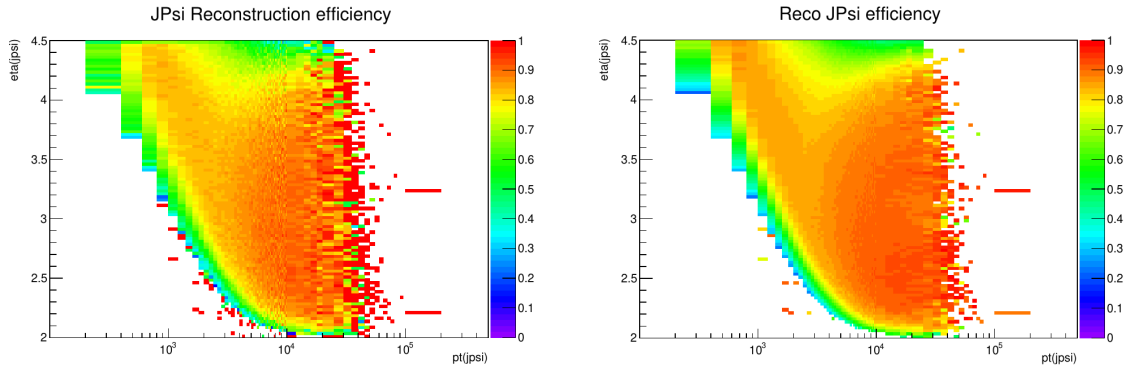

(a) Combine particles (b) Reweight as 1/eff(μ)*eff(μ)

Figure 6.19: J/ψ reconstruction efficiency for 2016 MC, where J/ψ's created from CombineParticles or from reweighting as 1/eff(μ)*eff(μ) *vs.* $\eta(J/\psi)$ and $p_{\mathrm{T}}(J/\psi)$. These plots include an IsMuon criterion as well.

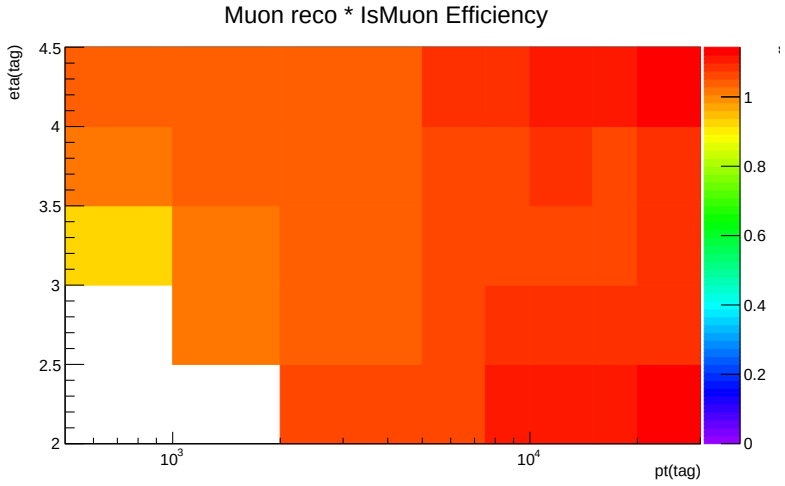

Figure 6.20: Closure test for reweighting the J/ψ reconstruction efficiency with the weight $1/\epsilon^{MC}_{reco\_\mu 1} \cdot \epsilon^{MC}_{reco\_\mu 2}$ using the muon reconstruction efficiency map from fig. 6.18.

6.2.1.2 data/MC ratio, $R_{data/MC}$

To obtain $R_{data/MC}$, a LHCb software package called TrackCalib was used [121]. This uses the tag-and-probe method on a mixture of J/ψ and Z^0 decays [122]. The tracks used in this analysis are long tracks, which generate hits in all parts of the tracking detector. This is shown in fig. 6.21. The tag-and-probe method uses one muon from the J/ψ or Z^0 as a fully reconstructed track. The probe then has the requirement that there are hits in the TT and muon stations. The long track efficiency is then the ratio of probe tracks that pass this requirement divided by

the total number of probes. The J/ψ is primarily used in this method, however Z^0 decays are used to obtain high p_{T} muons.

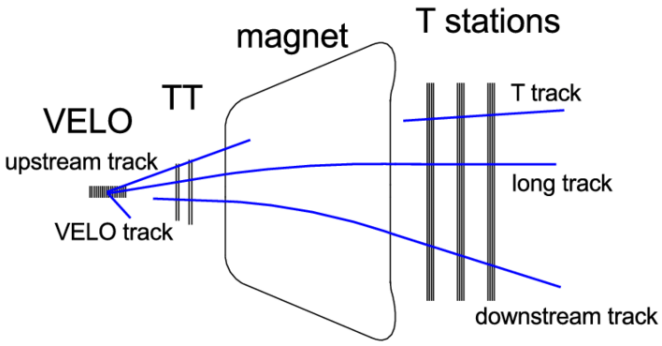

Figure 6.21: Different track types in LHCb [123].

This package provides data to MC ratios for different fiducial variables for different track types. Figure 6.22 shows 1D long track efficiency maps *vs.* p and η respectively. Figure 6.23 shows a 2D long track efficiency map *vs.* p and η, which is the final map used for the data/MC correction $R_{data/MC}$.

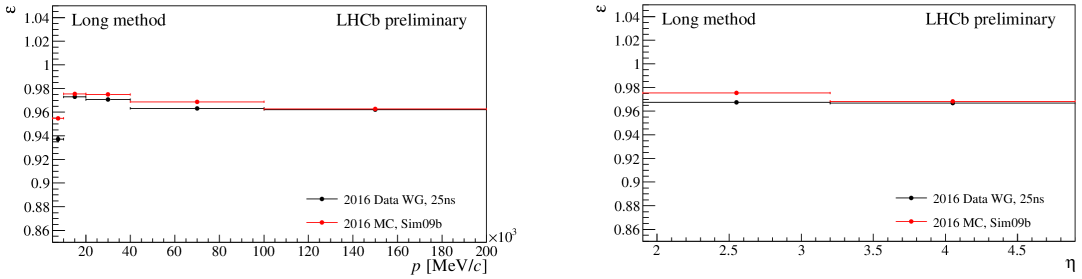

(a) p (b) η

Figure 6.22: Long track efficiency *vs.* p or η for Data and MC.

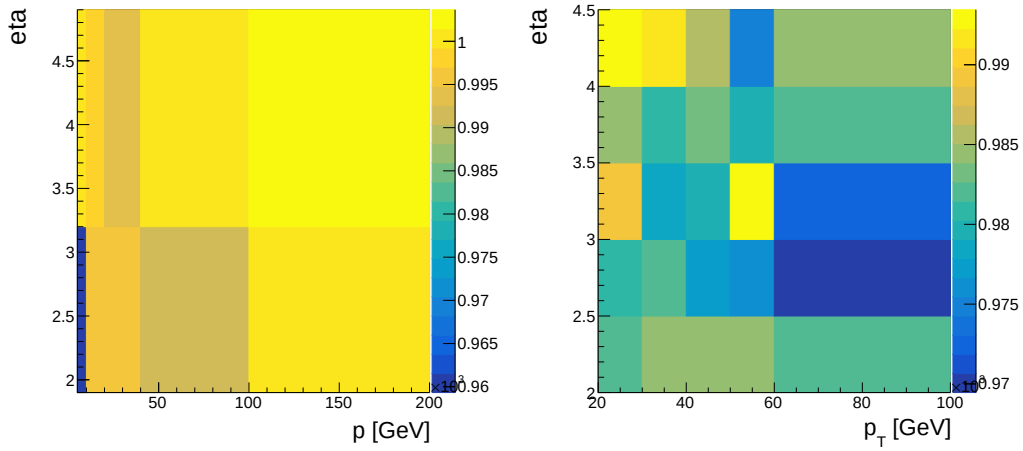

Figure 6.23: Ratio of data/MC for Long method tracking efficiency. Left, low part (p_{T} <20 GeV): η *vs.* p. Right, high momentum part (p_{T} >20 GeV): η *vs.* p_{T}.

6.2.2 Trigger efficiency

6.2.2.1 TCK selections

In this section the trigger efficiency is evaluated. Generally, throughout a year of data taking, the trigger conditions can vary quite a lot. Various cuts can be added, removed or altered depending on the output bandwidth of data required. Hence, the consistency of cuts used throughout 2016 needs to be checked. A year is split into separate runs, where each run is assigned a hexadecimal value called a TCK. Figures 6.24 and 6.25 show the cuts used for L0, HLT1 and HLT2 in each TCK. Green marks where the cuts are consistent. The white boxes differ, but do not effect the overall trigger efficiency much, so the cuts are consistent in L0, HLT1 and HLT2.

Trigger level	Condition	TCK Number – 2016 Mag Down								
		0x11291600 (~ 0.4 %)	0x11291603 (~ 2.3 %)	0x11291604 (~ 1.6 %)	0x11291605 (~ 5.1 %)	0x11371609 (~ 3.8 %)	0x1137160E (~ 1.4 %)	0x11381609 (~ 0.4 %)	0x1138160E (~ 1.9 %)	0x1138160F (~ 33.3 %)
L0DiMuon	$\sqrt{p_{T1}p_{T2}}$ > 1.3 – 1.5 GeV	DiMuonProd (Pt1Pt2) > 324 MeV$^{(2)}$	DiMuonProd (Pt1Pt2) > 400 MeV$^{(2)}$	DiMuonProd (Pt1Pt2) > 576 MeV$^{(2)}$	DiMuonProd (Pt1Pt2) > 676 MeV$^{(2)}$	DiMuonProd (Pt1Pt2) > 676 MeV$^{(2)}$	DiMuonProd (Pt1Pt2) > 676 MeV$^{(2)}$	DiMuonProd (Pt1Pt2) > 676 MeV$^{(2)}$	DiMuonProd (Pt1Pt2) > 676 MeV$^{(2)}$	DiMuonProd (Pt1Pt2) > 900 MeV$^{(2)}$
	N_{SPD} < 900	< 900	< 900	< 900	< 900	< 900	< 900	< 900	< 900	< 900
Hlt1DiMuon HighMass	$p_T(\mu)$ > 0.5 GeV	> 0.3 GeV	> 0.3 GeV	> 0.3 GeV	> 0.3 GeV	> 0.3 GeV	> 0.3 GeV	> 0.3 GeV	> 0.3 GeV	> 0.3 GeV
	$p(\mu)$ > 3 GeV	> 6 GeV	> 6 GeV	> 6 GeV	> 6 GeV	> 6 GeV	> 6 GeV	> 6 GeV	> 6 GeV	> 6 GeV
	Track χ^2/n_{dof} < 3	< 4	< 4	< 4	< 4	< 4	< 4	< 4	< 4	< 4
	Additional: TRGHOSTPROB < 999.0	None	None	None	None	< 999.0	< 999.0	< 999.0	< 999.0	< 999.0
	IsMuon	Yes	Yes	Yes	Yes	Yes	Yes	Yes	Yes	Yes
	DOCA < 0.2 mm	< 0.2 mm	< 0.2 mm	< 0.2 mm	< 0.2 mm	< 0.2 mm	< 0.2 mm	< 0.2 mm	< 0.2 mm	< 0.2 mm
	Vertex χ^2 < 25	< 25	< 25	< 25	< 25	< 25	< 25	< 25	< 25	< 25
	$m(\mu\mu)$ > 2.7 GeV	> 2.9 GeV	> 2.9 GeV	> 2.9 GeV	> 2.9 GeV	> 2.7 GeV	> 2.7 GeV	> 2.7GeV	> 2.7 GeV	> 2.7 GeV
	(QProd == -1) | (RV_MASS('mu+':'mu-')> 220.0 * MeV)	None	None	None	None	Implemented	Implemented	Implemented	Implemented	Implemented

Figure 6.24: TCK table Mag Down 2016 - L0 and HLT1.

Trigger level	Condition	TCK Number – 2016 Mag Down											
		0x212A1600 (~ 0.02 %) (0x11291600 ~ 0.02 %)	0x212C1600 (~ 0.35 %) (0x11291600 ~ 0.35 %)	0x212C1603 (~ 2.25 %) (0x11291603 ~ 2.25 %)	0x21311603 (~ 0.02 %) (0x11291603 ~ 0.02 %)	0x21311604 (~ 1.65 %) (0x11291604 ~ 1.65 %)	0x21311605 (~ 5.10 %) (0x11291605 ~ 5.10 %)	0x21371609 (~ 3.80 %) (0x11371609 ~ 3.80 %)	0x2137160E (~ 3.3 %) (0x1137160E ~ 1.4 %) (0x1138160E ~ 1.9 %)	0x21381609 (~ 0.44 %) (0x11381609 ~ 0.44 %)	0x2137160F (~ 3.06 %) (0x1138160F ~ 3.06 %)	0x2138160F (~ 17.34 %) (0x1138160F ~ 17.34 %)	0x2139160F (~ 12.91 %) (0x1138160F ~ 12.91 %)
Hlt2DiMuon JPsiTurbo	$p_T(\mu)$ > 0.5 GeV	> 0.5 GeV	> 0.5 GeV	> 0.5 GeV	> 0.5 GeV	> 0.5 GeV	> 0.5 GeV	> 0.5 GeV	> 0.5 GeV	> 0.5 GeV	> 0.5 GeV	> 0.5 GeV	> 0.5 GeV
	Track χ^2/n_{dof} < 3	< 5	< 5	< 5	< 5	< 5	< 5	< 5	< 5	< 5	< 5	< 5	< 5
	Vertex χ^2 < 25	< 25	< 25	< 25	< 25	< 25	< 25	< 25	< 25	< 25	< 25	< 25	< 25
	$\|m(\mu\mu) - m(J/\psi)\|$ < 0.15 GeV	< 0.12 GeV	< 0.12 GeV	< 0.12 GeV	< 0.12 GeV	< 0.12 GeV	< 0.12 GeV	< 0.12 GeV	< 0.12 GeV	< 0.12 GeV	< 0.12 GeV	< 0.12 GeV	< 0.12 GeV
	pt(J/ψ) > 0.0 GeV	> 0.0 GeV	> 0.0 GeV	> 0.0 GeV	> 0.0 GeV	> 0.0 GeV	> 0.0 GeV	> 0.0 GeV	> 0.0 GeV	> 0.0 GeV	> 0.0 GeV	> 0.0 GeV	> 0.0 GeV
	PIDmu > 1	> 1	> 1	> 1	> 1	> 1	> 1	> 1	> 1	> 1	> 1	> 1	> 1

Figure 6.25: TCK table Mag Down 2016 - HLT2.

6.2.2.2 Trigger efficiency in MC

To evaluate the trigger efficiency, the TIS-TOS method is used [124]. Firstly, J/ψ candidates are selected that pass an independent set of triggers to the ones that were selected for the analysis (TIS). Then from these TIS selected J/ψ candidates, J/ψ candidates are selected that pass the trigger lines for this analysis (TOS). This is to obtain an independent selection for the trigger efficiency. To be able to select J/ψ TIS candidates, the $B \to J/\psi K$ decay channel is used. These are obtained through the `FullDSTDiMuonJpsi2MuMuDetachedLine` stripping line. Stripping lines are further selection lines which are at a higher level than the trigger which are performed offline. The TIS triggers selected are then `L0Hadron`, `Hlt1.*TrackMVA.*` and `Hlt2Topo.*`, where `*` is a wildcard. The hadron line, `L0Hadron`, is used as an independent trigger, due to the fact that it triggers on the kaon in the $B \to J/\psi K$ decay rather than the J/ψ.

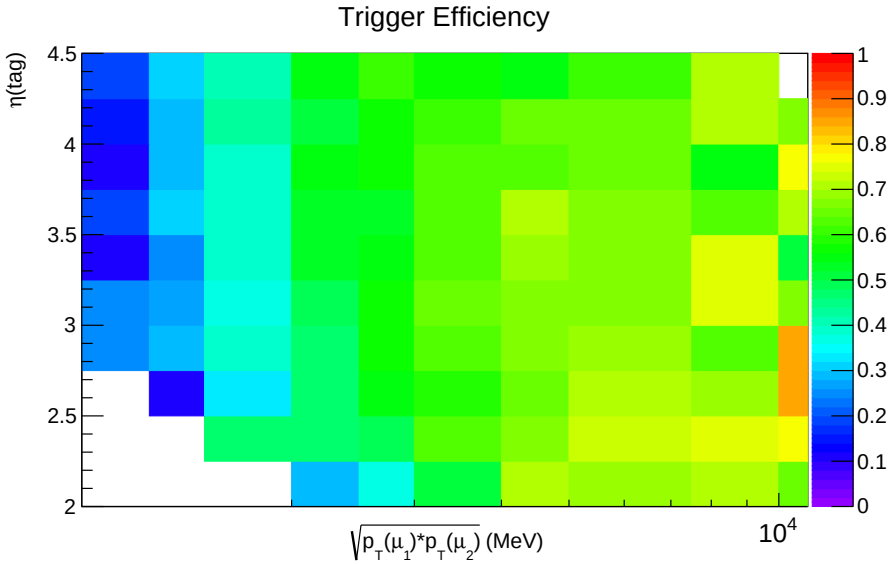

Figure 6.26: MC Trigger efficiency of $\eta(J/\psi)$ *vs.* $\sqrt{p_T(\mu_1)p_T(\mu_2)}$.

The main trigger inefficiencies are in the L0 trigger. Also, since the HLT1 and HLT2 trigger efficiencies are uniform in fiducial variables, the L0, HLT1 and HLT2 trigger efficiencies are combined into one map. This is shown in fig. 6.26 using $B \to J/\psi K$ MC. $\sqrt{p_T(\mu_1)p_T(\mu_2)}$ is used as a fiducial variable as this is the main selection variable used in the L0 trigger. To smooth out the trigger efficiency distribution shown in fig. 6.26, an interpolated fit is applied to the efficiency map. For each $\eta(J/\psi)$ bin, the function $a - be^{-cx}$ is fit *vs.* $\sqrt{p_T(\mu_1)p_T(\mu_2)}$. These functions are then used to obtain the trigger efficiency values. The interpolated fits for MC are shown in fig. 6.27.

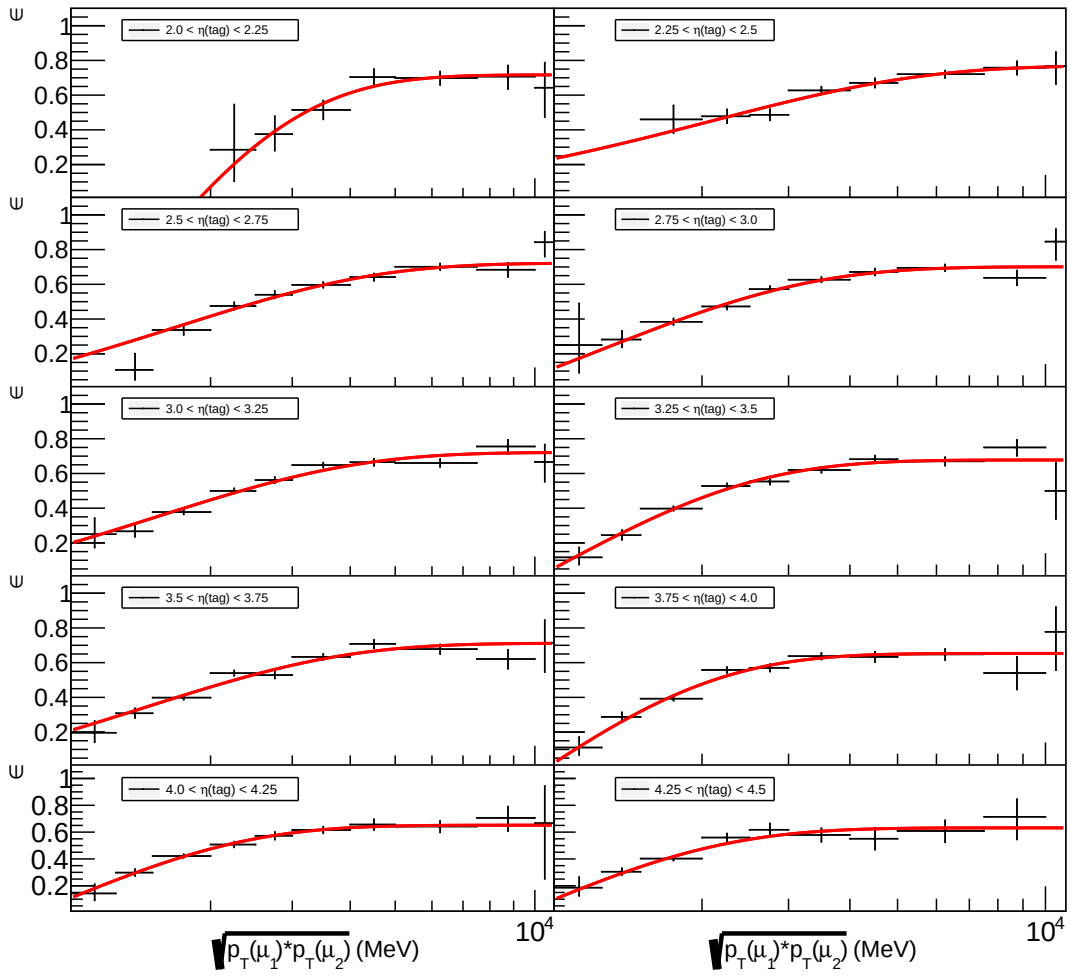

Figure 6.27: Interpolation fit of the trigger efficiency map shown in fig. 6.26 with the function $a - be^{-cx}$ *vs.* $\sqrt{p_T(\mu_1)p_T(\mu_2)}$ for different $\eta(J/\psi)$ bins with MC. These are in steps of 0.25 in $\eta(J/\psi)$ from 2.0-4.5.

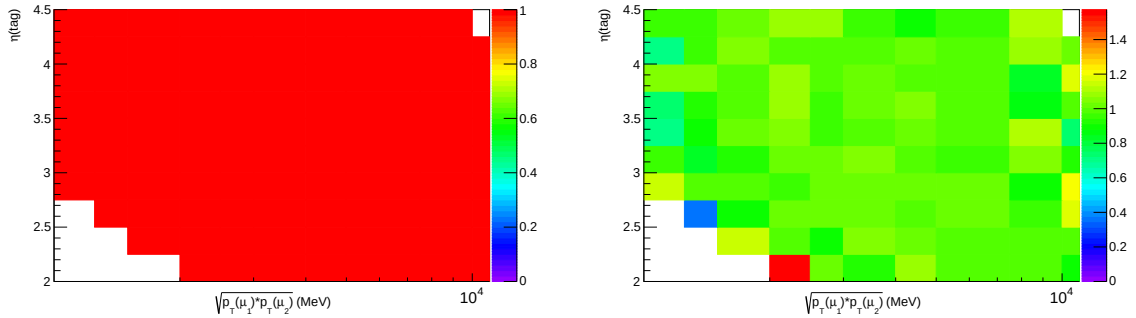

(a) Histogram. (b) Interpolated fit.

Figure 6.28: Closure test for trigger efficiency using the raw histogram in fig. 6.26 *vs.* the interpolated fits in fig. 6.27.

To check the trigger efficiency, a closure test is performed. The closure test is defined as the number of reweighted trigger efficiency TIS+TOS selected J/ψ candidates divided by the number of TIS selected J/ψ candidates. The left hand plot in fig. 6.28 shows the reweighting performed with the trigger efficiency map shown in fig. 6.26.

The reweighting in the right hand plot of fig. 6.28 uses the interpolated fits shown in fig. 6.27. Both closure tests are successful and give values around 1.

6.2.2.3 Closure test on inclusive J/ψ's

The final closure test is to validate fig. 6.26 and its interpolation in fig. 6.27 on not just the exclusive $B \to J/\psi K$ sample that created the maps, but on an inclusive $J/\psi \to \mu\mu$ data sample, to see if it matches the true J/ψ trigger efficiency. For the closure test, an inclusive J/ψ MC sample was used, and a yield ratio was obtained by applying LO+HLT1+HLT2 selection on candidates in the numerator. This ratio is then corrected with efficiency values from the TIS-TOS map (fig. 6.27), to evaluate the closure. Figure 6.29 displays the 2D result of the closure *vs.* $\eta(J/\psi)$ and $\sqrt{p_T(\mu_1)p_T(\mu_2)}$. Most values are within 5% of unity, hence this closure test is validated. Any differences from unity in the closure test are assigned as a systematic uncertainty.

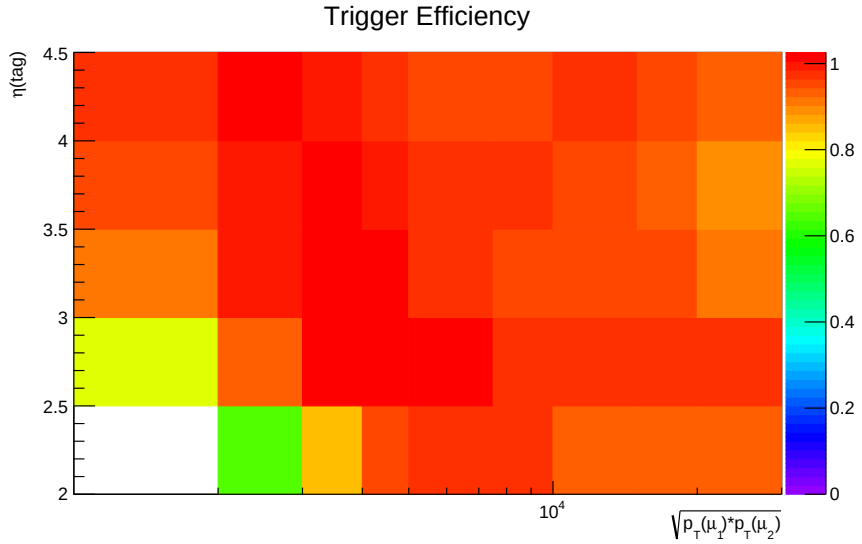

Figure 6.29: Closure test to test the TIS-TOS efficiency map on inclusive J/ψ, *i.e.* the true trigger efficiency, *vs.* $\eta(J/\psi)$ and $\sqrt{p_T(\mu_1)p_T(\mu_2)}$.

6.2.2.4 Trigger efficiency in Data

Since this procedure is verified with MC, the trigger efficiency in data can now be measured. Figure 6.30 shows the L0 +HLT1 +HL2 trigger efficiency map with data. The only difference between obtaining this and fig. 6.26 is that the ratio of signal yields in each bin is obtained from mass fits, due to the fact background is present. Figure 6.31 shows the interpolated fits of fig. 6.30 using $a - be^{-cx}$ like the MC case.

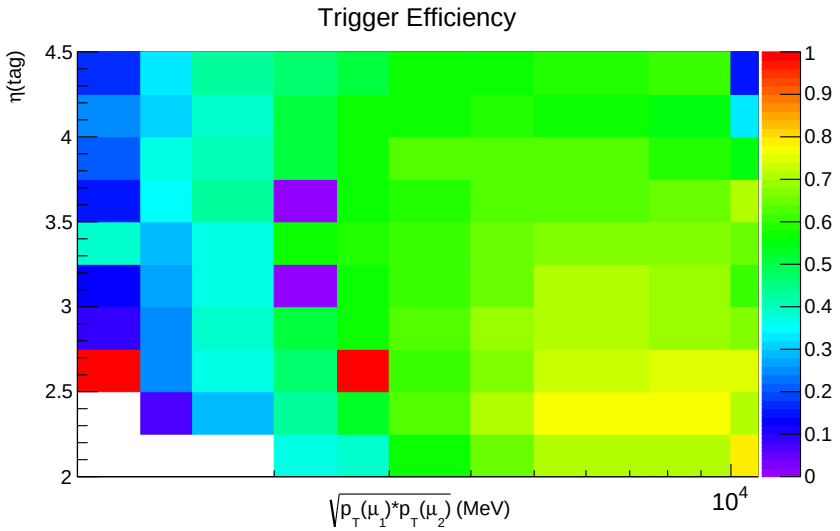

Figure 6.30: Trigger efficiency *vs.* $\eta(J/\psi)$ and $\sqrt{p_T(\mu_1)p_T(\mu_2)}$ with data.

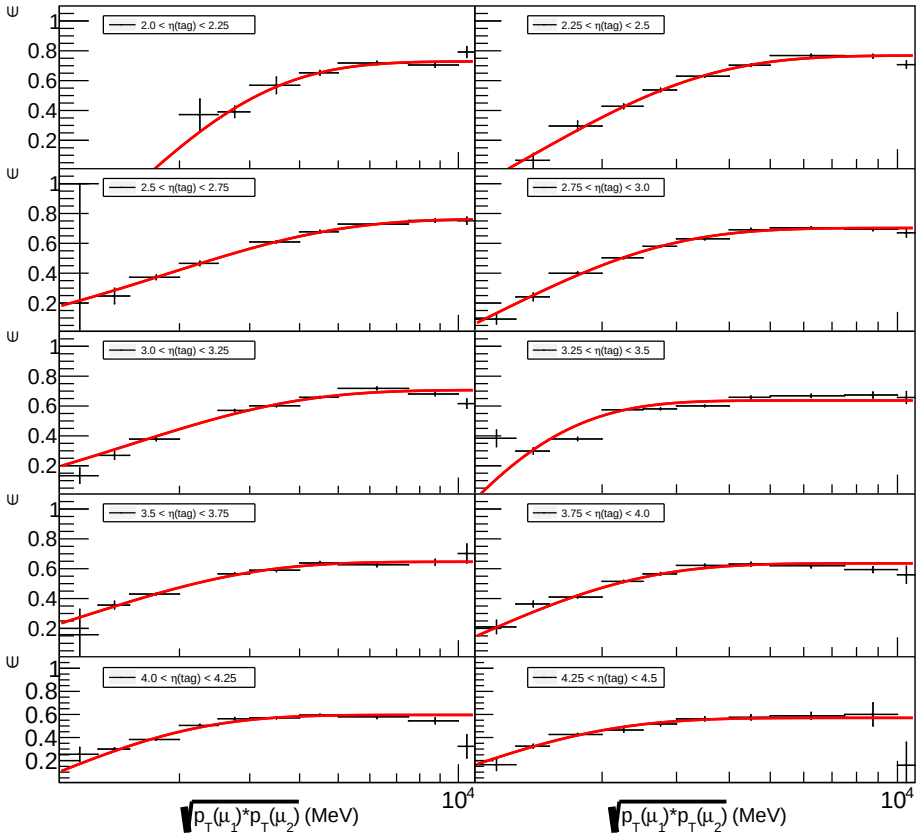

Figure 6.31: Interpolation fit of the trigger efficiency map shown in Fig. 6.30 with the function $a - be^{-cx}$ *vs.* $\sqrt{p_T(\mu_1)p_T(\mu_2)}$ for different $\eta(J/\psi)$ bins with data. These are in steps of 0.25 in $\eta(J/\psi)$ from 2.0-4.5.

6.2.2.5 Stripping line corrections

To be able to calculate the HLT2 trigger efficiency, the $B \to J/\psi K$ candidates from the `StrippingFullDSTDiMuonJpsi2MuMuDetachedLine` stripping line were used.

However, this stripping line already applies PID cuts on the muons, IsMuon and a PIDmu > 0, which have to be corrected for. Figure 6.32 shows the PID correction that has to be applied to each muon in addition to the trigger efficiency.

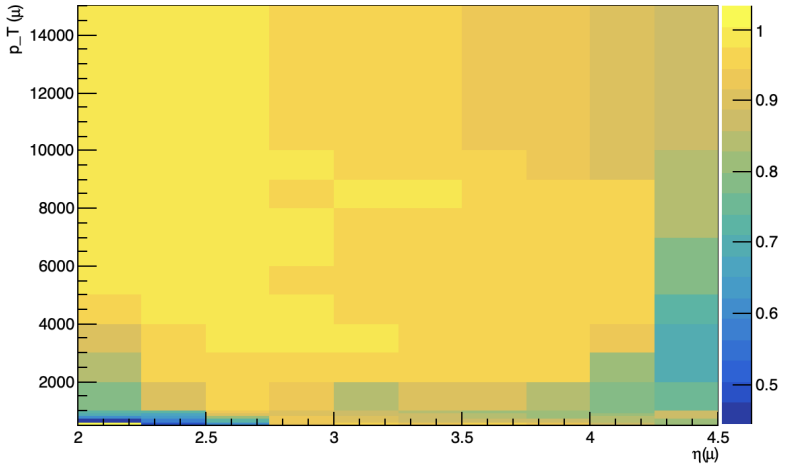

Figure 6.32: PID correction, PIDmu > 0 and IsMuon, for trigger efficiency, as these are already applied in the stripping line, which were calculated using PIDCalib2 [125].

6.2.3 Muon PID (ProbNNmu) efficiency

This efficiency corrects for the signal loss from applying the ProbNNmu > 0.8 cut on the muons. This is a per muon efficiency, so this is applied twice to the overall J/ψ candidate. When calculating this efficiency, all selection criteria are placed on the J/ψ candidates, including the trigger requirements. The denominator in the efficiency is then the number of remaining muons that have been selected in a specific $p_{\mathrm{T}}(\mu)$ and $\eta(\mu)$ range, and the numerator is the number of muons that pass these selection criteria and also ProbNNmu > 0.8 for that $p_{\mathrm{T}}(\mu)$ and $\eta(\mu)$ range.

6.2.3.1 ProbNNmu efficiency in MC

The procedure matches that of calculating the trigger efficiency, where the $B \to J/\psi\, K$ decay channel is used. The ProbNNmu efficiency map obtained from MC is shown in fig. 6.33. This is interpolated using the same function as for the trigger, except with different starting parameters. This is shown in fig. 6.34. Figure 6.35 shows the closure tests performed with the raw histogram and the interpolated fit. The result is roughly 1 for all values of $\eta(\mu)$ and $p_T(\mu)$ in both cases, so this efficiency map is validated.

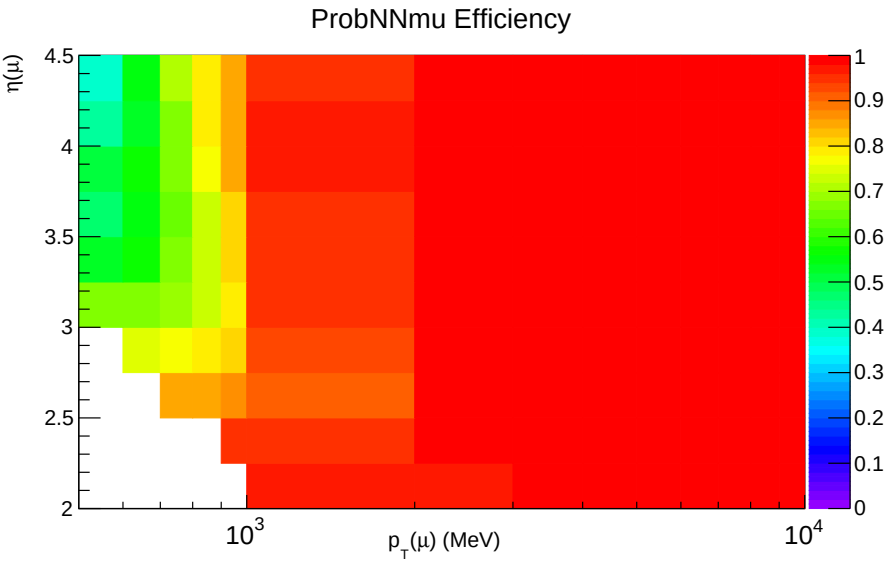

Figure 6.33: MC ProbNNmu efficiency of $\eta(\mu)$ *vs.* $p_T(\mu)$.

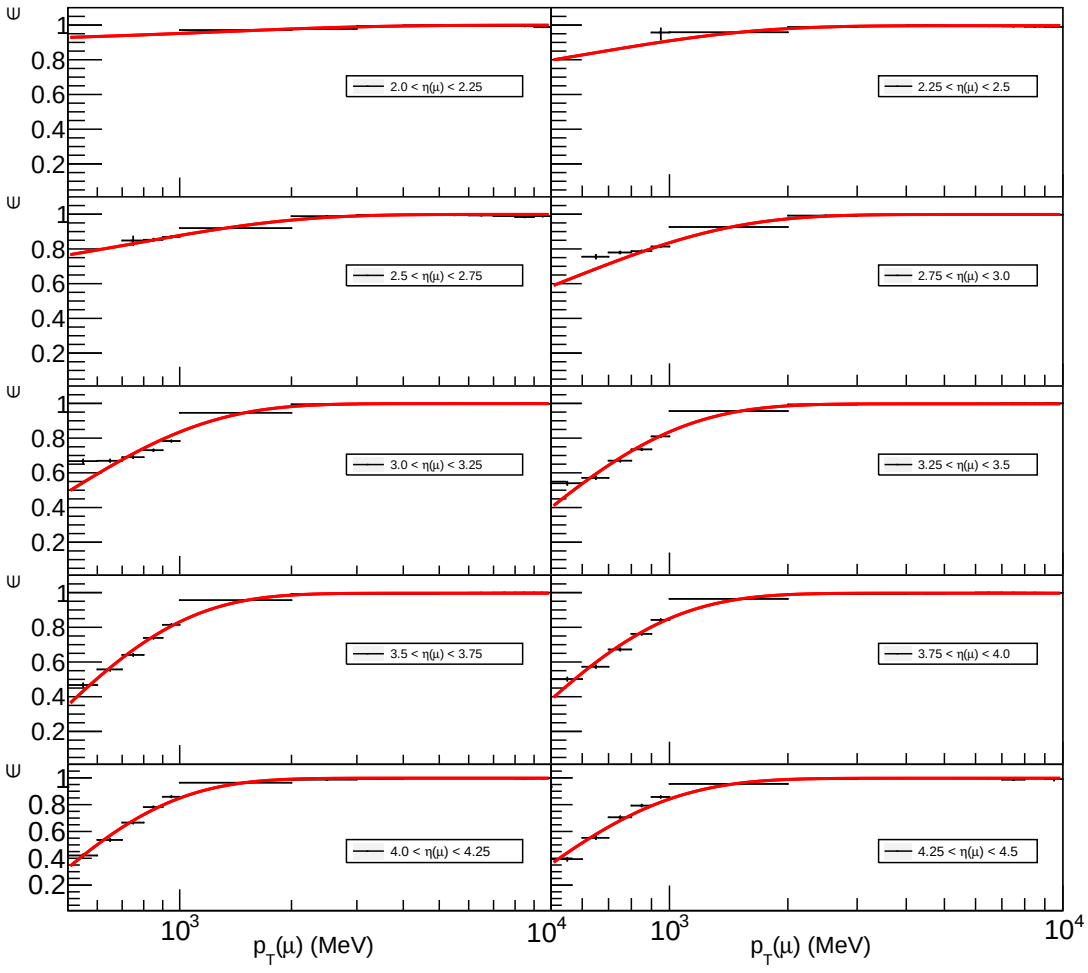

Figure 6.34: Interpolation fit of the ProbNNmu efficiency map shown in fig. 6.33 with the function $a - be^{-cx}$ *vs.* $p_T(\mu)$ for different $\eta(\mu)$ bins with MC. These are in steps of 0.25 in $\eta(\mu)$ from 2.0-4.5.

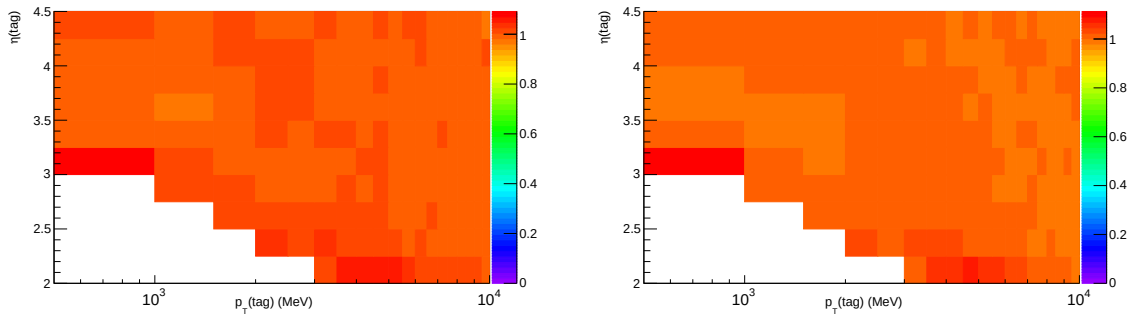

(a) Histogram (b) Interpolated fit

Figure 6.35: Closure test for ProbNNmu efficiency using the raw histogram in fig. 6.33 *vs.* the interpolated fits in fig. 6.34.

6.2.3.2 ProbNNmu efficiency in Data

The procedure for data again follows the same methods as for the trigger efficiency, by performing mass fits. The resulting raw histogram and interpolated fits are shown in fig. 6.36 and fig. 6.37 respectively.

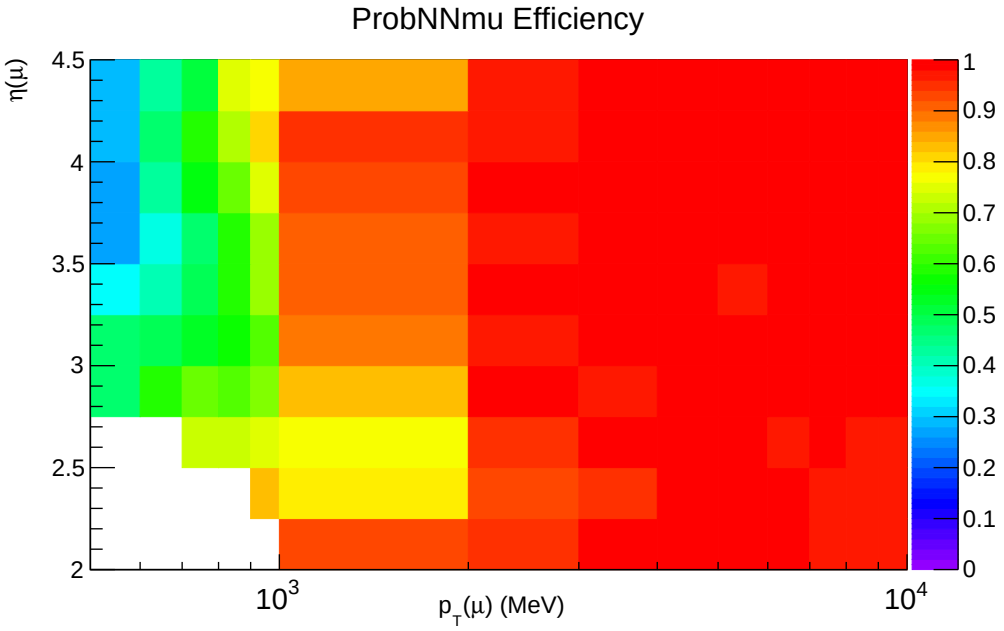

Figure 6.36: Data ProbNNmu efficiency of $\eta(\mu)$ *vs.* $p_T(\mu)$.

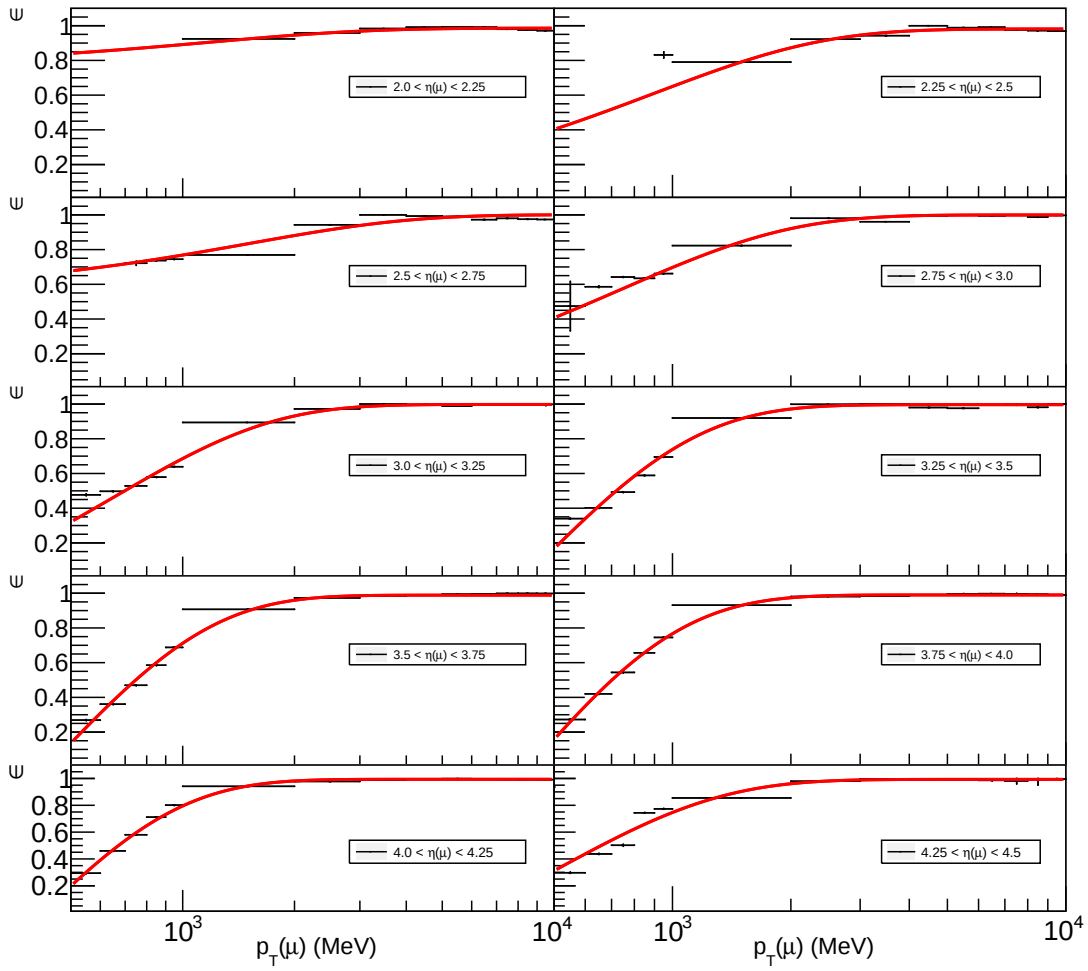

Figure 6.37: Interpolation fit of the ProbNNmu efficiency map shown in fig. 6.36 with the function $a - be^{-cx}$ *vs.* $p_T(\mu)$ for different $\eta(\mu)$ bins with data. These are in steps of 0.25 in $\eta(\mu)$ from 2.0-4.5.

6.2.4 Decay time of the J/ψ correction

The previously discussed correction factors do not account for a dependence of the reconstruction efficiency on the lifetime of the J/ψ. In order to correct for this, MC simulation of displaced (B decay) J/ψ's is used. The yield ratio (reconstructed level/generator level) of the reconstructed J/ψ's is evaluated as a function of J/ψ lifetime. Since all other correction factors were essentially obtained for t_Z=0, this decay time correction is a relative correction with respect to t_Z=0. The left hand plot in fig. 6.38 shows the ratio of tags reconstructed at detector level with respect to generator level as a function of t_Z, which was taken from the previous 2017 analysis [106,114]. The different colours in the left hand plot correspond to different $p_{\mathrm{T}}(J/\psi)$ ranges, where red corresponds to the lowest $p_{\mathrm{T}}(J/\psi)$ range and violet the highest.

This shows a drop in efficiency at large b-hadron decay times, where higher $p_{\mathrm{T}}(J/\psi)$ values have lower efficiencies. This then translates as a $p_{\mathrm{T}}(J/\psi)$ dependent correction as shown in the right hand plot of fig. 6.38, where the $p_{\mathrm{T}}(J/\psi)$ bins corresponds to the same ranges as used in the left hand plot of fig. 6.38. This happens in the active region of the VELO. Since the efficiency in $p_{\mathrm{T}}(J/\psi)$ is roughly close to unity, the lifetime correction is taken as a linear fit to the efficiency *vs.* $p_{\mathrm{T}}(J/\psi)$, to avoid over-correction. The different colours in the right hand plot correspond to different polarisations of the J/ψ, where black is unpolarised. This shows the correction is roughly independent of the polarisation of the J/ψ, with 1-2 % uncertainty.

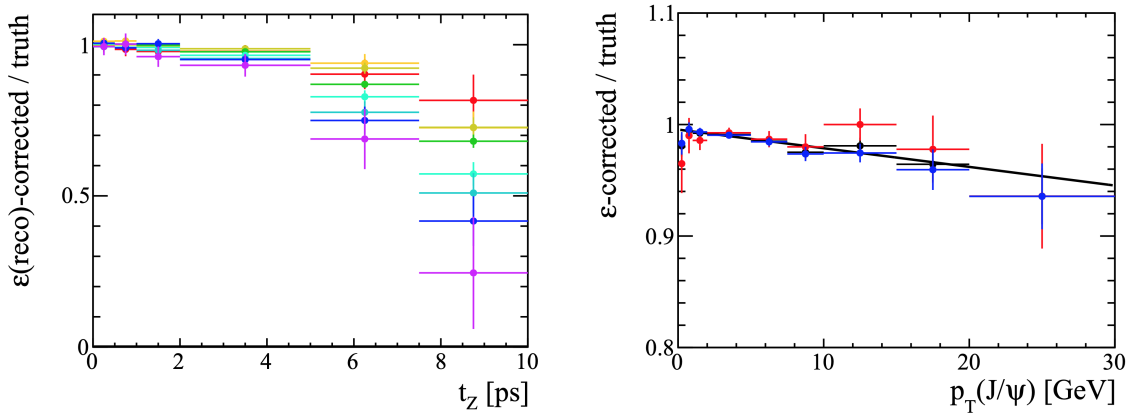

(a) Lifetime of J/ψ, t_Z.

(b) $p_{\mathrm{T}}(J/\psi)$.

Figure 6.38: Lifetime efficiencies obtained from simulated b $\rightarrow$ J/ψ decays, *vs.* different variables. The different colours in the left hand plot correspond to different $p_{\mathrm{T}}(J/\psi)$ ranges, where red corresponds to the lowest $p_{\mathrm{T}}(J/\psi)$ range and violet the highest. These match the $p_{\mathrm{T}}(J/\psi)$ ranges for each bin in the right hand plot. The different colours in the right hand plot correspond to different polarisations of the J/ψ, where black is unpolarised [106, 114].

6.2.5 Global event efficiencies

6.2.5.1 Number of PV's

The efficiency for the single primary vertex requirement is determined from minimum-bias data. The number of expected interactions in a minimum-bias event follows a Poisson distribution with probability $f(k, \mu)$, where k is the number of interactions and μ is the mean number of interactions. The number of expected interactions in an event with quarkonia production follows $1 + f(k, \mu)$ since this is, in comparison, a rare event. Therefore, specific events are selected for this evaluation, namely minimum-bias events where two opposite-sign tracks with kinematics similar to the

signal kinematics are required. This procedure is validated against MC simulation. The extracted efficiency value with this approach is, $\epsilon_{PV} = 73.8 \pm 0.5\%$.

6.2.5.2 Number of SPD hits

The number of SPD hits (multiplicity) was constrained to < 900 from the L0 trigger. It was evaluated from the SPD distribution in the tetraquark analysis, discussed in chapter 7, that the events outside this range are $\sim$0.005%. This number is negligible, so this does not need to be corrected for.

6.2.6 Applying the efficiency

To apply the efficiency correction, all factors introduced in this chapter and mentioned in eq. (6.8) are applied on an event-by-event basis to the reconstructed data. For example, for the reconstruction efficiency of one of the muons in a J/ψ, if the muon has a p_{T} of 700 GeV and η of 4.25, in the efficiency map fig. 6.18, this corresponds to a reconstruction efficiency of $\sim 75\%$. If the other muon has a reconstruction efficiency of 90%, this will correspond to a J/ψ reconstruction efficiency of 68%. The efficiency is then applied as a weight to each event to obtain the true J/ψ yield. The efficiency weight for each event is included in the mass and lifetime fits themselves, so is not applied as a yield correction post-fit. To test the typical efficiency correction factors obtained, 2D histograms of efficiency of J/ψ, ϵ, *vs.* $z(J/\psi)$ are shown in figs. 6.39 to 6.44, for each type of efficiency. The total efficiency *vs.* $z(J/\psi)$ is shown in fig. 6.45. The efficiencies shown are applied onto prompt and displaced J/ψ's separately in the p_{T}(jet) range of $20 < p_{\mathrm{T}}(\mathrm{jet}) < 30$ GeV.

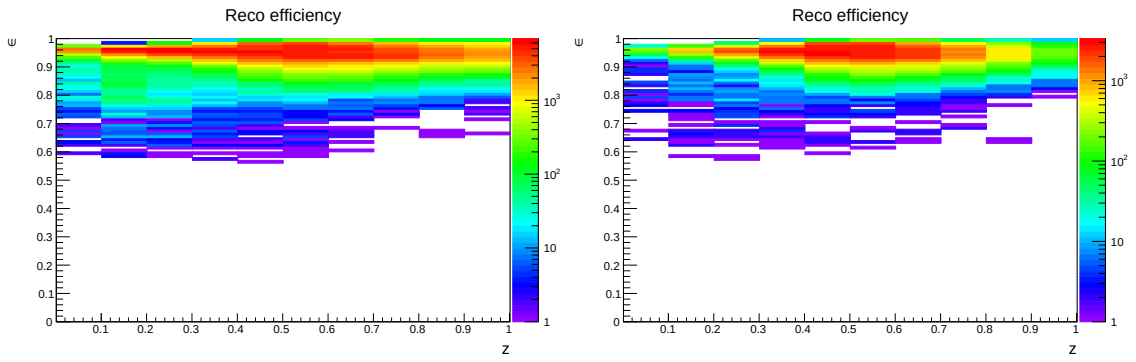

(a) Prompt. (b) Displaced.

Figure 6.39: Reconstruction efficiency using MC map *vs.* $z(J/\psi)$ for $20 < p_{\mathrm{T}}(\mathrm{jet}) < 30$ GeV with prompt and displaced decays. The z axis shows the number of J/ψ candidates.

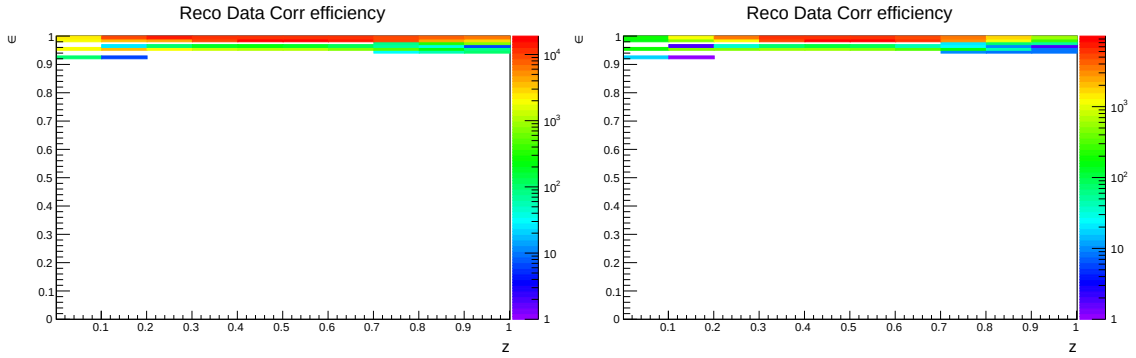

(a) Prompt. (b) Displaced.

Figure 6.40: Data correction to reconstruction efficiency *vs.* $z(J/\psi)$ for $20 < p_{\mathrm{T}}(\mathrm{jet}) < 30\,\mathrm{GeV}$ with prompt and displaced decays. The z axis shows the number of J/ψ candidates.

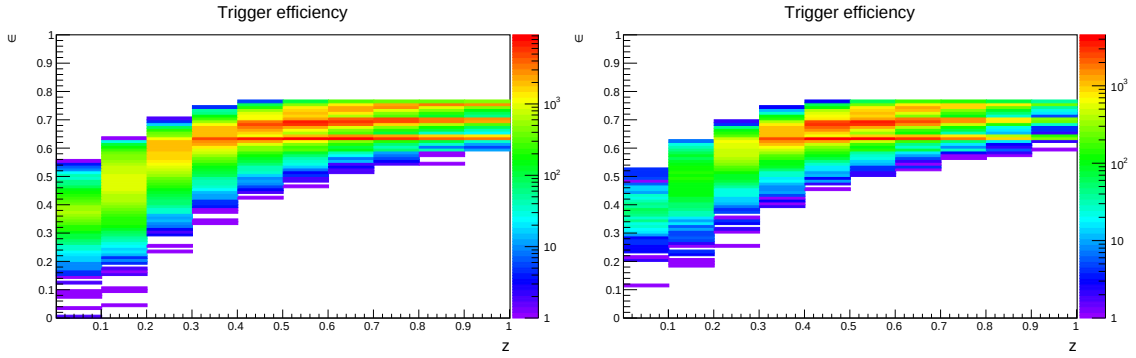

(a) Prompt. (b) Displaced.

Figure 6.41: Trigger efficiency *vs.* $z(J/\psi)$ for $20 < p_{\mathrm{T}}(\mathrm{jet}) < 30\,\mathrm{GeV}$ with prompt and displaced decays. The z axis shows the number of J/ψ candidates.

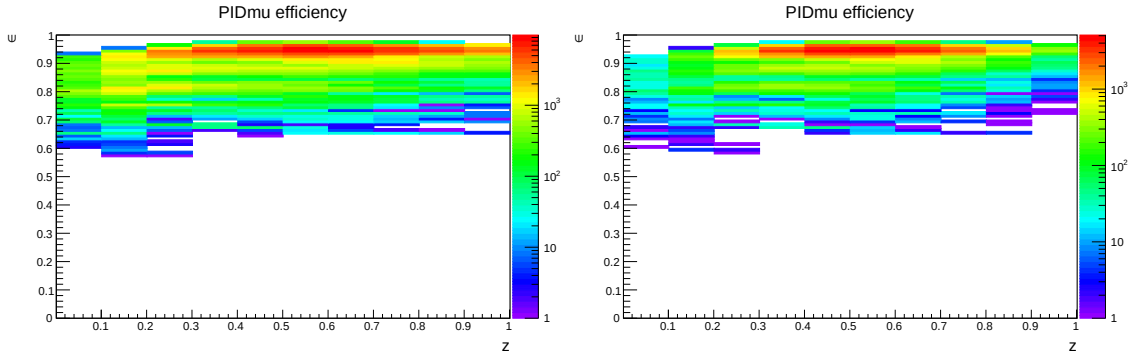

(a) Prompt. (b) Displaced.

Figure 6.42: The stripping line correction, PIDmu > 0 and IsMuon, efficiency *vs.* $z(J/\psi)$ for $20 < p_{\mathrm{T}}(\mathrm{jet}) < 30\,\mathrm{GeV}$ with prompt and displaced decays. The z axis shows the number of J/ψ candidates.

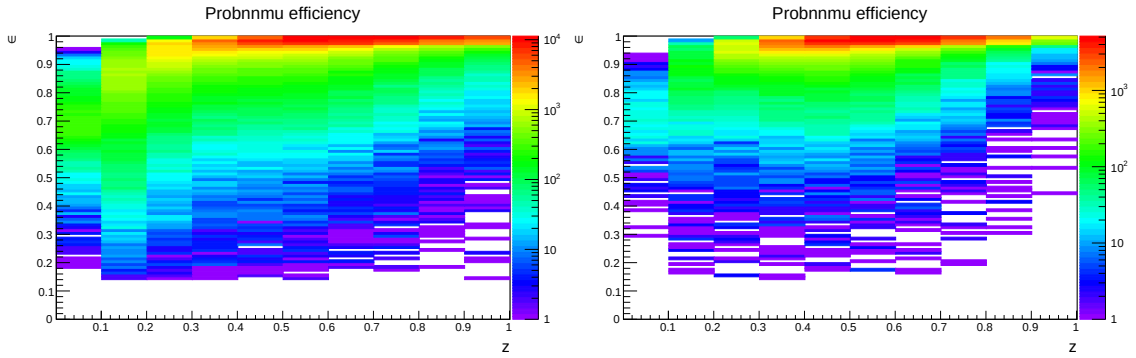

(a) Prompt. (b) Displaced.

Figure 6.43: ProbNNmu selection efficiency *vs.* $z(J/\psi)$ for $20 < p_{\mathrm{T}}(\mathrm{jet}) < 30\,\mathrm{GeV}$ with prompt and displaced decays. The z axis shows the number of J/ψ candidates.

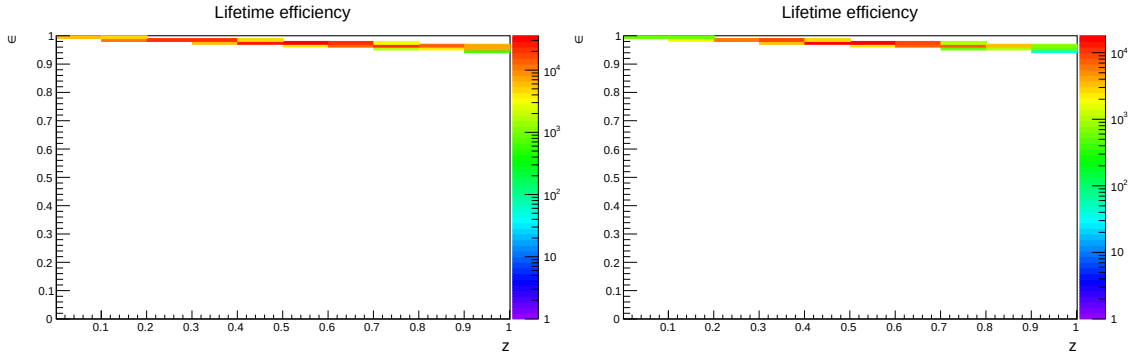

(a) Prompt. (b) Displaced.

Figure 6.44: Lifetime efficiency *vs.* $z(J/\psi)$ for $20 < p_{\mathrm{T}}(\mathrm{jet}) < 30\,\mathrm{GeV}$ with prompt and displaced decays. The z axis shows the number of J/ψ candidates.

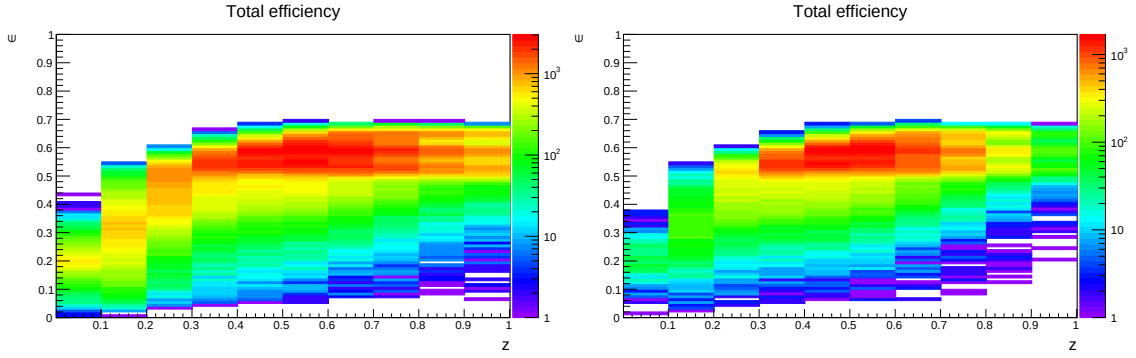

(a) Prompt. (b) Displaced.

Figure 6.45: Total efficiency *vs.* $z(J/\psi)$ for $20 < p_{\mathrm{T}}(\mathrm{jet}) < 30\,\mathrm{GeV}$ with prompt and displaced decays. The z axis shows the number of J/ψ candidates.

The efficiency that applies the biggest correction is trigger efficiency, in comparison to the lifetime and data corrected reconstruction efficiencies which apply the smallest. In the trigger efficiency map, there is a three prong structure. As the J/ψ candidate is made up of muons, this could be an incidence where one selected muon has a low efficiency and the other a high efficiency, but conversely, there are

regions where muons are selected both with a high efficiency. This could lead to this structure. The range of ProbNNmu efficiency values *vs.* z seems very large and suggests that large efficiency corrections could be applied. However, for the majority of candidates it applies nearly a 100 % efficiency correction. This is also true for the reconstruction efficiency obtained from MC. The average total efficiency to select either a prompt and displaced J/ψ is ∼60 %. An interesting feature to note is that for the prompt component, the average total correction seems to be applied across all $z(J/\psi)$ values. This is in comparison to the displaced component where the average correction is more central in $z(J/\psi)$ values of 0.5.

These correction factors shown in fig. 6.45 are applied to the raw yield distributions shown in fig. 6.7, which results in the normalised distributions shown in fig. 6.46. Overall the distributions seem to have not changed too much in shape. However, when comparing the raw distributions with the efficiency corrected distributions shown in fig. 6.47, the average $z(J/\psi)$ has been shifted to lower values. This is more prevalent in the prompt than the displaced component. The results in both distributions are for $p_{\mathrm{T}}(\mathrm{jet}) > 20\,\mathrm{GeV}$. This shift makes sense as the average efficiency correction shown in fig. 6.45 is larger for $z(J/\psi) < 0.3$, which is mainly to the trigger efficiency. This is because lower p_{T} values typically map to lower $z(J/\psi)$ values which is where the trigger is most inefficient.

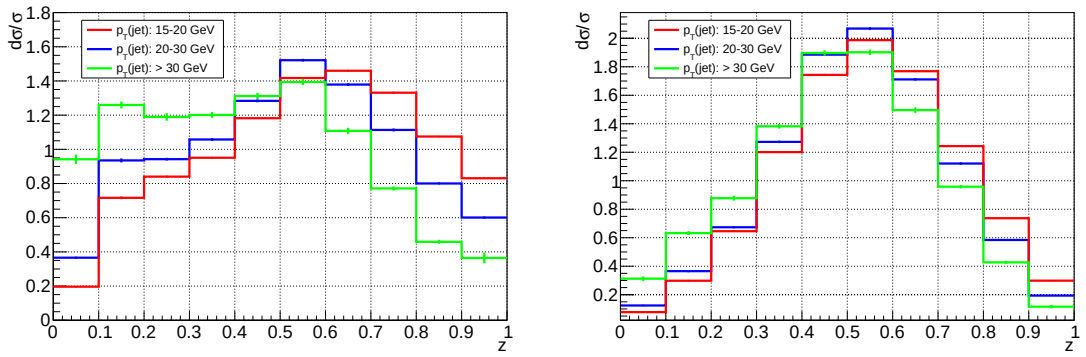

(a) Prompt. (b) Displaced.

Figure 6.46: Prompt and displaced normalised cross sections, $\mathrm{d}\sigma/\sigma$, *vs.* $z(J/\psi)$ in different $p_{\mathrm{T}}(\mathrm{jet})$ ranges with efficiency corrections. The plots are normalised as $1/N\,\mathrm{d}N/\mathrm{d}z$.

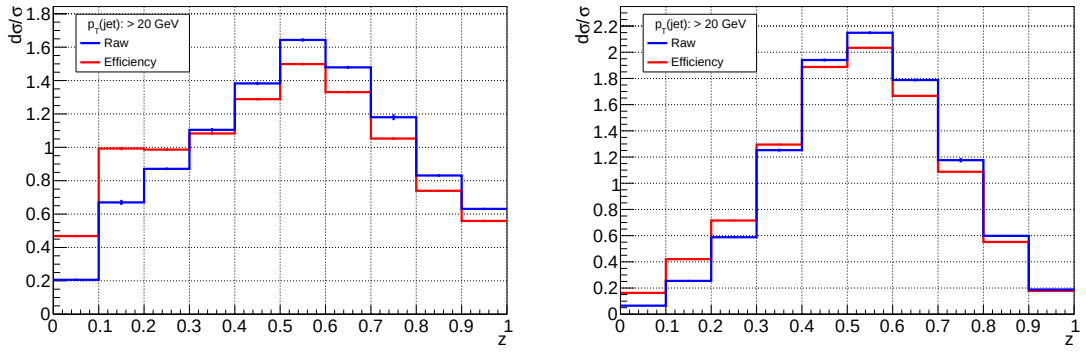

(a) Prompt. (b) Displaced.

Figure 6.47: Comparison of the raw and efficiency corrected prompt and displaced normalised cross sections, $\mathrm{d}\sigma/\sigma$, *vs.* $z(J/\psi)$ in different $p_{\mathrm{T}}(\mathrm{jet})$ ranges. The plots are normalised as $1/N\ \mathrm{d}N/\mathrm{d}z$.

The last step is to unfold the efficiency corrected prompt and displaced distributions. This corrects for the detector resolution in the jet reconstruction and is described in the subsequent sections.

6.2.7 Efficiencies for $\psi(2S)$

The efficiencies for the $\psi(2S)$ are applied in the same manner as for the J/ψ. All of the efficiency maps that were generated for the J/ψ are used for the $\psi(2S)$. For the reconstruction and PID efficiencies, this is a good assumption to make, as these are a per muon efficiency, so are independent of the candidate that generated them. The trigger efficiency is also taken from the J/ψ. This is because L0 and HLT1 used in the $\psi(2S)$ are exactly the same as for the J/ψ analysis. Also, the only difference in the HLT2 selection between the J/ψ and $\psi(2S)$ is the mass window requirement. Since the trigger is most inefficient at L0, and HLT2 is roughly 100 % efficient, the interpolated trigger efficiency map shown in fig. 6.31 is used for the $\psi(2S)$. A closure test can be performed to confirm this, but is not shown in this thesis. The lifetime efficiency for the displaced component is also taken from the J/ψ. There may be slight differences for the $\psi(2S)$ lifetime dependence in comparison to the J/ψ, however, since the correction is roughly 100 % efficient, this should not make much of a difference to the total distribution. The separate efficiency corrections *vs.* $z(\psi(2S))$ are shown in figs. 6.48 to 6.53 and show similar trends as for the J/ψ results. The total efficiency correction for the prompt and displaced components are shown in fig. 6.54, where the main efficiency correction is originating from the trigger efficiency. The average total efficiency to select a prompt or displaced $\psi(2S)$

is ∼60 %, which is similar to the J/ψ. However, for the prompt component there is an increased correction at lower $z(\psi(2S))$ values. This is because the $\psi(2S)$ shares more of the jet energy due to its higher mass, so any of the low p_{T} inefficiencies will be pushed down to even lower values of $z(\psi(2S))$.

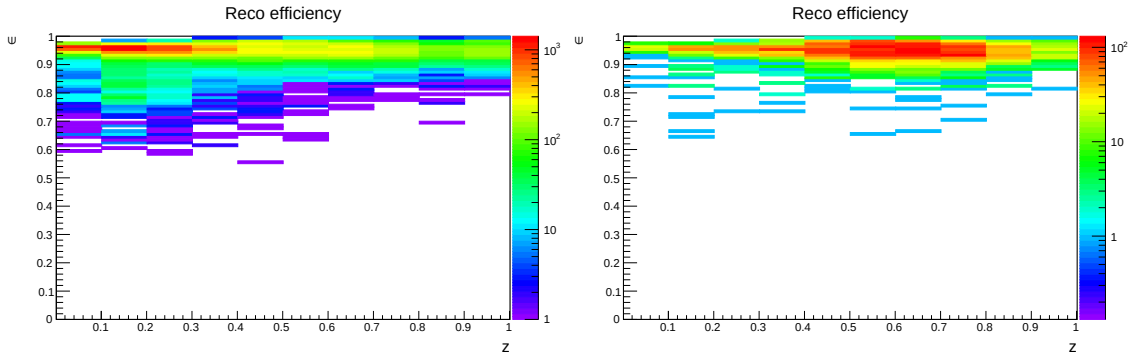

(a) Prompt. (b) Displaced.

Figure 6.48: Reconstruction efficiency using MC map *vs.* $z(\psi(2S))$ for $20 < p_{\mathrm{T}}(\mathrm{jet}) < 30\,\mathrm{GeV}$ with prompt and displaced decays. The z axis shows the number of $\psi(2S)$ candidates.

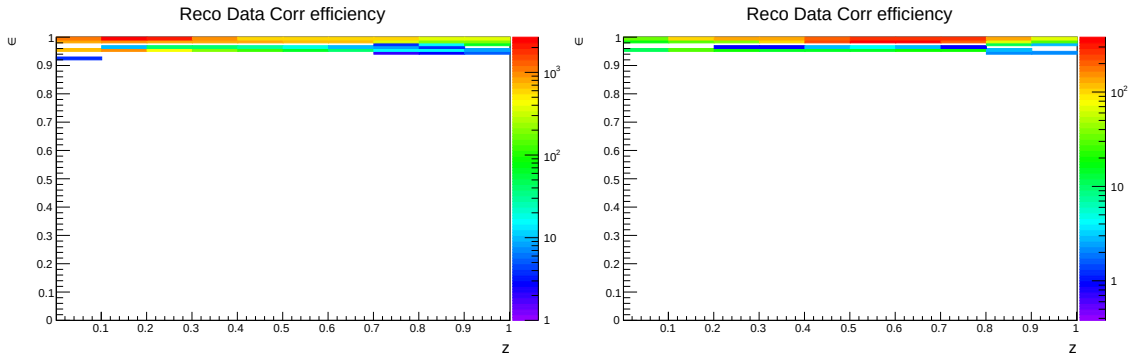

(a) Prompt. (b) Displaced.

Figure 6.49: Data correction to reconstruction efficiency *vs.* $z(\psi(2S))$ for $20 < p_{\mathrm{T}}(\mathrm{jet}) < 30\,\mathrm{GeV}$ with prompt and displaced decays. The z axis shows the number of $\psi(2S)$ candidates.

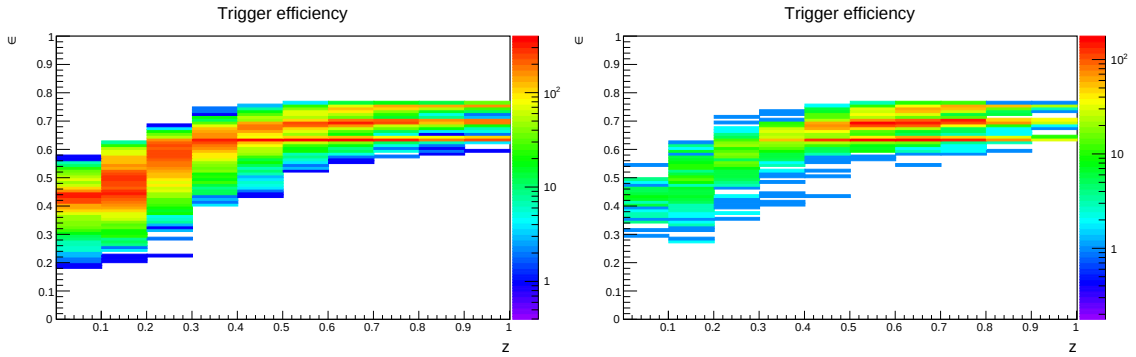

(a) Prompt. (b) Displaced.

Figure 6.50: Trigger efficiency *vs.* $z(\psi(2S))$ for $20 < p_{\mathrm{T}}(\mathrm{jet}) < 30\,\mathrm{GeV}$ with prompt and displaced decays. The z axis shows the number of $\psi(2S)$ candidates.

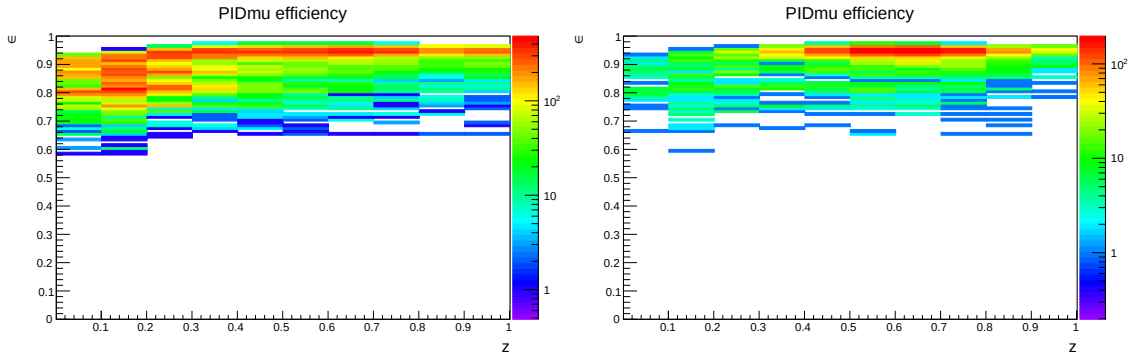

(a) Prompt. (b) Displaced.

Figure 6.51: The stripping line correction, PIDmu > 0 and IsMuon, efficiency *vs.* $z(\psi(2S))$ for $20 < p_{\mathrm{T}}(\mathrm{jet}) < 30\,\mathrm{GeV}$ with prompt and displaced decays. The z axis shows the number of $\psi(2S)$ candidates.

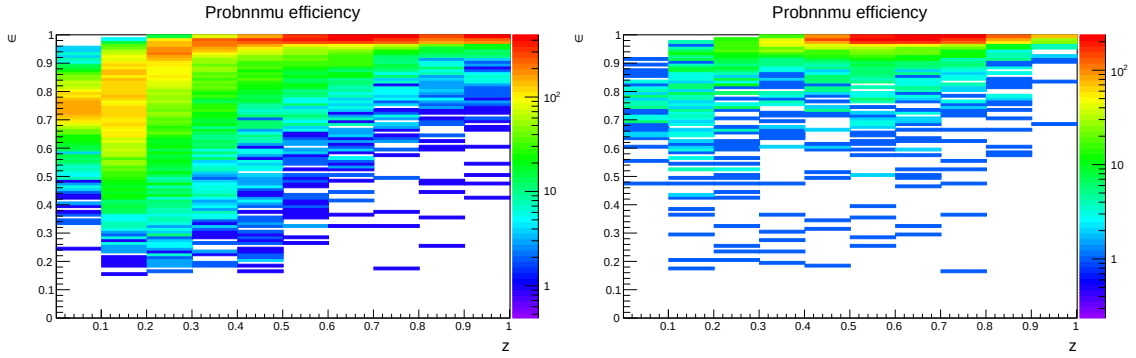

(a) Prompt. (b) Displaced.

Figure 6.52: ProbNNmu selection efficiency *vs.* $z(\psi(2S))$ for $20 < p_{\mathrm{T}}(\mathrm{jet}) < 30\,\mathrm{GeV}$ with prompt and displaced decays. The z axis shows the number of $\psi(2S)$ candidates.

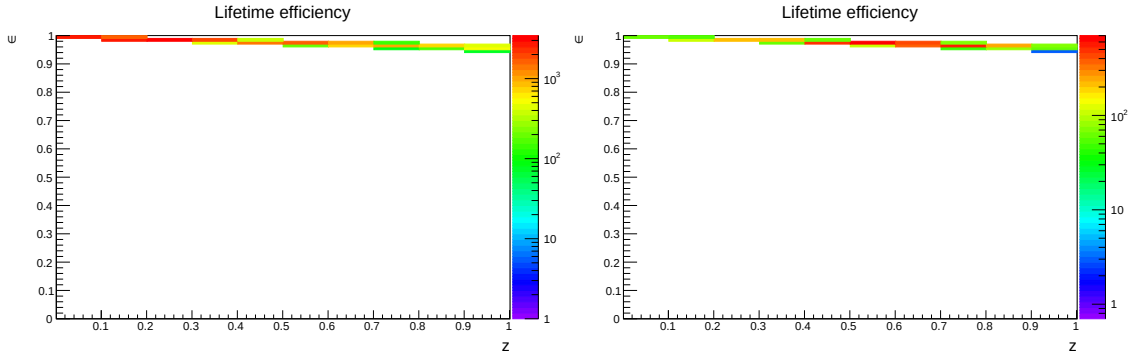

(a) Prompt. (b) Displaced.

Figure 6.53: Lifetime efficiency *vs.* $z(\psi(2S))$ for $20 < p_{\mathrm{T}}(\mathrm{jet}) < 30\,\mathrm{GeV}$ with prompt and displaced decays. The z axis shows the number of $\psi(2S)$ candidates.

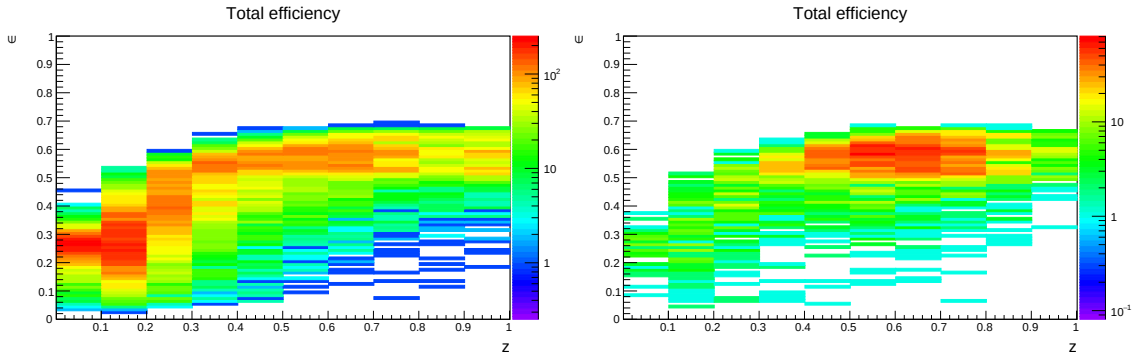

(a) Prompt. (b) Displaced.

Figure 6.54: Total efficiency *vs.* $z(\psi(2S))$ for $20 < p_{\mathrm{T}}(\mathrm{jet}) < 30\,\mathrm{GeV}$ with prompt and displaced decays. The z axis shows the number of $\psi(2S)$ candidates.

The correction factors shown in fig. 6.54 are applied to the raw yield distributions shown in fig. 6.12, which results in the distributions shown in fig. 6.55. Comparisons of the raw and efficiency corrected distributions are shown in fig. 6.56, which shows the same behaviour of shifting the overall distribution to lower $z(\psi(2S))$ values.

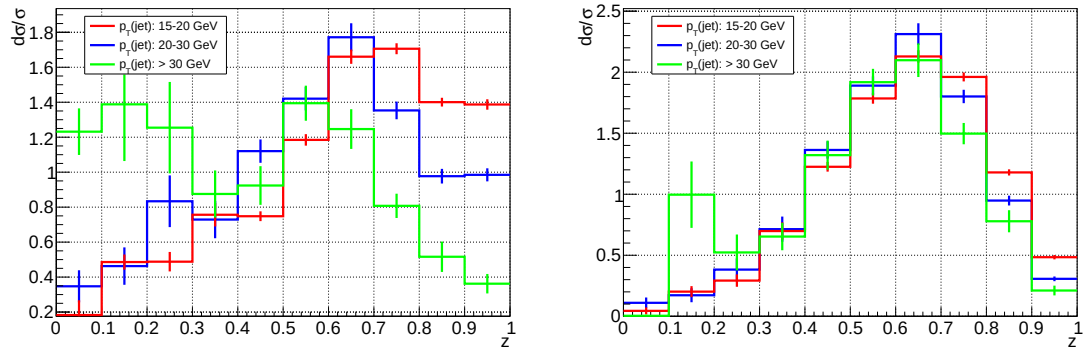

(a) Prompt. (b) Displaced.

Figure 6.55: Prompt and displaced normalised cross sections *vs.* $z(\psi(2S))$ in different $p_{\mathrm{T}}(\mathrm{jet})$ ranges with efficiency corrections, normalised as $1/N\ \mathrm{d}N/\mathrm{d}z$.

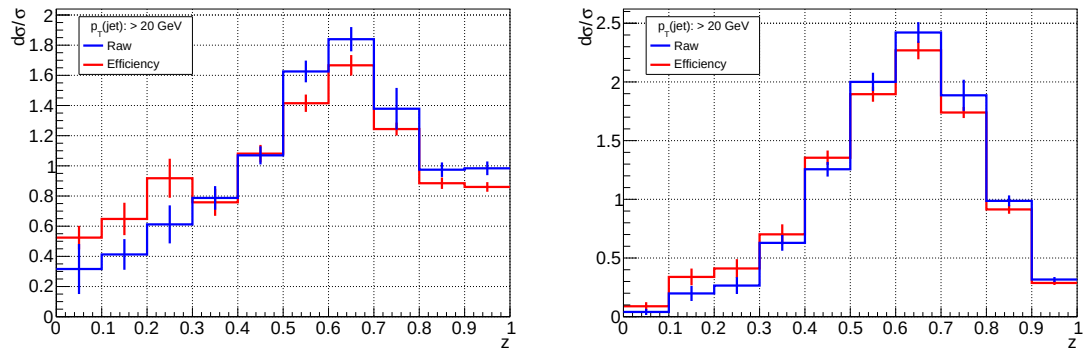

(a) Prompt. (b) Displaced.

Figure 6.56: Comparison of the raw and efficiency corrected prompt and displaced normalised cross sections, $\mathrm{d}\sigma/\sigma$, *vs.* $z(\psi(2S))$ in different $p_{\mathrm{T}}(\mathrm{jet})$ ranges. The plots are normalised as $1/N\ \mathrm{d}N/\mathrm{d}z$.

6.2.8 Efficiencies for $\Upsilon(1S)$, $\Upsilon(2S)$ and $\Upsilon(3S)$

The efficiencies for the Υ's are applied in the same manner as for the J/ψ. All of the efficiency maps that were generated for the J/ψ are used for the Υ's with the same reasoning as discussed for the $\psi(2S)$ in section 6.2.7, except, since there is no displaced components for the Υ's a lifetime correction does not need to be applied. The separate efficiency corrections *vs.* $z(\Upsilon)$ are shown in figs. 6.57 to 6.61 for each Υ and again show similar trends as for the J/ψ and $\psi(2S)$ results. The total efficiency corrections applied to each Υ are shown in fig. 6.62, where the main efficiency correction is originating from the trigger efficiency. The trigger correction seems to be more constant at ∼60 % for all $z(\Upsilon)$ values. This is because Υ's will typically decay into higher momentum particles than for the J/ψ, as there is a lot more phase space available. This means the inefficient tail at low p_{T} in the trigger is missed by the Υ candidates. The average total efficiency to select any Υ is ∼60 %, which is similar to the J/ψ and $\psi(2S)$. However, in all the Υ distributions there is a double peaking structure. The peak at low $z(\Upsilon)$ is due to similar reasons as for the $\psi(2S)$ where Υ's share even more of the jet energy due to its higher mass, so any low p_{T} inefficiencies will be pushed shown to even lower $z(\Upsilon)$ values. The peak at $z(\Upsilon) \simeq 1$ is due to the abundance of Υ candidates at $z(\Upsilon) \simeq 1$, which are roughly 2-3 orders of magnitude more than the lower $z(\Upsilon)$ bins.

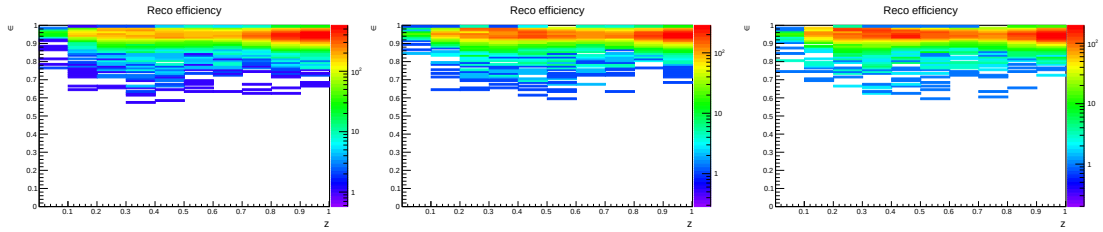

(a) $\Upsilon(1S)$. (b) $\Upsilon(2S)$. (c) $\Upsilon(3S)$.

Figure 6.57: Reconstruction efficiency using MC map *vs.* $z(\Upsilon)$ for $20 < p_{\mathrm{T}}(\mathrm{jet}) < 30\,\mathrm{GeV}$ for $\Upsilon(1S)$, $\Upsilon(2S)$ and $\Upsilon(3S)$. The z axis shows the number of Υ candidates.

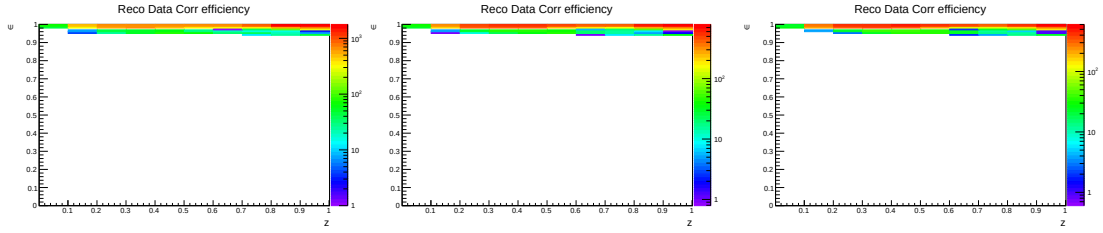

(a) $\Upsilon(1S)$. (b) $\Upsilon(2S)$. (c) $\Upsilon(3S)$.

Figure 6.58: Data correction to reconstruction efficiency *vs.* $z(\Upsilon)$ for $20 < p_{\mathrm{T}}(\mathrm{jet}) < 30\,\mathrm{GeV}$ for $\Upsilon(1S)$, $\Upsilon(2S)$ and $\Upsilon(3S)$. The z axis shows the number of Υ candidates.

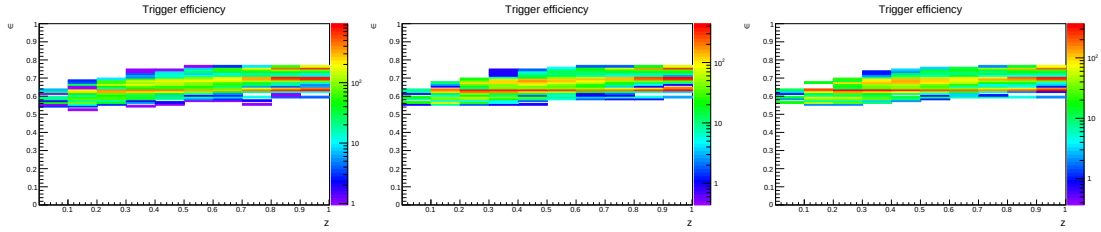

(a) $\Upsilon(1S)$. (b) $\Upsilon(2S)$. (c) $\Upsilon(3S)$.

Figure 6.59: Trigger efficiency *vs.* $z(\Upsilon)$ for $20 < p_{\mathrm{T}}(\mathrm{jet}) < 30\,\mathrm{GeV}$ for $\Upsilon(1S)$, $\Upsilon(2S)$ and $\Upsilon(3S)$. The z axis shows the number of Υ candidates.

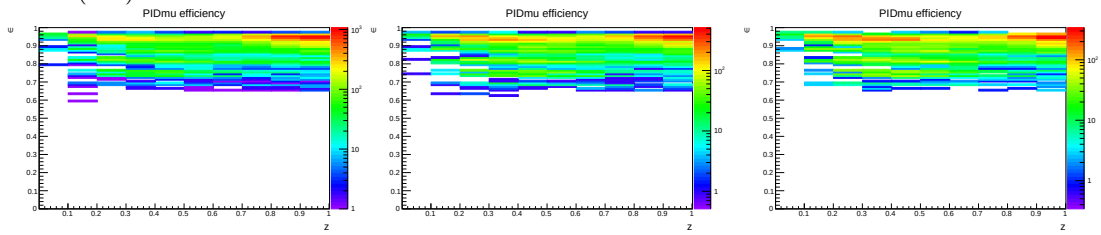

(a) $\Upsilon(1S)$. (b) $\Upsilon(2S)$. (c) $\Upsilon(3S)$.

Figure 6.60: PIDmu > 0 and IsMuon correction *vs.* $z(\Upsilon)$ for $20 < p_{\mathrm{T}}(\mathrm{jet}) < 30\,\mathrm{GeV}$ for $\Upsilon(1S)$, $\Upsilon(2S)$ and $\Upsilon(3S)$. The z axis shows the number of Υ candidates.

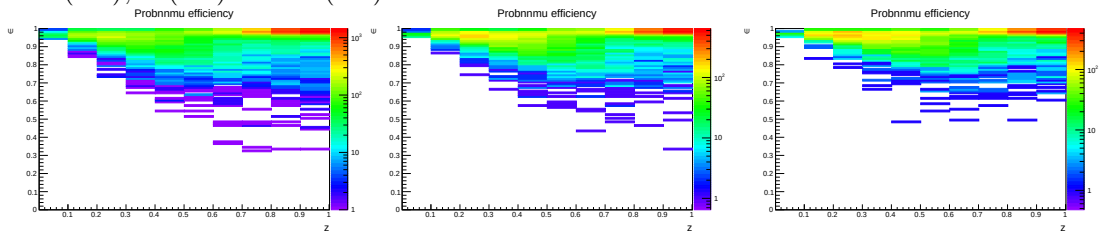

(a) $\Upsilon(1S)$. (b) $\Upsilon(2S)$. (c) $\Upsilon(3S)$.

Figure 6.61: ProbNNmu selection efficiency *vs.* $z(\Upsilon)$ for $20 < p_{\mathrm{T}}(\mathrm{jet}) < 30\,\mathrm{GeV}$ for $\Upsilon(1S)$, $\Upsilon(2S)$ and $\Upsilon(3S)$. The z axis shows the number of Υ candidates.

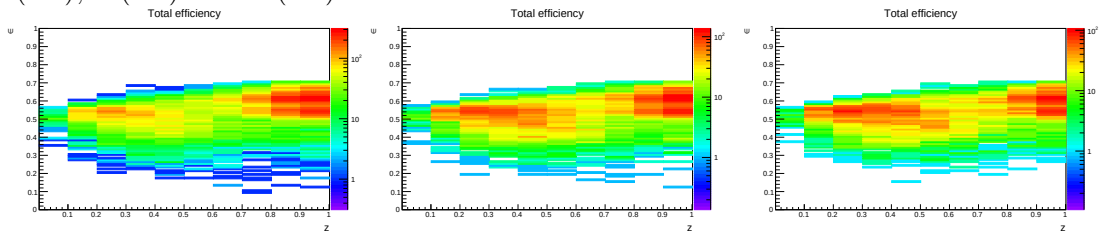

(a) $\Upsilon(1S)$. (b) $\Upsilon(2S)$. (c) $\Upsilon(3S)$.

Figure 6.62: Total efficiency *vs.* $z(\Upsilon)$ for $20 < p_{\mathrm{T}}(\mathrm{jet}) < 30\,\mathrm{GeV}$ for $\Upsilon(1S)$, $\Upsilon(2S)$ and $\Upsilon(3S)$. The z axis shows the number of Υ candidates.

Figure 6.63 shows normalised efficiency corrected distributions *vs.* $z(\Upsilon)$ for different Υ's and fig. 6.64 shows the normalised efficiency corrected distributions *vs.* $z(\Upsilon)$ but for different $p_{\mathrm{T}}(\mathrm{jet})$ ranges. The highest $p_{\mathrm{T}}(\mathrm{jet})$ distribution in fig. 6.64 is interesting as there is now a larger peak at $z(\Upsilon) \sim 0.35$. Since this is at the highest $p_{\mathrm{T}}(\mathrm{jet})$ bin, this could be a source of double parton scattering, or maybe even the fragmentation component.

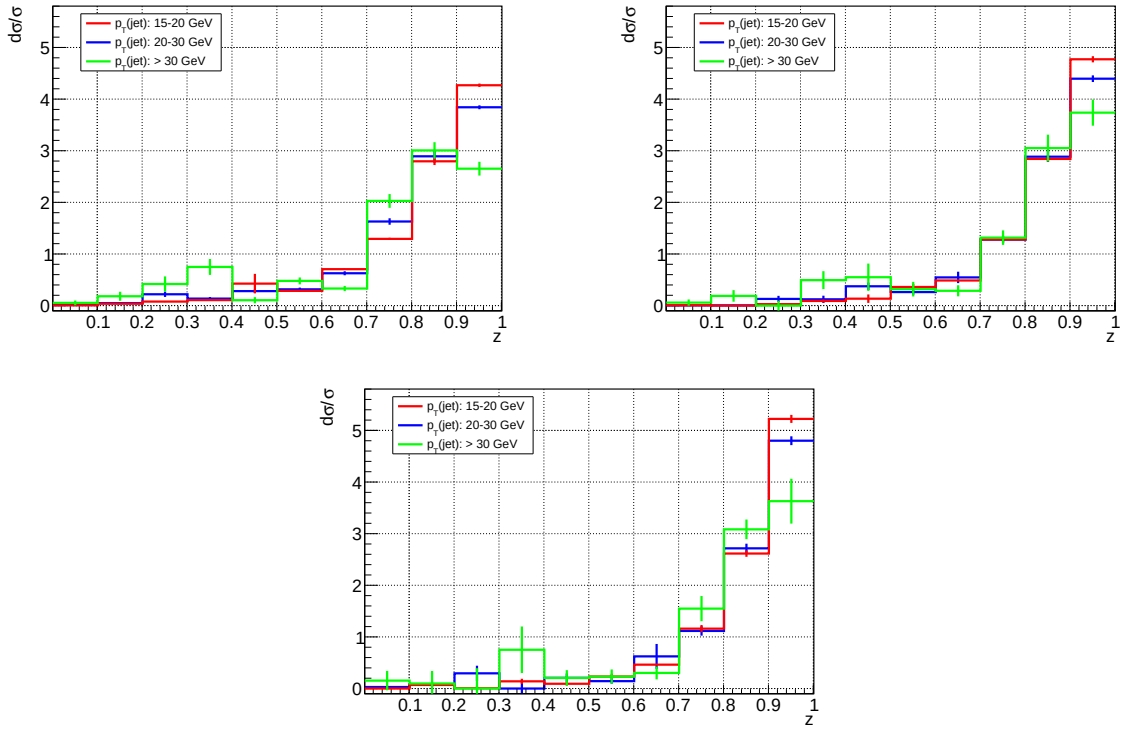

Figure 6.63: Normalised cross section distributions *vs.* $z(\Upsilon)$ in different $p_{\mathrm{T}}(\mathrm{jet})$ ranges for separated $\Upsilon(1S)$, $\Upsilon(2S)$ and $\Upsilon(3S)$ with efficiency corrections. The plots are normalised as $1/N\ \mathrm{d}N/\mathrm{d}z$. Left to right: $\Upsilon(1S)$, $\Upsilon(2S)$ and $\Upsilon(3S)$.

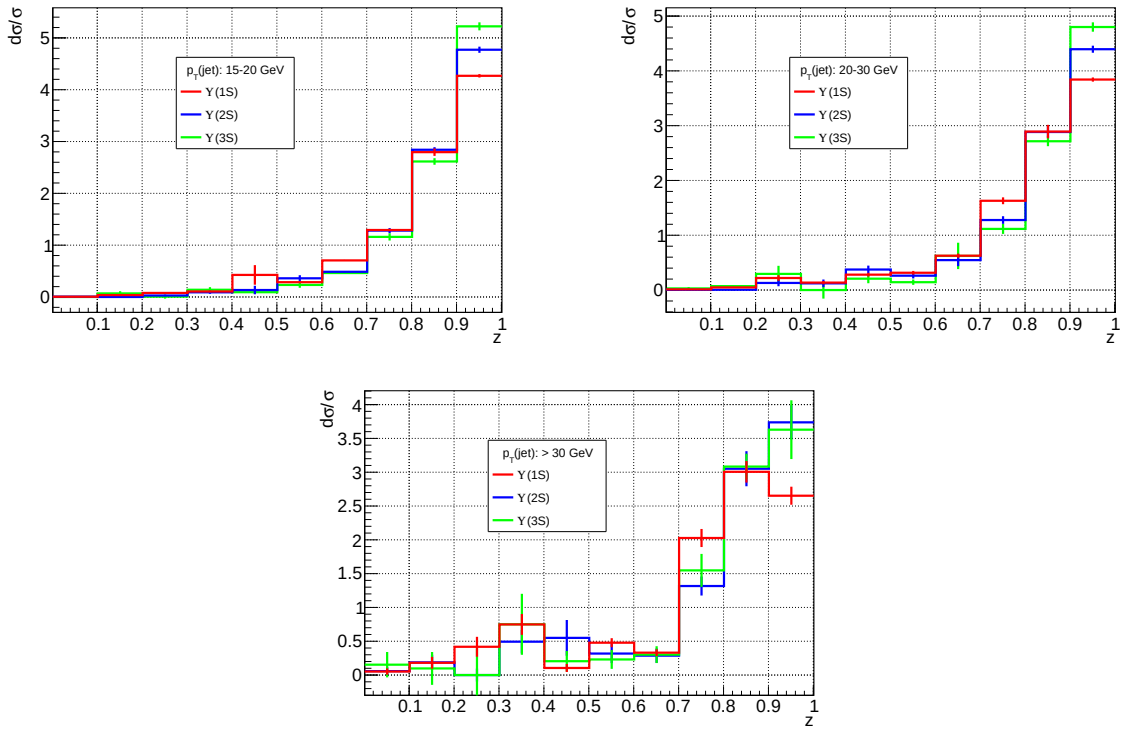

Figure 6.64: Normalised cross section distributions for $\Upsilon(1S)$, $\Upsilon(2S)$ and $\Upsilon(3S)$ *vs.* $z(\Upsilon)$ with efficiency corrections for different $p_{\mathrm{T}}(\mathrm{jet})$ ranges. The plots are normalised as $1/N\ \mathrm{d}N/\mathrm{d}z$. Left to right: $15 < p_{\mathrm{T}}(\mathrm{jet}) < 20\,\mathrm{GeV}$, $20 < p_{\mathrm{T}}(\mathrm{jet}) < 30\,\mathrm{GeV}$, and $p_{\mathrm{T}}(\mathrm{jet}) > 30\,\mathrm{GeV}$.

Figure 6.65 shows comparisons of the raw and efficiency corrected normalised distributions, and sees the same effect as seen for the J/ψ and $\psi(2S)$ where the average distribution is slightly shifted to lower $z(\Upsilon)$ values.

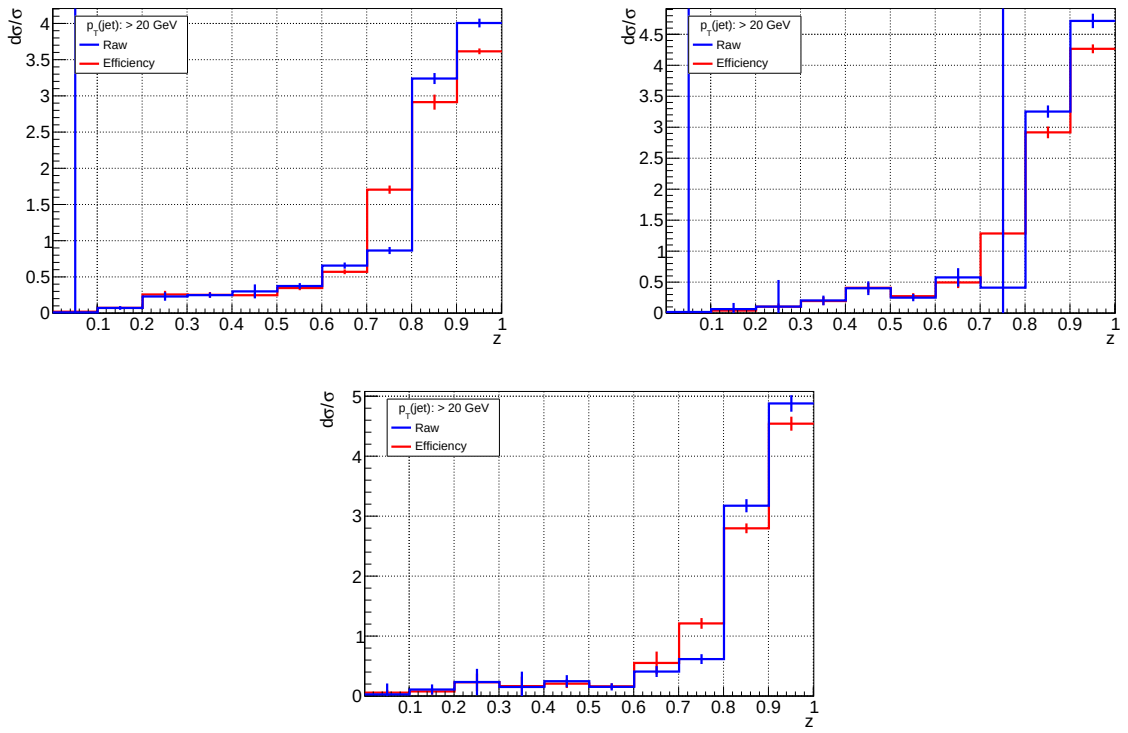

Figure 6.65: Comparison of the raw and efficiency corrected normalised cross section distributions *vs.* $z(\Upsilon)$ in different $p_{\mathrm{T}}(\mathrm{jet})$ ranges for separated $\Upsilon(1S)$, $\Upsilon(2S)$ and $\Upsilon(3S)$. The plots are normalised as $1/N\ \mathrm{d}N/\mathrm{d}z$. Left to right: $\Upsilon(1S)$, $\Upsilon(2S)$ and $\Upsilon(3S)$.

6.3 Unfolding

The unfolding procedure is used to correct for the finite detector resolution of the jet reconstruction process. This may lead to imperfections in the reconstructed jets and may have contributions from several sources. These may include deficiencies in pattern recognition that fails to reconstruct the trajectories of genuine particles, or the reconstruction of spurious tracks (often referred to as "fake" or "ghost" tracks) that may be clustered into jets. This can lead to differences in the p_{T} and energy of the jets that are reconstructed in comparison to their "true" p_{T} and energy values. Since z and $p_{\mathrm{T}}(\mathrm{jet})$ are the variables that are being measured in this analysis, this needs to be corrected for by unfolding them to their "true" values.

As the unfolding procedure was validated and cross-checked for the tetraquark analy-

sis which is discussed in chapter 7, the full details of the procedure and unfolding are discussed in section 7.3. However, some key points and differences in the procedure will be noted here.

The unfolding procedure is dependent on MC to model the differences due to detector reconstruction of the detector-level and generator jets. However, as was discussed in chapter 1 and chapter 3, and also shown in fig. 1.4, simulation describes production from b-decays fairly well, but not at all for prompt production. Not only is z not modelled correctly, but the number of constituents in the jets is underestimated as well in comparison to data. Hence, a dedicated MC sample needs to be created specifically for the purpose of unfolding the prompt distributions and an unfolding procedure needs to be defined which is relatively independent of needing to know the "true" distribution.

For reasons further discussed in section 7.3, it was decided to use the displaced sample for unfolding the prompt distributions, as it is provides a better description of more variables such as the number of constituents within the jet. However, there are differences between the number of hyperons in a jet for the prompt and displaced jet cases. Hyperons, such as a K^0_{s}, affect the jet reconstruction because they have very long decay times, and hence are not reconstructed in a jet. This means that the energy of a reconstructed jet is shifted away from the "true" jet energy, and the greater the number of hyperons, the greater the shift. This can be quantified in MC using the jet energy scale (JES) shift variable,

$$\mathrm{JES} = \left\langle \frac{\mathrm{p_T^{det}} - \mathrm{p_T^{gen}}}{\mathrm{p_T^{gen}}} \right\rangle, \tag{6.13}$$

where ${p_{\mathrm{T}}}^{\mathrm{det}}$ is the p_{T} of the jet at detector level and ${p_{\mathrm{T}}}^{\mathrm{gen}}$ is the generator level p_{T}. An example for such shifts from the tetraquark MC samples is shown in fig. 6.66, where JES is measured *vs.* p_T^{gen} for the hadronic part of the jet only, *i.e.* the jet does not include the quarkonium/tetraquark candidate. The nominal displaced sample, denoted `NP V0 mix`, contains ∼63 % of jets with hyperons. Another example is `P V0 mix`, which contains ∼28 % of jets with hyperons. This leads to a smaller shift in total energies of the jets. Hence, the proper hyperon fractions of jets need to be taken into account when preparing a MC sample which will unfold the data distributions.

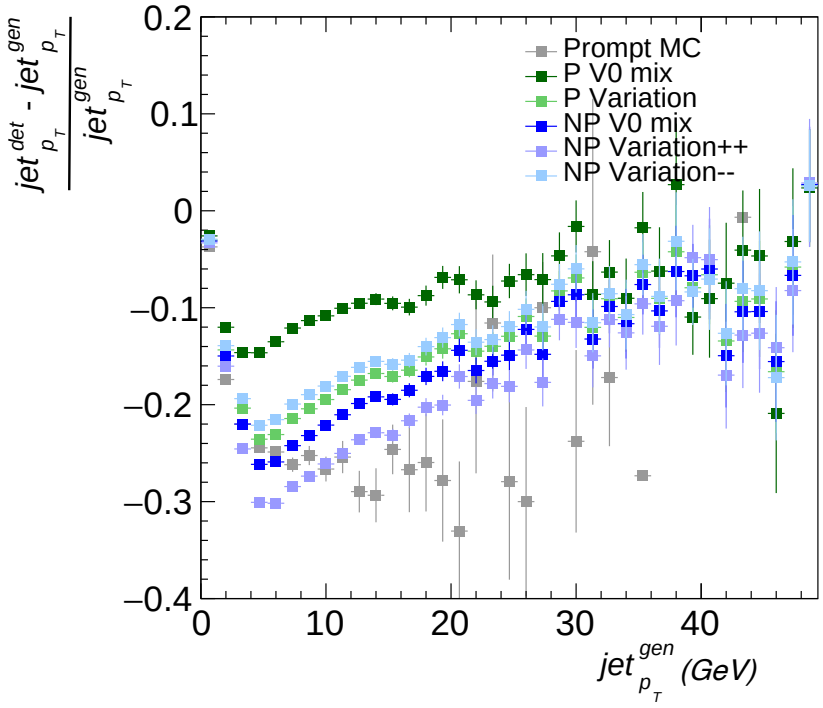

Figure 6.66: JES shift for different hyperon mixes for the hadronic part of the jet only. The nominal displaced sample, denoted `NP V0 mix`, contains ∼63 % of jets with hyperons. `NP Variation++` then represents ∼15 % more hyperons in the jet in comparison to `NP V0 mix`, and `NP Variation--` ∼15 % fewer hyperons in the jet. `Prompt MC` is the nominal prompt sample. `P V0 mix`, has ∼28 % of jets with hyperons and `P variation` has ∼55 % of jets with hyperons.

In the tetraquark analysis in chapter 7, the number of jets which contain hyperons was properly taken into account for the prompt and displaced distributions separately. In this analysis, inclusive MC samples were used, which properly take into account the hyperon ratios for the displaced components. However, the number of jets which carry a hyperon for prompt J/ψ and $\psi(2S)$ still needs further investigation. However, an unfolding procedure was still performed on prompt J/ψ and $\psi(2S)$ using their respective nominal displaced MC samples, to test the unfolding. Results for the normalised prompt and displaced J/ψ cross sections *vs.* $z(J/\psi)$ in different $p_{\mathrm{T}}(\mathrm{jet})$ ranges are shown in fig. 6.67. Also comparisons of the raw, efficiency corrected and unfolded distributions are shown in fig. 6.68. Overall, the distributions show that the unfolding shifts the total distribution to lower $z(J/\psi)$ values. This makes sense as energy losses of the jets due to not reconstructing hyperons are taken into account, so increase $p_{\mathrm{T}}(\mathrm{jet})$, and hence decrease $z(J/\psi)$.

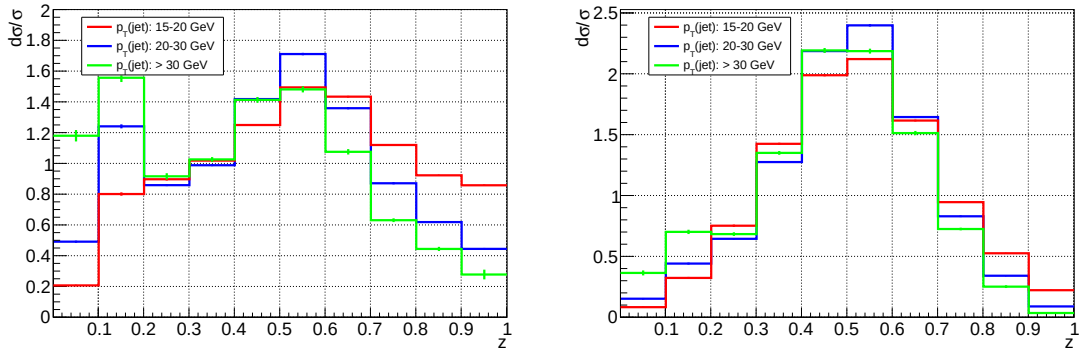

(a) Prompt. (b) Displaced.

Figure 6.67: Prompt and displaced normalised cross sections, $\mathrm{d}\sigma/\sigma$, *vs.* $z(J/\psi)$ in different $p_{\mathrm{T}}(\mathrm{jet})$ ranges which are unfolded. The plots are normalised as $1/N\ \mathrm{d}N/\mathrm{d}z$.

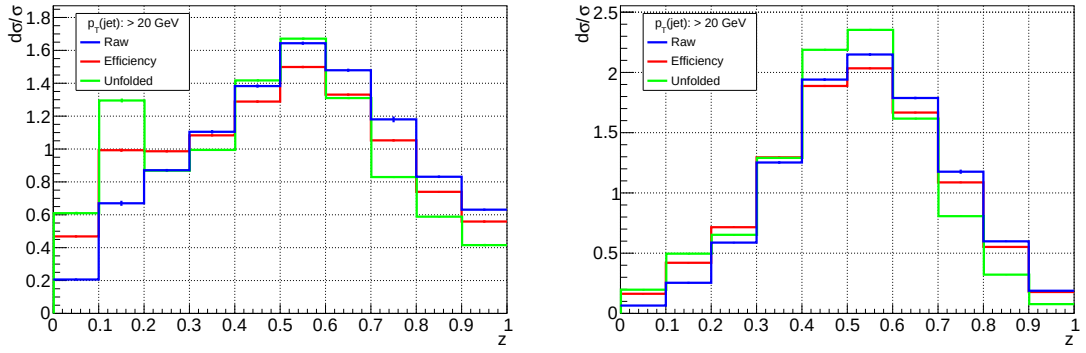

(a) Prompt. (b) Displaced.

Figure 6.68: Comparison of the raw, efficiency corrected and unfolded prompt and displaced normalised cross sections, $\mathrm{d}\sigma/\sigma$, *vs.* $z(J/\psi)$ in different $p_{\mathrm{T}}(\mathrm{jet})$ ranges. The plots are normalised as $1/N\ \mathrm{d}N/\mathrm{d}z$.

6.3.1 Unfolding of $\psi(2S)$ distributions

The procedure for unfolding the $\psi(2S)$ follows that as for the J/ψ. Results for the normalised prompt and displaced $\psi(2S)$ cross sections *vs.* $z(J/\psi)$ in different $p_{\mathrm{T}}(\mathrm{jet})$ ranges are shown in fig. 6.69. Also comparisons of the raw, efficiency corrected and unfolded distributions are shown in fig. 6.70, and again shift the distributions to lower $z(\psi(2S))$ values.

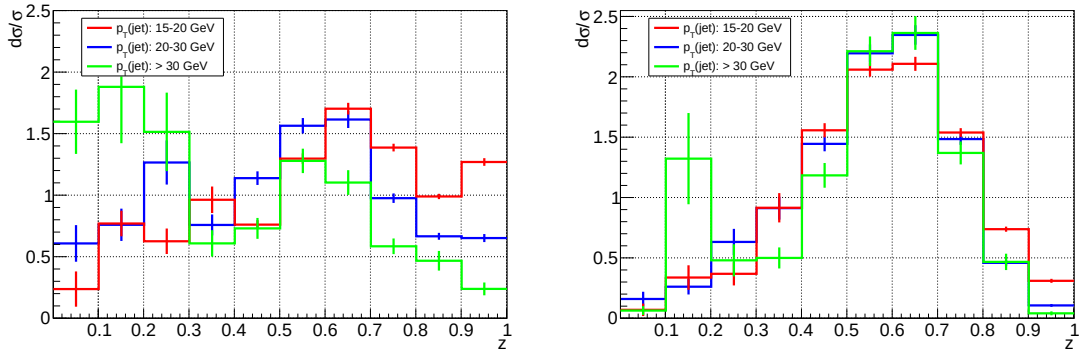

(a) Prompt. (b) Displaced.

Figure 6.69: Prompt and displaced normalised cross sections, $\mathrm{d}\sigma/\sigma$, *vs.* $z(\psi(2S))$ in different $p_{\mathrm{T}}(\mathrm{jet})$ ranges which are unfolded. The plots are normalised as $1/N\ \mathrm{d}N/\mathrm{d}z$.

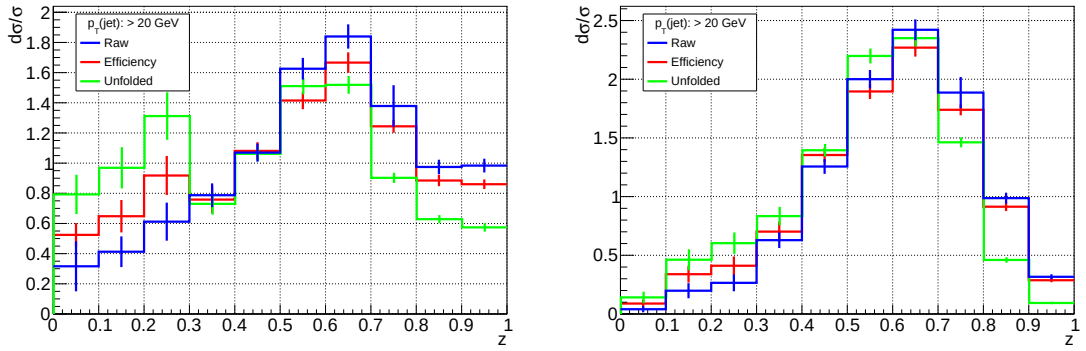

(a) Prompt. (b) Displaced.

Figure 6.70: Comparison of the raw, efficiency corrected and unfolded prompt and displaced normalised cross sections, $\mathrm{d}\sigma/\sigma$, *vs.* $z(\psi(2S))$ in different $p_{\mathrm{T}}(\mathrm{jet})$ ranges. The plots are normalised as $1/N\ \mathrm{d}N/\mathrm{d}z$.

6.3.2 Unfolding of $\Upsilon(1S)$, $\Upsilon(2S)$ and $\Upsilon(3S)$ distributions

The procedure for unfolding Υ's is slightly more straightforward, as Υ's cannot be produced from b-decays so they do not have a displaced component. Also, they seem to be more accurately described by MC at this energy scale, where MC also shows an isolated peak at $z(\Upsilon) \simeq 1$. Hence, the inclusive Υ LHCb samples are directly used with no alterations. Preliminary results for the normalised $\Upsilon(1S)$, $\Upsilon(2S)$ and $\Upsilon(3S)$ cross sections *vs.* $z(\Upsilon)$ in different $p_{\mathrm{T}}(\mathrm{jet})$ ranges are shown in figs. 6.71 and 6.72. Also comparisons of the raw, efficiency corrected and unfolded distributions are shown in fig. 6.70, which again shift the distributions to lower $z(\Upsilon)$ values.

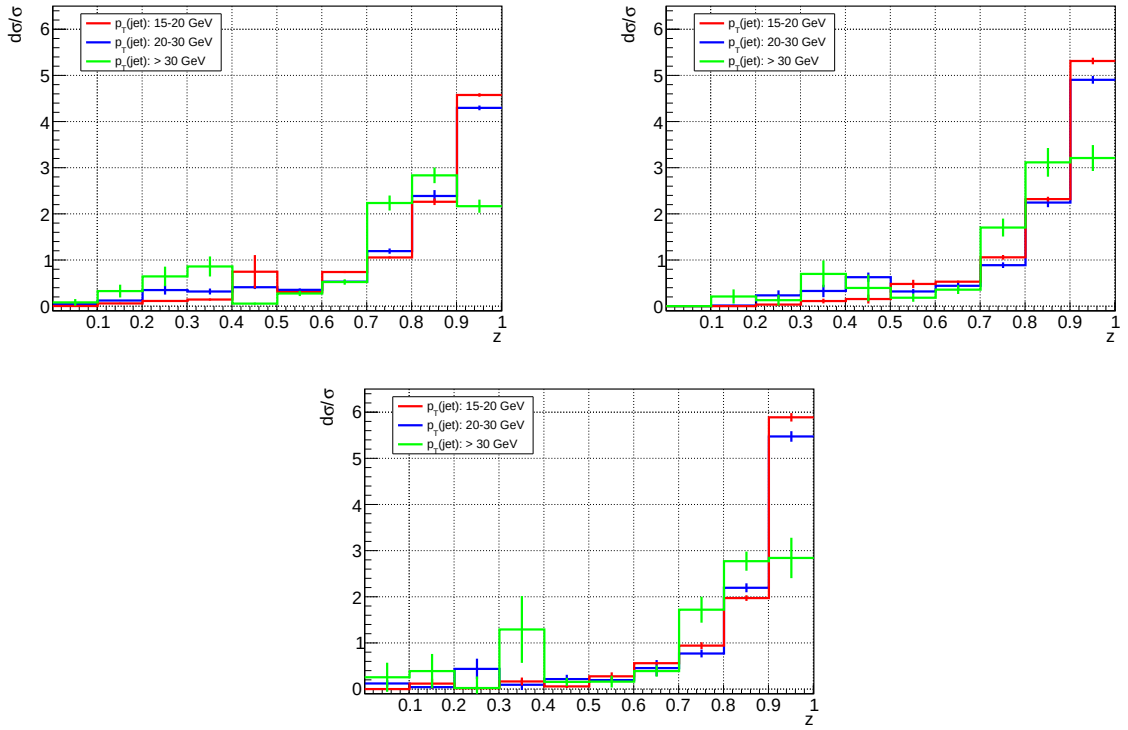

Figure 6.71: Normalised cross section distributions *vs.* $z(\Upsilon)$ in different $p_{\mathrm{T}}(\mathrm{jet})$ ranges for separated $\Upsilon(1S)$, $\Upsilon(2S)$ and $\Upsilon(3S)$ which are unfolded. The plots are normalised as $1/N\ \mathrm{d}N/\mathrm{d}z$. Left to right: $\Upsilon(1S)$, $\Upsilon(2S)$ and $\Upsilon(3S)$.

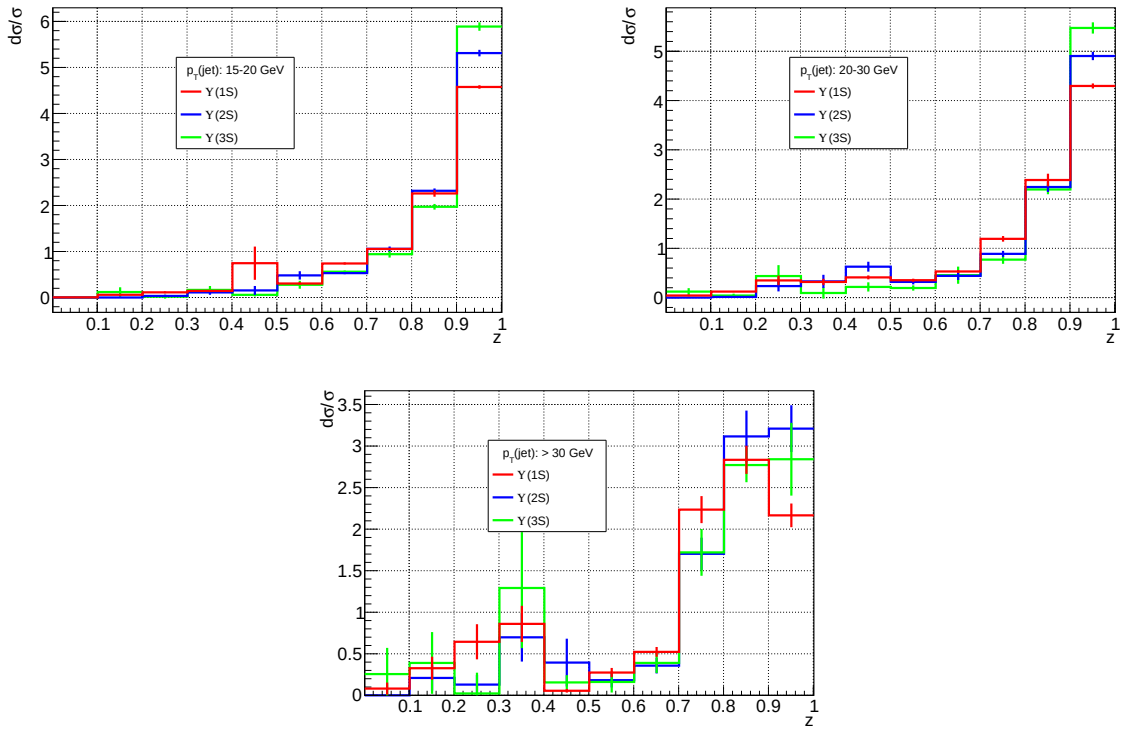

Figure 6.72: Normalised cross section distributions for $\Upsilon(1S)$, $\Upsilon(2S)$ and $\Upsilon(3S)$ *vs.* $z(\Upsilon)$ with efficiency corrections for different $p_{\mathrm{T}}(\mathrm{jet})$ ranges. The plots are normalised as $1/N\ \mathrm{d}N/\mathrm{d}z$. Left to right: $15 < p_{\mathrm{T}}(\mathrm{jet}) < 20\,\mathrm{GeV}$, $20 < p_{\mathrm{T}}(\mathrm{jet}) < 30\,\mathrm{GeV}$, and $p_{\mathrm{T}}(\mathrm{jet}) > 30\,\mathrm{GeV}$.

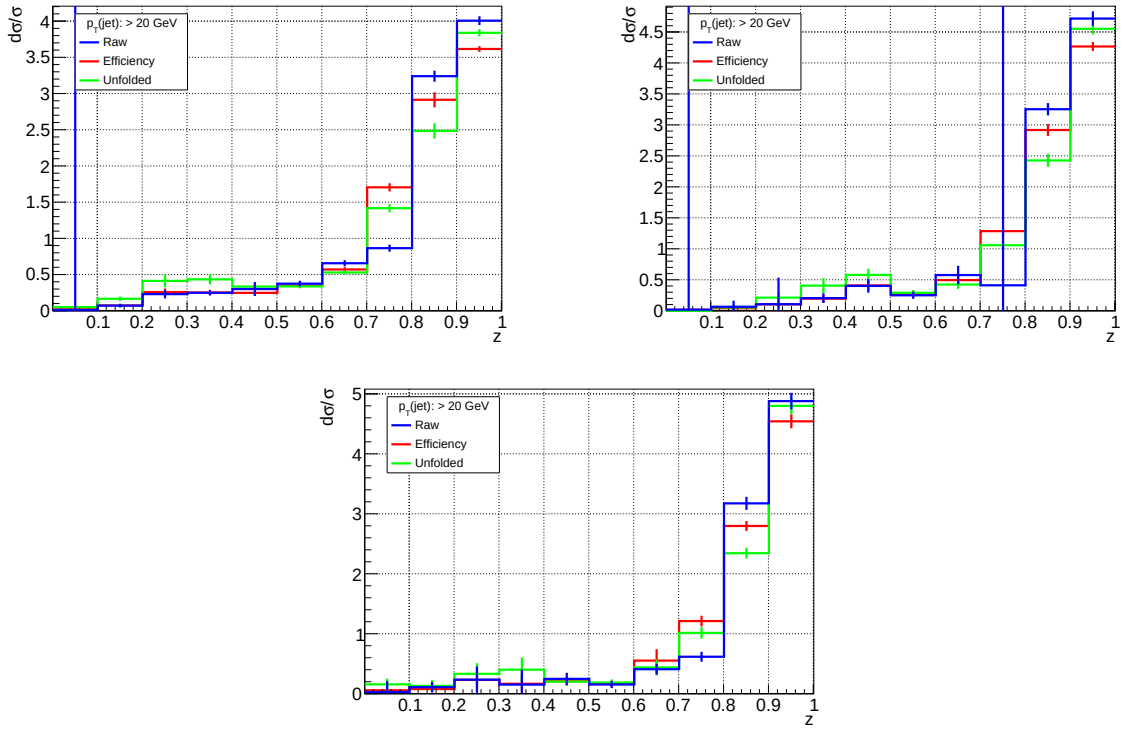

Figure 6.73: Comparison of the raw, efficiency corrected and unfolded normalised cross section distributions *vs.* $z(\Upsilon)$ in different $p_{\mathrm{T}}(\mathrm{jet})$ ranges for separated $\Upsilon(1S)$, $\Upsilon(2S)$ and $\Upsilon(3S)$. The plots are normalised as $1/N\ \mathrm{d}N/\mathrm{d}z$. Left to right: $\Upsilon(1S)$, $\Upsilon(2S)$ and $\Upsilon(3S)$.

6.4 Systematic uncertainties

In addition to statistical uncertainties there are also systematic uncertainties to take into account. These are divided into three categories, firstly the uncertainty from the signal yield extraction, *i.e.* mass and lifetime fits, secondly from the efficiency corrections, and finally from the unfolding procedure.

6.4.1 Signal fit uncertainty

As explained in section 6.1.2, the signal yield for prompt and displaced J/ψ was calculated in different $z(J/\psi)$ and $p_{\mathrm{T}}(\mathrm{jet})$ bins using mass fits and lifetime fits. The nominal mass fit uses a DCB model to fit the signal. To assess the uncertainty of this model, the DCB model is swapped with a SCB and a double Gaussian (DGauss) function separately. The same procedure is then followed where the efficiency correction is applied to reweight the data, the mass fit with the new signal model is

used and then a lifetime fit is performed. The systematic error due to the signal model assumption, σ_{signal}, is then assigned as the difference between the signal yield obtained from the double Gaussian/SCB fit, $S_{\text{DGauss/SCB}}$, and the nominal DCB fit, S_{DCB} divided by the nominal DCB signal yield,

$$\sigma_{\text{signal}} = \frac{|S_{\text{DGauss/SCB}} - S_{\text{DCB}}|}{S_{\text{DCB}}}, \tag{6.14}$$

for the prompt and displaced components separately in different $z(J/\psi)$ and $p_{\text{T}}(\text{jet})$ bins. The results are shown in figs. 6.74 and 6.75 using the DGauss and SCB models respectively. For the $z(J/\psi)$ bins, $0.0 < z(J/\psi) < 0.1$ and $0.1 < z(J/\psi) < 0.2$, the results are statistics limited as the background fractions in the signal fits are $\sim$ 96 %. This means repeating the signal fits in these bins with a different model will lead to overestimated systematic errors. Hence the systematics in these bins are extrapolated from the calculated values in the $0.2 < z(J/\psi) < 0.3$ bin. This method is used for all the systematic errors calculated. Figures 6.74 and 6.75 show that both the DGauss and SCB models give roughly the same systematic errors, with a mean of 2 % and ranging from 0.5 % to 5 %. Hence, the systematic is independent of the model chosen, so the DGauss model was used to evaluate the final systematic.

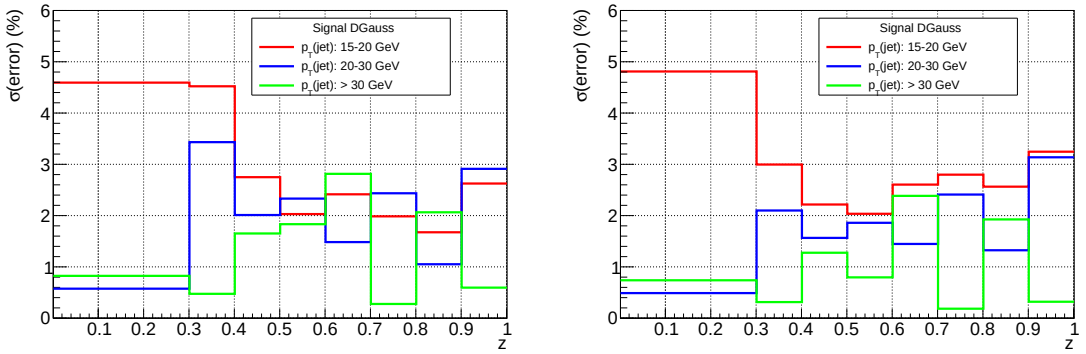

(a) Prompt. (b) Displaced.

Figure 6.74: Systematic uncertainty associated with the Double Gaussian signal fit *vs.* $z(J/\psi)$ in different $p_{\text{T}}(\text{jet})$ ranges.

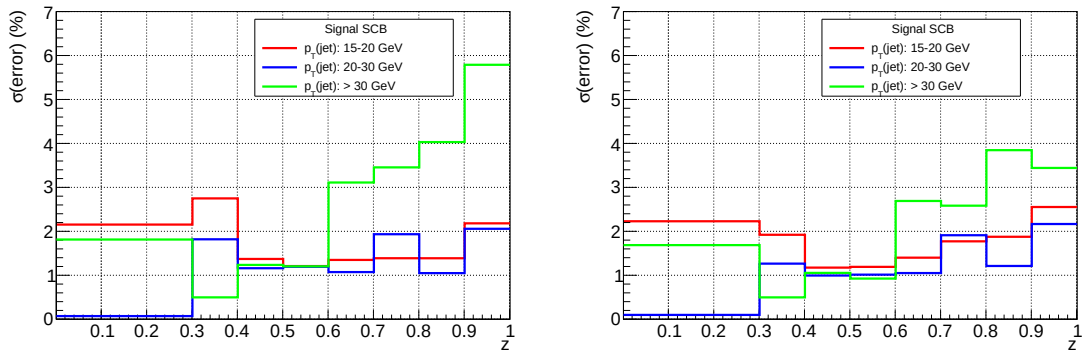

(a) Prompt. (b) Displaced.

Figure 6.75: Systematic uncertainty associated with the Single Crystal Ball signal fit *vs.* $z(J/\psi)$ in different p_{T}(jet) ranges.

6.4.2 Efficiency uncertainties

This systematic uncertainty is obtained from the efficiency maps used to correct for the loss of signal from the event selection. The uncertainties for each efficiency (*e.g.* reconstruction, trigger *etc.*) are calculated separately and then added together in quadrature. The reconstruction efficiency has three sources of error. The first is from the binning of the muon reconstruction efficiency map obtained from MC shown in fig. 6.18. This error is estimated by halving the number of bins in p_{T} and η and correcting the data with this efficiency map instead. The same procedure is then followed as discussed in section 6.4.1 by performing mass/lifetime fits on this new reweighted data and then error is the difference in signal yields divided by the nominal. The systematics from the half binning of the muon reconstruction MC efficiency map are shown in fig. 6.76. This method of calculation is used for most of the systematic errors described in this section.

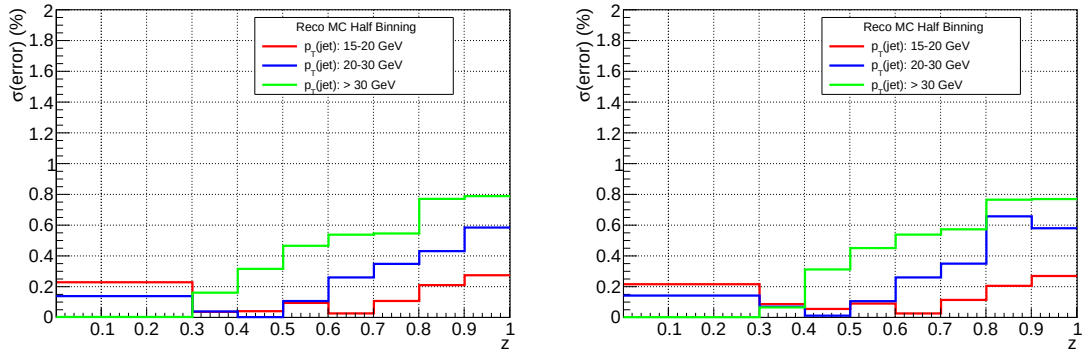

(a) Prompt. (b) Displaced.

Figure 6.76: Systematic uncertainty associated with the muon reconstruction MC efficiency map, using half binning, *vs.* $z(J/\psi)$ in different p_{T}(jet) ranges.

The second and third components of the reconstruction efficiency systematic are due to the data correction ratio $R_{\text{data/MC}}$ taken from TrackCalib [121] as shown in fig. 6.23. One is the statistical error and the other is the systematic error, which accounts for systematic uncertainties in the tag-and-probe method. Separately, each error is subtracted from the nominal $R_{\text{data/MC}}$ value. These new values of $R_{\text{data/MC}}$ are then used to reweight the data and new signal yields are obtained. All values are lowered by the error rather than increased to avoid instances where the efficiency would be greater than one. The systematic errors from the $R_{\text{data/MC}}$ correction are shown separately in figs. 6.77 and 6.78. The three sources of systematic uncertainties for the muon reconstruction efficiency are then summed in quadrature and the total is shown in fig. 6.79. This shows that the dominant source of systematic is from the data corrections, particularly the statistical part at high $z(J/\psi)$. This region corresponds to high p_{T} muons which fall between the J/ψ and Z tag coverage, resulting in a larger systematic uncertainty. It also shows the total systematic is $\sim$ 3 % across all $z(J/\psi)$ bins.

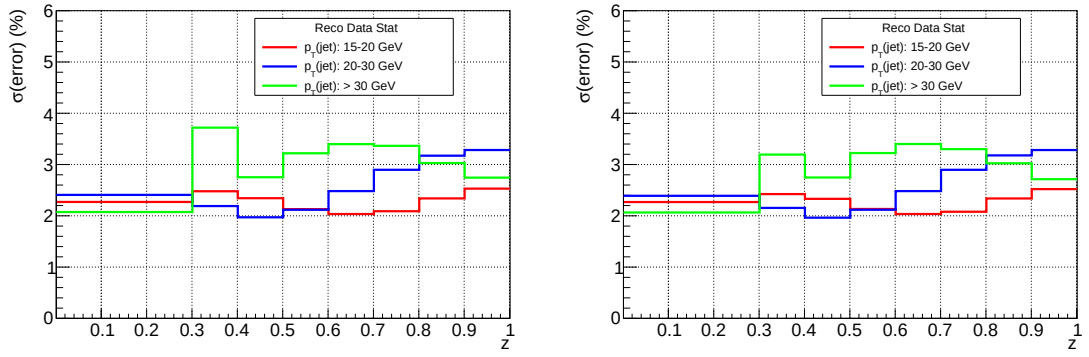

(a) Prompt. (b) Displaced.

Figure 6.77: Systematic uncertainty associated with the muon reconstruction $R_{\text{data/MC}}$ correction statistical error, *vs.* $z(J/\psi)$ in different p_{T}(jet) ranges.

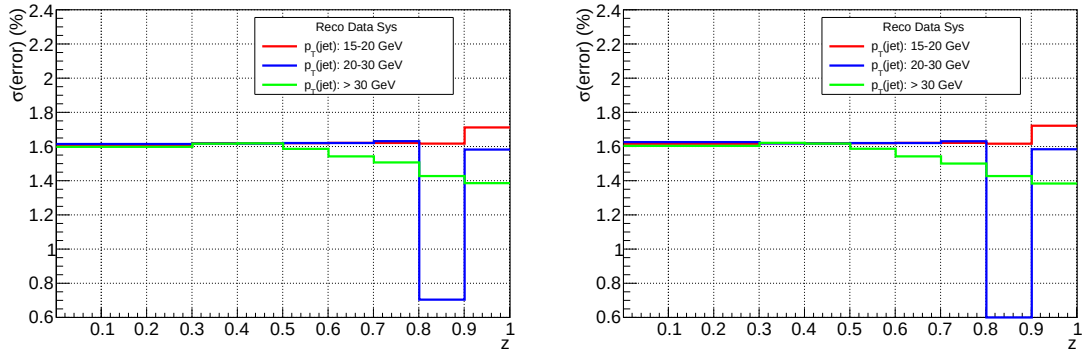

(a) Prompt. (b) Displaced.

Figure 6.78: Systematic uncertainty associated with the muon reconstruction $R_{\text{data/MC}}$ correction systematic error, *vs.* $z(J/\psi)$ in different p_{T}(jet) ranges.

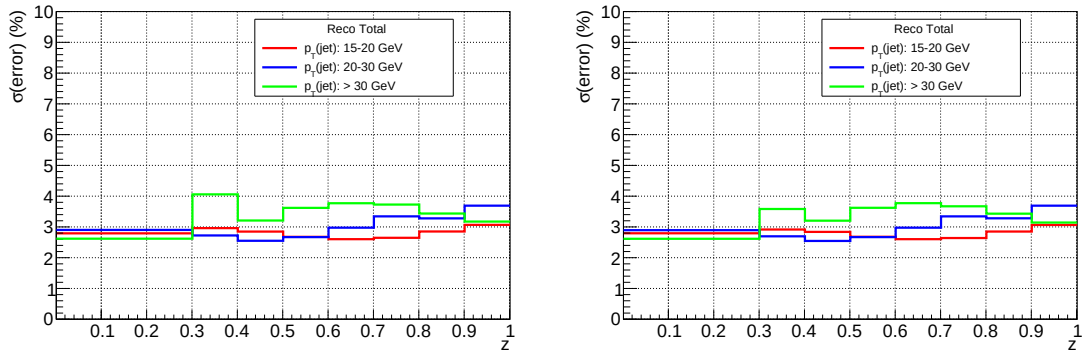

(a) Prompt. (b) Displaced.

Figure 6.79: Total systematic uncertainty associated with the muon reconstruction efficiency, *i.e.* the sum in quadrature of the three components, *vs.* $z(J/\psi)$ in different $p_{\mathrm{T}}(\mathrm{jet})$ ranges.

The trigger efficiency systematic is calculated using two different methods. To calculate the trigger efficiency, the 2D trigger efficiency histogram was interpolated using a 1D three parameter fit for each η (tag) bin *vs.* $\sqrt{p_{\mathrm{T}}(\mu_1)p_{\mathrm{T}}(\mu_2)}$. As there are 10 different η (tag) bins, this leads to 10 interpolated fit functions and hence a thirty parameter fit. The first method is to take the mean and sigma for these thirty different parameters from the nominal fits, construct a Gaussian for each parameter and then randomly sample a new value from each Gaussian. This leads to 30 new parameters to construct 10 new interpolated fit functions. These 10 new fit functions are then used to obtain to a new trigger efficiency weight to feed into the mass/lifetime fits. This then leads to new prompt/displaced yields. This process is repeated 100 times to obtain an average of these samplings. The systematic uncertainty of the trigger efficiency with this method, $\sigma_{\mathrm{trigger,gauss}}$, is calculated as,

$$\sigma_{\mathrm{trigger,gauss}} = \sqrt{\frac{\sum_i (S_{\mathrm{i,gauss}} - S_{\mathrm{nominal}})^2}{100}}, \tag{6.15}$$

where S_{nominal} is the nominal signal yield and $S_{\mathrm{i,gauss}}$ is the signal yield obtained for the i-th iteration of the sampling the fit parameters method, for each $z(J/\psi)$ and $p_{\mathrm{T}}(\mathrm{jet})$ bin. The results obtained using this method are shown in fig. 6.80. The range of the systematic uncertainty with this method is 0.5–4.0 % with the uncertainty increasing at lower $z(J/\psi)$ values. This is because $z(J/\psi)$ is highly correlated with $p_{\mathrm{T}}(J/\psi)$. In the trigger efficiency map in fig. 6.30, it can be interpreted as a binominal efficiency, where the trigger shows threshold behaviour above a given value of $\sqrt{p_{\mathrm{T}}(\mu_1)p_{\mathrm{T}}(\mu_2)}$. Hence, the efficiency can depend heavily on how the low $\sqrt{p_{\mathrm{T}}(\mu_1)p_{\mathrm{T}}(\mu_2)}$ tail is interpolated. This is in comparison to the high $z(J/\psi)$ region

which has quite small systematics and is relatively stable. Note, this method does not take into account correlations between the fit parameters, and the full correlation matrix from the fit would need to be used instead.

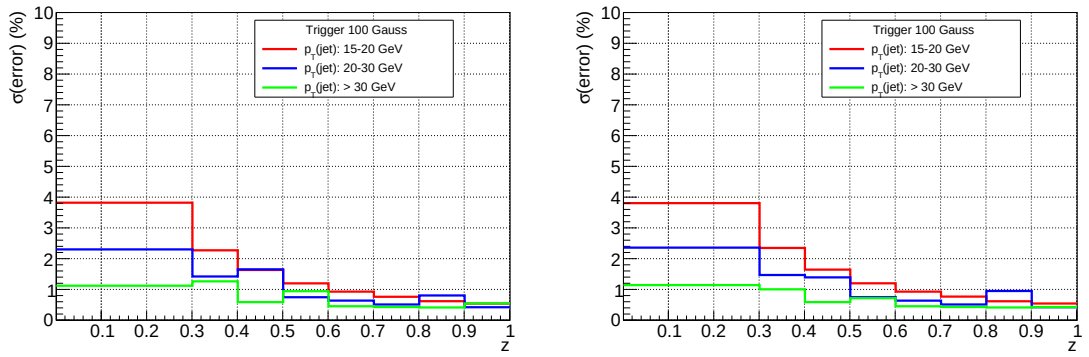

(a) Prompt. (b) Displaced.

Figure 6.80: Systematic uncertainty associated with the trigger efficiency, using the sampling of the fit parameters from 100 Gaussians method, *vs.* $z(J/\psi)$ in different $p_{\mathrm{T}}(\mathrm{jet})$ ranges.

The second method takes the nominal trigger efficiency map shown in fig. 6.30 and, as for the muon reconstruction MC efficiency map, halves the number of bins. This map is then interpolated to find 10 new interpolated fit functions to calculate the new trigger efficiency weight. The systematic uncertainty is then calculated using the form of eq. (6.14) which calculates the difference in signal yield values. The results using this method are shown in fig. 6.81. The total systematic is larger using the second method than the first, especially at low $z(J/\psi)$. This is because the half binning at low $\sqrt{p_{\mathrm{T}}(\mu_1)p_{\mathrm{T}}(\mu_2)}$ changes how this low tail is interpolated more significantly than when varying the fit parameters within their known uncertainties. This method may also take into account correlations between fit parameters, as the half binning method effectively interpolates a "new" efficiency map.

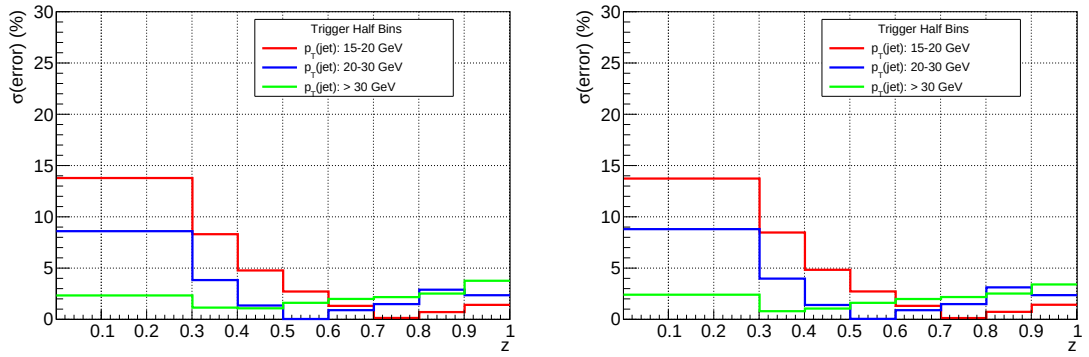

(a) Prompt. (b) Displaced.

Figure 6.81: Systematic uncertainty associated with the trigger efficiency, using the half binned map, *vs.* $z(J/\psi)$ in different $p_{\mathrm{T}}(\mathrm{jet})$ ranges.

An additional trigger systematic is needed to take into account differences from the true trigger efficiency, which were observed by performing a closure test shown in fig. 6.29. The systematic is calculated by first finding the difference of the closure test value from one for each event. This value is then subtracted from the nominal trigger efficiency value, to calculate the new trigger efficiency. This weight is then used to obtain the new signal yields. The results are shown in fig. 6.82. The systematic uncertainty increases at high $z(J/\psi)$, because of the statistics available for the closure test at high p_{T}.

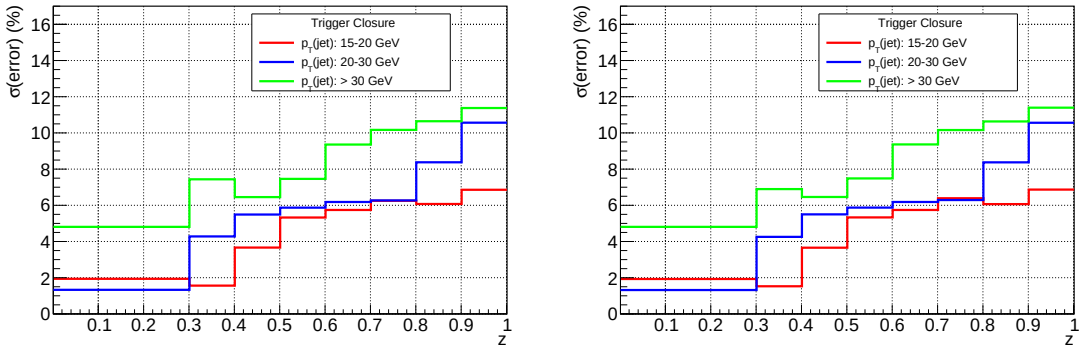

(a) Prompt. (b) Displaced.

Figure 6.82: Systematic uncertainty associated with the trigger efficiency, from the closure test, *vs.* $z(J/\psi)$ in different p_{T}(jet) ranges.

The total trigger systematic uncertainty is calculated from the combination of the uncertainty from the closure test with the uncertainty from the sampling of 100 Gaussians method, as shown in fig. 6.83. Alternatively, it can be the combination of the closure test uncertainty with the half binning method uncertainty fig. 6.84. After consideration, it was decided to take a more conservative approach for calculating the trigger systematic uncertainty by using the systematics calculated from the half binning method. This was to take into account possible correlations between the fit parameters and also the fitting of the low $\sqrt{p_{\mathrm{T}}(\mu_1)p_{\mathrm{T}}(\mu_2)}$ tail. Also, since the sources of the systematics for the closure test and half binning method are similar, the total trigger systematic is calculated by taking the variance of the individual systematics, rather than the sum in quadrature.

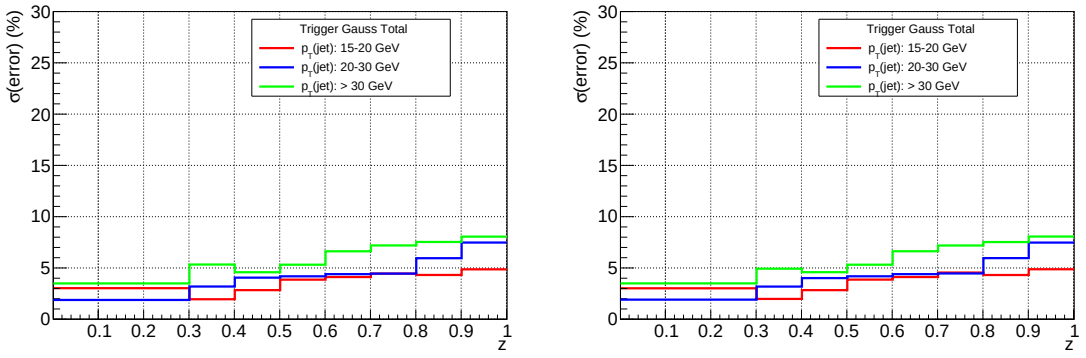

(a) Prompt. (b) Displaced.

Figure 6.83: Total systematic uncertainty associated with the trigger efficiency, *i.e.* the sum in quadrature of the systematic from the 100 Gaussian method plus the closure test, *vs.* $z(J/\psi)$ in different p_{T}(jet) ranges.

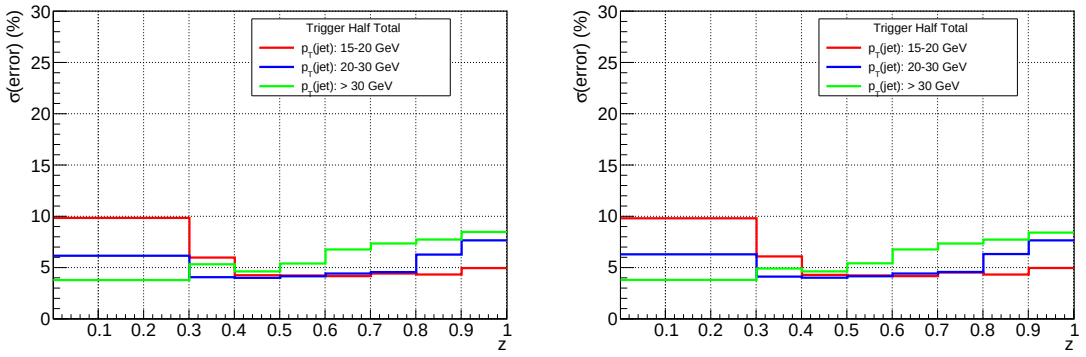

(a) Prompt. (b) Displaced.

Figure 6.84: Total systematic uncertainty associated with the trigger efficiency, *i.e.* the sum in quadrature of the systematic from the half binning method plus the closure test, *vs.* $z(J/\psi)$ in different p_{T}(jet) ranges.

For the stripping line correction, where particle ID is applied before the trigger selection as shown in fig. 6.32, to calculate the systematic uncertainty, the efficiency map is altered by lowering the efficiency value in each bin by the statistical uncertainty of that bin. This is then used to reweight the data and obtain new signal yields. The results are shown in fig. 6.85. This gives a small contribution to the total systematic in comparison to the trigger and muon reconstruction efficiencies. The systematic error increases with $z(J/\psi)$ as there are less statistics available at high p_{T}.

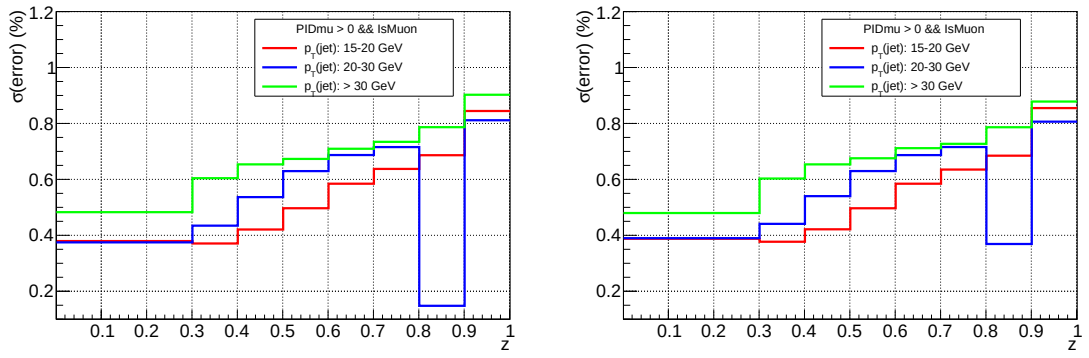

(a) Prompt. (b) Displaced.

Figure 6.85: Systematic uncertainty associated with the stripping line correction, PIDmu > 0 and IsMuon, *vs.* $z(J/\psi)$ in different p_{T}(jet) ranges.

The ProbNNmu efficiency is also calculated using an interpolated fit of the 2D efficiency histogram. Hence, the systematic uncertainty is calculated using the two methods as described for the trigger efficiency uncertainty. The sampling of 100 Gaussians method, which is shown in fig. 6.86, and then the half binning method, which is shown in fig. 6.87. The systematic uncertainties show the same behaviour as for the trigger uncertainties, where the systematics are higher at low $z(J/\psi)$ for the half binning method than the sampling method, due to the fit of the low p_{T} tail in the efficiency map. The fluctuations in the uncertainty are most likely to arise from the fitting process itself. Following the same reasoning as for the trigger uncertainties, the systematics calculated using the half binning method will be used.

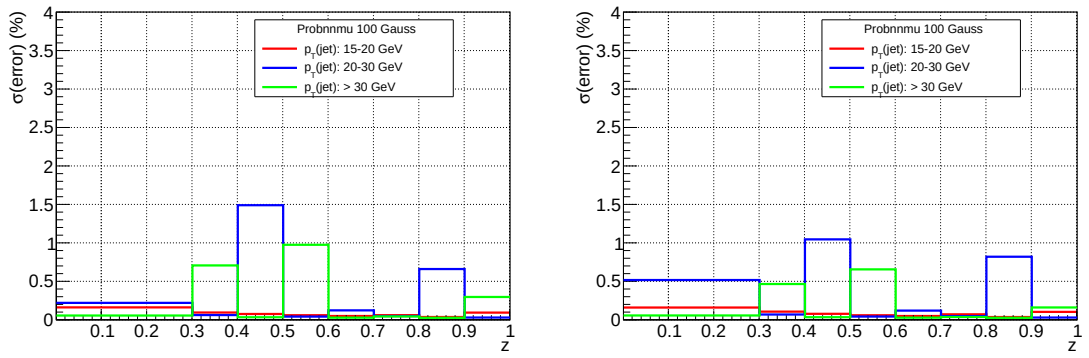

(a) Prompt. (b) Displaced.

Figure 6.86: Systematic uncertainty associated with the ProbNNmu efficiency, using the sampling of the fit parameters from 100 Gaussians method, *vs.* $z(J/\psi)$ in different p_{T}(jet) ranges.

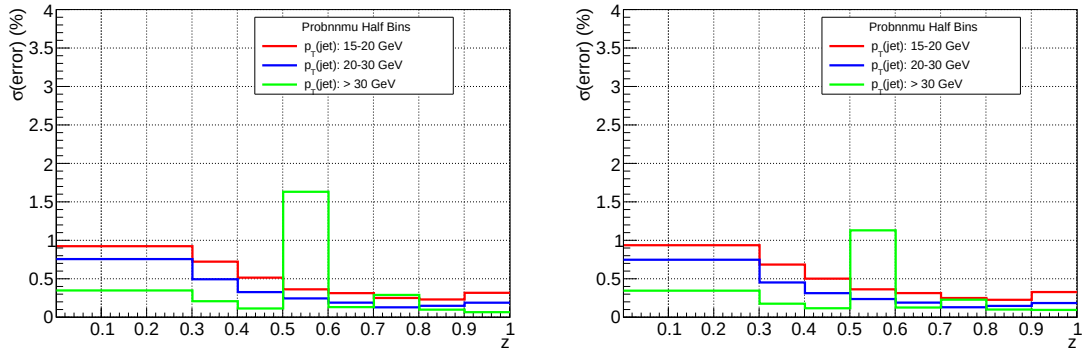

(a) Prompt. (b) Displaced.

Figure 6.87: Systematic uncertainty associated with the ProbNNmu efficiency, using the half binned map, *vs.* $z(J/\psi)$ in different p_{T}(jet) ranges.

6.4.3 Total systematics - signal fit + efficiency

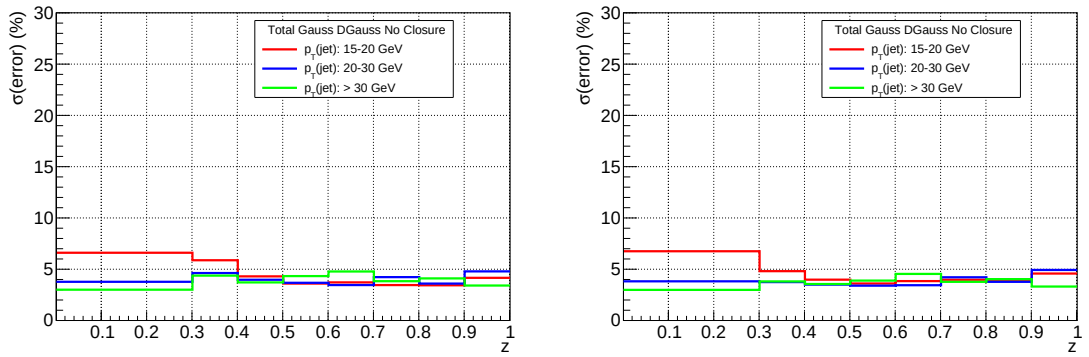

(a) Prompt. (b) Displaced.

Figure 6.88: Total systematic uncertainty associated from signal fit and all efficiency components, *vs.* $z(J/\psi)$ in different p_{T}(jet) ranges. This uses the 100 Gaussian method for trigger and ProbNNmu systematics, the Double Gaussian for the signal fit systematic but does not include the trigger closure test systematic.

The total systematic uncertainties, summing the signal fit uncertainties and efficiency uncertainties in quadrature, are discussed in this section. The unfolding systematics are discussed separately, as they are another dominant source of systematic uncertainty. Firstly, to check the calculation of the systematics, the values of the total systematics for this analysis were compared to the values obtained from the previous analysis published in 2017 [12, 114]. In the previous analysis, the method chosen to calculate the trigger and ProbNNmu systematics was similar to the sampling 100 Gaussians method. Also a systematic uncertainty due to the trigger closure test was not included in the total systematic. The results of the total systematics using similar methods to the previous analysis are shown in fig. 6.88. The results match that of the previous analysis, which quoted a 3–5 % total systematic uncer-

tainty from the signal fit and efficiency components [12, 114]. The results also show that the dominant sources of systematics are from the muon reconstruction and trigger efficiencies. However, the systematic from the trigger closure test needs to be included. Also, the trigger systematic calculated from sampling 100 Gaussians was swapped to using the half binning method to take into account correlations in the fit parameters. Therefore, the total systematics quoted for this analysis from signal fits and efficiency corrections are shown in fig. 6.89, where the trigger systematics calculated using the half binning method and the closure test are included. This shows a total 5–11 % systematic uncertainty.

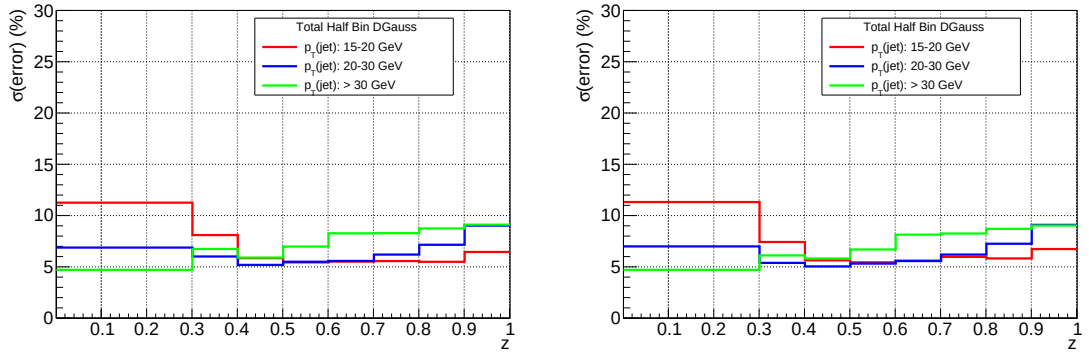

(a) Prompt. (b) Displaced.

Figure 6.89: Total systematic uncertainty associated from signal fit and all efficiency components, *vs.* $z(J/\psi)$ in different p_{T}(jet) ranges. This uses the half binning efficiency map for the trigger and ProbNNmu systematics, the Double Gaussian for the signal fit systematic and includes the trigger closure test systematic.

6.4.4 Unfolding systematics

The unfolding systematics are discussed in more detail in section 7.4.2, where the errors are split into those from the unfolding procedure, and then those from the input MC used to unfold the data. The only difference of procedure to note here is that to estimate the change of hyperon content in the jets, a JES shift is applied to each detector level jet in the MC to mimic more or fewer hyperons being used. This shift is taken from fig. 6.66, where the legend `NP Variation++` represents ∼15 % more hyperons in the jet, and `NP Variation--` ∼15 % fewer hyperons in the jet. The spread in the preliminary unfolding systematics for the displaced and prompt distributions are shown in figs. 6.90 and 6.91 respectively. These show that the dominant systematic is due to the estimated hyperon fraction. The regularisation parameter iteration of ± 1 from the chosen value can either be used a systematic uncertainty or as a cross-check only.

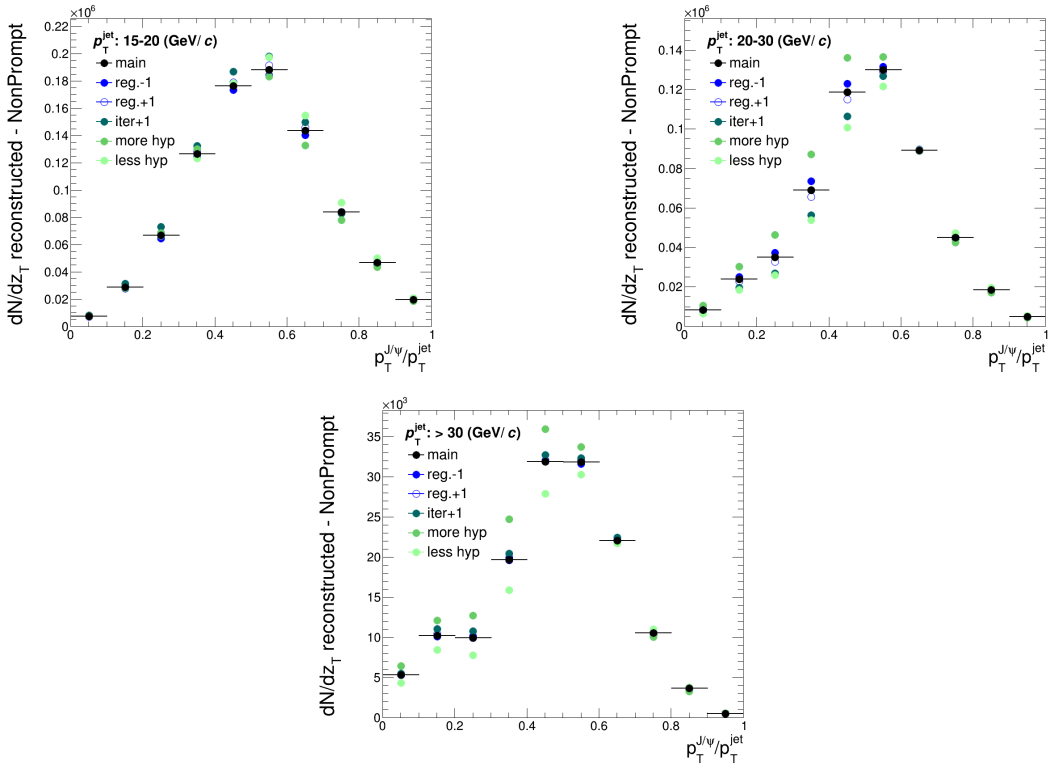

Figure 6.90: Displaced J/ψ unfolded distributions with various changes in the unfolding procedure *vs.* $z(J/\psi)$. The spread of distributions shows the systematic uncertainty associated to the unfolded result. The plots are normalised as $\mathrm{d}N/\mathrm{d}z$.

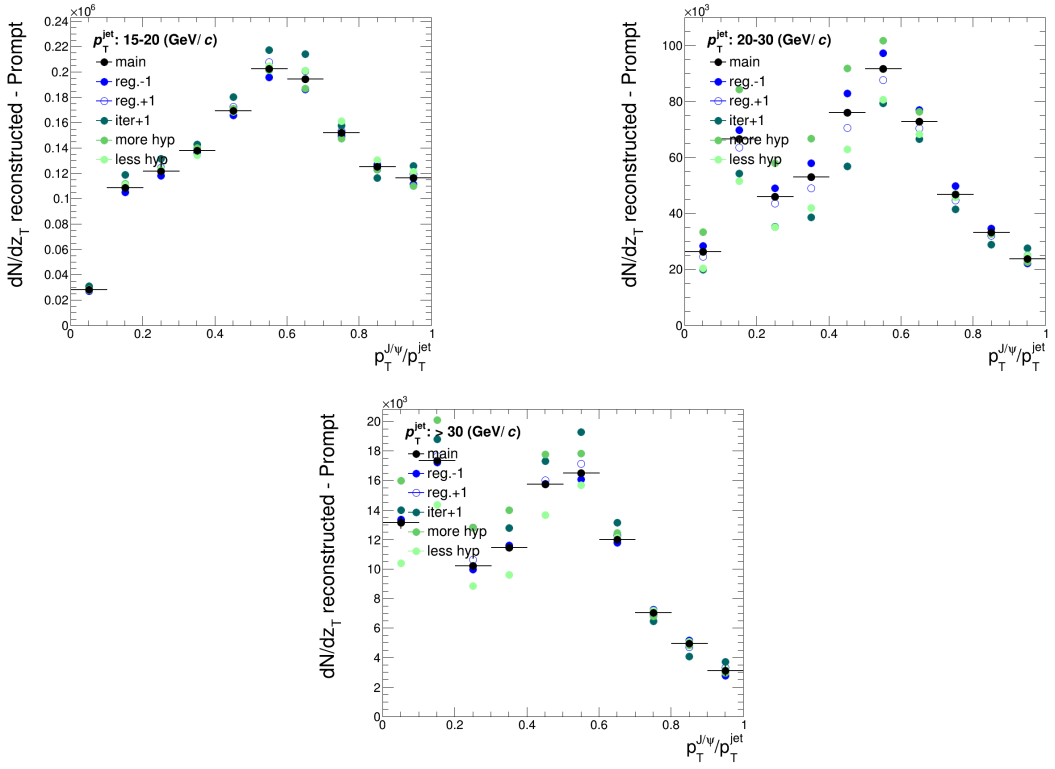

Figure 6.91: Prompt J/ψ unfolded distributions with various changes in the unfolding procedure *vs.* $z(J/\psi)$. The spread of distributions shows the systematic uncertainty associated to the unfolded result. The plots are normalised as $\mathrm{d}N/\mathrm{d}z$.

6.4.5 Systematic uncertainties for $\psi(2S)$ distributions

The systematics for the $\psi(2S)$ follow the exact same methods as for the J/ψ. Therefore, only the results of the total efficiency and signal fit systematics are shown. Figure 6.92 shows the results using similar methods to the previous 2017 analysis. This is not including the trigger closure test and uses the sampling method. Overall the systematics for the $\psi(2S)$ are larger than those shown for the J/ψ. This is mainly due to the fact that there are a lot less statistics available for the $\psi(2S)$. This affects mostly the lifetime fits because of the low purity at low $z(\psi(2S))$. However, at high $z(\psi(2S))$, the uncertainties are ∼3–7 %, ignoring the fluctuations in the highest p_{T}(jet) range. Figure 6.93 shows the total systematics taking the additional systematics due to the trigger closure test *etc.* into account. The systematics at high $z(\psi(2S))$ are higher than in fig. 6.92, with roughly ∼5–9 % uncertainty ignoring fluctuations. These are the final systematic uncertainties for the signal fit and efficiency corrections for the $\psi(2S)$. The preliminary unfolding systematics follow the same method as for the J/ψ, and are shown in figs. 6.94 and 6.95 for displaced and prompt $\psi(2S)$'s respectively. The dominant systematic is again due to the estimated hyperon fraction.

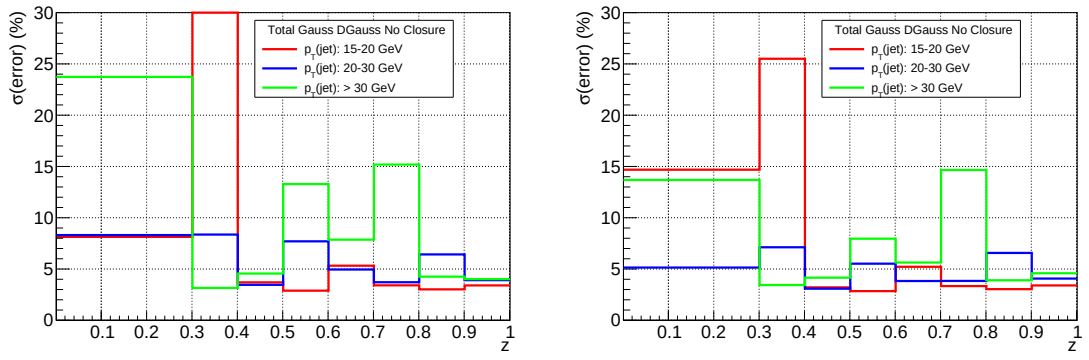

(a) Prompt. (b) Displaced.

Figure 6.92: Total systematic uncertainty associated from signal fit and all efficiency components, *vs.* $z(\psi(2S))$ in different p_{T}(jet) ranges. This uses the 100 Gaussian method for trigger and ProbNNmu systematics, the Double Gaussian for the signal fit systematic but does not include the trigger closure test systematic.

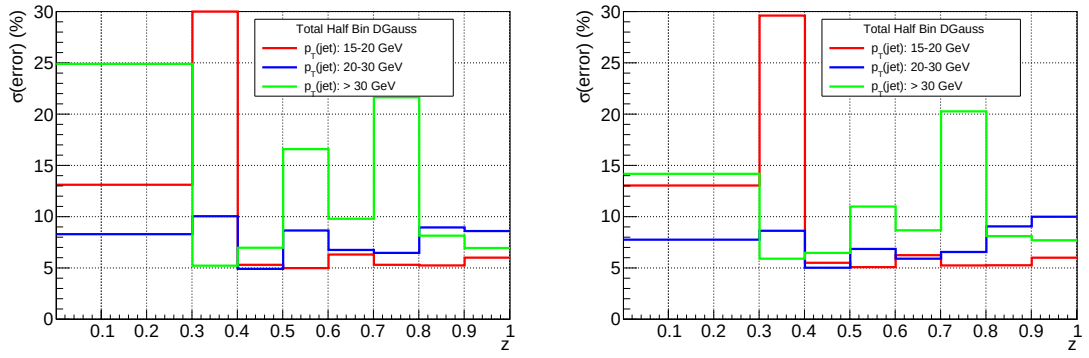

(a) Prompt. (b) Displaced.

Figure 6.93: Total systematic uncertainty associated from signal fit and all efficiency components, *vs.* $z(\psi(2S))$ in different $p_{\mathrm{T}}(\mathrm{jet})$ ranges. This uses the half binning efficiency map for the trigger and ProbNNmu systematics, the Double Gaussian for the signal fit systematic and includes the trigger closure test systematic.

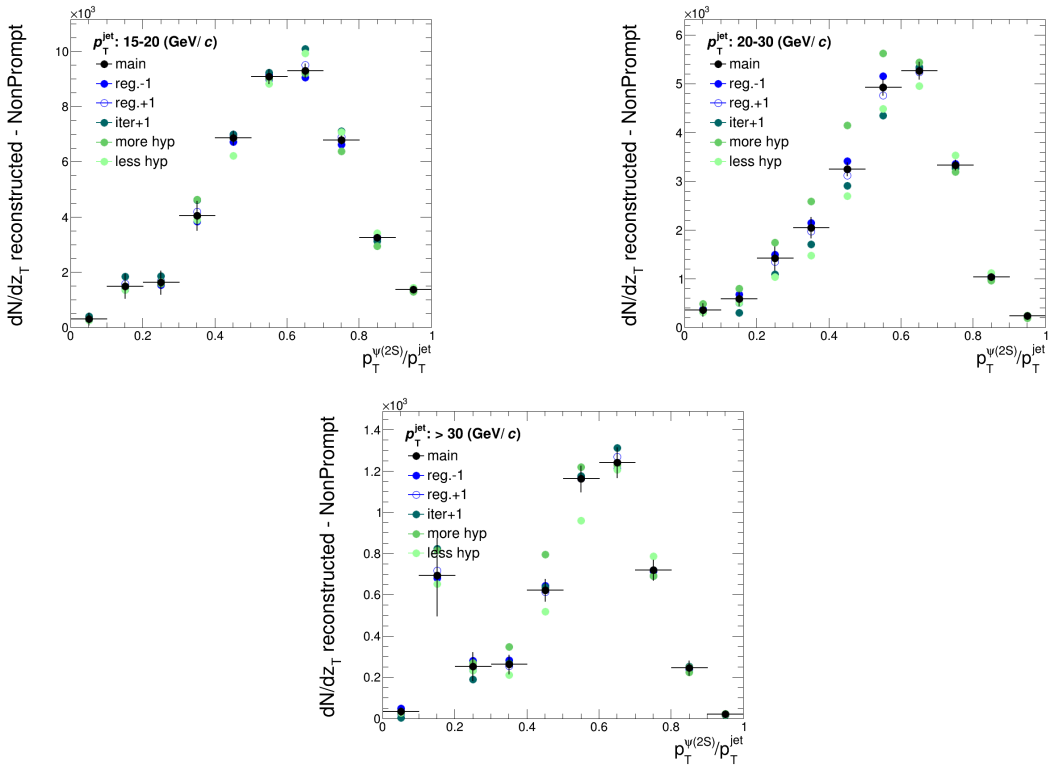

Figure 6.94: Displaced $\psi(2S)$ unfolded distributions with various changes in the unfolding procedure *vs.* $z(\psi(2S))$. The spread of distributions shows the systematic uncertainty associated to the unfolded result. The plots are normalised as $\mathrm{d}N/\mathrm{d}z$.

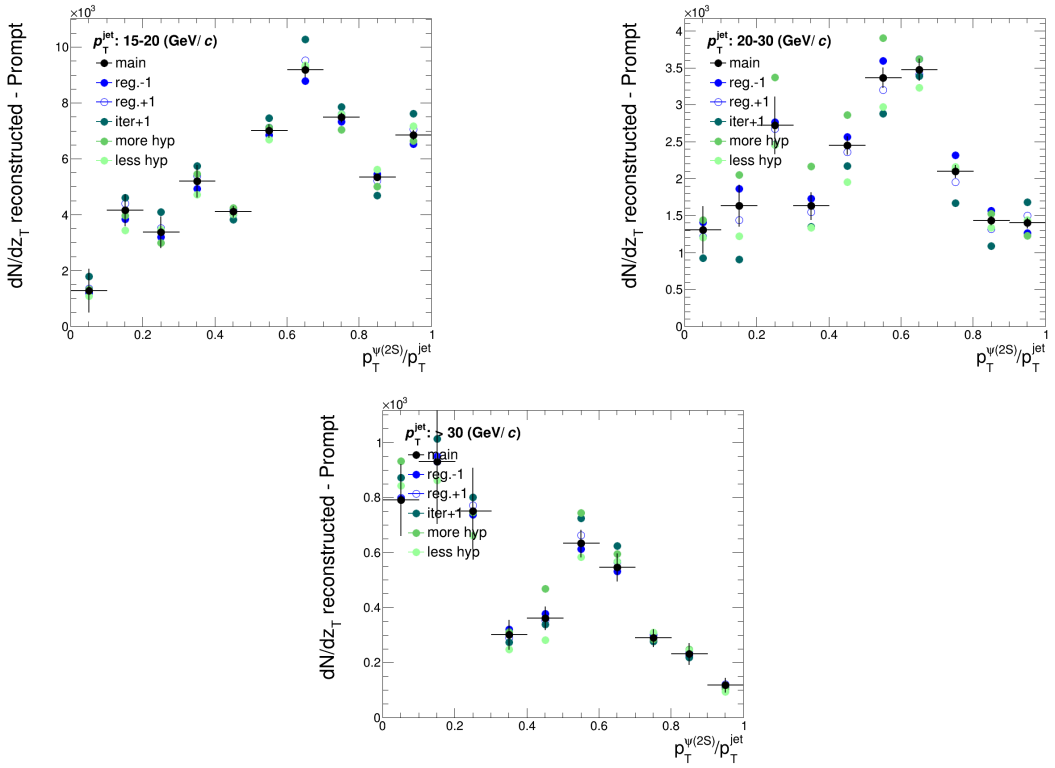

Figure 6.95: Prompt $\psi(2S)$ unfolded distributions with various changes in the unfolding procedure *vs.* $z(\psi(2S))$. The spread of distributions shows the systematic uncertainty associated to the unfolded result. The plots are normalised as $\mathrm{d}N/\mathrm{d}z$.

6.4.6 Systematic uncertainties for $\Upsilon(1S)$, $\Upsilon(2S)$ and $\Upsilon(3S)$ distributions

The method for calculating the Υ systematic uncertainties are slightly different from those calculated for the J/ψ and $\psi(2S)$. For $z(\Upsilon)$ values < 0.8, the signal yields are low and also the signal purity is low. This means the signal fits are not particularly stable when the total yield changes. Also, the total number of parameters in a given mass fit is larger because the three signal peaks are fit simultaneously. This is shown in fig. 6.96, where the DCB signal models are replaced by DGauss's and SCB's. The systematics evaluated are larger than anticipated for the signal uncertainty and further investigations are required to stabilise the fits. Hence, the total systematic presented for the Υ's does not include signal fit uncertainties pending these additional studies, which are beyond the scope of this thesis.

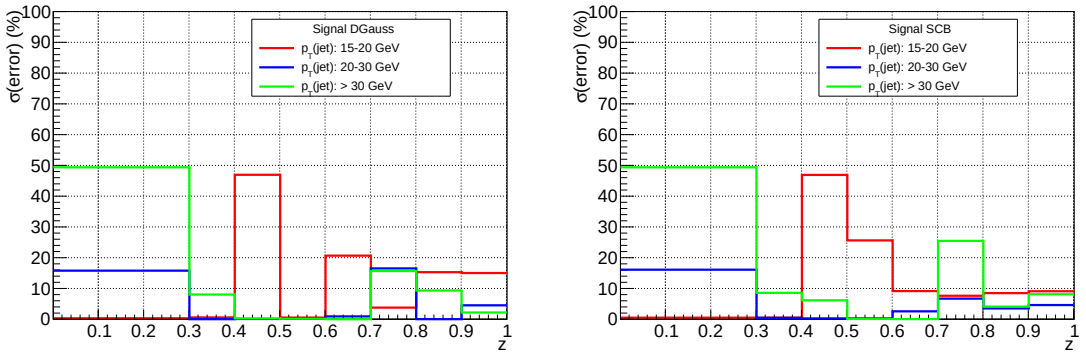

(a) Double Gaussian. (b) Single Crystal Ball.

Figure 6.96: Signal fit systematic uncertainty using the DGauss and SCB models *vs.* $z(\Upsilon)$ in different $p_{\mathrm{T}}(\mathrm{jet})$ ranges for $\Upsilon(1S)$.

However, the method has been altered slightly to be able to calculate systematic uncertainties from the efficiency corrections. Instead of performing a mass fit to retrieve a signal yield for each $z(\Upsilon)$ and $p_{\mathrm{T}}(\mathrm{jet})$ range, the total yield is extracted for each Υ. The total yield is extracted by creating a 3σ mass window from the nominal mass for each Υ, where σ is the mass resolution from the LHCb detector, and obtaining the yield within that window. At LHCb, this is 0.4 % of the nominal mass value for dimuon decay channels, *i.e.* a 120 MeV mass window. This is larger than the natural mass window of each Υ. This removes the need to perform a mass fit for each systematic uncertainty, and avoids overestimating the systematics. This method is reasonable to use, as the background yield is not expected to change with efficiency corrections. Also, the yield is not separated into prompt and displaced components like for the J/ψ and $\psi(2S)$.

The systematic uncertainties calculated using similar methods to the previous 2017 analysis are shown in fig. 6.97. The uncertainty values are in line with those seen in the J/ψ channel with values of ∼3–4 % and are relatively stable with $p_{\mathrm{T}}(\mathrm{jet})$ and each Υ. When including the full final systematics as shown in fig. 6.98, the systematic values range from ∼3–9 %. The dominant source of uncertainty is from the trigger efficiency. The systematics also increase with $p_{\mathrm{T}}(\mathrm{jet})$, due to the decrease in statistics. The systematics slightly alter between the three Υ states, but not significantly. The preliminary unfolding systematics follow the same method as for the J/ψ and $\psi(2S)$, except only the less hyperon systematic is used. The results are shown in figs. 6.99 to 6.101 for $\Upsilon(1S)$, $\Upsilon(2S)$ and $\Upsilon(3S)$ respectively.

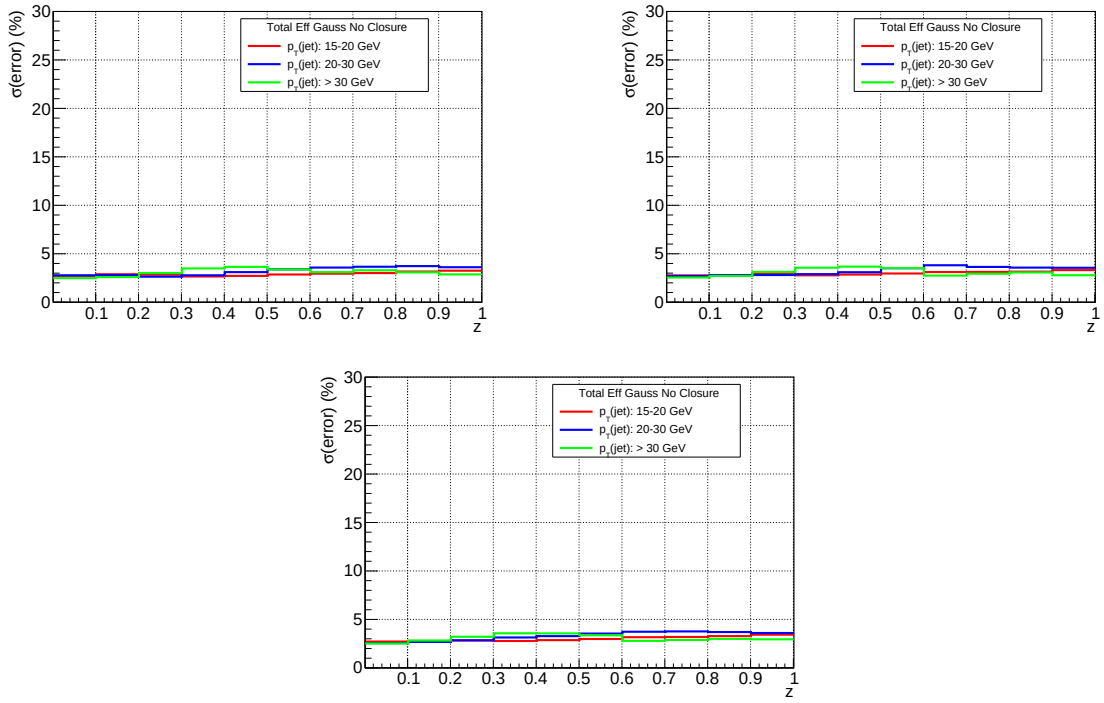

Figure 6.97: Total efficiency systematic uncertainty associated from all efficiency components, *vs.* $z(\Upsilon)$ in different $p_{\mathrm{T}}(\mathrm{jet})$ ranges for $\Upsilon(1S)$, $\Upsilon(2S)$ and $\Upsilon(3S)$ from left to right. This uses the 100 Gaussian method for trigger and ProbNNmu systematics, but does not include the trigger closure test systematic.

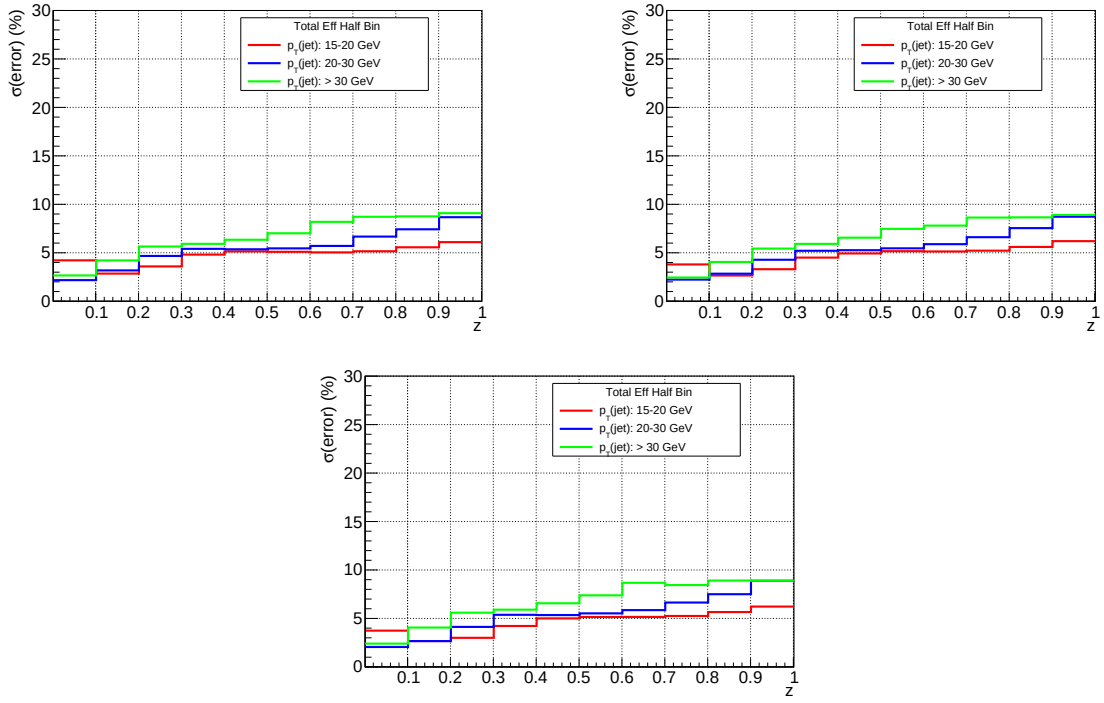

Figure 6.98: Total efficiency systematic uncertainty associated from all efficiency components, *vs.* $z(\Upsilon)$ in different $p_{\mathrm{T}}(\mathrm{jet})$ ranges for $\Upsilon(1S)$, $\Upsilon(2S)$ and $\Upsilon(3S)$. This uses the half binning efficiency map for the trigger and ProbNNmu systematics, and includes the trigger closure test systematic.

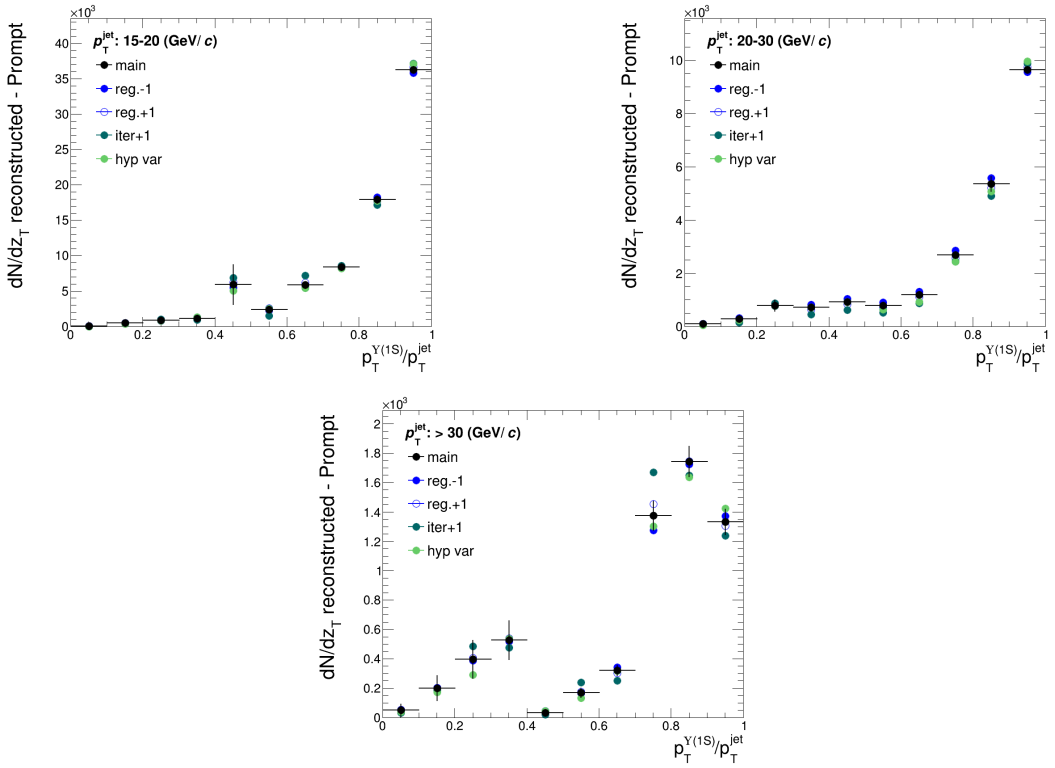

Figure 6.99: $\Upsilon(1S)$ unfolded distributions with various changes in the unfolding procedure *vs.* $z(\Upsilon)$. The spread of distributions shows the systematic uncertainty associated to the unfolded result. The plots are normalised as $\mathrm{d}N/\mathrm{d}z$.

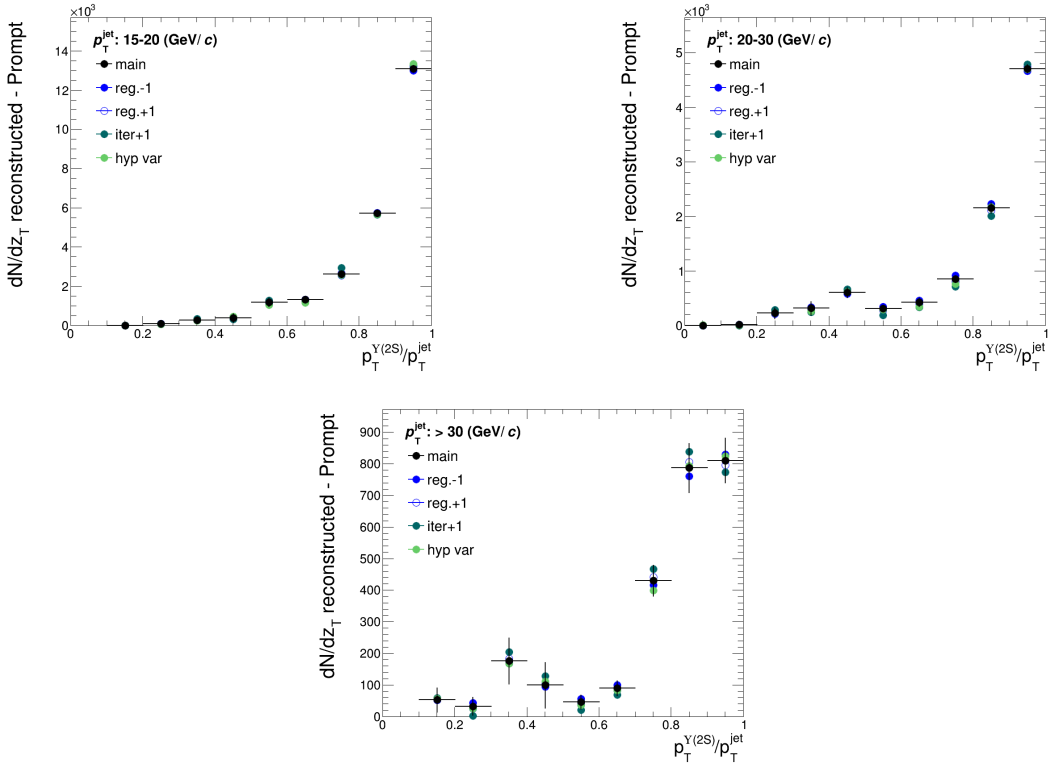

Figure 6.100: $\Upsilon(2S)$ unfolded distributions with various changes in the unfolding procedure *vs.* $z(\Upsilon)$. The spread of distributions shows the systematic uncertainty associated to the unfolded result. The plots are normalised as $\mathrm{d}N/\mathrm{d}z$.

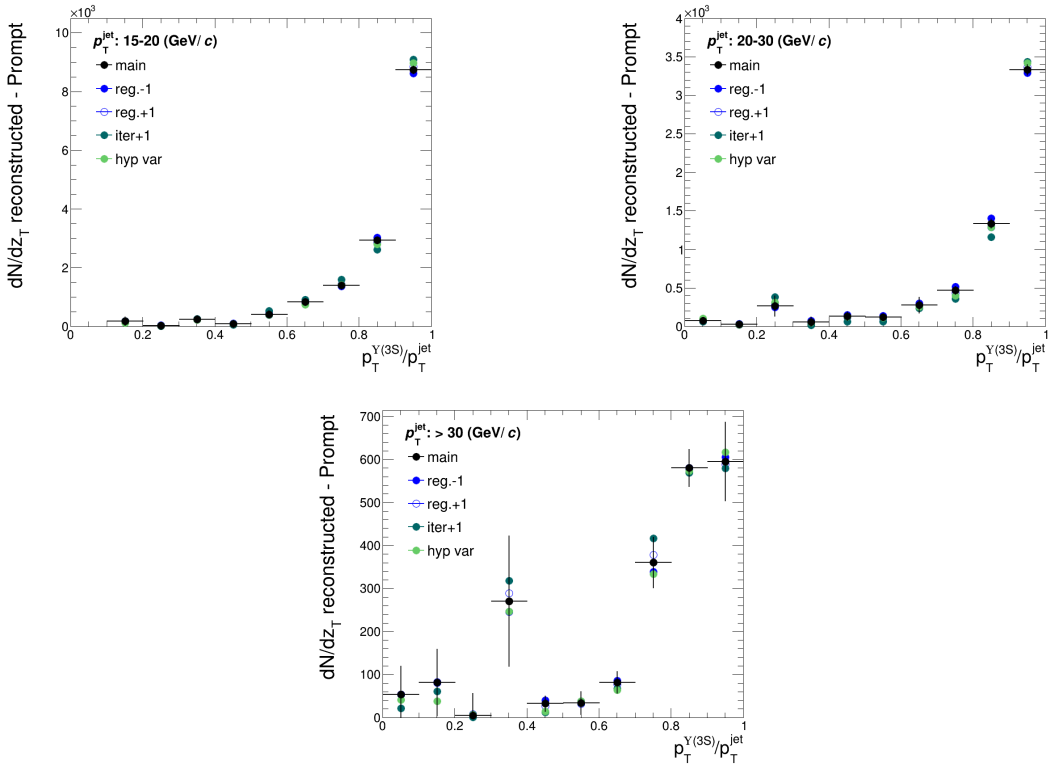

Figure 6.101: $\Upsilon(3S)$ unfolded distributions with various changes in the unfolding procedure *vs.* $z(\Upsilon)$. The spread of distributions shows the systematic uncertainty associated to the unfolded result. The plots are normalised as $\mathrm{d}N/\mathrm{d}z$.

6.5 Final results

The final results of the fragmentation functions of J/ψ, $\psi(2S)$, $\Upsilon(1S)$, $\Upsilon(2S)$ and $\Upsilon(3S)$ *vs.* z within fully reconstructed jets for several different $p_{\mathrm{T}}(\mathrm{jet})$ intervals are presented.

6.5.1 Final results for J/ψ

Figure 6.102 shows the results for the displaced fragmentation function of the J/ψ, which originate from b-decays. The errors displayed in the distributions are the statistical uncertainty (black), the systematic from the efficiency correction (blue box), and the systematic from the unfolding procedure (blue shaded area). The distribution is relatively stable with $p_{\mathrm{T}}(\mathrm{jet}) > 15\,\mathrm{GeV}$, with a peak around $z(J/\psi) \simeq 0.5$. This is consistent within systematic errors with the previous LHCb result published in 2017, shown in fig. 6.104.

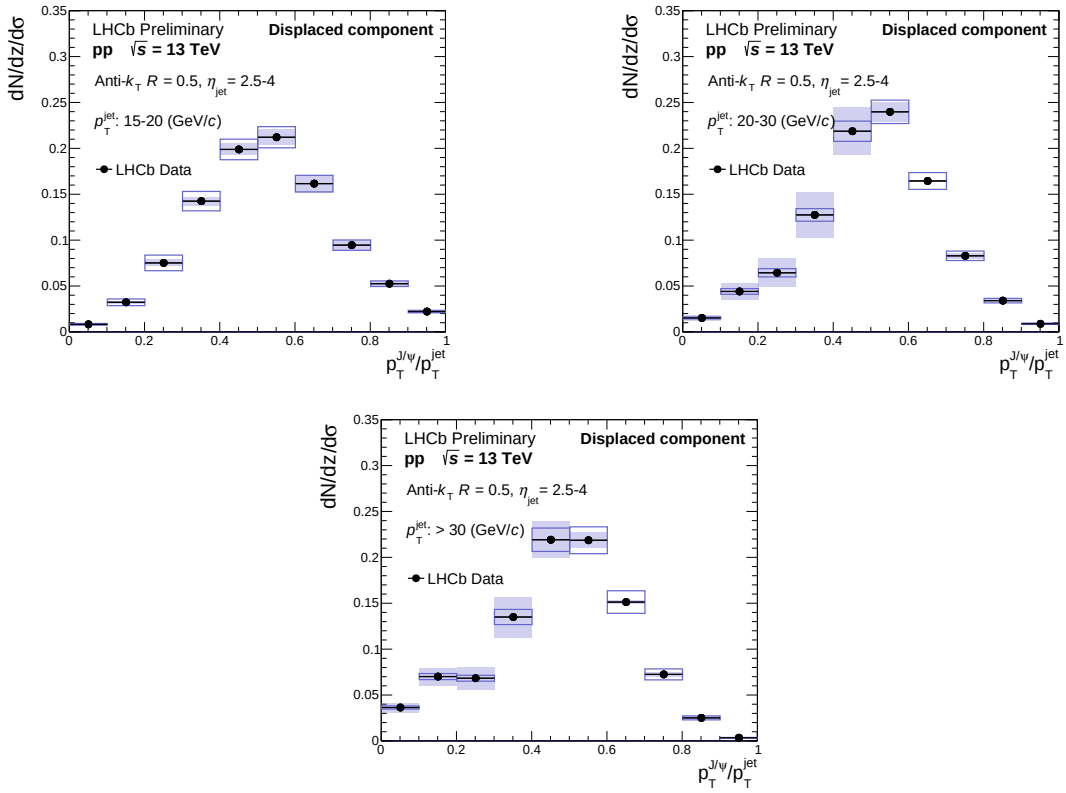

Figure 6.102: Final normalised cross section distributions for displaced J/ψ's *vs.* $z(J/\psi)$ in different $p_{\mathrm{T}}(\mathrm{jet})$ ranges. The plots are normalised as $\mathrm{d}N/\mathrm{d}z/\mathrm{d}\sigma$.

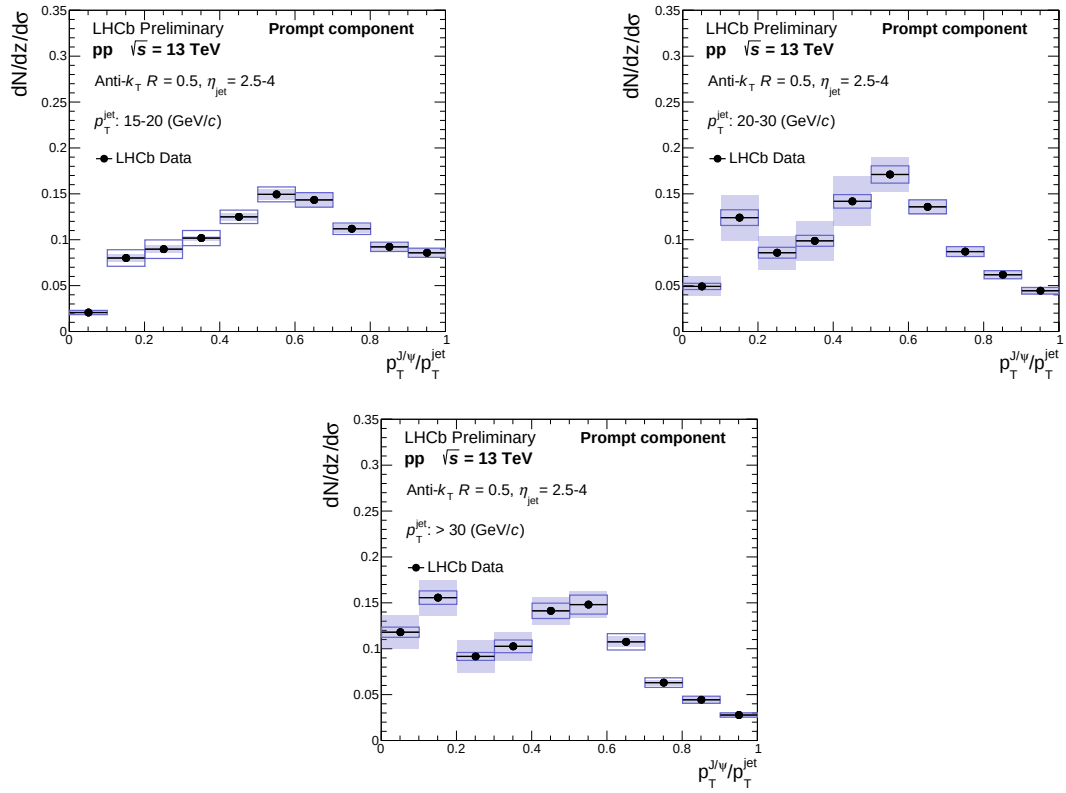

Figure 6.103: Final normalised cross section distributions for prompt J/ψ's *vs.* $z(J/\psi)$ in different $p_{\mathrm{T}}(\mathrm{jet})$ ranges. The plots are normalised as $\mathrm{d}N/\mathrm{d}z/\mathrm{d}\sigma$.

Figure 6.103 shows the fragmentation results for prompt J/ψ's, where the J/ψ's are produced at or very close to the collision vertex. The distribution has a peak, as for the displaced case, at $z(J/\psi) \simeq 0.5$. As $p_{\mathrm{T}}(\mathrm{jet})$ increases, $z(J/\psi)$ shifts to lower values. This result is consistent within systematic errors to the previous LHCb result published in 2017, shown in fig. 6.104, where there is not an isolated peak at $z(J/\psi) \simeq 1.0$ as predicted by PYTHIA 8 for $p_{\mathrm{T}}(\mathrm{jet}) > 20\,\mathrm{GeV}$.

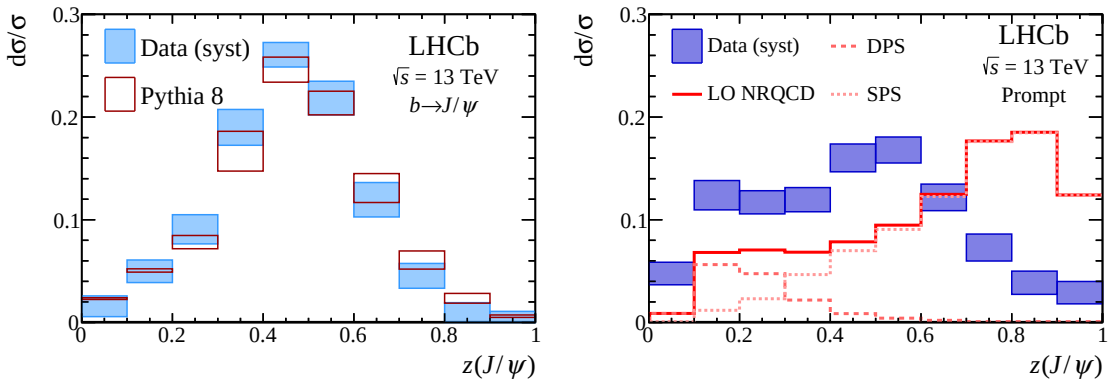

(a) Displaced component. (b) Prompt component.

Figure 6.104: Normalised prompt and b decay *vs.* $z(J/\psi)$ distributions from Ref. [12] for $p_{\mathrm{T}}(\mathrm{jet}) > 20\,\mathrm{GeV}$.

6.5.2 Final results for $\psi(2S)$

Figure 6.102 shows the results for the displaced fragmentation function of the $\psi(2S)$, where like for the J/ψ there is a central peak, expect it is shifted upwards to $z(\psi(2S)) \simeq 0.6$. This shift is most likely due to the heavier mass of the $\psi(2S)$ in comparison to the J/ψ, which shares more of the jet's energy. This is fairly consistent for all $p_{\mathrm{T}}(\mathrm{jet})$ ranges above 15 GeV. The statistical errors are larger for the $\psi(2S)$ than the J/ψ, because of the smaller production cross section and decay to the dimuon channel. Figure 6.106 shows the fragmentation results for the prompt $\psi(2S)$. This exhibits similar behaviour as for the J/ψ, with a central peak at $z(\psi(2S)) \simeq 0.6$, and the distribution shifting to lower values of $z(\psi(2S))$ with $p_{\mathrm{T}}(\mathrm{jet})$. The fluctuations at low $z(\psi(2S))$ for both the displaced and prompt distributions are most likely due to statistical fluctuations in the mass plus lifetime fits due to the low purity of signal combined with lack of statistics.

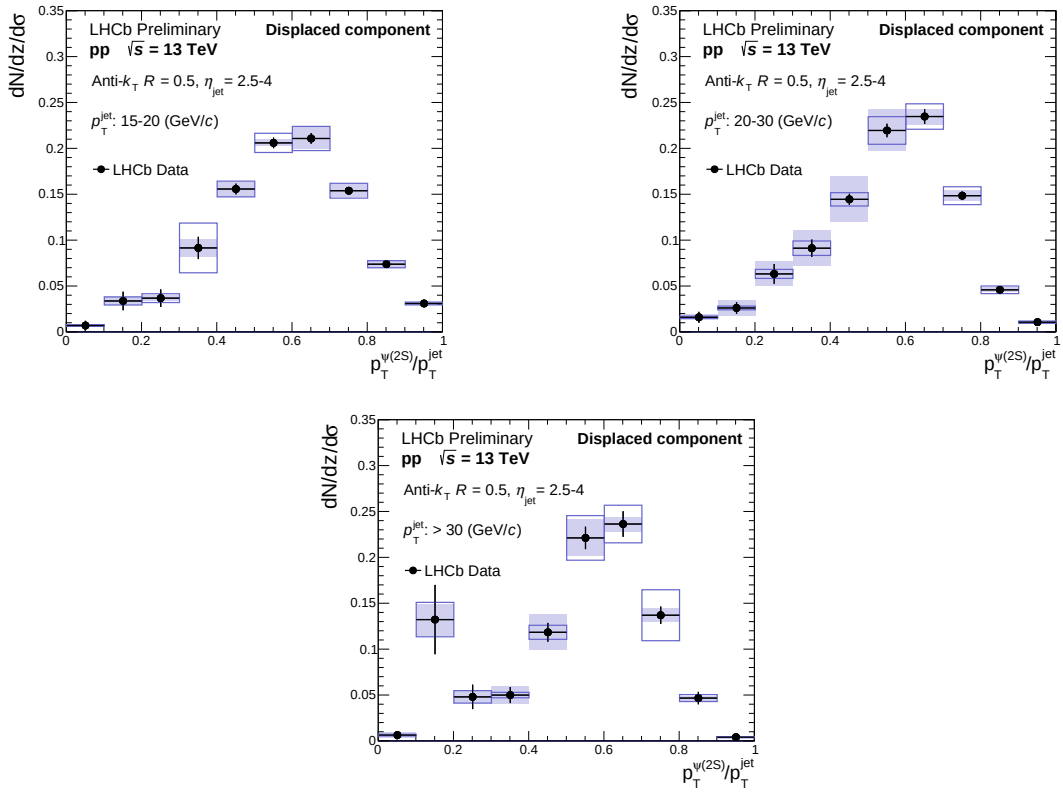

Figure 6.105: Final normalised cross section distributions for displaced $\psi(2S)$'s *vs.* $z(\psi(2S))$ in different $p_{\mathrm{T}}(\mathrm{jet})$ ranges. The plots are normalised as $\mathrm{d}N/\mathrm{d}z/\mathrm{d}\sigma$.

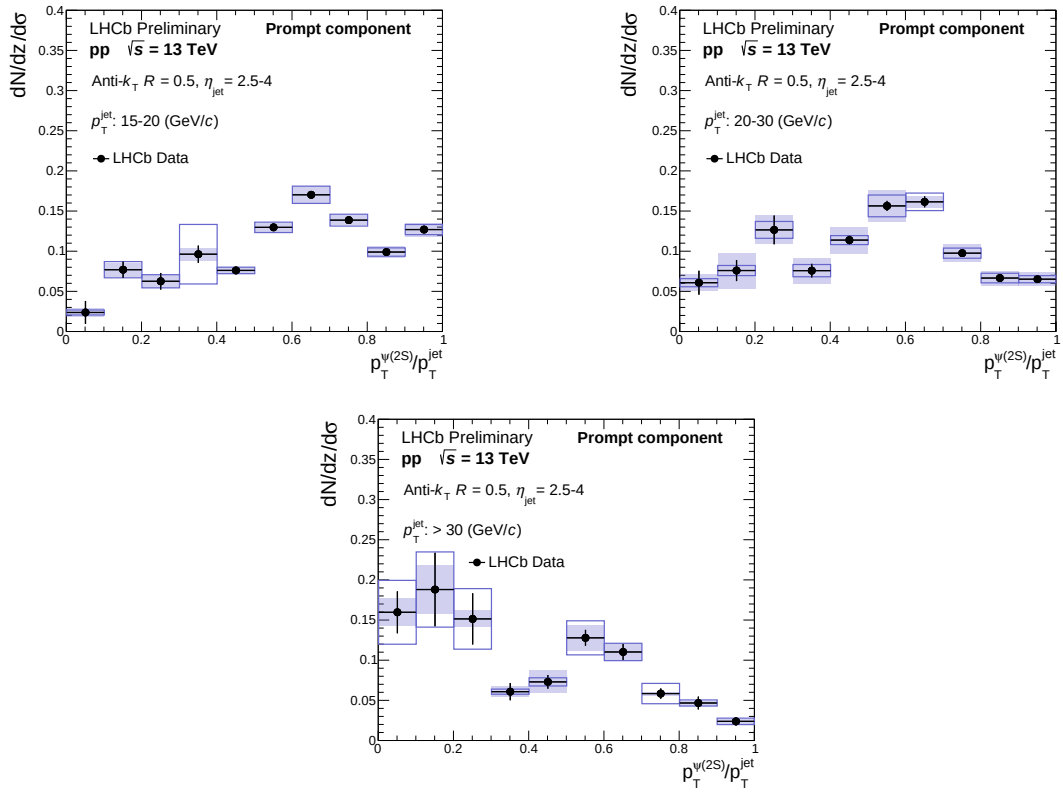

Figure 6.106: Final normalised cross section distributions for prompt $\psi(2S)$'s *vs.* $z(\psi(2S))$ in different $p_{\mathrm{T}}(\mathrm{jet})$ ranges. The plots are normalised as $\mathrm{d}N/\mathrm{d}z/\mathrm{d}\sigma$.

6.5.3 Final results for $\Upsilon(1S)$, $\Upsilon(2S)$ and $\Upsilon(3S)$

Figures 6.107 to 6.109 show the fragmentation results for the $\Upsilon(1S)$, $\Upsilon(2S)$ and $\Upsilon(3S)$ respectively for different $p_{\mathrm{T}}(\mathrm{jet})$ ranges. The results are very different to those of the J/ψ and $\psi(2S)$, with an isolated peak at $z(\Upsilon) \simeq 1$ that starts to shift to lower $z(\Upsilon)$ at higher $p_{\mathrm{T}}(\mathrm{jet})$ values. The peak at $z(\Upsilon) \simeq 1$ becomes more isolated the heavier the Υ particle. This is possibly because the heavier mass Υ's share more of the jet's energy, and hence have a larger $z(\Upsilon)$ value. A peak at $z(\Upsilon) \simeq 0.3$ is present for all $p_{\mathrm{T}}(\mathrm{jet}) > 30\,\mathrm{GeV}$ bins and may be either from a statistical fluctuation or some other underlying production mechanism such as double-parton scattering or from fragmentation processes.

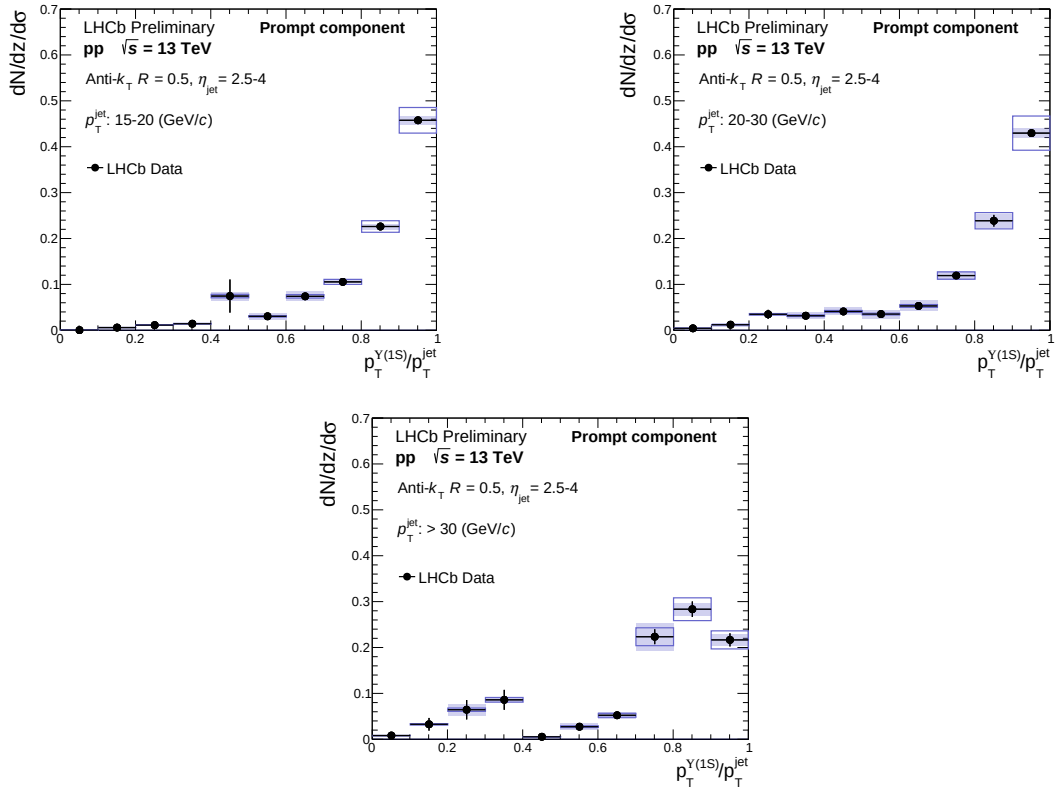

Figure 6.107: Final normalised cross section distributions for $\Upsilon(1S)$ *vs.* $z(\Upsilon)$ in different $p_{\mathrm{T}}(\mathrm{jet})$ ranges. The plots are normalised as $\mathrm{d}N/\mathrm{d}z/\mathrm{d}\sigma$.

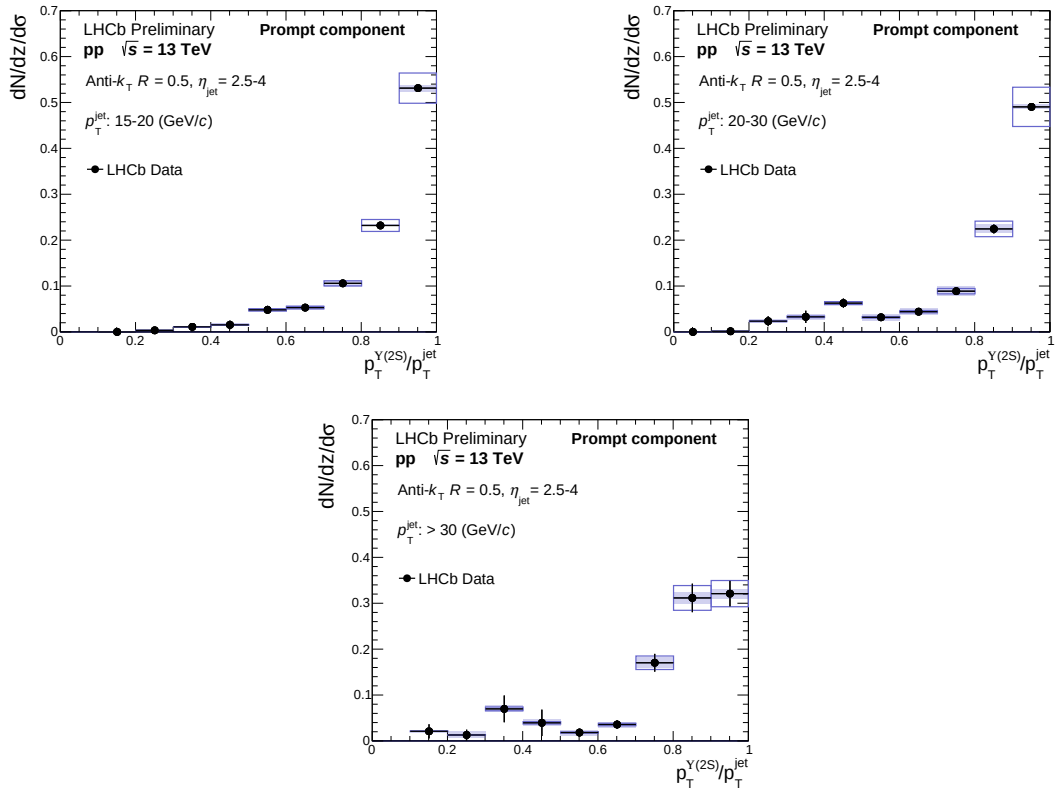

Figure 6.108: Final normalised cross section distributions for displaced $\Upsilon(2S)$'s *vs.* $z(\Upsilon)$ in different $p_{\mathrm{T}}(\mathrm{jet})$ ranges. The plots are normalised as $\mathrm{d}N/\mathrm{d}z/\mathrm{d}\sigma$.

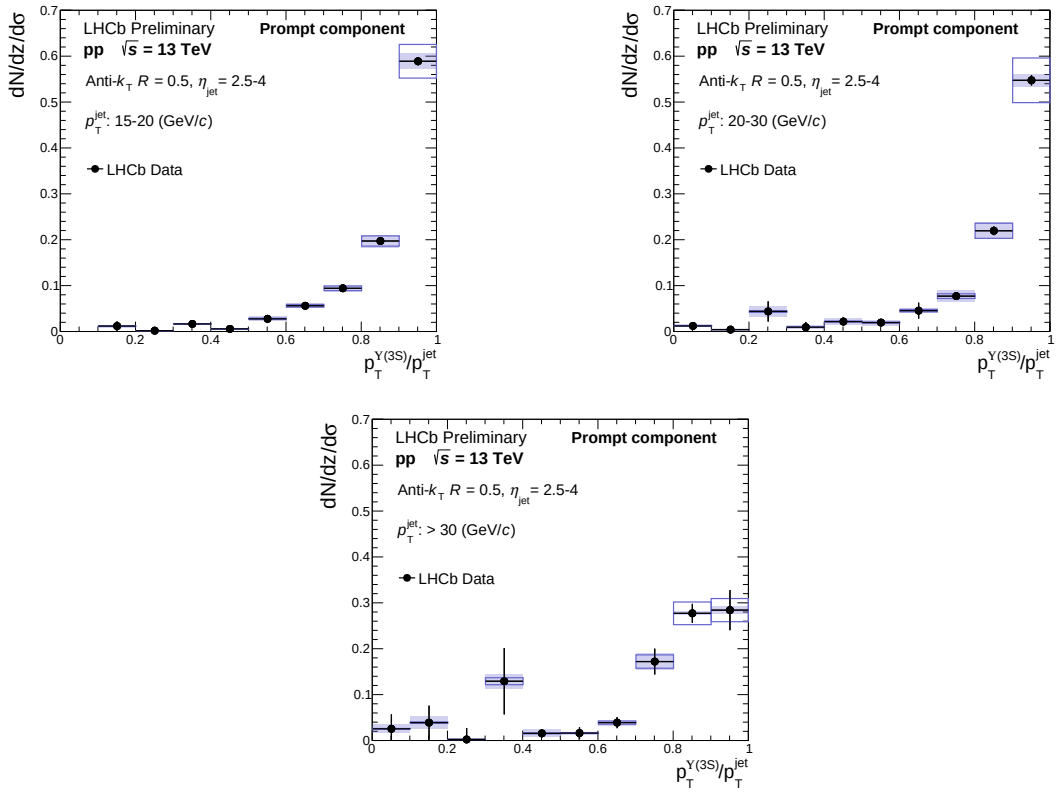

Figure 6.109: Final normalised cross section distributions for prompt $\Upsilon(3S)$'s *vs.* $z(\Upsilon)$ in different $p_{\mathrm{T}}(\mathrm{jet})$ ranges. The plots are normalised as $\mathrm{d}N/\mathrm{d}z/\mathrm{d}\sigma$.

6.5.4 Current theory predictions and discussion

The fragmentation results for all the different quarkonia results have been compared to current PYTHIA 8 MC predictions, *i.e.* through hard production only, for the $p_{\mathrm{T}}(\mathrm{jet})$ range, $20 < p_{\mathrm{T}}(\mathrm{jet}) < 30\,\mathrm{GeV}$. The comparisons for prompt and displaced J/ψ's are shown in fig. 6.110. The displaced component is consistent with data, as the gluon splitting $g \to b\bar{b}$ was not included in the generation, which would push the overall predicted distribution to lower $z(J/\psi)$ values. As observed in the 2017 LHCb analysis, the prompt MC prediction does not match data at all. The MC simulation includes contributions from feed-down from higher excited states such as the χ_{cJ} states, and also from double parton scattering (DPS). DPS results in the bump at $z(J/\psi) \simeq 0.15$. Similar results are exhibited for the $\psi(2S)$, where the displaced component is consistent with data without the $g \to b\bar{b}$ included. The prompt component is predicted to have an isolated peak at $z(\psi(2S)) \simeq 1.0$, in comparison to data which shows a central peak at $z(\psi(2S)) \simeq 0.6$. The $\psi(2S)$ MC prediction also includes DPS which results in the peak at $z(\psi(2S)) \simeq 0.15$. The $\psi(2S)$ MC prediction is more isolated than the J/ψ prediction, as there is negligible feed-down from higher excited states. The $z(\Upsilon)$ MC predictions also exhibit a more isolated peak the heavier the Υ particle. However, the predicted peak is still more isolated in all Υ's cases than is measured in data, where data shows some activity at low $z(\Upsilon)$. The Υ MC predictions also include DPS contributions.

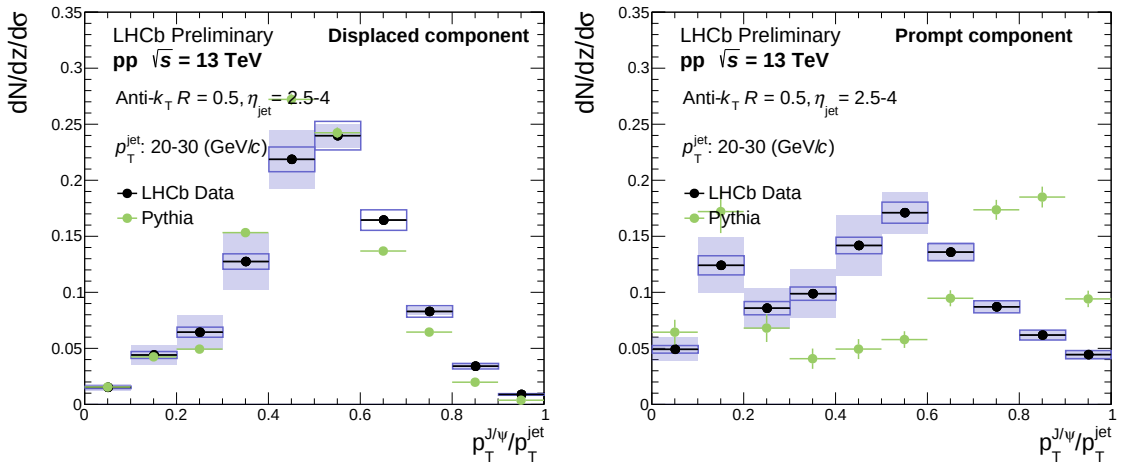

(a) Displaced component.

(b) Prompt component.

Figure 6.110: Final normalised cross sections for prompt and displaced J/ψ's *vs.* $z(J/\psi)$ with current PYTHIA 8 predictions, in $p_{\mathrm{T}}(\mathrm{jet})$ range of $20 < p_{\mathrm{T}}(\mathrm{jet}) < 30\,\mathrm{GeV}$. The plots are normalised as $\mathrm{d}N/\mathrm{d}z/\mathrm{d}\sigma$.

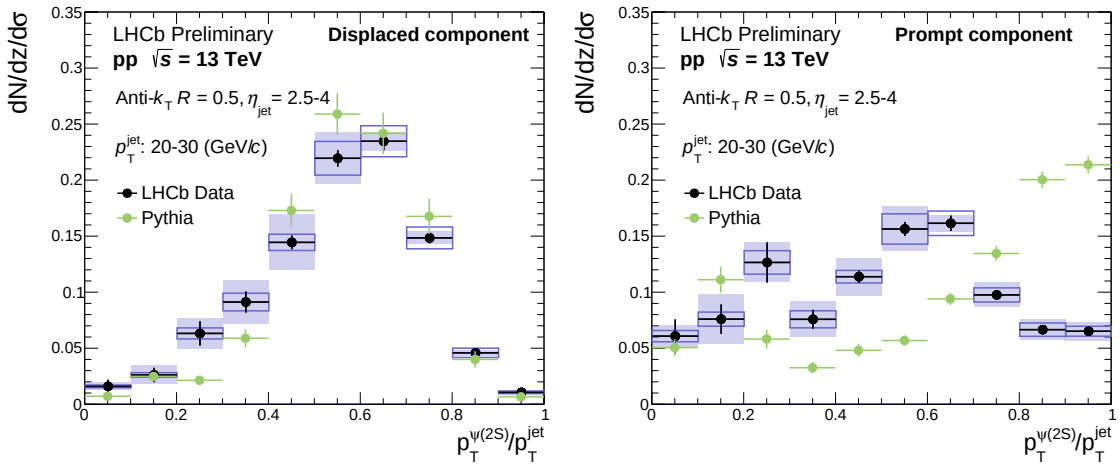

(a) Displaced component. (b) Prompt component.

Figure 6.111: Final normalised cross sections for prompt and displaced $\psi(2S)$'s *vs.* $z(\psi(2S))$ with current PYTHIA 8 predictions, in $p_{\mathrm{T}}(\mathrm{jet})$ range of $20 < p_{\mathrm{T}}(\mathrm{jet}) < 30\,\mathrm{GeV}$. The plots are normalised as $\mathrm{d}N/\mathrm{d}z/\mathrm{d}\sigma$.

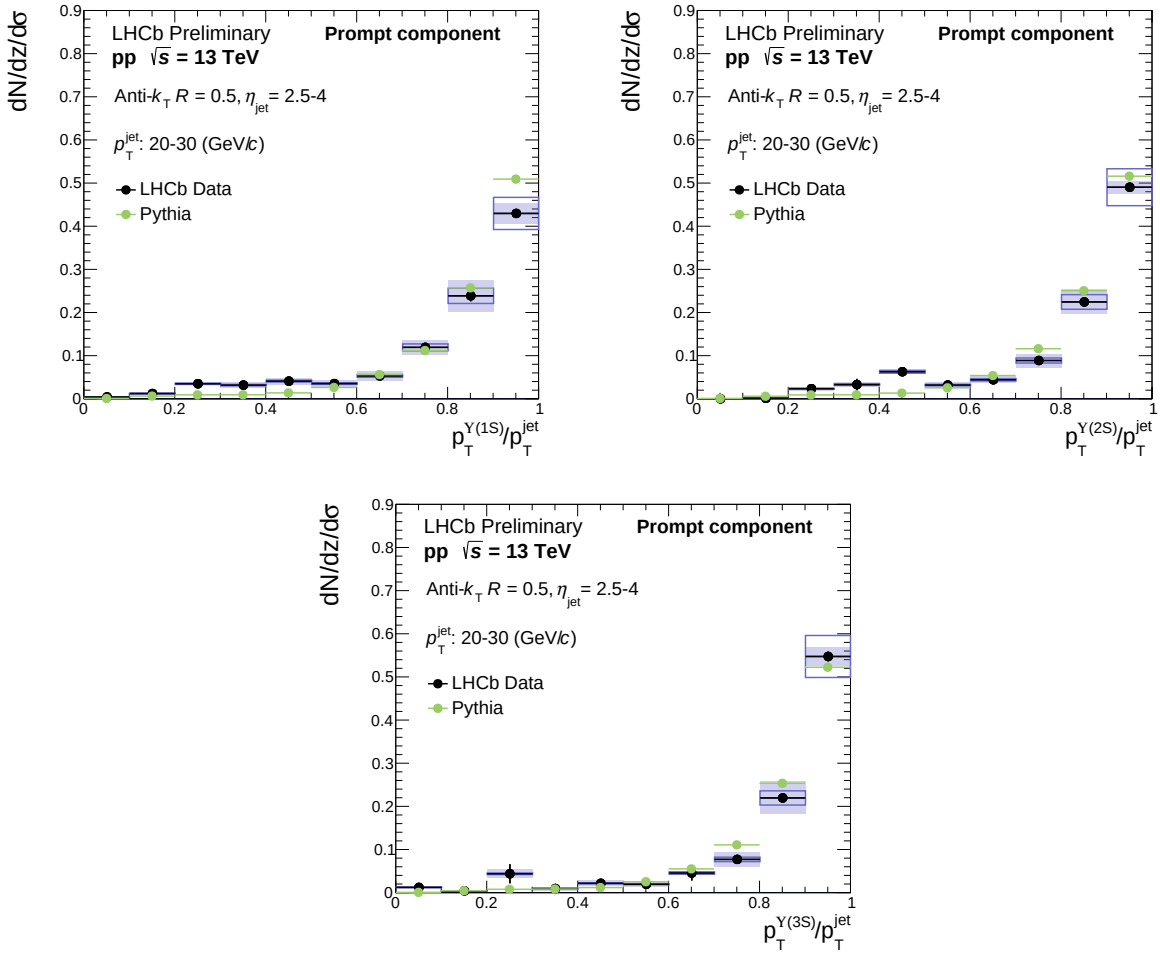

Figure 6.112: Final normalised cross section distributions for $\Upsilon(1S)$, $\Upsilon(2S)$ and $\Upsilon(3S)$ *vs.* $z(\Upsilon)$ with current PYTHIA 8 predictions, in $p_{\mathrm{T}}(\mathrm{jet})$ range of $20 < p_{\mathrm{T}}(\mathrm{jet}) < 30\,\mathrm{GeV}$. The plots are normalised as $\mathrm{d}N/\mathrm{d}z/\mathrm{d}\sigma$.

Overall, the displaced J/ψ and $\psi(2S)$, and the Υ's distributions are fairly consistent with PYTHIA 8 predictions, in contrast to the prompt J/ψ and $\psi(2S)$ which are not, and are a lot less isolated than predicted. This suggests there is a mechanism at play that is not modelled by PYTHIA 8. As explored in chapter 3, this could be the NRQCD fragmentation model, which is incorporated into PYTHIA 8 as part of this thesis. Further predictions using this new model for the different quarkonia states is the subject of future work.

6.5.5 Future prospects

There are many potential measurements that could be explored, to further understand quarkonia production in more detail. An example is to repeat these analyses with more statistics, which could lead to measurements with finer binning. Another is to repeat the measurements with updated full simulation using the PYTHIA 8 predictions discussed in chapter 3, to try and reduce the systematic due to the unfolding. Along with this, the hyperon fractions used for unfolding the prompt J/ψ and $\psi(2S)$ dimuon channels needs to be explored in more detail.

Other measurements could be to not only measure the jet fragmentation as a function of $z(Q)$, but also as a function of the jet radius, ΔR, and p_{T} of the quarkonia in question. These can give more hints to the fragmentation mechanisms involved in quarkonia production. Triple differentials of any of these two variables, along with $p_{\mathrm{T}}(\mathrm{jet})$ could also provide valuable information. However, this requires a more sophisticated unfolding procedure, which will need to be further explored.

A more detailed investigation into the feed-down contribution from χ_{cJ} states, for example in the case of prompt J/ψ's, would also be of interest, by measuring their fragmentation functions. Also, a measurement of the polarisation of the quarkonia *vs.* $z(Q)$ would give further insight into the different contributions from colour singlet production, colour octet production and fragmentation. An analysis to measure the polarisation of the J/ψ *vs.* $z(J/\psi)$ with LHCb data has begun as part of this thesis work. However, this measurement is in preliminary stages, and is beyond the scope of inclusion in the main body of this thesis, but is briefly discussed in appendix E. Interesting measurements of tetraquark production in jets have been measured, and is the subject of the next chapter in this thesis.

CHAPTER 7

Tetraquark in jets measurements

The first exotic state, X(3872), was discovered by the Belle collaboration in 2003 with the $B^{\pm} \to K^{\pm}\pi^{+}\pi^{-}J/\psi$ decay channel with a significance of 10σ [126]. This is of interest due the fact it seems to contain four quarks $c\bar{u}\bar{c}u$. It can be thought of as a new tetraquark state, as shown in fig. 7.1. Or since its mass has been found close to the sum of masses of D^0 and $\bar{D}^{*0}$, it may be thought of as a molecule of these two states, as also shown in fig. 7.1.

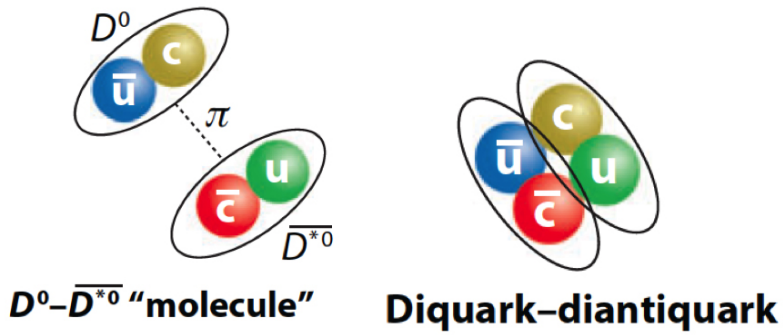

Figure 7.1: Molecular *vs.* tetraquark formation of the X(3872) [127].

To try and distinguish what this "particle" is, many observables have been measured. The LHCb collaboration has previously determined the quantum numbers of the X(3872) (J^{PC}=1^{++}) [128, 129] by its production in the $B^{+} \to$ X(3872)K^{+} decay channel. Its lineshape has also been studied as well as improving the precision of

its determined mass [130]. Various production mechanisms have been studied of the X(3872) [131–134], and LHCb has precisely studied the decay channels ($\psi(2S)$ γ) [135] and (J/ψ ω) [136]. The X(3872) production cross section relative to the $\psi(2S)$ as a function of p_{T} and rapidity in pp [137] and as a function of track multiplicity in pp and pPb have also been measured [138, 139]. However, even though all these variables have been measured, the debate still has not been settled [140–142].

Hence, this analysis is an expansion of the quarkonia production in jets analysis that was presented in the previous chapter and to previous X(3872) measurements provided by LHCb. This analysis will provide another variable of production through jet fragmentation, which should hopefully shed more light onto the production of this "particle".

7.1 Selection

For this analysis, the decay channel of X(3872) $\rightarrow J/\psi\,\pi\pi$ is used, as it has already been measured in previous analyses, and has been found to have a relatively large branching fraction (BF) of $(3.8 \pm 1.2)\%$. The $\psi(2S)$ also decays via this channel with a branching fraction (BF) of $(34.68 \pm 0.30)\%$, which is even larger than the $\psi(2S) \rightarrow \mu\mu$ channel of $(0.80 \pm 0.06)\%$ [20]. It is also roughly in the same mass range as the X(3872). Hence this is used as a control channel for the X(3872) analysis. It can also be used to cross check the fragmentation results for $\psi(2S) \rightarrow \mu\mu$ presented in the previous chapter. This analysis also uses the 2016 Turbo data set at $\sqrt{s}$ =13 TeV, like for the quarkonia analysis, with a total luminosity of $1.64\,\mathrm{fb}^{-1}$. DaVinci v45r6 is used for the data selection.

7.1.1 Meson and jet selection

To select $\psi(2S)$ and X(3872) candidates, J/ψ's are used as the triggered candidate. Pions which happen to be close to the J/ψ in space then combine to form the overall $\psi(2S)$ or X(3872) candidate. To simplify the naming a $\psi(2S)$ or X(3872) candidate shall be called a tag candidate. The triggers used are the same as the J/ψ in jets analysis (L0DiMuon+Hlt1DiMuonHighMass+Hlt2DiMuonJPsiTurbo), and the pions are taken from the StdAllNoPIDPions container, which contains all the pions reconstructed in an event. Several selection criteria are placed on the pions

and the tag candidate before they are fed into the particle flow algorithm, including constraining the mass using `DecayTreeFitter` [143]. Table 7.1 summarises the fiducial limits in which the results are presented.

particle	cut variable	value
π	p_{T}	$> 0.5\,\mathrm{GeV}$
π	p	$> 3\,\mathrm{GeV}$
μ	p_{T}	$> 0.5\,\mathrm{GeV}$
μ	p	$> 6\,\mathrm{GeV}$
Tag	p_{T}	$> 2\,\mathrm{GeV}$
Tag	η	2-4.5
Jet	η	2.5-4
Jet	constituents	> 1
Jet	p_{T}	$> 5\,\mathrm{GeV}$

Table 7.1: Fiducial Selection of the analysis. The signal loss due to these limitations is not corrected for.

particle	cut variable	value
π	TRCHI2DOF	< 3
π	TRGHOSTPROB	< 0.3
π	ProbNNpi	> 0.7
μ	IsMuon	True
μ	PIDmu	> 1
μ	TRCHI2DOF	< 4
J/ψ	$\sqrt{p_T(\mu_1)p_T(\mu_2)}$	$\sim> 324\,\mathrm{MeV}$
J/ψ	decay vtx χ^2	< 25
J/ψ	$\mathrm{DOCA}_{\mu\mu}$	$< 0.2\,\mathrm{mm}$
J/ψ	$\mathrm{mass}_{\mu\mu}$	$\mathrm{M} < 2900\,\mathrm{MeV}$
J/ψ	$\lvert\mathrm{mass}_{\mu\mu}$ - $\mathrm{mass}_{J/\psi}\rvert$	$< 120\,\mathrm{MeV}$
Tag	mass_{raw}	$\mathrm{M} < 4100\,\mathrm{MeV}$
Tag	mass_{fitted}	3635-3730 MeV || 3830-3920 MeV
Tag	$\mathrm{DOCA}_{(1,2\,\|\|\,2,3\,\|\|\,1,3)}$	$< 0.5\,\mathrm{mm}$
X(3872)-candidate	Q-value (M_{tag}-$\mathrm{M}_{J/\psi}$-$\mathrm{M}_{\pi\pi}$)	$< 150\,\mathrm{MeV}$
Global	N_{SPD}	< 900
Global	N_{PV}	$== 1$

Table 7.2: Analysis selection to increase signal-to-background in the mass spectrum. The majority of variables are defined in table 6.2, with the exception of TRGHOSTPROB is the probability that the track is a ghost, *i.e.* a fake track. ProbNNpi is a PID variable for the pion. mass_{raw} is the raw mass of the tag (di-muon di-pion) candidate, and mass_{fitted} is the refitted mass of the tag. $\mathrm{DOCA}_{(1,2\,\|\|\,2,3\,\|\|\,1,3)}$ is the distance of closest approach between the four decay products.

The second category of cuts are the analysis selection cuts that are used to increase

the signal to background ratio for a better fit of the yield in the mass spectrum. The loss of signal due to these selections are again corrected for, using efficiency maps already introduced in section 6.2 and additional maps due to the selection of pions for example, which will be discussed in section 7.2. All analysis selection cuts are listed in table 7.2. Those not including the trigger cuts are shown in table 7.3.

particle	cut variable	value
π	TRCHI2DOF	<3
π	TRGHOSTPROB	<0.3
π	ProbNNpi	>0.7
J/ψ	L0 && HLT1 && HLT2	True
Tag	mass_{raw}	$\text{M} < 4100\,\text{MeV}$
Tag	mass_{fitted}	3635-3730 MeV || 3830-3920 MeV
Tag	$\text{DOCA}_{(1,2\,\|\|\,2,3\,\|\|\,1,3)}$	$< 0.5\,\text{mm}$
X(3872)-candidate	Q-value (M_{tag}-$\text{M}_{J/\psi}$-$\text{M}_{\pi\pi}$)	$< 150\,\text{MeV}$
Global	N_{PV}	$== 1$

Table 7.3: Selection criteria when everything is included in trigger selection.

Once a tag candidate fulfills all these selection requirements, like for the quarkonia analysis, it is fed into the particle flow algorithm as a single particle while the three decay products are removed. However, in this case multiple J/$\psi\pi\pi$ combinations can fulfill all requirements, as there are lots of pions produced per event. Hence, only one candidate is randomly selected for the HLT jet builder. This is done to avoid introducing any bias on the selected J/$\psi\pi\pi$ combinations. However, the number of tag candidates that were rejected for each jet per event are saved to correct for this signal reduction. Again, the jets are build with the fast jet package Fastjet 3.3.2 [42, 144]. They are set to have a radius of R=0.5, using the anti-k_{T} algorithm and the p_{T} recombination scheme. If the jet p_{T} is greater than 5 GeV, the jet containing the tag is accepted for the analysis. The data are separated into the following bins:

A) p_{T}(jet) bins:

$$[5, 8, 11, 15, 20, 25, 30, 40, 60]\,\text{GeV for } \psi(2S),$$
$$[5, 8, 11, 15, 20, 25, 30, 40, 60]\,\text{GeV for X(3872)}$$

B) z_T bins:

$$[0, 0.3, 0.4, 0.5, 0.6, 0.7, 0.75, 0.8, 0.85, 0.9, 0.925, 0.95, 0.975, 1] \text{ for } \psi(2S),$$
$$[0.2, 0.5, 0.65, 0.75, 0.85, 0.95, 1] \text{ for X(3872)}$$

where z_T is the same variable as z. The signal yield extraction and separation into the prompt and displaced components follows very similar methods as with the quarkonia in jets analysis. In each of these bins the mass and lifetime distributions have been constructed.

7.1.2 Mass fits

For the mass distribution, the signal component is fit with a Double Crystal Ball (DCB) function for the $\psi(2S)$ and X(3872), like for the quarkonia in jets analysis. However, as there is also a hadronic component in the $J/\psi\pi\pi$ decay, a first order polynomial is used to fit the background component. For the DCB function here, n and α are taken from MC simulations.

In this manner, the mass distribution is fitted in different z_T ranges with different p_{T}(jet) ranges. The results of the raw yields are shown in figs. 7.2 and 7.3. The error in each bin is taken from the fit uncertainty of the signal yield from RooFit [113].

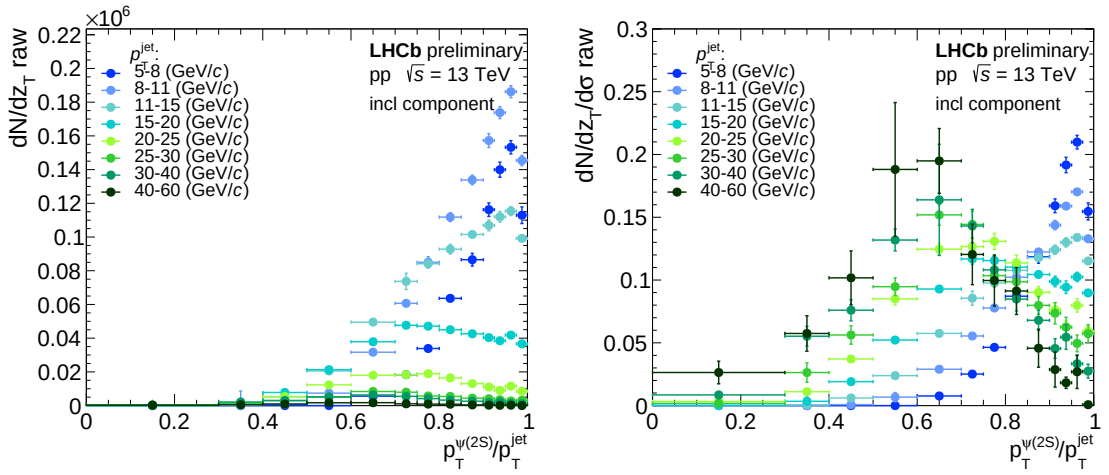

Figure 7.2: Raw inclusive yields for $\psi(2S)$ for each fitted bin. Left: absolute yield per z_T, right: normalised distributions to compare their shape.

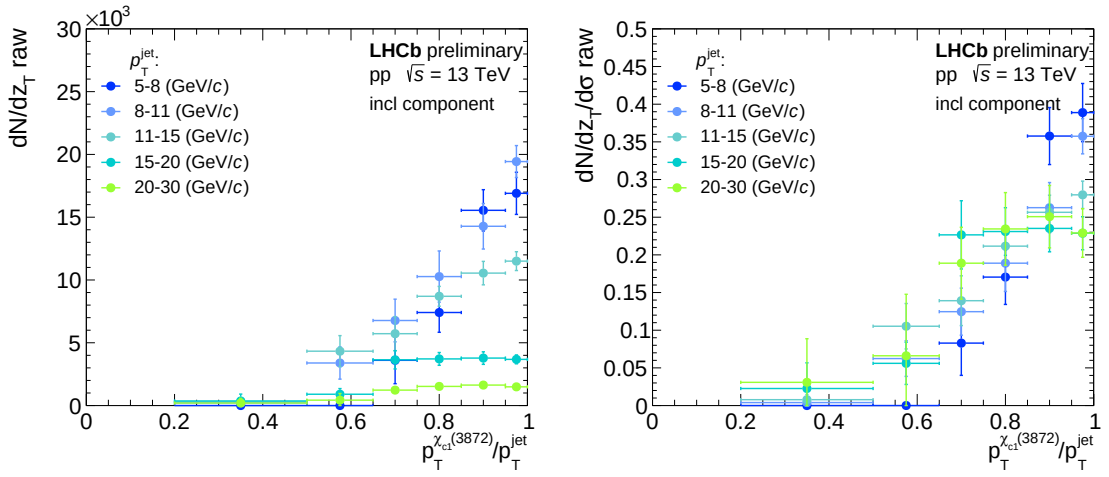

Figure 7.3: Raw inclusive yields for X(3872) for each fitted bin. Left: absolute yield per z_T, right: normalised distributions to compare their shape.

7.1.3 Separation of prompt and displaced signal component

In a final step of the yield extraction the inclusive yield is separated into prompt and displaced contributions. This follows the same method as the quarkonia in jets analysis. Figure 7.4 shows an example of a background lifetime fit to the side-band data sample and fig. 7.5 a signal lifetime fit for $\psi(2S)$ at p_{T}(jet) =15-20 GeV and z_T =0.6-0.75.

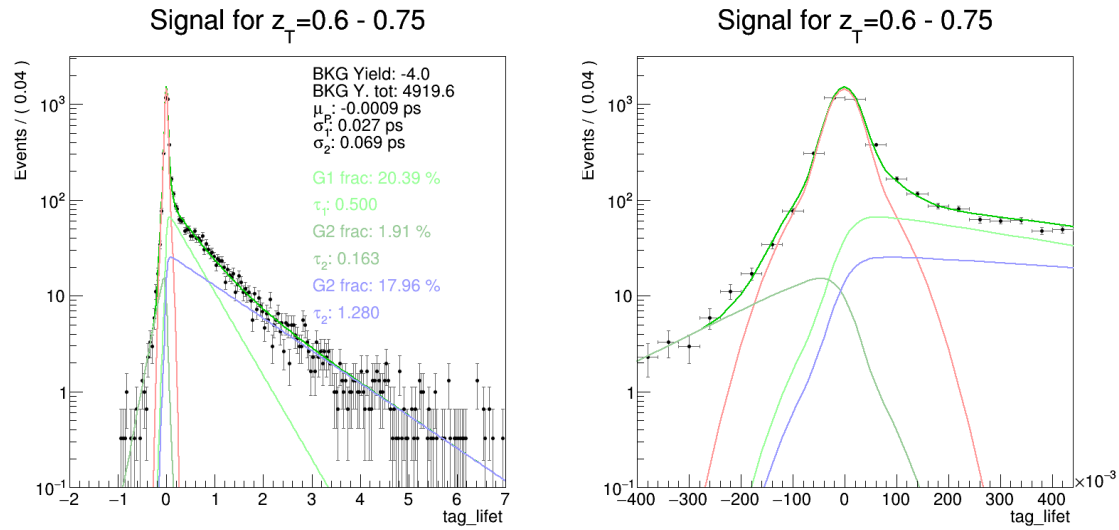

Figure 7.4: Pseudo-lifetime distribution for left and right side-bands of the $\psi(2S)$ mass distribution. For p_{T}(jet) =15-20 GeV and z_T =0.6-0.75. It consists of two negative exponentials and one positive exponential, each convolved with the same Double Gaussian PDF.

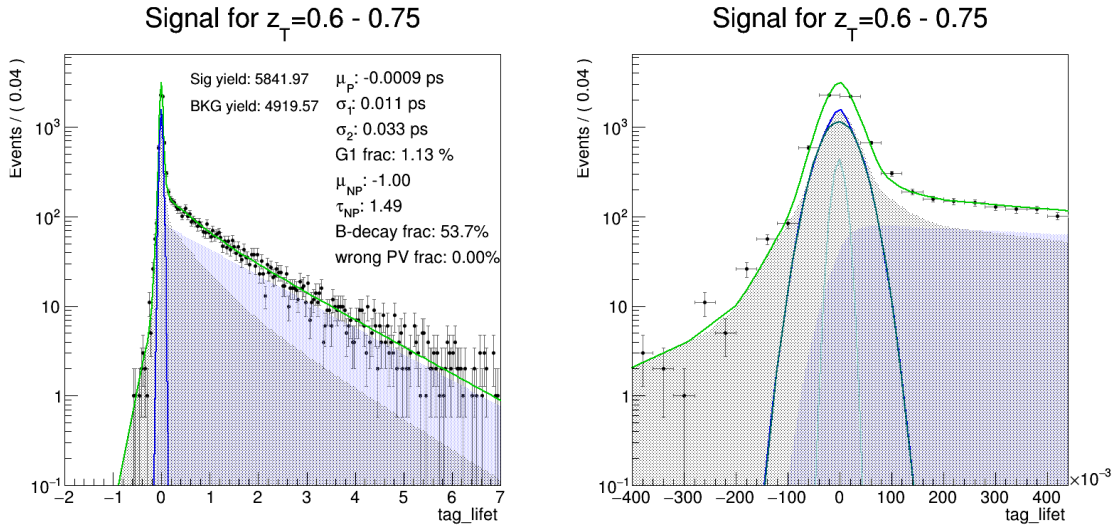

Figure 7.5: Pseudo-lifetime distribution for $\psi(2S)$ at p_{T}(jet) =15-20 GeV and z_T =0.6-0.75. The grey hashed area is the background contribution, which is an empirical fit to the sidebands of the mass fit, the blue curve describes the prompt component, which is a Double Gaussian, and the blue hashed describes the displaced component which is an exponential convolved with a Double Gaussian. The wrong PV component is too small to view. Left, shows the entire distribution, right shows the fit around the prompt component yield.

The main information extracted from these fits is the prompt and displaced fractions to the total yield. Displaced fractions *vs.* z_T in different p_{T}(jet) ranges for the $\psi(2S)$ and the X(3872) are summarised in fig. 7.6.

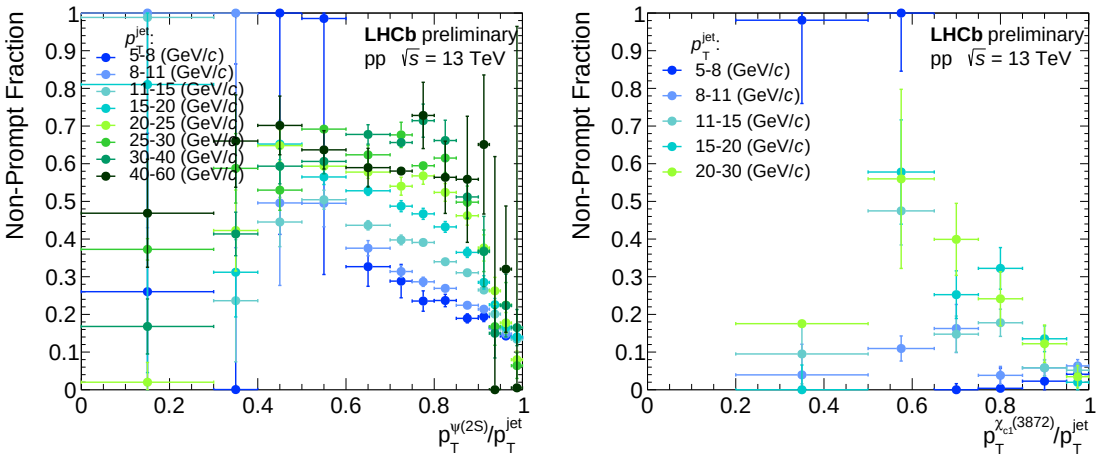

Figure 7.6: Result of the signal lifetime distribution fit resulting in the displaced fractions for the $\psi(2S)$ (left) and the X(3872) (right).

In the next section the signal is corrected for selection and reconstruction efficiency losses.

7.2 Efficiency Corrections

Many of the efficiency maps used to correct for signal losses were presented in section 6.2. However, additional selections were applied to build a $\psi(2S)$ and X(3872) candidate. The total efficiency, ϵ_{tot}, is again factorised into several sub-components. The efficiencies in black are taken from the quarkonia in jets analysis, and those in red are the additional efficiency maps that need to be obtained,

$$\epsilon_{tot} = \epsilon_{J/\psi} \cdot \epsilon_{\pi} \cdot \epsilon_{\psi(2S)/\mathrm{X}(3872)} \cdot \epsilon_{global} \tag{7.1}$$

where:

$$\epsilon_{J/\psi} = \epsilon_{reco}(\mu_1) \cdot \epsilon_{reco}(\mu_2) \cdot \epsilon_{trigger}, \tag{7.2}$$

$$\epsilon_{\pi} = \epsilon_{reco}(\pi_1) \cdot \epsilon_{selection}(\pi_1) \cdot \epsilon_{reco}(\pi_2) \cdot \epsilon_{selection}(\pi_2), \tag{7.3}$$

$$\epsilon_{\psi(2S)/\mathrm{X}(3872)} = \epsilon_{sel}(tag) \cdot \epsilon_{lifetime}, \tag{7.4}$$

$$\epsilon_{global} = \epsilon_{nPV} \cdot \epsilon_{nSPD} \cdot \epsilon_{Rnd}. \tag{7.5}$$

To calculate the efficiencies, again fiducial cuts are applied on the pions, muons and overall candidates which are shown in table 7.1. $\epsilon_{reco}(\pi)$ is the reconstruction efficiency of the pions. $\epsilon_{selection}(\pi)$ contains the additional PID and track quality cut selection efficiencies placed on the pions, shown in table 7.3. $\epsilon_{sel}(tag)$ are the selection cuts placed on the $\psi(2S)$/X(3872) tag candidate, shown in table 7.3. The efficiency due to randomly discarding a candidate inside a jet is ϵ_{Rnd}. These new efficiencies are shown in the following sections.

7.2.1 Pion efficiencies

7.2.1.1 Reconstruction efficiency for pions

The pion reconstruction efficiency is determined in the same fashion as the muon reconstruction efficiency. Firstly, an inclusive X(3872) $\rightarrow J/\psi\pi\pi$ sample was used with the StdAllNoPIDsPions container, and the resulting plot is shown in fig. 7.7a. This sample did not produce enough high p_{T} pions, so MC simulation of $Z \rightarrow \pi\pi$ was also used, shown in fig. 7.7b. These maps are then combined to produce the final pion reconstruction efficiency map, presented in fig. 7.8.

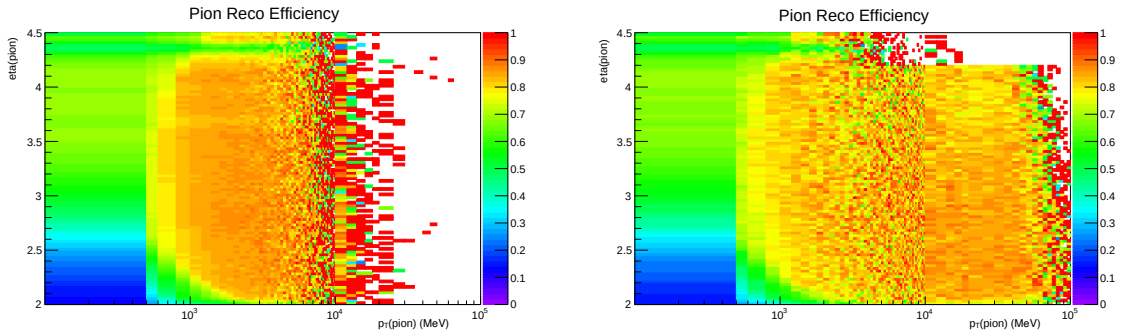

(a) X(3872) $\to J/\psi\pi\pi$ (b) $Z \to \pi\pi$

Figure 7.7: Pion reconstruction efficiency for 2016 MC (StdAllNoPIDsPions) in $\eta(\pi)$ *vs.* $p_T(\pi)$. Left shows MC of the process X(3872) $\to J/\psi\pi\pi$ and right shows MC of the process $Z \to \pi\pi$.

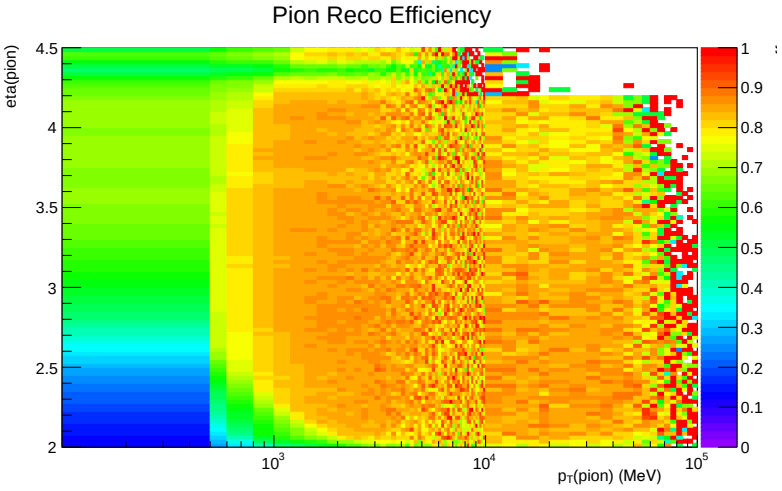

Figure 7.8: Combination of the two pion reconstruction efficiency maps shown in Fig. 7.7.

7.2.2 Selection efficiencies for pions

In this section, the calculation of $\epsilon_{selection}(\pi)$ is discussed. This contains three selection criteria: TRCHI2NDOF < 3 (the track fit quality χ^2 per degree of freedom), TRGHOSTPROB < 0.3 (the probability that the track is a ghost, *i.e.* a fake track) and ProbNNpi > 0.7 (the probability that the particle is a pion). This efficiency is applied on a per pion basis, with fiducial cuts applied. As this efficiency does not depend on any selection criteria placed before it, the data efficiency maps can be taken directly from PIDCalib2 [125], which is a LHCb software package that handles PID efficiencies. Figure 7.9 shows the combined selection efficiency of all three applied criterion on the pions. The criterion which has the largest effect is ProbNNpi > 0.7.

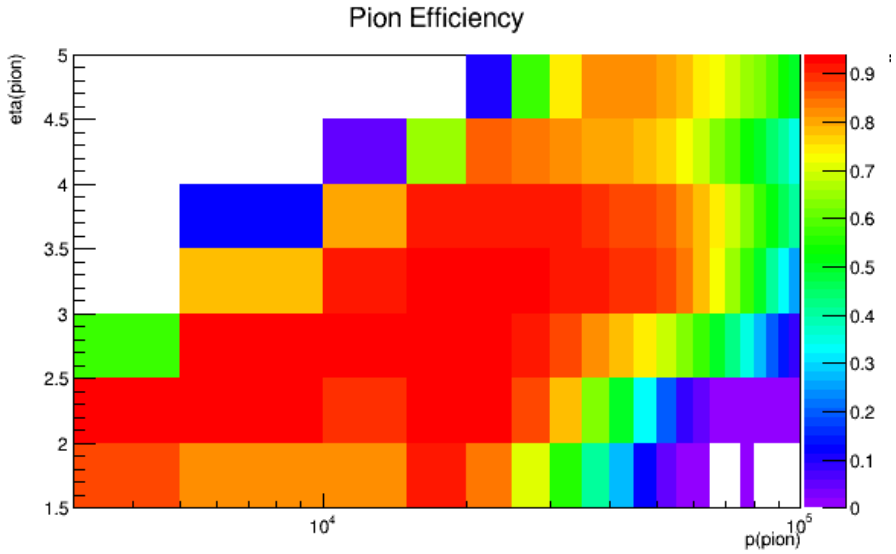

Figure 7.9: Combined pion selection efficiency taken from data using PIDCalib2 [125]. TRCHI2NDOF < 3 + TRACK_GHOSTPROB < 0.3 + ProbNNpi > 0.7.

7.2.3 Selection efficiencies for X(3872) and $\psi(2S)$

The only selections applied on the tags are the distance of closest approach selection (DOCA) for the three decay products, and in case of the X(3872) also a cut on the Q-value variable ($m_{\mathrm{X(3872)}} - m_{J/\psi} - m_{\pi\pi}$).

For the DOCA cut, the effect of applying this cut was tested on the signal and background yields. Figure 7.10 shows the mass distributions in different z_T bins, where the data in black is without a DOCA cut applied, and the data in red is with the DOCA cut applied.

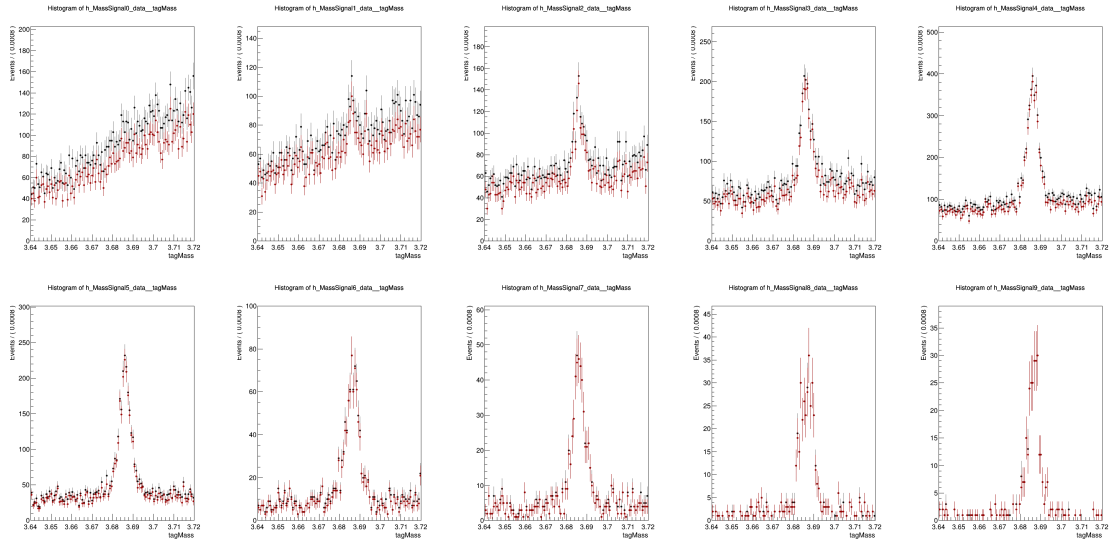

Figure 7.10: Mass spectra in different z_T bins for $p_{\mathrm{T}}(\mathrm{jet}) = 20\text{-}25\,\mathrm{GeV}$. Black data is without DOCA cut applied, red data is with DOCA cut applied

The DOCA cut mostly effects the background and not the signal. A detailed analysis was performed evaluating signal yield counts with and without the cut. The results were compatible with unity. Only the 5-10 GeV p_{T}(jet) bin showed a possible signal reduction of 1 %. Hence, it was decided to not apply any correction to the applied DOCA cut.

For the Q-value cut it was checked in simulation how many X(3872) were produced with a Q-value<150 MeV. Figure 7.11 shows the efficiency as a function of z_T for different p_{T}(jet) values. There is no dependence of the selection efficiency on any of the binning variables. Thus a global constant factor is used of,

$$\epsilon_{Q-value} = 0.8770 \pm 0.0018 \tag{7.6}$$

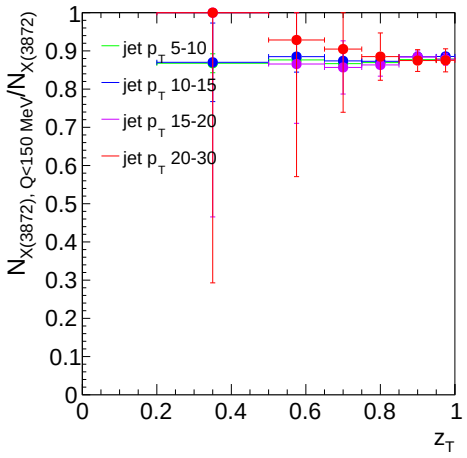

Figure 7.11: Efficiency of the X(3872) selection with Q-value cut $<$ 150 MeV.

7.2.4 Global event efficiencies

7.2.4.1 Random candidate rejection

The jets are built with the tag as a complete particle (not with the four decay tracks). In general there is only one J/ψ per event, but there are multiple pions which can combine with it. This sometimes leads to cases where there are multiple candidates in the allowed mass ranges that are fed into the jet finder. In order not to bias the analysis, in data, one candidate is randomly selected. This however throws out part of the statistics. This factor is independent of z_T but is evaluated for each p_{T}(jet) selection separately. The random selection correction factor used is depicted in figs. 7.12 and 7.13.

7.2.5 Applying the efficiency

To apply the efficiency correction, all factors shown in eq. (7.1) are applied on an event-by-event basis to the reconstructed data. The yield is compared before and after the event weighting to determine a correction factor in each p_{T}(jet) and z_T bin. If the weight factor is 0 the event is discarded in the numerator and the denominator. Figures 7.12 and 7.13 show all the effective correction factors for each bin in the analysis. The total corrections for each p_{T}(jet) range for the $\psi(2S)$ and X(3872) are shown in fig. 7.14.

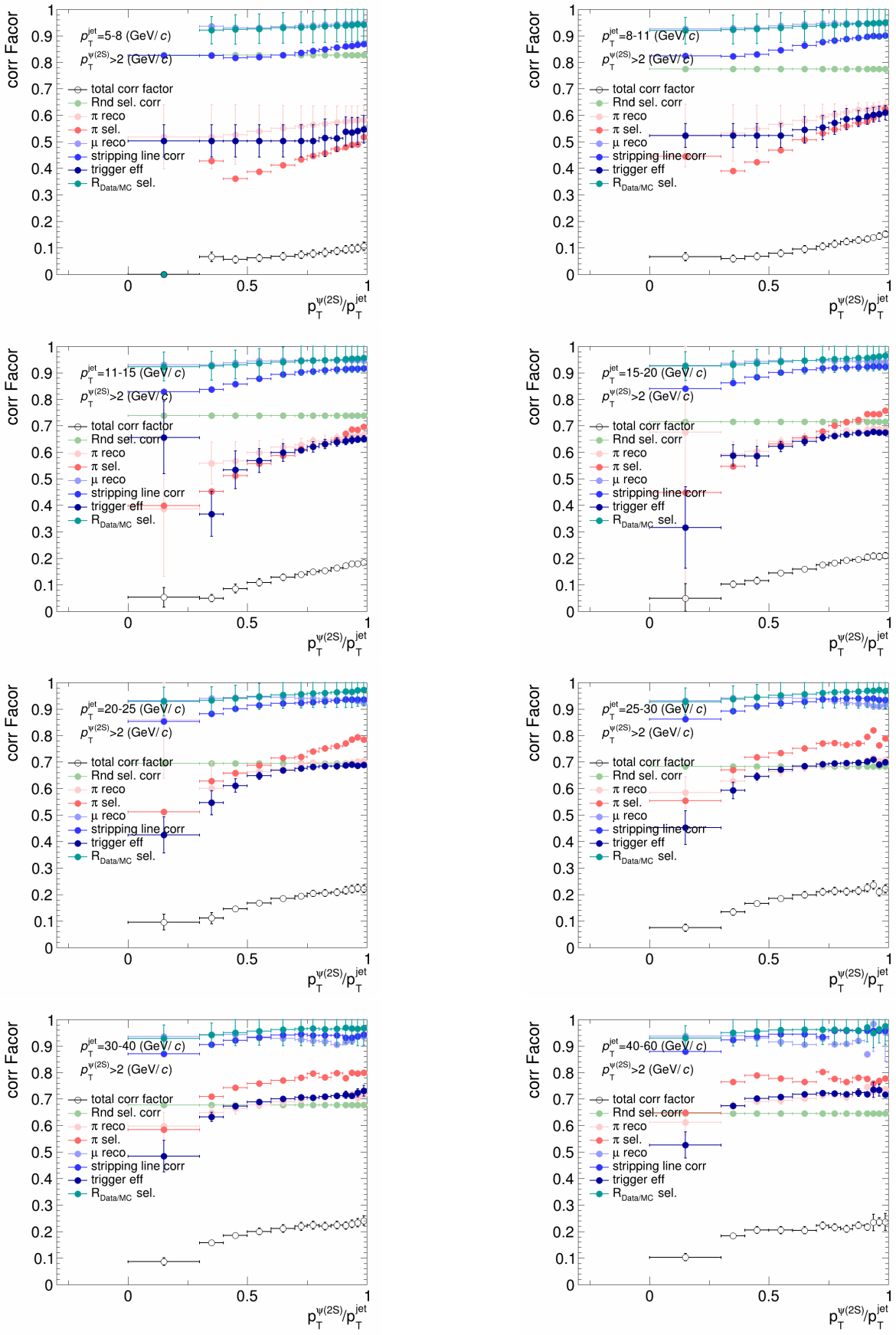

Figure 7.12: Total correction factors as a function of z_t for $\psi(2S)$ in all $p_{\mathrm{T}}(\mathrm{jet})$ bins.

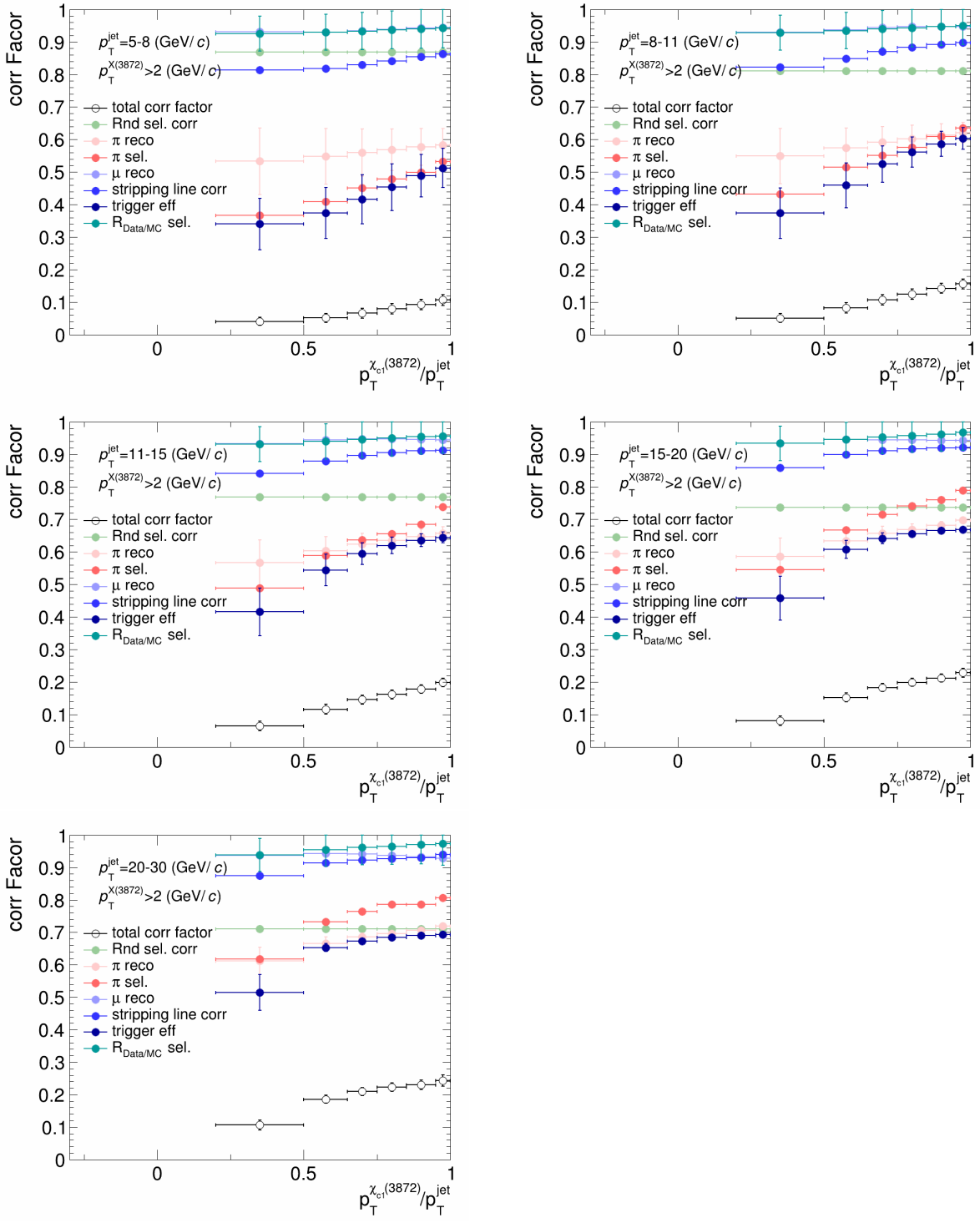

Figure 7.13: Total correction factors as a function of z_T for X(3872) in all p_{T}(jet) bins.

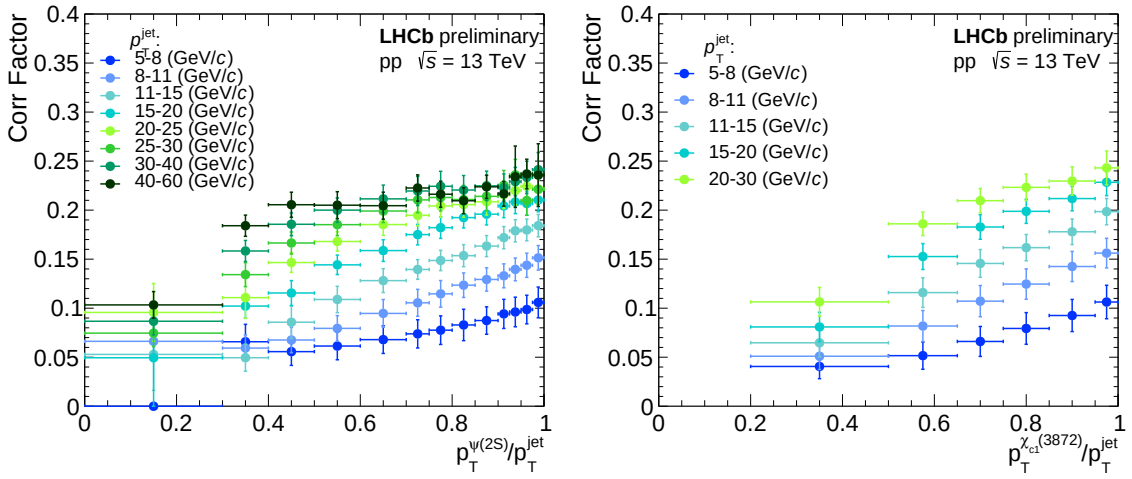

Figure 7.14: Total correction factors for p_{T}(jet)-z_T binning for $\psi(2S)$ and X(3872). These correction factors are applied to the inclusive raw yield distributions in figs. 7.2 and 7.3. These are shown in figs. 7.15 and 7.16.

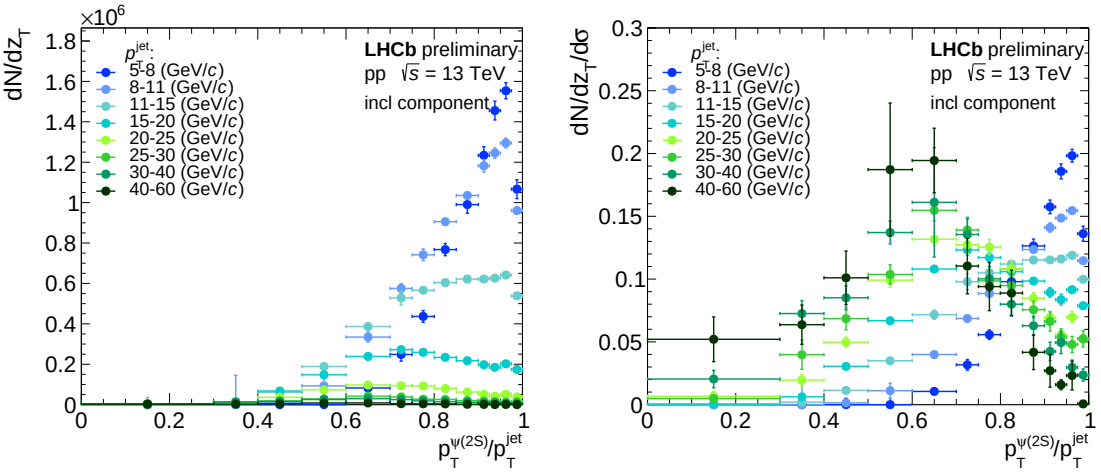

Figure 7.15: Corrected inclusive yields for $\psi(2S)$ for each fitted bin. Left: absolute yield per z_T, right: normalised distributions to compare their shape.

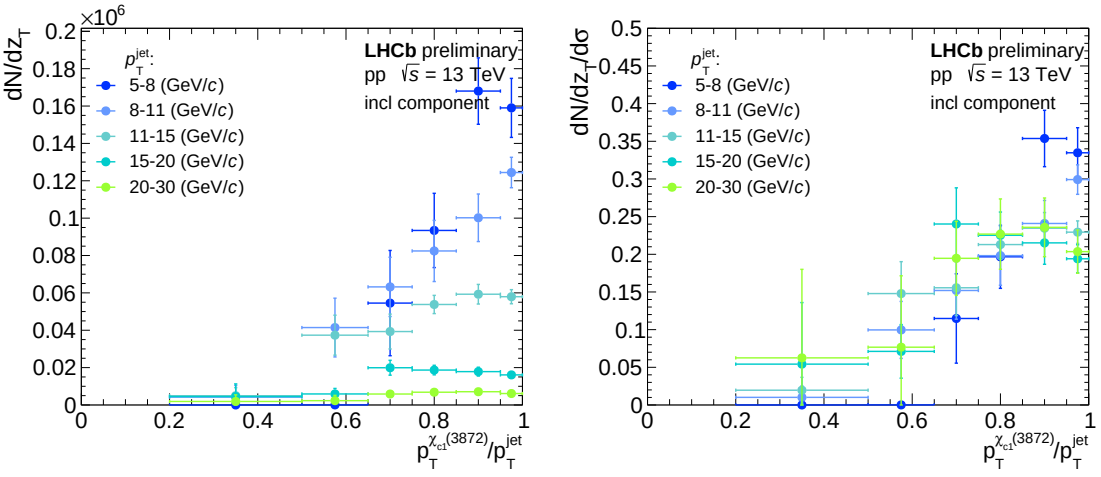

Figure 7.16: Corrected inclusive yields for X(3872) for each fitted bin. Left: absolute yield per z_T, right: normalised distributions to compare their shape.

These distributions are then split into the prompt and non-prompt components. These are shown in figs. 7.17 and 7.18.

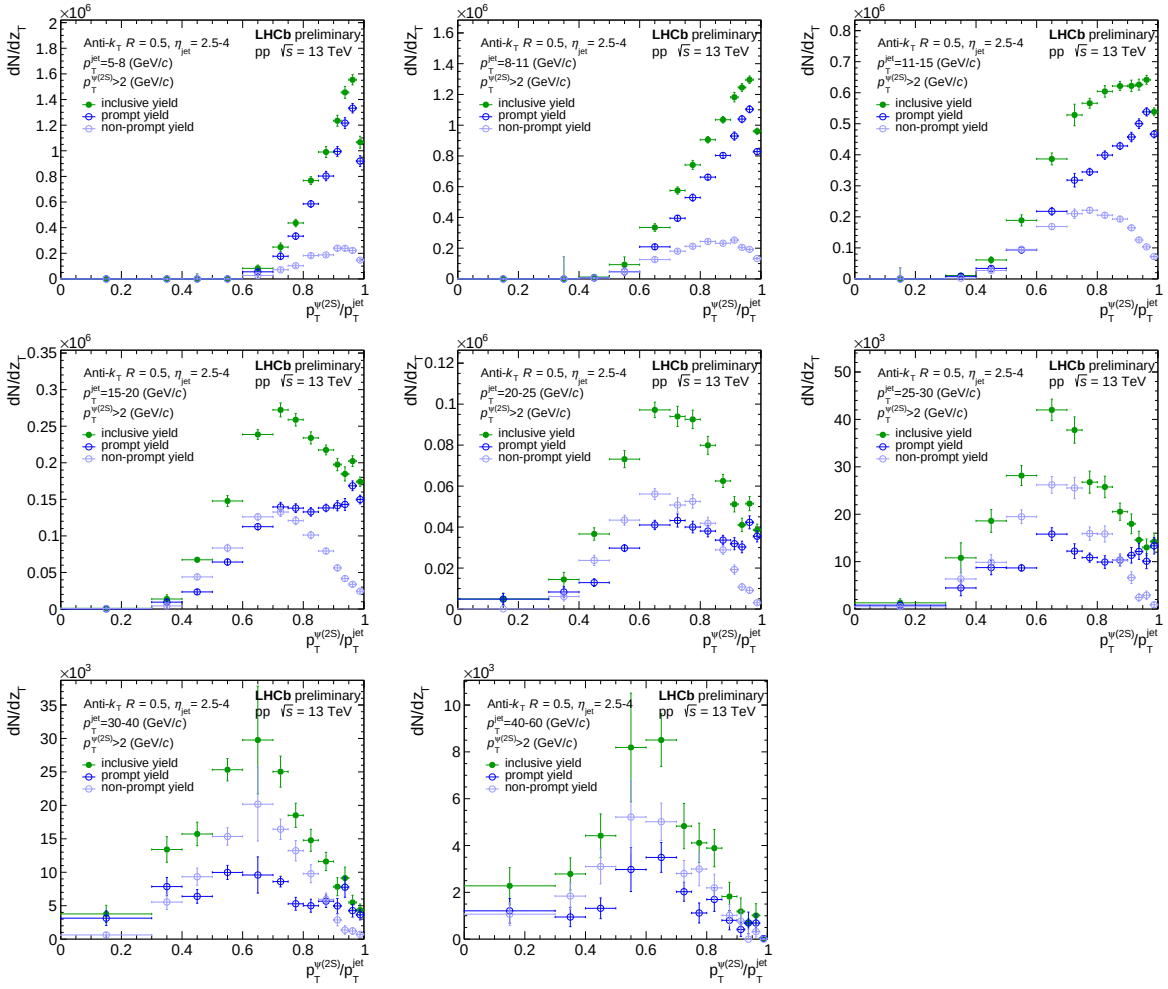

Figure 7.17: Corrected fragmentation functions of $\psi(2S)$ production within fully reconstructed jets at several p_{T}(jet). The distributions are corrected for multiple effects and split into their prompt and displaced contributions.

The last step remaining is the unfolding of the prompt and displaced distributions. This corrects for the detector resolution in the jet reconstruction and is described in the following sections.

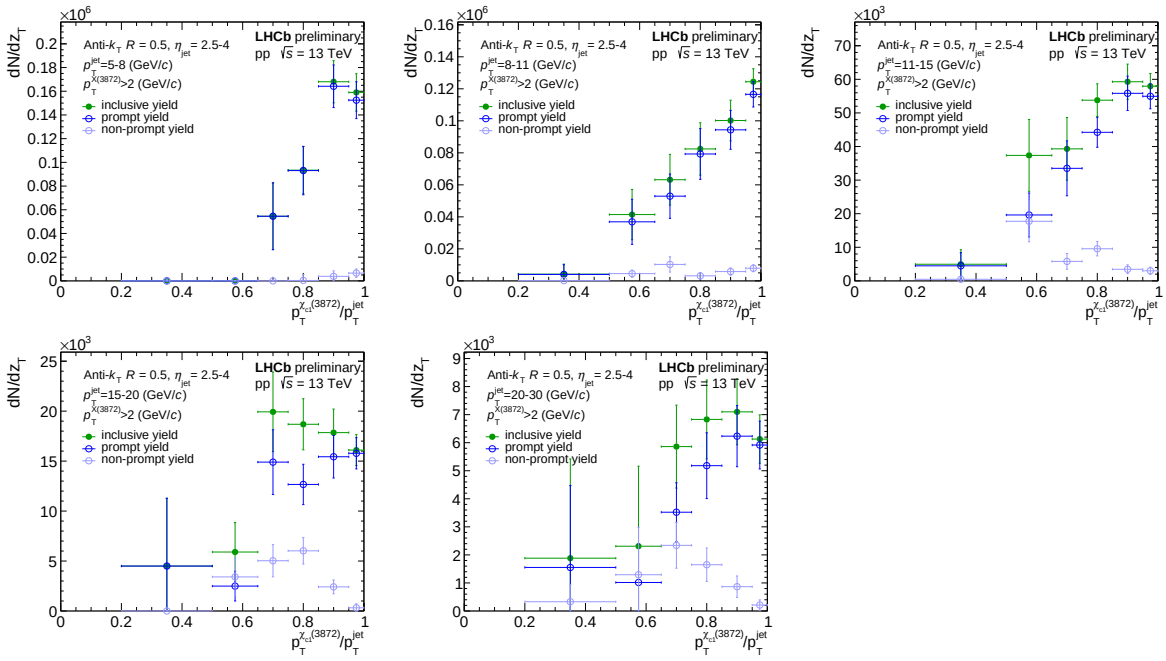

Figure 7.18: Corrected fragmentation functions of X(3872) production within fully reconstructed jets at several p_{T}(jet). The distributions are corrected for multiple effects and split into their prompt and displaced contributions.

7.3 Unfolding

The unfolding procedure is used to correct for the detector resolution of the jet reconstruction, which leads to jets not being reconstructed properly. This can come from several sources, for example where some particles are missing from the reconstruction, or fake tracks, called ghost tracks, can be clustered into jets. This can lead to differences in the p_{T} and energy of the jets that are reconstructed in comparison to their "true" p_{T} and energy values. Since z_T and p_{T}(jet) are the variables that are being measured in this analysis, and also the quarkonia in jets analysis discussed in chapter 6, this needs to be corrected for by unfolding them to their "true" values.

The unfolding procedure is hence dependent on MC to model the differences due to detector reconstruction of the detector-level and generator jets. However, as was discussed in chapter 1 and chapter 3, and also shown in fig. 1.4, MC describes production from b-decays fairly well, but not at all for prompt production. This means an unfolding procedure needs to be defined which is relatively independent of needing to know the "true" distribution. This means an MC sample needs to be created specially for the purposes of unfolding the prompt distributions. This will be discussed in more detail in the following sections along with the unfolding

procedure used. The methods described here for the unfolding are also applied to the different quarkonia distributions described in chapter 6.

7.3.1 MC samples for the unfolding

7.3.1.1 Investigating the current prompt PYTHIA sample

The samples used for this analysis were produced from PYTHIA. Since the z_T of the prompt distribution was so different to the measured distribution, it was decided to compare some key properties of the jets produced from simulated prompt, simulated displaced and finally data distributions, to see if the prompt MC was still usable. In b-decays, some of the decay products along with the J/ψ can be hyperons, for example a K^0_S. These have very long decay times, and hence do not get reconstructed in the jet. Hence, the displaced (also called non-prompt, NP) MC samples are separated into jets that contain hyperons and those that do not, and also a weighted mix of ∼60% hyperons. Figure 7.19 shows the number of jet constituents in different p_T(jet) ranges for each of the different MC samples in comparison to data. The data were selected for tags that were in the $\psi(2S)$ mass window, and with a short decay time to filter out displaced production.

Figure 7.19 shows that there is a clear discrepancy between prompt production MC and the data. The NP MC set describes the data much better, while no major difference between different hyperon contents is observed. Additionally, the number of jet constituents in the prompt MC sample does not seem to change with p_T(jet), with a maximum of around 4-5. Figure 7.20 also shows that the p_T(jet) distribution of the prompt MC is also too soft.

Based on these observations, it was decided to use the displaced MC sample for unfolding both the prompt and displaced measured distributions. However, the proper hyperon fractions for each of the prompt and displaced jets needs to be taken into account, as these can change what is reconstructed in the jet and hence p_T(jet) of the reconstructed jet. This is described in the next section.

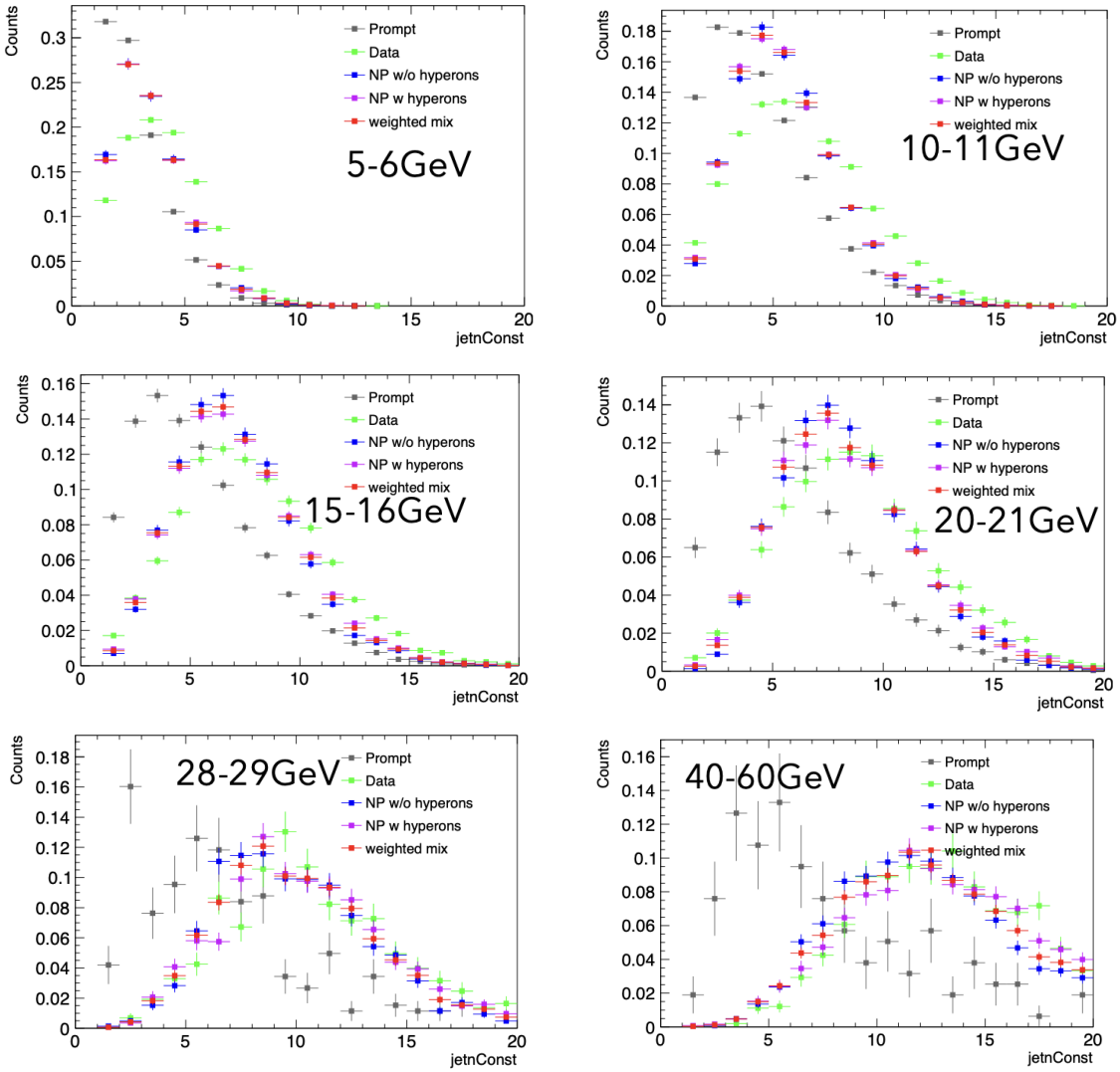

Figure 7.19: Distributions of number of jet constituents (charged+neutral) for different p_{T}(jet) ranges.

7.3.1.2 Hyperon content of jets

As mentioned in the previous section, when a hyperon such as a K^0_{S} is included in a jet, this is not reconstructed in the detector, and hence the measured energy of the reconstructed jet can be lower than the true jet energy. This leads to lower measured p_{T}(jet) values, and hence higher z_T values. This can be quantified by measuring the JES shift as shown in eq. (6.13) in section 6.3. Figure 7.21 illustrates the difference in JES for NP hyperon-free MC, NP containing all hyperons MC, a NP weighted mix of 60 % hyperons, and finally the prompt MC simulations to compare their properties. Prompt tag production MC and displaced tag production free of hyperons MC show a very similar behaviour in terms of jet energy scale

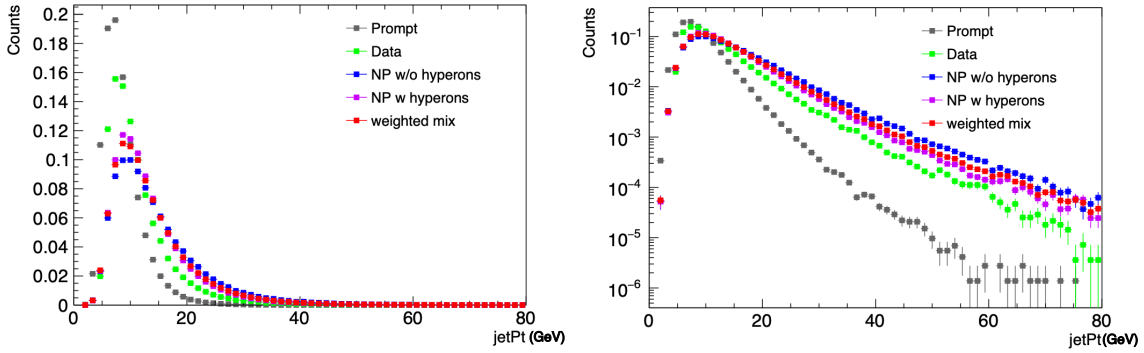

Figure 7.20: Jet p_{T} distributions for the different MC samples and mixes. Left: linear, right: log.

reconstruction. In both cases the jet energy can be reconstructed to a very precise level, missing only about 2 % for lower jet energies. The displaced MC with explicit hyperon content shows the strongest jet energy scale shift, where on average 10 % of the jet energy is lost in reconstruction.

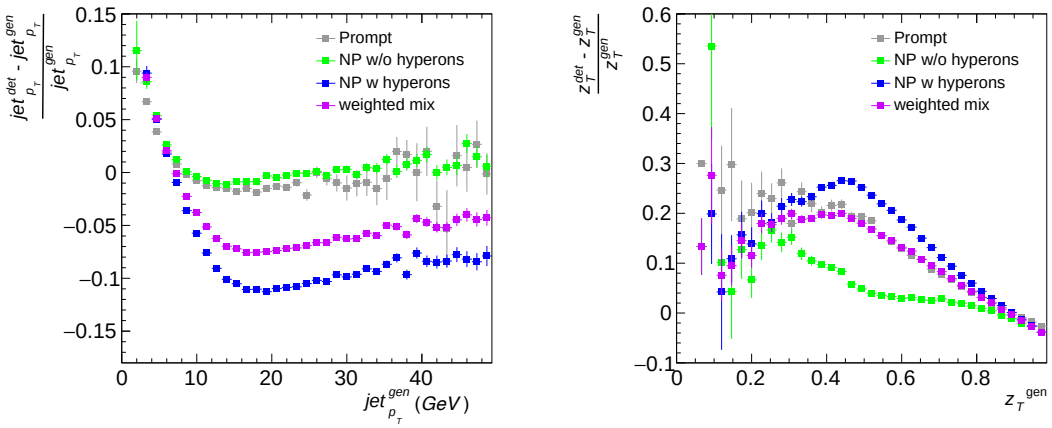

Figure 7.21: Left: jet energy scale shift for all the MC sets, right: z_T scale shift.

As the JES has a sizeable influence on the unfolded result due to the shift of energies, a precise determination of the hyperon content in jets for both prompt and displaced production is need. This has been determined separately for prompt and displaced production and is discussed in the next sections.

7.3.1.2.1 Displaced Mix

The different target ratios for the b-decay MC were extracted from PYTHIA simulations containing a B-meson. For B^+ decays, 61 % of events have jets which contain hyperons in comparison to 39 % without hyperons. For B^0 decays, 65 % of events have jets which contain hyperons in comparison to 35 % without hyperons. The

events are scaled further such that the ratio of B^+/B^0 decays is 1. For a systematic variation in the unfolding, weights which contain 20 % more or less hyperons are applied to the final combined response matrix (MC).

7.3.1.2.2 Prompt Mix

PYTHIA was used to find out the hyperon fraction that should be used to fill the prompt response matrix for the unfolding. This was done by checking the fraction of prompt jets that contained a hyperon. The jets were split by jet type, *i.e.* what was the origin of the jet such as a gluon or light quark. A second criterion is also applied which requires a tag particle in the jet, to see how this biases the composition. The results are presented in fig. 7.22. It shows the z_T of the hyperon produced in each case. The table in the figure shows the cross section of a specific jet type being produced, the mean z_T of the hyperon, and the overall fraction of events among these jets that contained a hyperon. The overall fractions are quite sizeable. The jets of interest here are ones that contain a J/ψ. Amongst these, the jets coming from a gluon have the highest cross section and thus are probably the most relevant. Hence, the prompt RM is composed with a hyperon content of 28%. Since these numbers are purely MC based, the b jet containing a J/ψ channel with a hyperon content of 55% is used as a systematic variation to the unfolding. Note, only the total hyperon fraction is adapted in the displaced MC sample. The z_T of the hyperons is not modelled in these MC.

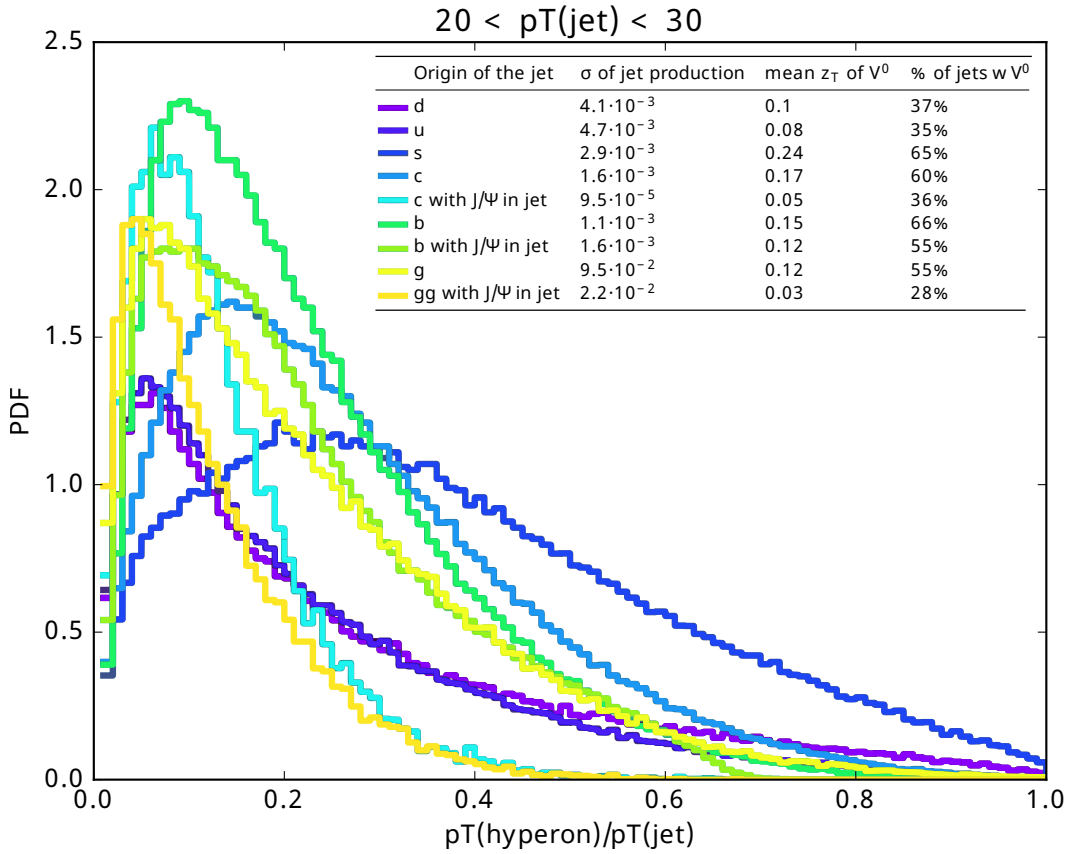

Figure 7.22: PYTHIA 8.3 study of different jet types to investigate the hyperon content of jets. In every case, a sizeable fraction of jets contain a hyperon, $\sim$ 30-60 %. The momentum fraction that the hyperons carry is very different amongst the jet types.

Figure 7.23 shows the JES and z_T scale shift of the jets after all scalings and variations are properly applied.

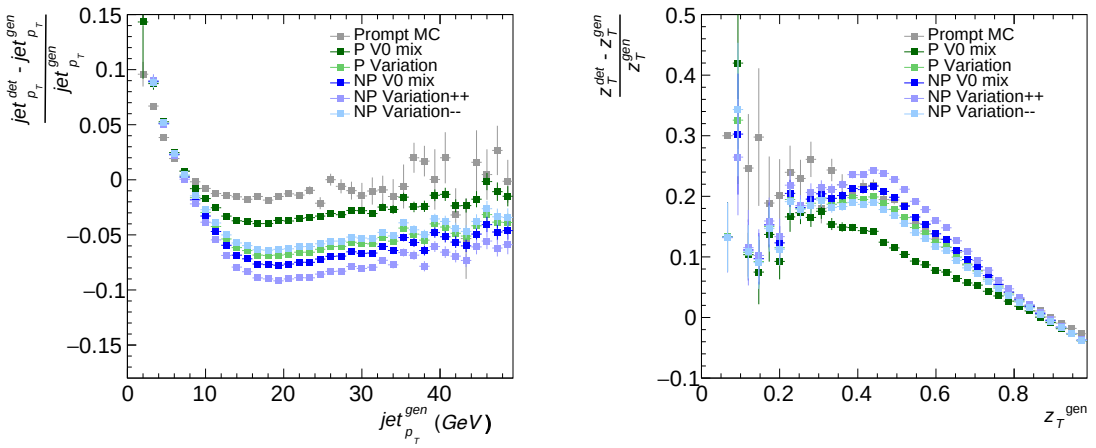

Figure 7.23: Left: JES shift for all final MC sets and their variations, including the discarded Prompt MC, and right: z_T scale shift.

7.3.2 Input to the unfolding - Response Matrix and Data

A response matrix maps and gives a graphical representation of the differences between generator level and detector level objects for a variable of interest. The variables of interest here to unfold are p_{T}(jet) and z_T, to correct for the jet energy resolution. The RM is then used to unfold the measured data to the true p_{T}(jet) and z_T values. To create the response matrix (RM), the MC jets reconstructed at detector level need to be matched to the jets at generator level. To match the jets, a list of jet objects that contain a reconstructed tag, *i.e.* a $\psi(2S)$ or X(3872), at both generator and detector level are geometrically matched using the radial distance, ($\Delta\mathrm{R}=\sqrt{(\Delta\varphi)^2+(\Delta\eta)^2}$), between the jet axes. For each generator level jet, the smallest distance to a detector level jet is determined. If for that detector level jet the matched generator level jet is also the closest jet, they are called a unique match and saved for the RM. A second approach can also be used where the tag is instead matched at generator and detector level. It is then checked if there was a successful reconstructed jets at both levels with these tags. Both approaches were found to be equally valid. If the jets are not matched, the are removed from the RM.

There are no selection cuts apart from fiducial requirements applied to the jet and tag objects since these are dedicated simulations without background events. All matched jets-pairs of the b-decay MC samples are accumulated and two RM with different hyperon weights are created. The measurement is performed double differentially in jet p_{T}-z_T. Hence, the RM and the unfolding is performed in two dimensions. Figure 7.24 shows an example RM for the displaced $\psi(2S)$. Section C.1 shows the RM's for the prompt $\psi(2S)$, and prompt and displaced X(3872).

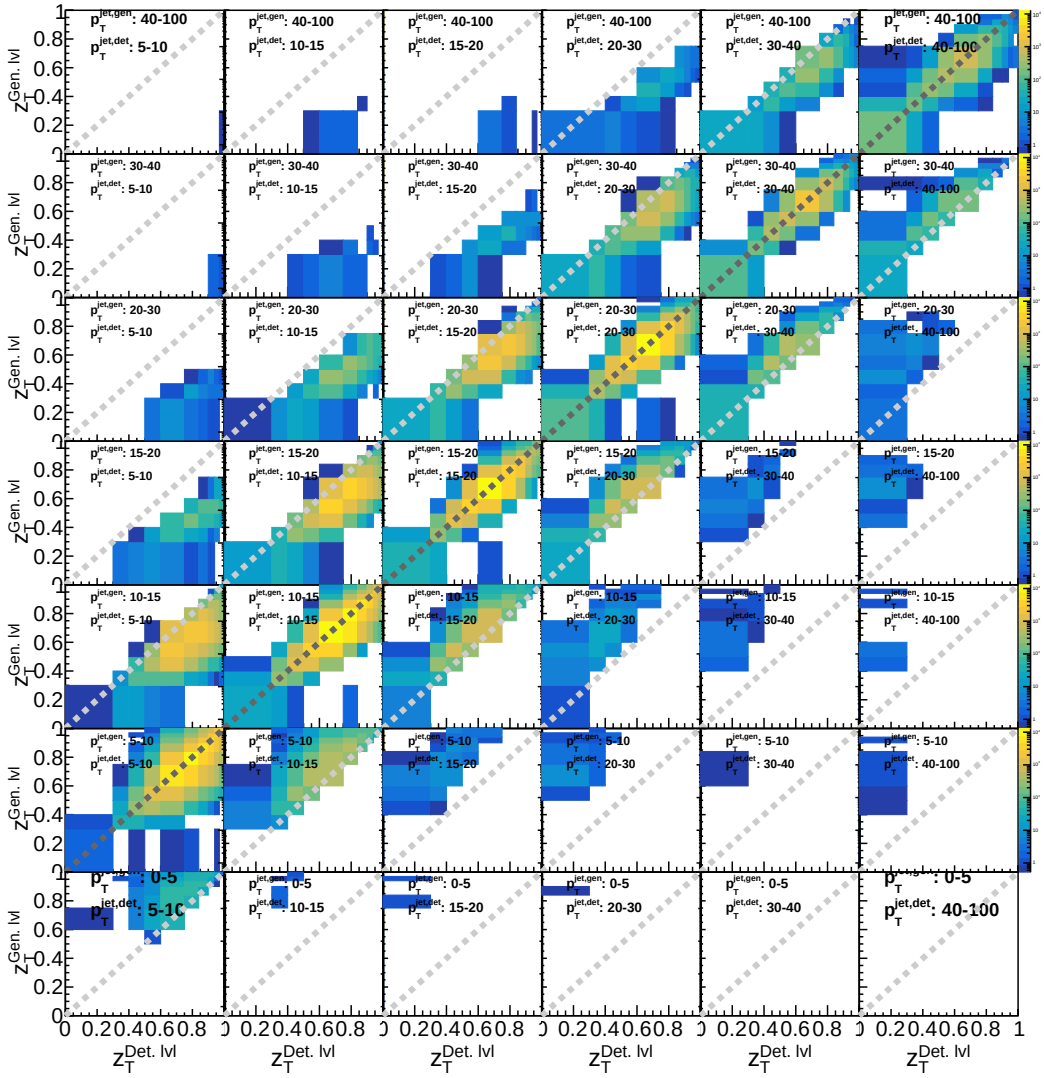

Figure 7.24: An example RM for the unfolding of displaced $\psi(2S)$. The MC is B-decay with a weight of ∼60% hyperons. The x-axis shows the measured quantities at detector level, the y-axis the initial quantities at generator level. The different tiles represent different p_{T}(jet) combinations at detector and generator level. The dark grey line represents the main diagonal line where the measured and reconstructed distribution is in the same p_{T}(jet) bin. The brighter grey diagonals show cases where the measured and reconstructed p_{T}(jet) differ so that the statistic measured in one bin is shifted to the next p_{T}(jet) bin during the unfolding procedure.

The measured results from data are used in a 2D representation for the unfolding. Figures 7.25 and 7.26 show the measured data that are fed into the unfolding algorithm for the $\psi(2S)$ and X(3872) respectively.

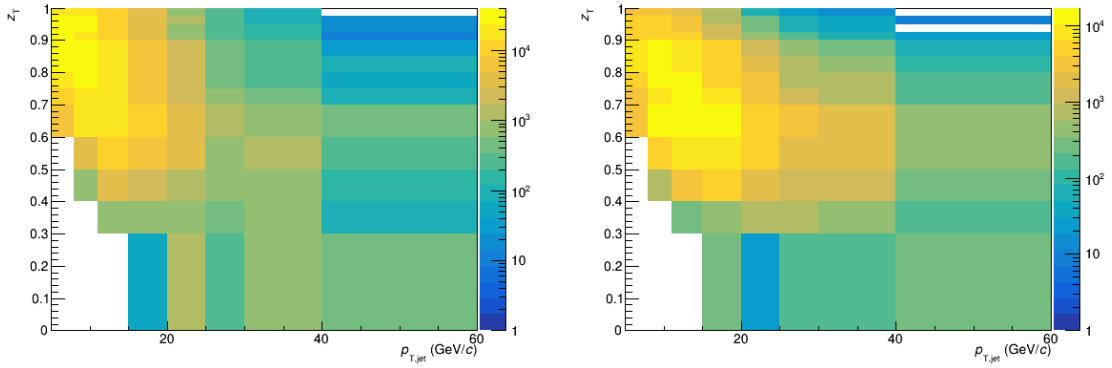

(a) Prompt (b) Displaced

Figure 7.25: 2D representations of the measured $\psi(2S)$ yield in p_{T}(jet) and z_T bins for prompt and displaced $\psi(2S)$'s respectively.

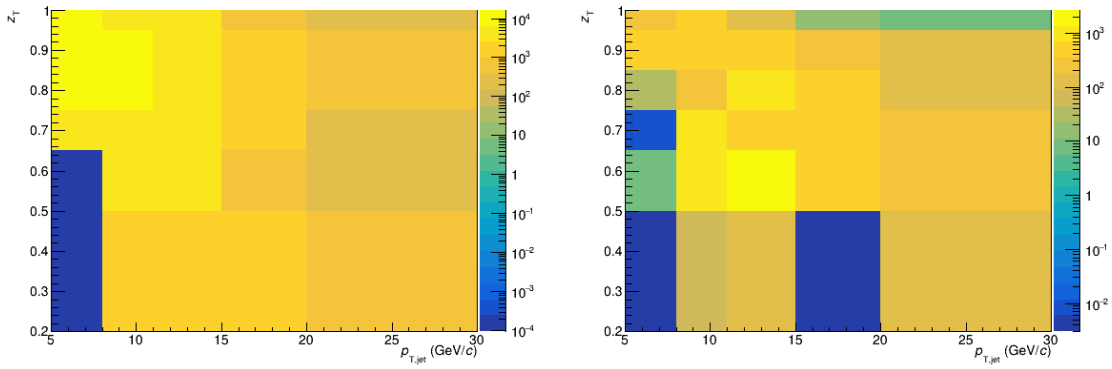

(a) Prompt (b) Displaced

Figure 7.26: 2D representations of the measured X(3872) yield in p_{T}(jet) and z_T bins for prompt and displaced X(3872)'s respectively.

7.3.3 Unfolding procedure

The unfolding is performed using the RooUnfold [145] package from ROOT [112]. The algorithm chosen to unfold with was the Bayesian unfolding algorithm and the statistical error estimator used was kCovToy [146]. To account for yield flowing into the measured range from ranges below and above the measured limits, 3 underflow and 2 overflow bins are added to the RM. These are p_{T}(jet) = [2-3,3-4,4-5] for the underflow bins, and p_{T}(jet) =[highLimit+20,highLimit+40] for the overflow bins, where the highLimit is 60 GeV for $\psi(2S)$ and 30 GeV for X(3872). The measured yield is unfolded to the same binning as used at detector level. The prior for the unfolding is the projection of the RM to the truth axis. The regularisation parameter used for all variations of unfolding is k=4.

There can be bin migration effects between different z_T bins, which are either due to minor p_{T}(jet) momentum shifts within the same p_{T}(jet) bin, or between different p_{T}(jet) bins due to major p_{T}(jet) momentum shifts. Hence, it can happen that reconstructed bins at the edge of the kinematic limits are dominated by statistics migrated into that bin from a region that is not covered by the measurement. This means that the yield would be purely modelled by the MC in the RM. The lowest p_{T}(jet) range suffers from out of bin migration specifically at low z_T. Hence, the lowest p_{T}(jet) bin is only used as input for the unfolding, and the final unfolded result is not reported.

7.3.4 Cross checks of the unfolding

In order to verify whether the unfolding results are stable and sensible, several cross checks are performed. First, the correlation coefficients can give insight about the right regularisation parameter choice. Figures 7.27 and 7.28 present the correlation coefficients for the regularisation parameters k=3,4 and 5 for prompt and displaced $\psi(2S)$ production respectively. Section C.2 shows the same figures for the X(3872) production. In these figures the regularisation parameter k=4 looks like a stable choice for all data sets.

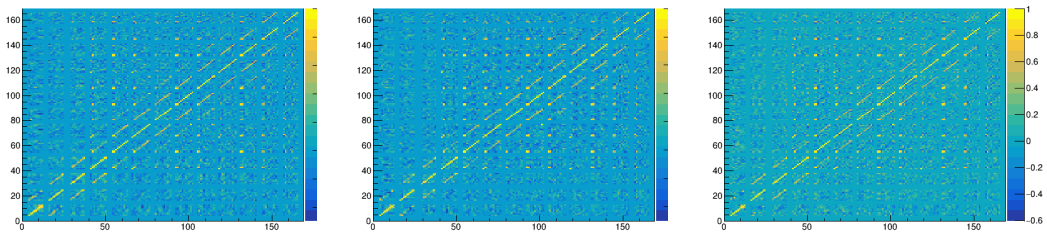

Figure 7.27: Correlation coefficients for regularisation parameters k=3,4,5 for $\psi(2S)$ prompt production and jet p_{T}-z_T binning. Regularisation parameter k=4 (middle) is used for the main result.

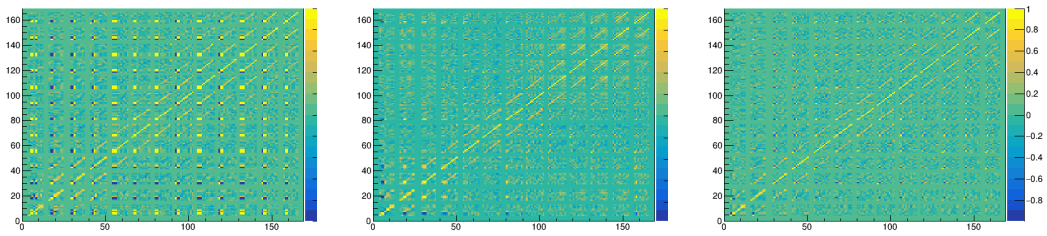

Figure 7.28: Correlation coefficients for regularisation parameters k=3,4,5 for $\psi(2S)$ non-prompt production. Regularisation parameter k=4 (middle) is used for the main result.

Apart from a reasonable covariance matrix, the unfolded spectra should also be stable when varying the regularisation parameter by ±1. This is presented in figs. 7.29 and 7.30 for $\psi(2S)$ production. Section C.3 shows the same figures for the X(3872) production. The unfolded results agree with each other within 5%. This value suggest a stable solution at k_{main}=4. The solutions at k_{main}±1 are used to quantify a systematic uncertainty on the result caused by the unfolding, which is detailed further in section 7.4.

Another cross check is a refolding test. This tests the stability of the result due to limited statistics in the RM. The statistics are divided in the RM into two separate random subsamples, RM1 and RM2. The data are then unfolded with RM1 and then refolded with RM2. The original raw data is then compared with the refolded data. The results of this test are shown in figs. 7.31 and 7.32. Section C.4 shows the same figures for the X(3872) production. The refolded spectrum agrees with the raw spectra within the statistical errors for most figures. Only the refolding of the last two bins of the 20-25 bin show some larger deviations.

The third cross check is a closure test. This test uses the MC jet spectrum at detector level and unfolds it with the RM. The unfolded detector level spectrum is compared to the generator level MC spectrum. If there are no intrinsic problems with the unfolding implementation and the RM, the comparison should yield a exact agreement. The closure test results are shown in figs. 7.33 and 7.34 for $\psi(2S)$. The tests show good stability by recovering the original PYTHIA spectrum within <2% accuracy. The only major difference is seen in the lowest p_{T}(jet) bins where some out of bin migration is occurring. The closure test results for X(3872) are shown in section C.5.

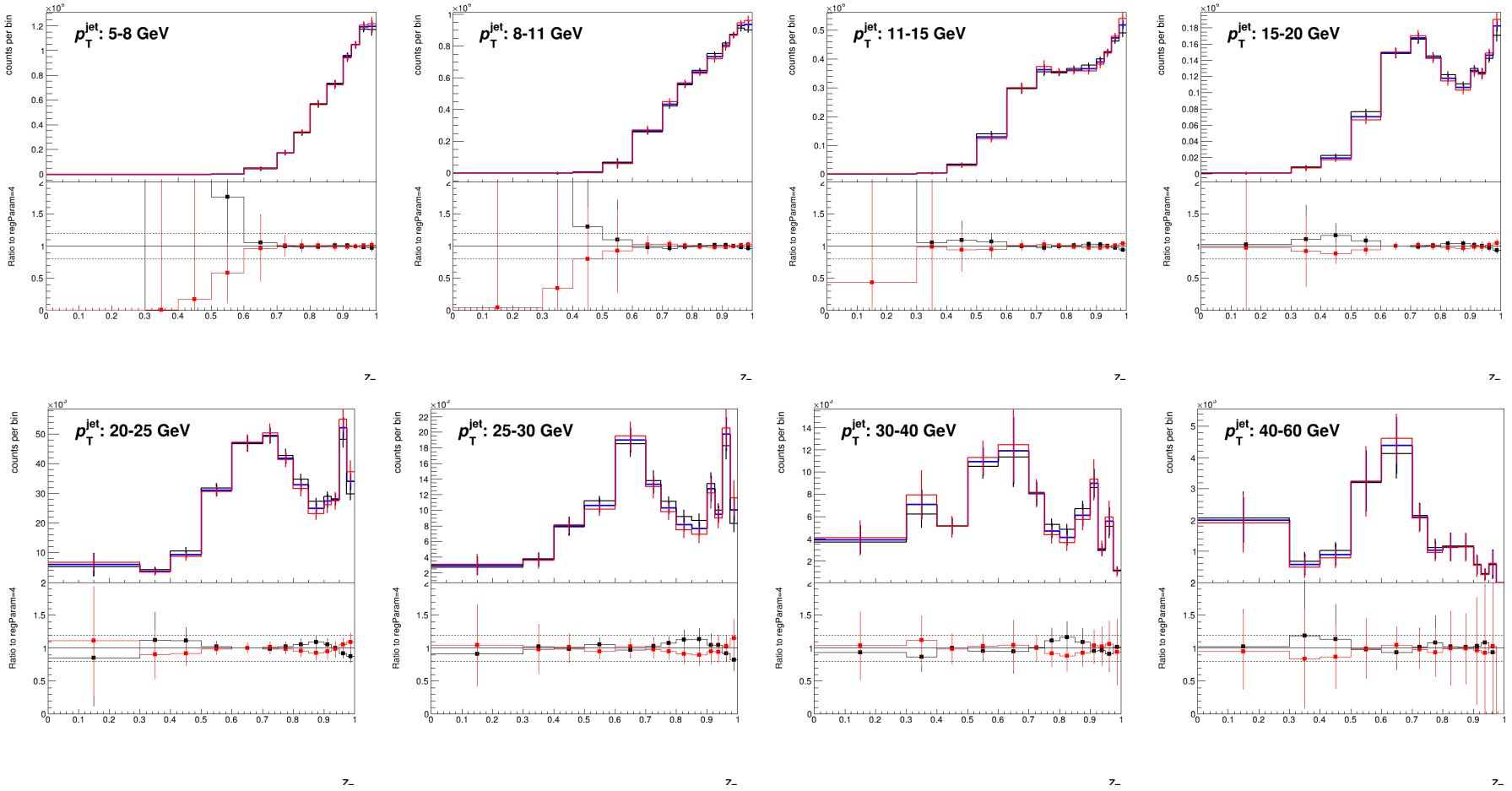

Figure 7.29: Unfolded result with regularisation parameter k=4 compared to k=3 and k=5 for prompt $\psi(2S)$ production. Left to right: Low p_{T}(jet) to high p_{T}(jet).

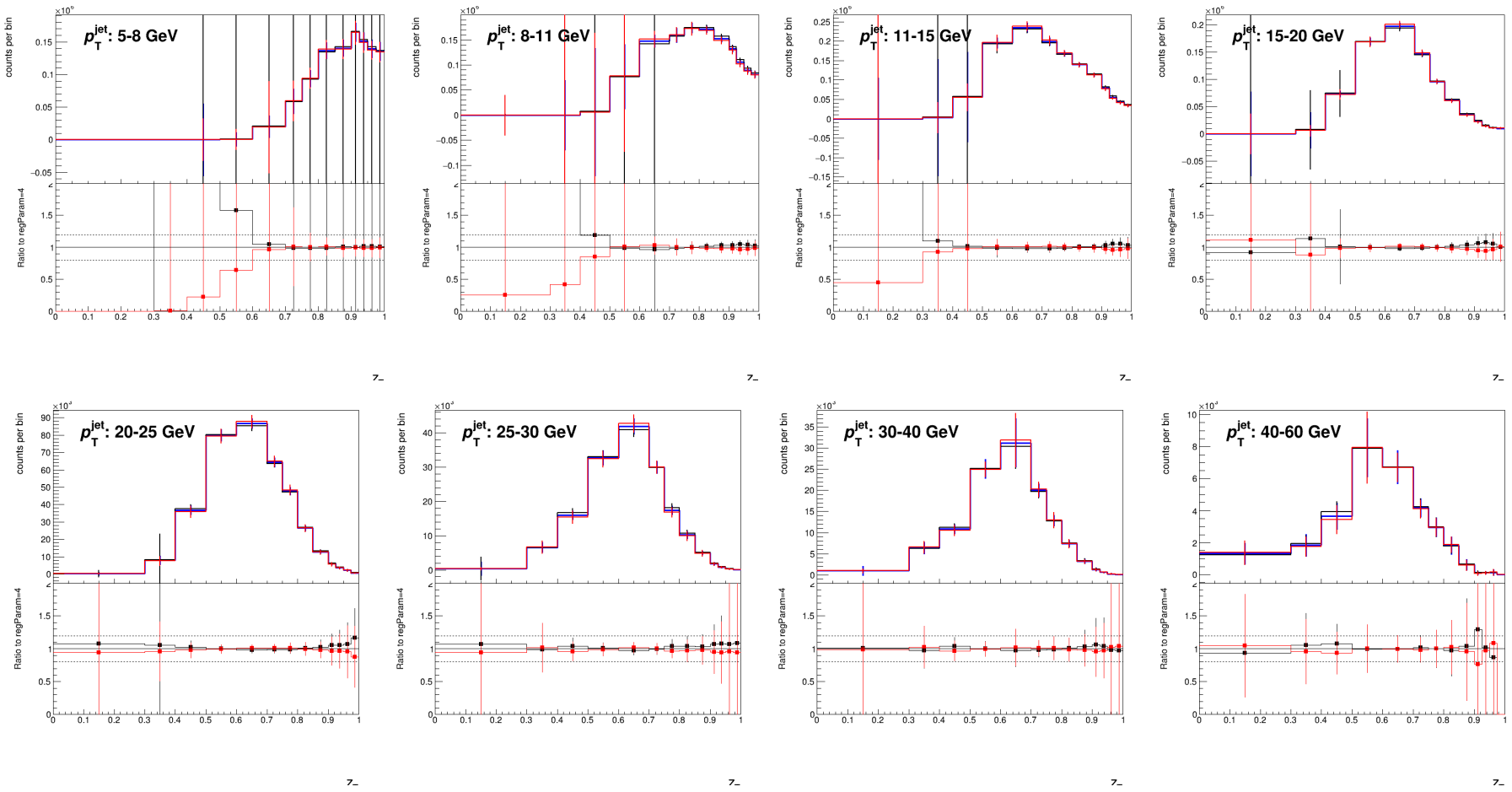

Figure 7.30: Unfolded result with regularisation parameter k=4 compared to k=3 and k=5 for displaced $\psi(2S)$ production. Left to right: Low p_{T}(jet) to high p_{T}(jet).

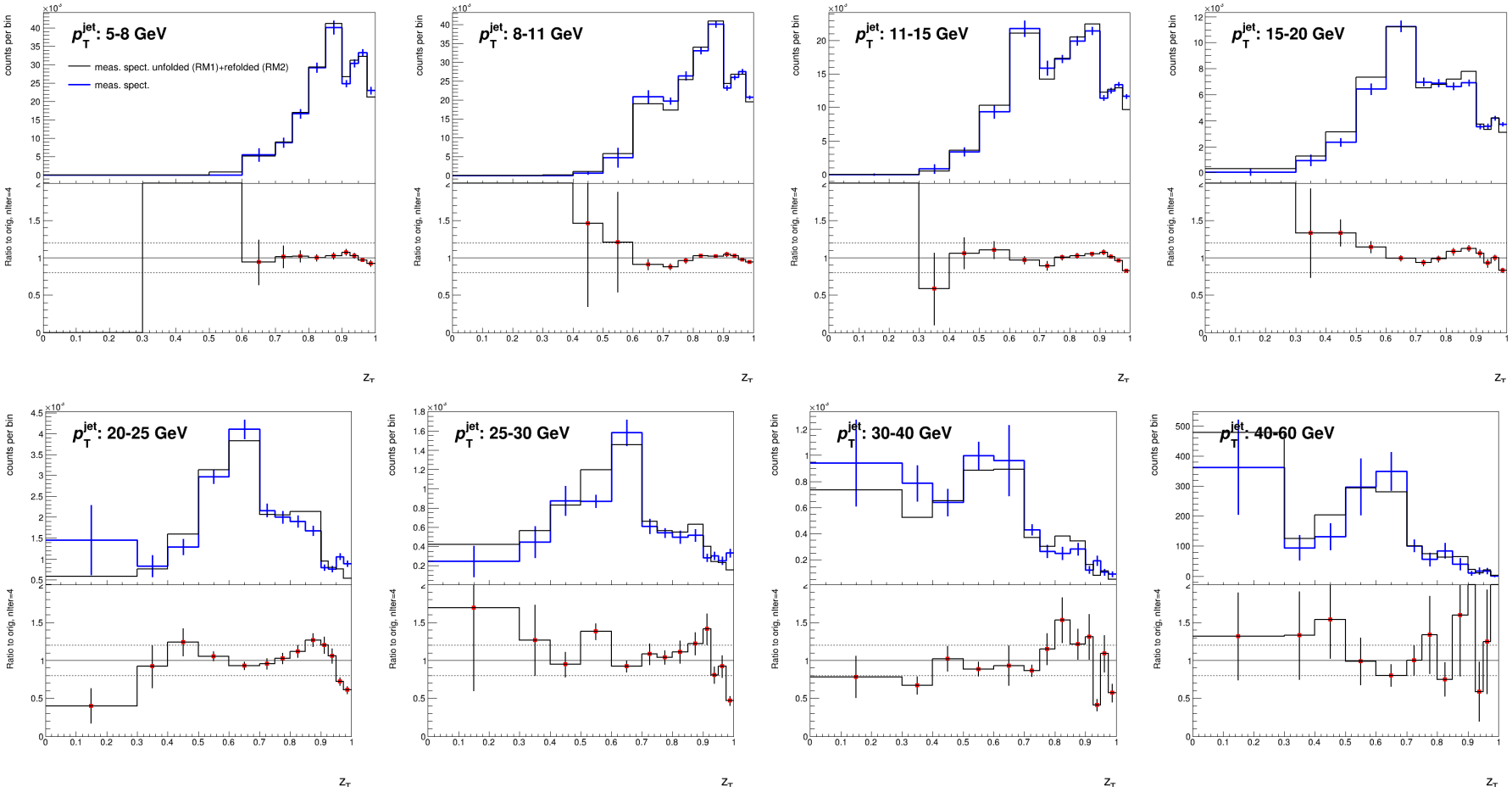

Figure 7.31: Refolding test for prompt $\psi(2S)$ production for k=4. The figures show different p_{T}(jet) bins. The measured spectrum was unfolded with half of the RM and refolded back with the other half of the RM.

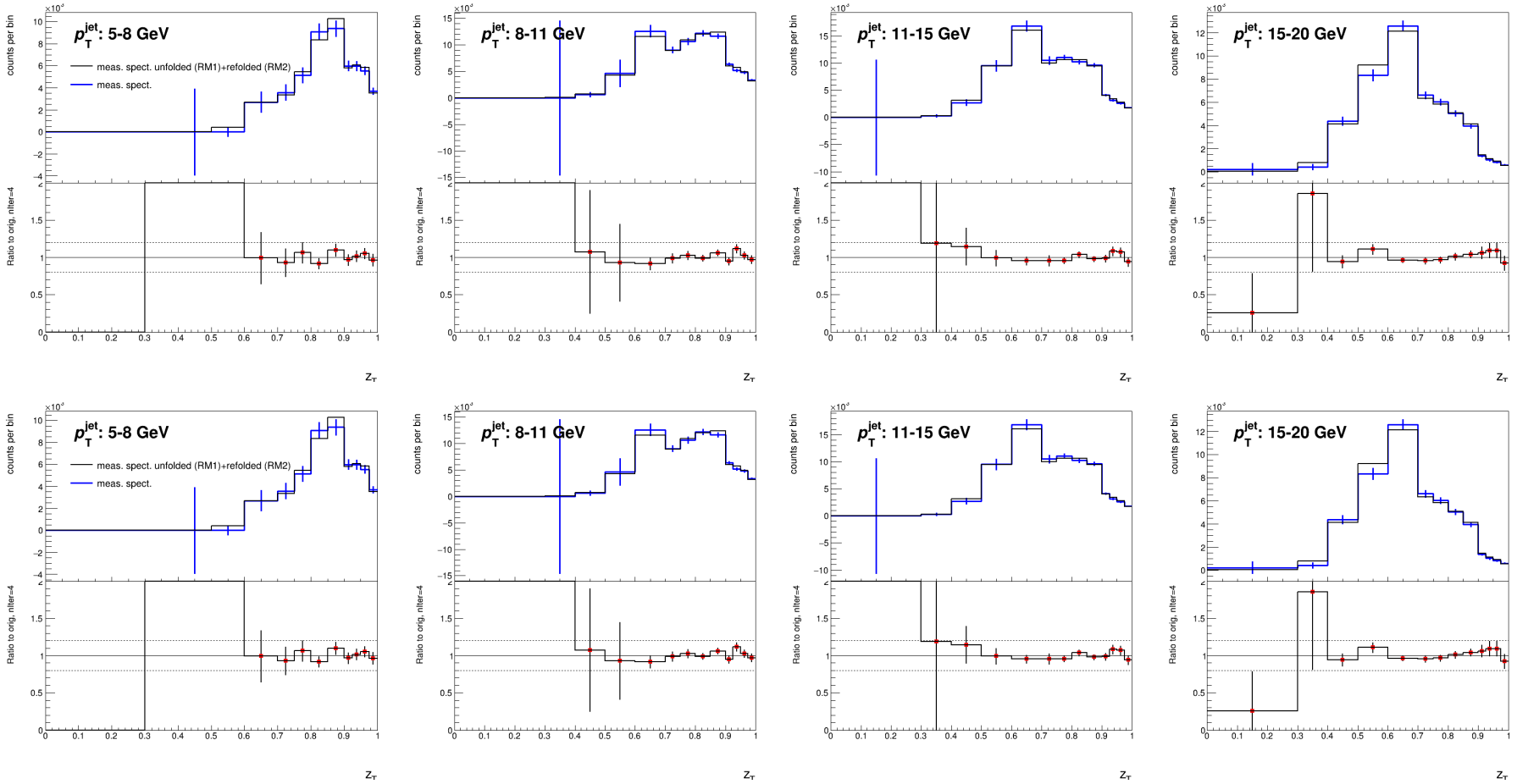

Figure 7.32: Refolding test for displaced $\psi(2S)$ production for k=4. The figures show different p_{T}(jet) bins. The measured spectrum was unfolded with half of the RM and refolded back with the other half of the RM.

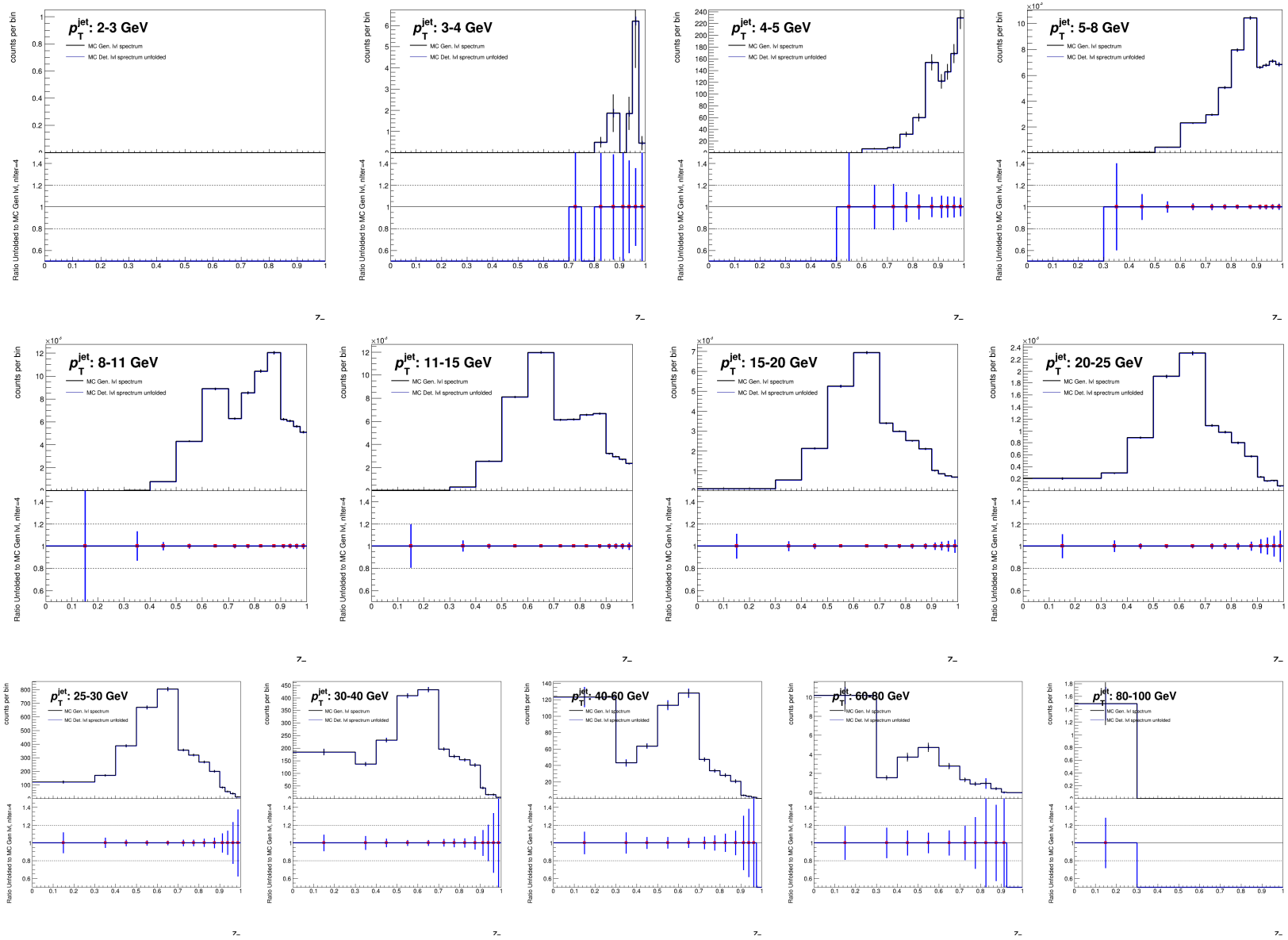

Figure 7.33: Closure test for prompt $\psi(2S)$ production for k=4. The errors reflect the statistical uncertainty of the unfolding. This is mostly due to limited statistics in the RM.

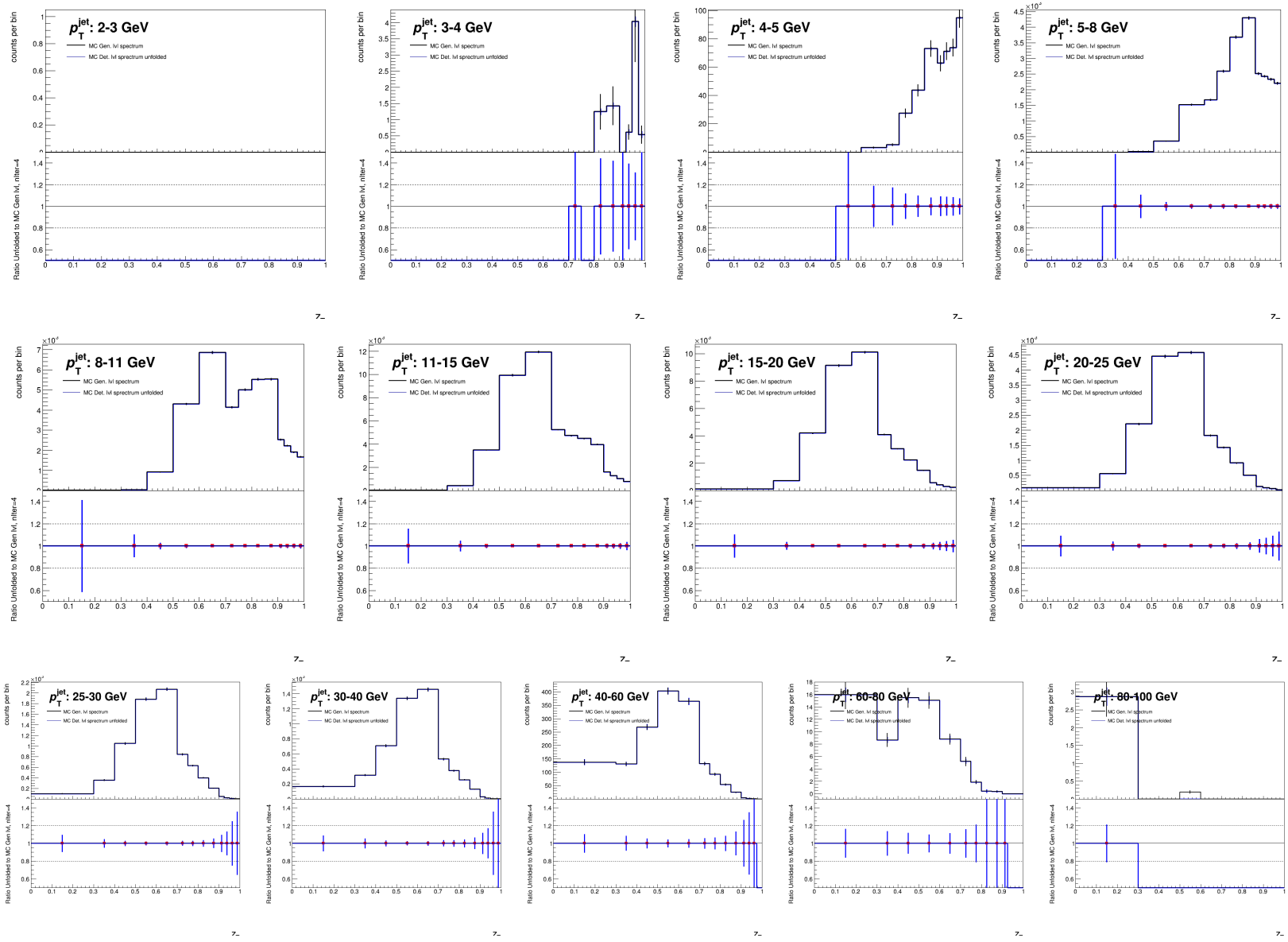

Figure 7.34: Closure test for displaced $\psi(2S)$ production for k=4. The errors reflect the statistical uncertainty of the unfolding. This is mostly due to limited statistics in the RM.

7.3.5 Unfolded Data

The results of the main unfolding procedure are presented in figs. 7.35 to 7.38. These figures compare the measured and unfolded spectra in each $p_{\mathrm{T}}(\mathrm{jet})$ bin side-by-side. Since the unfolding typically recovers lost jet energy, the denominator in the z_T variable grows and thus the distributions after the unfolding are shifted to lower z_T values. Figures 7.39 and 7.40 show all the unfolded results compared to each other. The prompt $\psi(2S)$ distributions show an isolated peak at high z_T values at high $p_{\mathrm{T}}(\mathrm{jet})$ values, even after unfolding.

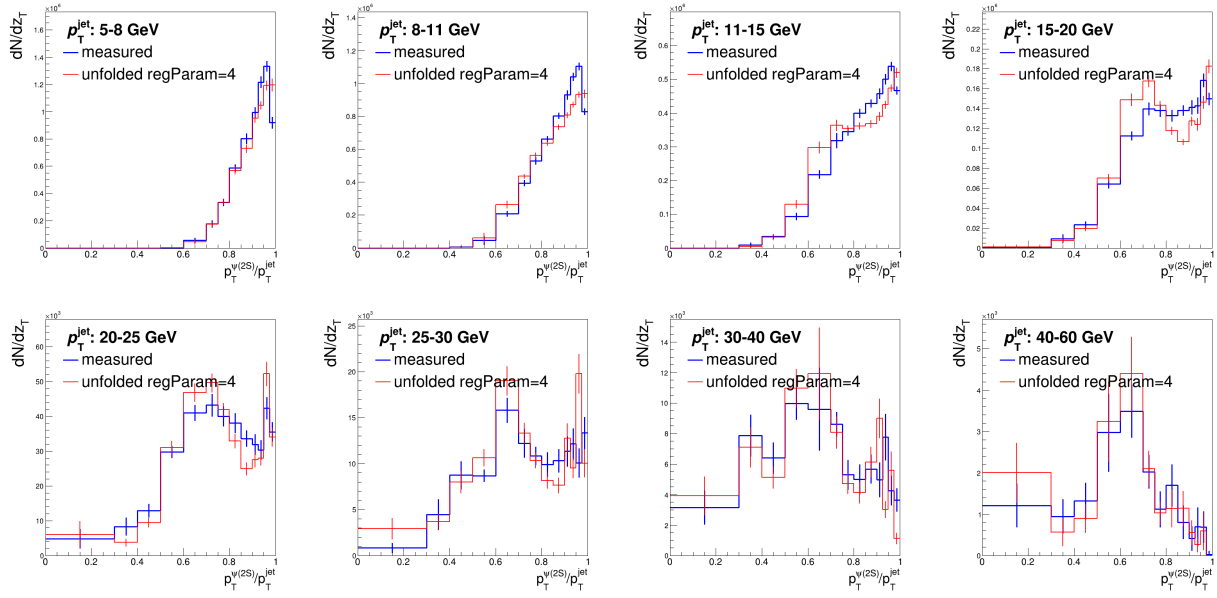

Figure 7.35: Measured and unfolded spectra for prompt $\psi(2S)$ production.

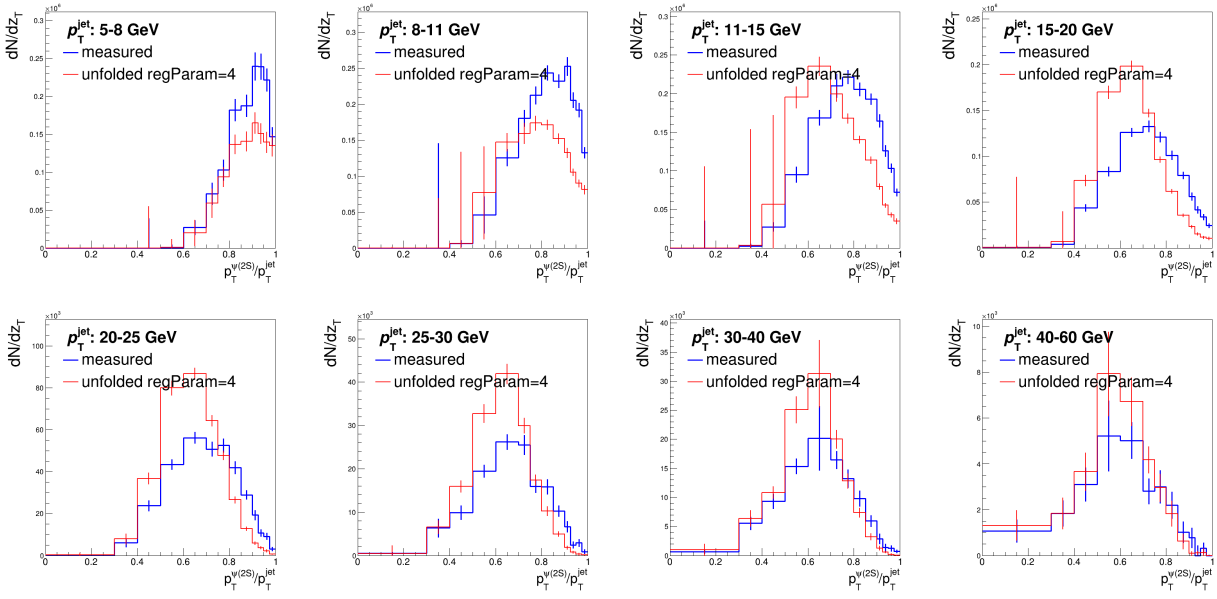

Figure 7.36: Measured and unfolded spectra for displaced $\psi(2S)$ production.

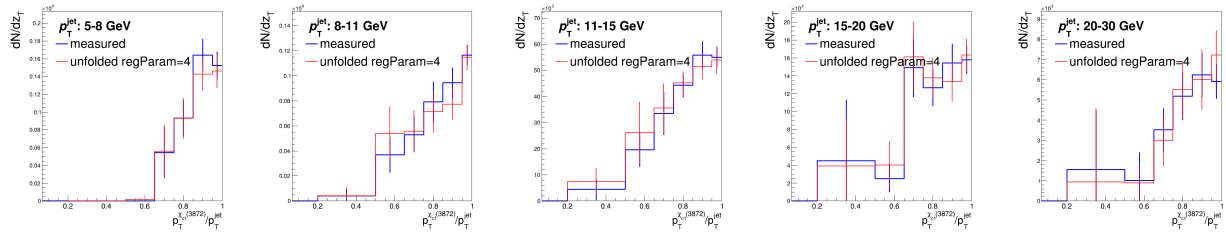

Figure 7.37: Measured and unfolded spectra for prompt X(3872) production.

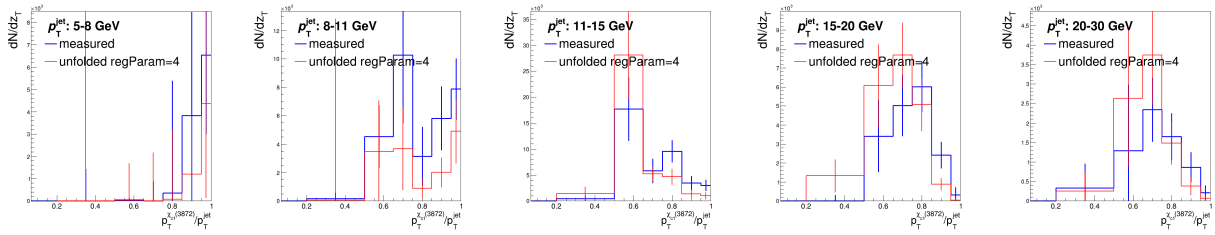

Figure 7.38: Measured and unfolded spectra for displaced X(3872) production.

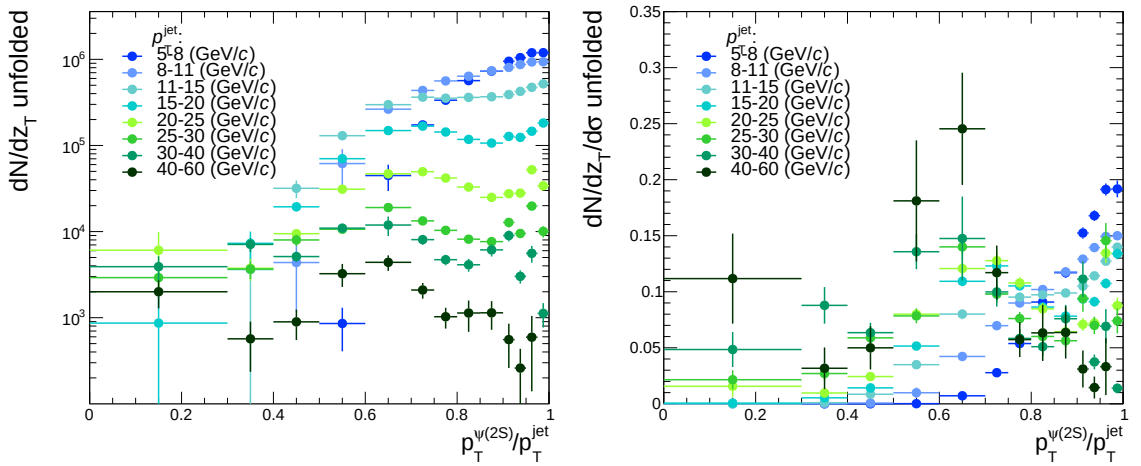

(a) Prompt $\psi(2S)$.

(b) Prompt $\psi(2S)$ normalised to integral.

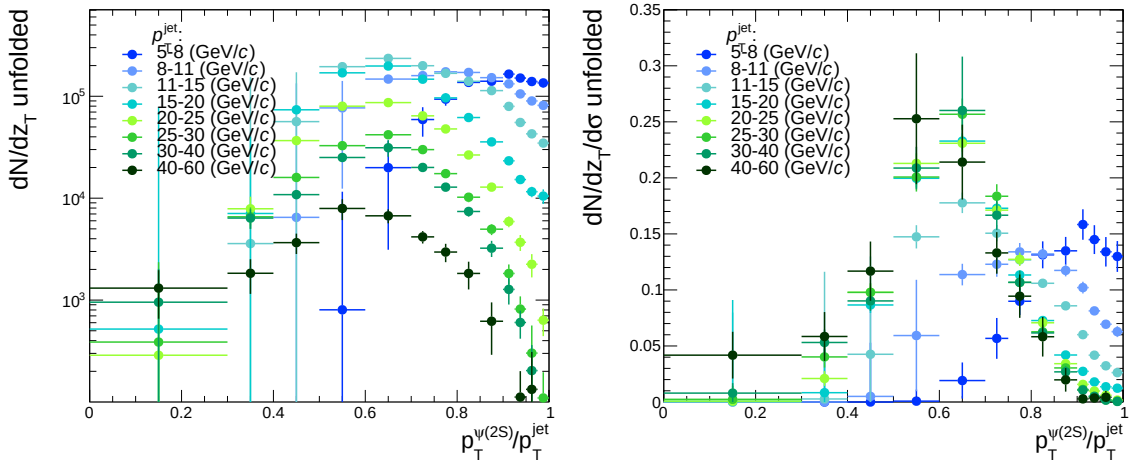

(c) Displaced $\psi(2S)$.

(d) Displaced $\psi(2S)$ normalised to integral.

Figure 7.39: Summary of the unfolded results for $\psi(2S)$ in bins of p_{T}(jet)-z_T.

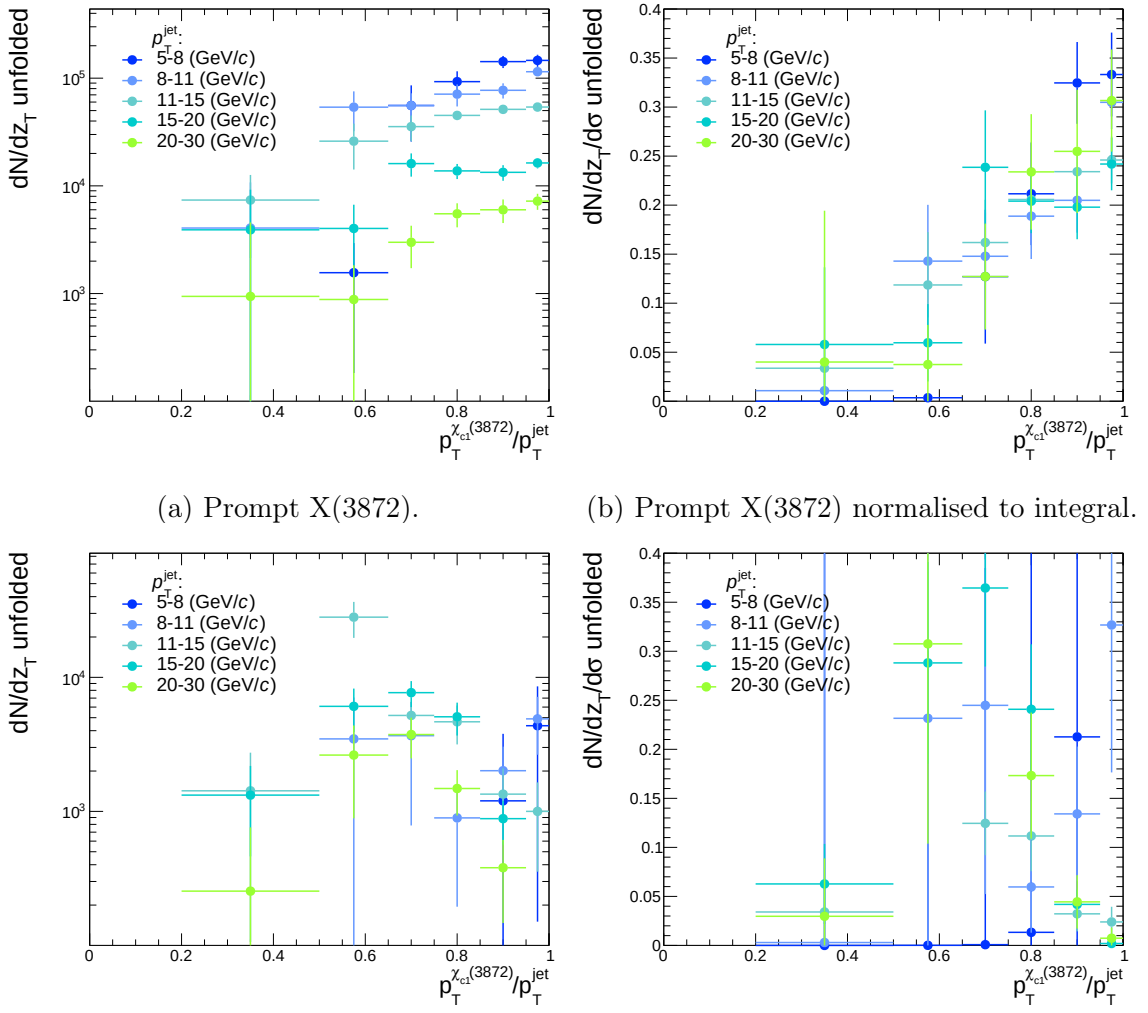

(a) Prompt X(3872).

(b) Prompt X(3872) normalised to integral.

(c) Displaced X(3872).

(d) Displaced X(3872) normalised to integral.

Figure 7.40: Summary of the unfolded results for X(3872) in bins of p_{T}(jet)-z_T.

7.4 Systematic uncertainties

As discussed in section 6.4, the three main sources of systematic errors are from i) the signal yield extraction, ii) the event selection and efficiency corrections and iii) the unfolding procedure. The signal yield extraction uses the same methods as described in section 6.4.1. Hence, it will not be discussed in detail here. However, the efficiency corrections and unfolding systematics will be described in more detail in the following sections.

7.4.1 Uncertainties from efficiency corrections

Each efficiency correction component has its own systematic error associated with it. The majority of the systematic errors are using the same methods as described in section 6.4.2, for example the trigger efficiency correction which uses a half binned map plus closure test uncertainty. The only uncertainties not taken into account are those associated with the pions. These are the pion reconstruction and selection (TRCHI2NDOF, TRACK_GHOSTPROB, ProbNNpi) efficiencies. The pion reconstruction efficiency is evaluated using a map with half bin sizes, and the selection efficiency by reducing the efficiency map content by 1σ error of the total value. The calculation of the total relative systematic uncertainties in each z_T and p_{T}(jet) bin then follow the same method as for the Υ's, as discussed in section 6.4.6, due to the lack of statistic for the X(3872).

Figures 7.41 and 7.42 show the summary of all the sub-components that contribute to the systematic uncertainty of the efficiency corrections. The overall systematic uncertainty, shown in black, is mostly around 6-8 % at high z_T and is dominated by the uncertainty on $\mathrm{R}_{data/MC}$.

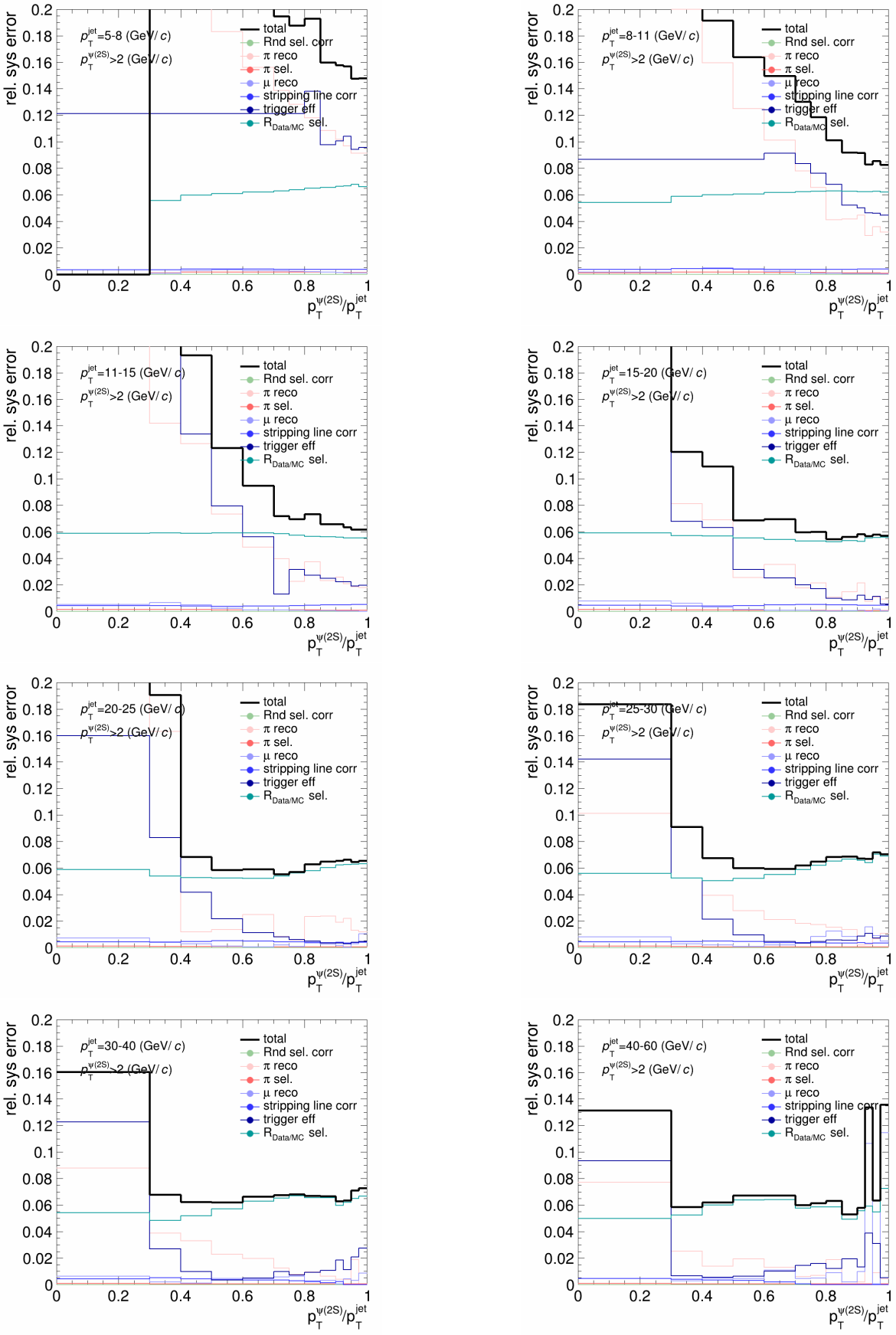

Figure 7.41: Summary of the total systematic uncertainty from the efficiency corrections split into its sub-components for the $\psi(2S)$ in different p_{T}(jet) bins.

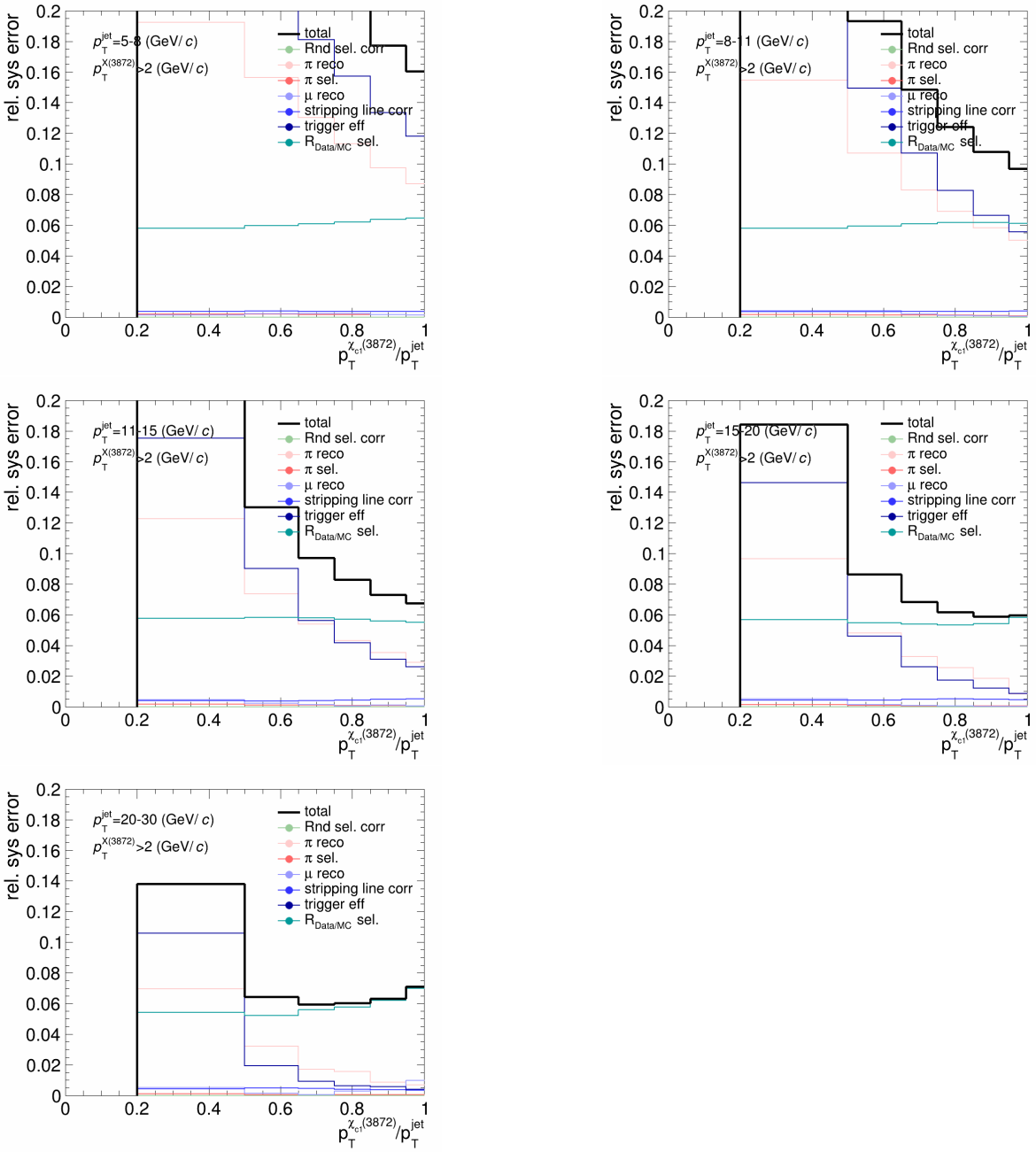

Figure 7.42: Summary of the total systematic uncertainty from the efficiency corrections split into its sub-components for the X(3872) in different p_{T}(jet) bins.

7.4.2 Uncertainties from the unfolding procedure

The uncertainties from the unfolding procedure are evaluated by varying the input criteria. One source of systematic uncertainty is the number of iterations selected in the unfolding procedure. Generally the results should have reached a stable condition and not vary too much with the main regularisation parameter. The choice in this analysis was $\mathrm{k}_{main} = 4$. The first uncertainty is evaluated by using

the unfolded results of $k_{main}\pm1$. This was discussed in section 7.3.4.

Another source of uncertainty is from the first initial prior (MC truth distribution) that is used for the unfolding. Since the MC simulations do not describe prompt $\psi(2S)$ and X(3872) production well, this is a source of an initial bias. To evaluate the sensitivity of the result on the prior, three variations have been used. First, a flat prior for the unfolding is used (uniform in dN/dz). Second, the prompt prior is swapped for the non-prompt RM and the non-prompt prior for the prompt RM. Third, the prior is weighted such that it matches the unfolded result and is then unfolded again with this adapted prior. Figures 7.43 and 7.44 show the nominal priors for the unfolding and the discrepancy between prior and final unfolded result in case of the prompt data.

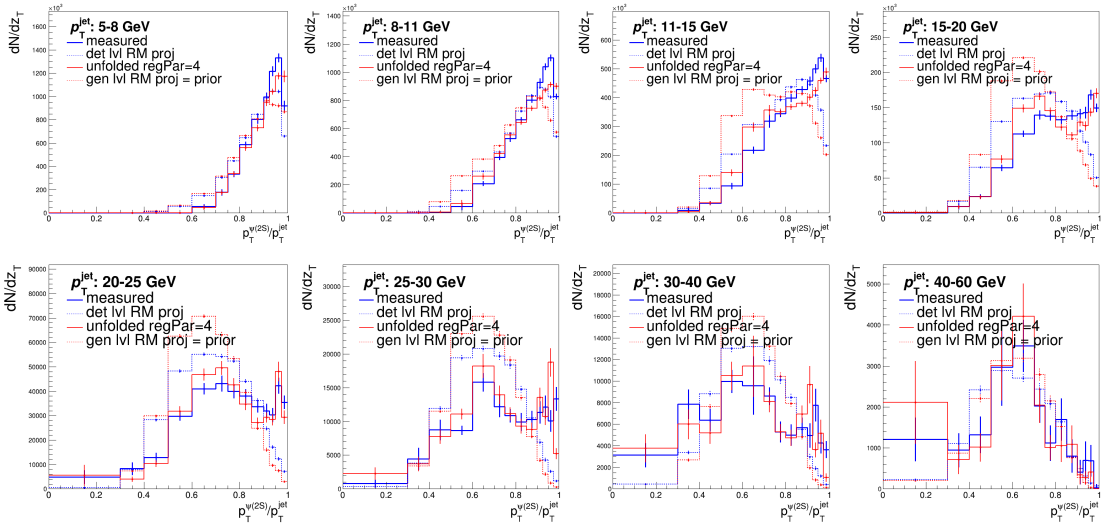

Figure 7.43: Prior with the measured and unfolded spectra for prompt $\psi(2S)$.

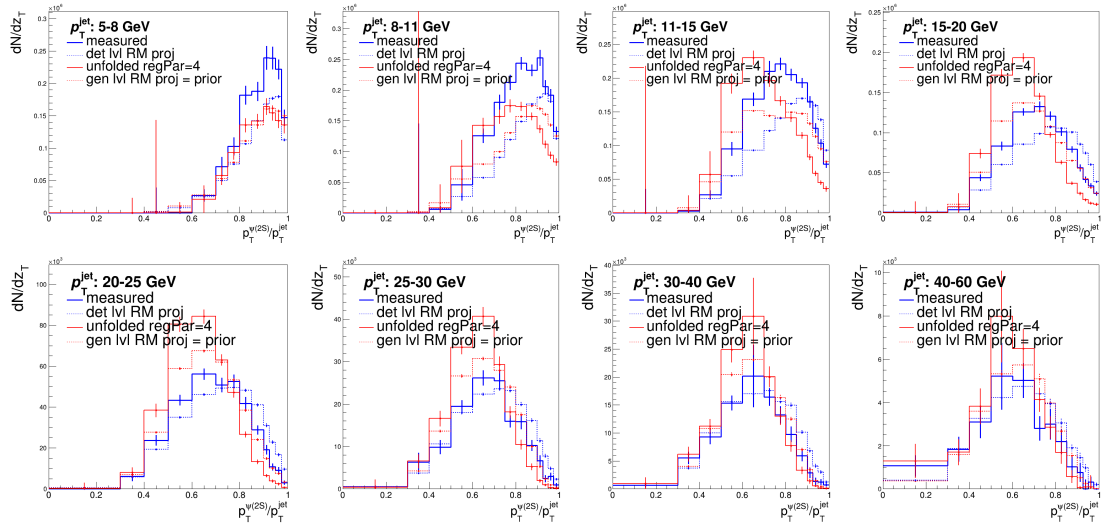

Figure 7.44: Prior with the measured and unfolded spectra for displaced $\psi(2S)$.

Additionally, the hyperon content in the RM is varied as an additional systematic, as mentioned in section 6.4.4. The difference between the main unfolded results and the unfolded results with various changes applied to them, as described above, are shown in figs. 7.45 and 7.46 for the prompt and displaced $\psi(2S)$ production. The unfolding systematics for the X(3872) are shown in section C.6. The results seem to be pretty stable against varying the regularisation parameter and are of the size of the statistical uncertainty or smaller. The largest source for the systematic uncertainty of the unfolding is due to the change in hyperon content, and can be roughly twice the statistical uncertainty.

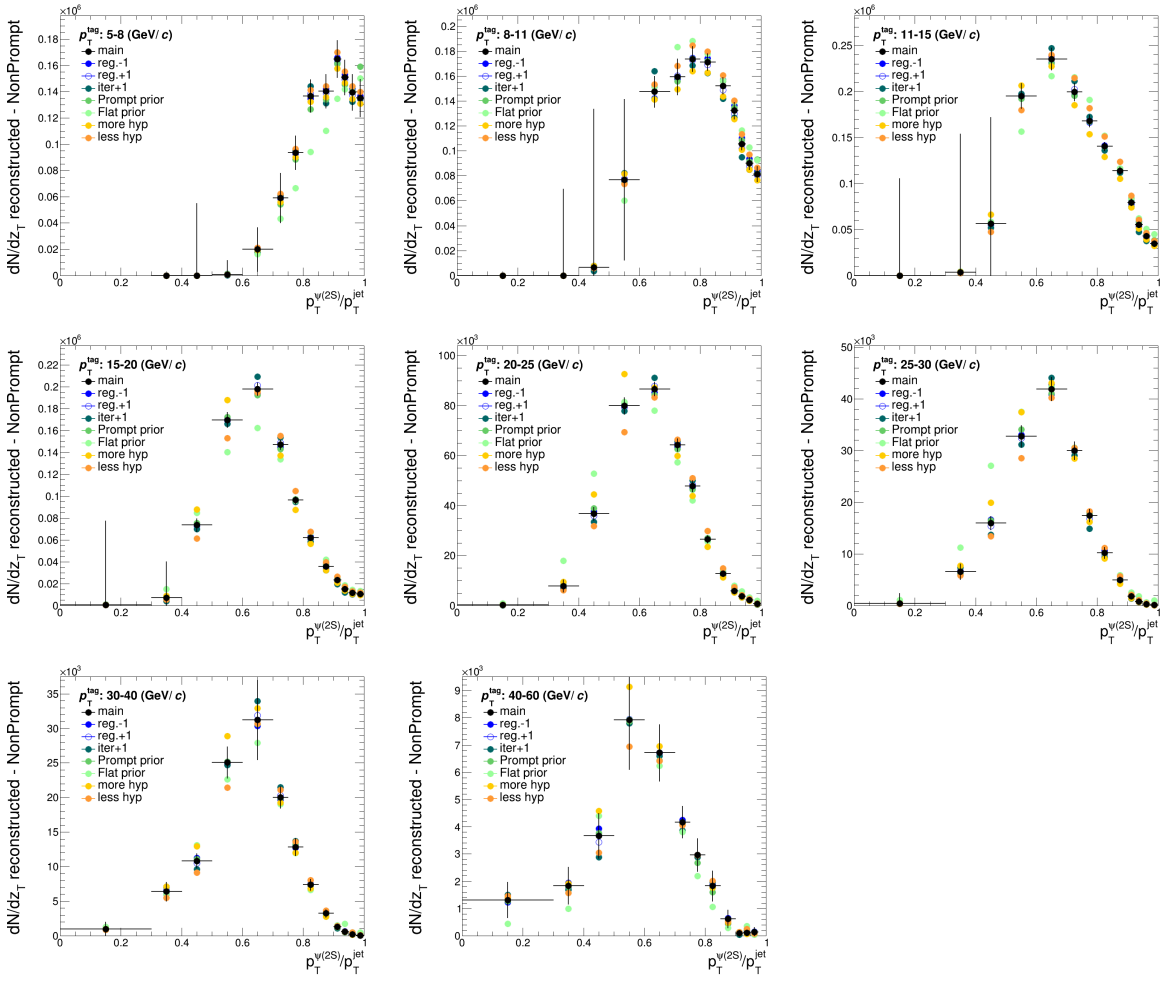

Figure 7.45: Displaced $\psi(2S)$ unfolded spectra with various changes in the unfolding procedure. The spread of distributions shows the systematic uncertainty associated to the unfolded result.

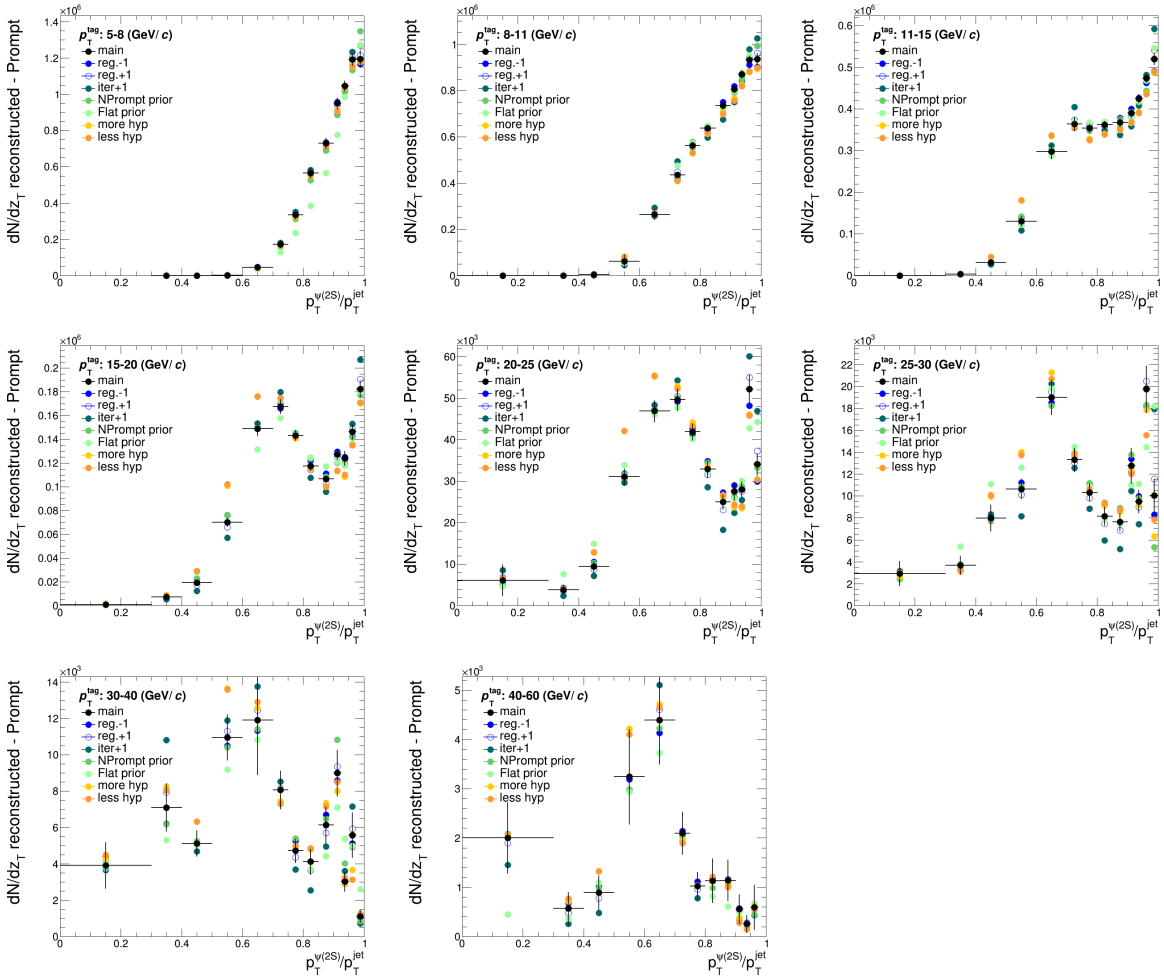

Figure 7.46: Prompt $\psi(2S)$ unfolded spectra with various changes in the unfolding procedure. The spread of distributions shows the systematic uncertainty associated to the unfolded result.

Since all the variations of the unfolding test the same source of systematic uncertainty, the combined error of the unfolding is calculated by the variance of the distributions,

$$\sigma = \sqrt{\frac{\sum_{i=0}^{N} \sigma_i^2}{N}}. \tag{7.7}$$

The final unfolded results presented with their errors are shown in section 7.5.

7.5 Final Results

The final results of the fragmentation functions of $\psi(2S)$ and X(3872) *vs.* z_T within fully reconstructed jets for several different p_{T}(jet) are presented.

7.5.1 Displaced and prompt $\psi(2S)$ and X(3872) production

Figures 7.47 and 7.48 present the displaced fragmentation functions of the $\psi(2S)$ and X(3872). These stem mostly from b-decays and hence indirectly probe the fragmentation of b-jets. The distributions shift to lower z_T at higher p_{T}(jet) values. This is most likely due to kinematic effects, as increasing p_{T}(jet) opens up the phase space to reach lower z_T values. This behaviour is shared between the $\psi(2S)$ and X(3872). Figures 7.49 and 7.50 then present prompt fragmentation functions of $\psi(2S)$ and X(3872) *vs.* z_T in different p_{T}(jet) ranges. This is when the $\psi(2S)$ or X(3872) is produced at or very close to the collision vertex. These distributions differ from the displaced component. All the figures which have bins that have a value of zero are where there is no signal yield. The errors displayed in the distributions are the statistical uncertainty (black), the systematic from the efficiency correction (blue box), and the systematic from the unfolding procedure (blue shaded area).

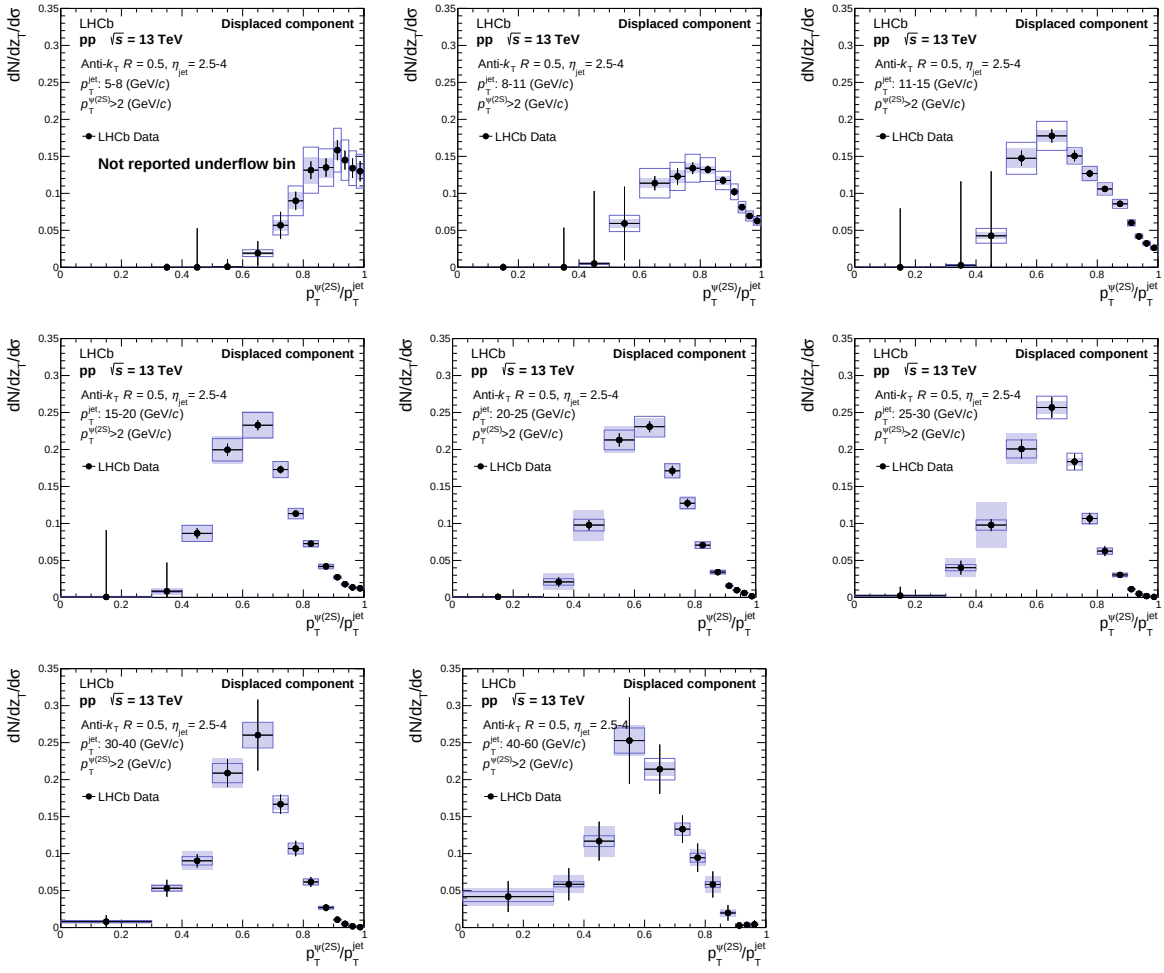

Figure 7.47: Displaced $\psi(2S)$ production *vs.* z_T within fully reconstructed jets at several p_{T}(jet), normalised as $\mathrm{d}N/\mathrm{d}z_T/\mathrm{d}\sigma$, where σ is the total cross section.

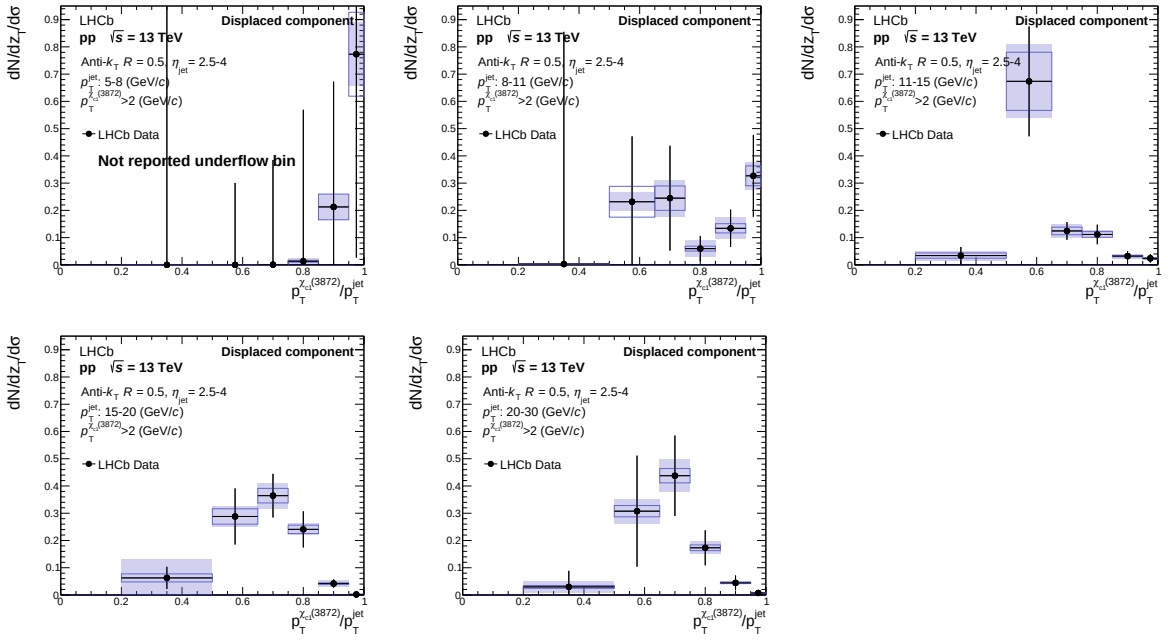

Figure 7.48: Displaced X(3872) production *vs.* z_T within fully reconstructed jets at several $p_{\mathrm{T}}(\mathrm{jet})$, normalised as $\mathrm{d}N/\mathrm{d}z_T/\mathrm{d}\sigma$, where σ is the total cross section.

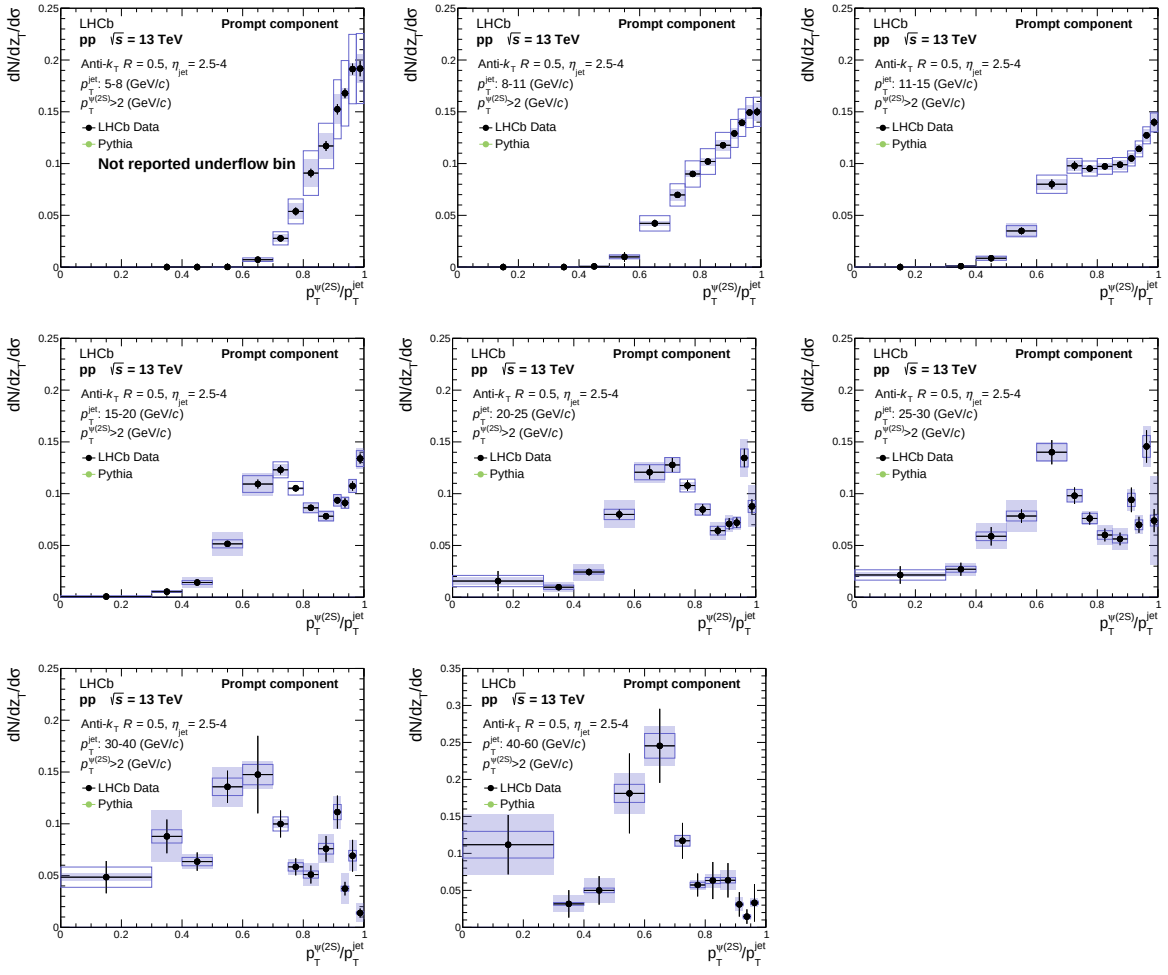

Figure 7.49: Prompt $\psi(2S)$ production *vs.* z_T within fully reconstructed jets at several $p_{\mathrm{T}}(\mathrm{jet})$, normalised as $\mathrm{d}N/\mathrm{d}z_T/\mathrm{d}\sigma$, where σ is the total cross section.

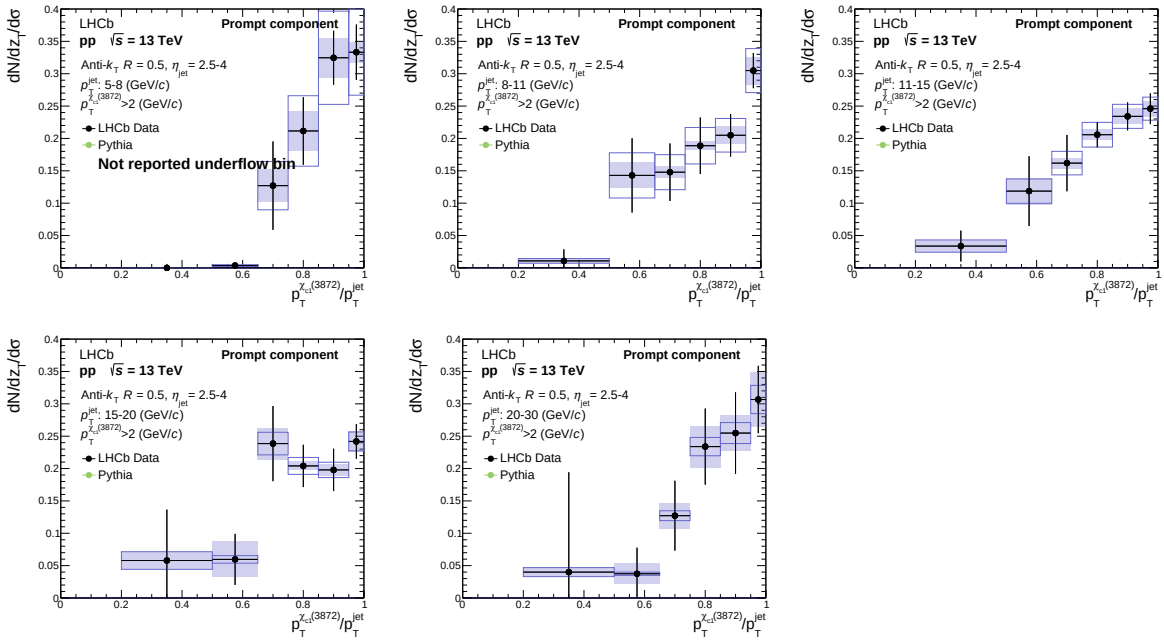

Figure 7.50: Prompt X(3872) production *vs.* z_T within fully reconstructed jets at several $p_{\mathrm{T}}(\mathrm{jet})$, normalised as $\mathrm{d}N/\mathrm{d}z_T/\mathrm{d}\sigma$, where σ is the total cross section.

7.5.2 Current theory predictions and discussion

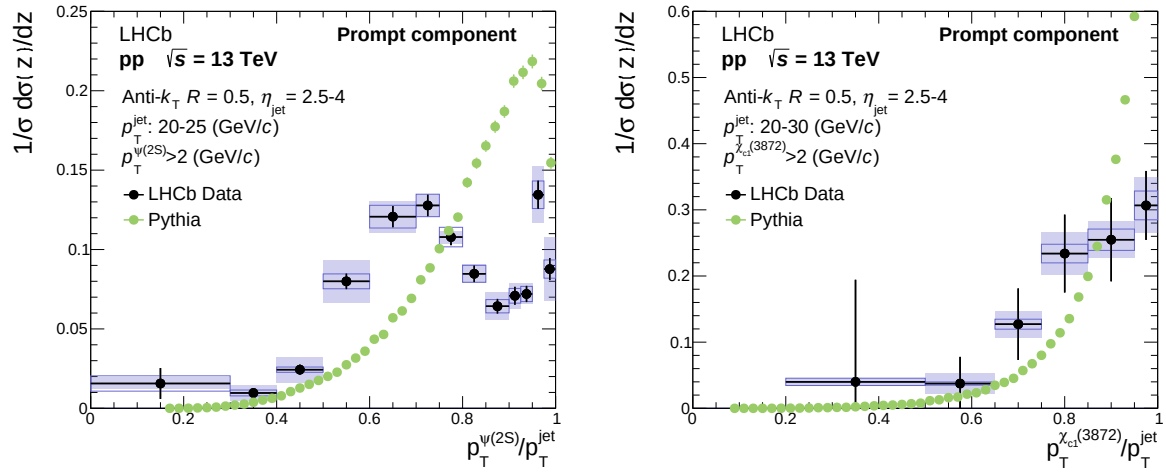

Figure 7.51: Comparison of the prompt fragmentation functions of $\psi(2S)$ and X(3872) with LHCb data and PYTHIA 8 MC predictions. The jets are required to have $p_{\mathrm{T}}(\mathrm{jet}) > 20\,\mathrm{GeV}$.

The displaced component for the $\psi(2S)$ follows the same trend as the $\psi(2S)$ results in chapter 6 with $p_{\mathrm{T}}(\mathrm{jet}) > 15\,\mathrm{GeV}$, with a central peak at $z_T \simeq 0.6$. The displaced X(3872) component has significantly lower statistics than the $\psi(2S)$, which is expected. However, at high $p_{\mathrm{T}}(\mathrm{jet})$ values, the peak has slightly moved towards higher

z_T values. This could be due to its heavier mass which means it shares more of the jet energy.

The prompt distributions for the $\psi(2S)$ and X(3872) are quite different from each other. The $\psi(2S)$ result, like that shown in chapter 6, shows a central peak at $z_T \simeq 0.6$. However, the X(3872) is more isolated towards high values z_T, which is more in line with the PYTHIA 8 prediction. As the masses of the two different particles are not too dissimilar from each other, this suggests there is another mechanism at play in the X(3872) fragmentation in comparison to the $\psi(2S)$. The $\psi(2S)$ also shows an isolated peak at high z_T values, which is observed due to the fact that the dimuon-dipion decay channel is $\sim$50 times larger than the dimuon channel, so the bins could be split more finely at high z_T. The central peak at $z_T \simeq 0.6$ could be interpreted as a possible production of the $\psi(2S)$ from fragmentation, and the peak at $z_T \simeq 1.0$ the hard scattering component. The peak is not as isolated in the dimuon decay channel. A series of cross-checks were performed between the two channels, to check for inconsistencies. The difference in the results is due to the fact there are different fiducial requirements between the two channels. The di-pion di-muon channel has additional fiducial requirements on the pions, which reduces the available phase space for the decay of the $\psi(2S)$. Once the difference in fiducial regions has been taken into account, the two channels are consistent with each other. This is shown in appendix D, along with other cross-checks such as measuring the b-decay fractions *vs.* $p_{\mathrm{T}}(\psi(2S))$ *etc.* However, the unfolding procedure for the prompt dimuon decay channel needs to take into account the prompt hyperon fraction of jets, which needs further investigation.

7.5.3 Future prospects

Analogous to the results presented in chapter 6, it would be beneficial to repeat these analyses with more statistics and also with a better MC prediction to be able to reduce the systematic certainty due to the unfolding. Also, additional fragmentation variables could be explored. This analysis gives further insight into the production of X(3872), which could be repeated for different exotic particles when enough statistics are available with Run 3 data.

CHAPTER 8

Conclusions

The work presented in this thesis has explored both theoretical and experimental measurements to understand quarkonia production in more detail. Chapter 3 details the incorporation of NRQCD fragmentation functions for various quarkonia states into the Pythia 8 parton shower. The results for the various quarkonia splitting functions, including from colour singlet production, colour octet production, and from feed-down have been presented and compared with LHCb data. The inclusion of these has the effect of pushing the predicted normalised cross section distribution to lower $z(J/\psi)$. These splittings are already extended into the bottomonium sector, although predictions have not yet been produced. More refined calculations can also be included, such as looking into double counting in the parton shower to the hard matrix element and also colour reconnection. The interference terms in the matrix element can also be taken into account between the c and $\bar{c}$. Further extensions of this work would be calculate its contribution to various inclusive branching fractions, to quarkonia production in heavy ion collisions and also polarisation effects.

Contributions to LHCb Upgrades 1 and 2 have also been discussed, with RICH detector and trigger work shown. In particular, preliminary measurements for the characterisation of LGAD sensors produced by *Micron* have been performed. The gain measurements before irradiation are consistent with the University of Glasgow measurements, where the gain increases with decreasing temperature. Preliminary results show that the gain decreases post-irradiation. However, more studies of

post-irradiated sensors need to be performed such as measuring the gain at higher voltages, and also the timing resolution of the sensor before and after irradiation.

Finally, normalised cross sections *vs.* z have been measured using Run 2 data collected by LHCb for different quarkonia states, namely the J/ψ, $\psi(2S)$, $\Upsilon(1S)$, $\Upsilon(2S)$ and $\Upsilon(3S)$, and also the X(3872) state. The measurements of prompt and displaced J/ψ's are consistent within errors to the analysis published by LHCb in 2017. Displaced $\psi(2S)$ PYTHIA 8 MC predictions are consistent with data from both the dimuon, and dimuon-dipion decay channels. However, prompt $\psi(2S)$ PYTHIA 8 predictions are again not consistent with data and predict an isolated peak at $z(\psi(2S))$ $\simeq 1$ in comparison to data which has a central peak at $z(\psi(2S)) \simeq 0.6$. The $\psi(2S)$ reconstructed from the dimuon-dipion decay channel also shows an isolated peak at $z(\psi(2S)) \simeq 1$, in comparison to the dimuon decay channel which is less isolated. This is due to the difference in fiducial requirements between the two decay channels, which is investigated in appendix D. Overall, both prompt J/ψ and $\psi(2S)$ distributions are much less isolated than current PYTHIA 8 predictions, which suggests an additional production mechanism is needed to explain this. This could be NRQCD fragmentation, or additional DPS components, or another additional mechanism. The Υ behave very differently to the J/ψ and $\psi(2S)$, which exhibits an isolated peak at $z(\Upsilon) \simeq 1.0$, and becomes more isolated for the higher mass Υ states. The distributions where $p_{\mathrm{T}}(\mathrm{jet}) > 30\,\mathrm{GeV}$ show a small peak at small $z(\Upsilon)$ values. It would be interesting to see if this peak disappears with more statistics. If not, it could be hints of DPS contributions, or maybe even fragmentation contributions. The prompt X(3872) results are different to those of the prompt J/ψ and $\psi(2S)$ where the distribution is shifted to high z values. This also suggests the mechanism for production is again different to the quarkonia, which needs to be explored.

A number of potential future measurements could be performed to increase the understanding of quarkonia and tetraquark production. First, the measurements should be repeated with higher statistics. Also, other experiments should measure these distributions, to investigate the production in different regions of phase space, which leads to better inputs for MC generators. The measurements could also be extended to other fragmentation variables, such as the jet radius, ΔR. Measurements of the polarisation *vs.* z are also important, where a preliminary investigation is explored for the J/ψ in appendix E, as they could give insight into different contributions from the colour singlet and colour octet states in the NRQCD framework.

REFERENCES

[1] A. Martin, *QUARKONIUM*, Comments Nucl. Part. Phys. **16** (1986) 249.

[2] A. Andronic *et al.*, *Heavy-flavour and quarkonium production in the LHC era: from proton–proton to heavy-ion collisions*, Eur. Phys. J. **C76** (2016) 107, arXiv:1506.03981.

[3] F. Yuan and K.-T. Chao, *Color-singlet direct j/ψ and ψ' production at the fermilab tevatron in the k_t factorization approach*, Phys. Rev. D **63** (2001) 034006.

[4] LHCb collaboration, R. Aaij *et al.*, *Measurement of forward J/ψ production cross-sections in pp collisions at $\sqrt{s} = 13$ TeV*, JHEP **10** (2015) 172, arXiv:1509.00771, [Erratum: JHEP 05, 063 (2017)].

[5] P. L. Cho and A. K. Leibovich, *Color octet quarkonia production*, Phys. Rev. **D53** (1996) 150, arXiv:hep-ph/9505329.

[6] P. L. Cho and A. K. Leibovich, *Color octet quarkonia production. 2.*, Phys. Rev. **D53** (1996) 6203, arXiv:hep-ph/9511315.

[7] Philip Ilten, *"quarkonia in jets"*, 9th May 2018. University of Birmingham Seminar.

[8] LHCb collaboration, R. Aaij *et al.*, *Measurement of J/ψ polarization in pp collisions at $\sqrt{s} = 7$ TeV*, Eur. Phys. J. **C73** (2013) 2631, arXiv:1307.6379.

[9] ALICE collaboration, B. Abelev *et al.*, *J/ψ polarization in pp collisions at $\sqrt{s} = 7$ TeV*, Phys. Rev. Lett. **108** (2012) 082001, arXiv:1111.1630.

[10] CDF collaboration, A. Abulencia *et al.*, *Polarization of J/ψ and ψ_{2S} Mesons Produced in $p\bar{p}$ Collisions at $\sqrt{s} = 1.96$-TeV*, Phys. Rev. Lett. **99** (2007) 132001, arXiv:0704.0638.

[11] CMS collaboration, S. Chatrchyan *et al.*, *Measurement of the Prompt J/ψ and $\psi(2S)$ Polarizations in pp Collisions at $\sqrt{s} = 7$ TeV*, Phys. Lett. **B727** (2013) 381, arXiv:1307.6070.

[12] LHCb collaboration, R. Aaij *et al.*, *Study of J/ψ Production in Jets*, Phys. Rev. Lett. **118** (2017) 192001, arXiv:1701.05116.

[13] T. Sjostrand, S. Mrenna, and P. Z. Skands, *PYTHIA 6.4 Physics and Manual*, JHEP **05** (2006) 026, arXiv:hep-ph/0603175.

[14] T. Sjöstrand *et al.*, *An Introduction to PYTHIA 8.2*, Comput. Phys. Commun. **191** (2015) 159, arXiv:1410.3012.

[15] CMS collaboration, A. Tumasyan *et al.*, *Fragmentation of jets containing a prompt J/ψ meson in PbPb and pp collisions at sNN=5.02TeV*, Phys. Lett. B **825** (2022) 136842, arXiv:2106.13235.

[16] E. Braaten, K. Cheung, and T. C. Yuan, *Z^0 decay into charmonium via charm quark fragmentation*, Phys. Rev. D **48** (1993) 4230.

[17] P. Ernstrom and L. Lonnblad, *Generating heavy quarkonia in a perturbative QCD cascade*, Z. Phys. **C75** (1997) 51, arXiv:hep-ph/9606472.

[18] R. Bain *et al.*, *Analytic and Monte Carlo Studies of Jets with Heavy Mesons and Quarkonia*, JHEP **06** (2016) 121, arXiv:1603.06981.

[19] *Standard model of elementary particles*, https://en.wikipedia.org/wiki/File:Standard_Model_of_Elementary_Particles.svg. Accessed: 2022-11-26.

[20] Particle Data Group, R. L. Workman and Others, *Review of Particle Physics*, PTEP **2022** (2022) 083C01.

[21] ATLAS collaboration, G. Aad *et al.*, *Combined measurements of Higgs boson production and decay using up to 80 fb^{-1} of proton-proton collision data at $\sqrt{s} = 13$ TeV collected with the ATLAS experiment*, .

[22] ATLAS collaboration, G. Aad *et al.*, *A search for the dimuon decay of the Standard Model Higgs boson in pp collisions at $\sqrt{s} = 13$ TeV with the ATLAS Detector* , CERN, Geneva, 2019. All figures including auxiliary figures are available at https://atlas.web.cern.ch/Atlas/GROUPS/PHYSICS/CONFNOTES/ATLAS-CONF-2019-028.

[23] LHCb collaboration, R. Aaij *et al.*, *Search for $A' \to \mu^+\mu^-$ Decays*, Phys. Rev. Lett. **124** (2020) 041801, arXiv:1910.06926.

[24] CDF collaboration, T. Aaltonen *et al.*, *High-precision measurement of the W boson mass with the CDF II detector*, Science **376** (2022) 170.

[25] Muon $g-2$ Collaboration, B. Abi *et al.*, *Measurement of the positive muon anomalous magnetic moment to 0.46 ppm*, Phys. Rev. Lett. **126** (2021) 141801.

[26] LHCb collaboration, R. Aaij *et al.*, *Test of lepton universality in beauty-quark decays*, Nature Phys. **18** (2022) 277, arXiv:2103.11769.

[27] B. Cabouat, *Monte-Carlo Modelling of Double Parton Scattering*, PhD thesis, Manchester U., 2020.

[28] S. Bethke, *The 2009 World Average of alpha(s)*, Eur. Phys. J. **C64** (2009) 689, arXiv:0908.1135, [,111(2009)].

[29] T. D. Lee and M. Nauenberg, *Degenerate Systems and Mass Singularities*, Phys. Rev. **133** (1964) B1549.

[30] T. Kinoshita, *Mass singularities of Feynman amplitudes*, J. Math. Phys. **3** (1962) 650.

[31] P. Skands, *Introduction to QCD*, in *Theoretical Advanced Study Institute in Elementary Particle Physics: Searching for New Physics at Small and Large Scales*, 341–420, 2013, arXiv:1207.2389.

[32] *Quark structure of proton*, https://en.wikipedia.org/wiki/Proton#/media/File:Quark_structure_proton.svg. Accessed: 2022-11-28.

[33] *Complex structure of proton*, https://www.desy.de/news/news_search/index_eng.html?openDirectAnchor=829. Accessed: 2022-11-28.

[34] V. N. Gribov and L. N. Lipatov, *Deep inelastic e p scattering in perturbation theory*, Sov. J. Nucl. Phys. **15** (1972) 438.

[35] G. Altarelli and G. Parisi, *Asymptotic Freedom in Parton Language*, Nucl. Phys. B **126** (1977) 298.

[36] Y. L. Dokshitzer, *Calculation of the Structure Functions for Deep Inelastic Scattering and e+ e- Annihilation by Perturbation Theory in Quantum Chromodynamics.*, Sov. Phys. JETP **46** (1977) 641.

[37] A. D. Martin, W. J. Stirling, R. S. Thorne, and G. Watt, *Parton distributions for the LHC*, Eur. Phys. J. C **63** (2009) 189, arXiv:0901.0002.

[38] NNPDF collaboration, R. D. Ball *et al.*, *Unbiased global determination of parton distributions and their uncertainties at NNLO and at LO*, Nucl. Phys. B **855** (2012) 153, arXiv:1107.2652.

[39] J. Pumplin *et al.*, *New generation of parton distributions with uncertainties from global QCD analysis*, JHEP **07** (2002) 012, arXiv:hep-ph/0201195.

[40] M. Cacciari, G. P. Salam, and G. Soyez, *FastJet User Manual*, Eur. Phys. J. **C72** (2012) 1896, arXiv:1111.6097.

[41] R. K. Ellis, W. J. Stirling, and B. R. Webber, *QCD and collider physics*, Camb. Monogr. Part. Phys. Nucl. Phys. Cosmol. **8** (1996) 1.

[42] M. Cacciari, G. P. Salam, and G. Soyez, *The anti-k_t jet clustering algorithm*, JHEP **04** (2008) 063, arXiv:0802.1189.

[43] J. M. Butterworth, A. R. Davison, M. Rubin, and G. P. Salam, *Jet substructure as a new Higgs search channel at the LHC*, Phys. Rev. Lett. **100** (2008) 242001, arXiv:0802.2470.

[44] P. Ilten, *Electroweak and Higgs Measurements Using Tau Final States with the LHCb Detector*, PhD thesis, University Coll., Dublin, 2013-09-06, arXiv:1401.4902.

[45] J. Bellm *et al.*, *Herwig 7.0/Herwig++ 3.0 release note*, Eur. Phys. J. C **76** (2016) 196, arXiv:1512.01178.

[46] T. Gleisberg *et al.*, *Event generation with SHERPA 1.1*, JHEP **02** (2009) 007, arXiv:0811.4622.

[47] C. Bierlich *et al.*, *A comprehensive guide to the physics and usage of pythia 8.3*, 2022. doi: 10.48550/ARXIV.2203.11601.

[48] T. Sjostrand and V. A. Khoze, *On Color rearrangement in hadronic W+ W- events*, Z. Phys. C **62** (1994) 281, arXiv:hep-ph/9310242.

[49] L. Lönnblad and T. Sjöstrand, *Modelling bose–einstein correlations at LEP 2*, The European Physical Journal C **2** (1998) 165.

[50] D. Amati and G. Veneziano, *Preconfinement as a property of perturbative qcd*, Physics Letters B **83** (1979) 87.

[51] T. Sjostrand and P. Z. Skands, *Transverse-momentum-ordered showers and interleaved multiple interactions*, Eur. Phys. J. C **39** (2005) 129, arXiv:hep-ph/0408302.

[52] A. Buckley *et al.*, *General-purpose event generators for LHC physics*, Phys. Rept. **504** (2011) 145, arXiv:1101.2599.

[53] G. Gustafson, *Dual Description of a Confined Color Field*, Phys. Lett. B **175** (1986) 453.

[54] G. Gustafson and U. Pettersson, *Dipole Formulation of QCD Cascades*, Nucl. Phys. B **306** (1988) 746.

[55] L. Lonnblad, *ARIADNE version 4: A Program for simulation of QCD cascades implementing the color dipole model*, Comput. Phys. Commun. **71** (1992) 15.

[56] Y. L. Dokshitzer and G. Marchesini, *Monte Carlo and large angle gluon radiation*, JHEP **03** (2009) 117, arXiv:0809.1749.

[57] E. Norrbin and T. Sjostrand, *QCD radiation off heavy particles*, Nucl. Phys. B **603** (2001) 297, arXiv:hep-ph/0010012.

[58] S. Hoeche *et al.*, *Matching parton showers and matrix elements*, in *HERA and the LHC: A Workshop on the Implications of HERA for LHC Physics: CERN - DESY Workshop 2004/2005 (Midterm Meeting, CERN, 11-13 October 2004; Final Meeting, DESY, 17-21 January 2005)*, 288–289, 2005, arXiv:hep-ph/0602031.

[59] S. Hoeche, *Introduction to Parton Showers and Matching*, MCnet Summer School Lecture, 2021.

[60] A. Deur, S. J. Brodsky, and G. F. de Teramond, *The QCD Running Coupling*, Nucl. Phys. **90** (2016) 1, arXiv:1604.08082.

[61] V. Papadimitriou, *Inclusive J/ψ, ψ (2S) and b quark production in $\bar{p}p$ collisions at $\sqrt{s}$ = 1.8-TeV*, AIP Conf. Proc. **272** (2008) 1086.

[62] E. Braaten, S. Fleming, and T. C. Yuan, *PRODUCTION OF HEAVY QUARKONIUM IN HIGH-ENERGY COLLIDERS*, Annual Review of Nuclear and Particle Science **46** (1996) 197.

[63] Z.-G. He, F. Ying, and K.-T. Chao, *Relativistic correction to e+e(-) -> j/psi plus gg at b factories and constraint on color-octet matrix elements*, Physical Review D - PHYS REV D **81** (2010) 054036.

[64] L3 collaboration, M. Acciarri *et al.*, *Heavy quarkonium production in Z decays*, Phys. Lett. B **453** (1999) 94.

[65] P. Cho and A. K. Leibovich, *Color-octet quarkonia production*, Phys. Rev. D **53** (1996) 150.

[66] A. Buckley *et al.*, *Rivet user manual*, Comput. Phys. Commun. **184** (2013) 2803, arXiv:1003.0694.

[67] E. Maguire, L. Heinrich, and G. Watt, *HEPData: a repository for high energy physics data*, J. Phys. Conf. Ser. **898** (2017) 102006, arXiv:1704.05473.

[68] A. Buckley *et al.*, *The HepMC3 event record library for Monte Carlo event generators*, Comput. Phys. Commun. **260** (2021) 107310, arXiv:1912.08005.

[69] R. Bain *et al.*, *NRQCD Confronts LHCb Data on Quarkonium Production within Jets*, Phys. Rev. Lett. **119** (2017) 032002, arXiv:1702.05525.

[70] L. Evans and P. Bryant, *LHC machine*, Journal of Instrumentation **3** (2008) S08001.

[71] S. Myers, *The LEP Collider, from design to approval and commissioning*, John Adams' Lecture, CERN, Geneva, 1991. Delivered at CERN, 26 Nov 1990.

[72] ATLAS collaboration, E. Boos *et al.*, *ATLAS: Letter of intent for a general purpose p p experiment at the large hadron collider at CERN*, .

[73] CMS collaboration, M. Della Negra *et al.*, *CMS: letter of intent by the CMS Collaboration for a general purpose detector at LHC* , CERN, Geneva, 1992. Open presentation to the LHCC 5 November 1992, M. Della Negra/CERN, CMS Spokesman.

[74] H. Dijkstra, H. J. Hilke, T. Nakada, and T. Ypsilantis, *LHCb Letter of Intent, LHCb Collaboration*, .

[75] ALICE collaboration, N. Antoniou *et al.*, *Letter of Intent for A Large Ion Collider Experiment*, .

[76] J. Haffner, *The CERN accelerator complex. Complexe des accélérateurs du CERN*, .

[77] T. Tantau, *The TikZ and PGF Packages*.

[78] LHCb collaboration, A. A. Alves, Jr. *et al.*, *The LHCb Detector at the LHC*, JINST **3** (2008) S08005.

[79] LHCb collaboration, R. Aaij *et al.*, *Observation of $J/\psi p$ Resonances Consistent with Pentaquark States in $\Lambda_b^0 \to J/\psi K^- p$ Decays*, Phys. Rev. Lett. **115** (2015) 072001, arXiv:1507.03414.

[80] LHCb collaboration, F. Betti, *Observation of CP violation in charm decays at LHCb*, in *54th Rencontres de Moriond on Electroweak Interactions and Unified Theories (Moriond EW 2019) La Thuile, Italy, March 16-23, 2019*, 2019, arXiv:1905.05428.

[81] LHCb collaboration, C. Elsässer, *$\bar{b}b$ production angle plots*, https://lhcb.web.cern.ch/lhcb/speakersbureau/html/bb_ProductionAngles.html.

[82] R. Alemany-Fernandez, F. Follin, and R. Jacobsson, *The LHCb Online Luminosity Control and Monitoring*, in *4th International Particle Accelerator Conference*, TUPFI010, 2013.

[83] L. Collaboration, *Standard set of performance numbers*, 2020.

[84] R. Aaij *et al.*, *The LHCb Trigger and its Performance in 2011*, JINST **8** (2013) P04022, arXiv:1211.3055.

[85] M. Patel, M. Losasso, and T. Gys, *Magnetic shielding studies of the lhcb rich photon detectors*, Nuclear Instruments and Methods in Physics Research Section A: Accelerators, Spectrometers, Detectors and Associated Equipment **553** (2005) 114, Proceedings of the fifth International Workshop on Ring Imaging Detectors.

[86] H. B.D̃ijkstra, *Cp violation prospects at the lhc*, Brazilian Journal of Physics - BRAZ J PHYS **34** (2004) .

[87] A. Piucci, *The LHCb upgrade*, Journal of Physics: Conference Series **878** (2017) 012012.

[88] LHCb collaboration, I. Bediaga *et al.*, *LHCb PID Upgrade Technical Design Report*, .

[89] V. Lukashenko, *LHCb RICH Upgrade 2019: CLARO calibration and MaPMT characterization*, .

[90] LHCb RICH Collaboration, E. Franzoso, *The upgrade and performance of the LHCb RICH detector*, Nuovo Cimento C **44** (2021) 46. 4 p.

[91] A. Dziurda, *The lhcb trigger and its upgrade*, Nuclear Instruments and Methods in Physics Research Section A: Accelerators, Spectrometers, Detectors and Associated Equipment **824** (2016) 277, Frontier Detectors for Frontier Physics: Proceedings of the 13th Pisa Meeting on Advanced Detectors.

[92] H. Abdolmaleki and A. Khorramian, *Parton distribution functions and constraints on the intrinsic charm content of the proton using the Brodsky-Hoyer-Peterson-Saka approach*, Phys. Rev. **D99** (2019) 116019, arXiv:1903.02583.

[93] LHCb collaboration, R. Aaij *et al.*, *Identification of beauty and charm quark jets at LHCb*, JINST **10** (2015) P06013, arXiv:1504.07670.

[94] C. M. LHCb Collaboration, *Framework TDR for the LHCb Upgrade II - Opportunities in flavour physics, and beyond, in the HL-LHC era* , CERN, Geneva, 2021.

[95] G. Lutz, *Semiconductor Radiation Detectors: Device Physics*, Springer, New York, 1999.

[96] E. Currás, M. Fernández, and M. Moll, *Gain suppression mechanism observed in Low Gain Avalanche Detectors*, Nucl. Instrum. Methods Phys. Res. , A **1031** (2022) 166530. 14 p, arXiv:2107.10022, 14 pages, 10 figures.

[97] N. Moffat *et al.*, *Low Gain Avalanche Detectors (LGAD) for particle physics and synchrotron applications*, JINST **13** (2018) C03014.

[98] T. Yang *et al.*, *Leakage current simulations of Low Gain Avalanche Diode with improved Radiation Damage Modeling*, Nucl. Instrum. Meth. A **1040** (2022) 167111, arXiv:2106.15421.

[99] M. Ferrero *et al.*, *An Introduction to Ultra-Fast Silicon Detectors: Design, Tests, and Performances*, Taylor & Francis, 2021.

[100] F. Hartmann, *Evolution of Silicon Sensor Technology in Particle Physics*, vol. 275 of *Springer Tracts in Modern Physics*, Springer, 2017.

[101] J. Mulvey, *Laser tct & strontium-90 ctt experimental procedure at the bilpa laboratory*, 2022.

[102] J. Mulvey. private communication.

[103] D. Thompson. private communication.

[104] M. Cristea, *Capacitance-voltage profiling techniques for characterization of semiconductor materials and devices*, SSRN Electronic Journal (2010) .

[105] E. Currás, M. Fernández, and M. Moll, *Gain reduction mechanism observed in Low Gain Avalanche Diodes*, Nucl. Instrum. Meth. A **1031** (2022) 166530, arXiv:2107.10022.

[106] LHCb collaboration, R. Aaij *et al.*, *Study of J/ψ Production in Jets*, Phys. Rev. Lett. **118** (2017) 192001, arXiv:1701.05116.

[107] D. Bjergaard, *A Measurement of the Radiation Environment Around Prompt J/ψ Events at ATLAS*, PhD thesis, Duke U., 2017.

[108] STAR collaboration, K. Shen, *Recent J/Ψ results in p+p and Au+Au collisions from STAR*, EPJ Web Conf. **259** (2022) 12002.

[109] X.-H. Mo, C.-Z. Yuan, and P. Wang, *Study of the rho-pi Puzzle in Charmonium Decays*, arXiv:hep-ph/0611214.

[110] S. Benson, V. V. Gligorov, M. A. Vesterinen, and J. M. Williams, *The LHCb Turbo Stream*, J. Phys. Conf. Ser. **664** (2015) 082004.

[111] G. Barrand *et al.*, *GAUDI - A software architecture and framework for building HEP data processing applications*, Comput. Phys. Commun. **140** (2001) 45.

[112] R. Brun and F. Rademakers, *ROOT: An object oriented data analysis framework*, Nucl. Instrum. Meth. **A389** (1997) 81.

[113] W. Verkerke and D. Kirkby, *The RooFit toolkit for data modeling*, arXiv e-prints (2003) physics/0306116, arXiv:physics/0306116.

[114] H. Diehl, P. Ilten and M. Williams, *"production of j/ψ mesons in jets"*, 6th December 2016. LHCb Analysis Note LHCb-ANA-2016-063.

[115] S. Coquereau, *Study of the B0→K*0μ+μ- decay with the LHCb experiment : angular analysis and measurement of the ratio RK*, PhD thesis, Paris U., VI-VII, 2016.

[116] LHCb collaboration, R. Aaij *et al.*, *LHCb Detector Performance*, Int. J. Mod. Phys. **A30** (2015) 1530022, arXiv:1412.6352.

[117] T. Skwarnicki, *A study of the radiative CASCADE transitions between the Upsilon-Prime and Upsilon resonances*, PhD thesis, Cracow, INP, 1986.

[118] LHCb collaboration, R. Aaij *et al.*, *Measurement of J/ψ production in pp collisions at $\sqrt{s} = 7$ TeV*, Eur. Phys. J. **C71** (2011) 1645, arXiv:1103.0423.

[119] J. Kim and C. D. Scott, *Robust Kernel Density Estimation*, arXiv e-prints (2011) arXiv:1107.3133, arXiv:1107.3133.

[120] ATLAS collaboration, S. Biondi, *Experience with using unfolding procedures in ATLAS*, EPJ Web Conf. **137** (2017) 11002.

[121] M. Alexander, *Tracking efficiencies*, https://twiki.cern.ch/twiki/bin/viewauth/LHCbInternal/LHCbTrackingEfficiencies, 2021.

[122] T. L. collaboration, *Measurement of the track reconstruction efficiency at lhcb*, Journal of Instrumentation **10** (2015) P02007.

[123] M. Stahl, *Machine learning and parallelism in the reconstruction of lhcb and its upgrade*, Journal of Physics: Conference Series **898** (2017) .

[124] S. Tolk, J. Albrecht, F. Dettori, and A. Pellegrino, *Data driven trigger efficiency determination at LHCb*, .

[125] D. Cervenkov, *Pidcalib2*, https://pypi.org/project/pidcalib2/#description, 2022.

[126] Belle Collaboration, S.-K. Choi *et al.*, *Observation of a narrow charmoniumlike state in exclusive $B^{\pm} \to K^{\pm}\pi^{+}\pi^{-}j/\psi$ decays*, Phys. Rev. Lett. **91** (2003) 262001.

[127] A. Fanfani and A. Meyer, *The x(3872) exotic charmonium: A charming puzzle*, https://cms.cern/news/x3872-exotic-charmonium-charming-puzzle, 2013.

[128] LHCb collaboration, R. Aaij *et al.*, *Determination of the X(3872) meson quantum numbers*, Phys. Rev. Lett. **110** (2013) 222001, arXiv:1302.6269.

[129] LHCb collaboration, R. Aaij *et al.*, *Quantum numbers of the $X(3872)$ state and orbital angular momentum in its $\rho^0 J\psi$ decay*, Phys. Rev. D **92** (2015) 011102, arXiv:1504.06339.

[130] LHCb collaboration, R. Aaij *et al.*, *Study of the lineshape of the $\chi_{c1}(3872)$ state*, Phys. Rev. D **102** (2020) 092005, arXiv:2005.13419.

[131] LHCb collaboration, R. Aaij *et al.*, *Study of $B_s^0 \to J\psi\pi^+\pi^-K^+K^-$ decays*, JHEP **02** (2021) 024, arXiv:2011.01867, [Erratum: JHEP 04, 170 (2021)].

[132] LHCb collaboration, R. Aaij *et al.*, *Study of the $\psi_2(3823)$ and $\chi_{c1}(3872)$ states in $B^+ \to (J\psi\pi^+\pi^-)\,K^+$ decays*, JHEP **08** (2020) 123, arXiv:2005.13422.

[133] LHCb collaboration, R. Aaij *et al.*, *Observation of the $\Lambda_b^0 \to \chi_{c1}(3872)pK^-$ decay*, JHEP **09** (2019) 028, arXiv:1907.00954.

[134] LHCb collaboration, R. Aaij *et al.*, *Observation of $\eta_c(2S) \to p\bar{p}$ and search for $X(3872) \to p\bar{p}$ decays*, Phys. Lett. B **769** (2017) 305, arXiv:1607.06446.

[135] LHCb collaboration, R. Aaij *et al.*, *Evidence for the decay $X(3872) \to \psi(2S)\gamma$*, Nucl. Phys. B **886** (2014) 665, arXiv:1404.0275.

[136] LHCb Collaboration, *Observation of sizeable ω contribution to $\chi_{c1}(3872) \to \pi^+\pi^- j/\psi$ decays*, 2022. doi: 10.48550/ARXIV.2204.12597.

[137] LHCb collaboration, R. Aaij *et al.*, *Measurement of $\chi_{c1}(3872)$ production in proton-proton collisions at $\sqrt{s}$ = 8 and 13 TeV*, JHEP **01** (2022) 131, arXiv:2109.07360.

[138] LHCb collaboration, R. Aaij *et al.*, *Observation of Multiplicity Dependent Prompt $\chi_{c1}(3872)$ and $\psi(2S)$ Production in pp Collisions*, Phys. Rev. Lett. **126** (2021) 092001, arXiv:2009.06619.

[139] J. Matthew Durham, Cameron Dean, Eliane Epple, Krista Smith, Cesar da Silva, Cheuk-Ping Wong, *Nuclear Modification of X(3872) and $\psi(2S)$ Production in pPb Collisions at $\sqrt{s}$ = 8.16 TeV*, LHCb-ANA-2022-009 (2022).

[140] A. Esposito *et al.*, *The nature of X(3872) from high-multiplicity pp collisions*, Eur. Phys. J. C **81** (2021) 669, arXiv:2006.15044.

[141] E. Braaten, L.-P. He, K. Ingles, and J. Jiang, *Production of $X(3872)$ at High Multiplicity*, Phys. Rev. D **103** (2021) L071901, arXiv:2012.13499.

[142] A. Esposito *et al.*, *From the line shape of the X(3872) to its structure*, Phys. Rev. D **105** (2022) L031503, arXiv:2108.11413.

[143] W. D. Hulsbergen, *Decay chain fitting with a kalman filter*, Nuclear Instruments and Methods in Physics Research Section A: Accelerators, Spectrometers, Detectors and Associated Equipment **552** (2005) 566.

[144] M. Cacciari, G. P. Salam, and G. Soyez, *The Catchment Area of Jets*, JHEP **04** (2008) 005, arXiv:0802.1188.

[145] T. Adye, *Unfolding algorithms and tests using RooUnfold*, in *PHYSTAT 2011*, (Geneva), 313–318, CERN, 2011, arXiv:1105.1160.

[146] G. D'Agostini, *A Multidimensional unfolding method based on Bayes' theorem*, Nucl. Instrum. Meth. A **362** (1995) 487.

[147] E. Braaten and T. C. Yuan, *Gluon fragmentation into heavy quarkonium*, Phys. Rev. Lett. **71** (1993) 1673, arXiv:hep-ph/9303205.

[148] E. Braaten and T. C. Yuan, *Gluon fragmentation into P wave heavy quarkonium*, Phys. Rev. D **50** (1994) 3176, arXiv:hep-ph/9403401.

[149] T. C. Yuan, *Perturbative qcd fragmentation functions for production of p-wave charm and bottom mesons*, Phys. Rev. D **50** (1994) 5664.

[150] P. Ernstrom, L. Lonnblad, and M. Vanttinen, *Evolution effects in z^0 fragmentation into charmonium*, doi: 10.48550/ARXIV.HEP-PH/9612408.

[151] J. G. Körner, *Helicity Amplitudes and Angular Decay Distributions*, in *Proceedings, Helmholtz International Summer School on Physics of Heavy Quarks and Hadrons (HQ 2013): JINR, Dubna, Russia, July 15-28, 2013*, 169–184, 2014, arXiv:1402.2787.

[152] R. Kutsche, *An angular distribution cookbook*, http://home.fnal.gov/~kutschke/, 1996. CLEO Internal note; Online; accessed 29 September 2019.

[153] Maddalena Frosini, Emanuele Santovetti and Yanxi Zhang, *"measurement of j/ψ polarization in pp collisions at $\sqrt{s}$ = 7 tev"*, 16th May 2013. LHCb Analysis Note LHCb-ANA-2013-018.

[154] PHENIX collaboration, A. Adare *et al.*, *Transverse momentum dependence of J/psi polarization at midrapidity in p+p collisions at s**(1/2) = 200-GeV*, Phys. Rev. **D82** (2010) 012001, arXiv:0912.2082.

[155] D. J. Lange, *The EvtGen particle decay simulation package*, Nucl. Instrum. Meth. **A462** (2001) 152.

[156] P. Ilten, *CIMBA: fast Monte Carlo generation using cubic interpolation*, arXiv:1908.08353.

APPENDIX A

PYTHIA 8 - Fragmentation functions

A.1 Summary of fragmentation functions

$Q \to Q \left[{}^3S_1^{(1)}\right]$	See section A.2.	[16](15)
$Q \to Q \left[{}^1S_0^{(1)}\right]$	See section A.3.	[16](19)
$g \to gg \left[{}^3S_1^{(1)}\right]$	See section A.4.	[147](9,10,11,12,13,14,15)
$g \to g \left[{}^1S_0^{(1)}\right]$	See section A.5.	[147](7)
$g \to g \left[{}^3P_0^{(1)}\right]$	See section A.6 and section A.6.1.	[148](1,4,8,9,10)
$g \to g \left[{}^3P_1^{(1)}\right]$	See section A.6 and section A.6.2.	[148](1,4,8,9,11)
$g \to g \left[{}^3P_2^{(1)}\right]$	See section A.6 and section A.6.3.	[148](1,4,8,9,12)
$Q \to Q \left[{}^3P_0^{(1)}\right]$	See section A.7 and section A.7.1.	[149](16,23,24,25,26,27,98,99)
$Q \to Q \left[{}^3P_1^{(1)}\right]$	See section A.7 and section A.7.2.	[149](16,23,28,29,30,31,98,99)
$Q \to Q \left[{}^3P_2^{(1)}\right]$	See section A.7 and section A.7.3.	[149](16,23,32,33,34,35,98,99)

$g \to \left[{}^3P_J^{(8)}\right]$	See section A.8.	[148](1,21,22)
$g \to \left[{}^3S_1^{(8)}\right]$	See section A.9.	[150](13) [17](4)
$Q \to Q\left[{}^3S_1^{(8)}\right]$	See section A.10.	[149](63,98)

Table A.1: Summary of the fragmentation functions, along with the papers they have been taken from, and their respective equation numbers in those papers.

A.2 $Q \to Q\left[{}^3S_1^{(1)}\right]$

Equation (15):

$$\begin{aligned}\int_0^1 dz\, D_{c\to\psi}(z) \;=\; & \frac{8{\alpha_s}^2|R(0)|^2}{27\pi m_Q}\int_0^\infty ds\frac{1}{(s-m_Q^2)^4}\int_0^1 dz\theta\left(s-\frac{4m_Q^2}{z}-\frac{m_Q^2}{1-z}\right)\\ & (s^2-2m_Q^2 s-47m_Q^4)-z(s-m_Q^2)(s-9m_Q^2)+\\ & +4\frac{z(1-z)}{2-z}s(s-m_Q^2)-4\frac{8-7z-5z^2}{2-z}m_Q^2(s-m_Q^2)\\ & +12\frac{z^2(1-z)}{(2-z)^2}(s-m_Q^2)^2\end{aligned} \tag{A.1}$$

A.3 $Q \to Q\left[{}^1S_0^{(1)}\right]$

Equation (19) full expansion:

$$\begin{aligned}\int_0^1 dz\, D_{c\to\eta_c}(z) \;=\; & \frac{8{\alpha_s}^2|R(0)|^2}{27\pi m_Q}\int_0^\infty ds\frac{1}{(s-m_Q^2)^4}\int_0^1 dz\theta\left(s-\frac{4m_Q^2}{z}-\frac{m_Q^2}{1-z}\right)\\ & (s+3m_Q^2 s)(s-5m_Q^2)-(s-m_Q^2)(s-9m_Q^2)z\\ & +4\frac{s-m_Q^2}{2-z}((s-m_Q^2)-(s-3m_Q^2)z)z\\ & +4\left(\frac{s-m_Q^2}{2-z}\right)^2 z^2(1-z)\end{aligned} \tag{A.2}$$

A.4 $g \to gg \left[{}^3S_1^{(1)}\right]$

Equation (9):

$$D_{g\to\psi}(z,2m_c) = \frac{5}{144\pi^2}\alpha_S(2m_c)^3\frac{|R(0)|^2}{M_\psi^3}\int_0^z dr\int_{(r+z^2)/2z}^{(1+r)/2} dy \frac{1}{(1-y)^2(y-r)^2(y^2-r)^2} \sum_{i=0}^{2} z^i\left(f_i(r,y)+g_i(r,y)\frac{1+r-2y}{2(y-r)\sqrt{y^2-r}}\log\frac{y-r+\sqrt{y^2-r}}{y-r-\sqrt{y^2-r}}\right), \tag{A.3}$$

where the integration variables are $r = 4m_c^2/s$ and $y = p\cdot q/s$. The functions f_i and g_i are shown in equations (10,11,12,13,14,15) respectively,

$$\begin{aligned} f_0(r,y) = {} & r^2(1+r)(3+12r+13r^2) - 16r^2(1+r)(1+3r)y \\ & - 2r(3-9r-21r^2+7r^3)y^2 + 8r(4+3r+3r^2)y^3 - 4r(9-3r-4r^2)y^4 \\ & - 16(1+3r+3r^2)y^5 + 8(6+7r)y^6 - 32y^7, \end{aligned} \tag{A.4}$$

$$\begin{aligned} f_1(r,y) = {} & -2r(1+5r+19r^2+7r^3)y + 96r^2(1+r)y^2 + 8(1-5r-22r^2-2r^3)y^4 \\ & + 16r(7+3r)y^4 - 8(5+7r)r^5 + 32y^6, \end{aligned} \tag{A.5}$$

$$\begin{aligned} f_2(r,y) = {} & r(1+5r+19r^2+7r^3) - 48r^2(1+r)y - 4(1-5r-22r^2-2r^3)y^2 \\ & - 8r(7+3r)y^3 + 4(5+7r)r^4 + 16y^5, \end{aligned} \tag{A.6}$$

$$\begin{aligned} g_0(r,y) = {} & r^3(1+r)(3+24r+13r^2) - 4r^3(7-3r-12r^2)y - 2r^3(17+22r-7r^2)y^2 \\ & + 4r^2(13+5r-6r^2)y^3 - 8r(1+2r+5r^2+2r^3)y^4 - 8r(3-11r-6r^2)y^5 \\ & + 8(1-2r-5r^2)y^6, \end{aligned} \tag{A.7}$$

$$\begin{aligned} g_1(r,y) = {} & -2r^2(1+r)(1-r)(1+7r)y + 8r^2(1+3r)(1-4r)y^2 \\ & + 4r(1+10r+57r^2+4r^3)y^3 - 8r(1+29r+6r^2)y^4 - 8(1-8r-5r^2)y^5, \end{aligned} \tag{A.8}$$

$$g_2(r,y) = r^2(1+r)(1-r)(1+7r) - 4r^2(1+3r)(1-4r)y \\ - 2r(1+10r+57r^2+4r^3)y^2 + 4r(1+29r+6r^2)y^3 + 4(1-8r-5r^2)y^4. \tag{A.9}$$

A.5 $g \to g\left[{}^1S_0^{(1)}\right]$

Equation (7):

$$\int_0^1 dz\; D_{g\to\eta_c}(z) = \frac{\alpha_s^2}{3\pi}\frac{|R(0)|^2}{2m_c}\int_{4m_c^2}^{\infty} ds \int_{4m_c^2/s}^1 dz \frac{s^2+16m_c^4-2z(s+4m_c^2)s+2z^2s^2}{s^2(s-4m_c^2)^2} \tag{A.10}$$

A.6 $g \to g\left[{}^3P_J^{(1)}\right]\mathbf{g}$

Equation (1):

$$D_{i\to\chi_{cJ}}(z,m_c) = \frac{H_1}{m_c}d_1^{(J)}(z,\Lambda) + (2J+1)\frac{H_8'(\Lambda)}{m_c}d_8(z) \tag{A.11}$$

Equation (4):

$$H_1 \approx \frac{9}{2\pi}\frac{|R_p'(0)|^2}{m_c^4}\,[1+O(v^2)] \tag{A.12}$$

Equation (8):

$$d_1^{(J)}(z,\Lambda) = \frac{\alpha_s^2}{27}\int_{4m_c^2/z}^{\infty} ds \frac{m_c^2}{s^2(s-4m_c^2)^4} f_J(s,z),\; z < \left(1+\frac{\Lambda}{m_c}\right)^{-1} \tag{A.13}$$

Equation (9):

$$d_1^{(J)}(z,\Lambda) = \frac{\alpha_s^2}{27}\int_{s_{min}(\Lambda)}^{\infty} ds \frac{m_c^2}{s^2(s-4m_c^2)^4} f_J(s,z),\; z > \left(1+\frac{\Lambda}{m_c}\right)^{-1} \tag{A.14}$$

A.6.1 $g \to g\left[{}^3P_0^{(1)}\right]\mathbf{g}$

Equation (10):

$$f_0(s,z) = (s-12m_c^2)^2[(s-4m_c^2)^2 - 2(1-z)(zs-4m_c^2)s] \tag{A.15}$$

A.6.2 $g \to g \left[{}^3P_1^{(1)}\right]\mathbf{g}$

Equation (11):

$$f_1(s,z) = 6s^2[(s-4m_c^2)^2 - 2(1-z)(zs-4m_c^2)(s-8m_c^2)] \tag{A.16}$$

A.6.3 $g \to g \left[{}^3P_2^{(1)}\right]\mathbf{g}$

Equation (12):

$$f_2(s,z) = 2[(s-4m_c^2)^2(s^2+96m_c^4) - 2(1-z)(zs-4m_c^2)s(s^2-24sm_c^2+96m_c^4)] \tag{A.17}$$

A.7 $Q \to Q \left[{}^3P_J^{(1)}\right]$

Equation (16):

$$D^{(1)}(z) = \int ds\, \theta\left(s - \frac{M^2}{z} - \frac{r^2M^2}{1-z}\right) D^{(1)}(z,s) \tag{A.18}$$

Equation (23):

$$D^{(1)}_{\bar{b}\to\bar{b}c({}^3P_J)}(z,s) = \frac{32\alpha_s^2(2m_c)}{243}\frac{r\bar{r}^3}{(1-\bar{r}z)^4}\sum_{n=0}^{3}\frac{f_n^{(J)}M^{(8-2n)}}{(s-\bar{r}^2M^2)^{5-n}} \tag{A.19}$$

Splitting kernel here is for $\bar{b} \to \bar{b}c$, where $M = m_b + m_c$, $r = m_c/M$ and $\bar{r} = m_b/M$. For χ_c states, which are $c\bar{c}$ states, replace any m_b with m_c. Hence, $M = 2m_c$, $r = \bar{r} = 1/2$. Equation (98):

$$\begin{aligned} D_{c\to\chi_{cJ}}(z,\mu_0) = {} & \frac{H_{1(c\bar{c})}}{m_c} D^{(1)}_{c\to c\bar{c}({}^3P_J)}(z,\Lambda) \\ & + (2J+1)\frac{H'_{8(c\bar{c})}(\Lambda)}{m_c} D^{(8)}_{c\to c\bar{c}({}^3S_1)}(z) \end{aligned} \tag{A.20}$$

Equation (99):

$$H_{1(c\bar{c})} \approx \frac{9}{2\pi}\frac{|R'_p(0)|^2}{m_c^4} \tag{A.21}$$

A.7.1 $Q \to Q \left[{}^3P_0^{(1)}\right]$

Equation (24):

$$f_0^{(0)} = 64r^2\bar{r}^3(1-\bar{r}z)^4 \tag{A.22}$$

Equation (25):

$$f_1^{(0)} = 8r\bar{r}(1-\bar{r}z)^3[1-18r+14r^2-2\bar{r}(1-2r+7r^2)z+\bar{r}^2(1+2r)z^2] \tag{A.23}$$

Equation (26):

$$\begin{aligned} f_2^{(0)} = -(1-\bar{r}z)^2[&2(1-4r)(1+6r-4r^2)-(5+14r-8r^2+80r^3-64r^4)z \\ &+2\bar{r}(2+9r+18r^2-28r^3-16r^4)z^2-\bar{r}^2(1+6r+16r^2-32r^3)z^3] \end{aligned} \tag{A.24}$$

Equation (27):

$$f_3^{(0)} = (1-z)[1-4r-(1-4r)(1-2r)z-r\bar{r}(3-4r)z^2]^2 \tag{A.25}$$

A.7.2 $Q \to Q \left[{}^3P_1^{(1)}\right]$

Equation (28):

$$f_0^{(1)} = 192r^2\bar{r}^3(1-\bar{r}z)^4 \tag{A.26}$$

Equation (29):

$$f_1^{(1)} = 24r\bar{r}(1-\bar{r}z)^3[2(1-r-r^2)-\bar{r}(3+10r-2r^2)z+\bar{r}^2z^2] \tag{A.27}$$

Equation (30):

$$\begin{aligned} f_2^{(1)} = -6(1-\bar{r}z)^2[&2(1+2r)-(5-2r+6r^2)z \\ &+2\bar{r}(2-3r-4r^2)z^2-\bar{r}^2(1-2r+2r^2)z^3] \end{aligned} \tag{A.28}$$

Equation (31):

$$f_3^{(1)} = 6(1-z)[1-2(1-2r)z+(1-4r)(1-2r)z^2+2r\bar{r}(1-2r)z^3+r^2\bar{r}^2z^4] \tag{A.29}$$

A.7.3 $Q \to Q\left[{}^3P_2^{(1)}\right]$

Equation (32):

$$f_0^{(2)} = 320r^2\bar{r}^3(1-\bar{r}z)^4 \tag{A.30}$$

Equation (33):

$$f_1^{(2)} = 8r\bar{r}^2(1-\bar{r}z)^3[2(4+13r)-(1+70r-26r^2)z-\bar{r}(7+8r)z^2] \tag{A.31}$$

Equation (34):

$$\begin{aligned} f_2^{(2)} = -4\bar{r}^2(1-\bar{r}z)^2[&4(1+4r)-(7+12r-32r^2)z \\ &+2(1+13r-26r^2+8r^3)z^2-(1-30r-5r^2+4r^3)z^3] \end{aligned} \tag{A.32}$$

Equation (35):

$$\begin{aligned} f_3^{(2)} = 4\bar{r}^2(1-z)[&2-4(1-2r)z+(5-8r+12r^2)z^2 \\ &+2(1-2r)(3+2r^2)z^3+(3-12r+12r^2+2r^4)z^4] \end{aligned} \tag{A.33}$$

A.8 $g \to \left[{}^3P_J^{(8)}\right]$

Equation (1):

$$D_{i\to\chi_{cJ}}(z,m_c) = \frac{H_1}{m_c}d_1^{(J)}(z,\Lambda)+(2J+1)\frac{H_8'(\Lambda)}{m_c}d_8(z), \tag{A.34}$$

Equation (21):

$$d_s(z) = \frac{\pi\alpha_s}{24}\delta(1-z), \tag{A.35}$$

Equation (22):

$$D_{g\to\chi_{cJ}}(z,2m_c) \approx \frac{2\alpha_s^2(2m_c)}{81}\frac{H_1}{m_c}\left[(2J+1)\frac{z}{(1-z)_+} + Q_J\delta(1-z) + P_J(z)\right] + (2J+1)\frac{\pi\alpha_s(2m_c)}{24}\frac{H_8'(m_c)}{m_c}\delta(1-z) \tag{A.36}$$

A.9 $g \to \left[{}^3S_1^{(8)}\right]$

Equation 13:

$$d_c^{\psi}(z,s) = \frac{\pi\alpha_s \langle 0|\, \mathcal{O}_8^{\psi}({}^3S_1)\, |0\rangle}{24m_c^3}\delta(1-z)\delta\left(1-\frac{s}{M_{\psi}^2}\right) \tag{A.37}$$

The sampling of z from a delta function of finite width:

$$\frac{1}{\epsilon}\theta(z-(1-\epsilon))\theta(1-z) \tag{A.38}$$

Equation 4:

$$d_{g\to\psi'}(z,S) = \frac{\pi\alpha_s \langle 0|\, \mathcal{O}_8^{\psi'}({}^3S_1)\, |0\rangle}{8m_c}\delta(1-z)\delta(S-4m_c^2) \tag{A.39}$$

A.10 $q \to q\left[{}^3S_1^{(8)}\right]$

For χ_c states. Equation (63):

$$D^{(8)}_{\bar{b}\to\bar{b}c({}^3S_1)}(z) = \frac{\alpha_s^2(2m_c)}{162}\frac{r\bar{r}^3 z(1-z)^2}{(1-\bar{r}z)^6} \left[2-2(3-2r)z+3(3-2r+4r^2)z^2-2\bar{r}(4-r+2r^2)z^3+\bar{r}^2(3-2r+2r^2)z^4\right] \tag{A.40}$$

Equation (98):

$$D_{c\to\chi_{cJ}}(z,\mu_0) = \frac{H_{1(c\bar{c})}}{m_c}D^{(1)}_{c\to c\bar{c}({}^3P_J)}(z,\Lambda) + (2J+1)\frac{H'_{8(c\bar{c})}(\Lambda)}{m_c}D^{(8)}_{c\to c\bar{c}({}^3S_1)}(z) \tag{A.41}$$

APPENDIX B

PYTHIA 8 - Quarkonia generation

B.1 $c \to J/\psi\, c$ - Steps of parton shower generation

This is a simplified list of the generation procedure of quarkonium production in the parton shower. For simplicity, only the $c \to J/\psi\, c$ splitting is allowed in the quarkonium splttings for now. Implemented in `SimpleTimeShower.cc`:

1. The starting $p^2_{\mathrm{T,evol}}$ scale of the parton shower is set up. This usually matches the $p^2_{\mathrm{T,evol}}$ scale of the outgoing partons in the hard process. In the next iteration of the shower, the starting $p^2_{\mathrm{T,evol}}$ scale is then set to the end $p^2_{\mathrm{T,evol}}$ value of the previous splitting.

2. All the possible dipoles are generated between all the outgoing partons, identifying the radiator, recoiler, dipole and their initial masses/kinematics. These are QCD, QED, Weak, Hidden Valley (if this process is turned on), and finally quarkonium (onium) dipoles. This is executed in `pT2next`.

3. Each generated dipole is passed to a separate method, where the onium dipoles are sent to `pT2nextOnium`. The main aim is to generate the end $p^2_{\mathrm{T,evol}}$ and z of the dipole.

4. In the `pT2nextOnium` method, firstly a cut off for the ending $p^2_{\mathrm{T,evol}}$ is established. This cannot be any smaller than the mass of the generated onium, or the scale set by the user, if this happens to be larger than the onium mass.

5. Rough initial values of $p^2_{\mathrm{T,evol}}$, z, Λ_{QCD} and α_s are then set.

6. The overestimates of the fragmentation function integrals are then set. If the radiator is a c or $\bar{c}$ then the $c \to J/\psi\, c$ splitting is allowed. This is set to be the value calculated in section 3.4.2.1. Otherwise the overestimate is set to zero.

7. The next section is then an iterative process:

   a. α_s and Λ_{QCD} is altered depending on the number of active flavours.

   b. The overestimate is altered to include integral limits on z, the enhance factor, sum of overestimates of each allowed process *etc.*

   c. $p^2_{\mathrm{T,evol}}$ is sampled as discussed in section 3.2.5.2 from the Sudakov factor, depending if α_s is running using eq. (3.42), or if is a fixed value eq. (3.34). b_0 and Λ_{QCD} is set to the number of active flavours. $p^2_{\mathrm{T,evol}_0}$ is the starting scale of the shower, R is a random number and total emission rate, E_{tot} in this case just the overestimate for $c \to J/\psi\, c$.

   d. If the new sampled $p^2_{\mathrm{T,evol}}$ is larger than the allowed minimum $p^2_{\mathrm{T,evol}}$ then the program is allowed to continue, if not then it returns 0.

   e. z is then sampled. For $c \to J/\psi\, c$, this is sampled from a flat distribution, $z = z_{min} + (1 - 2z_{min})R'$. For other distributions, this is sampled from a logarithmic distribution.

   f. Kinematics are corrected with these new sampled values, including the dipole mass *etc.*

   g. Firstly, the kinematics of $p^2_{\mathrm{T,evol}}$ and z are checked. $p^2_{\mathrm{T,evol}}$ is not a physical p_{T}, it is used as an evolution variable in the shower. $p^2_{\mathrm{T,evol}}$ is related to s, the centre of mass energy, with:

$$s = (p^2_{\mathrm{T,evol}}/(z * (1 - z))) + m_c^2; \tag{B.1}$$

   This is related to the physical p_{T} and if $(s <= ((4m_c^2/z) + (m_c^2/(1 - z)))$, then the splitting is not kept.

h. As explained before in section 3.2.5, the $p^2_{\mathrm{T,evol}}$ and z are sampled from an overestimate that is not the true integral (fragmentation function). Hence this needs to be accounted for.

i. Firstly, the value of the $c \to J/\psi\, c$ fragmentation function defined in eq. (3.52) is calculated using the generated $p^2_{\mathrm{T,evol}}$ and z values. This is the form of the fragmentation function translated from (s,z) variables to ($p^2_{\mathrm{T,evol}}$,z) variables. The functions for all splitting functions are defined in `OniaTools.cc`. This value will be called x.

j. Hence the value of the $c \to J/\psi\, c$ fragmentation function, x, is then divided by the overestimate value used, called y and the ratio x/y is calculated.

k. The α_s is also corrected for, as the α_s in the overestimate was calculated using the start $p^2_{\mathrm{T,evol}}$ value and not the current (end) $p^2_{\mathrm{T,evol}}$ value. In this example of $c \to J/\psi\, c$, one α_s is fixed at the mass of the onium and the other is set to the other running value of $p^2_{\mathrm{T,evol}}$.

l. As explained in section 3.2.5, if a random number generated R" $< x/y$, then this splitting is kept, and the generated $p^2_{\mathrm{T,evol}}$ and z for the dipole is saved. If not, then the program goes back to part a) to regenerate values of $p^2_{\mathrm{T,evol}}$ and z which pass the final R" $< x/y$ cut.

8. Out of all of the generated dipoles, QCD, onium, *etc.*, the dipole generated with the largest end $p^2_{\mathrm{T,evol}}$ is kept and the others are thrown away. This is to keep the p_{T} ordering of the shower.

9. This dipole is then passed to the branch method, which sorts out the final kinematics of the partons. For example, the generated $p^2_{\mathrm{T,evol}}$ and z neglect the fact that the radiating c quark has mass. The kinematics are altered using a modified mass procedure which is described in Ref. [57]. Also the dipoles change depending if they are IS or FS partons.

10. Once the final dipole kinematics are set, these generated partons (c and J/ψ) are added the PYTHIA event record.

11. This process is then started again, by going back to part 1) and using all the generated partons, where the starting $p^2_{\mathrm{T,evol}}$ scale is set to the end $p^2_{\mathrm{T,evol}}$ of the previous generation. The parton shower stops when $p^2_{\mathrm{T,evol}}$ is less than Λ_{QCD} ($\sim 0.5\,\mathrm{GeV}$), or to the ending value the user sets. This then goes to the string hadronisation stage of the generation.

APPENDIX C

Tetraquark in jets

C.1 RM for the $\psi(2S)$ and X(3872)

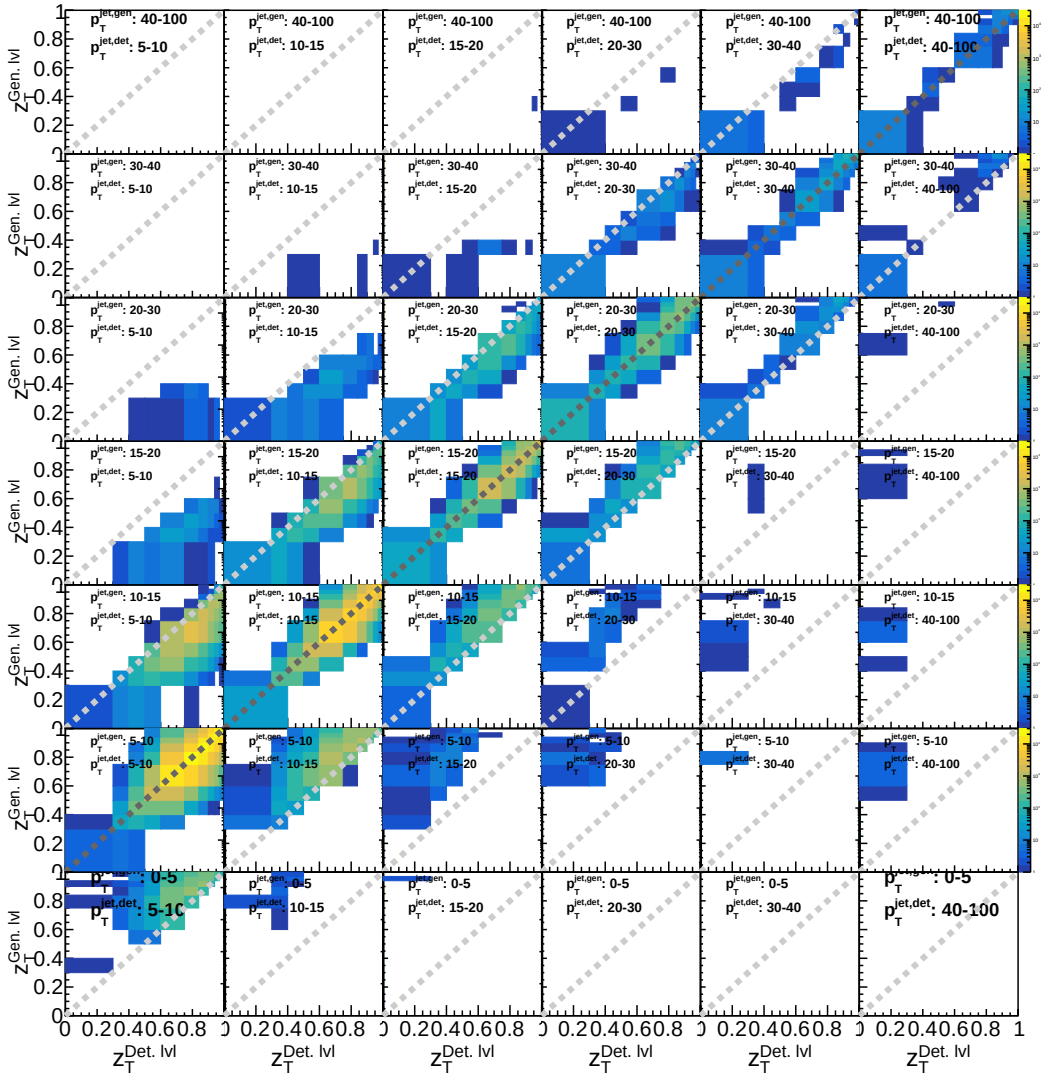

Figure C.1: An example representation of the RM for the unfolding of **prompt** $\psi(2S)$ signal. The MC is B-decay with a weight of 28% hyperons. The binning is according to the $\psi(2S)$ analysis. The x-axis shows the measured quantities at detector level, the y-axis the initial quantities at generator level. The different tiles represent different p_{T}(jet) combinations at detector and generator level. The dark grey line represents the main diagonal line where the measured and reconstructed distribution is in the same p_{T}(jet) bin. The brighter grey diagonals show cases where the measured and reconstructed p_{T}(jet) differ so that the statistic measured in one bin is shifted to the next p_{T}(jet) bin during the unfolding procedure.

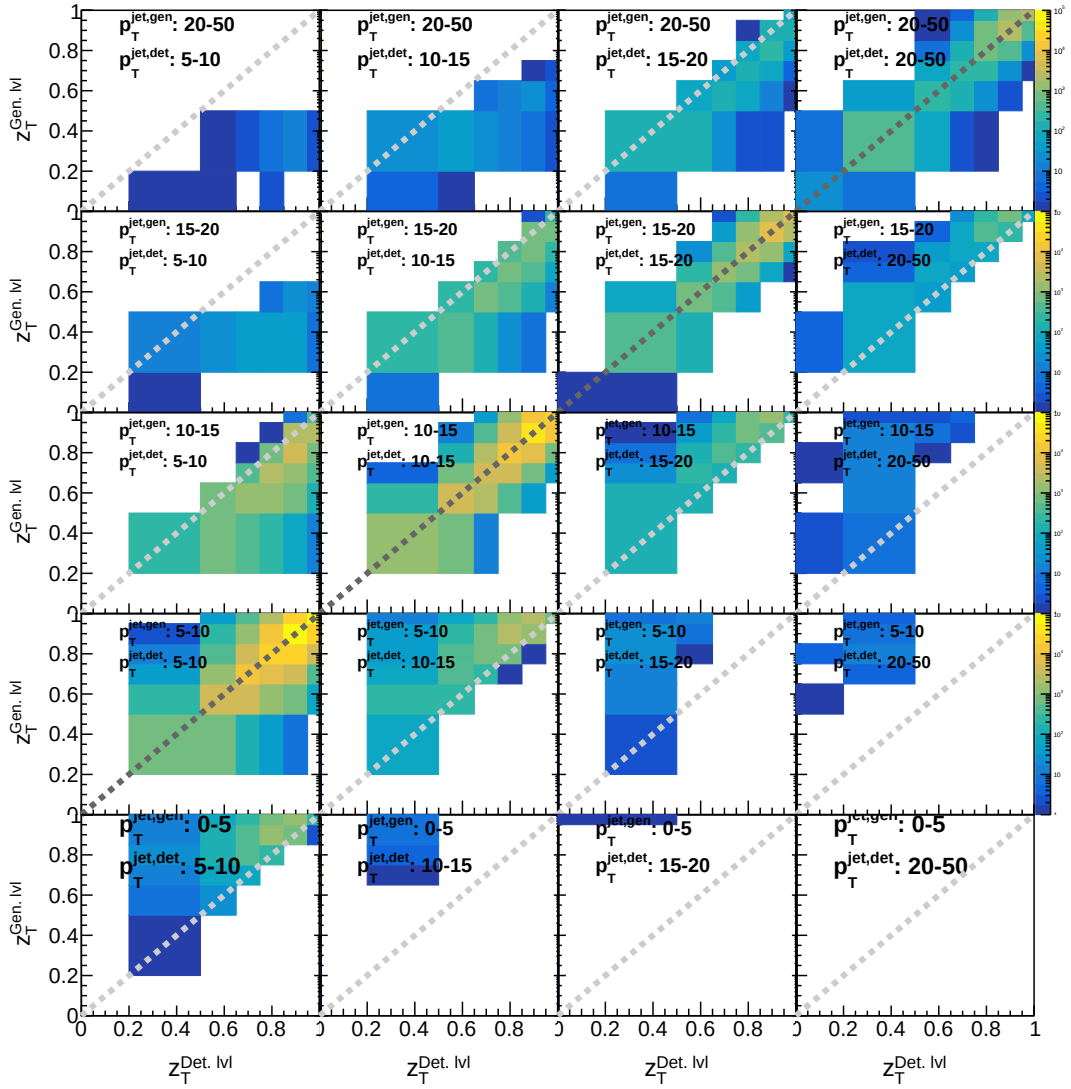

Figure C.2: An example representation of the RM for **prompt** X(3872) and $\psi(2S)$ production. The binning is according to the X(3872) analysis. The x-axis shows the measured quantities at detector level, the y-axis the reconstructed quantities at generator level. The different tiles represent different p_{T}(jet) combinations at detector and generator level. The dark grey line represents the main diagonal line where the measured and reconstructed distribution is in the same p_{T}(jet) bin. The brighter grey diagonals show cases where the measured and reconstructed p_{T}(jet) differ so that the statistic measured in one bin is shifted to the next p_{T}(jet) bin during reconstruction.

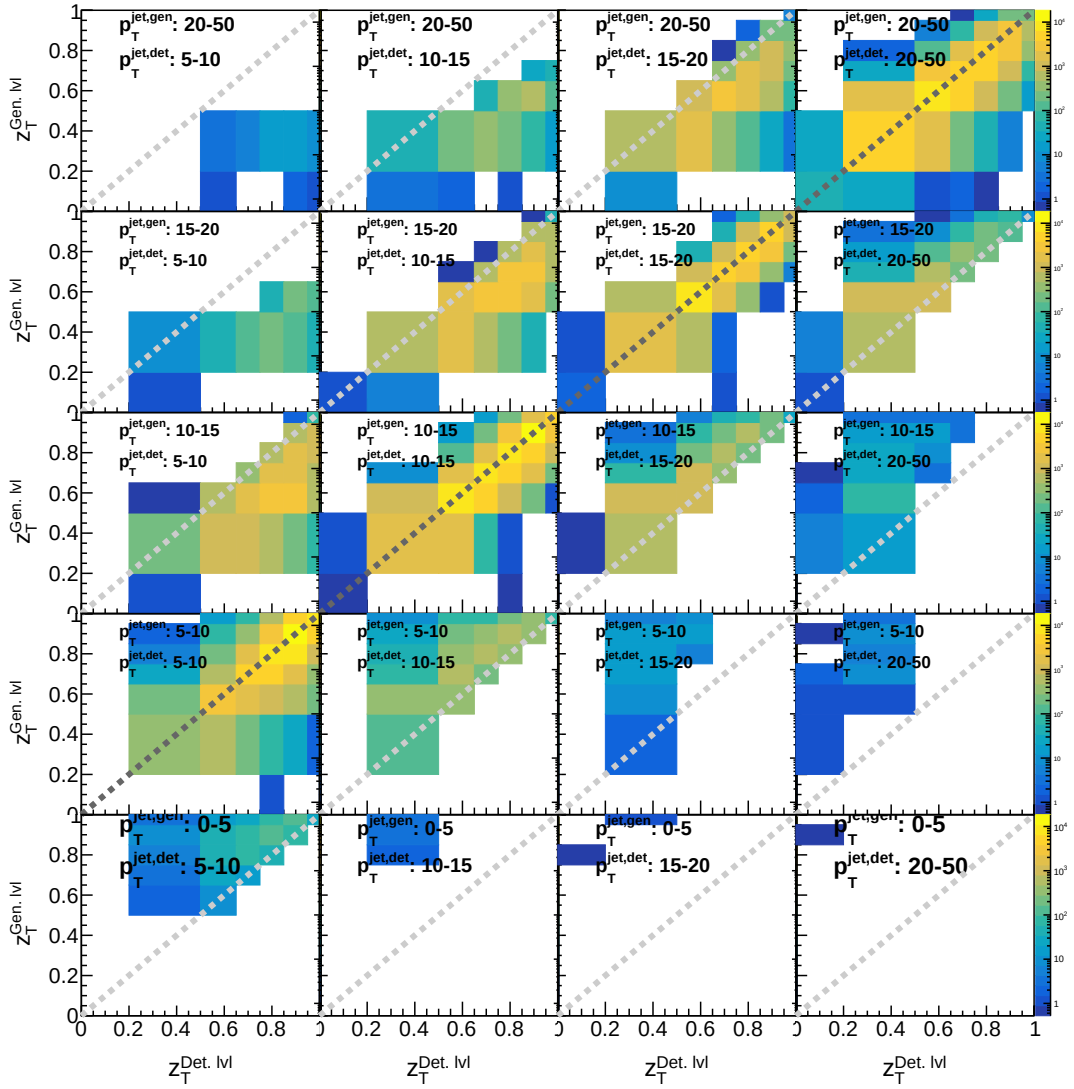

Figure C.3: An example representation of the RM for **displaced** X(3872) production from various B-decays. The binning is according to the X(3872) analysis. The x-axis shows the measured quantities at detector level, the y-axis the reconstructed quantities at generator level. The different tiles represent different p_{T}(jet) combinations at detector and generator lvl. The dark grey line represents the main diagonal line where the measured and reconstructed distribution is in the same p_{T}(jet) bin. The brighter grey diagonals show cases where the measured and reconstructed p_{T}(jet) differ so that the statistic measured in one bin is shifted to the next p_{T}(jet) bin during reconstruction.

C.2 Correlation Coefficients of X(3872) unfolding

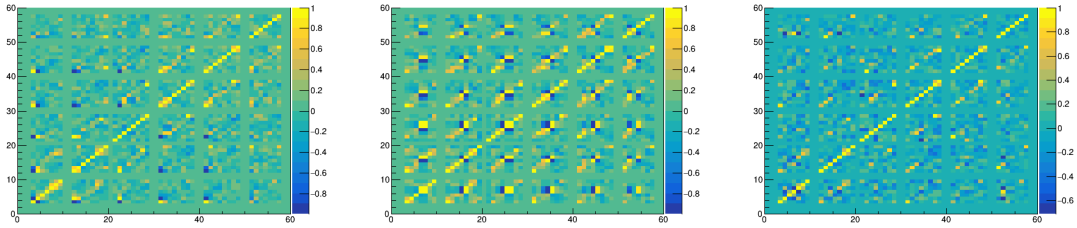

Figure C.4: Correlation coefficients for regularisation parameters k=3,4,5 for X(3872) displaced production in p_{T}(jet)-z_T binning.

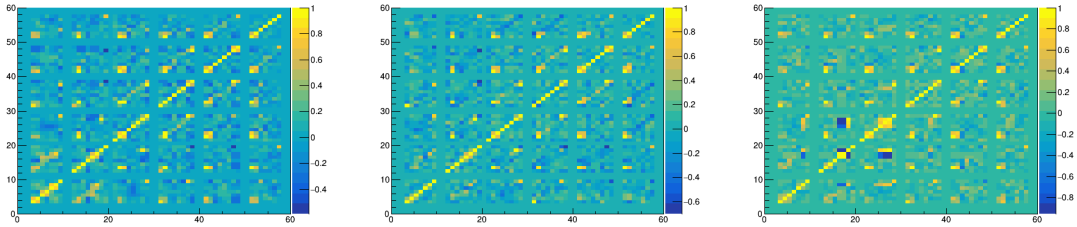

Figure C.5: Correlation coefficients for regularisation parameters k=3,4,5 for X(3872) prompt production in p_{T}(jet)-z_T binning.

C.3 Verification of the unfolding for X(3872) production

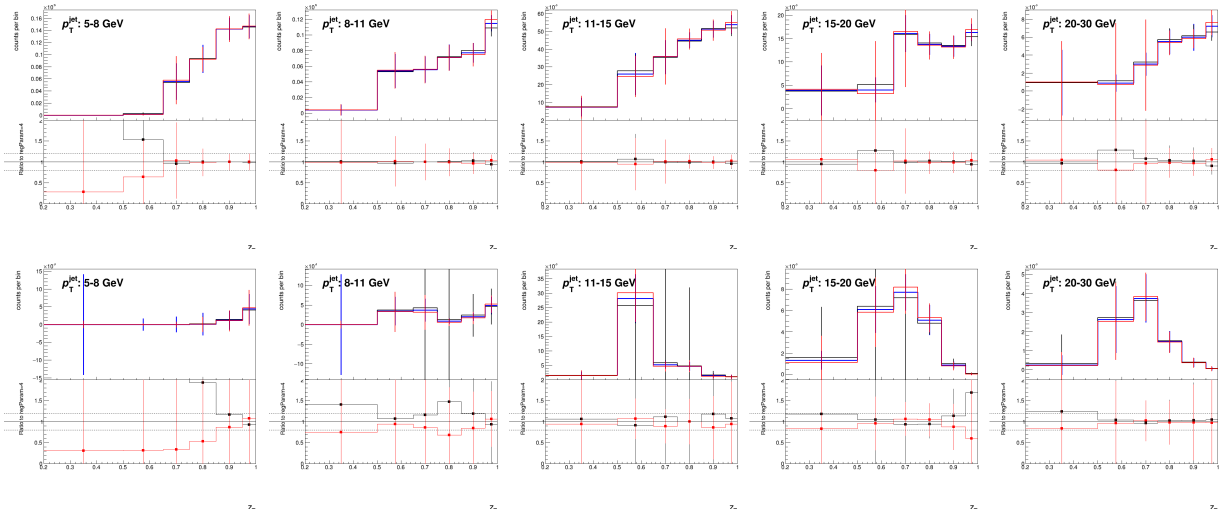

Figure C.6: Unfolded result with regularisation parameter k=4 compared to k=3 and k=5 for prompt (upper) and displaced (lower histograms) X(3872) production for p_{T}(jet)-z_T binning.

C.4 Refolding Test of the unfolding for X(3872) production

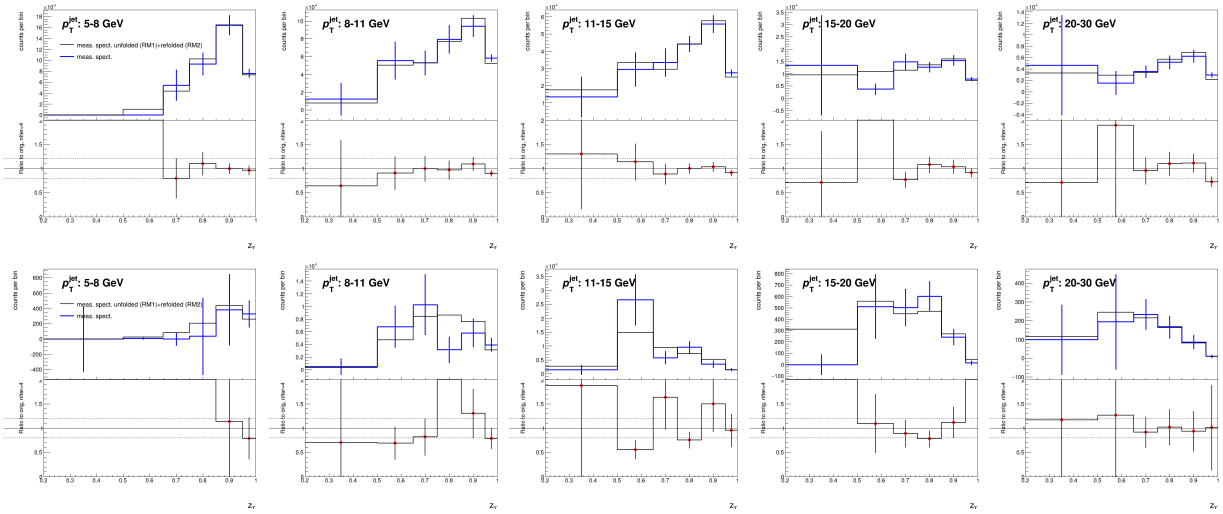

Figure C.7: Refolding test for prompt (upper) and displaced (lower histograms) X(3872) production for k=4. The figures show different bins of p_{T}(jet)-z_T.

C.5 Closure Test of the unfolding for X(3872) production

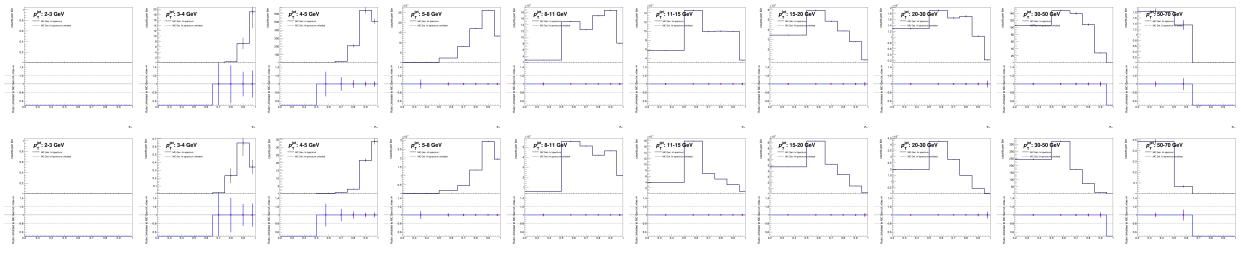

Figure C.8: Closure test for prompt (upper) and displaced (lower histograms) X(3872) production for k=4. The figures show different bins of p_{T}(jet)-z_T.

C.6 Systematic of the unfolding

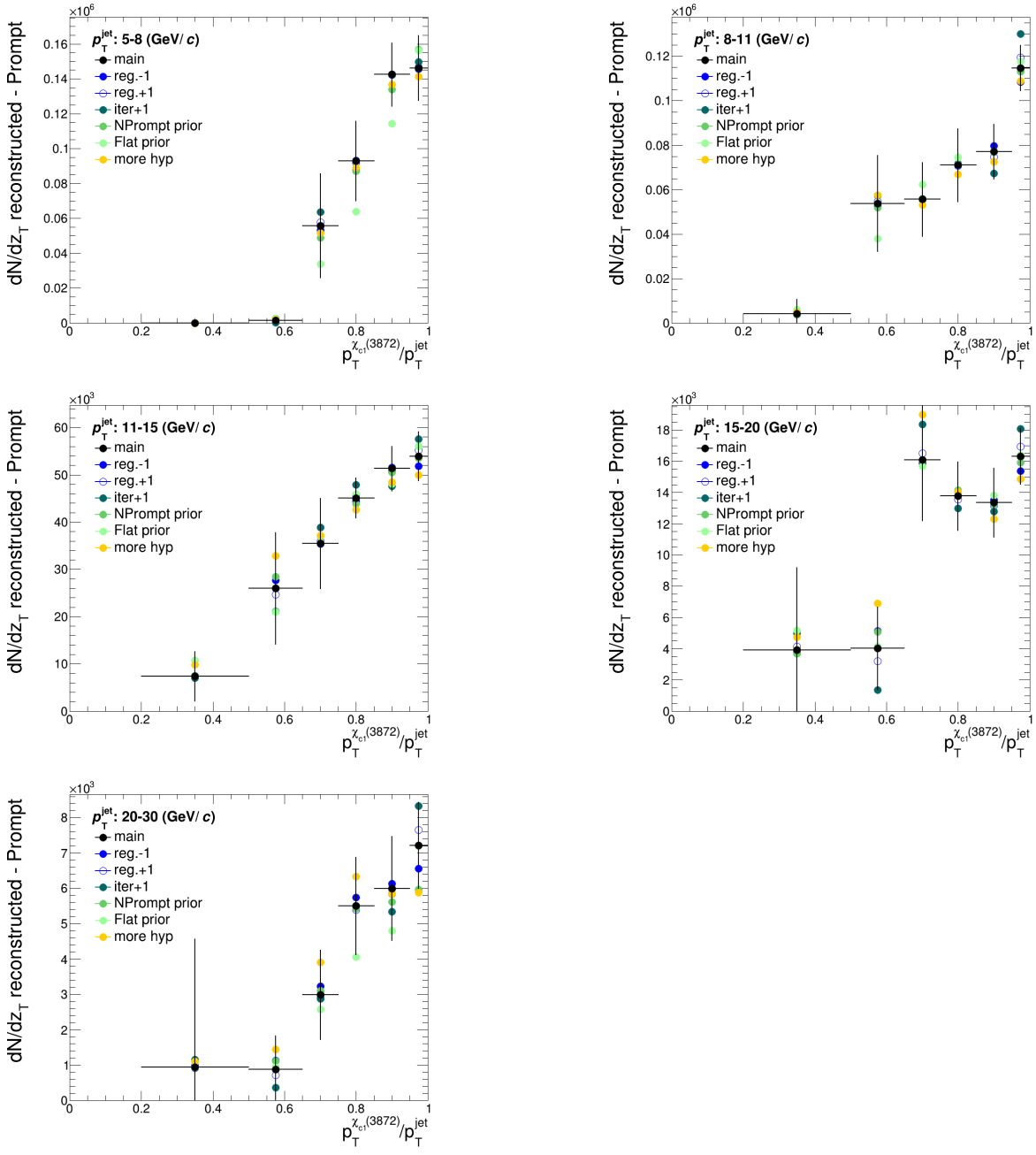

Figure C.9: Displaced X(3872) unfolded spectra for various changes in the unfolding procedure. The spread of distributions shows the systematic uncertainty associated to the unfolding procedure. In bins of p_{T}(jet)-z_T.

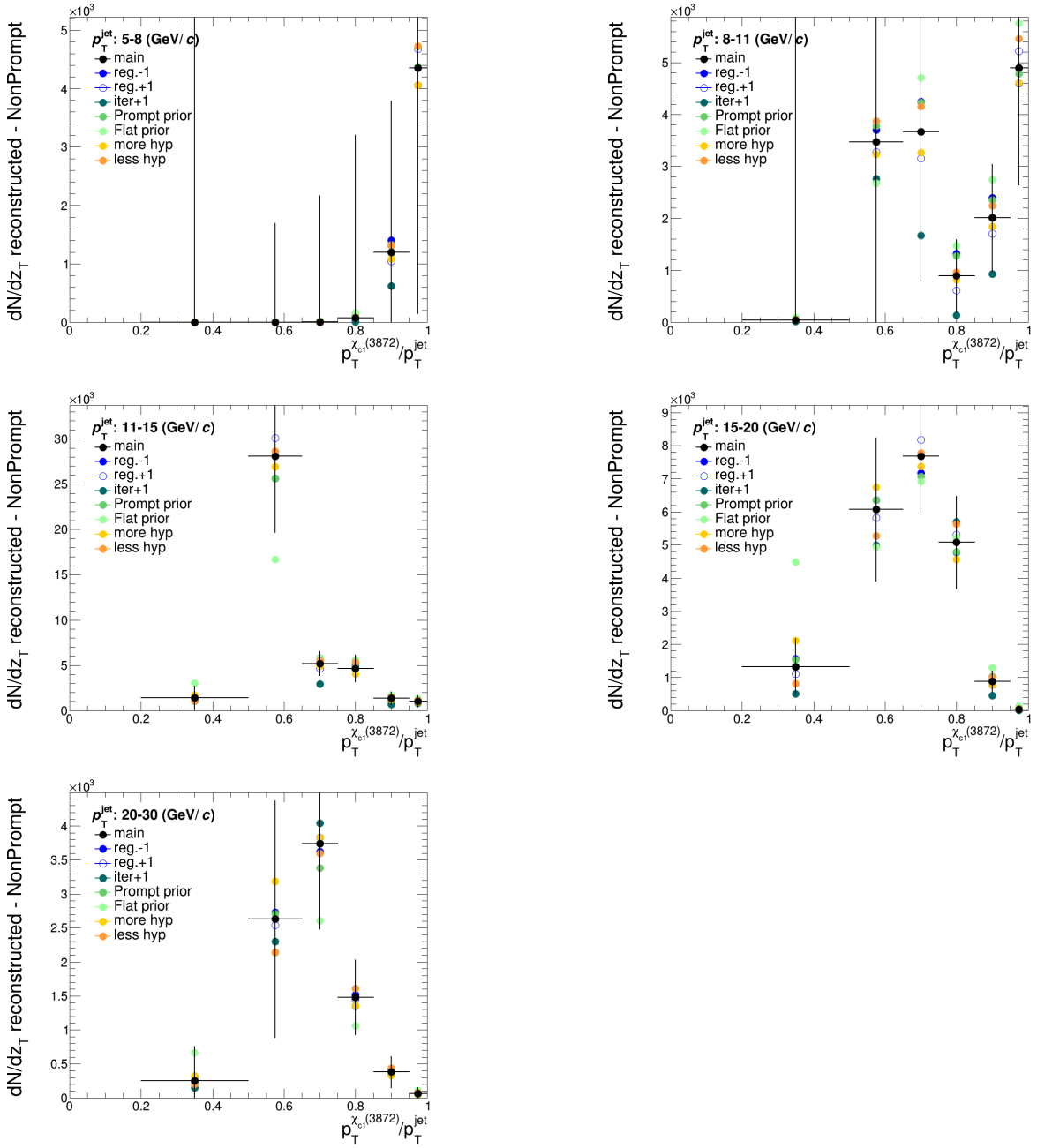

Figure C.10: Prompt X(3872) unfolded spectra for various changes in the unfolding procedure. The spread of distributions shows the systematic uncertainty associated to the unfolding procedure. In bins of p_{T}(jet)-z_T.

APPENDIX D

Cross-checks between $\psi(2S) \to \mu\mu$ and $\psi(2S) \to J/\psi\pi\pi$

D.1 Displaced fraction comparison

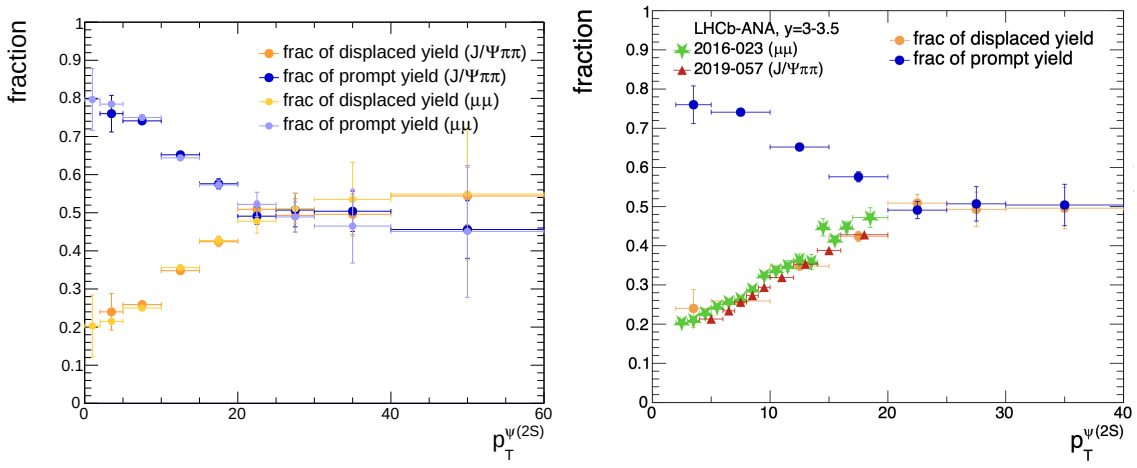

(a) Different channels.

(b) Comparison to previous results.

Figure D.1: a) Comparison of different channels displaced fraction values for $\psi(2S)$ and b) results in comparison to previous LHCb analyses vs. $p_{\mathrm{T}}(\psi(2S))$.

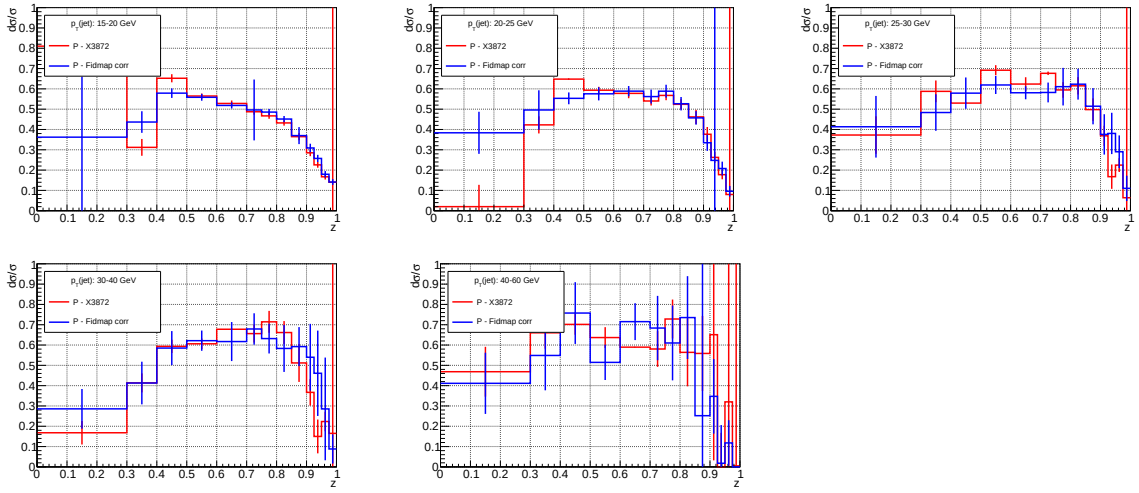

Figure D.2: Comparison of displaced fractions vs. $z(\psi(2S))$ for two different channels.

D.2 Fiducial region comparison

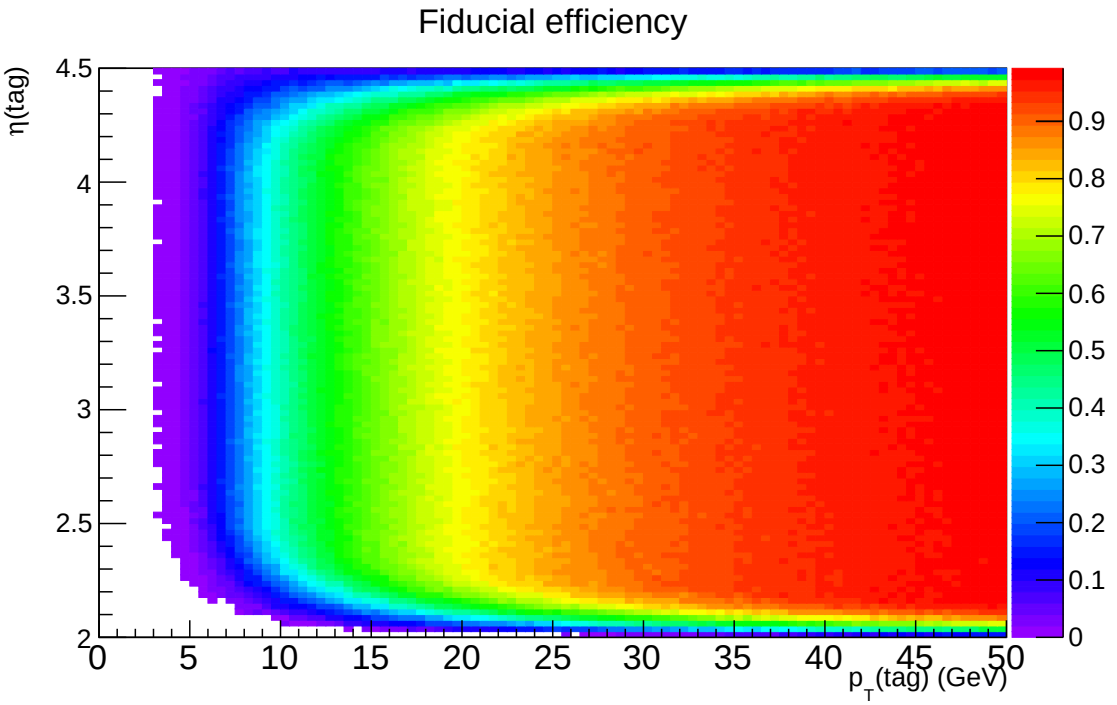

Figure D.3: Fiducial efficiency correction for the decays of $\psi(2S) \to J/\psi\ \pi\pi$ vs. $\psi(2S) \to \mu\mu$.

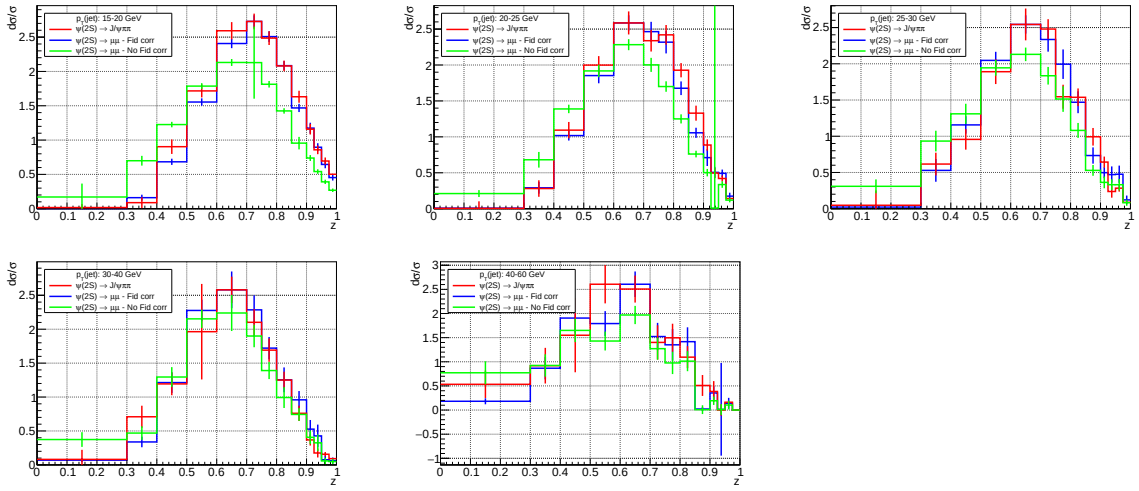

Figure D.4: Displaced $\psi(2S)$ comparisons of $\psi(2S) \to J/\psi\ \pi\pi$ vs. $\psi(2S) \to \mu\mu$ vs. $\psi(2S) \to \mu\mu$ fiducial efficiency corrected.

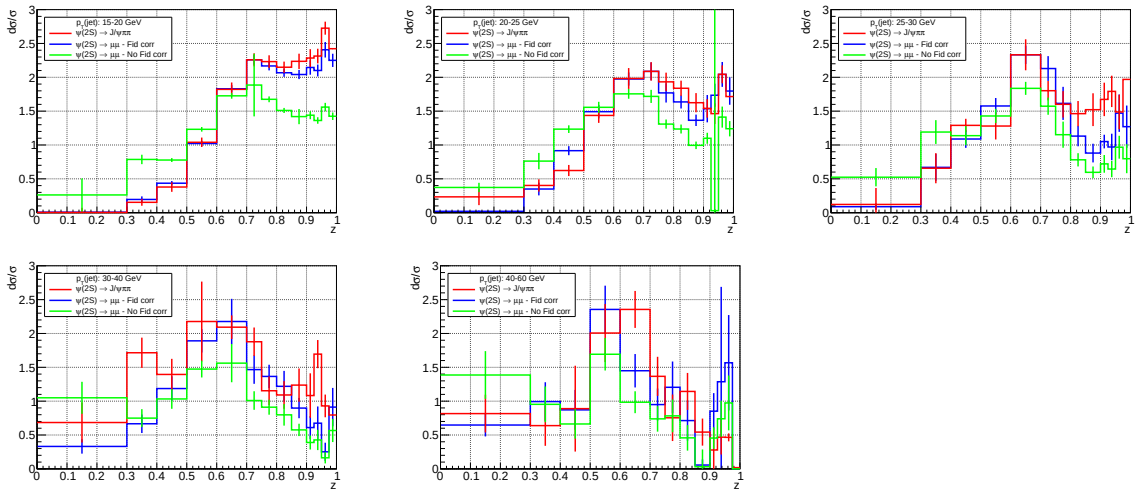

Figure D.5: Prompt $\psi(2S)$ comparisons of $\psi(2S) \to J/\psi\ \pi\pi$ vs. $\psi(2S) \to \mu\mu$ vs. $\psi(2S) \to \mu\mu$ fiducial efficiency corrected

APPENDIX E

Polarisation of J/ψ

E.1 Aims

The NRQCD parton shower model depicts the formation of J/ψ's, with minimal polarisation as one of its predictions. In direct contrast to this, in the hard production model, considerable transverse polarisation is predicted as $p_{\mathrm{T}}(J/\psi)$ increases. This is not observed in data. It is desirable, therefore, to determine a polarisation measurement of J/ψ's within jets. Polarisation will be measured in bins of $z(J/\psi)$ using jets rather than bins of $p_{\mathrm{T}}(J/\psi)$. The NRQCD parton shower production model for J/ψ's will be supported, if minimal polarisation is observed in each $z(J/\psi)$ bin. Different procedures followed to measure the polarisation of J/ψ's within jets is outlined in this chapter, with preliminary measurements with 2016 Turbo data shown. This approach could be repeated in the measurement of polarisation *vs.* $z(Q)$ for different quarkonia, Q.

E.2 The Helicity frame

The polarisation of a particle depends upon the angles of its decay products. This can be shown from first principles for different particle decays using methods as presented in "An angular distribution cookbook" and other texts [151, 152]. The polarisation of the J/ψ, can therefore be measured, and for $J/\psi \to \mu^+\mu^-$, its derived angular distribution is defined in eq. (E.1),

$$\frac{d^2N}{dcos\theta d\phi} \propto 1 + \lambda_\theta cos^2\theta + \lambda_{\theta\phi} sin2\theta cos\phi + \lambda_\phi sin^2\theta cos2\phi \tag{E.1}$$

where λ_θ, λ_ϕ and $\lambda_{\theta\phi}$ are parameters which depict the degree of polarisation [8]. The polarisation of the J/ψ can be determined, therefore, by measuring the angular distributions of the muons which decay from the J/ψ. It is necessary, however, to establish a frame in which to specify angles θ and ϕ. This is termed a polarisation frame and the direction of its chosen polarisation axis (z axis) determine the definition of the frame axes. The helicity frame is selected for this analysis, as it is the theoretically preferred frame in which to define these angles. It is preferable since the angular distributions are symmetrical, so $\lambda_\phi = \lambda_{\theta\phi} = 0$ and $\lambda_{\theta\phi}$ is maximised. (λ_θ, λ_ϕ, $\lambda_{\theta\phi}$) = (+1,0,0) characterises maximum transverse polarisation, (-1,0,0) maximum longitudinal polarisation and (0,0,0) zero polarisation (*i.e.* so the angular distributions are flat) [153]. Whilst this is purported to be true in the helicity frame, it requires testing. In addition, the λ variables are frame dependent. However, one can use a frame independent parameter, λ_{inv}, for polarisation, which is defined in eq. (E.2) [8],

$$\lambda_{inv} = \frac{\lambda_\theta + 3\lambda_\phi}{1 - \lambda_\phi}. \tag{E.2}$$

Nonetheless, $\lambda_\phi = 0$ in the helicity frame, therefore $\lambda_\theta = \lambda_{inv}$, so λ_θ is essentially frame invariant. The polarisation axis (z) in the helicity frame, is expressed as a unit vector in the direction of the J/ψ in the centre of mass frame of the two colliding protons. This is intrinsically the lab frame of LHCb. The production plane contains the direction of the J/ψ and the beam axis. The y-axis is then orthogonal to the production plane. Subsequently, the x axis is orthogonal to y and z in the right-handed coordinate system [8]. The polarisation measurement of the

J/ψ's is acquired from two angles. Firstly, θ, which is the angle between direction of the anti-muon in the centre of mass frame of the J/ψ and its polarisation axis (z). Secondly, ϕ, the angle between the direction of the anti-muon and the x axis. Figure E.1a [8] illustrates a schematic diagram of the helicity frame with the angles θ and ϕ configured for the example $J/\psi \rightarrow \mu^+\mu^-$. The z polarisation axes for different polarisation frames are represented in fig. E.1b [154]. These could be used the analysis to cross-check the polarisation measurement conducted in the helicity frame. The Collins-Soper frame for example is in the direction of the relative velocity of the two colliding proton beams and perpendicular to the helicity z axis [8].

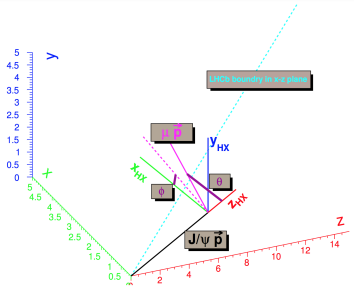

(a) Angles in helicity frame [153].

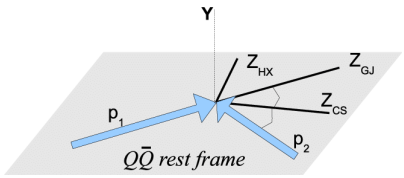

(b) Different polarisation axes [154].

Figure E.1: Definitions of polarisation frame.

The previous J/ψ polarisaton paper plots, "Measurement of J/ψ polarisation in pp collisions at $\sqrt{s} = 7\,\text{TeV}$" [8, 153], of $\cos\theta$ and ϕ were used to verify that the angles defined in the helicity frame were correct in this analysis. Measurements were made with J/ψ's not incorporated into jets, in this paper, however. So jets were eliminated, at first, in order to make an accurate comparison. Only prompt J/ψ's were used also in this analysis, so J/ψ's produced from b decays were extracted from the data sample. This was necessary as different polarisation's occur in J/ψ's created from prompt *vs.*b decays. A time significance criterion, τ_S, was applied to data, in order to eliminate the displaced component. This criterion is defined in eq. (E.3) as,

$$\tau_S = \frac{t_z}{\delta t_z}, \tag{E.3}$$

where t_z is as defined in eq. (6.4) as the lifetime of the J/ψ, and δt_z is the error on the lifetime of the J/ψ [153]. In this analysis, the criterion employed was $\mid \tau_S \mid < 4$. Furthermore, Monte Carlo (MC) generators do not precisely simulate particle production at extreme pseudo-rapidity values, *i.e.* at the edges of the LHCb detector acceptance. Consequently, a fiducial region is chosen where MC can adequately simulate the efficiency. To evaluate this, all the muon tracks are extrapolated back to

z = 1 m (just beyond the VELO). The transverse distance of tracks ($r_{xy} = \sqrt{x^2 + y^2}$) is then compared in MC and data. It was observed that MC does not sufficiently model data at $r_{xy} > 220$ mm, *i.e.* $\eta < 2.2$ [153]. These two criteria are utilised for cross-check purposes, but shall be removed for the jets analysis.

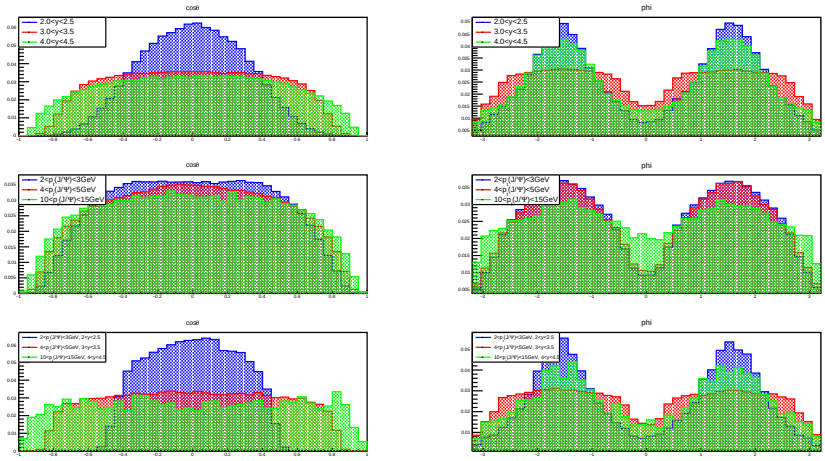

Figure E.2: Angular distributions, $\cos\theta$ and ϕ for $J/\psi \to \mu^+\mu^-$ using 2016 Turbo data without jets.

The distributions of $\cos\theta$ and ϕ defined in the helicity frame with 2016 Turbo Data are illustrated in fig. E.2 with the criterion specified above and normalised to one. The top row indicates the two distributions with three different rapidity ranges of the J/ψ, y applied. Rapidity is theoretically preferred to pseudo-rapidity since pseudo-rapidity is in the relativistic limit of rapidity (p $\simeq$ m). The middle row shows distributions captured at various $p_{\mathrm{T}}(J/\psi)$ ranges, and the lower row indicates these in varying rapidity and $p_{\mathrm{T}}(J/\psi)$ ranges. Green signifies a high, red a middle and blue a low $p_{\mathrm{T}}(J/\psi)$/y bin, respectfully. When $\cos\theta \simeq \pm 1$, both muons traverse exactly in the direction of the J/ψ, with the first in the absolute positive z direction and the second in the absolute negative z direction, in the centre of mass frame of the J/ψ. This denotes that at low $p_{\mathrm{T}}(J/\psi)$, the p_{T} of the J/ψ will not be sufficient to boost the muon in the -z direction to keep it within it the LHCb detector acceptance. This prevents numerous J/ψ's from becoming reconstructed around these values, indicated in the blue distribution. Nonetheless, a greater number of muons are boosted into the LHCb detector acceptance, as $p_{\mathrm{T}}(J/\psi)$ increases, indicating a growth in efficiency at high values of $|\cos\theta|$. At extreme rapidity ranges lower efficiencies are additionally observed at $\phi \simeq 0(\pm\pi)$. The J/ψ is at the utmost limit of the detector acceptance, so at $\phi \simeq 0(\pm\pi)$, in all probability, one of the muons will be beyond the limits of the detector acceptance. Additionally, there are also reconstruction efficiency effects at exceptional $p_{\mathrm{T}}(J/\psi)$/y ranges in addition

to geometrical aspects. Multiple scattering effects can occur at low $p_{\mathrm{T}}(J/\psi)$ values, for instance, culminating in lower efficiency at $\cos\theta \simeq \pm 1$. Furthermore, muons suffer from lower reconstruction efficiency at extreme rapidity values, given that the magnetic field can curve them beyond the LHCb acceptance, and diminishes efficiency at $\phi \simeq 0(\pm\pi)$. These distributions are similar to the distributions shown in fig. E.3, which are from "Measurement of J/ψ polarisation in pp collisions at $\sqrt{s} = 7\,\mathrm{TeV}$". This demonstrates that the definition of angles employed in this analysis are reliable and consistent when compared with previous analyses utilising the helicity frame [153].

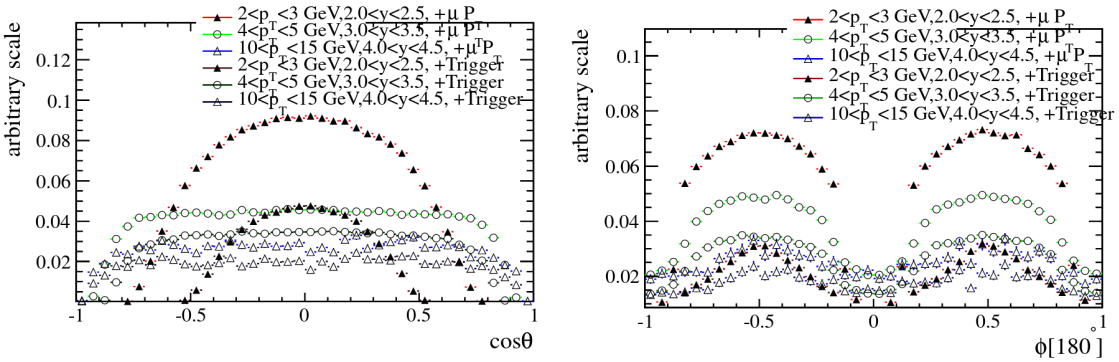

Figure E.3: Angular distributions for $\mathrm{J}/\psi \to \mu^+\mu^-$ in "Measurement of J/ψ polarisation in pp collisions at $\sqrt{s} = 7\,\mathrm{TeV}$" [153].

E.3 Binned maximum likelihood to measure polarisation

The angular distributions of $\cos\theta$ and ϕ are dependent on multiple factors, including the geometrical acceptance and reconstruction efficiency. It would be preferential to initially apply a model with accurate and accepted angular distributions for a specified decay. The efficiency effects can be progressively incorporated and the variation in angular distributions observed. In order to correct back to the true angular distributions, the reverse procedure of correcting for the efficiency effects can then be administered to 2016 data. A Monte Carlo (MC) generator is necessary to simulate these true distributions and Pythia 8.240 [13,14] is utilised in this analysis, to simulate hard $b\bar{b}$ events. EvtGen 1.07 [155] is employed to decay the interested particles to a decay channel selected by the user, for example $\mathrm{J}/\psi \to \mu^+\mu^-$.

First, a binned maximum likelihood method is adopted to determine the polarisation

of the true distributions. The angular distribution PDF in eq. (E.1) is applied to binned data in $\cos\theta$ and ϕ, by modifying the λ parameters to secure the maximum likelihood possible. In the helicity frame both λ_ϕ and $\lambda_{\theta\phi}$ are minimal values and λ_θ is maximal, as indicated earlier. Equation (E.1) is integrated by both variables distinctly to secure eqs. (E.4) and (E.5) respectively [153],

$$\frac{d^2N}{dcos\theta} \propto 2\pi(1 + \lambda_\theta cos^2\theta), \tag{E.4}$$

$$\frac{d^2N}{d\phi} \propto (2 + \frac{2}{3}\lambda_\theta) + \frac{4}{3}\lambda_\phi cos(2\phi). \tag{E.5}$$

.

A 1D binned maximum likelihood fit to $\cos\theta$ using eq. (E.4) is required, therefore, to acquire values for λ_θ only. Fewer statistics are also required to accomplish this fit in contrast to a 2D binned maximum likelihood fit, which helps the analysis. Discrete 1D binned maximum likelihood fits were conducted on true angular distributions, to verify this, for $J/\psi \to \mu^+\mu^-$ for the variables $\cos\theta$ and ϕ using eqs. (E.4) and (E.5), to see if it is feasible to ignore the variable ϕ when λ_ϕ it is negligible compared to λ_θ. Even though the polarisation is unknown for the prompt generation of J/ψ, techniques can be applied to fix the polarisation of the generated J/ψ's using EvtGen [155], which is independent of the production channel of the J/ψ (i.e. from b-decays or excited states). The binned maximum likelihood technique can be tested utilising varied initial polarisations of the J/ψ.

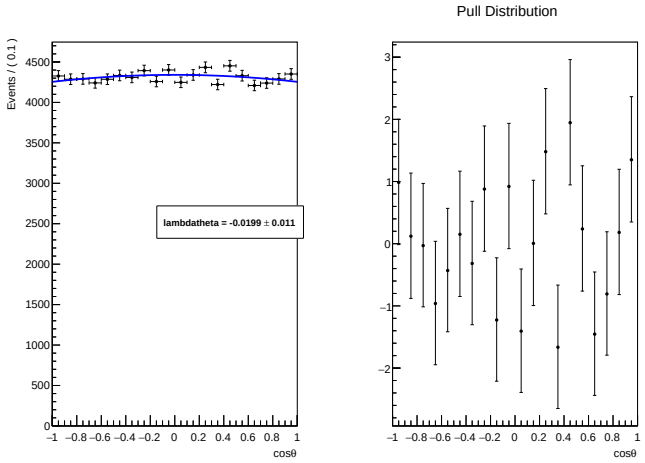

Figure E.4: J/ψ with no polarisation: binned Maximum Likelihood Fit of $\cos\theta$ for $J/\psi \to \mu^+\mu^-$.

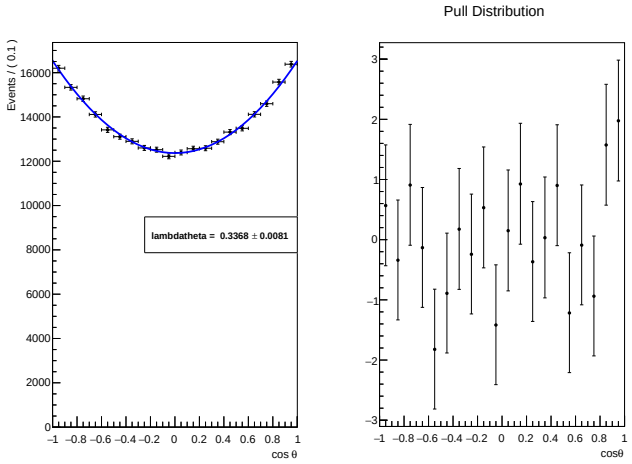

Figure E.5: J/ψ with maximum transverse polarisation: binned Maximum Likelihood Fit of $\cos\theta$ for $J/\psi \to \mu^+\mu^-$.

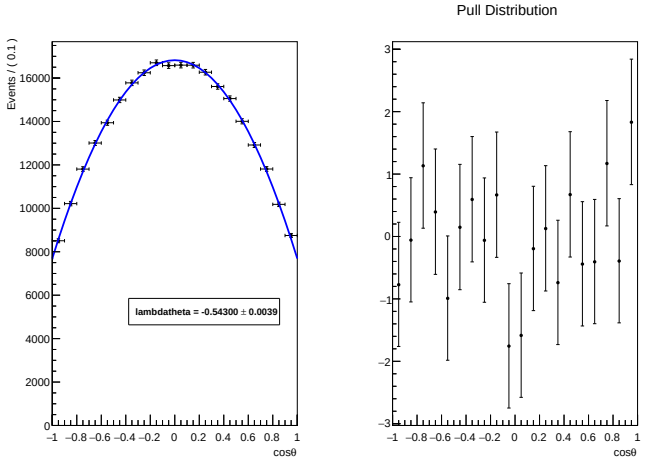

Figure E.6: J/ψ with maximum longitudinal polarisation: binned Maximum Likelihood Fit of $\cos\theta$ for $J/\psi \to \mu^+\mu^-$.

Binned maximum likelihood fits of the cosθ variable are illustrated in figs. E.4 to E.6, adopting eq. (E.4), where the J/ψ has zero, maximum transverse and maximum longitudinal polarisation, respectively. These are realised in RooFit [113] with 20 bins of equal width utilising $\sim$10x10^6 generated Pythia 8 [13, 14] events for each fit. The λ_θ variables acquired per fit are: -0.0199 $\pm$ 0.011 (i.e. predictively consistent with zero), 0.3368 $\pm$ 0.0061 and -0.54300 $\pm$ 0.0039, respectively. Binned maximum likelihood fits of the ϕ variable are illustrated in figs. E.7 to E.9, adopting eq. (E.5), where the J/ψ has zero, maximum transverse and maximum longitudinal polarisation, respectively. λ_θ is specified from each respective cosθ fit to determine λ_ϕ since eq. (E.5) is dependent on both λ_θ and λ_ϕ. The respective λ_ϕ variables acquired per fit are: -0.00624 $\pm$ 0.0072 (i.e. predictively consistent with zero), 0.0463 $\pm$ 0.0045 and -0.06642 $\pm$ 0.0033. Polarisation is not as sensitive to ϕ as cosθ

in the helicity frame as $\lambda_\theta \sim$10 times larger than λ_ϕ. Therefore, in order to determine the degree of polarisation of prompt J/ψ's, a 1D binned maximum likelihood fit in cosθ could be performed.

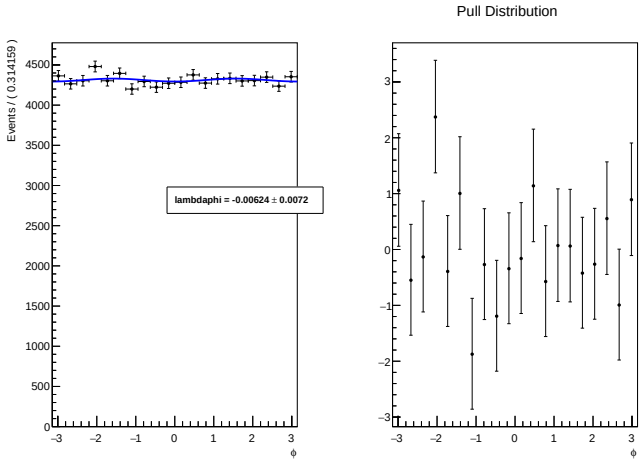

Figure E.7: *J/ψ* with no polarisation: binned Maximum Likelihood Fit of ϕ for J/$\psi \to \mu^+\mu^-$.

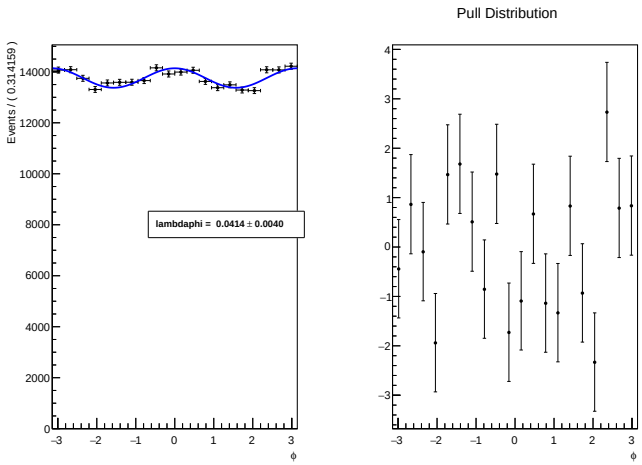

Figure E.8: *J/ψ* with maximum transverse polarisation: binned Maximum Likelihood Fit of ϕ for J/$\psi \to \mu^+\mu^-$.

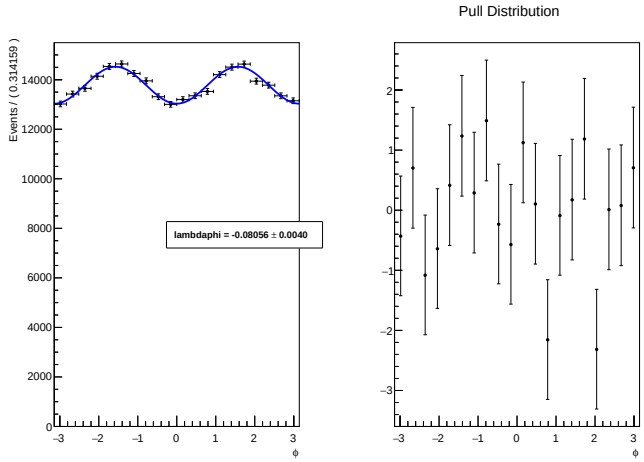

Figure E.9: J/ψ with maximum longitudinal polarisation: binned Maximum Likelihood Fit of ϕ for $\mathrm{J}/\psi \to \mu^+\mu^-$.

E.4 Efficiency effect considerations

The geometrical efficiency influences the appearance of the angular distributions, as discussed in section E.2. Figure E.10, by way of illustration, indicates true angular distributions for the $B^+ \to J/\psi + K^+$ composed by PYTHIA 8 [13,14] and EVTGEN [155] adopting the SVS model. The distributions in fig. E.11 are closely comparable to the distributions observed in data. In order to precure these distributions, the fiducial conditions administered to the 2016 Turbo data in section E.2 were also administered to this MC sample, $2.0 < \eta(J/\psi, \mu^+, \mu^-) < 4.5$, $p_T(\mu) > 0.5\,\mathrm{GeV}$ and $p(\mu) > 5\,\mathrm{GeV}$. Therefore, to acquire geometrical efficiency corrections to the $\cos\theta$ distribution in data, the alteration in yield is able to be explored in bins of $\cos\theta$ from the true versus the fiducial corrected MC distribution. This can then be applied to data. Examples of the effect of the fiducial cuts on the $\cos\theta$ and ϕ variables for different λ_θ values are shown in fig. E.12.

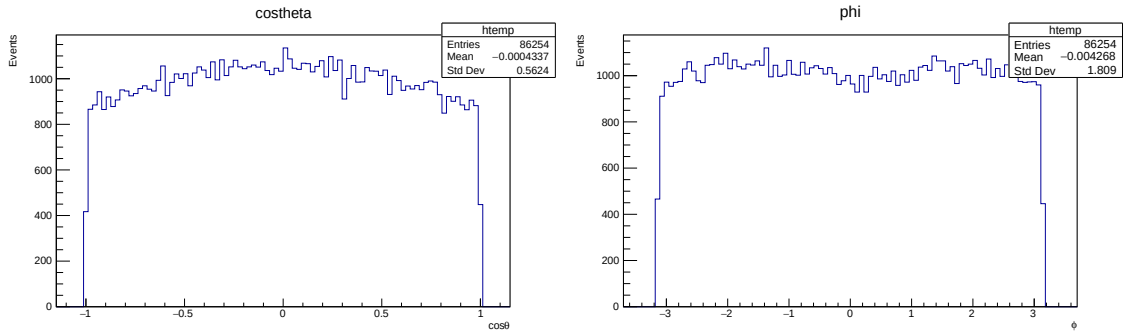

(a) $\cos\theta$ of positive muon.

(b) ϕ of positive muon.

Figure E.10: Angular distributions for $B^+ \to J/\psi + K^+$ decay, using the SVS model with full phase space with PYTHIA 8 [13, 14] and EVTGEN [155] simulation.

The $B^+ \to J/\psi + K^+$ channel has physical importance, on account of the fixed maximal longitudinal polarisation the J/ψ, by virtue of the conservation of angular momentum from the B^+ [153]. Furthermore, the polarisation of the J/ψ's generated promptly, is unknown and the geometrical efficiency is polarisation dependent. Therefore to examine this, the initial polarisation of the J/ψ can be amended, geometrical requirements applied, subsequently followed with an efficiency map of each $\cos\theta$ bin *vs.* the polarisation, as executed in section E.3 with EVTGEN [155]. Numerous MC samples with different polarisations would be necessary. Furthermore, to formulate sufficient statistics ($\sim$10x10^6 PYTHIA 8 [13, 14] events), employing the procedure in section E.3 to generate each prompt J/ψ polarisation sample necessitated a two-day simulation run. To resolve this it is essential to employ a particle gun system utilising CIMBA [156] to rapidly generate the J/ψ's. A requisite will also be to investigate trigger efficiencies and reconstruction efficiencies, however, with different MC incorporating LHCb detector effects. It will also be necessary to accommodate corrections for differences in data and simulation, on account of misunderstanding detector efficiencies in simulation. $B^+ \to J/\psi + K^+$ is employed as a control channel to account for the fact that J/ψ polarisation is fixed in this channel, and as a consequence the muon kinematics in data and simulation must match [153].

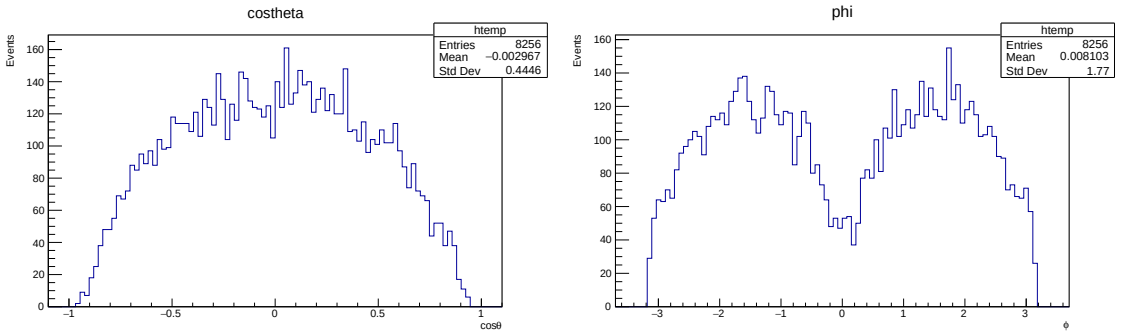

(a) $\cos\theta$ of positive muon. (b) ϕ of positive muon.

Figure E.11: Angular distributions for $B^+ \to J/\psi + K^+$ decay, using the SVS model with LHCb acceptance requirements with PYTHIA 8 [13, 14] and EVTGEN [155] simulation.

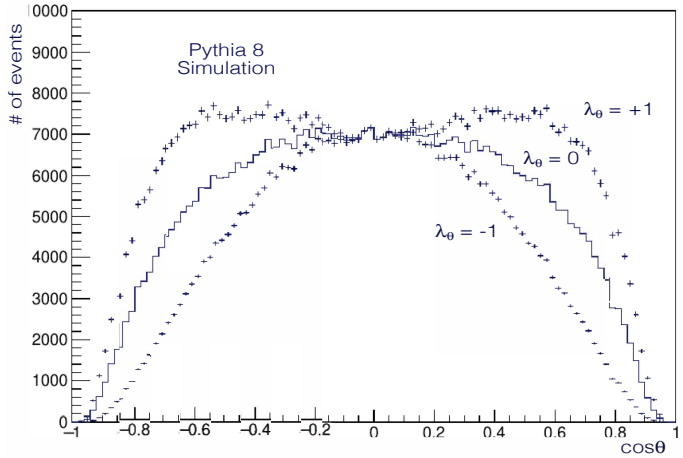

Figure E.12: Effect of fiducial requirements for J/ψ's with different polarisation on the variables $\cos\theta$ and ϕ with PYTHIA 8 simulation.

Ultimately, it is essential to amend the cosθ distributions on account of two different detector effects:

- The geometrical acceptance of the detector, imposed on both the J/ψ's and muons. This is remedied by employing generator level MC with PYTHIA 8 [13, 14] and EVTGEN [155].
- The impact of trigger and reconstruction effects on the efficiency of the detector. This is accounted for by MC incorporating detector effects. The differences in MC simulation detector effects and genuine detector effects observed in data are corrected for utilising the $B^+ \to J/\psi + K^+$ channel.

E.5 Preliminary binned $\cos\theta$ results with LHCb data

Adopting the identical approach taken in chapter 6, initial distributions for cosθ measurements for the prompt and displaced components are illustrated in fig. E.13. This was accomplished by firstly applying mass fits to obtain signal and background fractions, followed by conducting lifetime fits to achieve displaced and prompt fractions, implemented in equal bins of cosθ rather than bins of $z(J/\psi)$. The fact that the background and incorrect PV components are factored out of the distributions makes this approach have advantages to an unbinned maximum likelihood fit. The background must be flawlessly modelled in an unbinned fit, or assumptions made, if it is not possible. The paper, "Measurement of J/ψ polarisation in pp collisions at $\sqrt{s} = 7\,\text{TeV}$" outlines a similar approach, with the assumption that the background is flat [8, 153], which would not necessarily be made in this analysis. It would be worthwhile, nonetheless, to adopt this approach to cross-check the binned method. The distributions which are illustrated in fig. E.13 are not partitioned into distinct bins of p_{T}(jet) and $z(J/\psi)$ values. Figure E.14 shows an example cosθ distributions for $0.5 < z(J/\psi) < 0.6$.

As described in section E.1, a λ_θ (parameter that describe polarisation) versus z(J/ψ) for the prompt component, will be the final measurement to examine the parton shower interpretation of NRQCD. First, efficiency corrections will be need to be applied. As soon as corrections are considered, as depicted in section E.3, a binned maximum likelihood fit on the cosθ distributions to obtain λ_θ for each z(J/ψ) bin can be performed. The value of λ_θ will be $\simeq$ zero for all z(J/ψ) bins, if it predictably follows the parton shower version of NRQCD with the efficiency corrections. Ultimately, a cross reference can be undertaken with an alternative polarisation frame, namely, the Collins-Soper frame, since λ_θ is technically frame dependent. A 2D binned maximum likelihood fit with cosθ and ϕ with eq. (E.1) to determine all three λ variables would be comparably beneficial.

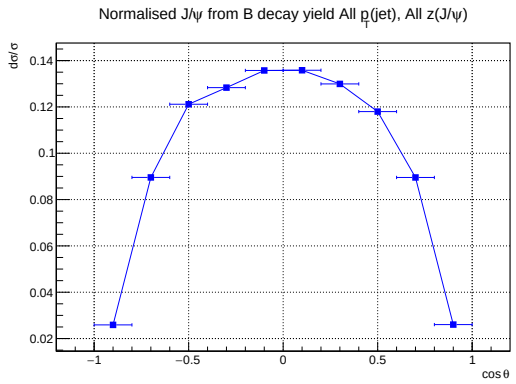

(a) Displaced component.

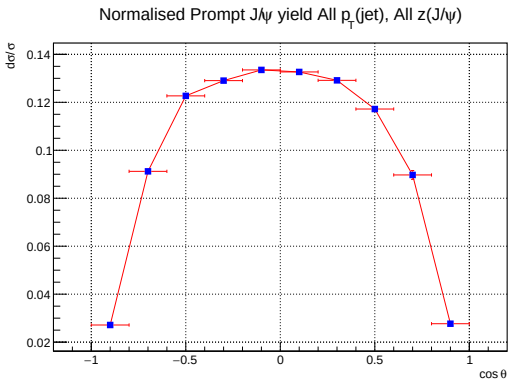

(b) Prompt component.

Figure E.13: Normalised cross section measurements *vs.* $\cos\theta$ for prompt and displaced J/ψ's using the full Turbo 2016 data set, using all $p_{\mathrm{T}}(\mathrm{jet})$ and all $z(J/\psi)$.

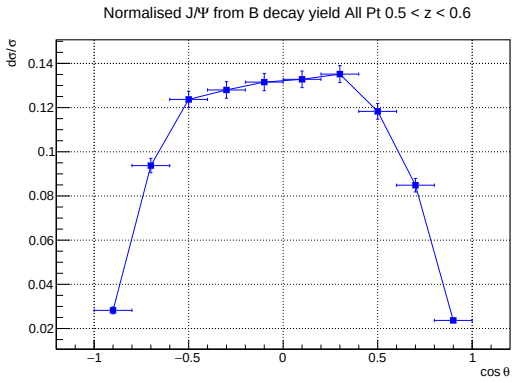

(a) Displaced component.

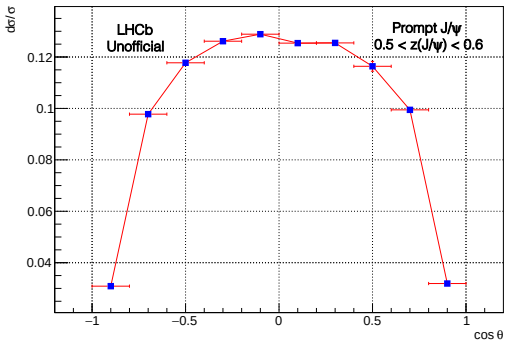

(b) Prompt component.

Figure E.14: Normalised cross section measurements *vs.* $\cos\theta$ for prompt and displaced J/ψ's using the full Turbo 2016 data set, using all $p_{\mathrm{T}}(\mathrm{jet})$ and $0.5 < z(J/\psi) < 0.6$.

E.6 Unbinned maximum likelihood method

To properly measure the three polarisation variables, an unbinned maximum likelihood method is needed to be performed. This method is more accurate to measure the polarisation, but has drawbacks when a binned unfolding procedure is needed to be performed on the jet resolution. However, the feasibility of this method has been tested. A 2D unbinned likelihood fit of variables cosθ and ϕ is performed, where the angles are defined in the helicity frame. The calculation of the likelihood is as follows,

$$\log \mathcal{L} = \alpha \sum_{i=1}^{n_{tot}} \omega_i \times \log \left[\frac{P(cos\theta_i, \phi_i | \lambda_\theta, \lambda_{\theta\phi}, \lambda_\phi)}{N(\lambda_\theta, \lambda_{\theta\phi}, \lambda_\phi)} \right] \tag{E.6}$$

where, ω_i is an s-weight to correct for the background component, and,

$$P(cos\theta, \phi|\lambda_\theta, \lambda_{\theta\phi}, \lambda_\phi) \equiv 1 + \lambda_\theta cos^2\theta + \lambda_{\theta\phi} sin2\theta cos\phi + \lambda_\phi sin^2\theta cos2\phi \tag{E.7}$$

which is the derived angular distribution equivalent to that from eq. (E.1), and,

$$N(\lambda_\theta, \lambda_{\theta\phi}, \lambda_\phi) \propto 1 + a\,\lambda_\theta + b\,\lambda_{\theta\phi} + c\,\lambda_\phi \tag{E.8}$$

which is the normalisation to correct for the fiducial requirements which is taken from MC.

This method was implemented and tested by using PYTHIA 8 simulation, generating J/ψ's which result in a λ_θ value of 0.6. The framework is validated, as the resulting measured λ_θ value with this method is also 0.6.

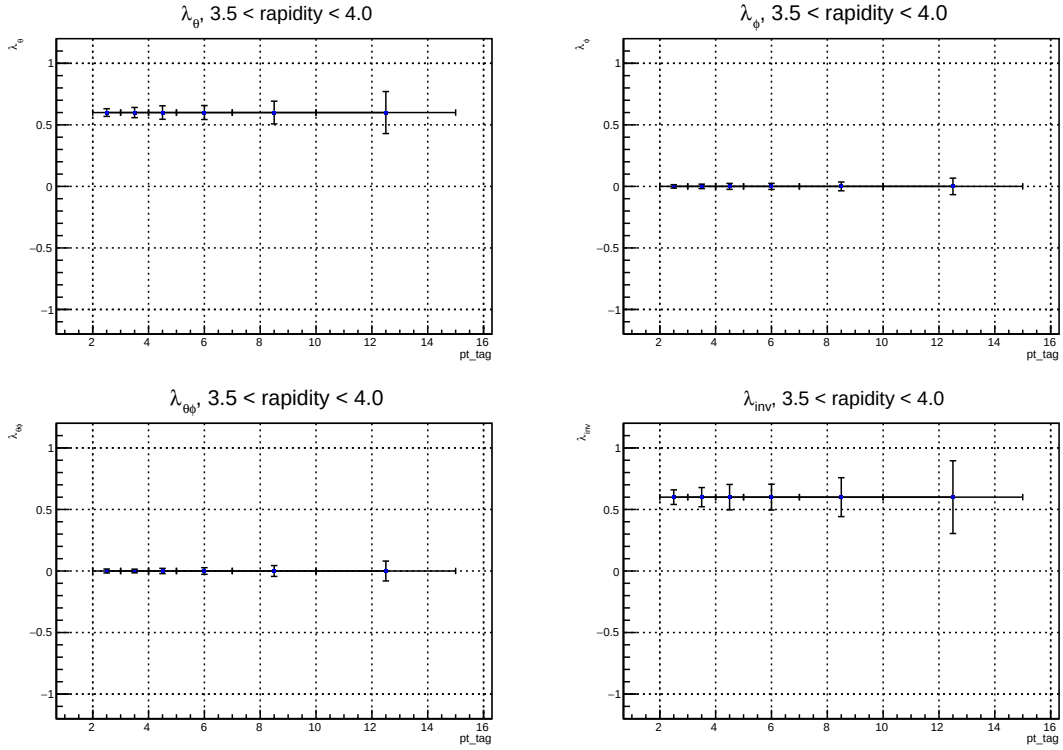

Figure E.15: Test of framework. Polarisation parameters vs. $p_{\mathrm{T}}(J/\psi)$ with an artifically reweighted PYTHIA 8 simulated mc sample with $\lambda_\theta = 0.6$. In $\mathrm{y}(J/\psi)$ range of 3.5-4.0.

This method was then implemented on the control channel, $B^+ \to J/\psi K^+$, using 2016 LHCb data, in rapidity range of $3.5 < \mathrm{y(J/}\psi) < 4.0$. This results in an output value which gives longitudinal polarisation which is expected for this decay channel. This procedure has been validated and can hence be applied to J/ψ's in jets.

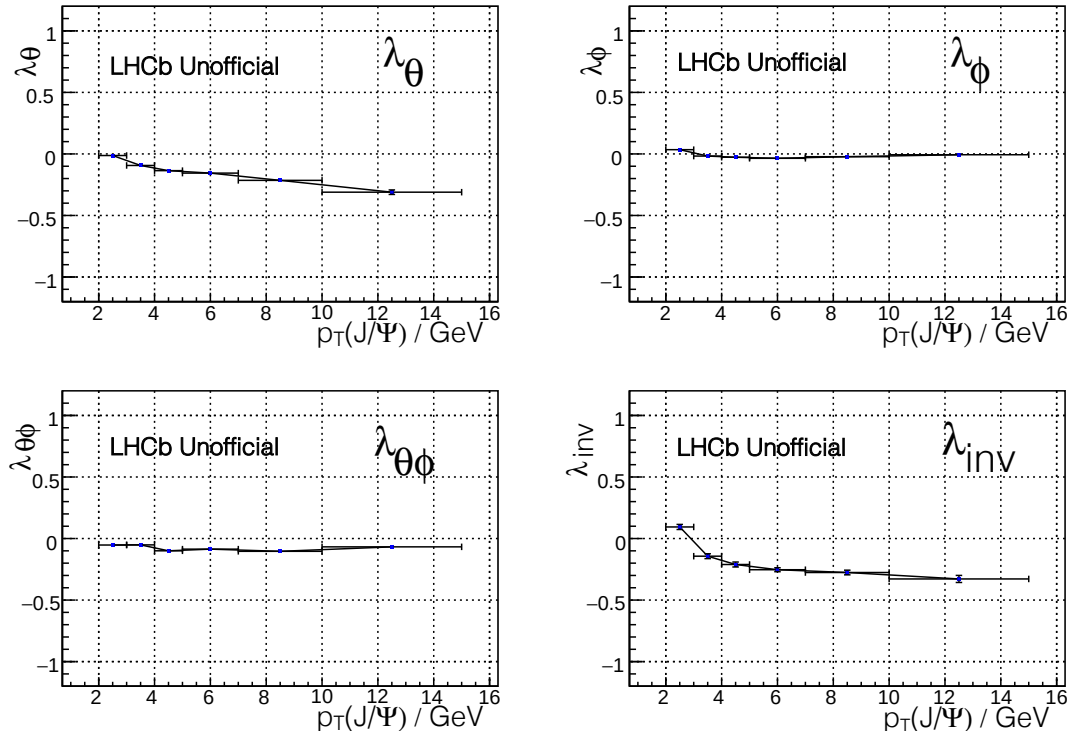

Figure E.16: Preliminary $B^+ \to J/\psi + K^+$ decay polarisation measurements with 2016 LHCb data. In rapidity(jpsi) range of 3.5-4.0.

E.7 Future prospects

There are advantages and disadvantages to both the binned and unbinned maximum likelihood method. The unbinned maximum likelihood method means all three polarisation variables can be measured simultaneously, but since the unfolding procedure needs a binned input, this has limitations. Further exploration is needed in order to encompass both techniques to produce a polarisation measurement, and also MC that more accurately describes prompt J/ψ's in jets.